THE THEORETICAL AND EXPERIMENTAL ELASTIC BEHAVIOUR OF BOX GIRDER BRIDGES

A thesis submitted for the degree of
Doctor of Philosophy
in the Faculty of Engineering of the
University of London

by

Colin John Billington, M.Sc(Eng), D.I.C., A.C.G.I.

Imperial College of Science and Technology
London
March 1974

ABSTRACT

This thesis concentrates on outstanding elastic problems in box girder bridge structures, in particular that of cross-sectional distortion and its effect on load distribution and transverse stress levels at the serviceability limit.

The beam on elastic foundation analogy for the analysis of box girders under distortional loading has been developed for straight, right supported, single cell structures by others. Additional verification in the form of comparisons with finite element and model analysis is given. The method is extended to continuous curved single cell box girders and validated by comparisons with finite element and model analysis.

A new approach, based on the combination of grillage and BEF analogy methods, is proposed to account for the effects of cross-sectional deformation in multibox structures. The approach, though approximate, is sufficiently accurate for design and results in considerable savings in computer costs. The method is shown to provide good agreement with finite element results.

The grillage-BEF method is applied to a model of a skew supported twin box structure in which distortional effects are accentuated by the skew. A study of several

3

diaphragming arrangements leads to recommendations as to the most efficient deployment of diaphragms in skew supported situations.

Extensive tests are reported on a series of small scale elastic models of bifurcated elevated highway structures with complex plan and cross sectional geometry. The three alternative forms of construction simulated are:

(i) Concrete spine box beam construction

(ii) Concrete multicellular box construction

(iii) Composite steel-concrete multibox construction.

Test results are analysed with particular attention given to the distribution of longitudinal and transverse stresses, distortion of the cross section, secondary warping, internal diaphragm behaviour and deflections. The composite multibox model provides a rigorous test for the grillage-BEF method.

Finally the results of a parametric study on the effects of distortion in steel box girders undertaken for the Merrison Committee are reported. Recommendations for design to account for such effects are included and particular attention is given to the positioning and proportioning of diaphragms.

ACKNOWLEDGEMENTS

The author wishes to express his gratitude to the following:

Dr. P.J. Dowling, who supervised this work, for all his encouragement and valuable advice throughout the project.

Dr. J.C. Chapman, now Technical Director, George Wimpey and Co. Ltd., who initiated the project and provided helpful suggestions from time to time during the course of the study.

Professor S.R. Sparkes, for the helpful way in which he accommodated the project as Head of the Engineering Structures Laboratories.

The Highway Engineering Computer Branch of the Department of the Environment for their financial support and also sponsorship of the Bifurcated Elevated Highways project. In particular Mr. F. Boeuf of HECB for his interest in the work.

The South Eastern Road Construction Unit of the Department of the Environment for their sponsorship of the work on the Merstham Interchange model.

Dr. P.T.K. Lim and Dr. K.R. Moffatt for making available their finite element system in such a helpful and

5

accommodating way and for providing some of the finite element results used for comparisons in Chapter Two.

The technical staff of the Engineering Structures Laboratory without whose experience and technical expertise the experimental content of the thesis would not have been possible. Special mention must be made in this context of Messrs. S.G. Casey, J. Davies, J. Galvin, B. Mourant and N. Smith working under the direction of Mr. J. Neale.

Mr. J. Cima for preparation of the figures, Miss J. Gurr for the photographs and Mrs. J.E. Slatford for help with some of the computation.

Finally, but in no way least, the author's wife, Pat, who so readily undertook the mammoth task of typing the manuscript and who has provided help and support in so many ways during the course of the study.

CONTENTS

	Page
ABSTRACT	2
ACKNOWLEDGEMENTS	4
CONTENTS	6
CHAPTER 1: INTRODUCTION	15
1.1 GENERAL	15
1.2 THE ELASTIC BEHAVIOUR OF THE BOX GIRDER WHEN SUBJECTED TO ECCENTRIC LOADING	18
1.3 METHODS FOR THE ANALYSIS OF BOX GIRDERS SUBJECTED TO ECCENTRIC LOADING	22
1.3.1 Single cell box girders with rigid cross section	22
1.3.2 Single cell box girders with deformable cross section	23
1.3.3 Multicell or multibox structures with rigid cross sections	26
1.3.4 Multicell or multibox structures with deformable cross sections.	27
1.4 OBJECTS OF THE THESIS	28
1.5 PRESENTATION OF THE THESIS	30
CHAPTER 2: SINGLE CELL BOX GIRDERS	32
2.1 GENERAL	32
2.2 THE BEAM ON ELASTIC FOUNDATIONS (BEF) ANALOGY	33
2.2.1 The differential equation	33
2.2.2 Calculation of stresses σ_{DB} and σ_{DW}	36
2.3 VERIFICATION OF THE BEF METHOD FOR STRAIGHT SINGLE CELL BOXES	38
2.3.1 Previous attempts at verification	38

Page

2.3.2 Additional verification of the BEF method using Finite Element analysis 40

2.3.3 Additional verification of the BEF method using model test results 41

2.3.4 Comparison of computer times for BEF and FE methods 42

2.4 EXTENSION OF THE BEF METHOD TO CURVED SINGLE CELL BOX GIRDERS 44

2.4.1 Proposed analytical method 44

2.4.2 Model tests on a curved box girder 49

2.4.3 Finite element and BEF analysis of the curved model 51

2.4.4 Comparison of BEF, FE and model test results 52

2.5 A PARAMETRIC STUDY OF THE BEHAVIOUR OF SINGLE CELL BOX GIRDERS USING THE BEF METHOD 55

2.5.1 General 55

2.5.2 Stress levels in steel and concrete boxes due to distortion 58

2.5.3 Trapezoidal boxes 59

2.5.4 Diaphragms 60

2.5.5 Effects of curvature in plan 62

2.5.6 Cross sectional properties of practical steel box girders 63

CHAPTER 3: MULTIBOX STRUCTURES 69

3.1 GENERAL 69

3.2 THE PROPOSED GRILLAGE - BEF APPROACH 71

3.3 ALTERNATIVE NON-ITERATIVE APPROXIMATE METHOD 78

CHAPTER 4: THE INFLUENCE OF SKEW SUPPORTS ON THE BEHAVIOUR OF MULTIBOX STRUCTURES 86

4.1 INTRODUCTION 86

4.2 DESCRIPTION OF THE MODEL TESTS 88

4.3 DESCRIPTION OF THE FINITE ELEMENT ANALYSIS 92

4.4 APPLICATION OF THE PROPOSED GRILLAGE-BEF METHOD 94

4.5 COMPARISON OF MODEL, FE AND GRILLAGE-BEF RESULTS 95

4.6 THE STRUCTURAL BEHAVIOUR OF THE UNDIAPHRAGMED MODEL 97

4.7 A STUDY OF VARIOUS DIAPHRAGMING ARRANGEMENTS FOR THE SKEW SUPPORTED MODEL 100

4.8 A COMPARISON OF THE SKEW STRUCTURE WITH A RIGHT SUPPORTED STRUCTURE OF EQUAL SPAN 105

CHAPTER 5: THE CONSTRUCTION, INSTRUMENTATION, AND TESTING OF THREE LINEARLY ELASTIC BIFURCATED ELEVATED HIGHWAY BOX GIRDER MODELS 107

5.1 INTRODUCTION 107

5.1.1 General 107

5.1.2 Junction layout and forms of construction 109

5.2 MODEL SCALE AND MATERIALS 111

5.2.1 Choice of materials 111

5.2.2 Model scale 111

5.2.3 Material properties 112

5.2.3.1 Araldite and sand 112

5.2.3.2 Steel 113

5.3 INSTRUMENTATION 115

5.3.1 General 115

Page

5.3.2 Deflections 115

5.3.3 Strains 116

5.3.4 Supports 118

5.3.5 Data logger 119

5.4 LOADING 121

5.4.1 Types of loading 121

5.4.1.1 Dead weight and uniformly distributed lane loading 121

5.4.1.2 HB vehicle loading 122

5.4.1.3 Knife edge loading 123

5.4.1.4 Point loading 123

5.4.1.5 Settlement of supports 123

5.4.2 Loading rig 124

5.4.3 Loading procedure 125

5.5 MODEL 1 - CONCRETE SPINE BEAM CONSTRUCTION 127

5.5.1 Manufacture of Araldite and sand components 127

5.5.2 Sequence of instrumentation and assembly 128

5.5.3 Layout of deflection gauges and support positions 129

5.5.4 Layout of strain gauge positions 130

5.6 MODEL 2 - CONCRETE MULTICELL CONSTRUCTION 132

5.6.1 Sequence of instrumentation and assembly 132

5.6.2 Layout of deflection gauges and support positions 132

5.6.3 Layout of strain gauge positions 133

Page

5.7 MODEL 4 - COMPOSITE BOX GIRDER CONSTRUCTION 135

5.7.1 Manufacture of steelwork 135

5.7.2 Sequence of instrumentation and assembly 136

5.7.3 Layout of deflection gauges and support positions 137

5.7.4 Layout of strain gauge positions 138

CHAPTER 6: RESULTS OF THE BIFURCATED ELEVATED HIGHWAY MODEL TESTS 139

6.1 GENERAL 139

6.2 ACCURACY OF RESULTS 140

6.2.1 Testing procedure and calculation of strains 140

6.2.2 Analysis of strain gauge faults and drifting 141

6.2.2.1 Analysis of strain gauge faults for Model 1 142

6.2.2.2 Analysis of strain gauge faults for Model 2 142

6.2.2.3 Analysis of strain gauge faults for Model 4 143

6.2.3 Support reaction checks 144

6.2.4 Moment equilibrium checks 144

6.2.4.1 Moment equilibrium checks for Model 1 145

6.2.4.2 Moment equilibrium checks for Model 2 145

6.2.4.3 Moment equilibrium checks for Model 4 146

6.3 PRESENTATION OF RESULTS 147

6.3.1 Plotting scales and units 147

Page

6.3.2 Description of result diagrams 148

6.3.2.1 Figures showing longitudinal stresses at extreme fibres 148

6.3.2.2 Figures showing in-plane and flexural components of longitudinal and transverse stresses 149

6.3.2.3 Figures showing principal stresses, maximum shear and the direction of the maximum principal stress, and figures showing transverse or vertical shears 149

6.3.2.4 Figures showing deflections 150

6.3.2.5 Sign convention for stress diagrams 150

6.4 RESULTS OF TESTS ON MODEL 1 - SPINE BEAM MODEL 152

6.4.1 Overall behaviour 152

6.4.2 Distribution of longitudinal stress 154

6.4.3 Transverse stresses 156

6.4.4 Shear stresses 157

6.4.5 Internal diaphragm behaviour 158

6.4.6 Principal stresses in Span BC 159

6.4.7 Deflections 160

6.4.8 Local effects due to HB loading 161

6.4.9 Knife edge and point loading test results 161

6.5 RESULTS OF TESTS ON MODEL 2 - MULTICELLULAR MODEL 163

6.5.1 Overall behaviour 163

6.5.2 Distribution of longitudinal stress 164

6.5.3 Transverse stresses 165

6.5.4 Principal stresses in Span BC 166

6.5.5 Deflections 167

6.5.6 Local effects due to HB loading 167

6.5.7 Knife edge and point loading test results 168

6.5.8 Support settlement test results 169

6.6 RESULTS OF TESTS ON MODEL 4 - COMPOSITE MULTIBOX MODEL 171

6.6.1 Overall behaviour 171

6.6.2 Warping stresses, σ_w 173

6.6.3 Effects of curvature on longitudinal stresses 175

6.6.4 Transverse stresses in the steel boxes 175

6.6.5 Transverse stresses in the deck slab 177

6.6.6 Principal stresses and transverse shears in Span BC 178

6.6.7 Deflections 179

6.6.8 Support reactions 180

6.6.9 Local effects due to HB loading 180

6.6.10 Knife edge and point loading test results 181

6.6.11 Support settlement test results 182

6.7 COMPARISON OF THE STRUCTURAL BEHAVIOUR OF THE VARIOUS FORMS OF CONSTRUCTION 184

CHAPTER 7: ANALYSIS OF THE COMPOSITE MULTIBOX BIFURCATED MODEL BY THE GRILLAGE-BEF METHOD 188

7.1 GENERAL 188

7.2 IDEALISATION OF THE STRUCTURE 189

7.3 COMPARISON OF MODEL TEST AND ANALYTICAL RESULTS 192

7.3.1 Plotting scales, units and legend 192

7.3.2 Comparison of deflections 193

7.3.3 Comparison of longitudinal stresses 193

7.3.4 Comparison of transverse distortional bending stresses 194

7.3.5 Compatibility of rotational deflections 195

CHAPTER 8: CONCLUSIONS AND METHODS FOR DESIGN 197

8.1 CONCLUSIONS 197

8.1.1 General conclusions 197

8.1.2 Particular conclusions relating to the distortional behaviour of straight single cell box girders 200

8.1.3 Particular conclusions relating to box girders curved in plan 202

8.1.4 Particular conclusions relating to the proposed analysis method for multibox structures 204

8.1.5 Particular conclusions relating to skew supported multibox structures 205

8.1.6 Particular conclusions relating to the behaviour of the Bifurcated Elevated Highways models. 207

8.2 DESIGN METHODS 211

8.3 FUTURE WORK 214

REFERENCES 217

APPENDIX A: DERIVATION OF THE GOVERNING DIFFERENTIAL EQUATION 226

APPENDIX B: DERIVATION OF BEF PROPERTIES 229

B1 RESISTANCE OF CROSS SECTION TO DEFORMATION 229

Page

B2 PROPERTIES OF DIAPHRAGMS 235

B2.1 Diagonal cross bracing 235

B2.2 Vee-type bracing 237

B2.3 Inverted vee-type bracing 239

B2.4 Ring stiffening 240

B2.5 Plate diaphragms 241

B3 WARPING STIFFNESS 243

B4 CALCULATION OF DISTORTIONAL SHEAR STRESSES AND DIAPHRAGM FORCES 245

B4.1 Distortional shear stresses 245

B4.2 Diaphragm forces 247

APPENDIX C: SETTING OUT DETAILS FOR BIFURCATED ELEVATED HIGHWAY MODEL 4 AND LOCATION OF INSTRUMENTATION SECTIONS ON THE MODELS 257

C1 SETTING OUT DETAILS FOR MODEL 4 257

C2 LOCATION OF INSTRUMENTATION SECTIONS 259

C2.1 Model 1 259

C2.2 Model 2 259

C2.3 Model 4 260

APPENDIX D: A DESIGN APPROACH FOR DISTORTION AND THE BASIS FOR INTERIM DESIGN RULES CLAUSES 6.3.4 AND 6.3.5 261

D1 DESIGN APPROACH 261

D2 BASIS FOR CLAUSES 6.3.4 AND 6.3.5 265

TABLES 275

FIGURES 294

NOTATION 525

CHAPTER 1: INTRODUCTION

1.1 GENERAL

It has been estimated[1] that £1,000m will be spent on the construction of elevated highways during the present decade, a large proportion of the structures being built in urban areas. The general requirements for elevated highway structures in urban areas are as follows:

(i) Flexibility in the positioning of supports,

(ii) Adaptability to changes in plan geometry to cope with small radius curves, bifurcations, carriageway widening, intersections, etc.,

(iii) Speed of erection,

(iv) Aesthetic acceptability,

(v) Shallow depth of construction, especially at multilevel interchanges,

(vi) Adaptability to modification as traffic densities change,

(vii) Ease of maintenance,

(viii) Economy.

The structural form which is best suited to meet these requirements is the box girder, the advantages of which stem from the high torsional stiffness of the closed section. This ensures good transverse distribution of eccentric forces (from both superimposed loading and irregularly positioned support reactions) such that efficient use is

16

made of the complete cross section with consequential savings in materials, and reduced depth of construction. Torsional forces may be carried by the boxes over several spans with simplified intermediate piers carrying only axial forces, and the box girder is ideally suited for situations in which additional torsional forces occur due to curvature in plan, bifurcations and intersections. The box's clean lines satisfy aesthetic criteria and make for ease of maintenance, and steel boxes in particular are suited to cases where speed of erection is essential.

Although the recent failures of steel boxes (Danube 1969, Milford Haven and Lower Yarra 1970, and Koblenz 1971) have highlighted the need for a greater understanding of tne non-linear behaviour of plate components of the box particularly under erection conditions, the large number of box girder structures currently in the design stage and under construction confirms the continuing popularity of this form of construction for medium and long span bridges.

The global analysis of box girders is at present accomplished on the basis of elastic theory and then, in the case of a steel box, plate panels and stiffening are proportioned to preclude instability. Global ultimate load analysis methods nave not been developed because the performance of the present generation of computers is such that the costs of these analyses would be prohibitive. Even when the development ot computer hardware makes ultimate load analysis possible, elastic methods will still be necessary for consideration of the various unserviceability limit states of stress, fatigue, crack widths,

vibration and deflection. This thesis concentrates on outstanding linear elastic problems which have immediate relevance to design with special attention given to those aspects of the behaviour peculiar to box sections, and particularly the effects of deformation of the cross section and their influence on load distribution.

Before discussing the programme of research in detail it is necessary to give a brief description of the elastic structural response of the box girder to arbitrary loading (Section 1.2) and also to review the various available analytical techniques (Section 1.3).

18

1.2 THE ELASTIC STRUCTURAL BEHAVIOUR OF BOX GIRDERS SUBJECTED TO ECCENTRIC LOADING

Loads applied to the bridge deck are transferred to the webs of the box girder by flexure. This flexure of the deck induces transverse bending stresses in the walls of the box girder but, provided these stresses are accounted for in the final analysis of the transverse bending effects, loads applied to the deck may be replaced by forces at the intersection of deck and web.

Consider a box of square cross section and uniform wall thickness, simply supported, and loaded eccentrically over one web by a point load at midspan. The eccentric load may be separated into three components (Figure 1) which are referred to as the bending, torsional and distortional components. Each of these components may be assumed to cause only the phenomenon suggested by its title and is treated independently. This assumption is not strictly correct for the majority of sections as there is some interaction between the torsional and distortional components of loading as will be described later. However, the effects of this interaction are small and have been shown to be negligible for the practical range of medium span bridge structures.[2,3].

The bending component of the loading produces bending moments and shears which may be treated by simple bending theory.

The torsional component of loading produces shears which twist the box. If the deformations due to twisting and shearing of the individual plates are not compatible with a rigid body rotation of the cross section, rigid body rotations of the individual plates in their own planes are required to satisfy compatibility of displacements at the box corners (Figure 2). These rigid body rotations of the plates result in longitudinal warping displacements and, where restraint of warping occurs, for example at positions of applied loading or diaphragms with high out-of-plane stiffness, longitudinal restrained warping stresses, σ_{TW}, result (Figure 3). For certain sections where the product of the wall thickness at any point and the perpendicular from the centre of rotation to the tangent at that point is constant at every point on the box wall, rigid body rotations of the plates are not necessary to provide compatibility of corner displacements and warping does not take place. These sections are described as 'warpless' sections and one such example is the square box with uniform wall thickness. Warping stresses are self equilibrating and therefore subject to the Principle of St. Venant which states that the strains which are produced in a body by the application to a small part of its surface of a system of forces statically equivalent to zero force and zero couple are of negligible magnitude at distances which are large

20

compared with the linear dimensions of the part. Where the magnitudes of warping stresses are changing in the longitudinal directions, in-plane shears are produced in the box walls which are also self equilibrating and of a distortional form. These second order shears produce the interaction of the torsional and distortional components of loading referred to above.

The distortional component of loading shown in Figure 1.1 may be replaced by forces acting at the box corners and the resultants of these forces act along the diagonals of the box producing racking of the cross section (Figure 4). Transverse bending moments are produced by the frame action of the box and transverse distortional bending stresses, σ_{DB}, result (Figure 5). Where the degree of distortion changes along the length of the box due to variations in distortional loading, in-plane bending of the walls takes place in such a way as to cause warping of the cross section and longitudinal distortional warping stresses, σ_{DW}, (Figure 5). Distortional in-plane shears are associated with changes of distortional warping stresses in the longitudinal direction. Distortional warping stresses may occur in boxes of any cross sectional dimensions including the torsional 'warpless' sections described above.

The components of eccentric vertical loading on rectangular and trapezoidal boxes are shown in Figure 6

together with the equivalent distortional loading for horizontally applied eccentric loading.

22

1.3 METHODS FOR THE ANALYSIS OF BOX GIRDERS SUBJECTED TO ECCENTRIC LOADING

Box girder bridge structures can be divided into four main types:

(i) Single cell boxes with rigid cross-section,

(ii) Single cell boxes with deformable cross-section,

(iii) Multicell or multibox structures with rigid cross-section,

(iv) Multicell or multibox structures with deformable cross-section.

The term 'multicell' is used to describe cross sections having several cells connected by continuous top and bottom flanges, and 'multibox' is used to describe cross sections having several separate cells connected by a continuous top flange only.

1.3.1 Single cell box girders with rigid cross-section

Maisel[4] lists 299 publications related to the analysis and design of thin-walled beams. Of these, 63 consider the elastic analysis of thin-walled beams of rigid cross-section, including the effects of torsion and restrained warping, and the analysis of such beams has been adequately summarized by Kolbrunner and Basler[5].

Providing the interaction between the torsional and distortional components of the loading can be neglected,

analysis methods for box girders of rigid cross-section may also be used to calculate the response of box girders of deformable cross-section to the torsional component of the loading.

1.3.2. Single cell box girders with deformable cross-section

Much literature in the field of aircraft structures is devoted to the problem of distortion of the cross section. Richmond[6] has devloped the early work of Reissner[7] and Ebner[8] in a form suitable for rectangular bridge structures. The box is represented by four longtudinal booms and four walls. It is assumed that the booms carry longitudinal bending forces only and the walls carry only shearing forces. The frame stiffness of the box is neglected and distortional loading is resisted only by diaphragms. An expression relating the internal forces in a cell to the displacements at the end of the cell is derived. By ensuring equilibrium at diaphragms an expression relating external loads (applied only at diaphragm positions) to the internal forces is found. These two steps are repeated for each cell and diaphragm respectively and together give a set of linear simultaneous equations which can be solved for the displacements. Dalton and Richmond[9] have extended this approach to trapezoidal boxes and Kuhn[10] describes a flexibility

24

solution for a similar idealisation. Moya[11] develops the displacement solution for curved single cell box girders.

Vlasov[12] draws the analogy between the differential equation describing the response of a box girder to the distortional component of the loading and that of the beam on elastic foundation (BEF). Wright, Abdel-Samad and Robinson[13] develop the analogy for single cell box girders with longitudinally and transversely stiffened plates. This method considers both the distortional stiffness of the box walls and that of intermediate diaphragms or cross bracing. Non-dimensional curves are presented which provide the maximum distortional stresses for boxes with regularly spaced interior diaphragms subjected to concentrated loading at mid-panel. The author has presented similar curves for uniformly distributed loading[14] which are more relevant to British Standard Highway loading[15].

Richmond[16] has derived the more general differential equation for the box girder subjected to both torsional and distortional components of loading and he describes its solution for simplified boundary conditions and loading. Dabrowski[17] presents a differential equation for a box girder curved in plan subjected to distortional loading which includes additional terms due to distortional forces caused by longitudinal bending moments.

Folded plate analysis has been developed by Scordelis for box girder bridges[18]. The method is restricted to structures simply supported at their extreme ends with plates of constant thickness and boxes of constant cross sectional dimensions. In certain cases difficulty can be experienced with concentrated loading conditions because of the poor convergence of the harmonic series used in the analysis.

The most general analysis method available to the engineer is the finite element (FE) method[19]. Special features encountered in practical box girders such as varying cross sectional properties, longitudinal and transverse stiffening, random spacing of diaphragming and supports and complicated loading combinations may all be accounted for. The development of new elements specifically for box girder analysis[20,21,22] has led to a reduction in the number of elements necessary to accurately describe the structure with consequent savings in data preparation and computer costs. However, the high computer costs involved with the use of large finite element systems has, in general, restricted their use to the more complicated structure. Various hybrid methods such as the finite segment method[18] and the finite strip method[23] have been developed in an attempt to reduce computational costs but this is only achieved with a sacrifice in generality.

26

1.3.3 Multicell and multibox structures with rigid cross sections

A number of the publications reviewed by Maisel[4] consider the torsion of multicell structures with rigid cross section. The work of Benscoter[24] deserves particular mention for the approximate solution given for non-uniform multicell boxes with arbitrary cross-sectional shape, loading and end conditions. The solution is in a form particularly suitable for design.

Grillage programs are extensively used by designers for the analysis of multibox systems assuming the box girders themselves have rigid cross sections. Sawko and Mosley[25] describe various grillage idealisations which replace the longitudinal boxes by either one member on the centre line or two members along the web lines. Stiff stub members may be used in the transverse direction across the width of the box so that the slab between boxes is of the correct stiffness and span.

Tung[26] proposes a method for the analysis of curved twin box girder bridges with boxes of rigid cross section. The solution is given in terms of Fourier series and a simplified solution is also provided for straight bridges

Hayward[27] has produced curves which enable the load distribution in straight twin box structures to be determined and comparisons with grillage results show good agreement.

1.3.4 Multicell or multibox structures with deformable cross sections

Several of the more general methods described in Section 1.3.2. for single cell box girders are also applicable to multicell and multibox bridges with deformable cross sections. The finite element method has been extensively used for the analysis of multicell structures[28-31] and the method has been applied to several multibox bridges at Imperial College[3,32,33] using the Imperial College Structural Analysis System (ICSAS)[34].

Few publications refer specifically to the problem of distortion of the cross section in multicell and multibox girders. Dalton and Richmond[9] have analysed a twin cell box using their displacement solution. Wright[35] proposes a simple distribution method for both multicell and multibox sections such that the distortional loading is found for each cell which is then treated independently using the BEF method for single cell boxes. This procedure has been shown to lead to very conservative results in some cases.

Mattock[36] examined the distortional stresses in a range of unstiffened, open-topped, composite multibox bridges using folded plate analysis. The results of this analysis were used to formulate a conservative design specification[37] which precludes the need for calculation of distortional stresses in certain ranges of cross sectional geometry.

28

1.4 OBJECTS OF THE THESIS

The effects of distortion of the cross section in box girders subjected to eccentric loading have been described in Section 1.2. The use of numerical techniques such as finite element and folded plate computer programs has made possible the accurate assessment of such effects. However, these methods are generally expensive and can be used indiscriminately without a physical understanding of the structural action. In such cases the analyst may not recognise the significant values in the mass of computer output. Therefore, a need exists for simple analysis methods in which the effects on the distortional behaviour of altering the various parameters are immediately obvious.

The analysis methods described in Section 1.3 have varying degrees of verification and claimed applicability. What little published experimental data there is mainly describes ad hoc testing undertaken to assess the adequacy of specific designs and is of limited use for comparison with analytical techniques.

The research described in this thesis was undertaken to fulfil the need for additional theoretical and experimental information about the elastic behaviour of elevated highway box girder structures. The general objectives of the research were therefore:

1. To develop an approximate analysis method for box girder structures with the generality necessary to cope with the complex geometry of modern elevated highways while retaining a degree of accuracy sufficient for design.
2. To provide comprehensive experimental data against which the approximate approach derived within this thesis and any other existing or future elastic analysis methods could be checked and also to elucidate aspects of the behaviour not directly apparent from current theoretical treatments.
3. To examine the elastic behaviour of box girder structures, in particular the effects of deformation of the cross section in multibox structures, and provide guidance on the design of box girders to account for such effects.

30

1.5 PRESENTATION OF THE THESIS

In Chapter 2 the BEF method for straight single cell boxes is reviewed. Additional verification is given and the method is extended to continuous curved girders. A parametric study of single cell box girders is presented.

The BEF method together with the use of grillage programs forms the basis of a simplified method for the analysis of multibox systems. The method is presented and compared with finite element analyses of a range of practical bridge structures in Chapter 3.

The problem of cross-sectional distortion is magnified in skew box structures. Chapter 4 describes the application of the BEF-grillage method to a skew supported twin box structure and compares the analysis with finite element and model test results. A study is made to determine the most efficient diaphragming arrangements for skew situations.

Chapter 5 describes an extensive series of tests on models of elevated highways of complex geometry. One of the models simulates composite multibox construction and provides a rigorous test for the method proposed in Chapter 3.

The three models simulate various forms of box girder construction as follows:

(i) Concrete spine beam construction,

(ii) Concrete multicellular construction,

(iii) Composite multibox construction.

The elastic behaviour of these models is discussed in Chapter 6.

The concluding chapter includes a section describing recommendations for design to account for distortion of the

cross section with particular reference to the code of practice used in the United States[37] and also the new British Interim Design Rules[38].

32

CHAPTER 2: SINGLE CELL BOX GIRDERS

2.1 GENERAL

The BEF analogy proposed by Wright et al[13] is reviewed in Section 2.2 and additional formulae are derived for Vee and inverted Vee type bracing. Further validation for the method in its application to single cell boxes is provided in Section 2.3 by comparison with model test results and finite element analyses.

Dabrowski's work on simply supported curved girders[17] is used as a basis for extending Wright's formulation of the BEF analogy to account for the behaviour of continuous curved girders in Section 2.4.

In Section 2.5 the BEF method is used to study the effects of altering the various distortional parameters on the behaviour of a wide range of practical single cell steel and concrete box girders.

2.2 THE BEAM ON ELASTIC FOUNDATIONS (BEF) ANALOGY

2.2.1 The Differential Equation

The differential equation describing the response of a box girder of deformable cross section to the distortional component of loading is

$$EI_w \frac{\partial^4 W}{\partial x^4} + KW = p(x) \quad \ldots\ldots\ldots\ldots\ldots\ldots\ldots\ldots (2.1)$$

where E is Young's modulus

I_w is a cross sectional property related to warping

W is the measure of distortion shown in Figure 5

K is the distortional stiffness of the box

p is the applied distortional loading.

The derivation of this equation and the assumptions necessary to the derivation are given in Appendix A.

The differential equation describing the deflection W of a beam of inertia I_b on a Winkler type elastic foundation (in which the reaction forces of the foundation are proportional at every point to the deflection of the beam at that point) of foundation modulus k loaded by distributed loading is

$$EI_b \frac{\partial^4 W}{\partial x^4} + kW = p(x) \quad \ldots\ldots\ldots\ldots\ldots\ldots\ldots\ldots (2.2)$$

34

The similarity of this equation to Equation 2.1 is evident and a direct analogy exists between the physical properties of the box and those of the BEF.

For convenience in treating standard bridge loading which is normally vertical Wright et al[13] developed the analogy with reference to the antisymmetrical component of the loading shown in Figure 1, but only the response to the distortional component of this loading is considered in the analysis. Also the differential equation is expressed in terms of a vertical deflection W at the top of the box web. This deflection is not strictly vertical but is directly proportional to the change in length of the diagonal of the box. The direction of W is influenced by the way in which the box is supported and the flexibility of support diaphragms. It is possible to envisage a situation where the distortion takes place only in the horizontal direction (for instance at the support section of a box with no support diaphragm), and perhaps a more concise treatment would have been to derive the differential equation in terms of the basic distortional deflection (the change in length of the diagonal) with respect to the distortional component of the loading. However for the sake of consistency Wright's formulation will be adhered to in this thesis.

The physical analogy between the box girder and the

BEF is summarised in Figure 7. The BEF deflection is proportional to the distortional deflection of the box cell and hence to σ_{DB}; the BEF bending moment is proportional to the box warping moment and hence σ_{DW}. Concentrated loads on the BEF correspond to concentrated antisymmetrical loads on the box and distributed BEF loading corresponds to distributed antisymmetrical loading on the box. The distortional or frame stiffness K of the box is analogous to the foundation modulus k of the BEF and the warping property I_w is analogous to the BEF inertia I_b. Diaphragms or cross bracing are analogous to point supports to the BEF. Diaphragms rigid in shear but free to warp correspond to pinned supports, diaphragms rigid in shear and warping correspond to encastre supports, diaphragms flexible in shear and free to warp correspond to vertical elastic supports and diaphragms flexible in shear and warping correspond to both vertical and rotational elastic supports.

Equations for distortional and warping stiffnesses are presented in Reference 13 together with diaphragm and bracing stiffnesses and the derivation of these is presented in Appendix B. Additional stiffness equations for V and inverted V type bracing are also derived in Appendix B. The formulae for diaphragm stiffnesses are summarised in Table 1.

36

Having calculated the properties of the analogous BEF, solution is required for Equation 2.2. Hetenyi[39] describes the solution for a range of cases. Solutions to more difficult problems such as beams with irregularly spaced diaphragms, changes in section, or complex loading, may be obtained by numerical procedures such as finite difference or finite element methods. These solution methods are well established and therefore it is unnecessary to give detailed descriptions in this thesis.

2.2.2 Calculation of stresses σ_{DB} and σ_{DW}

The BEF solution is obtained in terms of deflections and moments. The relationships between these quantities and σ_{DB} and σ_{DW} are given by the following expressions

$$\sigma_{DB} = KF_dW \qquad (2.3)$$

where K is the distortional stiffness

W is the BEF deflection

$F_d = \frac{b_B V}{2S}$ at the bottom of the box

or $F_d = \frac{b_T}{2S}\left[\frac{b_B}{b_T + b_B} - V\right]$ at the top of the box

where S is the relevant section modulus of the plate in question per unit length

b_T, b_B are top and bottom widths of box between web centrelines.

and V is the redundant out of plane shear force on the centre line of the bottom flange in a frame consisting of unit length of box subjected to unit distributed distortional loading (see Appendix B)

$$\sigma_{DW} = \frac{b_B \psi_b M}{2I_b} \quad \ldots\ldots\ldots\ldots\ldots\ldots\ldots\ldots\ldots\ldots (2.4)$$

where I_b is the BEF inertia

M is the BEF moment

ψ_b is a displacement coefficient for the bottom flange plate (see Appendix B)

σ_{DW} is the warping stress at the intersection of bottom flange and web.

σ_{DW} at the intersection of top flange and web is calculated from the value given above by the requirement that the warping stresses at a section are self equilibriating.

Distortional shear stresses and diaphragm forces may also be obtained from the BEF results and their calculation is described in Appendix B.

38

2.3 VERIFICATION OF THE BEF METHOD FOR STRAIGHT SINGLE CELL BOXES

2.3.1. Previous attempts at verification

Wright et al[13] present a comparison of the BEF method with a more refined procedure based on thin walled beam theory described in Reference 40. Four cross sections are considered, two of which are rectangular steel boxes with orthotropic decks, one with transversely stiffened plates, the other two being trapezoidal steel boxes with composite decks, one with transversely stiffened plates. Agreement for distortional warping stresses σ_{DW} is good but agreement for transverse distortional bending stresses σ_{DB} is less good, particularly for the stiffened boxes. However the application of the method may be criticised because of the use of an approximate value of the warping term I_b and also because transverse stiffeners on the box flanges are offset from those on the webs. In such cases a reduced frame stiffness should be used calculated for a section of the box with transverse stiffeners on opposite walls acting with an effective width of plate on adjacent walls as described in Reference 14.

The BEF method is also compared with a test on a model rectangular plexiglass box girder by Myers[41]. While qualitative agreement is obtained quantitative

agreement is not good. However this may be explained by one or more of the following deficiencies in Myers' experimental technique and application of the BEF method:

(i) Plexiglass is a material which creeps at constant load throughout the elastic range and is sensitive to small temperature changes. Although attempts were made to compensate for these effects the non-linearity of certain of the measurements suggests that the attempts were not always successful.

(ii) The top flange of the model was joined to the webs by screws at 4 inch centres. While these screws may be adequate to transfer in-plane shears it cannot be assumed that there is a continuous moment connection along the top edges of the webs.

(iii) Stresses were calculated from uniaxial strain gauge measurements. Stresses σ_x and σ_y on the surface of a plate subjected to applied forces in several directions should be calculated from orthogonal strain readings ε_x and ε_y according to the relationships:

$$\sigma_x = \frac{E}{(1-\nu^2)} (\varepsilon_x + \nu\varepsilon_y)$$

$$\sigma_y = \frac{E}{(1-\nu^2)} (\varepsilon_y + \nu\varepsilon_x)$$

where E is Young's Modulus

ν is Poisson's Ratio

40

(iv) BEF stresses are calculated for a panel adjacent to the model supports from Wright's curves for panels near midspan and therefore underestimate the model stresses.

In 1963 Florin[42] published a comparison of two theoretical analyses and test results on a rectangular plastic model box girder. The results from the theoretical analyses (due to Vlasov and Bjorklund) differed by only a few per cent, the differences being due to an allowance for shear deformation by Vlasov. Although not expressed in terms of the BEF analogy, the theories were based on the same differential equation. Florin found that the theoretical distortional displacements and transverse bending stresses agreed with the experimental results to within 15%. However the theoretical longitudinal distortional warping stresses were only about half the measured model stresses. This was probably due to the Poisson effect of the transverse strains being neglected in the longitudinal stress calculation.

2.3.2. Additional verification for the BEF method using Finite Element analysis

None of the foregoing comparisons are conclusive and therefore it was decided to carry out the following additional verifications. BEF results are compared with

those from finite element extensional flexural solutions of two examples using an element specially developed for box girder analysis[20]. The examples chosen are a 144 ft span, 6 ft square concrete box with 12 inch wall thickness (Example 1) and a trapezoidal stiffened steel box with the dimensions shown in Figure 8 (Example 2). Figure 9 shows longitudinal distributions of σ_{DB} and σ_{DW} for the concrete box (Example 1) and agreement is seen to be excellent. The results are presented in a non-dimensional form by dividing the actual stress under the load by the maximum possible bending stress under the same load calculated on the basis of simple bending theory.

Example 2 was analysed as part of a parametric study undertaken for the Merrison Committee[43]. Two loading conditions were considered - a concentrated load at midspan, and a uniformly distributed load. The finite element mesh used is shown in Figure 10 and the results of the analyses are shown non dimensionally in Figures 11-14. Again agreement is seen to be good.

2.3.3 Additional verification for the BEF method using model test results

A further comparison was made with the results of elastic tests on Box 7 of the series of ¼ scale steel box girders tested at Imperial College for the Merrison Committee.

42

The tests are fully reported by Frieze and Dowling[44]. Dimensions of the model are shown in Figures 15-17. Longitudinal strains measured during the elastic tests were generally very low and of the same order as errors induced by the electronic strain reading equipment and the stresses calculated from these strains were therefore unreliable. Significant transverse strains occurred in the transverse stiffeners, however, and the corresponding stresses have been used for the comparison with the BEF method. Transverse stresses in the end frame (Section C) were not considered because of the difficulty of assessing the section moduli of stiffener and plate at the end of the box. Results plotted for jack loads of 6 tons in Figures 18 and 19 show both model and BEF transverse stresses in plate and stiffeners for intermediate ring stiffeners at Sections B and E. BEF stresses generally underestimate stresses in the stiffeners but agreement is obtained for plate stresses. Model test results do not reflect the symmetry of the section but average values give reasonable agreement with the BEF predictions.

2.3.4. Comparison of computer times for BEF and FE methods

The above analytical and experimental comparisons provide more convincing verification for the BEF method. The usefulness of the BEF method is emphasized by the

following figures which show a comparison of computer time, storage and data preparation time for BEF and FE analyses of Example 2.

Analysis method	Computer time (seconds)	Computer storage	Approx. data preparation time
BEF	0.9	6K	5 mins
FE	400	60K	1 hour

The BEF program used (Program BEF6) was written to facilitate the research described in this thesis and computer times and storages are quoted for programs run on the London University CDC 6600 computer.

44

2.4 EXTENSION OF THE BEF METHOD TO CURVED SINGLE CELL BOX GIRDERS

2.4.1 Proposed analytical method

Additional distortional forces occur in box girders curved in plan due to the radial component of the longitudinal bending stresses. If it may be assumed that the cross-sectional dimensions are small in relation to the radius of curvature, the radial component, σ_R, of the longitudinal bending stress, σ_B, for unit length of the box is given by

$$\sigma_R = \frac{\sigma_B}{r} \qquad \text{.....(2.5)}$$

where r is the radius of curvature (see Figure 20).

Consider a unit length of a trapezoidal curved box girder (Figure 21). The total radial forces S_T and S_B in the top and bottom flanges respectively are given by

$$S_T = \frac{M_x . t_T (b_T + 2b_p) \bar{y}_T}{I_x . r} \qquad \text{.....(2.6)}$$

$$S_B = \frac{M_x . t_B . b_B \bar{y}_B}{I_x . r}$$

where M_x is the longitudinal bending moment

t_T, t_B are top and bottom flange thicknesses

$\bar{y}_T$, $\bar{y}_B$ are distances from the neutral axis of bending to the centroids of top and bottom flanges

I_x is the cross sectional inertia about the horizontal centroidal axis.

The radial stress σ_{RW} at a point in the web a distance $\bar{y}$ from the neutral axis is given by

$$\sigma_{RW} = \frac{M_x.\bar{y}}{I_x.r} \qquad \text{.....} \qquad (2.7)$$

The system of radial forces shown in Figure 21 can be replaced by a horizontal force acting through the shear centre and a pair of antisymmetrical horizontal forces (P_1) acting at the box corners producing a torque (see Figure 6b). The contributions to P_1 by the flanges are given by

$$P_{1T} = \frac{S_T y_s}{h} \quad \text{for the top flange}$$

$$P_{1B} = \frac{S_B (h-y_s)}{h} \quad \text{for the bottom flange} \qquad \text{.....} (2.8)$$

and for each web

$$P_{1W} = \int_o^{y_s} \sigma_{RWT} \frac{ct_w}{h} \left(1-\frac{y}{\bar{y}}\right)(y_s-y)dy +$$

$$\int_o^{h-y_s} \sigma_{RWB} \frac{ct_w}{h} \left(1-\frac{y}{h-\bar{y}}\right)(h-y_s-y)ds \quad \text{....} (2.9)$$

46

where σ_{RWT}, σ_{RWB} are the radial stresses at top and bottom of web

$$P_{lW} = \frac{\sigma_{RWT} c t_w y_s^2}{2h^2}\left[1-\frac{y_s}{3\bar{y}}\right] + \frac{\sigma_{RWB} c t_w (h-y_s)^2}{2h^2}\left[1-\frac{(h-y_s)}{3(h-\bar{y})}\right] \quad \ldots\ldots (2.10)$$

The equivalent vertical antisymmetrical loading P for a horizontal antisymmetrical load P_l is given by

$$P = \frac{P_l h}{b_T} \quad \ldots\ldots (2.11)$$

(see Figure 6c).

Therefore substituting for S_T etc. in the above expressions, the total equivalent vertical antisymmetrical load P for the radial component of the longitudinal bending stresses is given by

$$P = \frac{Mx}{I_x . r . b_T}\left\{t_T(b_T+2b_P)\bar{y}\, y_s + t_B b_B (h-\bar{y})(h-y_s) + \frac{t_w c}{h}\bar{y}\, y_s^2\left[1-\frac{y_s}{3\bar{y}}\right] + \frac{t_w c}{h}(h-\bar{y})(h-y_s)^2\left[1-\frac{(h-y_s)}{3(h-\bar{y})}\right]\right\} \quad \ldots\ldots (2.12)$$

The longitudinal bending moments in simply supported box girders are statically determinate and are therefore independent of the torsional moments. The total distortional stresses are obtained from a BEF analysis of the equivalent

straight box girder with a span equal to the developed length of the centre line of the curved box. The BEF loading is treated as sum of the antisymmetrical component of the loading and the antisymmetrical component of the radial forces given by Equation 2.12.

The distribution of bending and torsional moments in continuous curved girders and single span curved girders with indeterminate supports may be determined, for boxes with non-deformable cross sections, with the use of grillage analysis programs. Such programs are generally available to the designer and are used for the analysis of a wide range of bridge structures. The curved box is represented by a series of single members along its centre line to which bending and twisting loads are applied. However, if deformation of the cross section is permitted, the interaction between the bending and torsional moments is influenced by the distortional deflections. The distortional deflections can be thought of as rotations of the flanges which are additive to the torsional rotations. An increase in rotation is equivalent to a decrease in torsional stiffness and the influence of distortion is to reduce the effective torsional rigidity of the cross sections. Therefore the effects of distortion can be allowed for in the grillage analysis by reducing the torsional stiffness property of the longitudinal members.

48

An iterative procedure leads to the final solution which is obtained when a compatibility condition is satisfied. The compatability criterion is that the torsional rotations (θ_G) given by the final grillage analysis should be equal to the sum of the distortional rotations (θ_D) given by the BEF analysis of the equivalent straight girder, and the torsional rotations (θ_T) obtained from the application of the torsional moments given by the final grillage analysis to the girder having its full torsional stiffness. The criterion is expressed by the following equation

$$\theta_G = \theta_D + \theta_T \quad \text{.....(2.13)}$$

Successive reductions of the torsional stiffness are made on the basis of a comparison of rotations until Equation 2.13 is satisfied. It is shown in Chapter 3 where a similar procedure is proposed for multibox systems that the magnitude of torsional moments given by the grillage analysis is not sensitive to small changes in torsional stiffness. A study of a large number of practical steel box girder bridges shows that in many cases no reduction is necessary to obtain accuracy sufficient for design, and that in such cases an overestimate is made of torsional moments and hence distortional stresses. This is because the box having a higher torsional stiffness in relation to bending stiffness attracts greater torsional moments.

2.4.2 Model tests on a curved box girder

The method outlined in 2.4.1 is compared in 2.4.4 with the results of the tests described in this section and FE results described in 2.4.3.

The dimensions of the model are given in Figure 22 and a general view of the model is shown in Figure 23. The loading and support arrangement (Figure 24) is such that the model simulates a semicircular girder with encastre supports. The model material is an Araldite 219 casting resin and sand mixture which was developed at Imperial College to produce elastic models of concrete structures. This material has several advantages over other commonly used model materials such as perspex or other plastics viz:

(i) The Araldite casting resin is available in liquid form.

(ii) It has a reasonable pot life (up to 24 hours).

(iii) Both mixing of Araldite ingredients and casting can be carried out at room temperature.

(iv) It can be both hot and cold cured.

(v) The curing rate can be controlled.

(vi) Shrinkage both during and after curing is outstandingly low and the cured products are dimensionally very accurate.

(vii) It is less sensitive to small changes in ambient temperature

50

(viii) The creep rate is very low - virtually no creep at working strains.

(ix) It can be readily cast to complex shapes.

(x) Its elastic properties are similar to those of concrete (Young's Modulus of 1.4 - 2 x 10^4 N/mm^2 (2 - 3 x 10^6 p.s.i.), Poisson's ratio 0.2 - 0.25) with a high tensile strength so that it is ideal for modelling reinforced concrete.

Test specimens were made from the Araldite and sand mixes used for casting the model and tensile tests gave the following elastic properties:

Young's Modulus (E) = 2.35 x 10^6 p.s.i.

Poisson's ratio (ν) = 0.24.

This material has been described in some detail here as the same material is used for several other models referred to in subsequent chapters. Additional information is given in Reference 45.

The model was cast in two parts each consisting of a flange and half the depth of the webs. Diaphragms were cemented inside the box at the support sections and after internal strain gauges had been positioned the two halves of the model were bonded together with an Araldite epoxy adhesive.

Electrical resistance strain gauge rosettes with 3 mm gauge lengths were located at two sections shown in Figure 22.

The disposition of gauges at these sections is shown in Figure 25. Gauges were located on the inside and outside walls of the box at coincident positions so that the in-plane and flexural components of longitudinal and transverse stresses could be separated. Strains were measured at a total of 168 locations, using an electronic data logging system designed to record information from up to 300 strain gauge bridges at the rate of ten channels per second.

Vertical deflections were measured below the web centrelines at the strain gauge sections using dial gauges with a resolution of 0.0001 inches. It can be seen from Figure 24 that deflections measured under the loaded part of the model will be double those measured under the equivalent encastre girder because of the nature of the support conditions.

Two loading cases were considered, namely concentrated loads separately applied above the centre lines of inner and outer webs at midspan.

2.4.3 Finite element and BEF analysis of the curved model

A finite element extensional-flexural solution of the equivalent full scale structure was carried out using the Imperial College Structural Analysis System (ICSAS). The mesh incorporated one element over the depth of each web

52

and two elements over the width of the box. Advantage was taken of the symmetry of the structure in that a quadrant of the structure was analysed with the correct boundary conditions imposed at midspan necessary to provide continuity. A total of eight elements were used along the length of the box between the support and midspan sections.

The proposed BEF-grillage analysis was carried out using the grillage program from ICSAS with a total of 32 elements over the quadrant. The torsional stiffness of the grillage elements was the full torsional stiffness of the box cross sections with a single line of elements along the centreline of the box. The antisymmetrical loading equivalent to the radial component of the bending forces was calculated at each grillage node using Equation 2.12 and applied to the equivalent straight BEF.

2.4.4 Comparison of BEF, FE and model test results

The test results from the two loading cases were combined to give stresses for the symmetrical and antisymmetrical components of concentrated loading applied at midspan. The cross sectional distribution of σ_{DB} at midspan due to the symmetrical component of loading is shown in Figure 26 and that due to the antisymmetridal component is shown in Figure 27. Corresponding BEF and FE results are also shown in Figures 26 and 27 and cross sectional distributions of σ_{DB}

for a FE analysis of the equivalent straight box are shown in Figure 28. Stresses are non-dimensionalised with respect to the maximum 'simple' bending stress as before. Unfortunately three of the internal strain gauge elements failed during manufacture of the model so that transverse bending stresses could not be obtained at these locations. However sufficient gauges remained in working order for a comparison of model, FE and BEF results to be made. Cross sectional distributions of longitudinal extreme fibre stresses for the two components of load are shown in Figures 29 and 30.

The cross sectional distributions of σ_{DB} and σ_{DW} show reasonable agreement between the three analyses. The finite element stresses are in general larger in the side of the box nearer the centre of curvature but average FE values for the two sides of the box agree closely with BEF values. FE and BEF results both slightly underestimate model stresses for the symmetrical component of loading but close agreement is obtained for σ_{DB} due to the antisymmetrical component. BEF stresses σ_{DW} for the symmetrical component are lower than those from the other analyses but average longitudinal stresses are in agreement. BEF stresses σ_{DW} due to the antisymmetrical component overestimate model stresses but when longitudinal stresses due to the two components are combined agreement is good.

The results show that in this particular case further

54

grillage analyses with reductions to torsional stiffness properties are unnecessary. Agreement between the three analysis methods is adequate for design purposes and maximum stress values for the three analyses agree closely. A comparison of the finite element results shown in Figure 27 with those for the equivalent straight box shown in Figure 28 demonstrates the validity of separating the two components.

2.5 A PARAMETRIC STUDY OF THE BEHAVIOUR OF SINGLE CELL BOX GIRDERS USING THE BEF METHOD

2.5.1 General

The response of a single cell box girder to an arbitrary eccentric load has been described in Section 1.2 Having established the validity of the BEF method in the previous sections, it is used in this section to investigate the effects of altering the various parameters of the box on its distortional behaviour. A selection of the results presented here have also been included in a paper with other authors[3]. The examples are based on a two lane highway with piers at 144 ft centres and although the structures are not actual designs, the proportions are representative of practical bridge cross sections. The dimensions of the examples used in this section are given in Figure 31 and Tables 2 and 3. Results are presented in a non-dimensional form by dividing the actual stress under a given load by the maximum possible bending or shear stress under the same load calculated on the basis of simple bending theory. Deflections are non-dimensionalised with respect to the bending deflections in a similar manner.

Consider Section 1 which is square in cross section with wall thicknesses representative of a concrete box. Figure 9 shows the longitudinal distribution of σ_{DB} and σ_{DW}

56

for both BEF and FE solutions. The distortional stresses increase rapidly towards the load because the high transverse stiffness of the thick walled box restricts the deflections due to distortion to the region of the load. Consequently the distortional stresses are sensitive to the length over which the load is applied. Figure 32 shows the variation of peak midspan σ_{DB} and σ_{DW} with loaded length for Section 1 under a fixed load distributed over an increasing length. As the loaded length increases σ_{DB}/σ_B approaches a constant value and σ_{DW}/σ_B at midspan reduces to zero. Distortional curvature is confined to the regions at the ends of the distributed load where distortional warping stresses result.

Figure 33 shows the variation of maximum stresses σ_{DB} and σ_{DW}, distortional deflection, and transverse distortional moment with wall thickness for a 6 ft x 6 ft box girder under central point load. Distortion of the cross section is resisted by "frame action" of the box walls and by warping. When the wall thickness is small the frame action is negligible and distortion is resisted only by warping with maximum values of σ_{DW} and distortional deflection. As the wall thickness is increased the frame action becomes more important with consequent decreases in σ_{DW} and distortional deflection, but increases in transverse moment and σ_{DB}. With further increases of thickness a peak value of σ_{DB} is reached after

which the section modulus of the box wall (proportional to the square of the wall thickness) increases more rapidly than the transverse moment with a resulting reduction of σ_{DB}.

The use of transverse stiffeners makes possible a study of the effects of altering the frame stiffness of the box while keeping the wall thickness and hence the warping stiffness constant. The variation of maximum transverse distortional moment and the corresponding stresses, σ_{DB}, for a 6 ft x 6 ft box with 0.5 inch plates under central point load as the distortional stiffness of the section is increased is shown in Figure 34. The transverse distortional moments increase with frame stiffening. The maximum stress in the frame depends upon the section modulus of the stiffener together with an associated effective width of plate and it can be seen that the addition of stiffening does not necessarily reduce the transverse stresses. It has been the practice to proportion transverse stiffening by buckling considerations and often such stiffeners attract high distortional stresses especially at the corners of the boxes where welding details may impose limitations on stress levels due to the limit state of fatigue. In single cell boxes distortional stresses are often fully reversible and particular care must be taken in the choice of stiffening so that the fatigue life of corner connections is not impaired.

58

2.5.2 Stress levels in steel and concrete boxes due to distortion

Concrete Section 3 and steel Section 6 have the same overall cross sectional dimensions. The midspan cross sectional distributions of σ_{DB} and σ_{DW} for antisymmetrical loading at midspan for Sections 3 and 6 are shown in Figures 35 and 36. It can be seen that the stresses in the concrete box are all less than σ_B whereas the stresses in the steel box are much greater and σ_{DB} in the web stiffener is several times σ_B. However the web stiffeners in the steel box are designed as buckling stiffeners according to BS153, and not to resist distortion of the cross section. If the stiffening is increased to that for Section 6A (Table 3), the maximum value of σ_{DB} reduces from $9.81\sigma_B$ to $0.32\sigma_B$. Alternatively diaphragms may be used to restrict σ_{DB} and to a lesser extent σ_{DW} and their effectiveness is examined in Section 2.5.4.

The effect of varying the cross sectional side ratio is studied with concrete Sections 2, 3 and 4 and steel Sections 5, 6 and 7. In each case the bottom section modulus is kept constant by varying the bottom flange thickness and the load is applied 9 ft from the longitudinal centre line. The variation of σ_{DB} and σ_{DW} is shown for concrete and steel boxes subjected to concentrated and distributed loads in Figures 37 to 39. Again the stresses are greater in the steel boxes but no significant trend emerges in the results.

2.5.3 Trapezoidal boxes

The effect of sloping the webs is studied by reference to concrete Sections 8, 9 and 10 and steel Sections 11, 12 and 13. The bottom flange thickness is adjusted so that the bottom section modulus remains constant for either concrete or steel sections. Figures 40 to 42 show the maximum mid-span values of σ_{DB} and σ_{DW} for central concentrated loading and uniformly distributed line loading on both steel and concrete boxes. In all cases a reduction in stress occurs as the bottom flange becomes more narrow. This is because the frame stiffness of the box is increased and in the extreme with a zero bottom flange width the section becomes triangulated and non-deformable. Figure 43 which shows cross sectional distributions of σ_{DB} for Sections 8 to 10 demonstrates how the position of maximum σ_{DB} may vary as the slope of the web is changed.

Transverse in-plane forces are introduced into the flanges when the webs are sloped. Tensile stresses result in the top flange at midspan and compressive forces occur at the supports in the bottom flange and diaphragms and these must be considered in design. Figure 44 shows cross sectional distributions of transverse in-plane stresses obtained from FE analyses of Sections 8 and 10.

60

2.5.4 Diaphragms

The diaphragm spacings and stiffnesses required to restrict distortional stresses to acceptable levels depend upon the transverse stiffness of the box or, more precisely, upon the parameter β which is given by

$$\beta = \sqrt[4]{\frac{K}{4EI_w}} \quad \ldots\ldots\ldots\ldots\ldots\ldots\ldots\ldots\ldots\ldots (2.14)$$

(See also Appendix B).

β has the dimensions of $(\text{length})^{-1}$ and a dimensionless panel length (βL_D) may be defined as the product of β and the diaphragm spacing, L_D. Curves may be plotted of dimensionless BEF deflection, moment, support reaction and shear for specific load cases. Wright et al[13] present curves for central point load and Figure 45 shows similar curves of dimensionless BEF deflection (proportional to σ_{DB}) for a uniformly distributed load. Diaphragms at dimensionless spacings greater than 5 do not significantly affect maximum values of σ_{DB}. An intermediate range exists from $\beta L_D = 1$ to $\beta L_D = 5$ over which the diaphragm spacing is the dominant parameter and below $\beta L_D = 1$ diaphragm stiffness becomes more important. Below $\beta L_D = 0.2$ stiffness alone controls distortion. These ranges vary slightly for different loading cases but as a general rule for proportioning diaphragms these ranges may be used.

The influence of diaphragm stiffness and spacing is illustrated by reference to Section 11. Figure 46 shows the longitudinal distribution of σ_{DB} in Section 11 for different numbers of diaphragms with the load applied in each case midway between the most central diaphragms. It can be seen that five ½ in. plate diaphragms are necessary to reduce σ_{DB} to a value less than σ_B.

Figures 47 and 48 show the effect of different numbers of alternative diaphragms on the maximum values of σ_{DB} and σ_{DW}. Curves for the point load case illustrate that for few diaphragms stress levels are controlled by the diaphragm spacing, and for seven or more diaphragms stresses are controlled by diaphragm stiffness. Diaphragms are less efficient in the control of warping stresses which if critical are best controlled by increasing the flange areas. Three alternative diaphragms are studied. The plate diaphragms each contain about the same weight of steel as two diaphragms made from 8 x 8 x ⅝ in. angles or three made from 6 x 6 x ¾ in. angles. For a point load, σ_{DB} is reduced to about $0.8\sigma_B$, if three internal ½ in. plate diaphragms, five 8 x 8 cross bracings, or seven 6 x 6 cross bracings are used. On the basis of weight the third alternative is the most efficient and this arrangement also leads to the lowest σ_{DW}.

For a rigid diaphragm all of the distortional component of eccentric concentrated load applied at the diaphragm is

62

resisted by the diaphragm. In practice the diaphragm has a finite stiffness and some of the distortional force is resisted by the frame action of the box and by adjacent diaphragms. For example, for seven 6 x 6 x ½ in bracings the maximum stress in the angles would be $2.1\sigma_B$ if the bracings were assumed rigid, but is $1.0\sigma_B$ when the actual stiffness is used in the BEF solution.

Figure 49 shows the effect of introducing different numbers of 12 in. concrete diaphragms into concrete Section 8. The number of diaphragms has a marked effect on σ_{DB} but little effect on σ_{DW} over the range shown. A slight increase in σ_{DW} may be noticed for four diaphragms. This may be explained by reference to the moment response of the analogous BEF shown in Figure 50. If diaphragms are placed beyond A-A they will not affect σ_{DW} at midpanel. If diaphragms are placed between A and B it can be seen that midpanel moments are slightly increased (corresponding to four diaphragms in Figure 49). Similarly σ_{DB} may be increased slightly if the diaphragm spacing corresponds to supports between A and B[46].

2.5.5 Effects of curvature in plan

Distortional effects due to curvature may be accounted for by the method described in Section 2.4. If the values of σ_{DB} and σ_L shown in Figures 26-30 for symmetrical and antisymmetrical components of load are combined to give the

stresses for single point loads applied above the centre-line of each web separately (Figure 51) it can be seen that maximum values of σ_{DB} and σ_{L} are obtained when the load is applied above the inner web. In such a case the distortional forces due to the radial component of the longitudinal bending stresses are additive to the distortional forces due to the antisymmetrical component of the loading and higher values of σ_{DB} and σ_{DW} result.

2.5.6 Cross sectional properties of practical steel box girders

The distortional properties of 28 recent steel box girder bridge designs were studied in order to investigate possible simplifications to the BEF method, and more particularly to the calculation of the distortional properties I_{w} and K, for use in design. The details of the bridges were supplied by the DoE and the bridge names and reference numbers are given in Table 4. Although the majority of the structures are of multibox construction, the analysis method proposed for such structures in Chapter Three makes use of the BEF method for single cell boxes to determine distortional effects in each cell separately. Therefore the calculation of the distortional properties of a multi-box bridge is approached by the calculation of the properties of each cell as an independent box. The properties studied

64

are listed for each bridge in Table 5 from which the following observations may be made:

(i) βL (span) - the dimensionless panel length of the span of the box. If this is greater than approximately 2.5 the influence of the support diaphragms on distortional stresses at midspan is small and the box may be analysed as an infinite BEF for which there is a simple solution. Table 5 shows that all the bridges studied have βL (span) greater than 2.5.

(ii) βL_D (panel) - the dimensionless panel length between diaphragms or cross bracing. The influence of diaphragms on mid-panel stresses depends to a certain extent on the loading case. If βL_D is less than 2.0 diaphragms control the stresses under both distributed and concentrated loading. If βL_D is less than 0.2 diaphragm stiffness alone is the controlling factor. Therefore as a general rule diaphragms are most effective if spaced in the range $0.2 < \beta L_D < 2.0$. Of the thirteen structures with internal diaphragms only one had $\beta L_D < 0.2$ (Porton Road Bridge) and one had $\beta L_D < 2.0$ (Thornham East Bridge).

(iii) $I_x/4I_b$, r_β, r_s. The expressions leading to the warping stiffness property I_b are complicated and

the use of an approximate value of $I_x/4$ has been suggested[13]. The warping stiffness is used in the BEF analysis at two stages - in the calculation of the β parameter and secondly in the calculation of warping stresses from the BEF moment. A further approximation may be introduced into the warping stress calculation by using the analogy to bending about the horizontal axis as

$$\sigma_{DW} = E\bar{y}W \qquad (2.15)$$

where $\bar{y}$ is the distance from the neutral axis of bending to the extreme fibres

W is the BEF deflection.

In Table 5 the value $I_x/4I_b$ gives a comparison of approximate and exact values for warping stiffness and r_β is a measure of the error in β resulting from the use of $I_x/4$. r_s is a measure of the error resulting from the use of Equation 2.15 rather than the exact expression for σ_{DW}. Expressions leading to r_β and r_s are given in Appendix B. Table 5 shows that the maximum value of r_β is 1.19 - an error of 19% - but in only two cases r_β shows errors greater than 10%. Values of r_β greater than unity lead to conservative values of σ_{DW} and values of r_β calculated to be less than unity do not exceed 6%

error. The approximation of Equation 2.15 measured by r_s leads to somewhat larger errors, the maximum being 25%. However where values of r_s are small, representing large errors in σ_{DW}, values of r_β are generally greater than unity and discrepancies tend to compensate. The maximum error in σ_{DW} in using Equation 2.15 together with $I_x/4$ is 19%. Since the warping stresses are generally of less importance than σ_{DB} the above figures suggest that the use of these approximations leads to sufficient accuracy for design.

(iv) V_D - the redundant shear at a cut on the centre line of the bottom flange of unit length of the box subjected to unit antisymmetrical load. The expression for V_D is complicated and is used in the calculation of the frame stiffness K. The value of V_D is almost always between 0.2 and 0.25 and if an approximate value of say 0.225 could be used the calculation of K would be greatly simplified. However Table 5 shows that for two bridges V_D is outside the normal range and for Bridge 1 the use of a value of .225 would lead to large errors. Bridge 1 is peculiar in that although substantial transverse web stiffening is used (12" bulb flats) there are no transverse stiffeners on the bottom

flange. Such a detail could lead to high stress concentrations in the bottom flange plate adjacent to the web stiffners and is therefore in general to be avoided.

(v) γ and λ - geometrical properties of the box used to define the practical ranges of box girders. For rectangular boxes $\gamma = 1$ and trapezoidal boxes obviously have $\gamma < 1$. λ - the ratio of slant height to top flange width varies between 4 and 0.24.

(vi) α and ν - ratios of transverse flexural rigidities of bottom to top flanges and web to top flange respectively. These ratios have a large influence in the calculation of the frame stiffness of the box cell and they reflect the levels of σ_{DB} in the various plates of the box. Where there is a large difference in flexural rigidities of adjacent box walls, transverse stresses may often be high in the wall with the smaller flexural rigidity especially where the section modulus of the stiffener-plate combination is low. Transverse stiffeners are in general proportioned for considerations other than that of controlling distortional stresses and this frequently leads to large differences in flexural rigidity and hence high stress levels. Table 5

68

shows that almost half the bridges investigated have values of ν less than 0.002.

The above observations lead to simplifications in calculation of BEF parameters and in particular the approximate warping property Ix/4. Ratios γ, λ, α, and ν may be used to simplify the calculation of K with the use of curves as shown in Appendix B. The clauses dealing with distortion of the cross section in the new British Interim Design Rules are based on the use of a simplified BEF method resulting from the above study. They will be discussed further in Chapter Eight.

CHAPTER 3: MULTIBOX BRIDGE STURCTURES

3.1 GENERAL

A recent feature survey of 173 concrete box girder bridges[47] shows that of the total, 53 are single cell, 59 are multicell and the remainder (61) are multibox. A similar survey of data on 62 steel box girder bridges compiled for the Merrison Committee Parametric Studies[48] reveals that fifteen are single cell, four are multicell and 43 are multibox. An analysis method which accounts for distortional effects in single cell box girders has been described in Chapter Two. It is clear, however, that for the method to be of more general use to the designer, it must also be applicable to multibox structures. A report by Kee[49] provides the basis for an approximate method of calculation of load distribution and hence distortional effects in multicell box girders. The literature survey of Section 1.3 demonstrates the lack of alternative analysis methods to the finite element approach for general multibox structures and highlights the need for more economic methods suitable for design.

In this Chapter a method is proposed, based on a combination of grillage and BEF methods, to account for distortional

70

effects in complex multibox elevated highway structures. Validation is provided by comparison with finite element results, and the method is used to investigate the influence of the distortional stiffness on load distribution and distortional stresses for a typical twin box structure.

3.2 THE PROPOSED GRILLAGE - BEF APPROACH

Standard computer programs for the analysis of grillages are widely used in the design office for the analysis of many forms of bridge superstructure. Sawko and Mosley[50] describe the application of such programs to box girder bridges with undeformable box cross-sections. If deformation of the cross section is permitted the effects are similar to those described for curved continuous single cell boxes in Section 2.4. Antisymmetrical vertical displacements of the box corners which result from deformation can be considered as rotations of the flanges which are additional to the pure torsional rotations and which reduce the effective torsional stiffness of the box section. This conception of the structural action leads to an analysis method utilising standard grillage programs with reduced torsional stiffness properties (GJ) for the longitudinal members to make allowance for deformation of the cross section. The torsional stiffness GJ is the Bredt-Batho value for closed undeformable sections and is given by

$$GJ = \frac{4GA^2}{\oint \frac{ds}{t}}$$

where G is the shear modulus

A is the enclosed area of the box cross section

t is the wall thickness

s is the distance along the box wall.

The degree of reduction to GJ is dependent upon the distortional properties of the box cells, the span and spacing of the boxes, and the loading. The following iterative procedure provides the final solution which results when compatibility of vertical antisymmetrical deflections of the box corners is obtained:

Step 1 Carry out a grillage analysis of the structure assuming the longitudinal members have the full GJ as given above.

Step 2 Carry out a BEF analysis of each box with antisymmetrical loading equivalent to the torsional moments given by Step 1.

Step 3 At key sections compare the sum of the BEF distortional deflection δ_D and the torsional deflection δ_T with the grillage torsional deflection δ_G. (δ_D is the vertical distortional deflection at the top corner of the box defined by W in Figure 5, δ_T and δ_G are the relevant torsional rotations multiplied by half the top width of the box defined by δ_T in Figure 2. δ_T is obtained from the grillage results by dividing δ_G by the torsional stiffness reduction factor and therefore, for the full torsional stiffness grillage, $\delta_G = \delta_T$).

Step 4 Calculate a new torsional stiffness equal to the previous torsional stiffness divided by the reduction

factor R which is given by:

$$R = \frac{\delta_T + \delta_D}{\delta_G} \quad \ldots\ldots\ldots\ldots\ldots\ldots\ldots\ldots\ldots\ldots (3.1)$$

Step 5 Carry out a further grillage analysis with the new GJ.

Step 6 Carry out a BEF analysis of each box with antisymmetrical loading equivalent to the torsional moments given by Step 5.

Step 7 Repeat Steps 3 to 6 until the following compatibility criterion is obtained at Step 3.

$$\delta_G = \delta_T + \delta_D \quad \ldots\ldots\ldots\ldots\ldots\ldots\ldots\ldots\ldots\ldots (3.2)$$

The previous grillage and BEF analysis will have given the correct distribution of bending and torsional moments and deflections, and distortional stresses and deflections.

The procedure is illustrated by reference to the twin box structure shown in Figure 52. The cross section consists of two open-topped steel boxes with a composite reinforced concrete deck. The four webs are equally spaced at eight feet centres and a concentrated load is applied above an outer web at midspan.

The idealisation used for the grillage analysis is shown in Figure 53 and consists of a single line of longitudinal members along the centre-line of each box with

74

transverse members to represent the boxes and slab. Slab members with high stiffness are used across the width of the box so that the transverse members which represent the slab between boxes have the correct span and stiffness properties. Cantilevered transverse box members are used over the outer half of the box so that loads can be applied above the outer webs. Member properties are given in Table 6.

A three dimensional finite element 'shell' analysis was also performed using ICSAS. The applied loading is separated into symmetrical and antisymmetrical components and it is then possible to analyse only a quarter of the structure resulting in large savings in computer time. The mesh selected for the analysis consists of rectangular plate elements (Figure 54). The number of nodes in the cross section is the minimum necessary to define the geometry and the mesh length is equal to one sixteenth of the span.

Finite element transverse distortional bending stresses, σ_{DB}, and deflections for a concentrated load of 1 ton applied above one of the outer webs at midspan are given in Figure 55 and Table 7 respectively. The grillage analysis for longitudinal members having the full torsional stiffness (GJ) gives an antisymmetrical deflection for the loaded box of $\delta_G = 0.224 \times 10^{-3}$ in. and the BEF analysis of the corresponding torsional moments gives a distortional deflection δ_D of 0.403×10^{-2} in. The sum of δ_D and the torsional

deflection δ_T (=0.224 x 10^{-3}in.) gives

$$\frac{\delta_G}{\delta_D + \delta_T} = \frac{0.224 \times 10^{-3}}{0.425 \times 10^{-2}} = \frac{1}{19} \quad \ldots\ldots\ldots (3.3)$$

which suggests a reduction of GJ to one nineteenth of the full value. Transverse distortional bending stresses σ_{DB} for the BEF analysis of torsional moments given by the full GJ grillage are also shown in Figure 55 and it can be seen that the stress levels are approximately double the finite element values.

The results of a grillage-BEF analysis for GJ/19 are given in Table 7 and Figure 55 and a comparison of deflections for this case gives:

for the loaded box $\quad \frac{\delta_G}{\delta_D + \delta_T} = \frac{1}{0.971}$

and for the unloaded box $\quad \frac{\delta_G}{\delta_D + \delta_T} = \frac{1}{1.115}$ $\quad \ldots\ldots\ldots\ldots (3.4)$

Figure 55 shows that the maximum σ_{DB} calculated by grillage-BEF is within six per cent of the finite element values - an accuracy quite sufficient for design. The factors from Equation 3.3 when multiplied by GJ/19 suggest values of GJ/19.45 for the loaded box and GJ/21.18 for the unloaded box. A further grillage-BEF analysis using these figures gives even closer agreement with the FE analysis (Figure 55 and Table 7).

76

The above figures show that two grillage-BEF analyses are sufficient to calculate the effects of distortion for the loading case considered. The above FE and grillage-BEF results were obtained from computer programs run on the University of London CDC6600 computer. The central processing time used for the FE run was 96 seconds compared with a total of 17 seconds for two grillage-BEF runs. However the FE approach has the advantage that additional load cases can be considered at little extra cost because the major part of the computer time is taken in the inversion of the structure stiffness matrix. If one reduction factor for the torsional stiffness could be used for all loading cases which still retaining sufficient accuracy for design, additional loading cases could also be calculated by the grillage-BEF method for a relatively small increase in computer time. Therefore two additional load cases were calculated by the grillage-BEF method with the longitudinal members having a torsional stiffness of one nineteenth of the full value. The load cases consisted of a uniformly distributed line load applied above an outer web, and a concentrated load applied at midspan above one of the inner webs. In both cases the total applied load was 1 ton.

A comparison of antisymmetrical deflections for the most critically distorted box gives:

For the concentrated load above an inner web

$$\frac{\delta_G}{\delta_D + \delta_T} = 1.053$$

and for the uniformly distributed line load

$$\frac{\delta_G}{\delta_D + \delta_T} = 0.932,$$

differences of five and seven per cent respectively.

The transverse distortional stresses for the two load cases together with corresponding FE results are given in Figures 56 and 57. The results show very good agreement for the two methods and give the important result that the same reduction factor for the torsional stiffness may be used for different load cases with consequent savings in computer costs.

Longitudinal stresses are also predicted accurately by the grillage-BEF approach and Figure 58 shows a comparison of longitudinal stresses with FE results for a central concentrated load above an outer web of the twin box example.

78

3.3 ALTERNATIVE NON-ITERATIVE APPROXIMATE METHOD

The procedure for calculation of distortional effects using the grillage-BEF method proposed in 3.2 could be abbreviated if the final torsional stiffness reduction factor could be estimated with acceptable accuracy without iterating the solution. In the method described in 3.2 reductions to the torsional stiffness are calculated on the basis of a comparison of antisymmetrical deflections until the compatibility criterion of Equation 3.2 is satisfied. An alternative approximate basis for calculation of the reduction factor could be the condition that the strain energy of torsion, U_T, and distortion U_D, in the actual box should be equal to the strain energy ($U_{T(reduced)}$) due to pure torsion in an idealised non-deformable box with a reduced torsional stiffness.

i.e. $$U_{T(reduced)} = U_T + U_D \quad \ldots\ldots\ldots\ldots\ldots\ldots \quad (3.5)$$

This approach has been used by Pelikan and Esslinger[66] for estimating a reduced torsional stiffness of orthotropic decks with closed stringers.

$$U_T = \frac{b_T^2}{2GJ} \int_o^L P^2 \, ds \quad \ldots\ldots\ldots\ldots\ldots\ldots \quad (3.6)$$

where b_T is the top width of the box

P is the antisymmetrical loading

s is the distance along the beam.

The distortional strain energy is the sum of the strain energy due to distortional bending, U_{DB}, and that due to distortional warping, U_{DW}.

$$U_D = U_{DB} + U_{DW} \quad \ldots\ldots\ldots\ldots\ldots\ldots\ldots\ldots (3.7)$$

where U_{DB} is given by

$$U_{DB} = K\int_o^L W^2 ds \quad \ldots\ldots\ldots\ldots\ldots\ldots\ldots\ldots (3.8)$$

and U_{DW} is given by

$$U_{DW} = EI_b\int_o^L (W'')^2 ds \quad \ldots\ldots\ldots\ldots\ldots\ldots\ldots\ldots (3.9)$$

where K is the foundation modulus of the BEF

I_b is the inertia of the BEF

W is the BEF deflection

therefore

$$\frac{b_T^2}{2GJ_{(reduced)}}\int_o^L P^2 ds = \frac{b_T^2}{2GJ}\int_o^L P^2 ds + U_{DB} + U_{DW}$$

and

$$\frac{GJ}{GJ_{(reduced)}} = \frac{U_T + U_{DB} + U_{DW}}{U_T} \quad \ldots\ldots\ldots\ldots\ldots\ldots (3.10)$$

However the distributions of torsional moments and BEF deflection and moments are not known without preliminary analysis. If it is assumed that the torsional moments are distributed over the span in a sinusoidal form,

80

and if it is further assumed that distortion is resisted by the frame stiffness of the box alone and also that distortional deflections have a sinusoidal distribution, then a direct calculation of the reduced torsional stiffness can be made as shown below. (Longitudinal distributions of torsional moments and distortional deflections in general approximate sinusoidal configurations).

Applied torsional moments m_T are distributed according to

$$m_T = P.b_T \sin \frac{\pi x}{L} \quad \ldots\ldots\ldots\ldots\ldots\ldots\ldots\ldots (3.11)$$

where P is the antisymmetrical load

x is the distance along the span from one support

L is the span length.

The total torsional moment M_T at a distance x from the support is therefore given by

$$M_T = \int_x^{L/2} P.b_T \sin \frac{\pi x}{L} \, dx = P.b_T \frac{L}{\pi} \cos \frac{\pi x}{L} \quad \ldots\ldots (3.12)$$

The torsional strain energy U_T is given by Equation 3.6 therefore

$$U_T = \left(\frac{P.b_T}{2GJ}\right)^2 . \frac{L}{\pi}^2 . \frac{L}{2} \quad \ldots\ldots\ldots\ldots\ldots\ldots\ldots\ldots (3.13)$$

For the idealised non-deformable box with a reduced torsional stiffness $GJ_{(reduced)}$ the torsional strain energy $U_{T\ (reduced)}$ is given by

$$U_{T\ (reduced)} = \frac{(P.b_T)^2}{2GJ_{(reduced)}} \cdot \left(\frac{L}{\pi}\right)^2 \cdot \frac{L}{2} \quad \ldots\ldots (3.14)$$

The distortional strain energy is calculated by the summation of the strain energies due to bending in each of the box walls. The transverse bending moment diagram for a unit length of the box subjected to a unit distributed antisymmetrical load is shown in Figure 59. V_D is the redundant shear at the centre line of the bottom flange and its value is derived in Appendix B. Distortional bending moments m_D are distributed according to

$$m_D = M.\ \sin \frac{\pi x}{L} \quad \ldots\ldots\ldots\ldots\ldots\ldots\ldots\ldots (3.15)$$

where M is the value given by Figure 59.

The distortional bending strain energy for the top flange U_1 is given by

$$U_1 = 2\int_o^{b_T/2}\int_o^{L} \frac{M^2}{2EI} .\sin^2\frac{\pi x}{L}\, dx.dy$$

therefore

$$U_1 = 2\int_o^{b_T/2}\int_o^{L} \frac{\left(\frac{b_B}{b_T+b_B} - V_D\right)^2 x^2 .\sin^2\frac{\pi x}{L}}{2EI_t}\, dx.dy$$

82

therefore

$$U_1 = \frac{\left(\frac{b_B}{b_T+b_B} - V_D\right)^2 b_T^{\,3} L}{48EI_1} \quad \ldots\ldots\ldots\ldots\ldots\ldots (3.16)$$

where I_1 is the inertia of unit length of the top flange plate for transverse bending.

Similarly for the bottom flange the distortional bending strain energy U_2 is given by

$$U_2 = \frac{V_D^{\,2} b_B^{\,3} L}{48EI_2} \quad \ldots\ldots\ldots\ldots\ldots\ldots\ldots\ldots (3.17)$$

and for the two webs the strain energy U_3 is given by

$$U_3 = \frac{cL}{2EI_3}\left[C_1^{\,2} - C_1C_2 + \frac{C_2^{\,2}}{3}\right] \quad \ldots\ldots\ldots (3.18)$$

where $C_1 = b_B . V_D/2$

$$C_2 = \frac{b_T}{2}\left(\frac{b_B}{b_T+b_B} - V_D\right) + C_1$$

and I_2, I_3 are the bottom flange and web inertias equivalent to I_1 for the top flange.

Equating the strain energies gives

$$U_{T(\text{reduced})} = U_T + U_1 + U_2 + U_3 \quad \ldots\ldots\ldots (3.19)$$

and substituting from Equations 3.12 to 3.17

$$R = \frac{GJ}{GJ_{(reduced)}} = 1 + \frac{GJ}{12b_T^2 E}\left(\frac{\pi}{L}\right)^2 \cdot \left\{ \left(\frac{b_B}{b_T+b_B} - V_D \right)^2 \cdot \frac{b_T^3}{I_1} + \frac{V_D^2 b_B^3}{I_2} + \frac{24c}{I_3}\left(C_1^2 - C_1C_2 + \frac{C_2^2}{3} \right) \right\}$$

.....(3.20)

Equation 3.20 may be used to calculate a reduction factor, R, for the torsional stiffness of longitudinal members of the grillage analysis without recourse to preliminary analysis. The assumptions necessary to the derivation of Equation 3.19 make the expression approximate especially for distortionally flexible boxes. For example the structure used to illustrate the grillage-BEF approach in 3.2, which has no transverse stiffening or diaphragming and was selected as an extreme example to test the method, has a reduction factor calculated from Equation 3.19 of R = 26.4. In order to determine the errors produced by the use of this value rather than the value of GJ/19 suggested by the iterative procedure, a grillage-BEF analysis for boxes having GJ/26.4 was carried out. The results of this analysis are included in Figures 60-65 which show the maximum torsional moments, deflections, transverse slab moments, distortional effects and longitudinal bending moments for a range of grillage-BEF analyses of the twin box example for torsional stiffnesses ranging from the full Bredt-Batho value to zero.

84

Figures 60-65 show that the behaviour of the structure is insensitive to small changes in the torsional stiffness of the longitudinal members. Large changes in GJ produce much smaller changes in the structural response. For example a reduction of GJ from the full Bredt-Batho value to GJ/2 (i.e. 50% reduction) produces an increase of less than 6% in the maximum deflections and longitudinal bending moments and a decrease of only 9% in the maximum torsional moment. Similarly a reduction of the torsional stiffness from GJ/10 to GJ/100 (a reduction of 90%) produces an increase of 30% in the maximum deflection but a decrease of 70% in the torsional moments and hence distortional stresses. Calculations on other practical bridge designs suggest that, in general, the behaviour is insensitive to small changes to GJ[32,51,52]. Conservative results for distortional stresses are obtained when the effective torsional stiffness is overestimated. The use of GJ/26.4 suggested by Equation 3.19 produces errors in maximum deflections and bending moments of less than 4% and an error of 16% in the maximum stress σ_{DB}. This gives sufficient accuracy for preliminary design and if the distortional effects prove to be critical a further grillage analysis may be necessary for an accurate assessment of distortional effects.

The torsional stiffness reduction factors necessary for practical box girder designs vary widely according to

the geometry of structures. Reduction factors for the steel bridge designs referred to in 2.5 vary between 1.6 and 17.8.

Where internal diaphragms are incorporated into the box distortion of the cross section is largely limited to the loaded panel. In such cases it may be assumed that the sinusoidal distribution of distortional forces is effectively restricted to the diaphragm spacing whereas the torsional moments remain distributed over the entire torsional span. This results in a modified form of Equation 3.20 where the reduction factor for internal diaphragms R_D is given by

$$R_D = \frac{GJ}{GJ_{red}} = 1 + \frac{GJ\ L_D}{12 b_T^{\,2} EL}\left(\frac{\pi}{L}\right)^2 \left[\left(\frac{b_B}{b_T+b_B} - V_D\right)^2 \frac{b_T}{I_1} + \frac{V_D^{\,2} b_B^{\,3}}{I_2} + \frac{24c}{I_3}\left(c_1^{\,2} - c_1 c_2 + \frac{c_2^{\,2}}{3}\right)\right] \quad \ldots\ldots\ldots\ldots\ldots\ldots \quad (3.21)$$

Therefore

$$R_D = 1 + \frac{L_D}{L}(R-1) \quad \ldots\ldots\ldots\ldots\ldots\ldots\ldots\ldots \quad (3.22)$$

The use of equation 3.21 for internal diaphragms is demonstrated in Chapter Seven.

86

CHAPTER 4: THE INFLUENCE OF SKEW SUPPORTS ON THE BEHAVIOUR OF MULTIBOX STRUCTURES

4.1 INTRODUCTION

The layout of modern motorway and urban highway grade separated interchanges often necessitates the use of skew supports for the elevated structures. The particular advantages of the box section over other forms of construction in such situations are discussed in Chapter One. Skew supports introduce higher torsional moments into the box girders than occur in the equivalent right supported bridge and distortional effects are correspondingly more pronounced. In this chapter the behaviour of skew supported multibox structures is illustrated by reference to theoretical and model analyses of the Merstham Interchange Slip Road Structures. These analyses also provide additional comparisons for the analysis method presented in Chapter Three.

The four level Merstham Interchange is at present being constructed at the intersection of the M23 and M25 Motorways near Merstham, Surrey. The layout of the interchange (Figure 66) necessitates a high degree of skew at the supports of the lower slip road structures which will carry two traffic

lanes over four spans varying in length between 76 feet and 126 feet. The original design for the superstructure consisted of two rectangular stiffened steel box girders with a composite reinforced concrete deck. Details of the stiffening for the steel plates of the boxes are shown in Figure 67. There were no diaphragms within the spans but ½ in. stiffened plate diaphragms were incorporated into the boxes above the bearings. The supports consisted of a single bearing which allowed both rotation and translation located centrally beneath each box at the pier positions. An alternative design proposed by the contractor which employs concrete for the boxes rather than steel was finally adopted for construction but the results described in this chapter are related to the steel design in which the effects of skew are more severe.

The model tests, and the finite element and grillage-BEF analyses of the undiaphragmed structure are described in Sections 4.2 to 4.4. The results of the three analysis methods are compared in Section 4.5 and the structural behaviour is discussed in Section 4.6. The results indicate that the distortional stress levels in the undiaphragmed structure are unacceptable. Subsequently a study of a number of possible diaphragm arrangements was undertaken using the finite element program to determine the most efficient diaphragming system for the skew situation. This study is reported in Section 4.7.

88

4.2 DESCRIPTION OF THE MODEL TESTS

The model dimensions are shown in Figure 68. The model was constructed to a scale of 1/30 of the full scale structure as this was the most suitable for the available materials and laboratory testing apparatus. It was thought unnecessary to reproduce exactly all the features of the prototype structure although the overall dimensions of the superstructure and the thickness of the slab were scaled down exactly. It was necessary to represent the stiffened plates of the full scale structure by unstiffened plates in the model and therefore it was not possible to scale down the extensional and flexural plate stiffnesses in the same proportions. The investigation was concerned more with the transverse distortional stresses in the boxes than with longitudinal stresses so it was decided to choose a model plate thickness which would provide the correct scale transverse flexural stiffness. This resulted in greater extensional stiffnesses of the plates and the inertia of the cross section was increased by 19.8%.

The steel boxes were each manufactured from a single sheet of Birmingham Gauge 24 (0.02476 in.) mild steel which was folded around a specially prepared former to produce the box section. The boxes were formed so that there was a longitudinal joint along the centre line of the bottom

flange. At this location the distortional warping stresses and transverse distortional bending stresses are both theoretically zero and only vertical shears act across the joint. An adhesive with a high shear strength was used to bond 1 in. wide strips of 0.005 in. thick steel both inside and outside the bottom flange to complete the joint. The strips gave sufficient area to provide the shear connection but added very little to the total inertia of the cross section.

The model slab was made from the Araldite CY219 casting resin and sand mixture described in Section 2.5. The slab was cast in a steel mould and after curing the boxes were bonded to the under surface of the of the slab with an epoxy adhesive. The completed model is shown in Figures 69 and 70 and the elastic properties of the model materials measured by tensile tests are given in Table 8.

The bearings consisted of ½ in. diameter, 1/32in. thick rubber pads mounted on columns instrumented to measure the support reactions. The columns were located on a heavy steel I-section girder which was supported about three feet above the laboratory floor. The moving loading frame also rested on the I-section with the load hanging beneath from the frame. The general testing arrangement is shown in Figure 71. The load, which was applied to a simulated HB vehicle of the correct scale, was chosen in the correct

proportion to give the same stresses in the model as would occur in the equivalent full scale structure so that the results would be directly meaningful. Thus for the correct stresses the bending moment scale was 1:27000 and the shear force scale was 1:900. The concentrated load scale was 1:900 and the distributed load scale 1:30 for the same unit length. One HB wheel load of 11.25 tons was represented by a model load of 28 lb. and 45 units of HB loading (180 tons) was represented by 448 lb.

Strains, deflections and reactions were measured experimentally. The strains were measured in both the longitudinal and transverse directions by electrical resistance strain gauges bonded to the model surfaces. Gauge lengths of 3 mm were used on the steel and 5 mm on the Araldite and sand. Strain gauges were located at three cross sections which coincided with Sections 10, 12 and 14 of the FE mesh and the layout of these strain gauges is shown in Figure 72. The strain gauge readings were processed to give stresses in the longitudinal and transverse directions. Vertical and horizontal deflections were measured with dial gauges having a resolution of 0.0001 in.. Sufficient deflections were measured at Sections 10 and 14 to define the movements of the four corners of each box so that the distorted shape of the cross section could be determined. Vertical deflections of the model were also measured above the support

positions so that the settlement of the rubber bearings could be allowed for in the comparison of theoretical and experimental results.

92

4.3 DESCRIPTION OF THE FINITE ELEMENT ANALYSIS

The Imperial College Structural Analysis System (ICSAS)[34] was used to analyse the model. The mesh selected for the analysis consisted essentially of rectangular elements with triangular elements used only where the geometry made this necessary at the ends of the model. The stiffness matrix of the rectangular elements is a combination of the stiffness matrix of the standard flexural element[19] and that of a plane stress element developed specially for box girder analysis[20]. The stiffness matrix of the triangular elements is a combination of the stiffness matrix of the standard flexural element[53] and that of the standard plane stress element[19].

Figure 73 illustrates the mesh used in the analysis. The longitudinal mesh lines are the minimum required to define the geometry of the cross section and the support positions. Analytical tests on a single cell box[20] suggested that satisfactory accuracy would be obtained with this layout. These tests also indicated that only 10 web elements were necessary along the span.

The composite plates which formed the top flanges of the box girders were represented by equivalent homogeneous plates for which the appropriate value of Poisson's ratio ν_{eff} was given by

$$\nu_{eff} = \sqrt{\nu_{steel} \times \nu_{concrete}}$$

and the thickness t_{eff} and Young's Modulus E_{eff} were then calculated from the simultaneous equations

$$\frac{E_{eff} t_{eff}^3}{12(1-\nu_{eff}^2)} = D_{composite}$$

and

$$\frac{E_{eff} t_{eff}}{(1-\nu_{eff}^2)} = C_{composite}$$

where $D_{composite}$ and $C_{composite}$ are the flexural and extensional rigidities of the composite plate. The elastic properties of the top flange plate used in the analysis were: $\nu_{eff} = 0.261$, $t_{eff} = 0.356$ in., $E_{eff} = 3.95 \times 10^6$ p.s.i.

94

4.4 APPLICATION OF THE PROPOSED GRILLAGE-BEF ANALYSIS

The idealisation used for the grillage analysis of the Merstham model is shown in Figure 74 and consists of a single longitudinal line of grillage elements along the centre-line of each box with stiff transverse members over the width of the boxes, and transverse members spanning between the edges of the boxes to represent the slab. The member properties used for the grillage analysis are listed in Table 9.

A reduction factor R for the torsional stiffness of the longitudinal members was calculated from Equation 3.20 and resulted in the initial use of GJ/16 for both lines of longitudinal elements of the grillage.

4.5 COMPARISON OF MODEL, FE AND GRILLAGE-BEF RESULTS

The loading case used for the comparison is Load case 2 of Figure 75 which consists of an HB vehicle placed at its maximum eccentricity opposite one of the inner supports. Figure 76 shows FE and model test transverse distortional bending stresses σ_{DB} at Section 12 together with the corresponding grillage-BEF stresses for a torsional stiffness of GJ/16. Grillage-BEF results for the full GJ case are also included for interest. A comparison of grillage-BEF deflections suggests a further reduction of the torsional stiffness of the unloaded box to GJ/25 and stresses σ_{DB} at Section 12 for the loaded box having GJ/16 and the unloaded box having GJ/25 are also shown in Figure 76.

Close agreement is obtained between the three methods for stresses in the loaded box. The grillage-BEF results overestimate the stresses in the unloaded box but further adjustments to the torsional stiffness suggested by a comparison of grillage-BEF deflections would reduce these stresses. It is interesting to note that a large reduction in torsional stiffness of the unloaded box from GJ/16 to GJ/25 has a negligible effect on the behaviour of the loaded box.

FE, model, and grillage-BEF transverse bending stresses σ_{DB} at Section 10 are shown in Figure 77 and FE and grillage-

96

BEF stresses at Section 14 are shown in Figure 78. Stresses at both sections are in close agreement in the loaded box. A single grillage-BEF analysis is sufficient to obtain an accurate assessment of the stresses in the loaded box in which the maximum distortional stresses are obtained. A comparison of computer times for FE and grillage-BEF programs run on the University of London CDC6600 Computer illustrates the advantage of the latter method in terms of cost.

Analysis method	Computer time (seconds)	Computer storage
FE	1,420	82K
Grillage-BEF	20	50K

4.6 THE STRUCTURAL BEHAVIOUR OF THE UNDIAPHRAGMED MODEL

Finite element results for three loading cases (Figure 75), including that used for the comparison of analysis methods in Section 4.5, were used to study the structural bahaviour of the undiaphragmed model. FE deflections and flexural components of transverse stresses for the three loading cases are plotted in Figures 79-81 and 82-84 respectively. It was found to be useful to superimpose the deflections at several cross sections for any particular loading case so that the influence of the skew supports on the response of the complete structure can be seen more clearly.

The support diaphragms prevent distortion of the box girders above the piers but the central bearing does not provide a torsional restraint. The torsional resistance is provided by the slab spanning between the box girder supports. Maximum vertical deflections occur under the outer web of the loaded box at Section 13 for Load cases 1 and 2.

Considering the Load case 1 results, and progressing along the loaded box from the support diaphragm at Section 8, the deformations and distortional stresses increase rapidly away from the support. The maximum transverse distortional stress (8135 p.s.i.) occurs at Section 12 (Figure 82, Point A). There is a high differential deflection between the inner

98

webs of the two boxes opposite the inner support which reduces towards mid-span as the support at Section 18 is approached until, at Section 18, the distortions and deflections occur in the unloaded box only. The transverse slab stresses are high near the supports (Figure 82, Point B), where the differential deflection is large, and locally under the axles of the HB vehicle (Figure 82, Point C). The high differential deflection and large rotation at the diaphragmed inner support result in an upward deflection of the unloaded cantilever.

The results for Load case 2 may be studied in a similar way. The differential deflections between the boxes opposite the inner support at Section 10 are now larger because the HB vehicle is opposite the support and at the position of maximum eccentricity. The rotation of the diaphragm is greater, the upward deflection of the cantilever is greater and the distortional stresses in the loaded box are also high. The maximum transverse distortional stress (11377 p.s.i.) occurs at Section 12 (Figure 83, Point D). Because of the high differential deflection, the maximum transverse slab stress is also larger and occurs where the slab joins the inner edge of the box at the diaphragm (Figure 83, Point E). The diaphragm prevents the relief of the slab stresses which occurs elsewhere where the distortion of the box reduces the otherwise rapid change of curvature in the slab at the edge of the box.

For Load case 3 the deflected shape is quite different and the differential deflections between the two boxes are low. The distortional stresses in the boxes are low (4086 p.s.i. maximum Figure 84, Point F), but the maximum distortions still occur near the inner supports at Section 10 and 18. The upper surface of the slab is concave between the boxes and the structure tends to span between the inner supports with small uplift forces at the outer supports. The maximum transverse slab stresses occur at Section 14 (Figure 84, Point G) under one of the axles of the HB vehicle.

The results of all three loading cases show how the inner supports act as eccentric loads on the unsupported box producing large distortions of the cross section and correspondingly large transverse bending stresses opposite the inner supports.

The magnitudes of the model stresses are not high and their full significance is only realised when the full scale transverse moments, calculated from model stresses, are applied to the combined stiffener and effective width of plate section of the prototype structure. For the maximum model stress (11377 p.s.i.) the equivalent full scale stress approaches yield stress which is clearly unacceptable. Longitudinal stresses and transverse slab stresses are directly applicable to the full scale structure and with suitable steel reinforcement in the slab they can be readily catered for in the design.

100

4.7 A STUDY OF VARIOUS DIAPHRAGMING ARRANGEMENTS FOR THE SKEW SUPPORTED MODEL

The analysis of the undiaphragmed model described in 4.6 showed that transverse distortional bending stresses reached unacceptable levels under working loads. Therefore a study was carried out using the FE program to evaluate the effects of different diaphragm layouts on the transverse distortional stresses in the box girders and the transverse stresses in the slab. The various diaphragm configurations considered are shown in Figure 85 and the results relating to these positions were also compared with the equivalent right bridge (Figure 86), with a span of 46.4 in., to isolate the effects of skew on the distortional behaviour. Bar elements in the form of cross bracing were used to simulate the diaphragms as these could be introduced into the FE analysis without altering the remainder of the data for the program. The bar elements were proportioned to provide the same distortional stiffness as ½ in. plate diaphragms in the full scale structure. The load positions used in the study were the same as those used in the original analysis of the undiaphragmed model as these were judged to approximate closely the critical positions for the various diaphragm configurations considered. The results of the study are summarised in Figures 87 to 89 which show the maximum transverse

box and slab stresses for each diaphragm arrangement. The results have been presented also as cross-sectional plots in a report for the DoE South Eastern Road Construction Unit[33].

High transverse distortional bending stresses, σ_{DB}, occurred in the box girders opposite inner skew supports. It would appear therefore that one possible modification which would restrict these stresses would be to provide diaphragming within the box in this region. To this end, the analysis of Diaphragm Layout 2, which incorporates cross bracing at Sections 10 and 18, was carried out. Figures 87 to 89 show that the maximum σ_{DB} in the loaded box is reduced from 11,377 p.s.i. for Load case 2 at Section 12 to 5,824 p.s.i. for Load case 2 at Section 13 and the maximum σ_{DB} in the unloaded box is almost unchanged (6,515 p.s.i. for the undiaphragmed case to 6,152 p.s.i. - both for Load case 1 at Section 13). However the maximum transverse slab stress at Section 10 for Load case 2 is increased from 951 p.s.i. to 1,511 p.s.i. and the latter value would be unacceptable in the full scale structure. The undiaphragmed box, due to its lack of distortional stiffness, can more readily follow the transverse deflected shape of the slab and therefore transverse moments are lower than those obtained when the distortion is prevented and a hard point is produced at the intersection of the edge of the box and slab. There are two

102

possible solutions to this problem. One is to remove the hard spot by moving the diaphragm in the loaded box away from the support so that there are not two diaphragms at the same section. The distortion is then resisted elsewhere and some distortion is allowed at the support section so that a compromise is obtained between the maximum box and slab stresses. The other solution is to prevent differential deflection of the two boxes at the support section by providing diaphragms between the boxes at these points and the transverse slab moments are then reduced to negligible proportions at that section. The latter solution has the disadvantage that the diaphragms interfere aesthetically with the clean lines of the underside of the structure.

Both possible solutions were investigated with the FE program. Diaphragm Layouts 3 and 4 (Figure 85) were analysed in order to study the effects of moving the diaphragms away from the support sections and Diaphragm Layout 5 (Figure 85) simulates diaphragming between the box girders at support sections.

The results for Diaphragm Layouts 2,3 and 4 are summarised in Figures 87-89 and show how the transverse slab stresses at Section 10 decrease as the diaphragm is moved away from the support region. The maximum transverse slab stresses occur near the diaphragms (1,285 p.s.i. at Section 11 for Layout 3, 1,140 p.s.i. at Section 13 for Layout 4 - both for

Load case 2, c.f. 1,511 p.s.i. for Layout 2). The maximum σ_{DB} in both boxes are also reduced as the distortional spans decrease.

The results for Diaphragm Layout 5 (bracing in and between the boxes at support sections) have also been incorporated into Figures 87-89. They show that although there is a considerable reduction in the transverse slab stresses at the support section, the maximum transverse slab stress for Load case 3 (1,068 p.s.i. at Section 14) is only marginally below that of other diaphragm layouts. The maximum σ_{DB} is 5,791 p.s.i.

The results show that, of the diaphragm configurations considered, Layouts 4 and 5 are the best solutions, the maximum transverse slab stresses being marginally higher for Layout 4 and the maximum σ_{DB} marginally higher for Layout 5. Diaphragm Layout 4 would appear to have the advantage in terms of cost and ease of fabrication.

Diaphragm Layout 6 is a fully diaphragmed scheme with bracing both in and between the boxes at even numbered sections (see Figure 85). This layout is included as a similar arrangement was considered by the SERCU when the results of the undiaphragmed test became available. Transverse stresses in both the slab and the box girders were low. While this stiffening system would be effective in limiting both transverse slab and distortional bending stresses in the boxes to acceptable levels, the alternative solutions considered

104

in Diaphragm Layouts 2 to 5 suggest that a similar objective may be achieved with possible savings in fabrication costs and considerable savings in maintenance costs by the omission of diaphragms between boxes.

4.8 A COMPARISON OF THE SKEW STRUCTURE WITH A RIGHT SUPPORTED STRUCTURE OF EQUAL SPAN

An equivalent right supported structure with a span of 46.4 in. (Figure 86) was analysed. The load cases were chosen to be symmetrical about midspan so that it was only necessary to analyse a quarter of the structure (loads were applied as symmetrical and antisymmetrical components which were superimposed to obtain the results for eccentric loads). This resulted in large savings in computer time and storage. The results of Load case 4 are comparable with those of Load case 3 on the skew structures, while those of Load case 5 may be compared with Load case 1 on the skew structures. Two support systems were considered - Type A with a single support centrally below the box as for the skew structures, and Type B which has supports under both webs of each box at the pier positions. Thus the effects of resisting the torsional loading at the supports rather than by the slab spanning between the boxes could be investigated. The results of the analysis which are included in Reference 33 show that the transverse slab stresses are higher for support Type A where torsion is resisted by the transverse action of the slab, although for this structure differences are only marginal (maximum slab stress for Type A - 1,164 p.s.i., for Type B - 1,106 p.s.i., Figure 90). The boxes resist the rotation of the slab and consequently attract higher

106

stresses than if they were free to rotate. This is reflected by higher transverse slab stresses at the edge of the unloaded box for Load case 5 (Figure 91).

It is interesting to compare the results of the analysis of Diaphragm Layout 5 (bracing at support sections in and between the boxes) with the results for the right bridge structure (Figures 90-91). The results for both structures show very similar behaviour, the main difference being the higher values of σ_{DB} for the right bridge structure which has a longer distortional span. This suggests that distortional effects in skew structures with bracing of the type used in Layout 5 could be evaluated by analysing a right supported structure with a span equal to the distance between inner skew supports.

CHAPTER 5: THE CONSTRUCTION, INSTRUMENTATION AND TESTING OF THREE LINEARLY ELASTIC BIFURCATED ELEVATED HIGHWAY BOX GIRDER MODELS

5.1 INTRODUCTION

5.1.1 General

The program of construction for elevated highway structures over the next ten years involves the expenditure of a considerable amount of public money. Consequently the need to identify the analytical methods which are the most efficient in terms of accuracy, computer time, and costs from those which are already available and those which may be developed in the near future, is apparent. In particular, the special structural problems associated with elevated roads, especially in urban areas, such as decks which are sharply curved in plan, bifurcated junctions, and discrete randomly spaced supports, can only be tackled by a limited number of available computer programs, and very little experimental data exists against which the accuracy of such programs may be established.

In 1968 a joint Ministry of Transport Bridge Engineering

108

Section and Road Research Laboratory committee was formed to investigate the structural problems associated with elevated highways. The first project undertaken by the committee was the testing and verification of analytical techniques so that a working suite of programs would eventually become generally available.

The committee divided the verification work into four phases viz:-

1. Comparison of analytical techniques with results of model tests on quadrilateral decks. Three types of decks were to be considered -
   (i) Solid reinforced concrete slab
   (ii) Voided reinforced concrete slab
   (iii) Stiffened composite steel and concrete deck.
2. Comparison of analytical techniques with results of tests on four idealised, small scale, bifurcated bridge models in the linear elastic range.
3. Comparison of analytical techniques with results of tests to loads above the normal working range on four larger scale micro concrete-steel bifurcated bridge models.
4. Assessment of the results from first three phases and user testing of selected programs.

This chapter describes the manufacture, instrumentation and testing arrangement for the three models of Phase 2 of the above program which simulate different forms of box

girder construction. The fourth model is of plate girder construction and is reported elsewhere[45,58,59]. Test results for the box girder models are presented in Chapter Six.

5.1.2 Junction Layout and Forms of Construction

The models represent a bifurcated junction in a section of continuous elevated urban highway. Such a section was chosen as it incorporated many of the features which would normally not be amenable to conventional hand analytical methods. The models have identical plan layouts and span dimensions but are designed to represent alternative forms of construction. The full scale dimensions of the plan layout are shown in Figure 92. The spans and curvatures were chosen to be representative of those found in urban highway structures. The carriageway layout consists of four traffic lanes splitting into three and two lane carriageways at the bifurcation.

The four alternative forms of construction reproduced in the models are:

(i) Prestressed concrete spine box construction - Model 1

(ii) Prestressed concrete multicellular construction - Model 2

110

(iii) Composite steel and concrete plate girder construction - Model 3

(iv) Composite steel and concrete box girder construction - Model 4.

All the schemes represent viable economic alternatives for the spans considered. The three schemes described in this chapter ((i), (ii) and (iv) above) are of box girder construction, a form which lends itself particularly to curvature in plan and random support layouts on account of its high torsional stiffness.

5.2 MODEL SCALE AND MATERIALS

5.2.1 Choice of Materials

It was decided at an early stage that the most suitable materials for the construction of the models are an Araldite casting resin and sand mixture to represent concrete parts of the models and thin steel sections for steel parts of the models. The Araldite and sand material was described in detail in 2.4.

5.2.2 Model Scale

The choice of scale depended upon the following:

(i) Minimum possible thickness of materials

(ii) Minimum dimensions necessary for installation of the available instrumentation

(iii) Magnitude of loads

(iv) Size of loading and support rig in relation to grid of locating bolts on laboratory floor.

After a series of experiments with the Araldite and sand material it was decided that the most suitable scale is 1:50. The minimum Araldite and sand thickness is then 4.5 mm (0.1773 in) with a maximum sand grain size of 1.2 mm (0.0473 in). The tests showed that this material could be worked easily and that consistent elastic properties could be obtained.

112

5.2.3 Material Properties

5.2.3.1 Araldite and Sand

The matrix material is an epoxy casting resin (Araldite 219) manufactured by C.I.B.A. of Duxford, Cambridge. It consists of three parts - CY219 casting resin, a liquid of medium viscosity, HY219 hardener and DY219 accelerator, both liquids of low viscosity. These are mixed in the following ratio by weight.

	Parts by weight
Araldite CY219	100
Hardener HY219	50
Accelerator DY219	0-10 depending on desired curing time

Two parts by weight of Accelerator DY219 were used for the model material. This gives up to two hours for casting and a curing time of two days at 20°C.

The sand used was a fine builders sand passing B.S. sieve No. 14. This was mixed with the Araldite in the ratio of 4 parts sand : 1 part Araldite 219 using a small electrically powered mixer.

Test specimens were made from each of the Araldite and sand mixes used for casting the model. The specimens were of three types - tension, compression and bending. Poisson's ratio, , and Young's Modulus, E, were obtained for each of the

specimens from strain gauge readings. TML electrical resistance strain gauges manufactured by Tokyo Sokki Kenkyujo Co. Ltd. of Tokyo, with gauge lengths of 3mm and 5mm and a nominal gauge factor of 2 were used. Strain gauges were bonded to opposite sides of each specimen using a special epoxy cement (Flemming Services resin 104 and hardener 103). The longitudinal strains measured by the strain gauges were checked against readings from both Lambs and Amslers mechanical extensometers and good agreement was obtained.

Average values of E and ν for each of the four models are given in Table 10 together with confidence limits. The average density of the material was found to be 2272 Kg/m^3 (142 lb/ft^3). The stress-strain relationship is linear up to 1000 $\mu\varepsilon$ in compression and 450 $\mu\varepsilon$ in tension. Above these values the creep rate becomes appreciable. The ultimate tensile strain varies between 600 $\mu\varepsilon$ and 800 $\mu\varepsilon$ and the ultimate compressive strain is approximately 7000 $\mu\varepsilon$ at a stress of approximately 80 N/mm^2 (13000 p.s.i.).

5.2.3.2 Steel

The steel used for the manufacture of the composite models was cut from cold rolled mild steel sheet. Table 11 shows the Birmingham Gauge numbers and thicknesses of the material used. Tensile specimens were cut from each of the

114

sheets used and the elastic properties were measured in the same way as those of the Araldite and sand. Values of E and ν may be found in Table 12.

5.3 INSTRUMENTATION

5.3.1 General

The models were instrumented to measure deflections, strains and reactions. The instrumentation was concentrated at sections which were judged to be the most critical both from the magnitude and distribution point of view. In general, instrumentation was carried throughout the models so that at least one section in each span was fully instrumented and the outer spans were not used simply to provide continuity to the more interesting central bifurcated span.

5.3.2 Deflections

Previous experience at Imperial College has shown that dial gauges with a resolution of .0025 mm (.0001 in) are sufficient for measuring the deflections of this type of model. However in view of the very extensive instrumentation on the models, it was considered essential to read the deflections electronically rather than visually. Therefore special transducers were purpose made for this project by Research Models and Equipment of Twyford, Berks. They consist essentially of a 'tuning fork' arrangement of two cantilevers between which a conical plunger moves. The cantilevers have linear strain gauges on both sides and the total strain difference for the four gauges caused by

116

movement of the plunger can be converted by callibration to a deflection. The cantilevers are protected by a 12.7 mm (0.5 in) diameter tube and the complete transducer is about 76 mm (3 in) long. The transducers are wired into four arm bridge circuits in an automatic data logger (see Section 5.3.5 in such a way that total strain (in microstrain) is obtained for the four gauges. The resolution of the transducers is therefore 1 με which is approximately equivalent to a deflection of .0012 mm (.00005 in). The exact locations of transducers for the models are described in Sections 5.5.3, 5.6.2 and 5.7.3.

5.3.3 Strains

The T.M.L. electrical resistance strain gauges referred to in 5.2.3.1 were used throughout all four models for strain measurement. The gauges are of the polyester type which consists of a grid of copper-nickel alloy resistance wire on a supporting base impregnated with polyester resin. The features of this type of strain gauge are:

(i) Far better insulation than paper backed gauge, therefore measurements are stable

(ii) Easy in application and needs no pressure or heat

(iii) Moisture proof

(iv) The transparent base makes it possible to detect improper setting

(v) Heat resistant - no creep up to 80°C

(vi) Insensitive to strains perpendicular to direction of gauge.

The gauge factor is approximately 2.0 with a tolerance of ±1%. The gauge resistance is nominally 120 ohms with a maximum variation of resistance of 119.7 to 120.3 ohms.

A gauge length of 3 mm was used throughout. This is the minimum size that will not be influenced by individual sand grains situated under the gauge, and enables localised stresses to be measured so that a complete stress distribution may be obtained at any section.

Uniaxial, biaxial and triaxial gauges were used. Rosette gauges (triaxial) were used where the principal stress directions were not known, cross gauges (biaxial) were used where stresses were only required in the longitudinal and transverse directions, and linear gauges (uniaxial) were used at positions of uniaxial stress in the plate girder model. In most locations gauges were bonded to both sides of the box walls or slab in order to separate in-plane and flexural components of stress.

The adhesive used to bond the gauges to the model surface was a special gauge adhesive manufactured by Flemming Services. This consists of two parts - resin 104 and hardener 103 - which are mixed in the ratio 4:1. P.V.C. covered 10 strand, 0.1 mm miniature wire leads are used to

118

connect the strain gauges to the data logger.

5.3.4 Supports

The model supports are instrumented so that support reactions may be measured. The bearings consist of a 10 mm (0.394 in) diameter pad of 0.794 mm (1/32 in) thick neoprene rubber which is designed to allow rotation and translation in the horizontal plane. The bearing pad is bonded to the model and to a 12.7 mm (½ in) diameter disc which is brazed to the top of the support column so that both tensile and compressive reactions may be transmitted to the column. The column itself consists of a 9.52 mm (⅜ in) O.D. 22 gauge mild steel tube which is 1 inch in height. Two biaxial strain gauges are bonded to the outer surface of the column at diametrically opposite positions. A state of vertical uniaxial stress in the column produces horizontal Poisson's ratio strains and the leads from the four strain gauge elements are wired into a four-arm bridge circuit of the data logger in a similar fashion to the transducers such that the strains are additive. This gives a resolution of 1 με for the four gauges, and the support columns (together with the bearing pads) were calibrated for reaction and vertical deflection using a proving ring and transducers. This gave a calibration of approximately 1 με equivalent to a force of 17N (3.8 lbf)

and vertical deflection of .00012 mm (.00005 in). Exact calibration values were used to process the results of tests.

The base of the tubular column is brazed to a 1 in. square base plate which is bolted to the top of the support rig. The support rig itself consists of steel frames which are bolted to the laboratory floor under each pier position. The top of the support rig is 4 ft above the floor so that there is ample room for mounting vertical deflection gauges beneath the models and placing leads from the instrumentation to the data logger leaving the top surfaces of the models, which are at convenient working level, clear for the placing of loads. A general view of the support rig arrangement with one of the models in position is shown in Figure 93.

5.3.5 Data logger

Two data logging systems were used for this project - a 300 channel Solartron logger and a 500 channel Compulog. Both systems incorporate fast scanning speeds, analogue to digital conversion, print out and punch tape output so that temperature changes do not affect the measured parameter values during the scanning period. Strain gauges, transducers and support columns are permanently wired into 25 channel Amphinol plugs which are plugged into 'active' sockets in the rear of the loggers. For every 'active' gauge there is a temperature compensating dummy gauge which is bonded to a

120

similar material (Araldite and sand or steel) and kept at a constant state of strain. The dummy gauges are generally housed in boxes of 25 and then connected to the 'dummy' sockets of the logger.

The 300 channel logger was used for Model 1 (spine beam construction) and the 500 channel system, which was brought into commission during this project, was used for the remaining models. Neither system has sufficient channels to read all the gauges on any one model so it was decided to separate the gauges into two groups - main stress gauges, and secondary stress gauges - which were wired into separate plugs. The main stress gauges are key gauges at each section which provide the longitudinal extreme fibre stresses at selected points in the cross section and which were read for every load case. The gauges can be considered as recording the overall behaviour of the models. The secondary stress gauges are the remainder and provide detailed stress distributions at each section. It was only necessary to measure 'secondary' strains at sections in the region of applied loading. In this way it was possible to obtain an overall stress distribution and detailed stress distributions at key sections.

5.4 LOADING

5.4.1 Types of Loading

The following types of loading were considered:

(i) Dead weight

(ii) Uniformly distributed lane loading

(iii) HB vehicle loading

(iv) Knife edge loading

(v) Point loading

(vi) Settlement of supports

A summary of the load magnitudes may be found in Tables 13 and 14.

5.4.1.1 Dead Weight and Uniformly Distributed Lane Loading

These were both simulated by one loading arrangement. The traffic lane positions are marked out on the top surfaces of the models (dimensions in Figure 94). Loading pads were shaped to fit between the lane markings. The pads consist of 12.7 mm (½ in) plywood bonded to 3.2 mm (⅛ in) dense sponge rubber. A steel disc locates in a hole in the top of the pad and load hangers rest in a conical depression in the disc. The pads are the same width as the lanes and approximately square so that there are 11 pads along each lane of the outer spans and 16 pads along the lanes in the

122

bifurcated span (except lane 3A - see Figure 94). For any particular lane of each span the pads have the same centre line arc length so that the pad area is constant.

Loads were applied to the pads in lane-span units so that 14 load cases were necessary to cover the complete carriageway area (Figure 95). Results are presented for the scale HA uniformly distributed loading for the full scale lane lengths (Knife edge loading separately). The intensities of loading for the 14 load cases are given in Table 13. The results may be combined therefore to obtain any desired combination of lane loadings and if all the results (multiplied by suitable factors) are summed, the dead load stresses may be closely approximated.

5.4.1.2 HB Vehicle Loading

A scale simulated HB vehicle was constructed with wheel dimensions as shown in Figure 96. This was loaded with the scale HB load of 721 N (162 lbf) for which results are given. One HB loading case was carried out for each lane of each span resulting in 14 load cases for Model 1. For subsequent models one HB loading case was carried out for each outer span and four were carried out for the bifurcated span. For Model 1 the HB vehicle was placed symmetrically about the midspan of each lane of the outer spans (see Figure 97). The positions of the HB vehicle in the bifurcated span vary

for the four models because of the different web positions and are shown in Figures 97-99.

5.4.1.3 Knife Edge Loading

The knife edge consists of a steel bar, 12 mm (0.5 in) deep, 6 mm (0.25 in) wide and with a length equal to the lane width, bonded to a pad of 2 mm (.08 in) thick rubber which rests on the model. Results are presented for a model knife edge load of 222.5 N (50 lbf). The knife edge was applied to each model at four positions in the bifurcated span (see Figures 100-102).

5.4.1.4 Point Loading

The point loading pad consists of a steel disc 10 mm (0.39 in) diameter bonded to a pad of 3 mm (0.125 in) thick rubber which rests on the model. Results are presented for a model point load of 222.5 N (50 lbf). The point load positions are shown in Figures 103-105.

5.4.1.5 Settlement of Supports

This loading case is simulated by loading directly above a support column. The columns are bolted to the top of the support rig so that metal shims can be introduced below the columns. The settlement is made up of a differential

124

level of the support columns due to the shims plus the deflection of the rubber bearing pad due to loading directly above the bearing. The locations at which this procedure was carried out are shown in Figures 106-107.

5.4.2 Loading Rig

The loading rig consists of a mobile gantry which straddles the model and incorporates a hydraulic jack for lifting and placing the loads. The jack is suspended from the centre of the gantry cross member and is operated by a hand pump which is attached to one of the gantry legs. The load which is in the form of a yoke is suspended below the jack with a cord and spring linkage. As the hydraulic pressure in the jack is released the load falls gently until a conical pin below the centre of the yoke locates in a conical depression in the loading pad and the linkage becomes slack. A general view of the loading rig is shown in Figure 108.

The lane loading tests require a number of loads to be placed simultaneously. For these tests a plate, which has holes drilled directly above the centres of the loading pads, is suspended below the jack. A separate yoke is suspended via a cord and spring linkage from each hole and the complete plate is then raised or lowered by the jack.

5.4.3 Loading Procedure

Preliminary tests were carried out on each model to check the operation of the instrumentation and to establish the locations and magnitudes of critical strains so that the model would not be damaged. The instrumentation was checked by taking successive readings at zero load and checking for drift in gauge readings. Then alternate pads were loaded in lane-span units to establish the critical strain positions and from this the maximum load which could be applied to complete lane-span units, was determined. The loads which were finally used in the lane loading tests were 178N (40 lbf) per pad on the outer spans and 89N (20 lbf) per pad on the bifurcated span but results are presented for the loadings shown in Tables 13 and 14. The test loads resulted in maximum strains of approximately 400 με in the Araldite and sand.

Each load case test consisted of readings taken for the following sequence of loads:

OO LL OO LL OO

where O represents one set of readings at zero load

L represents one set of readings with the load applied to the model.

This sequence includes two complete loading cycles, readings with which drift checks can be carried out, and

126

duplicate readings in case of spurious readings due to transient electronic faults. On application or removal of the loading a period of two minutes was allowed to elapse before readings were taken. A further period of two minutes was then allowed to elapse before the second set of readings were taken and then the loading was removed or reapplied. This ensured that any time dependent effects would be exposed. A detailed explanation of the interpretation of results from this loading sequence is given in Chapter Six.

5.5 MODEL 1 - CONCRETE SPINE BEAM CONSTRUCTION

5.5.1 Manufacture of Araldite and Sand Components

The dimensions of the model are shown in Figures 109-112. The top flange, including portions of the webs down to the bottom of the top corner haunches and the bottom flange up to the top of the bottom corner haunches, were each cast in one piece and the constant thickness portions of the webs were cast separately in flat sheets which were cut to the required depth and then formed to the correct curvature. The flat strips were placed on a curved steel former which was then heated in an oven to 100^{o}C at which temperature the web strips took up the curvature of the former. The curvature of the former could be very accurately controlled by adjustment of a threaded tie bar. The web strips were weighted with bags of lead shot while cooling so that the correct shape was retained. Tests were carried out to check that the material properties were not altered by the heating process. Specimens treated in the following ways were cut from the same sheet and tested:

(i) Unheated

(ii) Heated but not curved

(iii) Heated and curved, then cooled and reheated to flatten out for testing

128

No significant difference was observed between the properties of all three specimens.

Diaphragms were also cut from a flat sheet of Araldite and sand and shaped using a compressed air driven diamond grinder.

The dimensional accuracy of all the Araldite and sand components was carefully checked before assembly of the model commenced and was found to be within $\pm$ .127 mm (.005 in).

5.5.2 Sequence of Assembly and Instrumentation

The strain gauges located inside the boxes on the top and bottom flanges were fixed in position first. The underside of the top flange is shown in Figure 113. The webs were then cut to length and clamped to the bottom flange so that the positions of instrumentation on the webs could be made coincident with those on the flange. The webs were then instrumented on both sides and, together with diaphragms, were then bonded to the bottom flange. The adhesive used was an Araldite epoxy glue consisting of AV100 resin and HV100 hardener mixed in equal parts. Photographs taken at this stage of construction are shown in Figures 114-116. These show the mass of instrumentation and wiring, and the wooden clamps and web spacers which were removed before fixing the top flange. Wires from instrumentation inside the outer spans were brought out through grooves cut in the

top of the end diaphragms and wires from the bifurcated span were brought out through grooves cut in the tops of the webs at sections away from the gauge positions. With all the internal instrumentation complete the top flange was bonded to the tops of the webs and finally exterior instrumentation was located on the flanges.

5.5.3 Layout of Deflection Gauges and Support Positions

The locations of instrumented sections are shown in Figure 117. Deflections were measured at all sections except 1-1, 4-4, 5-5, 8-8 and 12-12 which are positions where strain gauges measured web and diaphragm shears.

At support sections vertical deflections were measured directly above the support columns providing a check on the calibration of the columns, and the horizontal deflections at the lower flange level of the box were also measured.

At Sections 2-2, 5-5, 7-7, 10-10 and 14-14 sufficient deflections were measured to define the movements of the box corners. In general this consisted of vertical deflections below the web centre lines and horizontal deflections at the top and bottom flange centre line levels.

Two support columns are positioned at the extremity of each arm of the structure providing torsional restraints. Single columns only are provided at intermediate supports (Sections 3-3, 9-9 and 13-13) with no torsional restraint.

130

The philosophy behind this support layout is to make use of the high torsional stiffness of the box section to carry torsional moments to the abutments of the structure, with the result that intermediate supports need carry only vertical loads and are, therefore, simpler and consequently cheaper.

5.5.4 Layout of Strain Gauge Positions

Strains were measured at all sections shown in Figure 113 except Sections 0-0, 11-11 and 15-15. The layout of strain gauges at a typical instrumentation section is shown in Figure 118. The exact locations of all the gauges are given in Reference 45. A total of 724 strain gauge elements, (143 main stress elements and 581 secondary stress elements), were measured on this model.

Triaxial strains were measured at Section 1-1 at the mid-point of each wall to provide some indication of shear flow around each cell at this position of maximum torsional moment. Sections at the mid-point of all three outer spans were fully instrumented with biaxial gauges measuring strains in the longitudinal and transverse directions (Sections 2-2, 10-10 and 14-14). Main stress gauges are located above and below the centre lines of the webs and these give longitudinal stresses for all loading cases. Secondary stress gauges are located on both sides of each wall near the corners of

boxes giving a complete sectional distribution of longitudinal and transverse stresses near the position of maximum distortional and longitudinal stresses. Main stresses are measured at the intermediate support Sections 3-3, 9-9 and 13-13 with biaxial gauges.

The central bifurcated span is gauged more fully than the outer spans. Triaxial main and secondary stress gauges are located at Sections 5 and 6 (before and after the bifurcation) providing longitudinal, transverse, and principal stresses. These sections are mid way between diaphragms at positions of maximum cross-sectional distortion. Vertical shears are measured in the webs at Sections 4-4, 8-8 and 12-12 near the intermediate support positions. The diaphragms and webs at Section 5-5 are instrumented with triaxial gauges to determine the shear distribution before, through, and after the diaphragms so that the load distributing action of the diaphragms can be compared with that of the box sections.

132

5.6 MODEL 2 - CONCRETE MULTICELL CONSTRUCTION

The dimensions of the model are shown in Figures 119-122. Casting of the flange and web pieces was carried out in the same way as Model 1 (see Section 5.5.1). The Polyfilla mould is shown in Figure 123, the casting process is shown in Figures 124 and 125 and the underside of the cured top flange casting after extraction from the mould is shown in Figure 126.

5.6.1 Sequence of Instrumentation and Assembly

This was similar to that of Model 1 (see Section 5.5.2). It commenced by the forming of the web sections to their correct radii. The strain gauges were then bonded to the inside surface of the bottom flange and both surfaces of the webs were bonded to the bottom flange (Figure 127). The same adhesives were used as for Model 1. All the wires from the internal gauges were brought out through the ends of the model through holes in the diaphragms. The top flange was then bonded to the webs and finally the instrumentation of the underside of the bottom flange was completed (Figure 128).

5.6.2 Layout of Deflection Gauges and Support Positions

The locations of instrumented sections are shown in Figure 129. Deflections were measured at all sections except

4-4, 7-7 and 11-11 which are sections where strain gauges measured web shears. Deflection gauges were deployed in similar positions as for Model 1. At support sections vertical deflections were measured directly above the support columns and horizontal deflections were measured at the lower flange level. Elsewhere the horizontal and vertical deflections of the box were measured.

The support system is similar to that of Model 1 with twin support columns at the extremity of each arm of the structure and single columns at intermediate support sections.

5.6.3 Layout of Strain Gauge Positions

Strains were measured at all sections shown in Figure 129 except Sections 1-1, 10-10 and 14-14. The layout of gauges at a typical section is shown in Figure 130. A more detailed description of the location of instrumentation is given in Reference 45. A total of 1411 strain gauge elements (172 main stress elements and 1239 secondary stress elements), were measured on this model.

The deployment of strain gauges on Model 2 was similar to that on Model 1. Main stress gauges are located above and below selected web centre lines at all strain gauged sections except 4-4, 7-7 and 11-11. At the latter sections vertical shears are measured in the webs. Biaxial gauges are used at Sections 2-2, 9-9 and 13-13 (located at midspan

134

positions) to obtain cross sectional distributions of longitudinal and transverse stresses and triaxial gauges are similarly used at Sections 5-5 and 6-6 in the bifurcated span.

5.7 MODEL 4 - COMPOSITE BOX GIRDER CONSTRUCTION

5.7.1 Manufacture of Steelwork

The dimensions of the model are shown in Figures 131-134. The design calls for open topped steel boxes, each of which was made from seven components. The webs were made in the form of channel sections with outstands of 5 mm to which the flange plates were bonded. The web thickness of 0.508 mm was designed to satisfy the requirements of BS153 for unstiffened webs. The outstand was restricted to 5 mm by the cold rolling process used to shape the web sections to their correct radius. 5 mm by 5 mm angles of 0.508 mm thick steel were bonded to the outside of the webs at the top to carry the upper flange plates which were cut to the desired radii from flat sheets of steel. The widths of the top flange plates vary to obtain the correct flange area so that the upper surface of the boxes was kept flat for bonding to the slab. Bottom flange plates were also cut to the correct radii from flat steel sheets and the thickness was varied to obtain the desired flange area. Each complete box was made from several lengths joined together. Joins in the various components were staggered and cover plates were bonded over the join to ensure continuity. In the support sections a single longitudinal stiffener is bonded to the longitudinal centre

136

line of each box. The stiffener consists of a 3 mm x 3 mm x 0.508 mm angle. Transverse stiffeners 5 mm wide and 10 mm deep were cut from an Araldite and sand sheet and are located at 30 mm centres on the bottom flange in the support sections. Diaphragms were also cut from 5 mm Araldite and sand sheets and have 10 mm diameter holes through which wires from internal instrumentation pass.

5.7.2 Sequence of Instrumentation and Assembly

The webs, top flange angles and top flange plates, diaphragms and bottom flange stiffeners were assembled first. The adhesive used throughout this model was Devcon 101 with Devcon 'Flex' hardener mixed in the ratio Resin 101:Flex of 5:1. This adhesive gives a much higher peeling strength than ordinary Devcon 101 and is necessary for connections at the corners of the boxes where high transverse moments occur. Before the bottom flange plates and the slab were located, all the strain gauges were bonded in position except those on the upper surface of the top flange. The 4.5 mm thick slab was then clamped to a level surface with its underside uppermost and the steelwork (without bottom flange plates) was fixed in position. Wires from internal instrumentation were threaded through the holes in the diaphragms before the bottom flange plates were fixed in position. Finally the upper surface of the slab was gauged.

Figures 135-138 show Model 4 during construction. In all these photographs the steelwork was laid on the slab for visual effect and the bottom flange plates were also laid in position for Figure 138. Final fixing did not take place until the instrumentation was in position as described above. Figure 136 shows the bottom flange stiffening in the support region. Figure 137 is a close-up of the bifurcation showing how the shear from the bifurcated web is transferred by diaphragm to the webs of the central box. Figure 138 shows the bottom flange plates in position and the bottom flange cover plates in the support regions can also be seen.

5.7.3 Layout of Deflection Gauges and Support Positions

The locations of instrumented sections are shown in Figure 139. Vertical deflections are measured under each web at Sections 3-3, 5-5, 6-6 and 11-11. Horizontal deflections of the slab are measured at these sections and horizontal deflections of the bottom flanges are measured at undiaphragmed sections (6-6 and 11-11).

The support layout is similar to that of Models 1 and 2 with twin columns at the ends of each arm of the structure providing torsional restraints, and single columns at intermediate piers.

138

5.7.4 Layout of Strain Gauge Positions

Strains are measured at all sections shown in Figure 139 except 1-1, 9-9 and 12-12. The layout of strain gauges at a typical section is shown in Figure 140. A total of 603 strain gauge elements (208 main stress elements and 395 secondary stress elements) are measured on this model.

Main stress gauges measure longitudinal stresses at the box corners at all strain gauge sections. Where possible these gauges are used in conjunction with gauges on the opposite side of the box wall to measure secondary stresses. At undiaphragmed sections (2-2, 6-6 and 11-11) biaxial or triaxial (Section 6-6) strains are measured on both sides of the walls at each box corner giving a detailed distribution of longitudinal and transverse stresses.

CHAPTER SIX: RESULTS OF THE BIFURCATED ELEVATED HIGHWAY MODEL TESTS

6.1 GENERAL

The results of tests on the bifurcated elevated highways models, the manufacture, instrumentation and testing of which were described in Chapter Five, are presented in this Chapter. The testing program incorporated some 30 to 40 tests on each model and the test data and results are presented in ten reports[45,54-62] which include some 4000 diagrams. No attempt has been made to reproduce all the information in this thesis but representative diagrams which illustrate particular aspects of the structural behaviour are included. The behaviour of the models is studied with particular attention being given to the cross sectional distributions of longitudinal and transverse stresses, secondary warping, distortion of the box cross section, principal stresses, deflections and internal diaphragm behaviour.

140

6.2 ACCURACY OF RESULTS

6.2.1 Testing procedure and calculation of strains

Each load case test consisted of readings taken for the following sequence of loads (see also 5.4.3):

OO LL OO LL OO

where O represents one set of readings at zero load

L represents one set of readings with the load applied to the model.

This information is provided by the data logger in the form of punched tape which is processed by one of a number of computer programs available at Imperial College. Having read the strain data, the average strain differences for each of the two loading cycles are required. This process is illustrated by Figure 141. The values of each pair of readings (e.g. OO or LL) are compared and the average values are printed out (e.g. O, L, etc.) and where differences occur they are categorised and printed out. For these tests, drift limits of 5 $\mu\varepsilon$ and 20 $\mu\varepsilon$ were used so that the gauge numbers of strain gauge elements that drifted between 5 $\mu\varepsilon$ and 20$\mu\varepsilon$, and those that drifted more than 20$\mu\varepsilon$, on any pair of readings, were listed. The mean values of the averages of the first and second pair of zeros were

then taken and printed out (O_I) together with drifting gauge numbers. These mean values were subtracted from the average of the first pair of loads ($L_1 - O_I$) to give the factored strains (ε_I) for the first load cycle. A similar procedure was followed for the second and third pairs of zeros (O_2 and O_3) and the second pair of loads (L_2) so that the factored strains for the second loading cycle were obtained (ε_{II}). The factored strains (ε_1 and ε_{II}) were then multiplied by the gauge factor to obtain the actual strains which were used to calculate stresses.

6.2.2 Analysis of strain gauge faults and drifting

Before results were plotted the readings from gauges which drifted more than 20 με were rejected. Almost invariably any particular gauge only drifted on one of the loading cycles in which case the results from the other loading cycle were used, but in the small number of cases where this was not possible the model was retested. If gauges failed during the tests in general they were replaced but if this was not possible notes to this effect are attached to the results diagrams.

The maximum error due to drift for a gauge drifting between 5 and 20 με on successive scans at the same load or on averages of successive pairs of zero readings can be

142

shown to be 14 με and the maximum error due to drift for a gauge drifting both on successive scans and successive zeros is 21 με. Maximum measured strains were of the order of 400 με.

6.2.2.1 Analysis of strain gauge faults for Model 1

Out of a total of 580 strain gauge elements on this model, two failed and could not be replaced. The results of four of the lane loading tests were chosen at random and an analysis was made of drifting. It was found on average that 1.2% of gauges drifted between 5 με and 20με on successive readings at the same load, 2.3% of gauges drifted between 5 με and 20 με on averages of successive pairs of zero readings and only 0.7% drifted on both successive readings and the averages of successive pairs of zero readings. The results of six of the other tests (three HB, two point load, and one knife edge) were also scrutinised for gauge drifting and it was found on average that the corresponding figures were 0.75%, 2.61% and 0.61% respectively.

6.2.2.2 Analysis of strain gauge faults for Model 2

Out of a total of 1239 strain gauge elements on this model, three failed and could not be replaced. Similar checks to those described in 6.2.2.1 for Model 1 were carried

out and resulted in the following figures:

For lane loading:

1.6% of gauges drifted on successive readings at the same load

3.1% of gauges drifted on the averages of successive pairs of zeros

0.9% of gauges drifted on both successive readings and successive pairs of zeros.

For HB, point and knife edge loads, the figures were 0.9%, 3.4% and 0.4% respectively.

6.2.2.3 Analysis of strain gauge faults for Model 4

Out of a total of 394 strain gauge elements on this model, three failed and could not be replaced. Similar checks to those described in 6.2.2.1 for Model 1 were carried out and resulted in the following figures:

For lane loading:

0.9% of gauges drifted on successive readings at the same load

18.3% of gauges drifted on the averages of successive pairs of zeros

0.3% of gauges drifted on both successive readings and successive pairs of zeros.

144

For HB, point and knife edge loads, the figures were 0.7%, 18.8% and 0.2% respectively. In view of the large number of gauges drifting on the averages of successive pairs of zeros a further analysis of these results was made which showed that only 1.8% of gauges drifted between 10 με and 20 με on the averages of successive pairs of zeros.

6.2.3 Support reaction checks

The sum of the measured reactions was compared with the total applied load. For Model 1, the maximum error in reactions was 4.6% for Load case 9 and the average error for all load cases was 2.2%. 4.6% represents an average error of 2 με per support column. For Model 2, the maximum error in reactions was 5.8% for Load case 8 and the average error was 2.5%. 5.8% represents an average error of less than 3 με per support column. For Model 4, the maximum error in reactions was 4.3% for Load case 8 and the average error was 1.6%. 4.3% represents an error of less than 2 με per support column.

6.2.4 Moment equilibrium checks

The average stress values were checked at several sections by comparing the moment calculated from the stress results with the moment calculated from the reactions and applied loading.

6.2.4.1 Moment equilibrium checks for Model 1

The moment at midspan AB for Load case 1 calculated from the reactions given in Figure 142 and the applied loading is 40858 N.mm. and the moment calculated from the longitudinal stresses given in Figures 143 and 144 is 40044 N.mm which represents an error of 2%. The moment at midspan AB for Load case 20 calculated from the reactions given in Figure 145 is 85282 N.mm. and the moment calculated from the longitudinal stresses given in Figure 146 and 147 is 86651 N.mm. which represents an error of 1.6%. Similar checks were carried out for several load cases and the average error was found to be 2.9%.

6.2.4.2 Moment equilibrium checks for Model 2

The moment at midspan AB for Load case 1 calculated from the reactions given in Figure 148 is 37839 N.mm. and the moment calculated from the longitudinal stresses given in Figures 149 and 150 is 38159 N.mm. which represents an error of 0.85%. The moment at Instrumentation Section 5 for Load case 22 calculated from the reactions given in Figure 151 is 57616 N.mm. and that calculated from the longitudinal stresses shown in Figures 152 and 153 is 59014 N.mm. representing an error of 2.4%. A number of similar checks were carried out at other sections and the average error was found to be 2.5%.

146

6.2.4.3 Moment equilibrium checks for Model 4

Equilibrium checks were carried out for Load cases 1 and 16 on this model. For Load case 1 at Section 3 the moment calculated from the reactions of Figure 154 is 34969 N.mm. and that calculated from the longitudinal stresses of Figure 155 is 36441 N.mm. which represents an error of 4.21%. For Load case 16 at Section 3 the moment calculated from the reactions of Figure 156 is 98525 N.mm. and that calculated from the longitudinal stresses of Figure 157 is 103273 N.mm. representing an error of 4.8%

6.3 PRESENTATION OF RESULTS

Stress and deflection results are presented in the form of cross sectional plots produced by a computer program which makes use of the various plotting facilities of the University of London and Imperial College Computer Centres. The program draws a line skeleton of the cross section, plots the stresses at strain gauge positions in graphical and numerical form and writes titles, figure numbers, etc.

6.3.1 Plotting scales and units

The cross section is plotted to a scale of 0.52 full size which was convenient for the paper size and means that figure heights are exact multiples of plotter increments. Stresses are plotted to a scale of 10.41 mm = 1 N/mm^2 for stresses in the Araldite and sand material and 10.41 mm = 10 N/mm^2 for stresses in the steel parts of Model 4. Deflections are plotted to 52 times full scale. These scales should not be used to calculate stress and deflection values as there is a slight magnification of the diagram during reproduction. The numerical values of all stress and deflection results are given on the diagrams, stresses being given in N/mm^2 units and deflections in millimetres. Support reactions are plotted on a plan drawing of the

148

model adjacent to the support positions and numerical values of the reactions are given in Newtons above the vertical support deflection in millimetres (negative values denote uplift).

6.3.2 Description of result diagrams

At each strain gauged section several diagrams are used to show the results, each showing a different type of stress or stress component. The system of main and secondary stress gauges was described in Chapter Five and the result of this system is that only longitudinal stresses are plotted at key points at the majority of cross sections for each load case. At sections in the region of the applied load a more detailed distribution of longitudinal and transverse stresses, and in some cases principal and shear stresses, is plotted.

6.3.2.1 Figures showing longitudinal stresses at extreme fibres

The main stress gauges are located on the centre lines of each of the webs. Longitudinal main stresses are calculated from longitudinal and transverse strains and are plotted on vertical lines extending above and below the webs. Stress results are joined with straight lines, the only purpose of which is to emphasize the overall stress distribution. The sign convention is that given in 6.3.2.5.

6.3.2.2 Figures showing in-plane and flexural components of longitudinal and transverse stresses

Where gauges are located on both sides of the box walls, in-plane and flexural components of longitudinal and transverse stresses are calculated. The in-plane component of longitudinal stress is equivalent to the longitudinal stress at the centre of the wall. The flexural component of longitudinal stress includes the effects of stress gradient due to eccentricity from the neutral axis, the effects of secondary warping and those of local bending under applied loading. Transverse stresses are joined by straight lines which are linearly extrapolated to the flange-web intersections where discontinuities occur. The sign convention is that given in 6.3.2.5.

6.3.2.3 Figures showing principal stresses, maximum shear and the direction of maximum principal stress, and figures showing transverse or vertical shears

At each secondary stress rosette (triaxial) strain gauge position results are plotted for gauges on the positive surface of each wall as defined in 6.3.2.5. Four results are given for each gauge and these are listed as follows:

150

Maximum principal stress	σ_1
Minimum principal stress	σ_2
Maximum shear stress	τ_{12}
Clockwise angle from diagonal element direction to direction of σ_1 (in degrees)	θ_1

The magnitudes of transverse or vertical shear stresses are plotted adjacent to the strain gauge position.

6.3.2.4 Figures showing deflection

The horizontal and vertical deflections of the corners of the boxes are plotted using the scales given in 6.3.1. Deflections are plotted relative to the undeflected cross sectional profile which is shown on the diagrams. The deflected positions of the box corners are joined by straight lines which have no meaning other than to emphasize corner deflections. Figures adjacent to the deflected position of the box corners give the magnitudes of the deflections in millimetres, the vertical deflection value being given above the horizontal value.

6.3.2.5 Sign convention for stress diagrams

Tensile stresses are positive, compressive stresses are negative. Positive stresses are plotted outside the

boxes and above the top flange. For internal webs in the twin cell sections of Model 1 and throughout Model 2, positive stresses are plotted to the right of the web (i.e. on the inside of the curve).

152

6.4 RESULTS OF TESTS ON MODEL ONE - SPINE BEAM MODEL

Results were obtained for fourteen lane loading cases, thirteen HB loading cases, four knife edge and six point load cases. The simulated HB vehicle was placed symmetrically about midspan in each of the outer span lanes and symmetrically about strain gauge (S.G.) section 5 in each lane of the bifurcated span. The results of each HB loading case can be related to those for uniformly distributed loading in the same lane. The magnitudes of stress caused by HB loading are generally higher than those caused by uniformly distributed loading because the loads are higher but the general structural response is much the same for both types.

6.4.1 Overall behaviour

The overall behaviour is studied using the longitudinal main stress gauge results. The most noticeable feature of these results is the very good transverse distribution of eccentric loads that is obtained by the box section by virtue of its high torsional stiffness (e.g. Figs. 158 and 159).

The results for each of the outer spans, which are circular in plan, illustrate the effect of curvature on the stress levels. In all cases when the load is on the

inside of the curve the maximum longitudinal stresses are greater than when the load is on the outside of the curve (e.g. Fig. 143 c.f. 158, 160 c.f. 161, and 162 c.f. 146). This phenomenon is caused by the distortional warping stresses due to the radial component of the bending moments which are additive to the longitudinal stresses when the load is applied above the inner web (see 2.4).

Intermediate piers (B, C_1 and C_2) have a single support column under the longitudinal centreline of the structure. At Pier B a main stress gauge is located on the longitudinal centreline of the compression flange adjacent to the support position. In several cases this gauge measures a tensile stress (e.g. Fig. 163) and in all other cases the gauge measures a much lower compressive stress than the gauges located on the underside of the outer webs. This is partly due to the position of the gauge which is slightly offset from the centreline of the pier and also due to the Poisson effect from transverse bending of the support diaphragm. Gauges on the cantilevers of the tension flange measure lower longitudinal stresses than those above the diaphragm due to the effects of shear lag.

The maximum measured longitudinal stress for the lane loading cases is 1.735 N/mm^2 for Load case 9 (Fig. 164) and for the HB loading cases the maximum is 3.829 N/mm^2 for Load case 38 (Fig. 165).

154

6.4.2 Distribution of longitudinal stress

A detailed cross sectional distribution of longitudinal stress is obtained at loaded sections from the secondary strain gauge readings. Secondary stress gauges are located on the box walls adjacent to web-flange intersections. The main stress gauge results showed a good transverse distribution of stress with a gradual reduction in magnitude away from the loaded lane. Secondary gauge results while exhibiting this overall behaviour also show a localised increase in stress across the width of each web in a direction away from the load and a rapid decrease in stress in between webs. When the stress points across the width of the flanges are joined by straight lines, the values obtained on the web centrelines agree closely with those measured by the main stress gauges (e.g. Figs. 143 and 144). The phenomenon which causes the increase in stress across the webs is that of secondary warping[63] and occurs when the wall thickness is not extremely small compared with the depth of the box. A secondary stress system develops which has a linear variation of normal stresses over the wall thickness. Shears perpendicular to the wall are produced and a secondary warping torque develops. The maximum stress values measured on the flanges adjacent to the webs can be appreciably larger than the values on the web centreline (e.g. Load

case 1 maximum value on web centreline 0.971 N/mm^2, value on flange adjacent to web 1.144 N/mm^2 representing an increase of 17.8%) and as the web centreline values are those obtained by conventional analysis methods (e.g. grillage, finite element 'shell' analysis) which treat the structure as thin walled, this behaviour may be significant.

Secondary stress gauges are located on both surfaces of the box walls at each strain gauge location and therefore it has been possible to separate longitudinal and transverse stresses into in-plane and flexural components. The in-plane component represents the value of stress at the middle plane of each wall and the flexural component includes the effects of secondary warping and that of eccentricity from the neutral axis of bending. For example, consider Figures 166 and 167. Fig. 166 shows the smooth transverse distribution of the in-plane component whereas Fig. 167 shows the change in sign of the flexural component across the width of the webs caused by the secondary warping.

For the lane loading cases, longitudinal stresses are greatest when the central span (BC) is loaded and the maximum measured longitudinal stress (1.749 N/mm^2) occurs at S.G. Section 6 for Load case 9 (Fig. 168). The maximum stress in span AB (1.144 N/mm^2) occurs when the inside lane is loaded for Load case 1 (c.f. 0.607 for Load case 4, Figs. 144 and 169)

156

6.4.3 Transverse stresses

Transverse stresses measured by secondary strain gauges are also separated into in-plane and flexural components. The measured in-plane transverse stresses are all very low as might be expected away from support diaphragms but flexural stresses are large and of the same order as longitudinal stresses. The flexural stresses arise from two effects. Loads applied to the deck between webs are transferred to the webs of the boxes by flexure and this induces transverse moments in the webs and bottom flanges and hence transverse stresses. Other stresses are caused by the resultant loads acting above the webs producing differential deflection of the webs and distortion of the cross section. This cross sectional distortion also produces transverse flexural stresses.

Curvature of the outer spans has a similar effect on transverse stresses to its effect on longitudinal stresses described in 6.4.1. Transverse stresses are significantly higher when the inside lane is loaded (e.g. Load case 1 (inside lane) $\sigma_{DB} = 1.208$ N/mm^2 (Fig. 170), Load case 4 (outside lane) $\sigma_{DB} = 0.864$ N/mm^2 (Fig. 171).

Maximum transverse bending stresses for lane loading occur at Section 1 for Load case 1 (1.208 N/mm^2, Fig. 170). Stresses in spans C_2D and C_1E are much lower (maximum 0.456 N/mm^2, Fig. 172) and the maximum stress σ_{DB} in the

bifurcated span occurs at S.G. Section 6 for Load case 9 (0.869 N/mm^2, Fig. 173). Maximum transverse stresses caused by HB loading also occur at Section 1 (3.526 N/mm^2 for Load case 15, Fig. 174). The maximum HB flexural stress in Span BC is 1.389 N/mm^2 for Load case 29 (Fig. 175).

Load cases in the bifurcated span produce significant transverse stresses in the deck slab between the boxes near the bifurcation. The maximum occurs for Load case 29 at S.G. Section 6 (2.267 N/mm^2, Fig. 176).

Rapid changes in transverse moments also imply high vertical shearing forces (not measured) in the slab between the boxes.

Where loads are applied to the cantilever parts of the deck, transverse stresses are measured near the cantilever root. Similar values are obtained for each lane loading case (e.g. Load case 1: 0.772 N/mm^2 (Fig. 170), Load case 10: 0.701 N/mm^2 (Fig. 177), Load case 12: 0.730 N/mm^2 (Fig. 178).

6.4.4 Shear stresses

Vertical shear stresses are measured in the webs of the bifurcated span adjacent to intermediate support diaphragms. At Support B the distribution of shear between the webs is influenced by the complex geometry of the bifurcation and no consistent overall pattern emerges.

158

For example for Load case 5 (inside lane loaded, Fig. 179) the shear stress in the inside web is approximately double that in the centre web whereas for Load case 9 (outer lane loaded, Figure 180) all three webs have similar shears but the inner web has the largest shear of the three. At Supports C_1 and C_2 the shear distribution between webs reflects the loading position and shears of opposite sign are obtained at Support C_1 for Load cases 5, 6 and 7 (Figs. 181-183) and at Support C_2 for Load case 9 (Fig. 184)

6.4.5 Internal diaphragm behaviour

The internal diaphragm at S.G. Section 4 was extensively strain gauged on both faces and gauges were also placed on the longitudinal webs on both sides of the diaphragm. Where eccentric loads are applied to the inner cell and no loads are applied above the diaphragm (e.g. Load cases 5, 8 and 9), the principal action of the diaphragm is to resist distortion of the cross section and the principal stresses are obtained on the diagonals of the box with maximum shears acting in the vertical and horizontal directions. For example, Figure 185 (Load case 5) shows that the angle that the maximum positive principal stress makes with the diagonal strain gauge element is very near 0^{o} or 90^{o} for all gauges and therefore the maximum shears which

occur at 45° to the principal stress direction are parallel to the box walls. The directions and magnitudes of the principal stresses given in Figure 185 are illustrated in Figure 186. Vertical shears are of similar value at the bottom and at mid height of the diaphragm.

Where loads are applied directly above the diaphragm the bearing stresses change the direction of the principal stresses and the direction of the maximum compressive principal stress rotates towards the vertical.

6.4.6 Principal stresses in Span BC

Triaxial strain gauges were used at S.G. Sections 5 and 6 in order to define the directions of principal stresses in the region of the complex geometry of the bifurcation. Results show that the directions of principal stresses in the box under the loaded lane approximate closely to the longitudinal and transverse directions. The directions of principal stresses in the unloaded box do not agree as closely with these directions but the maximum longitudinal stresses obtained at each point in the flanges at S.G. Sections 5 and 6 agree closely with the greatest principal stresses at these points (e.g. for lane loading maximum longitudinal stress at S.G. Section 6 = 1.749 N/mm^2 (Figure 168), greatest maximum principal stress = 1.749 N/mm^2

160

(Figure 187); for HB loading, maximum longitudinal stress at S.G. Section 5 = 3.806 N/mm^2 (Figure 188), greatest maximum principal stress = 3.835 N/mm^2 (Figure 189)).

6.4.7 Deflections

Horizontal and vertical deflections are plotted for loaded spans at S.G. Sections at midspan of the outer spans and at S.G. Sections 5 and 6 of Span BC. Horizontal deflections are generally low due to the considerable transverse stiffness of the flanges bending in their own planes, and where distortion of the cross section occurs it is largely confined to the vertical direction with the webs remaining parallel to the vertical (e.g. Figure 190).

The maximum vertical deflections of the outer spans are measured under the outer webs when the outer lanes are loaded (e.g. Figures 191, 192) whereas maximum longitudinal and transverse stresses occur when inner lanes are loaded (see 6.4.1). The exaggerated deflection scale emphasises the distortion of the cross section and shows that the changes in length of diagonals of the boxes are greatest for cases when inside lanes are loaded.

8 Local effects due to HB loading

Local bending of the deck occurs in the vicinity of HB vehicle due to the concentrated nature of the ling. Where the load is applied to the cantilever, gitudinal hogging moments are produced in the centre he vehicle, giving tensile stresses on the top surface. ome cases these stresses are larger than the compressive esses in the deck due to overall bending of the section g. Fig. 193 longitudinal tensile stress of 0.651 N/mm^2 the cantilever). Transverse bending stresses in the tilevers are also produced, the maximum measured value ng 2.504 N/mm^2 for Load case 20 (Fig. 194).

Longitudinal and transverse moments occur in the top ges of the boxes when the load is applied between the s. Again longitudinal hogging moments are produced at centre of the vehicle giving reduced total longitudinal esses on the top surface (e.g. Fig. 195) and transverse ging moments are produced in the top flange midway een the webs.

.9 Knife edge and point loading test results

Four knife edge loading cases were tested (load cases 9) and results are presented for a load of 222.5 N (50 lb).

162

The loads were applied above S.G. Section 5 which is approximately at midspan BC. The results when suitably scaled may be added to the uniformly distributed lane loading results described in 6.4.1 to obtain full HA loading for Span BC. Maximum longitudinal stresses are obtained at the tip of the cantilever for Load case 49 (-1.898 N/mm^2, Fig. 196) and maximum transverse stresses occur at the root of the cantilever for load case 46 (2.078 N/mm^2, Fig 197).

A series of six point load cases was tested (load cases 54-59, Fig.103) and results are presented for a load of 222.5 N (50 lb). The results again demonstrate the good load distribution properties of the boxes (e.g. Fig. 198). High local stresses arise due to longitudinal and transverse bending of the deck under the concentrated load especially for load cases 55 and 58 where the load is placed midway between webs. For load case 55 the maximum longitudinal stresses of -3.024 N/mm^2 occurs directly under the load (Fig. 199) and the transverse flexural stress at this location is 4.311 N/mm^2 (Fig. 200). Where the load is applied above the webs transverse distortional bending stresses are obtained in the box walls (e.g. 1.118 N/mm^2 for Load case 59, Fig. 201) and Load cases 57 and 59 produce local longitudinal bending of the deck and high longitudinal stresses near the top of the webs (e.g. Fig. 202).

6.5 RESULTS OF TESTS ON MODEL 2 - MULTICELLULAR MODEL

Several aspects of the structural behaviour of the spine beam model (Model 1) described in 6.4 are also exhibited by the multicellular model. These points, as illustrated by Model 2, are summarised below, together with a more detailed description of those aspects of the behaviour peculiar to this model.

6.5.1 Overall behaviour

The results of the tests on this model also display the very good transverse distribution of eccentric loads obtained with the closed section (e.g. Figures 203, 204).

The results for the outer spans illustrate the effects of curvature on the stress levels. For Spans AB and C_1E, when the load is on the inside of the curve the maximum longitudinal stresses are greater than when the load is applied to the outside of the curve as was also described in 6.4.1 for Model 1 (e.g. for Model 2, Figs. 149 c.f. 205 and 206 c.f. 207). For Span C_2D stresses are approximately equal for loads applied to the inside and outside of the curve (e.g. Figs. 208 c.f. 209). However Span C_2D differs from the other outer spans in that in C_2D the outer lane is above a cantilevered part of the

164

deck which therefore has a greater eccentricity from the shear centre than the inner lane. In this span, the higher longitudinal stresses, which are normally obtained by loading in the inside lane and which are caused by the addition of distortional warping stresses induced by the radial component of the bending moment, are offset by the higher torsional moments obtained when loading is on the outer lane.

The maximum longitudinal stress caused by the lane loading cases and measured by the main stress gauges is 1.581 N/mm^2 for Load case 5.

6.5.2 Distribution of longitudinal stress

The secondary warping behaviour described in 6.4.2 is also displayed by the secondary stress results for Model 2. The maximum stress values measured on the flanges adjacent to the webs can be appreciably larger than the values on the web centre lines (e.g. Load case 37, maximum value on the web centreline = 3.582 N/mm^2, value on flange adjacent to web = 4.487 N/mm^2, representing an increase of 25.3% (Figs 210, 211); maximum value on the web centre line for all tests = 4.701 N/mm^2 for Load case 35 and the maximum value on the flange = 6.172 N/mm^2 representing an increase of 31.1% (Figs. 212, 213)). The separation of longitudinal stress in the box

walls into in-plane and flexural components demonstrates that the secondary warping stresses have a flexural distribution across the wall thickness (e.g. Figs. 214, 215).

6.5.3 Transverse stresses

Transverse stresses measured by secondary strain gauges are also separated into in-plane and flexural components. Measured in-plane stresses are generally low and the maximum value is of the order of thirty per cent of the flexural component. Flexural stresses are large and of the same order as longitudinal stresses.

Curvature of the outer spans has a similar effect on transverse stresses to its effect on longitudinal stresses described in 6.5.1. Transverse stresses in Spans AB and C_1E are significantly higher when the inside lane is loaded (e.g. Load case 1 (inside lane) σ_{DB} = 1.421 N/mm^2 (Fig. 216), Load case 4 (outside lane) σ_{DB} = 0.970 N/mm^2 (Fig. 217)). Loading on the outer lane of Span C_2D produces maximum transverse stresses because of the greater eccentricity of this lane from the shear centre.

For lane loading the maximum measured transverse flexural stress occurs at Section 13 for Load case 12 (1.558 N/mm^2, Fig. 218) for loading applied above the cantilever. The maximum transverse flexural stresses

166

in Spans AB and C_1E are 1.421 N/mm^2 (Fig. 216) and 1.259 N/mm^2 (Fig. 219) respectively. In the bifurcated span (BC) transverse stresses are measured at Sections 5 and 6 and for all load cases except Load case 7, which consists of loading only over part of the span, the maximum stresses occur at Section 5, the overall maximum being 1.151 N/mm^2 for Load case 5 (Fig. 220).

For HB loading the maximum transverse bending stresses occur at Instrumentation Section 13 for Load case 35 (6.452 N/mm^2, Fig. 221). The maximum flexural stress in the boxes of the bifurcated span occurs at Instrumentation Section 6 for Load case 22 (4.359 N/mm^2, Fig. 223).

Load cases in the bifurcated span produce significant transverse stresses in the deck slab between the boxes near the bifurcation. The maximum occurs for Load case 27 at Instrumentation Section 6 (2.766 N/mm^2, Fig. 224). Significant transverse in-plane stresses also occur in the slab at the bifurcation (1.25 N/mm^2 Fig. 225).

6.5.4 Principal stresses in Span BC

Results show that the directions of principal stresses in the cells under the load approximate closely to the longitudinal and transverse directions, as was observed for Model 1. The directions of principal stresses in

the unloaded cells do not agree as closely with these directions but the maximum longitudinal stresses obtained at each point in the flanges at Instrumentation Sections 5 and 6 agree closely with the greatest principal stresses at these points (e.g. maximum longitudinal stress at Section 6 = 3.897 N/mm^2, Fig. 226; maximum principal stress = 3.899 N/mm^2, Fig. 227).

6.5.5 Deflections

Horizontal deflections are largely restricted by the high in-plane bending stiffnesses of the flanges. Where distortion of the cross section does occur it is mainly confined to the vertical direction with the webs remaining parallel to the vertical (e.g. Fig. 228).

6.5.6 Local effects due to HB loading

Local bending of the deck occurs in the vicinity of the HB vehicle due to the concentrated nature of the loading. Local bending effects are minimised by the close spacing of the webs which restricts the number of wheel loads on any one axle acting above a cell to two. Where the HB vehicle is situated partly on the cantilevered section of the deck for Load case 35, high transverse bending stresses are induced at the root of

168

the cantilever and the transverse distortional stresses in the adjacent cells are the maximum obtained throughout the structure (6.452 N/mm^2, Fig. 221).

6.5.7 Knife edge and point loading test results

Four knife edge loading cases were tested (Load cases 50-53) and results are presented for a load of 222.5N (50 lbf). The loads were applied above Instrumentation Section 6 which is at the bifurcation of the top flange. Local effects are obtained in the top flange under the knife edge where maximum longitudinal stresses result (-2.566 N/mm^2, Fig. 229). High transverse flexural stresses occur in the slab at the bifurcation for Load case 51 (1.872 N/mm^2, Fig. 230) and the maximum transverse bending stress in the cell walls is also produced by this loading case (2.374 N/mm^2, Fig. 230).

Four point load cases were tested (Load cases 60-63) and results are presented for a load 222.5N (50 lbf). High local stresses arise due to longitudinal and transverse bending of the deck under the concentrated load, especially for Load case 62 where the load is placed on the cantilevered part of the section at the bifurcation. The maximum measured longitudinal stress of 6.429 N/mm^2 (Fig. 231) occurs under the load and the transverse flexural stress at this location is 8.221 N/mm^2 (Fig. 232). The high local stresses alter

the principal stress directions in the vicinity of the loading in the top flange and the maximum measured principal stress is -10.680 N/mm^2 (Fig. 233).

6.5.8 Support settlement results

Two support settlement cases were considered - Load case 86 which is the settlement of the inner support at Pier A, and Load case 87 which is the settlement of Pier C_2. For Load case 86, results are presented for a support settlement of 2.03 mm (0.08 in) which was achieved by removing a 2.54 mm (0.1 in) packing piece from beneath the support column and applying a load of 845N (190 lbf) directly above the column. Load case 87 results are presented for a support settlement of 1.52 mm (0.06 in) which was achieved by removing a 1.52 mm (0.06 in) packing piece from beneath the column and applying a load of 356N (80 lbf).

For Load case 86 the maximum longitudinal stress measured on the web centreline occurs at Section 6 (2.256 N/mm^2, Fig. 234). Secondary stress gauge measurements were taken for Section 2 and the results exhibited the secondary warping phenomenon referred to in Section 4.1 (Figs. 235 and 236).

For Load case 87, main stress gauges and deflections

170

only were measured. Maximum longitudinal stresses occurred at Pier C_2 (3.318 N/mm^2, Fig. 237) and high longitudinal stresses were obtained at Sections 6 (2.096 N/mm^2), 8 (1.993 N/mm^2) and 13 (2.082 N/mm^2). The maximum vertical deflection was obtained at Section B (1.208 mm, Fig. 238) and an upwards deflection resulted at Section 2 (-0.358 mm, Fig. 239).

6.6 RESULTS OF TESTS ON MODEL 4 - COMPOSITE MULTIBOX MODEL

6.6.1 Overall behaviour

The overall behaviour exhibited by the main stress gauge results varies significantly between the different spans due to the different diaphragming arrangements. Indeed, the original choice of diaphragm spacing was made to study the effects of having different numbers of diaphragms in each of the three outer spans which are otherwise fairly similar. Span C_2D has no internal diaphragms, Span AB has internal diaphragms at midspan, and Span C_1E has internal diaphragms at the quarter points. A marked improvement in load distribution is achieved with increasing numbers of diaphragms. If the average stress in the bottom flange at midspan of a box is taken as an indication of the load carried by that box the transverse distribution of eccentric loading can be compared quantitatively as shown in Table 15. The table is arranged with the results for the outer span having the smallest number of diaphragms at the top with results for spans having increasing numbers of diaphragms listed below. Although Span BC does not consist of a single circular curve the results obtained in this span support those from the circular spans to a large extent. Results for the two loading cases with the

172

greatest eccentricities are shown for each span with the results for the innermost lane shown above those for the outermost lane. With an increasing number of diaphragms there is a significant decrease in the percentage of the total load carried by the loaded box and a corresponding increase in the percentage of the total load carried by the box adjacent to the loaded box. Because the number and spacing of boxes is not the same for each span the percentage of load in the loaded box carried by the adjacent box has also been calculated to obtain an assessment of load distribution. These figures show a marked increase from a minimum of 11.7% for Span C_2D (no internal diaphragms) to a maximum of 77.9% for Span C_1E (three internal diaphragms). A comparison of the cross sectional distributions of longitudinal stresses for these loading cases confirms the improvement in transverse distribution (Figs. 240 and 241).

Longitudinal stresses are measured at two Instrumentation Sections (5 and 6) in Span BC. Instrumentation Section 5 coincides with internal diaphragming and Section 6 is midway between diaphragms. Results at both sections exhibit the good distribution obtained with the diaphragmed box section (Figs. 242-245) with approximately fifty per cent of the total load carried by the loaded box. The maximum longitudinal steel stress in Span BC (37.18 N/mm^2)

occurs at Section 6 for Load case 73 (Fig. 246) and the maximum slab stress is -3.324 N/mm^2.

The overall maximum longitudinal steel stress occurs in Span C_2D at Section 11 for Load case 32 (90.00 N/mm^2, Fig. 248), where the maximum longitudinal slab stress is -8.60 N/mm^2. High warping stresses also occur in Span C_2D due to the action of loads in the bifurcated span (e.g. Fig. 249).

6.6.2 Warping stresses, σ_W

Warping stresses are calculated by subtracting the average longitudinal extreme fibre stress on the flange (σ_B) from the stress at the edge of the box. Warping stresses are included in Table 15 and are non-dimensionalised against σ_B. σ_W/σ_B is tabulated for the loaded box and also for the box adjacent to the loaded box. A marked reduction in σ_W/σ_B is obtained with an increasing number of diaphragms from a maximum of 334.9% for Load case 10 on Span C_2D (Fig. 240) to a corresponding value of 19.2% for Load case 14 on Span C_1E (Fig. 241). The maximum longitudinal stress of 32.185 N/mm^2 in Span C_2D compares with a maximum of 20.812 N/mm^2 in Span C_1E although maximum values of σ_B are 18.25 N/mm^2 for Span C_2D and 18.500 N/mm^2 for Span C_1E.

174

Warping stresses are measured at two sections in Span AB (2 and 3) and it is of interest to observe how σ_W changes sign between the two sections (Figs. 250 and 155). The distributions of longitudinal stresses at Section 2 show a smooth decrease in stress away from the load in the transverse direction and warping stresses are smaller than those at Section 3 where rapid changes in distortional deflection (W_D) occur due to the prescence of the diaphragms. The rapid changes in deflection are accompanied by high curvatures and hence high values of σ_W (proportional to $\partial^2 W_D/\partial x^2$).

6.6.3 Effects of curvature on longitudinal stresses

The effect of curvature on the stress levels in the outer spans is also illustrated by Table 15. For each span, results for loading on the innermost lane are tabulated above those for loading on the outermost lane. In all cases the warping stresses, and hence maximum longitudinal stresses, are significantly greater when the innermost lane is loaded. When the loading is applied above the inside lane the distortional warping stresses caused by the radial component of the longitudinal stresses are additive to the ordinary warping stresses and when the loading is applied above the outside lane the two stress systems are of the opposite sense (see 2.4).

6.6.4 Transverse stresses in the steel boxes

In-plane components of transverse stress are generally low and only of significance where bearing stresses occur in the webs due to superimposed loading. Flexural stresses σ_{DB} are high and of the same order as maximum longitudinal stresses.

Transverse stresses in the boxes are measured at Section 2 in Span AB, at Section 6 in Span BC and at Section 11 in Span C_2D. A comparison of the results for lane loading on the different spans illustrates the effect

176

of diaphragm spacing on the transverse stress levels. In Span C_2D which has no internal diaphragms the maximum stress is 46.384 N/mm^2 (Fig. 251), in Span AB with one internal diaphragm per box the maximum stress is 17.696 N/mm^2 (Fig. 252) and in Span BC a maximum value of 5.472 N/mm^2 (Fig. 253) is obtained.

Curvature of the outer spans has a similar effect on transverse stresses to its effect on warping stresses described in 6.6.3. Transverse stresses are significantly higher when the inside lane is loaded (e.g. Load case 1 (inside lane) σ_{DB} = 17.696 N/mm^2 (Fig. 252), Load case 4 (outside lane) $\sigma_{DB\ max}$ = 9.483 N/mm^2 (Fig. 254).

Transverse flexural stresses measured at Section 6 in the bifurcated span are of a different pattern from those measured in the outer spans and at first sight there does not appear to be moment equilibrium at the bottom corners of the box. The measured stresses are very low and it is possible that this is due to local effects induced by the corner detail of the box which are over-shadowed by the much higher transverse distortional stresses in the outer spans. The maximum flexural component of transverse stress occurs for Load case 32 at Section 11 (135.0 N/mm^2, Fig. 255).

6.6.5 Transverse stresses in the deck slab

Transverse bending stresses in the slab arise from three effects. Loads applied to the deck are transferred to the webs by local flexure inducing transverse stresses. Stresses also arise due to differential deflection between boxes and finally stresses arise due to distortion of each box cross section caused by the resultant loads acting above the webs.

As might be expected the maximum transverse slab stresses, in the parts of the deck forming the top flange of the box girders, are highest in Span C_2D where maximum σ_{DB} stresses in the boxes occur. The maximum value for lane loading of 2.245 N/mm^2 is obtained for Load case 10 (Fig. 251). The spacing of webs in Span C_2D is greater than in other spans and consequently the slab has a greater span in the transverse direction.

However, the maximum measured transverse bending stresses in the slab between boxes do not occur in Span C_2D but in Span AB at Section 3 where diaphragms are incorporated into the boxes. Here extremely high stresses are measured, the maximum being 20.79 N/mm^2 for Load case 16 (Fig. 256). Transverse stresses are also measured at Section 2 in Span AB where they are much smaller (maximum 3.28 N/mm^2 for Load case 16, Figure 257) and therefore it would

178

appear that the presence of the diaphragms at Section 3 is instrumental in producing the very high slab stresses. Unfortunately Section 3 is the only section that incorporates instrumentation on the slab between boxes at a diaphragmed location. However a similar phenomenon was observed in the study of diaphragming for the Merstham Interchange model reported in Chapter Four. When diaphragms are absent, the box, due to its lack of distortional stiffness, can more readily follow the transverse deflected shape of the slab and therefore transverse moments are lower than those obtained when the distortion is prevented and a 'hard' point is produced at the intersection of the edge of the box and slab. There are several possible solutions to this problem which are discussed in detail in Chapter Four.

6.6.6 Principal stresses and transverse shears in Span BC

Triaxial strain gauge rosettes were also used at Section 6 of this Model in order to define the directions of principal stresses in the region of the complex geometry of the bifurcation. Results again show that the directions of principal stresses in the box under the loaded lane approximate closely to the longitudinal and transverse directions. The directions of principal stresses in the

other boxes do not agree as closely with these directions but the maximum longitudinal stresses obtained at each point in the flanges agree closely with the greatest principal stresses at these points (e.g. maximum longitudinal extreme fibre stress at Section 6 = 37.180 N/mm^2 (Fig. 246) and the greatest maximum principal stress = 37.490 N/mm^2 (Fig. 258).

6.6.7 Deflections

Horizontal and vertical deflections of the box corners are plotted for loaded spans at sections at midspan of the outer spans and at Sections 5 and 6 in the bifurcated span. At diaphragmed sections the horizontal deflections of the bottom flange are calculated from the vertical deflections of the slab assuming that the cross section does not distort. Horizontal transverse deflections of the slab are small and where distortion of the cross section occurs it is largely confined to the vertical direction with the webs remaining parallel to the vertical (e.g. Fig. 259).

The maximum vertical deflections of the outer spans are measured under the outer webs when the outer lanes are loaded (maximum longitudinal and transverse stresses occur when the inner lanes are loaded). The exaggerated deflection scale emphasises the distortion of the cross

180

section at Sections 6 and 11 and shows that the changes in lengths of the diagonals of the boxes are greatest when the inside lane is loaded (e.g. Figs. 259 and 260).

6.6.8 Support Reactions

The comparison of the sum of the reactions with the applied load was referred to in Section 6.2.3 and discrepancies were shown to be small. Reactions are shown on a plan of the structure together with vertical displacements of the structure above the supports due to the elasticity of the rubber bearings. The magnitudes of deflections reflect the positions of applied loading (e.g. Fig. 154).

6.6.9 Local effects due to HB loading

Local bending of the deck slab occurs in the vicinity of the HB vehicle due to the concentrated nature of the loading and local longitudinal and transverse stresses are produced. For example, consider the results of Load case 16 at Section 2. Figure 261 shows the longitudinal stresses at the extreme fibres and illustrates the high longitudinal stresses in the loaded box. The in-plane component of longitudinal stress shows a more smooth distribution of stress (Fig. 262) and the flexural component (Fig. 263) includes the local longitudinal bending

effects in the slab. Similarly the flexural components of transverse stress (Fig. 264) are high in the loaded box with a maximum stress of -4.216 N/mm^2.

6.6.10 Knife edge test results

Four knife edge loading cases were tested (Load cases 82-85) and results are presented for a load of 222.5N (50 lbf). Local effects are obtained in the top flange under the knife edge where high longitudinal stresses result (-3.579 N/mm^2, Fig. 265). High transverse flexural stresses also occur in the slab (e.g. 6.155 N/mm^2, Fig. 266). Maximum longitudinal steel stresses are obtained for Load case 84 (14.98 N/mm^2, Fig. 267) and the maximum transverse bending stress in the boxes is obtained for Load case 82 (11.29 N/mm^2, Fig. 268).

A series of four point load cases was tested (Load cases 68-71) and results are presented for a load of 222.5N (50 lbf). High local stresses arise due to longitudinal and transverse bending of the deck under the concentrated load especially for Load case 62 where the load is placed on the deck between two boxes. The maximum measured longitudinal slab stress of 4.645 N/mm^2 (Fig. 269) occurs near to the load and the transverse flexural stress at this location is 11.130 N/mm^2 (Fig. 270). Maximum steel

182

stresses are 12.79 N/mm^2 longitudinal for Load case 71 (Fig. 271) and 15.31 N/mm^2 transverse for Load case 68.

6.6.11 Support settlement test results

Two support settlement cases were considered - Load case 88 which is the settlement of the inner support at Pier A, and Load case 89 which is the settlement of Pier C_2. For Load 88, results are presented for a support settlement of 2.54 mm (0.1 in) which was achieved by removing a 2.54 mm (0.1 in) packing piece from beneath the support column and applying a load of 845N (120 lbf) at a distance of 25.4 mm (1 in) from the column in a radial direction away from the centre of curvature. Load case 89 results are presented for a support settlement of 2.54 mm (0.1 in) which was achieved by removing a 2.54 mm (0.1 in) packing piece from beneath the column and applying a load of 356N (150 lbf) at a distance of 25.4 mm (1 in) from the column along the arc in Span C_2D.

For Load case 88 the maximum longitudinal stresses occur at Section 4 (17.71 N/mm^2, Fig. 273) and high longitudinal stresses also occur in the bifurcated span (e.g. 12.90 N/mm^2 at Section 6, Fig. 274). Transverse stresses were measured by the secondary stress gauges at Section 2 where a maximum transverse flexural stress of 18.07 N/mm^2

was recorded (Fig. 275). Deflections were measured throughout the structure and upwards deflections at one side of the section were recorded at all sections but Section 11.

For Load 89 the maximum longitudinal stresses occur at Section 10 where the settlement is imposed (68.74 N/mm^2 in the steel and 5.41 N/mm^2 in the slab, Fig. 276) and as might be expected the effects of settlement at this single column inner support are much greater than those measured for Load case 88 where the load is carried by the adjacent column.

184

6.7 COMPARISON OF THE STRUCTURAL BEHAVIOUR OF THE VARIOUS FORMS OF CONSTRUCTION

The models were designed by selecting overall dimensions and wall thicknesses typical of existing structures of similar full scale spans and carriageway layout. Very few calculations were carried out other than to check the approximate magnitudes of maximum strains by simple bending theory so that the models were not overstressed during the initial trial loading period. Rigorous analyses by the finite element or grillage methods were not carried out at the design stage and no attempt was made to produce structures which would be competitive on economic grounds. The details of the models and their instrumentation were intended to produce information against which computer programs could be tested and also to provide insight into the structural behaviour of the various forms of construction. To this latter end some of the details such as, for example, the number of diaphragms in the outer spans of the composite multibox scheme, were varied throughout the structures although this obviously would not be done in practice.

The two models which simulate concrete structures provide an interesting comparison in that their cross sectional areas are similar except for Span C_2D which in

Model 2 has a large cantilever on one side. The cross sectional areas are as follows:

Span	Cross sectional areas (mm^2)	
	Model 1	Model 2
AB	4302	4349.25
C_1E	2435.5	2360
C_2D	3973.5	3098.25

The outer spans of both models have no internal diaphragms. Table 16 lists various stresses in all three models. Maximum longitudinal stresses due to lane loading in Models 1 and 2 and in the deck of Model 4 are all very similar and of the same order as maximum distortional stresses σ_{DB} in the concrete models. The high maximum slab transverse bending stress in Model 4 is due to the positioning of internal diaphragms in Span AB. Redesign to reduce this stress and also the even higher stress caused by the HB loading was discussed in 6.6. The various maximum stresses shown in the HB loading section of Table 16 were in general isolated values and do not reflect the overall stress levels. The high stresses in Model 2 occurred due to HB loading on the cantilevered part of the slab in Span C_2D. As described in 6.6,

186

the stresses in Model 4 are largely dependent on the number of internal diaphragms but it is interesting to note that the stresses in the bifurcated span (BC), which was well diaphragmed, are similar in magnitude to the stresses in the concrete models when the latter are multiplied by the modular ratio.

The principal stress directions in the loaded boxes in the bifurcated spans coincide with the longitudinal and transverse directions in all three models and therefore maximum longitudinal stresses approximate closely to the maximum principal stresses.

It is of interest to compare the cross sectional distributions of longitudinal stresses at Midspan AB for the lane loading cases on the three models (e.g. Figs. 144, 150, 155 for Models 1, 2 and 4 respectively). Models 1 and 2 both exhibit the secondary warping behaviour caused by the relatively thick walls with an increase in stress across the webs and a more rapid decrease across the width of the box cells. The results for Model 4 show an increase in stress across the width of each box and a decrease across the slab between boxes with apparently a similar distribution to those of the concrete boxes, the steel box being analogous to the thick concrete web. However, the increase in stress across the steel box is due to the high local curvatures associated with a rapid decrease in distortion in the

vicinity of the internal diaphragm. These curvatures produce warping stresses of opposite sign to those at midpanel where the more normal smooth distribution of stress is obtained.

The three forms of construction considered then are all viable structural alternatives. Where high stresses were encountered in the models they could be reduced by changes to the design details and were not due to a basic fault in the structural system . Good transverse distribution of eccentric loading is obtained with the box section when it is adequately diaphragmed to fully mobilise its high torsional stiffness. This transverse distribution of eccentric loading produces a complex three dimensional stress system which must be considered in the design of both concrete and steel box girder structures.

188

CHAPTER 7: ANALYSIS OF THE COMPOSITE MULTIBOX BIFURCATED MODEL BY THE GRILLAGE-BEF METHOD

7.1 GENERAL

The proposed grillage-BEF analysis method has been applied to box girder structures of varying complexity in Chapters Two, Three and Four. The composite multibox bifurcated model described in Chapters Five and Six provides a rigorous test for the proposed method and its analysis is described in this Chapter. The model incorporates many of the features associated with modern elevated highway structures and includes changes in plate thickness and cross sectional dimensions, various diaphragming arrangements, curvature in plan, random spacing of supports and the bifurcation itself.

7.2 IDEALISATION OF THE STRUCTURE

The dimensions of the model are shown in Figures 131-134 and the positions of instrumentation are shown in Figure 139. Model test results are described in Section 6.5. The grillage idealisation is shown in Figure 277 and consists of single line of elements along the centreline of each box with transverse elements to represent the slab. The rigidity of the transverse elements (EI) is increased, to allow for the increased span of the slab between the box centrelines, in proportion to the increase in length so that the stiffness (EI/L) remains constant. This device was used in order to reduce the total number of nodes in the structure (reduced from 178 with additional nodes at the edge of the box to 84 without) and hence the computer time and storage. The work of Sawko and Mosley[25] suggests that the errors induced by such an idealisation for the transverse members will be small.

The manufacture of the steel boxes from their various components is described in 5.7 and a typical cross section is shown in Figure 133. The steel boxes which are open topped consist essentially of two channel sections which form the webs with flange plates bonded to the flanges of the channels. The exact calculation of the sectional

190

properties for such boxes is not possible using the equations given in Appendix B and some idealisation of the section was necessary for calculation of the bending rigidity, EI_c, the torsional rigidity, GJ, the warping rigidity, EI_w and the frame stiffness, k. The main idealisation was the replacement of the open topped box by an equivalent closed topped box with equal flange area. The outstands of the web channels were also smeared across the box width. This resulted in a close approximation to EI_c, slightly increased values of GJ and k and a slightly reduced value of EI_w. Longitudinal grillage members in the bifurcated span which incorporated changes in cross sectional dimensions were assumed to have average properties calculated midway between nodes.

Torsional stiffness reduction factors were calculated from Equation 3.21 which includes the influence of internal diaphragming. Reduction factors vary from 46.9 for Span C_2D which has no internal diaphragms to 2.0 for that part of Span BC nearest Pier C_1. Reduction factors together with beam properties are given in Table 17.

The analysis of the model was carried out for the reduced torsional stiffness values given in Table 17 and also for the full Bredt-Batho torsional stiffness values which would have normally been used by the designer. The following three loading cases were used for the comparison

of model and analytical results:

Load Case Number	Description
1	Uniformly distributed lane loading in Lane 1 of Span AB (Figure 95)
10	Uniformly distributed lane loading in Lane 1 of Span C_2D (Figure 95)
73	HB vehicle loading in Lane 1 of Span BC (Figure 99)

The load cases were chosen to test the analysis method for both concentrated and distributed loading on spans with differing amounts of diaphragming and hence a wide range of torsional stiffness reduction factors.

192

7.3 COMPARISON OF MODEL TEST AND ANALYTICAL RESULTS

Model test and analytical results are shown in Figures 278 to 288. Model test results are plotted in the same way as is described in Chapter Six except that the following larger scales were used:

7.3.1 Plotting scales, units and legend

The cross section is plotted to a scale of 0.736 full size. Stresses are plotted to a scale of 14.72 mm = 1 N/mm^2 for the Araldite and sand deck and 14.72 mm = 10 N/mm^2 for stresses in the steel. Deflections are plotted to 73.6 times full scale. These scales should not be used to calculated stress and deflection values as there is a slight magnification of the diagram during reproduction. The numerical values of stress and deflection results are given on the diagrams, stresses being given in N/mm^2 units and deflections in millimetres.

Experimental results are shown as crosses which are joined by solid straight lines, the only purpose of which is to emphasize the experimental points. Theoretical results for the reduced torsional stiffness analysis are shown as dashed lines and theoretical results for the full torsional stiffness analysis are shown as broken lines of

dots and dashes. Important numerical values for the reduced torsional stiffness analysis are shown in parentheses.

7.3.2 Comparison of deflections

Deflections for the three loading cases are plotted in Figures 281, 284, 287 and 288. Theoretical deflections for Load cases 1 and 10 with reduced torsional stiffnesses agree closely with experimental values. Deflections are plotted at Sections 5 and 6 for Load case 73 and theoretical values in general overestimate those obtained from the tests. However if vertical deflections are non-dimensionalised by dividing by the average deflection, δ_B, close agreement is obtained between theoretical and experimental results. Non-dimensionalised values are shown on Figures 287 and 288. The agreement of non-dimensionalised values indicates that the analysis with reduced torsional stiffness has provided a good estimate of the transverse distribution of loading.

7.3.3 Comparison of longitudinal stresses

Longitudinal stresses are shown in Figures 278, 280, 282, 285 and 286. Close agreement between theoretical results for reduced torsional stiffnesses and model results

194

is obtained for longitudinal stresses in the steel boxes and in general theoretical values slightly overestimate experimental values. Theoretical results for the full torsional stiffnesses show a greater transverse distribution of loading and considerably overestimate warping stresses in the bottom flanges.

Theoretical results are in general agreement with experimental values in the deck slab except in the vicinity of applied loading where the experimental values include additional local bending effects.

7.3.4 Comparison of transverse distortional bending stresses

Transverse distortional bending stresses in the steel boxes are shown in Figures 279 and 283. Stresses are not plotted for the full torsional stiffness case for Load case 10 as the analysis overestimated the stresses to such an extent that the results would not all fit on to the page with the plotting scales adopted.

Theoretical results for reduced torsional stiffnesses and test results are in general agreement. However some of the test results show large variations between corresponding values on opposite sides of the boxes where theoretical values are identical. Similar variations

were experienced with the results of the Merstham Interchange model described in Chapter Four and are largely due to small imperfections in the manufacture of the model. If model results on opposite sides of the boxes were to be averaged it can be seen that model and theoretical results would be in close agreement.

7.3.5 Compatibility of rotational deflections

The torsional stiffness reduction factors used in the grillage analysis were selected using Equation 3.2.1. Although the comparison of theoretical and experimental results described in the previous sub-sections shows good agreement, it is advisable to consider the compatibility criterion of Equation 3.2 to ensure that the approximate theoretical solution approaches the compatible solution.

Reduction factors calculated from Equation 3.1 for the reduced torsional stiffness analyses are included in Table 17. These values indicate that further reductions could be made to the torsional stiffness of Spans AB and C_2D to obtain full compatibility. It is of interest to examine the reduction factors obtained by the application of Equation 3.1 to the results of the full torsional stiffness analysis. These reduction factors are also included in Table 17 and indicate similar reductions to those given

196

by Equation 3.2.1. In view of the insensitivity of the analysis to small changes in torsional stiffness demonstrated in Chapter Three, and the good agreement between theoretical and experimental results further analyses were thought to be unnecessary.

CHAPTER 8: CONCLUSIONS AND METHODS FOR DESIGN

8.1 CONCLUSIONS

8.1.1 General Conclusions

(1) An approximate elastic analysis method for single and multibox structures which is economical in both computer storage and costs, and is capable of coping with the complex geometry of modern elevated highways has been developed within this thesis. The method is equally applicable to concrete, steel and composite structures accounts for the effects of cross sectional distortion and can, if desired, include the effects of transverse stiffening, cross frames and diaphragms of various types. The method can account for the effects of curvature in plan, variations in cross-sectional dimensions and properties, and skew supports or random positioning of bearings for multibox structures. The response to standard types of loading can be considered including concentrated and distributed loading, HB vehicle loading, and also horizontally applied forces on single cell box girders.

(2) Results from an extensive experimental program of tests on small scale elastic model box girder structures have been made available. Incremental loading demonstrated

198

that the behaviour of the models was linearly elastic. The repeatability of strain and deflection measurements, and appropriate equilibrium checks provided validation for the experimental results. The results of the bifurcated elevated highways models are to be used as standard tests for bridge analysis computer programs by the Department of the Environment.

(3) Comparisons of the proposed theoretical approach with model test results and three dimensional finite element analyses show good agreement.

(4) A parametric study of a wide range of practical box girder bridge structures has resulted in a simplified design procedure to account for the effects of cross sectional deformation. This procedure has been incorporated in the Department of the Environment's Interim Design Rules for steel box girder bridges.

(5) The results presented in this thesis relate to linear elastic behaviour which is of importance in the assessmnet of the unserviceability limit state for factored working loads. Much of the information given shows how the behaviour in the elastic range departs from that given by the simple theories of bending and torsion used by standard grillage analysis programs. The principal effects

which cause this departure are:

(i) Shear lag

(ii) Distortion of the cross section and distortional warping

(iii) Torsional warping

(iv) Secondary warping.

Information on shear lag may be obtained from the Bifurcated Elevated Highways models results. For example, the longitudinal stresses for Model 1 at Pier B, when compared with those obtained from the bending moment calculated from the reactions and applied loading, indicate that, due to shear lag, there is a reduction in the effective breadth of the top flange of 5%. Moffatt[64] has given an extensive treatment of the effects of shear lag.

The effects of distortion of the cross section have been investigated in this thesis and are discussed in detail in 8.1.2. The transverse distortional bending stresses and distortional warping stresses produced by cross sectional distortion can be large in magnitude and must be considered in design. Torsional warping stresses are generally of secondary importance in practical box girder structures. Their magnitudes can be calculated approximately by the simplified procedure given in the Interim Design Rules[38].

200

Secondary warping stresses are developed when the wall thickness is not extremely small compared with the depth of the box. The results of Bifurcated Elevated Highways Models 1 and 2 which represent two forms of concrete construction showed secondary warping stresses with maximum values of approximately 30% of the longitudinal bending stresses under the same loading. In order to assess their significance in relation to the total longitudinal stresses due to dead and live loading, the results for one of the outer spans of Model 2 were combined to give totals for dead load with one third HA loading on one lane and an HB vehicle on the other lane. The total stresses are shown in Figures 290 and 291 which indicate that an increase of 15% in maximum longitudinal stress is caused by secondary warping.

8.1.2 Particular conclusions relating to the distortional behaviour of straight single cell box girders

(1) Additional validation is provided within this thesis for the beam on elastic foundations analogy for the analysis of distortional effects in single cell straight box girders. The method is compared with three dimensional finite element analyses and a quarter scale stiffened steel box girder model.

(2) Maximum transverse distortional bending stresses in the concrete boxes studied were found to be of similar magnitude to maximum bending stresses under the same loading. Maximum distortional warping stresses were found to be of the order of 30% of the maximum bending stresses.

(3) Transverse distortional bending stresses in stiffened steel box girders are extremely sensitive to the cross sectional properties of the transverse stiffeners employed. Maximum stresses can be reduced from several times the maximum bending stress to acceptable levels by a judicious choice of transverse stiffener section while maintaining a constant distortional stiffness. Higher distortional stresses in general occur in the stiffener outstand which has a large eccentricity from the neutral axis of the combined stiffener and effective width of plate section. Peak distortional stresses occur at the box corners where transverse stiffeners on adjacent corners of the box intersect. It is generally necessary to employ a low class welding detail at this intersection and therefore transverse distortional bending stresses are of primary importance in the assessment of the fatigue life of such welds, particularly because the stresses can be fully reversible subjecting the weld to a high stress range.

202

(4) The use of a trapezoidal cross section, in which the webs are sloped, reduces transverse distortional bending stresses but transverse in-plane stresses are induced into the flanges.

(5) The effectiveness of internal diaphragms in resisting distortion depends upon their spacing and stiffness. The spacing of diaphragms can be expressed non-dimensionally by the product βL_D and four ranges of diaphragm effectiveness can be observed which are defined by ranges of βL_D. Diaphragms at spacings corresponding to βL_D greater than 5.0 do not significantly affect maximum distortional stresses at midpanel. An intermediate range exists from $\beta L_D = 1$ to $\beta L_D = 5$, over which the diaphragm spacing is the dominant parameter in controlling distortion, but below $\beta L_D = 1$ diaphragm stiffness becomes more important and below $\beta L_D = 0.2$ stiffness alone controls distortion.

(6) A study of the distortional properties of 28 practical steel box girder bridge designs showed that the use of $I_x/4$ as an approximation to the warping property I_b gives sufficient accuracy for design.

8.1.3 Particular conclusions relating to box girders curved in plan

(1) Additional distortional forces occur in box girders

curved in plan due to the radial component of the longitudinal bending stresses. In this thesis the BEF analogy has been extended to include the effects of these additional forces on simply supported curved box girders. An analytical method has been proposed based on the combined use of standard grillage analysis programs and the BEF method to account for the effects of the radial component in continuous curved girders. The method is shown to give satisfactory agreement with model tests and finite element analysis.

(2) Maximum longitudinal stresses and transverse distortional bending stresses are obtained when loads are applied above the inner web. In such a case the distortional forces due to the radial component of the longitudinal stresses are additive to the distortional forces due to the antisymmetrical component of the loading and higher values of transverse distortional bending stresses and distortional warping stresses result. When the loads are applied above the outer web the distortional forces due to the radial component are subtractive. This phenomenon was observed in the circular box model described in Chapter Two in which the radial component produced transverse distortional bending stresses which were approximately 50% of those due to the antisymmetrical component of the loading. Similar behaviour was also observed in the curved

204

outer spans of the bifurcated elevated highways models.

8.1.4 Particular conclusions relating to the proposed analysis method for multibox structures

(1) An analytical method for multibox structures has been developed within this thesis and is based upon the combined use of standard grillage analysis programs with the BEF analogy. The method consists essentially of making reductions to the torsional stiffness properties of the longitudinal members of the grillage to allow for apparent increased rotations about the longitudinal axis due to distortion of the cross section. The increased rotations reduce the effective torsional stiffness and affect the transverse distribution of loading. Having obtained the correct distribution of load, the distortional effects are assessed separately for each box by the BEF method.

(2) The effective torsional stiffness values for practical box girders were found to vary over a wide range. Torsional stiffness reduction factors (i.e. the ratio of the full Bredt-Batho torsional stiffness to the effective value) for the steel box designs referred to in Chapter Two vary between 1.6 and 17.8. Still larger reductions were necessary for the analysis of the Merstham Interchange

model and the Bifurcated Elevated Highways model, and, although the analysis method was shown to be insensitive to small changes in torsional stiffness properties, the large reductions necessary for the more flexible designs had marked effects on the transverse distribution of load.

(3) Standard grillage analyses using the full Bredt-Batho torsional stiffness without an allowance for distortion overestimate the torsional moments and therefore provide conservative results for distortional stresses. However, they also overestimate the degree of transverse distribution of loading and therefore provide non-conservative results for longitudinal bending stresses.

8.1.5 Particular conclusions relating to skew supported multibox structures

(1) Skew supported multibox structures were studied with particular reference to a model which simulated a trial design for the slip road structures of Merstham Interchange. It was found that the effects of the skew supports were to produce high differential deflections between the box girders, which initially had internal diaphragms only above the bearings, in the region of the inner skew support, thus accentuating the distortional stresses in the box girders and the transverse stresses in the deck slab.

206

(2) A study of a number of alternative internal and external diaphragming arrangements was made in an attempt to overcome this problem. It was found that, if internal diaphragms were placed in adjacent boxes on a cross section perpendicular to the longitudinal axis, transverse stresses in the deck slab could be increased significantly. This is because the undiaphragmed box, due to its lack of distortional stiffness, can more readily follow the transverse deflected shape of the slab and therefore transverse moments are lower than those obtained when the distortion is prevented and a hard point is produced at the intersection of the edge of the box and slab.

(3) It was found that a compromise between maximum transverse slab and box stresses could be obtained by siting diaphragms in adjacent boxes in such a way that they were offset longitudinally. Alternatively diaphragming could be extended between the boxes largely eliminating differential deflections, but this solution is likely to be less acceptable in terms of cost, aesthetics and ease of maintenance.

(4) If rigid diaphragms are provided in and between the box girders at skew support positions in a direction perpendicular to the span, the distortional response of the structure between support diaphragms is similar to

that of the equivalent right supported structure with a span equal to the distance between inner skew supports.

(5) The equivalent right bridge structure was analysed with both single and twin supports under each box to determine the effect of providing an individual torsional restraint for each box. The differences between the two analyses were small as the torsional response was overshadowed by the distortional deflections, but they do indicate that the torsional stiffness of each box is small when compared with the torsional stiffness of the complete structure restrained by single supports under each box. The use of a single bearing at each support position simplifies pier and foundation design.

8.1.6 Particular conclusions relating to the behaviour of the bifurcated elevated highways models

(1) The choice of Araldite and sand, and steel for the modelling materials resulted in a high degree of dimensional accuracy and consistent material properties. The material properties were such that testing was largely time and temperature independant. The instrumentation proved to be extremely reliable and very few gauges failed during testing.

208

(2) Both concrete models exhibited the secondary warping behaviour associated with thick webs referred to in 8.1.1. This could lead to increases in longitudinal stress of up to 30% of the longitudinal stress which would be obtained for the same loading by theories which treat the section as thin walled and could result in an increase of up to 15% on the maximum overall longitudinal stress.

(3) Transverse in-plane stresses were generally low and only of siginificance where bearing stresses occurred in the webs.

(4) Transverse flexural stresses were significant and of the same order as longitudinal stresses for the same load in the concrete models. Transverse flexural stresses in the composite multibox model varied between spans according to the number of internal diaphragms used but again maximum values were of the same order as maximum longitudinal stresses.

(5) Large transverse bending stresses were produced in the deck slabs of all three models between the boxes at the bifurcation. These stresses would be controlled in practice by diaphragming between the boxes. Large stresses were also produced in the deck of the composite multibox model in the vicinity of internal diaphragms which were located in adjacent boxes at coincident cross sections.

These stresses could be reduced by the methods described in 8.1.5 for the Merstham Interchange model.

(6) Principal stresses were measured at gauge positions near the bifurcations. It was found that the principal stress directions in the flanges of loaded box cells coincided with the longitudinal (i.e. spanwise) and transverse directions and that maximum longitudinal stresses agreed closely with maximum principal stresses. The directions of principal stresses in unloaded cells did not conform as closely with the longitudinal and transverse directions.

(7) One of the internal diaphragms in the concrete spine beam model was instrumented to read principal and shear stresses. When loads were not applied directly above the diaphragm the principal stresses acted along the diagonals and maximum shear stresses occurred in the vertical plane. The principal action of the diaphragm was to resist distortion of the cross section and stresses on both faces of the diaphragm were in agreement showing that out of plane bending effects were small. Where loads were applied above the diaphragm the principal stresses were modified by bearing stresses which had the effect of rotating the principal directions towards the horizontal and vertical.

210

(8) All three models demonstrated the high degree of transverse distribution of loading obtained with effectively diaphragmed box girders by virtue of their high torsional stiffness. This transverse distribution of eccentric loading produces a complex three dimensional stress system which must be considered in the design of both steel and concrete box girder structures.

8.2 DESIGN METHODS

Two principal design specifications which give guidance on the effects of distortion and transverse load distribution are the American Association of State Highway Officials (AASHO) "Standard Specification for Highway Bridges"[37] and the British Interim Design Rules (IDR)[38] issued by the Department of the Environment.

The treatments given to the subject of distortion by these documents differ radically in emphasis. The AASHO rules are restricted to composite multibox bridges in which the spacing between boxes is approximately equal to the box width. Other dimensional restrictions are also imposed. A simple empirical formula is given for determining the transverse distribution of loading based on analytical and experimental studies of a wide range of structures of this particular type. The studies also indicated that for the range considered it was not necessary to consider the effects of distortion of the cross section even if diaphragms were provided only at pier positions.

No such dimensional restrictions are imposed by the British I.D.R. which are applicable to all steel and composite box girder structures except suspension bridges.

212

The approach adopted in the I.D.R. is to provide a simplified design method with which the designer can assess the distortional behaviour of his structure. The method resulted from the parametric studies described in Chapter Two of this thesis and is based on a simplified beam on elastic foundation analogy method in which limits are placed on the minimum stiffness of diaphragms so that the non-dimensionalised design curves (e.g. Fig. 45) can be replaced by simple expressions relating transverse distortional bending stresses and distortional warping stresses to the antisymmetrical loading and the distortional properties of the box cross section. The basis for the design method is given in Appendix D. In addition design aids are given to assist in the calculation of the distortional parameter β (see Appendix B) and to provide the summation of the effects of the four axles of the HB vehicle (Fig. 289). The method considers a single cell cross section but it is applicable to separate boxes in multibox structures if the distribution of applied torques is known for each cell. The designer is left to choose an analysis method to obtain the load distribution.

Undoubtedly the I.D.R. for distortional effects are simple to use and quickly give an assessment of peak distortional effects but they have the disadvantage that they can be applied without the physical understanding of

the structural action which the full BEF method can supply. A knowledge of the ranges of diaphragm effectiveness discussed in 8.1.2 enables the designer to proportion diaphragms efficiently. The other disadvantage is that if the designer uses standard grillage programs for global analysis without making allowance for distortional deflections, he will obtain an overestimate of distortional stresses but an underestimate of maximum longitudinal bending stresses. The combined use of grillage and BEF methods proposed in this thesis provides a close approximation to the correct degree of load distribution and the prevailing stress levels. It would, of course, be possible to use a grillage analysis with the torsional stiffness reduction factor suggested in this thesis and then to use the I.D.R. for calculation of distortional stresses, but it seems that while employing a computer program for the grillage analyses, it would be sensible to have a single program comprising grillage and BEF sub programs to carry out the complete analysis.

214

8.3 FUTURE WORK

Attention has been drawn in this thesis to the potential fatigue problem at the intersection of transverse stiffeners at the corners of stiffened steel box girders. The transverse distortional bending stresses, which may be fully reversible and which cause the fatigue problem, are calculated for the transverse stiffener acting with an effective width of plate obtained from Equation B9 given in Appendix B. This formula was derived by Wright[13] from curves given in the A.I.S.C. manual[65]. The effective width is used in two stages of the analysis - in the calculation of the frame stiffness of the cross section, and in the calculation of stresses from transverse moments. Equation B9 is adequate for the calculation of transverse stiffness but it does not represent the variation in effective width which occurs near the corners of the box and which affects the stress levels at this location. The intersection of stiffener outstands on adjacent plates occurs at some distance from the box corner where the effective width is, in general, approaching the value given by Equation B9 but an experimental investigation of the variation in effective width appropriate for stress calculations in the vicinity of the box corner

would enable the complete distribution of stress at the box corner to be obtained.

Having calculated the stresses at the box corners, it is necessary to consider the fatigue performance of the corner welds. The longitudinal weld joining adjacent flange and web plates is subjected to longitudinal direct stresses, shear stresses, transverse bending stresses and bearing stresses. The fillet welds used for joining transverse stiffeners are subjected to shearing caused by distortion of the cross section. Little fatigue data is available for the performance of such welds and there is a need for a comprehensive experimental study of this problem.

The two Bifurcated Elevated Highways models which simulated concrete structures exhibited the phenomenon of 'secondary warping' which manifests itself as an increase in longitudinal stress across the width of thick webs in a direction away from eccentrically applied loading. This behaviour represents a departure from normal thin-walled theory and the test results indicate that the magnitudes of the increases in longitudinal stress can be significant. It is hoped that a study of larger scale micro-concrete box girder models at present being carried out at Imperial College will provide further information on this topic.

216

A possible extension to the BEF-grillage analysis would be the derivation of the warping property I_b and the frame stiffness k for a multicellular cross section. This would lead to a more rigorous treatment of multi-cell structures than that proposed by Kee[49] referred to in Chapter Three.

This thesis has concentrated largely on the effects of cross sectional distortion at the serviceability limit state and a rational basis for the proportioning of internal diaphragming has been provided. It is expected that in many cases this will obviate the need for internal diaphragming especially in concrete box structures. Recent box girder research has concentrated almost exclusively on the ultimate behaviour under symmetrical loading, and the implications for collapse under eccentric loading on undiaphragmed structures must not be overlooked. The way now appears to be open for the development of an ultimate global analysis method based on the grillage-BEF approach for considera-tion of the collapse limit state.

REFERENCES

1. Chapman, J.C. and Dowling, P.J. Proposed Research on Steel Elevated Highways. Research Report, Engineering Structures Laboratories, Imperial College, June 1969.

2. Dabrowski, R. Influence of shear deformation on the warping torsion of box girders with deformable profiles having flexural stiffness. Der Bauingenieur. Vol. 40, No. 11, November 1965.

3. Chapman, J.C., Dowling, P.J., Lim, P.T.K. and Billington, C.J. The structural behaviour of steel and concrete box girder bridges. Structural Engineer, Vol. 49, March 1971, pp 111-120.

4. Maisel, B.I. Review of literature related to the analysis and design of thin-walled beams. London, Cement and Concrete Association, 1970.

5. Kolbrunner, C.F. and Basler, K. Torsion in structures - an engineering approach. Berlin, Springer-Verlag, 1969.

6. Richmond, B. Twisting of thin-walled box girders. Proceedings of the Institution of Civil Engineers, Vol. 33, April 1966, pp 659-675.

7. Reissner, H. Neuere Probleme der Flugzeugstatik. Z. flugtech. Motorluft, 1926, Vol. 17, No. 18, pp 384-393.

8. Ebner, H. Die Beanspruchung dunnwandiger Kastentrager auf Drillung bei behinderter Querschnittswolbung. Z. flugtech. Motorluft, 1933, Vol. 24, No. 24, pp 684-692.

218

9. Dalton, D.C. and Richmond, B. Twisting of thin-walled box girders of trapezoidal cross section. Proceedings of the Institution of Civil Engineers, Vol. 39, January 1968, pp 61-73.

10. Kuhn, P. Stresses in aircraft and shell structures. New York, McGraw Hill, 1956.

11. Moya, V.S. Twisting of thin walled box beams. M. Phil. thesis, University of Surrey, 1967.

12. Vlasov, V.Z. Thin-walled elastic beams. U.S. Department of Commerce, PST Catalogue No. 428, 1959.

13. Wright, R.N., Abdel-Samad, S.R. and Robinson, A.R. BEF analogy for the analysis of box girders. Journal of the Structural Division, ASCE, Vol. 94, No. ST7, July 1968.

14. Billington, C.J. The behaviour of steel box girder bridges under eccentric loading. M.Sc. thesis, University of London, 1969.

15. Specification for steel girder bridges, BS153: Part 3A, Loads. British Standards Institution, London, 1958.

16. Richmond, B. Trapezoidal boxes with continuous diaphragms. Proceedings of the Institution of Civil Engineers, Vol. 43, August 1969, pp 641-650.

17. Dabrowski, R. Curved thin-walled girders. Berlin, Springer-Verlag, 1968.

18. Scordelis, A.C. Analysis of simply supported box girder bridges. Berkeley, University of California, Department of Civil Engineering, October 1966.

19. Zienkiewicz, O.C. The finite element method in engineering science. London, McGraw-Hill, 1971.

20. Lim, P.T.K., Kilford, J.T. and Moffatt, K.R. Finite element analysis of curved box girder bridges. Proc. International Conference on Developments in Bridge Design and Construction, Cardiff, March 1971.

21. Sisodiya, R.G. and Cheung, Y.K. A higher order in-plane parallelogram element and its application to skewed curved box girder bridges. Proc. International Conference on Developments in Bridge Design and Construction, Cardiff, March 1971.

22. Scordelis, A.C. Analysis of continuous box girder bridges. Berkeley, University of California, Department of Civil Engineering, November 1967.

23. Cheung, Y.K. Analysis of box girder bridges by the finite strip method. Paper presented at the American Concrete Institute Annual Convention, Chicago, 1969.

24. Benscoter, S.V. A theory of torsion bending for multicell beams. Journal of Applied Mechanics, Vol. 21, March 1954.

25. Sawko, F. and Mosley, W.H. Grillage analysis of composite box girder bridge decks. Civil Engineering and Public Works Review, October 1969, pp 979-981.

220

26. Tung, D.H.H. Analysis of curved twin box girder bridges. Proc. ASCE Structural Engineering Conference, Seattle, 1967.

27. Hayward, A.C.G. Interaction between twin beam and deck systems. Civil Engineering and Public Works Review, October 1969, pp 1164-1166.

28. Lim, P.T.K. Elastic analysis of bridge structures by the finite element method. Ph.D. thesis, University of London, 1971.

29. Krisfield, M.A. Finite element methods for the analysis of multicellular structures. Proceedings of the Institution of Civil Engineers, Vol. 48, 1971, pp 413-437.

30. Willam, K.T. and Scordelis, A.C. Cellular structures of arbitrary plan geometry. Journal of the Structural Division, ASCE, Vol. 98, No. ST7, November 1967.

31. Billington, C.J. Batheaston By-Pass North Loop Viaduct - Finite element analysis. Report for S.W.R.C.U., March 1972.

32. Billington, C.J. and Chapman, J.C. Huntworth Viaduct - BEF and finite element analysis. Report for S.W.R.C.U., Engineering Structures Laboratories, Imperial College, May 1971.

33. Billington, C.J. and Dowling, P.J. Merstham Interchange lower slip road structures - finite element and model analysis. CESLIC Report MI1, Imperial College, April 1972.

34. Lim P.T.K. and Moffatt, K.R. A general purpose finite element program. Proc. P.T.R.C. Bridge Program Review Symposium, London, January 1971.

35. Wright, R.N. Design of box girders of deformable cross section. Highway Research Record, No. 295, 1970.

36. Mattock, A.H. and Johnston, S.B. Behaviour under load of composite box girder bridges. Journal of the Structural Division, ASCE, Vol. 94, No. ST10, October 1968.

37. Standard Specifications for Highway Bridges. American Association of State Highway Officials, Tenth Edition, 1969.

38. Committee of Investigation into the Design and Erection of Steel Box Girder Bridges. Interim Design Rules. Department of the Environment, London, February 1973.

39. Hetenyi, M. Beams on elastic foundations. Ann Arbor, The University of Michigan Press, 1946.

40. Abdel-Samad, S.R., Wright, R.N. and Robinson, A.R. Analysis of box girders with diaphragms. Journal of the Structural Division, ASCE, Vol. 94, No. ST10, October 1968.

222

41. Myers, D.E. and Cooper, P.B. Box girder model studies. Journal of the Structural Division, ASCE, Vol. 95, No. ST12, December 1969.

42. Florin, G. Comparison of various theories for twisted rectangular box girders with no stiffening at load point by experiment. Der Stahlbau, February 1963, pp 51-56.

43. Billington, C.J., Ghavami, K. and Dowling, P.J. Steel box girders - Parametric study of cross-sectional distortion due to eccentric loading. CESLIC Report BG16, Imperial College, September 1972.

44. Frieze, P.A. and Dowling, P.J. Steel box girders. Model 7 - Progress Report 2. CESLIC Report BG20, Imperial College, (in preparation).

45. Billington, C.J. and Dowling, P.J. Bifurcated Elevated Highways - construction, instrumentation and testing of four linearly elastic models. CESLIC Report BB1, Imperial College, January 1972.

46. Discussion on paper by Chapman, J.C., Dowling, P.J., Lim, P.T.K. and Billington, C.J. The structural behaviour of steel and concrete box girder bridges. The Structural Engineer, Vol. 50, No. 1, January 1972.

47. Swann, R.A. A feature survey of concrete box spine-beam bridges. C. and C.A. Technical Report 42.469, June 1972.

48. Flint, A.R. and Horne, M.R. Conclusion of research program and summary of parametric studies. Proc. International Conference on Steel Box Girder Bridges, The Institution of Civil Engineers, London, 1973.

49. Kee, K.P. The effects of cross sectional deformation in multicellular box girder bridges. M.Sc. thesis, University of London, 1970.

50. See Reference 25.

51. Billington, C.J. Teesbridge - BEF distortional analysis. Report for Dobbie, Sandford, Fawcett and Partners, Imperial College, July 1971.

52. Billington, C.J. New Scotswood Bridge - BEF distortional analysis. Report for Mott, Hay and Anderson, December 1972.

53. Cheung, Y.K., King, I.P. and Zienkiewicz, O.C. Slab bridges with arbitrary shape and support conditions: a general method of analysis based on finite elements. Proceedings of the Institution of Civil Engineers, Vol. 40, 1968, pp 9-36.

54. Billington, C.J. and Dowling, P.J. Bifurcated Elevated Highways Model 1 - spine beam construction. Results of lane loading tests. CESLIC Report BB2, Imperial College, September 1972.

55. Billington, C.J. and Dowling, P.J. Bifurcated Elevated Highways Model 1 - spine beam construction. Results of HB, knife edge and point loading tests. CESLIC Report BB3, Imperial College, January 1973.

224

56. Billington, C.J. and Dowling, P.J. Bifurcated Elevated Highways Model 2 - multicellular construction. Results of lane loading tests. CESLIC Report BB4, Imperial College, July 1973.

57. Billington, C.J. and Dowling, P.J. Bifurcated Elevated Highways Model 2 - multicellular construction. Results of HB, knife edge, point loading and settlement tests. CESLIC Report BB5, Imperial College, August 1973.

58. Billington, C.J. and Dowling, P.J. Bifurcated Elevated Highways Model 3 - composite plate girder construction. Results of lane loading tests. CESLIC Report BB6, Imperial College, (in preparation).

59. Billington, C.J. and Dowling, P.J. Bifurcated Elevated Highways Model 3 - composite plate girder construction. Results of HB, knife edge and point loading tests. CESLIC Report BB7, Imperial College, (in preparation).

60. Billington, C.J. and Dowling, P.J. Bifurcated Elevated Highways Model 4 - composite multibox construction. Results of lane loading tests. CESLIC Report BB8, Imperial College, November 1973.

61. Billington, C.J. and Dowling, P.J. Bifurcated Elevated Highways Model 4 - composite multibox construction. Results of HB, knife edge, point loading and settlement tests. CESLIC Report BB9, Imperial College, November 1973.

62. Billington, C.J. and Dowling, P.J. Bifurcated Elevated Highways - Elastic Models Final Report. CESLIC Report BBlO, Imperial College, (in preparation).

63. Oden, J.T. Mechanics of Elastic Structures. McGraw Hill, New York, 1967.

64. Moffatt, K.R. The finite element analysis of box girder bridges. Ph.D. thesis, University of London, 1974.

65. American Institute of Steel Construction. Design Manual for orthotropic steel plate deck bridges. A.I.S.C., New York, 1963.

66. Pelikan, W. and Esslinger, M. Die Stahlfarhrbahn Berechnung und Konstruktion M.A.N. Forschungsheft, No. 7, 1957.

226

APPENDIX A. DERIVATION OF THE GOVERNING DIFFERENTIAL EQUATION

An energy argument leads to Equation 2.1. The component of displacement in the plane of the cross section and in the direction along the tangent, s, to the section is denoted by v(x,s) and the warping displacement by u(x,s). The basic assumption of negligible shear strains may be expressed as

$$\frac{\partial u(x,s)}{\partial s} + \frac{\partial v(x,s)}{\partial x} = 0 \qquad \text{(A1)}$$

The term $\partial v/\partial x$ is found from the distortional deflection W(x) shown in Figure 5 and v(x,s) is expressed as the product W(x).V(s). Therefore

$$u(x,s) = - W'(x)\Omega_d(s) \qquad \text{(A2)}$$

where $$\Omega_d(s) = \int_{s_o}^{s} V(s)\,ds + C$$

The strain energy U_1, corresponding to the warping stresses is given by

$$U_1 = \frac{E}{2}\int_o^L \left[\iint_A \left(\frac{\partial u(x,s)}{\partial x}\right)^2 dA\right] dx$$

therefore

$$U_1 = \frac{1}{2} E C_d \int_o^L (W'')^2 \, dx \quad \ldots\ldots\ldots\ldots\ldots\ldots \quad (A3)$$

where $C_d = \int_A \Omega_d^2(s) \, dA$

$$= \oint \Omega_d^2(s) \, t(s) \, ds$$

and t is the plate thickness

L is the span.

The energy, U_2, required to distort a length dx of the box cell is given by

$$dU_2 = \frac{1}{2} K W^2 dx$$

therefore

$$U_2 = \frac{1}{2} K \int_o^L W^2 \, dx \quad \ldots\ldots\ldots\ldots\ldots\ldots \quad (A4)$$

where K is the frame stiffness per unit length.

The energy U_3 of the external forces is given by

$$U_3 = - \int_o^L p \, W \, dx \quad \ldots\ldots\ldots\ldots\ldots\ldots \quad (A5)$$

where p is the generalised force per unit length.

The total potential energy U is given by

$$U = U_1 + U_2 + U_3$$

228

therefore

$$U = \frac{1}{2} E C_d \int_o^L (W'')^2 \, dx + \frac{1}{2} K \int_o^L W^2 dx - \int_o^L pW dx \quad \ldots\ldots\ldots \quad (A6)$$

The usual processes of calculus for minimising the total potential energy result in the Euler-Lagrange equation for W which is identical to Equation 2.1.

APPENDIX B. DERIVATION OF BEF PROPERTIES

B.1 RESISTANCE OF CROSS SECTION TO DEFORMATION

The load-displacement relationship for the box cross section subjected to distortional loading is computed by taking a unit length of the cell loaded by a unit generalised distortional force and finding the redundant forces by the influence coefficient method. The distortional deflection δ_1 can be found by the principle of virtual displacements. The cross sectional dimensions are shown in Figure B1 and a unit generalised distortional load is shown in Figure B2.

Considering bending energy only, release the structure at the centre of the bottom wall giving the M_o diagram (Figure B3). From conditions of skew symmetry, there is only one redundant force which is a vertical shear. Placing a unit load at the release position gives the M_1 diagram (Figure B4):

Now $$f_{11} = \int \frac{M_1^2}{EI}\, ds$$

$$\frac{f_{11}}{2} = \frac{1}{D_B}\left[\frac{b_B}{2}\left(\frac{b_B}{2}\right)^2 \cdot \frac{1}{3}\right] + \frac{1}{D_T}\left[\frac{1}{3} \cdot \frac{b_T}{2}\left(\frac{b_T}{2}\right)^2\right]$$

$$+ \frac{1}{D_C}\left[\frac{c}{6}\left\{2 \cdot \left(\frac{b_T}{2}\right)^2 + \frac{2b_T b_B}{4} + 2\left(\frac{b_T}{2}\right)^2\right\}\right]$$

230

therefore

$$f_{11} = \frac{-1}{12}\left[\frac{b_T^3}{D_T} + \frac{2c}{D_c}\left(b_T^2 + b_T b_B + b_B^2\right) + \frac{b_B^3}{D_B}\right]$$

$$U_o = \int \frac{M_1 M_o}{EI}\, ds$$

therefore

$$U_o = \frac{2}{(b_T+b_B)24}\left[\frac{c}{D_c} b_T b_B\,(b_B+2b_T) + \frac{1}{D_T}.b_B.b_T^3\right]$$

$$f_{11}V + U_o = 0$$

therefore

$$V = \frac{\frac{1}{D_c}\left[(2b_T+b_B)\; b_T b_B c\right] + \frac{1}{D_T}\left[b_B b_T^3\right]}{(b_T+b_B)\left[\frac{b_T^3}{D_T} + \frac{2c}{D_c}.(b_T^2+b_T b_B+b_B^2) + \frac{b_B^3}{D_B}\right]}$$

..... (B1)

The bending moment diagram is shown in Figure B5. The displacements are most easily found by applying a virtual unit load to an idealised structure at the point where the deflection is required. The idealised structure consists of half the box held in equilibrium under the applied load by in-plane shears in the proportion of the Bredt-Batho shear flows (Figure B6).

Deflections are computed relative to the centre of the top flange.

(i) Vertical deflection at top of web, δ_1

$$\delta_1 = \int \frac{MM'}{EI}\, ds$$

$$M_D' = \frac{b_T b_B}{2(b_T+b_B)}$$

hence

$$\delta_1 = \frac{b_T b_B}{24(b_T+b_B)} \left(\frac{c}{D_c} \left[\frac{2b_T b_B}{(b_T+b_B)} - V\ (2b_T+b_B) \right] + \frac{b_T^2}{D_T} \left[\frac{b_B}{(b_T+b_B)} - V \right] \right) \quad \text{..... (B2)}$$

δ_1 is the deflection of the box cell under a unit generalised distortional load and it is therefore the distortional flexibility of the cell. The relative deflections of the other corners of the cell will now be computed for use in defining the deformation of cross bracing and diaphragms. It is not necessary to repeat the above calculation for other unit loads as the M' diagrams are of the same form and the deflections can therefore be found from proportions.

$$\text{Deflection} = M_D \left(\frac{b_T+b_B}{b_T b_B} \right) \delta_1$$

(ii) Horizontal deflection at top of web

The horizontal deflection relative to the centre of the top flange is zero. From inspection it can be seen that

232

the M' diagram is zero.

(iii) Vertical deflection at bottom of web δ_{VB} (see Figure B7).

$$M_D' = \frac{b_T^2}{2(b_T+b_B)}$$

therefore

$$\delta_{VB} = \frac{b_T \delta_1}{b_B}$$

(iv) Horizontal deflection at bottom of web δ_{HB} (see Figure B8).

$$M_D' = \frac{b_T h}{(b_T+b_B)}$$

therefore

$$\delta_{HB} = \frac{2h}{b_B} \delta_1$$

The distortional stiffness K (= $1/\delta_1$) is computed from Equations B1 and B2. In order to simplify the calculation of the β parameter, the expression for which includes K, curves were derived for inclusion in the Interim Design Rules. If the dimensionless groups $\gamma(= B_B/B_T)$, $\lambda(= C/B_T)$, $\alpha(= D_{YB}/D_{YT})$, and $\nu(= D_{YC}/D_{YT})$ are substituted into Equation B2 this equation reduces to

$$K = 1/\delta_1 = \frac{24 D_{YT} R}{B_T^3}$$

where

$$R = \frac{1 + \alpha}{\gamma\{\frac{\lambda}{\nu}\left[\frac{2\gamma}{1 + \gamma} - (2 + \gamma)S\right] + \frac{\gamma}{1 + \gamma} - S\}}$$

and

$$S = \frac{(\gamma\lambda/\nu).(2 + \gamma) + \gamma}{1 + \gamma + \frac{2\lambda}{\nu}(1 + \gamma)(1 + \gamma + \gamma^2) + \frac{\gamma^3(1 + \gamma)}{\alpha}}$$

then

$$\beta = \sqrt[4]{\frac{24D_{YT}R}{EI_C B_T^3}}$$

For rectangular boxes, $\gamma = 1$ and the equation for R reduces to

$$R = \frac{2}{\frac{\lambda}{\nu}\left[1 - \frac{3(3\lambda/\nu + 1)}{(2 + 12\lambda/\nu + 2/\alpha)}\right] + \frac{1}{2} - \frac{(3\lambda/\nu + 1)}{(2 + 12\lambda/\nu + 2/\alpha)}}$$

This expression for R is in terms of two variables only (λ/ν and α) and therefore a family of curves can be plotted for R against α for different values of λ/ν. Values of λ/ν and α in Table 5 suggest that the practical range of α is from 1 to 2500. Values of R are plotted for these ranges in Figure B17.

The general expression for R for trapezoidal boxes has the additional variable γ which may be related to λ by the expression

$$\lambda = (1 - \gamma)/2 \cos \theta$$

where θ is the side slope of the box.

234

Curves similar to those for the rectangular box may be plotted for particular values of θ and λ. A common side slope is 60° and it was decided that a series of curves for evaluation of R for this slope would be useful. Curves were plotted for values of λ of 0.8, 0.5 and 0.3 and are shown in Figures B18-20 for the practical range of parameters. Values of R for other values of λ may be found by logarithmic interpolation between the curves for particular values of α and λ/ν.

B2 PROPERTIES OF DIAPHRAGMS

Diaphragms, cross bracings and ring stiffeners restrain deformation of the box cross section just as intermediate supports restrain the deflection of a BEF. The diaphragm stiffness analogous to the support stiffness of the BEF is evaluated for various diaphragm configurations. Bracings are considered first. The bracing stiffness is defined as the magnitude of concentrated antisymmetric load producing a unit distortional deflection of the bracing. This may be calculated by applying the distortional component of this loading as four concentrated loads acting at the corners of the box along the diagonals (Figure B9).

B2.1 Diagonal Cross Bracing

Consider the loading of Figure B9. By antisymmetry the forces in AB and DC are zero. Resolving the forces horizontally and vertically at A gives a force P in the diagonal brace, and zero force in the web member. Each brace of a pair has the properties: Length L_b; area A_b; and Young's Modulus E_b. The change in length of the diagonals, δ_b, for unit antisymmetrical load is calculated by resolving the deflections of diagonally opposite nodes in the direction of the diagonal (Figure B10).

236

Therefore

$$\delta_b = \delta' + \delta'' + \delta'''$$

where $$\delta' = \frac{h\delta_1}{L_b}$$

$$\delta'' = \frac{h}{L_b}\,\delta_{VB}$$

$$\delta''' = \frac{(b_T+b_B)}{2L_b}\,\delta_{HB}$$

therefore

$$\delta_b = \frac{2\left(1+\frac{b_T}{b_B}\right)}{\sqrt{1+\left(\frac{b_T+b_B}{2h}\right)^2}}\,\delta_1 \qquad \text{(B3)}$$

From Figure B9

$$Q = \frac{2\left(1+\frac{b_T}{b_B}\right)}{\sqrt{1+\left(\frac{b_T+b_B}{2h}\right)^2}}$$

Now $$\frac{P}{A_b} = E_b \cdot \frac{\text{extension}}{L_B}$$

for unit vertical distortional deflection the extension is δ_b/δ_1 and Q is then the diaphragm stiffness.

Substituting for P and extension

$$\frac{\delta_1 Q}{\delta_b A_b} = \frac{E_b}{L_b}\,\frac{\delta_b}{\delta_1}$$

Therefore

$$Q = \frac{E_b A_b}{L_b}\left(\frac{\delta_b}{\delta_1}\right)^2 \quad \text{..... (B4)}$$

B2.2 V-type bracing

The stiffness of this type of bracing is calculated in a similar way. Considering Figure B11 and resolving vertically at B

$$P \sin\phi = F \cos\theta$$

therefore

$$F = \frac{P_c}{L_d}$$

Resolving vertically at A

$$R \cos\psi = P \sin\phi + F \cos\theta$$

therefore

$$R = \frac{2PL_b}{L_d}$$

$$Q = \frac{\delta_b}{\delta_1} P$$

therefore

$$R = \frac{2\delta_1 L_b}{\delta_b L_d} Q$$

238

The extension, δ, of the brace is calculated by resolving the deflections at each end of the brace in the direction of the brace (Figure B12).

Therefore

$$\delta = \delta' + \delta'' = \frac{\delta_1 h}{L_b} + \frac{2h\delta}{b_B} 1 \cdot \frac{b_T}{2L_b}$$

$$= \frac{\delta_1 h}{L_b}\left(1 + \frac{b_T}{b_B}\right)$$

for unit distortional deflection

$$\delta = \frac{h}{L_b}\left(1 + \frac{b_T}{b_B}\right) \quad \text{..... (B5)}$$

$$\frac{R}{A_b} = \frac{E_{b.extension}}{L_b}$$

therefore

$$\frac{2\delta_1 L_b}{\delta_b L_d}\frac{Q}{A_b} = \frac{E_b}{L_b}\frac{h}{L_b}\left(1 + \frac{b_T}{b_B}\right)$$

therefore

$$Q = \frac{E_b A_b h}{2L_b^3}\left(1 + \frac{b_T}{b_B}\right) L_d \frac{\delta_b}{\delta_1}$$

$$Q = \frac{E_b A_b h}{2L_b^3} \cdot L_d \left(1 + \frac{b_T}{b_B}\right) \frac{\delta_b}{\delta_1} \quad \text{..... (B6)}$$

B2.3 Inverted V-type bracing

Considering Figure B13 and resolving vertically at A,

$$F = \frac{P_c}{L_d}$$

Resolving vertically at B

$$R \sin \theta = \frac{2Ph}{L_d}$$

Therefore

$$R = \frac{2PL_b}{L_d}$$

$$Q = \frac{\delta_b}{\delta_1} P$$

Therefore

$$R = 2\frac{\delta_1 L_b}{\delta_b L_d} \cdot Q$$

The extension, δ, of the brace is calculated by resolving the deflections at each end of the brace in the direction of the brace (Figure B14).

Therefore

$$\delta = \delta' + \delta'' = \frac{h\delta_1}{L_b} + \frac{b_T}{b_B} \cdot \frac{h}{L_b} \delta_1$$

$$= \frac{\delta_1 h}{L_b} \left(1 + \frac{b_T}{b_B} \right) \quad \text{..... (B7)}$$

240

but

$$\frac{R}{A_b} = \frac{E_{b.extension}}{L_b}$$

Substituting for R and extension

$$Q = \frac{E_b A_b h L_d}{2L_b^3}\left(1 + \frac{b_T}{b_B}\right)\frac{\delta_b}{\delta_1} \quad \ldots\ldots\ldots\ldots\ldots\ldots \text{(B8)}$$

B2.4 Ring Stiffening

The diaphragm stiffness of ring stiffening can be calculated from Equation B2 for δ_1 when D_c, D_B and D_T are replaced by the EI of the relevant stiffener plus associated effective width of plate d_o which may be calculated from

$$d_o = \frac{b \tanh\left(5.6\frac{b}{a}\right)}{\frac{5.6b}{a}(1-\nu^2)} \quad \ldots\ldots\ldots\ldots\ldots\ldots \text{(B9)}$$

where b is the stiffener spacing

a is the span of the plate in the transverse direction.

Stiffeners on opposite walls of the box but not on adjacent walls at coincident sections (e.g. Fig. B15) can be treated by a similar approach. The effective width of unstiffened wall, which acts with the combined stiffener and effective width of plate on the adjacent plate, is

computed by considering the behaviour of an infinitely long plate with a width equal to the span of the plate in the transverse direction, subjected to a concentrated moment on one edge. The governing differential equation for this problem and its solution are described in Reference 14. Figure B16 shows the effective widths for plates varying in span from three to ten feet. Having obtained the effective width its EI is used in Equation B2 to compute δ_1 and hence Q. This procedure may also be used where transverse stiffeners on webs are offset longitudinally from those on flanges by an amount greater than the effective plate widths. Where stiffeners are not offset by this amount a complex interaction exists and an intermediate stiffness between the full interaction and zero interaction values should be used.

B2.5 Plate diaphragms

The stiffness of a plate diaphragm may be approximated by replacing it with an equivalent pair of cross braces. A rectangular plate diaphragm in pure shear would have the same stiffness as cross bracing of area A_b given by

$$A_b = \frac{G_p t_p L_b^3}{2E_b A_p} \quad \text{..... (B10)}$$

where G_p, t_p, A_p are the shear modulus, thickness and middle surface area of the plate.

242

For a trapezoidal diaphragm the equivalent bracing area can be approximated by

$$A_b = \frac{G_p t_p h^2}{E_b (b_T+b_B)} \left[1 + \left(\frac{b_T+b_B}{2h} \right)^2 \right]^{3/2} \quad \ldots\ldots \quad (B11)$$

The formulae for diaphragm and bracing stiffnesses are summarised in Table 1.

B3 WARPING STRESSES

Wright et al[13] suggest the use of $I_c/4$ as an approximation to the warping property which is analogous to the inertia of the BEF. They also give a procedure which leads to an exact warping property I_b but unfortunately there are misprints in the paper which make some of their expressions dimensionally incorrect. The derivation of the exact warping stiffness which is lengthy is not repeated here but the correct expressions leading to I_b are given below.

$$I_b = \frac{b_B}{4} \psi_B \left(\psi_T q_{WT} + \psi_B q_{WB} + 2\psi_C q_{WC} \right) \ldots\ldots \quad (B12)$$

where

$$\psi_T = \alpha_3$$

$$\psi_B = \alpha_1 - 2h/b_T - \alpha_3$$

$$\psi_C = h/c + (b_T - b_B)\ \alpha_3/2c$$

$$\alpha_1 = \frac{2h}{b_B} \left(1 + \frac{b_B}{b_T} \right)$$

$$\alpha_2 = 1.0$$

$$\alpha_3 = \frac{2h \left(\frac{q_{BB}}{b_B} - \frac{q_{BC}}{c} \right)}{\left(q_{BT} + q_{BB} + \frac{|b_T - b_B|\ q_{BC}}{c} \right)}$$

244

$$q_{BT} = \frac{t_T}{6}\left(b_T + 2b_p\right)^3 + \frac{t_w b_T c}{4}\left(b_T+b_B\right)$$

$$q_{BB} = \frac{t_B\, b_B^3}{6} + \frac{t_w b_B c}{4}\left(b_T+b_B\right)$$

$$q_{BC} = \frac{t_w c^2}{12}\left(b_T-b_B\right)$$

$$q_{WT} = \frac{t_T r_w}{6b_T}\left(b_T+2b_p\right)^3 - \frac{\left(1-r_w\right) t_w c b_T}{4}$$

$$q_{WB} = \frac{t_B b_B^2}{6} + \frac{\left(1-r_w\right) b_B c\, t_w}{4}$$

$$q_{WC} = \frac{\left(1+r_w\right) c^2\, t_w}{12}$$

and

$$r_w = \frac{b_B^2 t_B + c\left(b_T+2b_B\right) t_w}{\frac{\left(b_T+2b_p\right)^3}{b_T}\, t_T + c\left(2b_T+b_B\right) t_w}$$

The errors resulting from the use of the approximate warping property $I_x/4$ and Equation 2.15 for calculating warping stresses are defined by the following ratios:

(i) r_β - the error in β

$$r_\beta = \sqrt[4]{\frac{4I_b}{I_x}}$$

(ii) r_s - the error in σ_{DW} resulting from the use of Equation 2.15 rather than Equation 2.4

$$r_s = \frac{2(h-\bar{y})}{b_B \psi_b}$$

B4 CALCULATION OF DISTORTIONAL SHEAR STRESSES AND DIAPHRAGM FORCES

The calculation of transverse distortional bending stresses σ_{DB} and distortional warping stresses σ_{DW} from the deflections and moments given by the solution of the analogous BEF are given in Chapter Two. In addition, distortional shear stresses and diaphragm forces can also be calculated from BEF results. Distortional shear stresses are analogous to BEF shears and diaphragm forces are analogous to BEF support reactions.

B4.1 Distortional shear stresses

The derivation of I_b in Reference 13 shows that the increase in in-plane shear q_w^* per unit length of box in the spanwise direction for an element of width dx is given by

$$q_w^* = q_w \frac{d^2 s}{dx^2} \cdot dx \quad \text{..... (B13)}$$

where q_w is the relevant value of q_{WT}, q_{WB} or q_{WC} given in B3

s is the distortional warping stress at the bottom of a web and is given by

$$s = \frac{E b_B \psi_B W''}{2}$$

246

The total distortional shear force Q_w in any plate is given by the integration of Equation B13.

Therefore

$$Q_w = q_w \frac{ds}{dx}$$

but

$$s = \frac{Eb_B\psi_B}{2} \frac{M}{EI_b} = \frac{b\psi_B M}{2I_b}$$

where M is the BEF moment.

Therefore

$$\frac{ds}{dx} = \frac{b\psi_B}{2I_b} \cdot \frac{dM}{dx}$$

and $\frac{dM}{dx}$ is the BEF shear force Q_{BEF}

Therefore

$$Q_w = \frac{q_w b\psi_B Q_{BEF}}{2I_b} \quad \ldots\ldots\ldots\ldots\ldots\ldots\ldots\ldots \quad (B14)$$

The average distortional shear stress τ_D in any plate is then given by

$$\tau_D = \frac{Q_w}{bt} \quad \ldots\ldots\ldots\ldots\ldots\ldots\ldots\ldots\ldots\ldots \quad (B15)$$

where b is the span of the plate in the transverse direction

t is the plate thickness.

B4.2 Diaphragm forces

The diaphragm or bracing stiffness Q is defined as the magnitude of concentrated vertical antisymmetrical load acting above the bracing which would deform the bracing to produce unit deflection W. The bracing forces are related to Q in B2. If the support reaction given by solution of the analogous BEF is R then the forces in bracing are found by multiplication of the expressions for bracing forces in terms of Q by R/Q.

The corresponding shear stress τ_p in a plate diaphragm is given by

$$\tau_p = \frac{R\ b_T}{h(b_T+b_B)\,t_p} \qquad \text{(B16)}$$

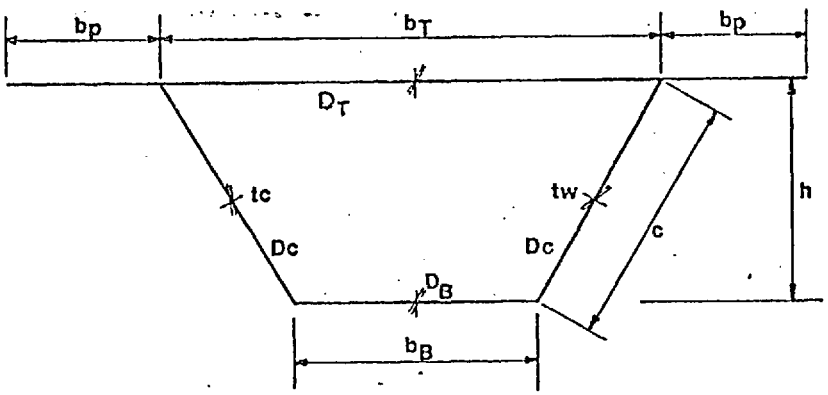


Fig.B1

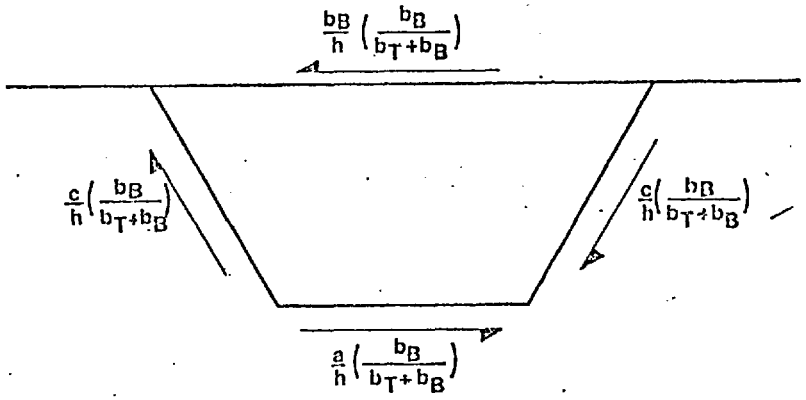


Fig.B2

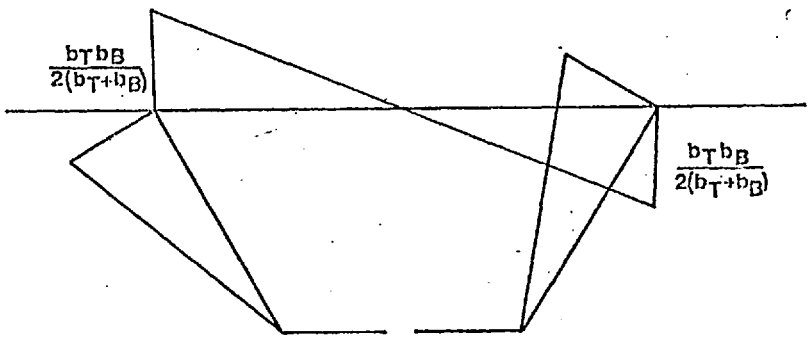


Fig.B3

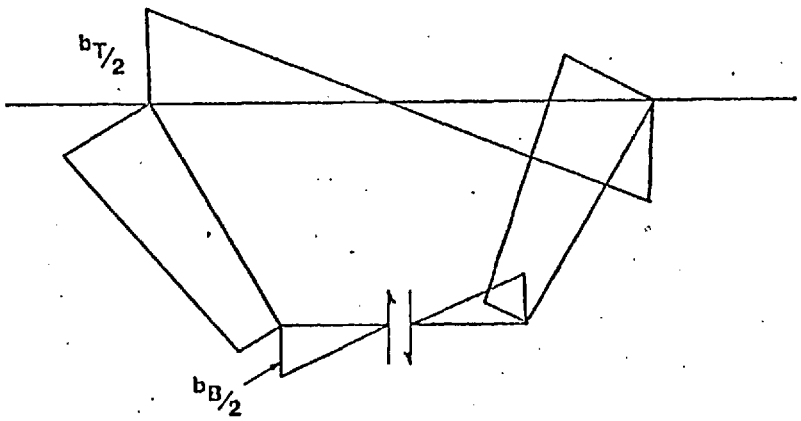


Fig.B4

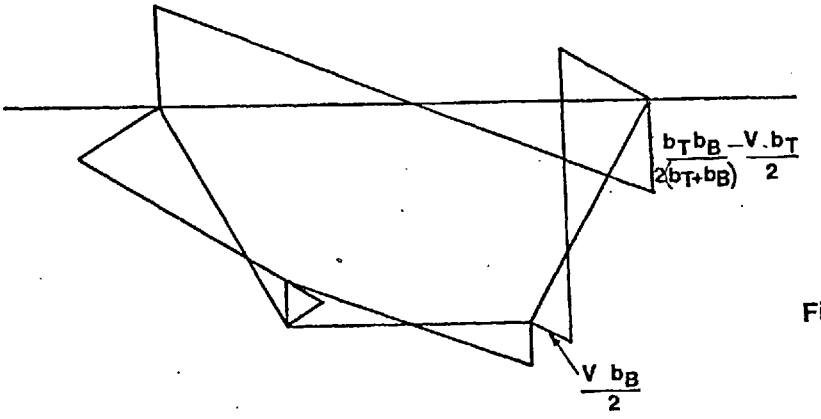


Fig.B5

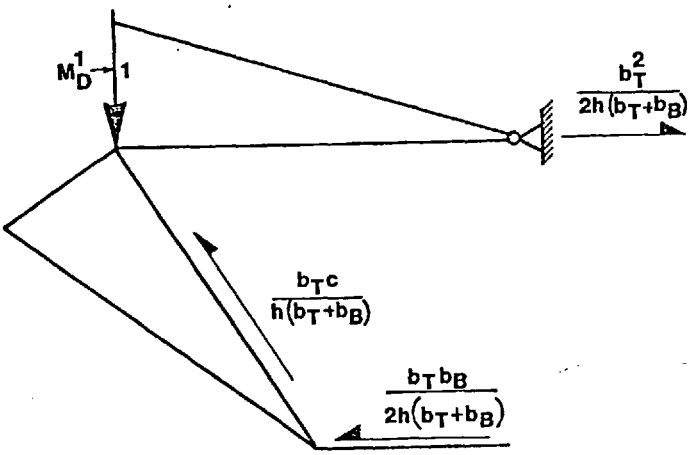


Fig.B6

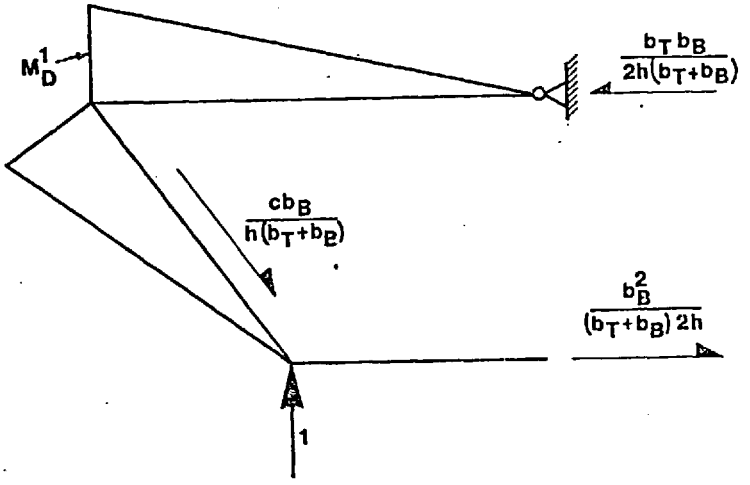


Fig.B7

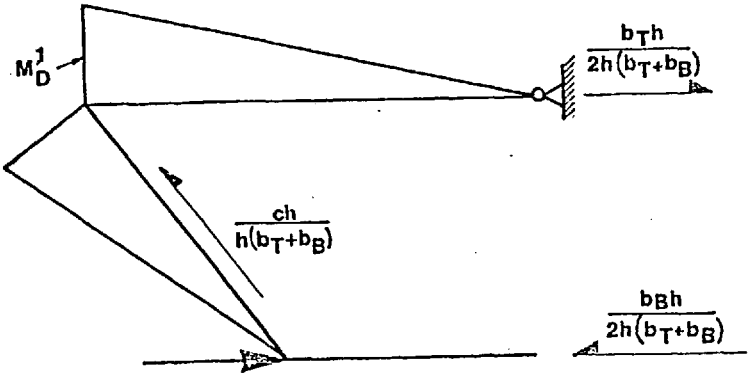


Fig.B8

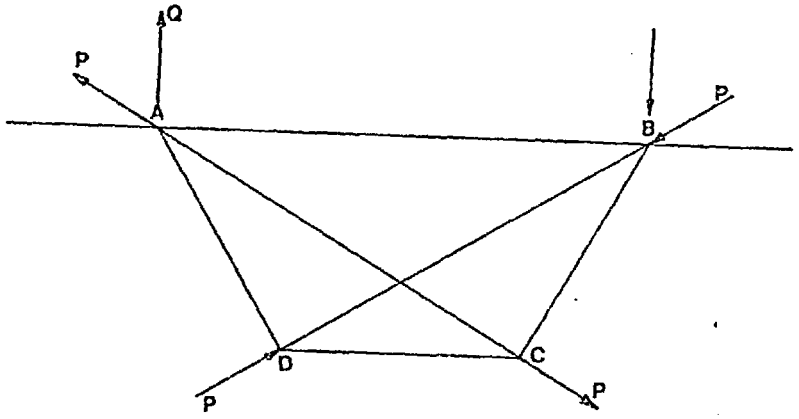


Fig.B9

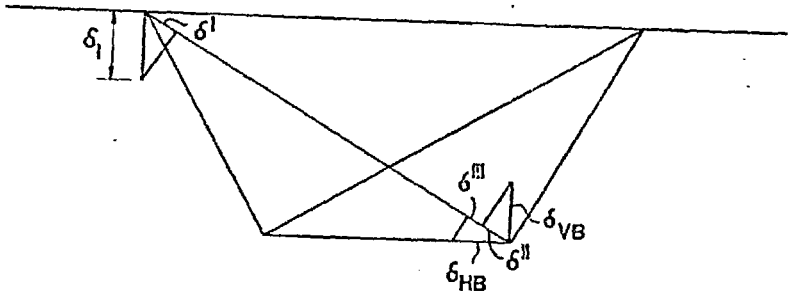


Fig.B10

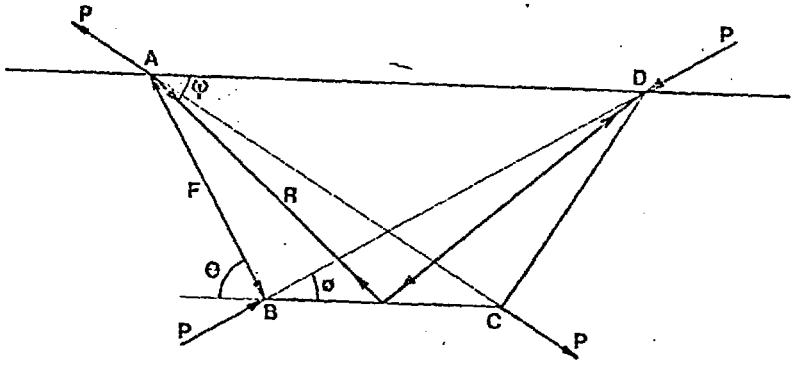


Fig.B11

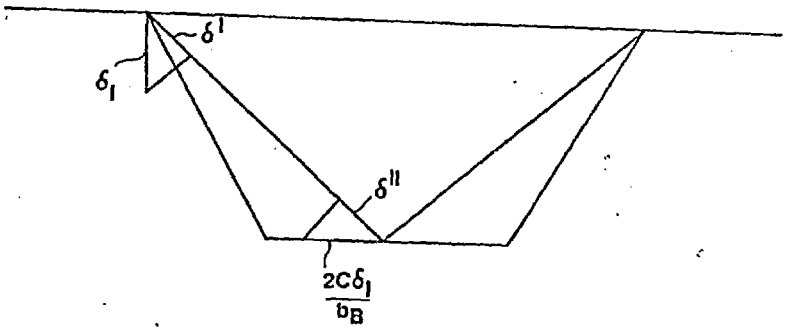


Fig.B12

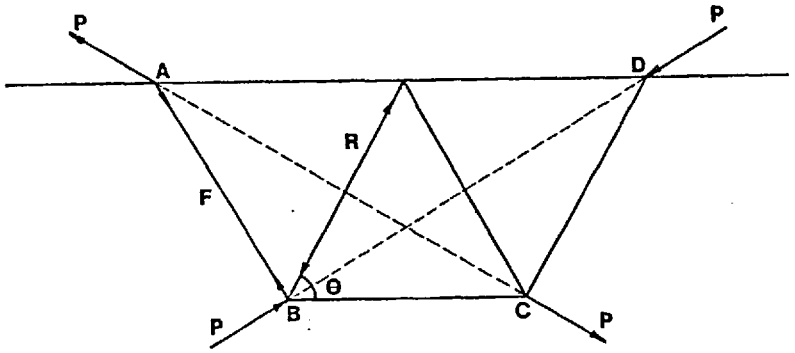


Fig.B13

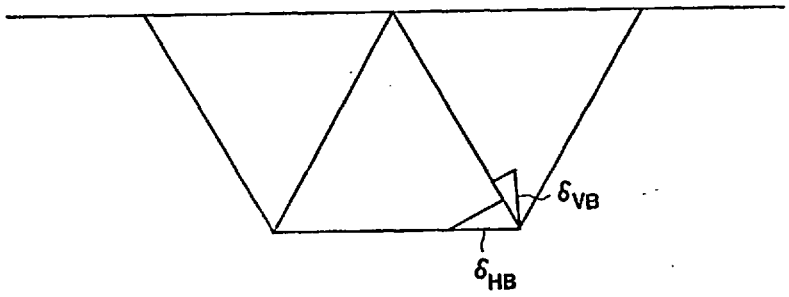


Fig.B14

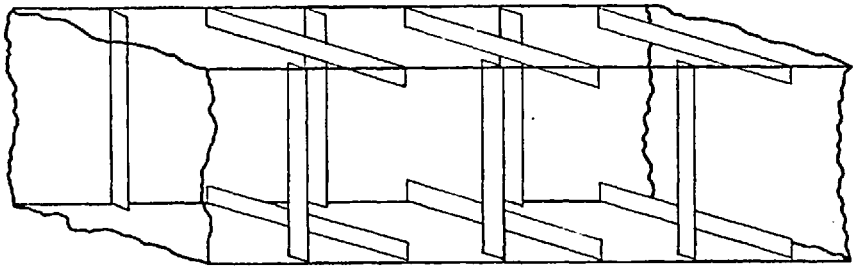


Fig.B15

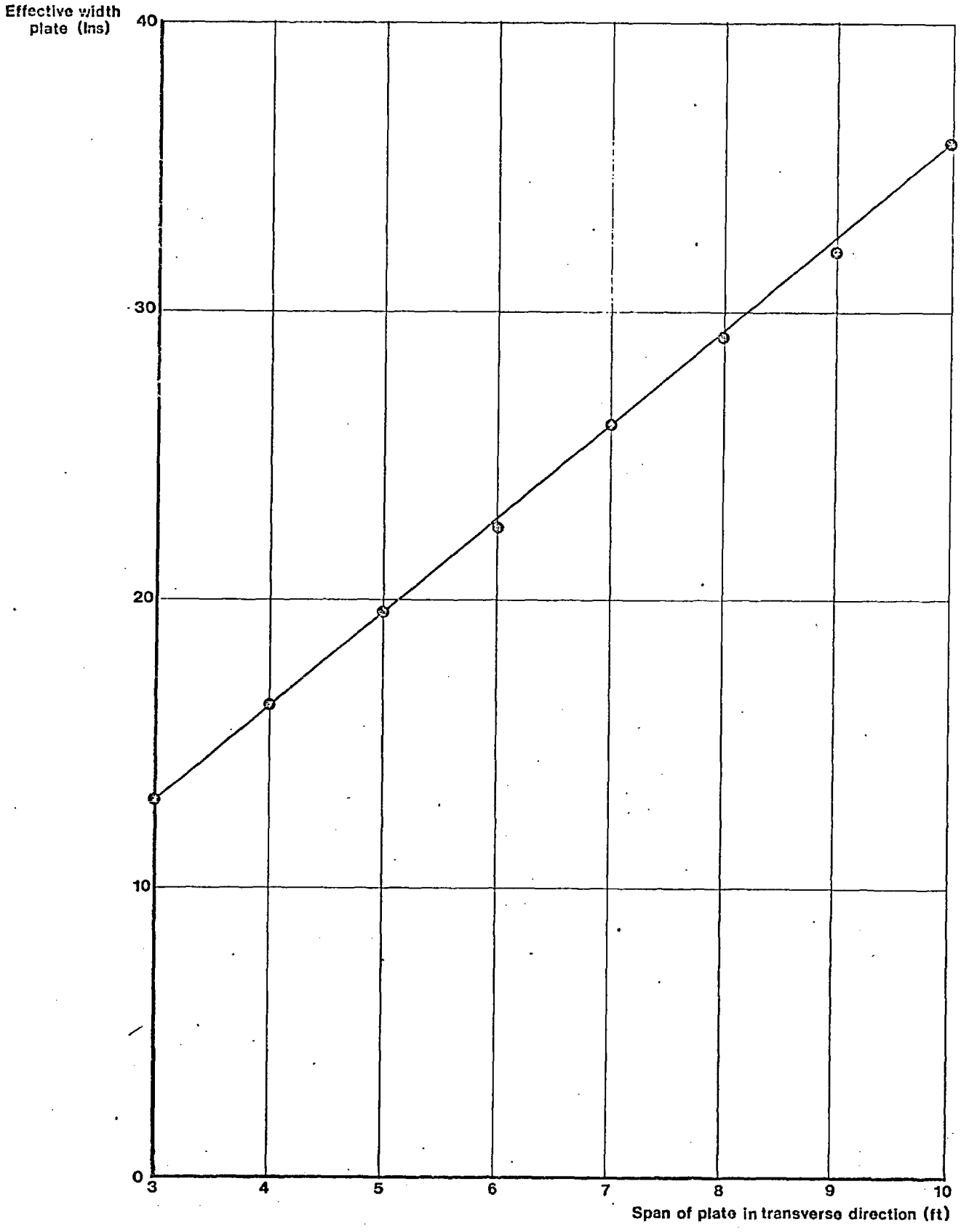


Fig.B16 Effective width of unstiffened plate acting with transverse stiffener on an adjacent plate

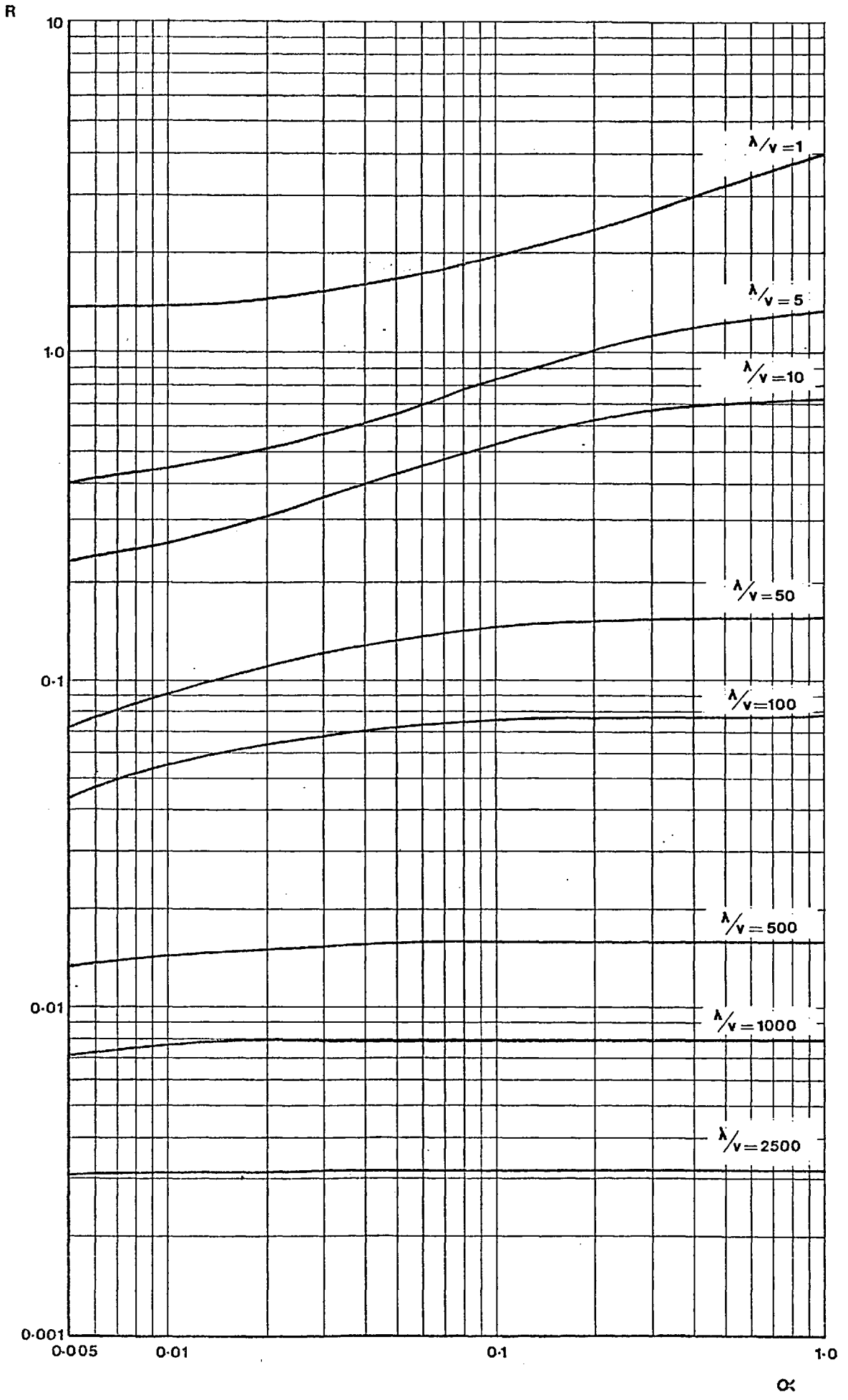


Fig.B17 Simplification of β calcs. for rectangular box
i.e. α=1

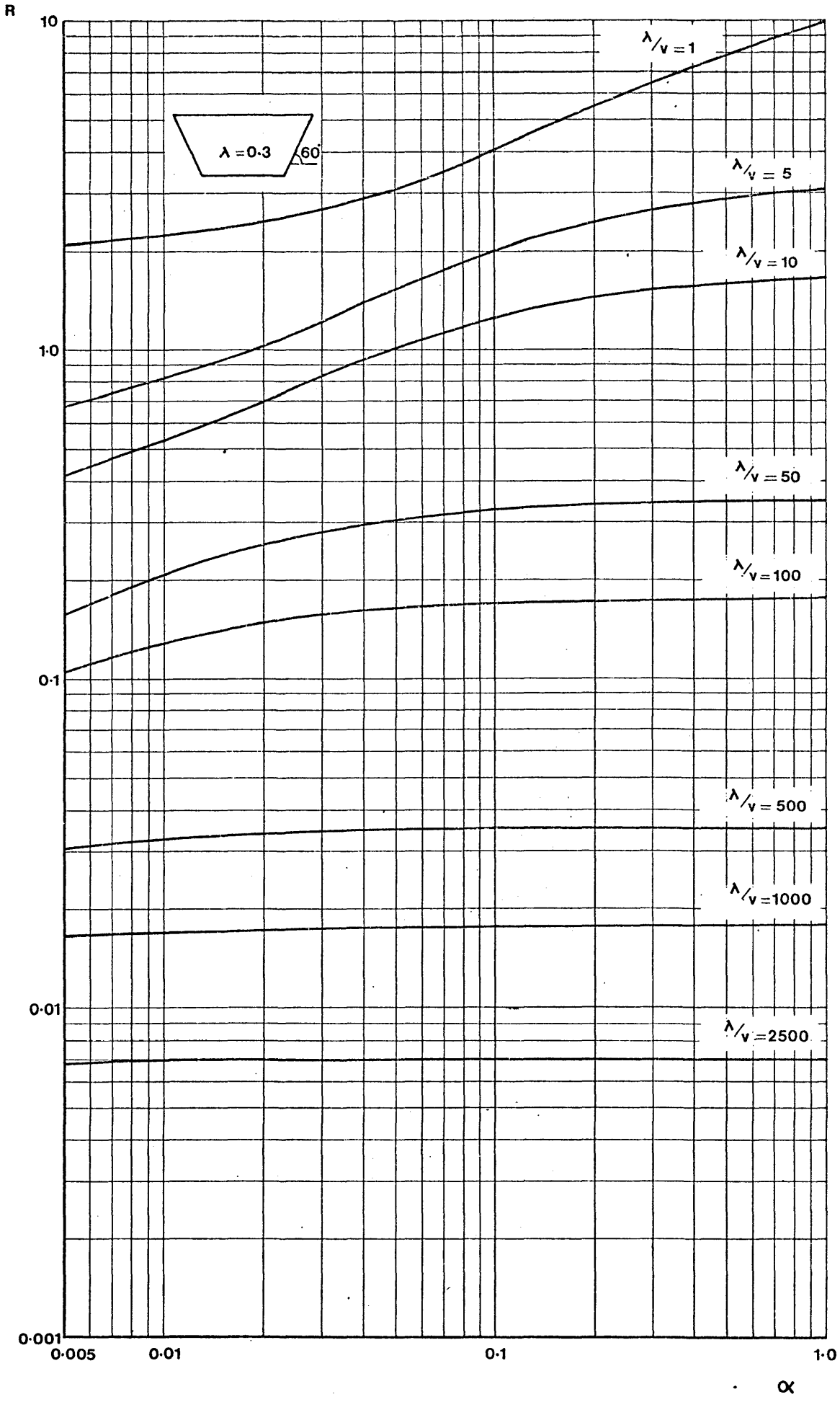


Fig.B18 Simplification of β calcs. for 60° trapezoidal box when λ = 0·3

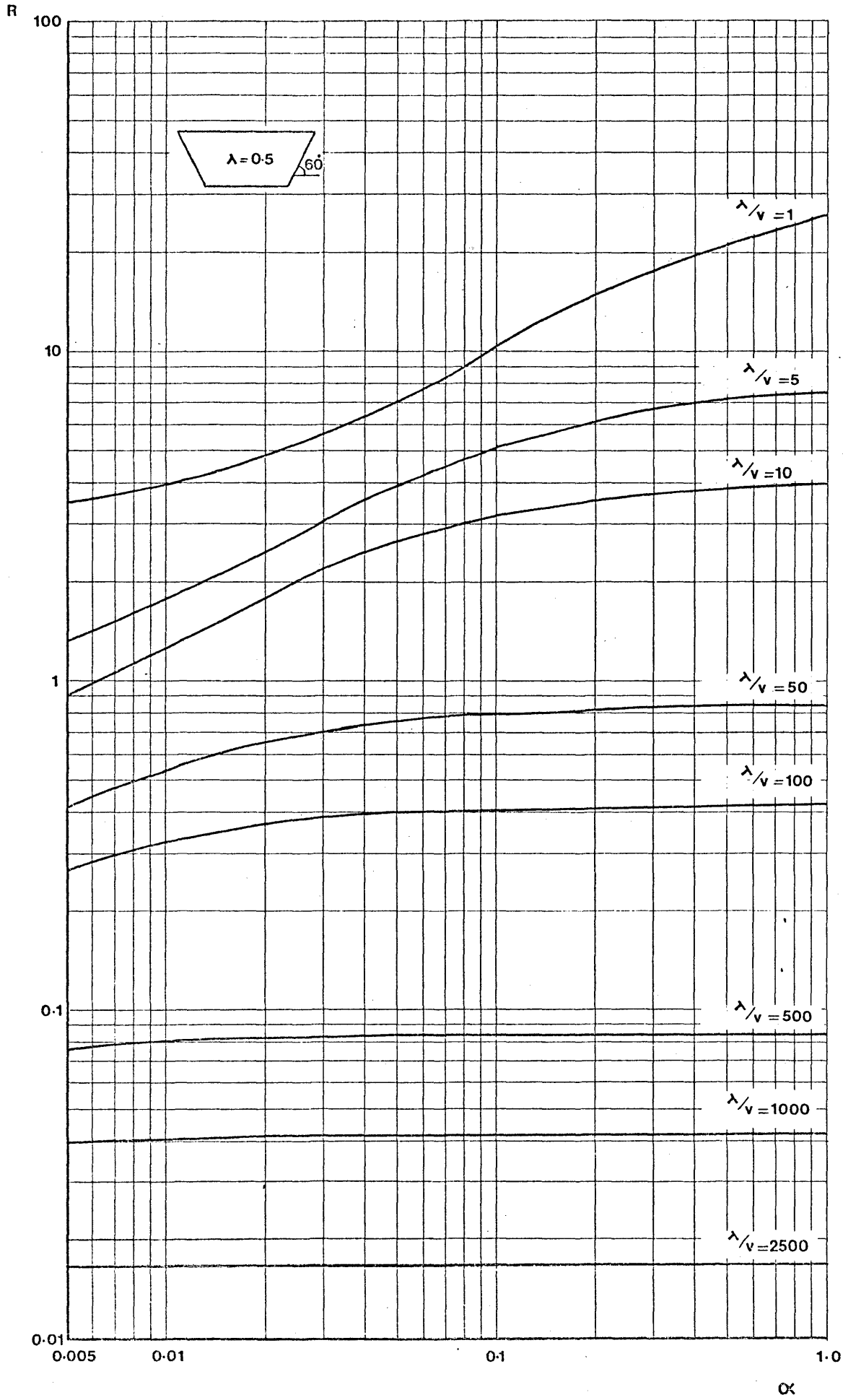


Fig.B19 Simplification of β calcs. for 60° trapezoidal box when λ=0·5

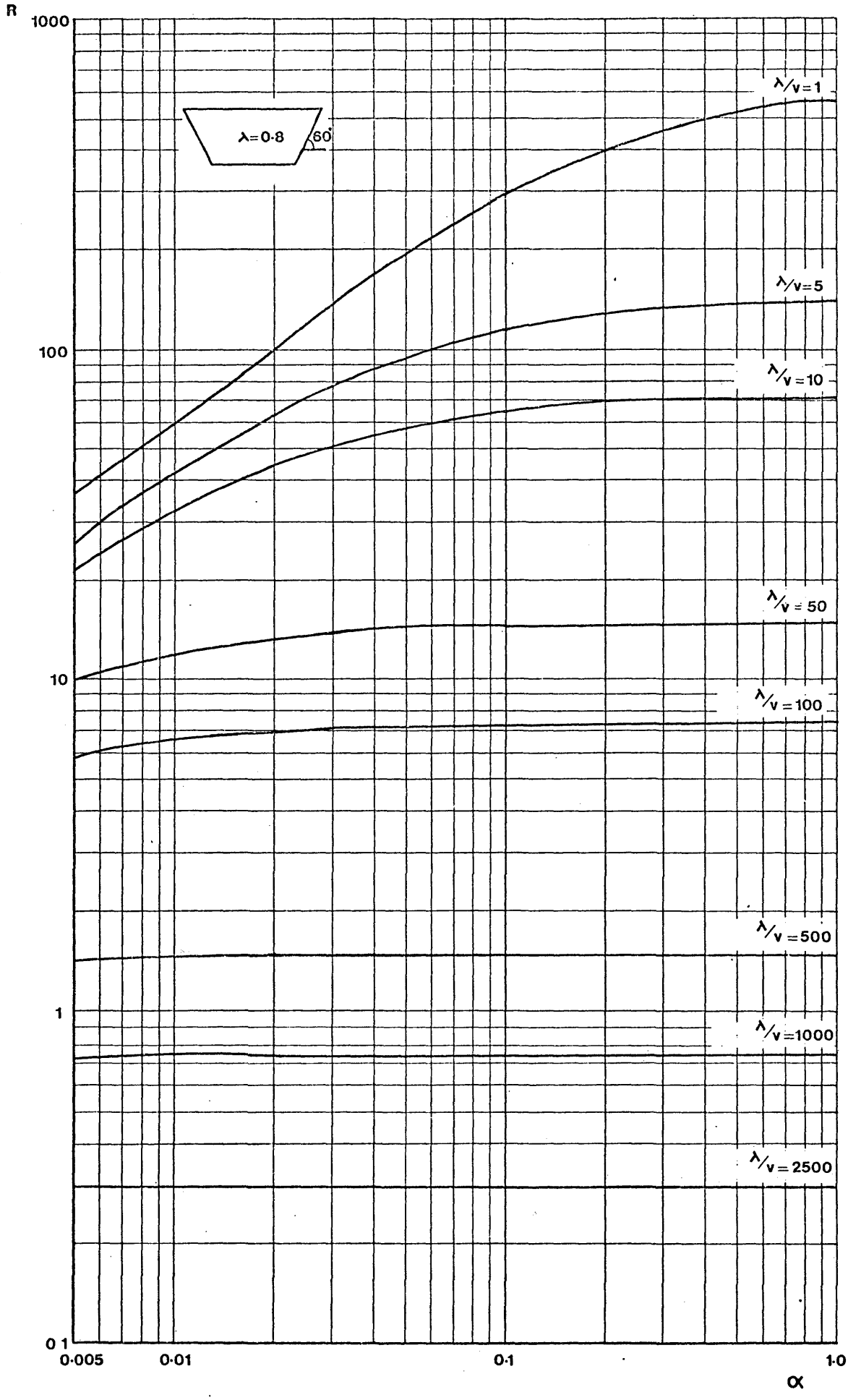


Fig.B20 Simplification of β calcs. for 60° trapezoidal box when λ=0·8.

APPENDIX C. SETTING OUT DETAILS FOR BIFURCATED ELEVATED HIGHWAY MODEL 4 AND LOCATION OF INSTRUMENTATION SECTIONS ON THE MODELS

C1. SETTING OUT DETAILS FOR MODEL 4

(1) Arcs BF, FG, GJ, JK and KC_2 are equal

(2) Diaphragm lines FF', GG', JJ' and KK' are radial

(3) Web 1 has constant centre line radius of 1220.5 mm

(4) Web 6 has radius of 1500.5 from BB' to curve reversal line RR' and then a reverse curve of 1541.5 mm radius

(5) Web 2 has radius of 1276.5 mm from BB' to GG' at (i) and radius of 1288.5 mm from (ii) to C_2C_2'. (i) to (ii) is a straight

(6) Web 3 has radius of 1332.5 mm from BB' to GG' at (iii) and radius of 1356.5 mm from (iv) to C_2C_2'. (iii) to (iv) is a straight

(7) Web 3A (radius 1424.5 mm) and Web 4A (reverse radius 1679.5 mm) meet at (v)

(8) A straight from (iv) to (v) meets the reverse curve of web 4A (radius 1633.5 mm) at (vi) and (vi) - (vii) is radial to the reverse curves

(9) Web 4 has radius of 1388.5 mm from BB' to FF' at (viii) and a straight joins (viii) to (vi)

(10) (x), (xi), (xii) are the midpoints of (iii) - (ix), (iii) - (iv) and (ix) - (vi) respectively

(11) Web 5 has radius of 1444.5 mm from BB' to (xiii) and reverse radius of 1587.5 mm from (xiv) to C_1C_1'. (xiii) to (xiv) is a straight.

C2. LOCATION OF INSTRUMENTATION SECTIONS.

C2.1 Model 1 (Figure 117)

(i) Instrumentation Sections 0-0, 3-3, 9-9, 11-11, 13-13 and 15-15 are on the centre lines of support diaphragms

(ii) Instrumentation Sections 2-2, 10-10 and 14-14 are at midspan of the outer spans

(iii) Instrumentation Sections 1-1, 4-4, 8-8 and 12-12 are 4.5 mm from the face of the support diaphragms (i.e. 22.5 mm from the centre line of the diaphragms)

(iv) Instrumentation Section 5-5 is on the line of the diaphragm with gauges on the webs 4.5 mm from both faces of the diaphragm, and gauges on both faces of the diaphragm

(v) Instrumentation Section 6-6 is radial, midway between the two diaphragms, to the centre line of Web 3, and then radial to the reverse curve

(vi) Instrumentation Section 7-7 is radial to both curves from the inside of the bifurcation radius.

C2.2 Model 2 (Figure 129)

(i) Instrumentation Sections 1-1, 3-3, 8-8, 10-10, 12-12 and 14-14 are on the centre lines of the support diaphragms

(ii) Instrumentation Sections 2-2, 9-9 and 13-13 are at midspan of the outer spans

(iii) Instrumentation Sections 4-4, 7-7 and 11-11 are 4.5 mm from the faces of the support diaphragms

(iv) Instrumentation Section 5-5 is on the curve reversal line

(v) Instrumentation Section 6-6 is radial to both curves from the inside of the bifurcation radius

C2.3 Model 4 (Figure 139)

(i) All Instrumentation Sections except 2-2, 6-6 and 11-11 are on diaphragm lines

(ii) Instrumentation Section 2-2 is at the quarter point of Span A-B

(iii) Instrumentation Section 6-6 is radial midway between diaphragms to Web 3A and then radial to the reverse curve

(iv) Instrumentation Section 11-11 is at midspan of Span C_2D.

APPENDIX D. A DESIGN APPROACH FOR DISTORTION AND THE BASIS FOR INTERIM DESIGN RULES CLAUSES 6.3.4 AND 6.3.5

D1 DESIGN APPROACH

The dimensional span length, βL, for most practical box girder structures is such that the support diaphragms do not significantly affect distortional stress levels at midspan. If internal diaphragms are for the moment neglected, each box can be analysed as a separate infinite BEF for which the following simple solution for peak stresses exists:

(a) For uniformly distributed loads

$$\sigma_{DW} = \frac{P_{UDL} \cdot \bar{y}}{\beta^2 \cdot I_x}$$

$$\sigma_{DB} = \frac{P_{UDL} \cdot F_D}{2}$$

(b) For knife edge loads

$$\sigma_{DW} = \frac{P_{KE} \cdot \bar{y}}{\beta \cdot I_x}$$

$$\sigma_{DB} = \frac{P_{KE} \cdot F_D \cdot \beta}{2}$$

.....(D1)

(c) For one axle of HB loading

$$\sigma_{DW} = \frac{P_{HB} \cdot \bar{Y}}{\beta \cdot I_x}$$

$$\sigma_{DB} = \frac{P_{HB} \cdot F_D \cdot \beta}{2} \qquad \text{..... (D1)}$$

The effects of the four axles of the HB vehicle are obtained by the summation:

$$\sigma_{DW(total)} = \sigma_{DW} \sum (C_{\beta x})$$

$$\sigma_{DB(total)} = \sigma_{DB} \sum (A_{\beta x}) \qquad \text{..... (D2)}$$

where

$$A_{\beta x} = e^{-\beta x}(\cos\beta x + \sin \beta x)$$

$$C_{\beta x} = e^{-\beta x}(\cos\beta x - \sin \beta x)$$

x is the longitudinal distance of the axle from midspan.

If σ_{DB} are unacceptable they may be reduced by diaphragming or by the redesign of transverse stiffening, and if σ_{DW} are unacceptable they may be reduced by diaphragming or by increasing the flange areas. Reduction factors which depend upon diaphragm spacing, βL_D, may be applied to the upper bound values of σ_{DB} and σ_{DW} given by Equations D1 and D2 when internal diaphragms are provided.

If R_W and R_B are the desired fractions of the values

of σ_{DW} and σ_{DB} with no diaphragming then the diaphragm spacings necessary to achieve these reductions are given by:

(a) For knife edge, HB and point loads

$$L_D = \frac{R_W}{\beta}$$

$$L_D = \frac{2\,(R_B)^{0.35}}{\beta}$$

(b) For uniformly distributed loads ..... (D3)

$$L_D = \frac{2.1\sqrt{R_W}}{\beta}$$

$$L_D = \frac{2.2\,(R_B)^{0.27}}{\beta}$$

i.e. σ_{DW} desired $= R_W \cdot \sigma_{DW}$ with no diaphragms.

Equations D3 are derived from the dimensionless curves given by Wright et al[13] for concentrated loads and Billington[14] for uniformly distributed loads and reproduced in Figures D1 to D8. Provided the diaphragms have a dimensionless stiffness q (see curves) such that the dimensionless BEF moment, m, or deflection, w, is the minimum for a given value of βL, then Equations D3 represent the sloping straight line of the curves. In other words, the effective diaphragm rigidity is infinite and Table 18 gives the minimum diaphragm stiffness for

given values of βL to achieve this. Expressions for q for various types of diaphragming are given in Table 1. Diaphragms are then designed to take the full distortional loading. For plate diaphragms the shear stress τ_D is given by:

$$\tau_D = \frac{P.b_T}{h(b_T+b_B)t_p} \quad \ldots\ldots\ldots\ldots\ldots\ldots\ldots \quad (D4)$$

For cross bracing with the compression brace fully effective, the force F_B in each brace is given by:

$$F_B = \frac{\sqrt{1+\left(\frac{b_T+b_B}{2h}\right)^2}}{2\left(1+\frac{b_T}{b_B}\right)} \cdot P \quad \ldots\ldots\ldots\ldots\ldots\ldots \quad (D5)$$

where P = antisymmetrical distortional load acting above one web

D = depth of box

t_p = thickness of plate diaphragm.

D2 BASIS FOR DESIGN RULES

Clauses 6.3.4 and 6.3.5 of the Interim Design Rules[38] are largely based on the simplified design approach described in D1 but Equations D1 and D3 are combined to allow for the influence of diaphragms directly as it was felt that it was often necessary to space internal diaphragms for considerations other than that of controlling distortion.

The combination of Equations D1 and D3 leads to the following maxima for σ_{DW} and σ_{DB}

(i) For a uniformly distributed applied torque T_{UDL} per unit length of span

$$\sigma_{DW} = \frac{T_{UDL}\ \bar{y}\ L_D^2}{4.5\ b_T\ I_x} \qquad \text{for } \beta L_D < 1.6$$

$$\sigma_{DW} = 0.6\ \frac{T_{UDL}\ \bar{y}\ L_D^2}{(\beta L_D)^2\ b_T\ I_x} \qquad \text{for } \beta L_D \geqslant 1.6$$

$$\sigma_{DB} = \frac{T_{UDL}\ F_D}{b_T\ Z} \qquad \text{for } \beta L_D > 2.65$$

$$\sigma_{DB} = \frac{T_{UDL}\ F_D}{2\ b_T\ Z}\left(\frac{\beta L_D}{2.2}\right)^{3.7} \qquad \text{for } \beta L_D \leqslant 2.65$$

(D6)

(ii) For a single applied torque T due to axle or knife edge loading applied midway between diaphragms

$$\sigma_{DW} = \frac{T\ \bar{y}\ L_D}{b_T\ I_x} \qquad \text{for } \beta L_D \leq 1.0$$

$$\sigma_{DW} = \frac{T\ \bar{y}\ L_D}{(\beta L_D)\ I_x\ b_T} \qquad \text{for } \beta L_D > 1.0$$

$$\sigma_{DB} = \frac{T\ F_D\ (\beta L_D)}{2 b_T\ L_D\ Z} \qquad \text{for } \beta L_D > 2$$

$$\sigma_{DB} = \frac{T\ F_D}{15.5 b_T\ L_D\ Z} (\beta L_D)^{3.9} \qquad \text{for } \beta L_D \leq 2 \qquad \text{(D7)}$$

The design rules incorporate the curves provided for the simplification of the β calculation described in Appendix B. Also the summation factors for the HB vehicle used in Equation D2 are plotted for the range of β over which there is interaction between the effects of adjacent axles (see Figure 289).

The rules as drafted provide a simple method for assessing the importance of distortional stresses in steel box girders. Approximations used in the rules lead to conservative results.

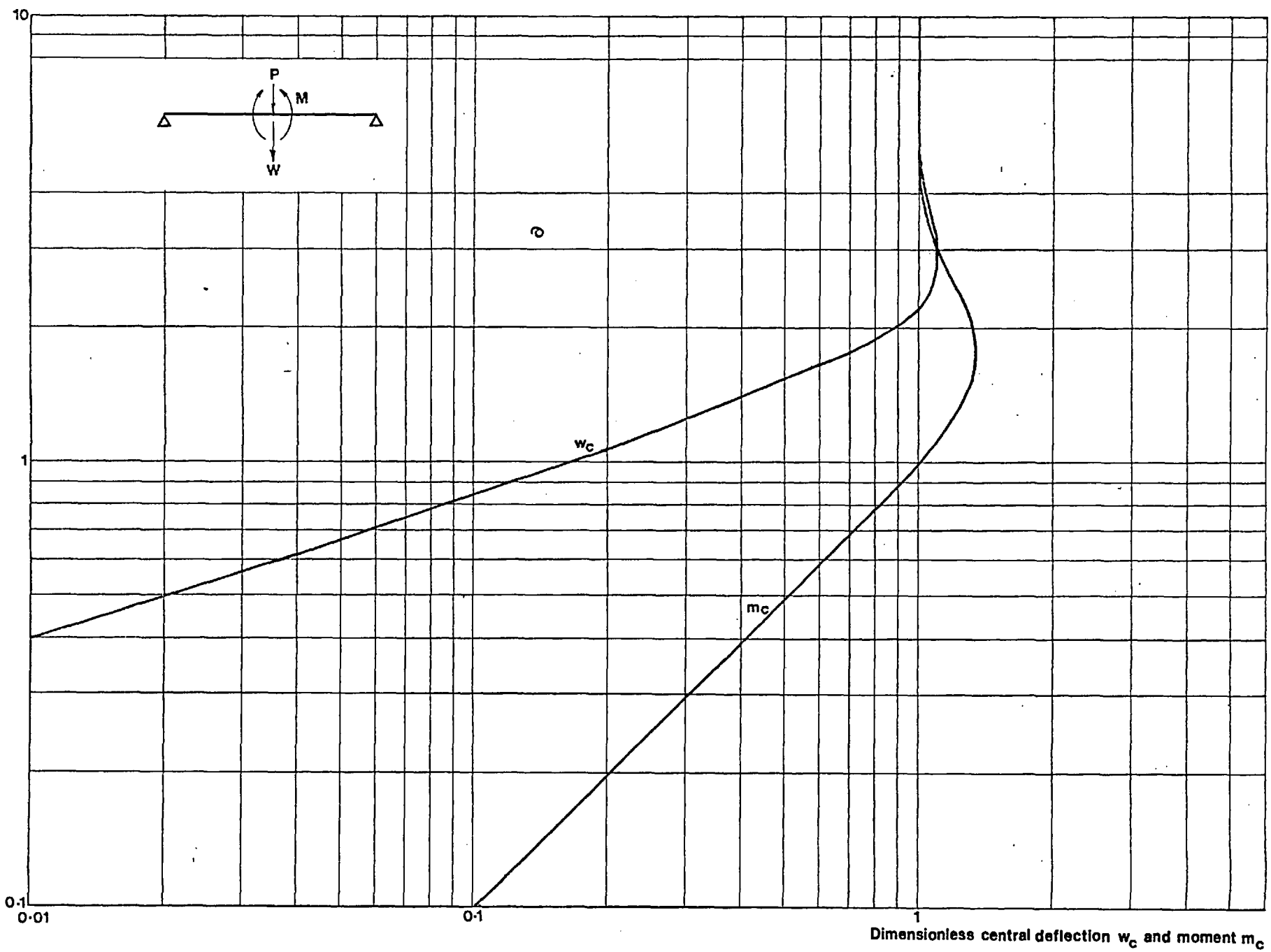


Fig.D1
Reproduced from Ref.13

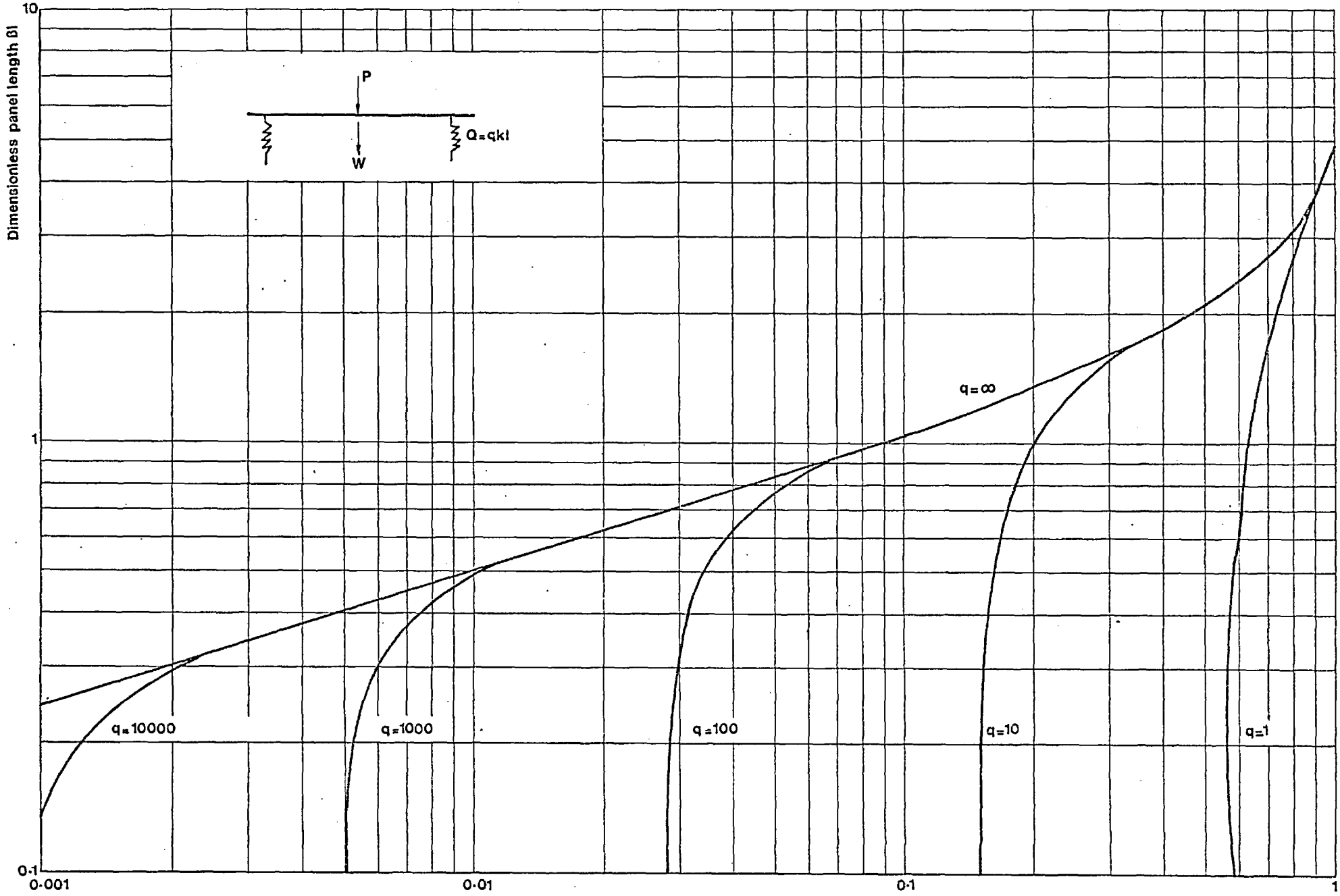

Dimensionless panel length ßl
10
1
0·1
0·001
0·01
0·1
1
P
W
Q=qkl
q=∞
q=10000
q=1000
q=100
q=10
q=1
Dimensionless central deflection $w_c = \frac{8EI_b ß^3 W}{P}$

Fig.D2

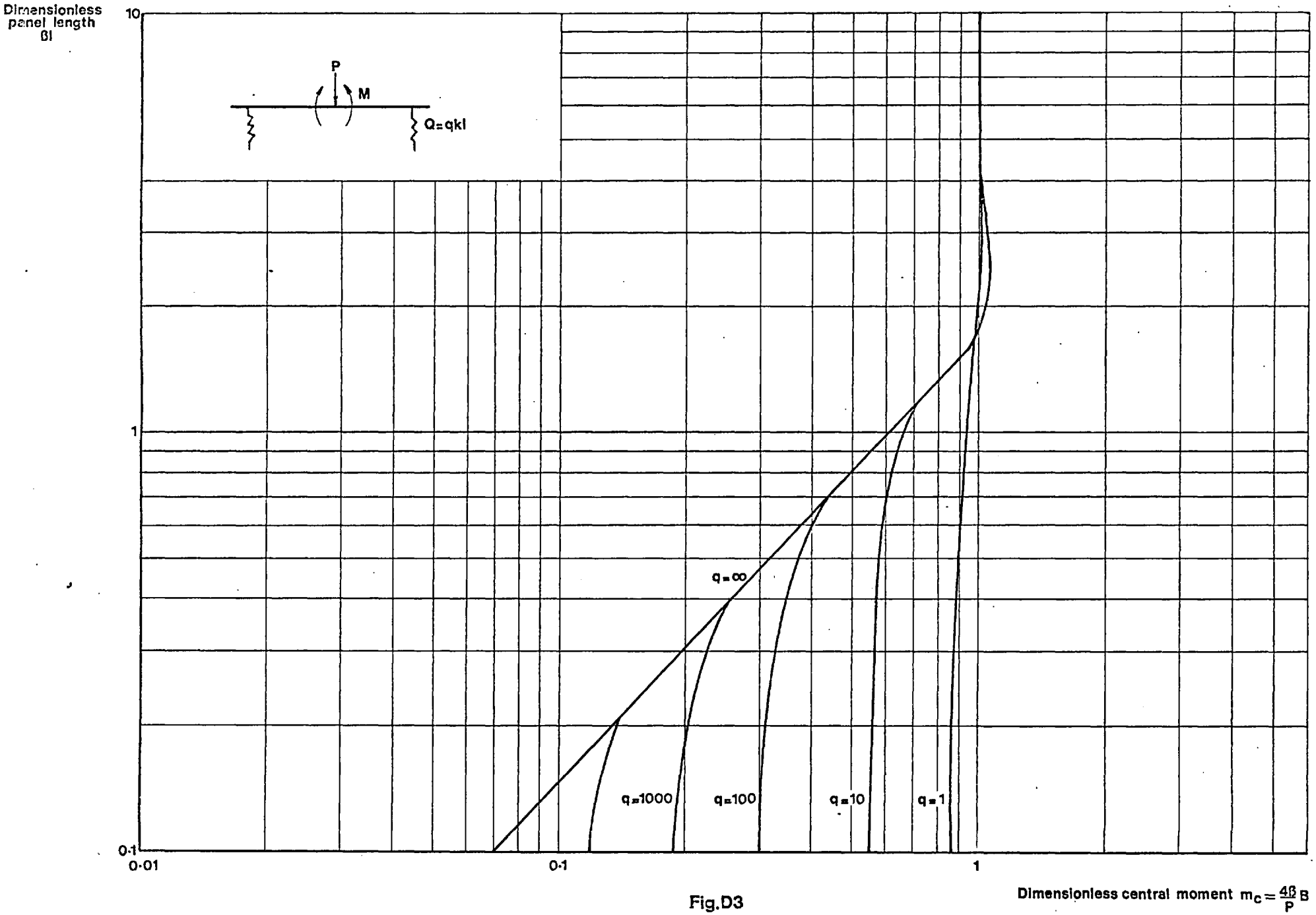


Fig.D3
Reproduced from Ref.13

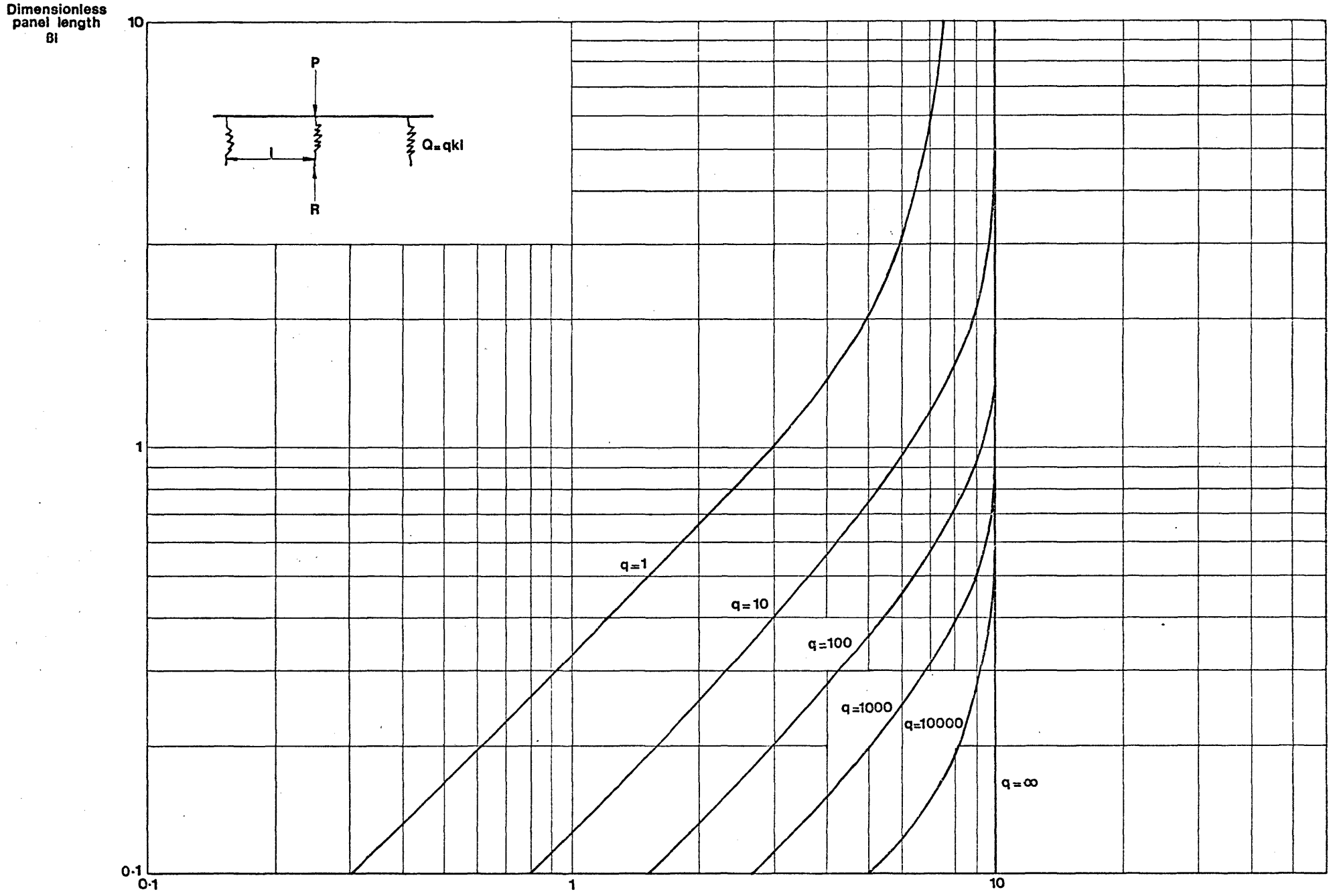

Dimensionless panel length βl
10
1
0·1
0·1
1
10
P
R
l
Q=qkl
q=1
q=10
q=100
q=1000
q=10000
q=∞
Dimensionless support reaction r=R/P

Fig. D4

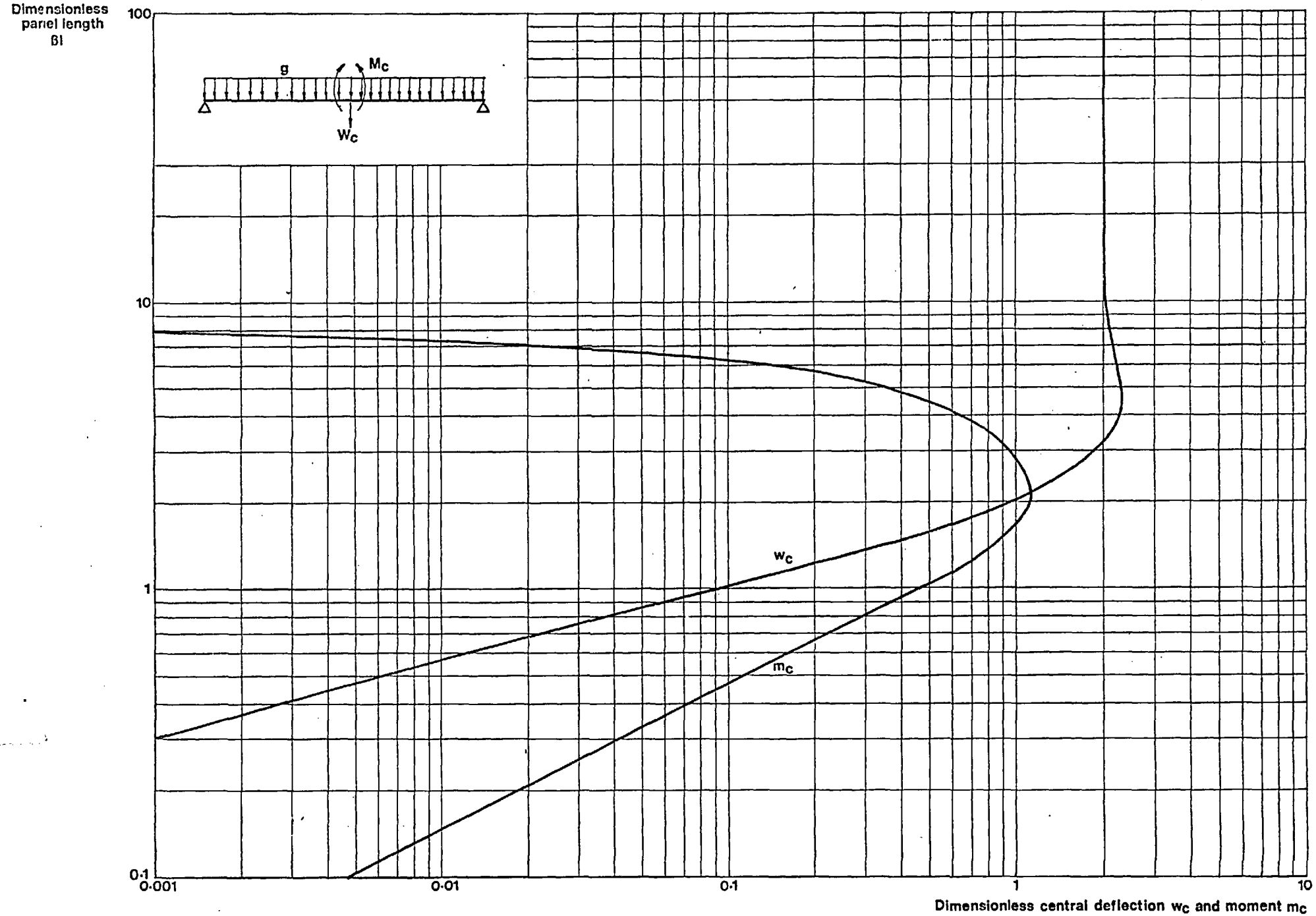


Fig.D5
Reproduced from Ref.14

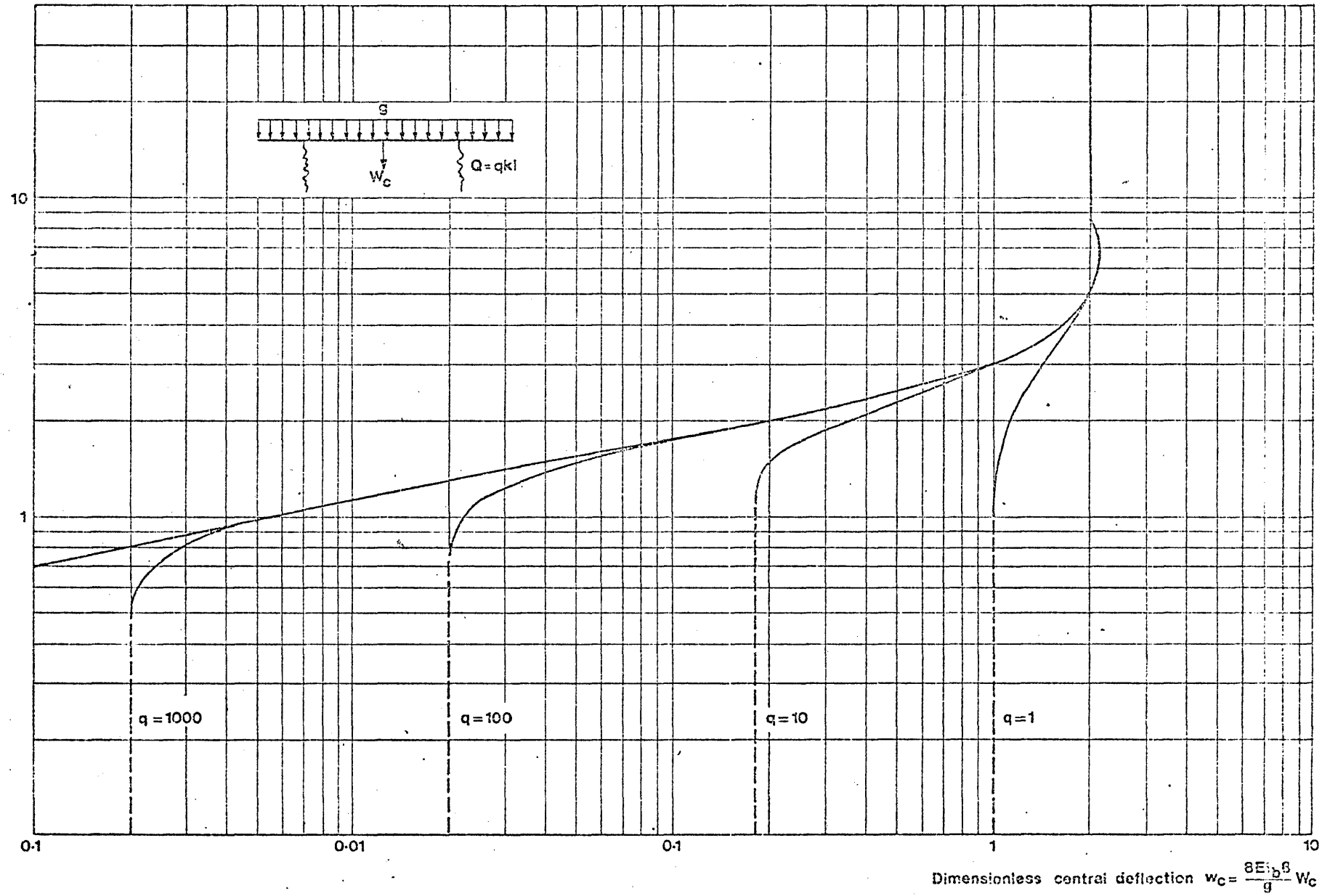


Fig. D6 Reproduced from Ref. 14

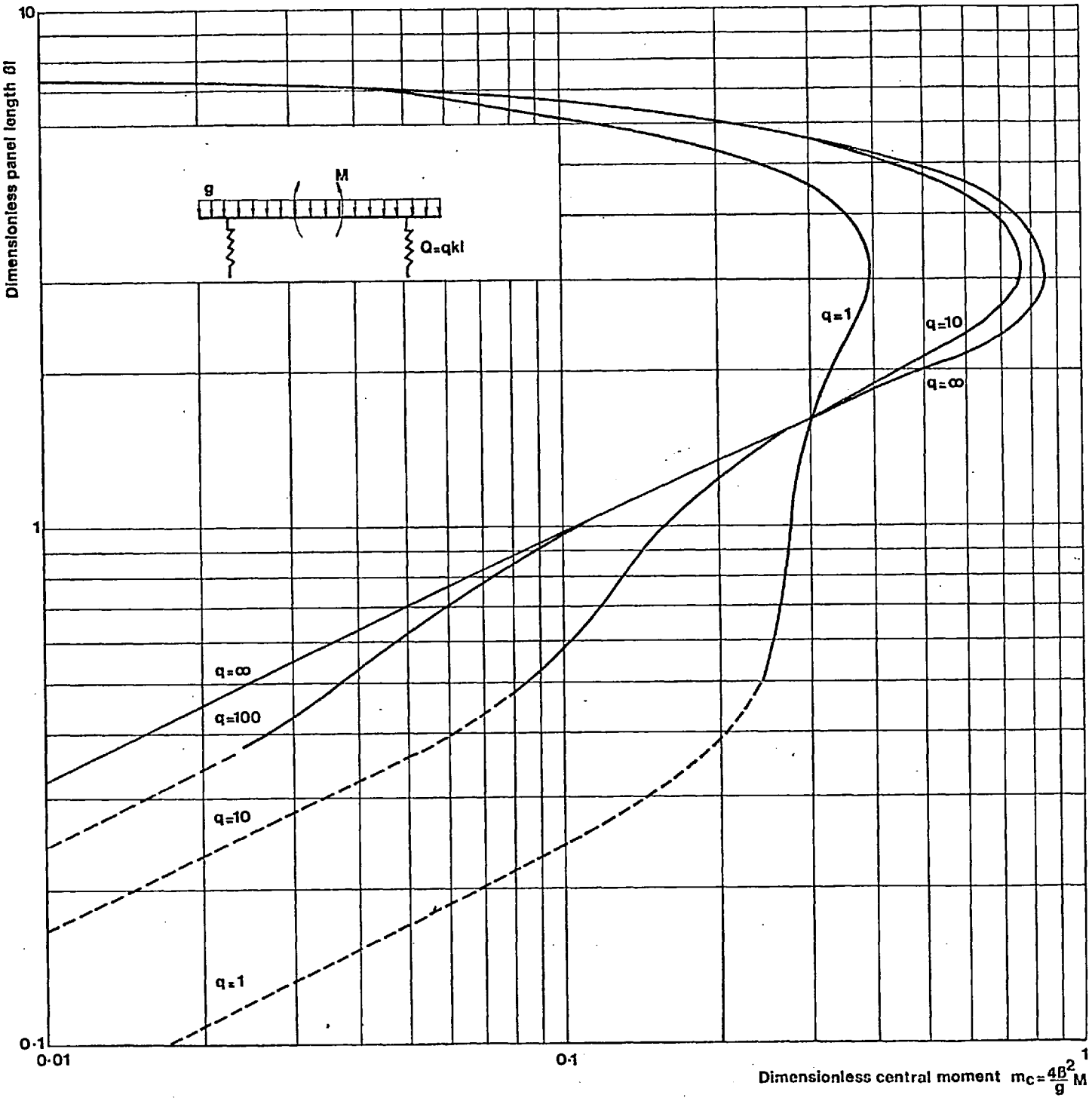


Fig.D7
Reproduced from Ref.13

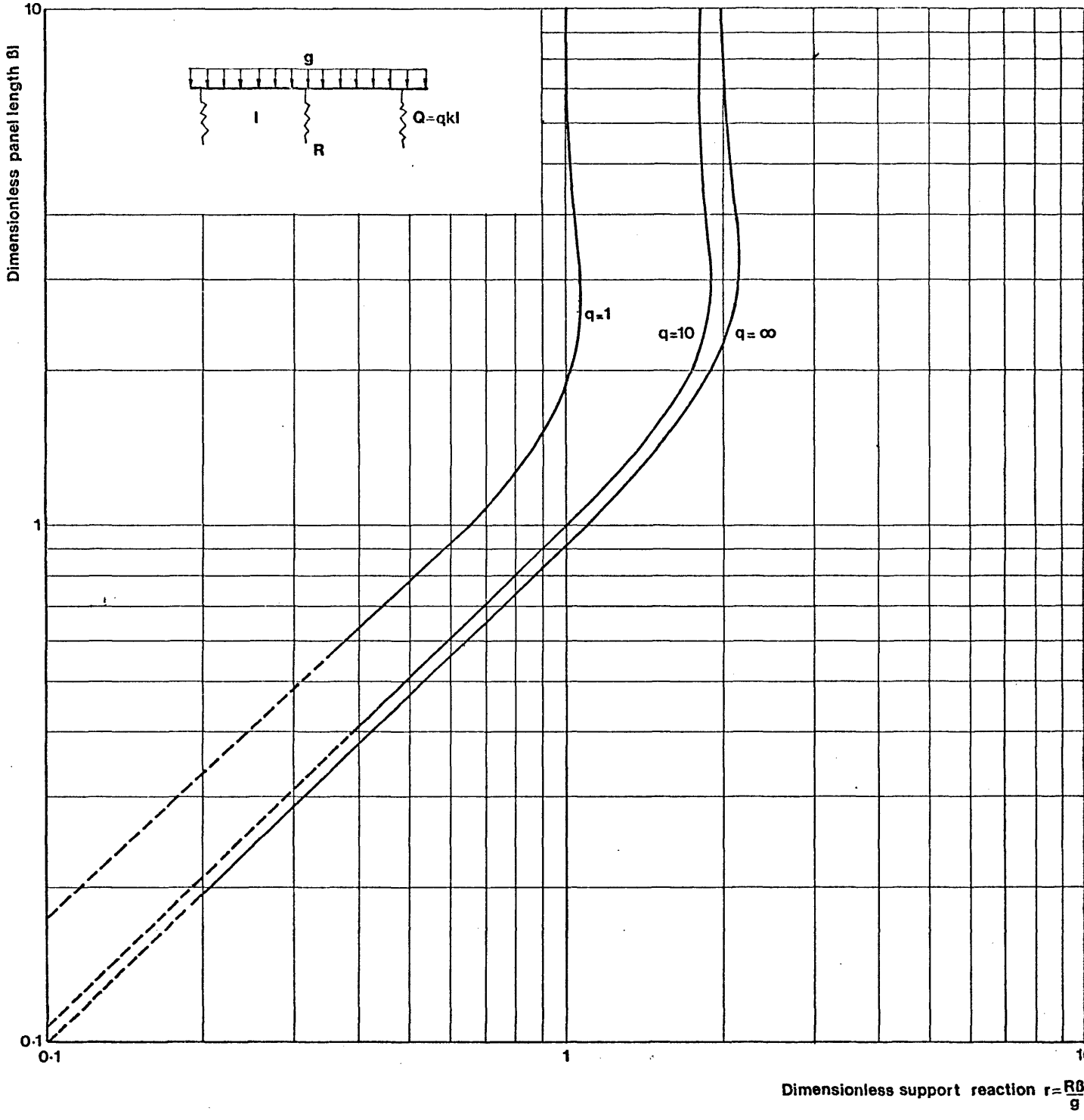


Fig. D8
Reproduced from Ref.14

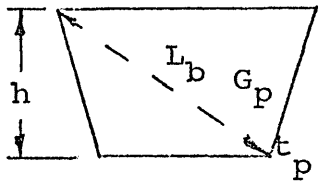
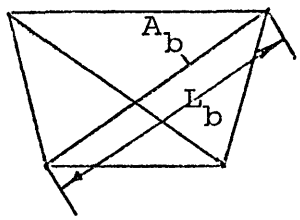
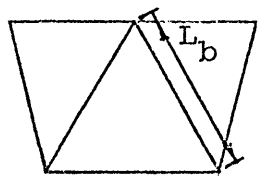
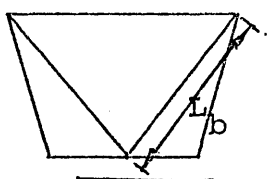
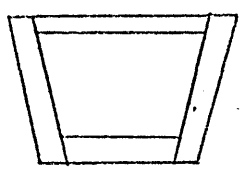
Diaphragm type	Q	q
Plate diaphragm (spacing 1)  Area of X-sect = A_p	$\dfrac{G_p t_p L_b^2 \delta_b^2}{2A_p \delta_1^2}$ $A_b = \dfrac{G_p t_p L_b^3}{2E_p A_p}$	$\dfrac{G_p t_p L_b^2 \cdot \delta_b^2}{2A_p \cdot 1 \cdot \delta_1}$
Cross bracing  	$\dfrac{E_b A_b}{L_b}\left(\dfrac{\delta_b}{\delta_1}\right)^2$ $t_p = \dfrac{2A_b E_p A_p}{G_p L_b^3}$	$\dfrac{E_b A_b}{L_b 1} \cdot \dfrac{\delta_b^2}{\delta_1}$
K bracing  $L_b = \sqrt{h^2 + \left(\frac{b_B}{2}\right)^2}$	$\dfrac{E_b A_b h L_d}{2L_b^3}\left(1+\dfrac{b_T}{b_B}\right)\dfrac{\delta_b}{\delta_1}$	$q = \dfrac{Q\delta_1}{1}$
Inverted K  $L_b = \sqrt{h^2 + \left(\frac{b_T}{2}\right)^2}$	$\dfrac{E_b A_b h L_d}{2L_b^3}\left(1+\dfrac{b_T}{b_B}\right)\dfrac{\delta_b}{\delta_1}$	$q = \dfrac{Q\delta_1}{1}$
Ring Stiffener 	$\dfrac{1}{\delta_1}$ $t_p = \dfrac{1b^2}{4G_p h\left(b_T+b_B\right)\cdot\delta_1}$	1
where	$\delta_1 = \dfrac{1}{K}$,	$\delta_b = \dfrac{2\left(1+\dfrac{b_T}{b_B}\right)\delta_1}{\sqrt{1+\left(\dfrac{b_T+b_B}{2h}\right)^2}}$

Table 1. Diaphragm formulae

SECTION NUMBER	A metres (feet)	B metres (feet)	C metres (feet)	D metres (feet)	t_a mm (inches)	t_b mm (inches)	t_d mm (inches)
1	1.8 (6)	1.8 (6)	1.8 (6)	1.8 (6)	300 (12)	300 (12)	300 (12)
2	3.6 (12)	3.6 (12)	9 (30)	1.8 (6)	300 (12)	225 (9)	600 (24)
3	5.4 (18)	5.4 (18)	9 (30)	1.8 (6)	300 (12)	150 (6)	600 (24)
4	7.2 (24)	7.2 (24)	9 (30)	1.8 (6)	300 (12)	113 (4½)	600 (24)
5	3.6 (12)	3.6 (12)	9 (30)	1.8 (6)	13 (½)	25 (1)	13 (½)
6	5.4 (18)	5.4 (18)	9 (30)	1.8 (6)	13 (½)	16 (⅝)	13 (½)
7	7.2 (24)	7.2 (24)	9 (30)	1.8 (6)	13 (½)	11 (7/16)	13 (½)
8	5.4 (18)	5.4 (18)	5.4 (18)	1.8 (6)	300 (12)	150 (6)	600 (24)
9	5.4 (18)	4.05 (13.5)	5.4 (18)	1.8 (6)	300 (12)	200 (8)	600 (24)
10	5.4 (18)	2.7 (9)	5.4 (18)	1.8 (6)	300 (12)	300 (12)	600 (24)
11	5.4 (18)	5.4 (18)	5.4 (18)	1.8 (6)	13 (½)	16 (⅝)	13 (½)
12	5.4 (18)	4.05 (13.5)	5.4 (18)	1.8 (6)	13 (½)	21 (5/6)	13 (½)
13	5.4 (18)	2.7 (9)	5.4 (18)	1.8 (6)	13 (½)	32 (1¼)	13 (½)

Table 2. Centreline dimensions and wall thicknesses of examples used in 2.5.

SECTION NUMBER		5	6 and 11	7	12	13	6A
TOP FLANGE PLATE	Thickness t	½ in	½ in	½ in	½ in	½ in	½ in
	Longitudinal stiffening	8 in x ½ in flats @ 12 in c/c	8 in x ½ in flats @ 12 in c/c	8 in x ½ in flats @ 12 in c/C	8 in x ½ in flats @ 12 in c/c	8 in x ½ in flats @ 12 in c/c	8 in x ½ in flats @ 12 in c/c
	Transverse stiffening	15 in x ¼ in web 6 in x ½ in flange @ 6 ft c/c	24 in x ½ in web 6 in x ½ in flange @ 6 ft c/c	28 in x ½ in web 6 in x ½ in flange @ 6 ft c/c	24 in x ½ in web 6 in x ½ in flange @ 6 ft c/c	24 in x ½ in web 6 in x ½ in flange @ 6 ft c/c	24 in x ½ in web 6 in x ½ in flange @ 6 ft c/c
BOTTOM FLANGE PLATE	Thickness	1 in	⅝ in	7/16 in	5/6 in	1¼ in	⅝ in
	Longitudinal stiffening	5 in x ½ in flats @ 2 ft c/c	5 in x ½ in flats @ 2 ft c/c	5½ in x ½ in flats @ 2 ft c/c	8 in x ½ in flats @ 2 ft c/c	8 in x ½ in flats @ 2 ft c/c	5 in x ½ in flats @ 2 ft c/c
	Transverse stiffening	10 in x ½ in flats @ 12 ft c/c	12 in x ½ in flats @ 12 ft c/c	12 in x ⅝ in flats @ 12 ft c/c	10 in x ½ in flats @ 12 ft c/c	8 in x ½ in flats @ 12 ft c/c	12 in x ½ in flats @ 6 ft c/c
WEB PLATE		All ½ in plate with 4 in x ⅜ in flats transverse at 6 ft c/c					½ in plate Transverse stiffeners as bottom flange

Table 3. Details of stiffening used in the steel bridge examples of 2.5

Bridge No.	Name	DoE ref	Type
1	Fylde Bridge	4/1	3 cell rectangular m'cell
2	Irwell Valley Bridge	4/2	Trapezoidal multibox
3	Samlesbury Bridge	4/3	Rectangular multibox
4	Rosebank Bridge	4/7	Rectangular
5	Bidston Moss Viaduct	4/11a	Twin rectangular box
6	Porton Road Bridge	6/5	Rectangular
7	Red Lane Dyke	9/10	Single rectangular box
8	Lofthouse Interchange	9/11a	Trapezoidal multibox
9	Neath Bridge 15	10/3a	Rectangular
10	Taff River Bridge	10/4	Rectangular
11	Neath Bridge 4	10/7a	Trapezoidal
12	Coombe Lane Flyover	11/1	Rectangular multibox
13	Watford By-Pass	11/9	Rectangular multibox
14	Elstree Road Bridge	11/10	Rectangular
15	Kirkless Viaduct	14/1	Rectangular multibox
16	Blakelow Lane Bridge	14/3	Rectangular
17	Foxcover Lane Overbridge	14/11	Twin rectangular boxes
18	South Moor Accom. Bridge	14/15	Trapezoidal
19	Hylton Bridge	14/23	Twin rectangular boxes
20	Wrey Bridge	15/1	Trapezoidal multibox
21	Monks Lane Bridge	15/2	Trapezoidal
22	Thornham East Bridge	15/4	Rectangular
23	Wardley Moss Bridge	15/6	Trapezoidal multibox
24	Station Road Bridge	16/15	Trapezoidal multibox
25	Roughetts Road Bridge	16/16	Trapezoidal multibox
26	Huntworth Viaduct	17/2	Twin rectangular boxes
27	Huntworth Lodge Accom. Bridge	17/9	Single trapezoidal box
28	Over Bridge Gloucester		Trapezoidal

Table 4. List of practical bridge examples referred to in 2.5

Bridge No	Bl span	Bl panel	$I_c/4I_b$	r_β	r_S	ν	$\gamma = \frac{b_B}{b_T}$	$\lambda = \frac{C}{b_T}$	$\alpha = \frac{D_{YB}}{D_{YT}}$	$\nu = \frac{D_{YC}}{D_{YT}}$	λ/ν
1	8.55	0.95	1.00	1.00	0.98	0.060	1	1.71	.00940	.327	5.23
2	6.70	1.67	0.82	1.06	0.77	0.247	.667	.917	.248	.159	5.77
3	12.36	-	0.64	1.12	0.91	0.241	1	4.00	.203	.237	16.9
4	9.67	-	0.88	1.03	1.09	0.255	1	3.53	1.50	1.29	2.74
5	3.33	-	1.01	1.00	0.84	0.243	1	.566	.0105	.00101	560.
6	3.54	0.19	1.24	0.95	0.93	0.248	1	.755	.0232	.000670	1120.
7	8.26	0.25	1.10	0.98	0.85	0.251	1	.750	54.1	.0153	49.0
8	10.79	0.69	0.88	0.97	0.98	0.243	.545	1.09	.0509	.0285	38.2
9	6.48	-	1.13	0.97	0.94	0.250	1	1.25	.878	.000520	2385.
10	6.75	-	1.19	0.96	1.01	0.229	1	.824	.0506	.0242	34.0
11	7.47	-	1.12	0.97	0.92	0.238	.862	.552	.388	.269	2.05
12	4.85	0.56	0.75	1.08	0.79	0.230	1	1.61	.418	.0156	103.2
13	12.21	0.92	1.27	0.95	0.99	0.249	1	1.52	.0179	.00127	1197.
14	2.72	1.12	1.13	0.97	0.87	0.249	1	1.61	.460	.00191	843.
15	8.12	-	0.91	1.03	0.83	0.202	1	1.33	.0410	.0284	46.8
17	5.78	1.35	0.80	1.06	0.81	0.156	1	1.29	.0401	.207	5.23
18	3.74	0.93	1.23	0.95	1.00	0.241	.924	.453	.0120	.00181	250.
19	8.26	-	0.88	1.03	0.79	0.230	1	.956	.179	.114	8.38
20	6.02	0.41	0.51	1.19	0.54	0.210	.364	.538	.0106	.000550	971.
21	8.12	0.24	0.91	1.03	0.83	0.202	.333	.528	.134	.0869	6.07
22	7.99	2.50	1.26	0.94	1.01	0.242	1	.650	.00360	.000450	1438.
23	3.27	-	1.25	0.94	0.91	0.213	.843	.243	.0523	.0233	10.4
26	7.02	-	0.77	1.07	0.75	0.225	1	.783	.0114	.00620	126.

Table 5. Table of parameters for practical boxes of 2.5

(See Table 3 for list of bridge numbers)

Member Type	Bending Rigidity (EI) Kip. ins	Torsional Rigidity (GJ) Kip. ins	Shear Rigidity (GA) Kip. ins
Longitudinal	1.278×10^{10}	7.190×10^{9}	1.246×10^{6}
Transverse box	1.0×10^{10}	1.0×10^{10}	2×10^{6}
Transverse slab	6.221×10^{7}	1.037×10^{8}	1.440×10^{6}

Table 6. Twin box example of Chapter 3.
Member properties for initial grid analysis with the full torsional stiffness.

Description of analysis	Loaded box			Unloaded box		
	δ_B (in)	$\delta_T+\delta_D$ (in)	$\delta_{T(GRID)}$ (in)	δ_B (in)	$\delta_T+\delta_D$ (in)	$\delta_{T(GRID)}$ (in)
Finite element	$.7056 \times 10^{-2}$	$.1599 \times 10^{-2}$	-	$.1610 \times 10^{-2}$	$.1147 \times 10^{-2}$	-
Grid - BEF (full GJ)	$.4788 \times 10^{-2}$	$.4253 \times 10^{-2}$	$.2240 \times 10^{-3}$	$.3966 \times 10^{-2}$	$.2485 \times 10^{-2}$	$.1241 \times 10^{-3}$
Grid - BEF (GJ/19 for both boxes)	$.7074 \times 10^{-2}$	$.1598 \times 10^{-2}$	$.1646 \times 10^{-2}$	$.1681 \times 10^{-2}$	$.1256 \times 10^{-2}$	$.1127 \times 10^{-2}$
Grid - BEF (GJ/18.45 for loaded box GJ/21.18 for unloaded box)	$.7102 \times 10^{-2}$	$.1652 \times 10^{-2}$	$.1651 \times 10^{-2}$	$.1653 \times 10^{-2}$	$.1157 \times 10^{-2}$	$.1148 \times 10^{-2}$

Table 7. Twin box example of Chapter 3

Deflections in inches (δ_B= bending deflection, δ_T = torsional deflection, δ_D = distortional deflection, $\delta_{T(GRID)}$ = torsional deflection from grid analysis).

Material	E(lb/in^2)	t(in)	ν
Steel	28×10^6	0.02476	0.3
Araldite and sand	2.38×10^6	0.299	0.227
Equivalent composite plate	3.95×10^6	0.356	0.261

Table 8. Merstham Interchange Model

Table of material properties

Member Type	Bending Rigidity (EI) Kip. ins	Torsional Rigidity (GJ) Kip. ins	Shear Rigidity (GA) Kip. ins
Longitudinal	6225.5	4400.8	4598.5
Transverse box	10000	1000	10000
Transverse slab	30.75	23.41	1663.8

Table 9. Merstham Interchange Model

Member properties for initial grid analysis with the full torsional stiffness.

Model No	No of test specimens	Young's Modulus			Poisson's ratio	
		N/mm^2	lb/in^2	$\pm$		$\pm$
1	4	1.72×10^4	2.5×10^6	5%	.26	4%
2	7	1.63×10^4	2.37×10^6	4%	.25	4%
4	2	1.67×10^4	2.43×10^6	4%	.25	4%

Table 10. Elastic properties of Araldite and sand material used for the Bifurcated Elevated Highways models

Birmingham Gauge No	Thickness	
	mm	inches
22	0.7938	0.03125
24	0.6289	0.02476
26	0.4981	0.01961
27	0.4432	0.01745
28	0.3969	0.01563
32	0.2489	0.0098

Table 11. Bifurcated Elevated Highways Models

Birmingham steel gauge thicknesses. These are the nearest Birmingham gauges to those used. Where thicknesses are not exact Birmingham gauge the correct thicknesses are given on the diagrams.

Model No	No of test specimens	Young's Modulus			Poisson's ratio	
		N/mm^2	lb/in^2	$\pm$		$\pm$
4	2	2.01×10^5	29.2×10^6	2%	0.3	2%

Table 12. Bifurcated Elevated Highways - Model 4

Elastic properties of steel.

Load case	Span	Lane	Total Load	
			N	lb
1	AB	1	411.2	92.4
2	AB	2	423.6	95.2
3	AB	3	436.1	98.0
4	AB	4	447.2	100.5
5	BC	1	486.8	109.4
6	BC	2	500.6	112.5
7	BC	3A	511.8	115.0
8	BC	3B	505.1	113.5
9	BC	4	503.4	113.1
10	C_2D	1	417.0	93.7
11	C_2D	2	430.8	96.8
12	C_2D	3A	441.4	99.2
13	C_1E	3B	435.2	97.8
14	C_1E	4	424.1	95.3

Table 13. Bifurcated Elevated Highways Models

Lane loading intensities.

Load case	Type of load	Model	Span	Lane	Total Load		Figure
					N	lb	
15	HB	1	AB	1	721	162	32a
16	"	2	AB	1	"	"	32b
17	"	1	AB	2	"	"	33a
18	"	3,4	AB	2	"	"	33b
19	"	1	AB	3	"	"	34
20	"	1	AB	4	"	"	35
21	"	1	BC	1	"	"	36a
22	"	2	BC	1	"	"	36b
23	"	1	BC	2	"	"	37
24	"	2	BC	2/3	"	"	38a
25	"	3	BC	2/3	"	"	38b
26	"	4	BC	2/3	"	"	38c
27	"	2	BC	3A	"	"	38d
28	"	1	BC	3B	"	"	39
29	"	1	BC	4	"	"	40a
30	"	2	BC	4	"	"	40b
31	"	1	C_2D	1	"	"	41a
32	"	3,4	C_2D	1	"	"	41b
33	"	1	C_2D	2	"	"	42
34	"	1	C_2D	3A	"	"	43a
35	"	2	C_2D	3A	"	"	43b
36	"	1	C_1E	3B	"	"	44a
37	"	2,4	C_1E	3B	"	"	44b
38	"	1	C_1E	4	"	"	45
46-49	Knife edge	1	BC	-	225.5	50	47
50-53	" "	2	BC	-	"	"	48
54-59	Point load	1	BC	-	"	"	52
60-63	" "	2	BC	-	"	"	53
64-67	" "	3	BC	-	"	"	54
68-71	" "	4	BC	-	"	"	55
72	HB	3	BC	1	721	162	36c
73	"	4	BC	1	"	"	36d
74	"	3	BC	3A	"	"	38e
75	"	4	BC	3A	"	"	38f
76	"	3	BC	4	"	"	40c
77	"	4	BC	4	"	"	40d
78-81	Knife edge	3	BC	-	222.5	50	49
82-85	" "	4	BC	-	"	"	50
86-87	Settlement	2	-	-	-	-	56
88-89	"	4	-	-	-	-	57

Table 14. Bifurcated Elevated Highways Models

Table of loading cases other than Lane Loadings.

Span	No. of internal diaphragms	Load case	% of total load carried by loaded box	% of total load carried by adjacent box	% of load in loaded box carried by adjacent box	σ_W/σ_B for loaded box (%)	σ_W/σ_B for adjacent box (%)
C_2D	0	10	89.5	10.5	11.7	106.6	334.9
		12	76.8	23.2	30.2	0.3	97.4
AB	1	1	62.5	23.4	37.4	65.6	122.4
		4	62.9	28.3	45.0	5.7	94.3
C_1E	3	14	56.2	43.8	77.9	12.5	19.2
		13	59.5	40.5	68.1	1.9	6.8
BC	4	5	50.3	30.0	59.6	20.2	39.1
		9	53.1	31.9	60.1	27.9	39.1

Table 15. Bifurcated Elevated Highways - Model 4

Effect of number of internal diaphragms on load distribution and warping stresses.

QUANTITY	Model 1	Model 2	Model 4 steel	Model 4 slab
U.D. Lane loading tests				
(i) Moment at midspan AB due to L/C1	40858	37839	34969	-
(ii) Max. longitudinal stress (main stress gauges)	1.735	1.581	32.185	1.701
(iii) Max. longitudinal stress (secondary stress gauges)	1.749	1.656	32.185	1.701
(iv) Max. longitudinal stress in Span BC	1.749	1.244	12.966	1.235
(v) Max. principal stress at location of (iii)	1.749	1.264	12.981	-
(vi) % increase in longitudinal stress due to secondary warping in Span AB	17.8	19	-	-
(vii) Max. σ_{DB} due to L/C1	1.208	1.421	17.696	-
(viii) Max. σ_{DB} due to L/C4	0.864	0.970	9.483	-
(ix) Max. σ_{DB} overall	1.208	1.558	46.384	-
(x) Max. σ_{DB} in Span BC	0.869	1.151	5.472	-
(xi) Max. slab transverse bending stress	1.463	0.741	-	6.836
HB loading tests				
(xii) Max. longitudinal stress	3.967	6.172	90.0	8.860
(xiii) Max. σ_{DB}	3.526	6.452	135.0	-
(xiv) Max. σ_{DB} in Span BC	1.389	4.359	20.31	-
(xv) Max. slab transverse bending stress	2.504	6.452	-	12.260
(xvi) Max. longitudinal stress in Span BC	3.806	3.897	37.180	3.973
(xvii) Max. principal stress at location of (xvi)	3.835	3.899	37.490	-

- continued -

QUANTITY	Model 1	Model 2	Model 4 steel	Model 4 slab
Knife edge loading tests				
(xix) Max. longitudinal stress	1.898	2.566	14.980	3.579
(xx) Max. σ_{DB}	2.078	2.374	11.290	-
Point loading tests				
(xxi) Max. longitudinal stress	3.024	6.429	12.790	4.645
(xxii) Max. σ_{DB}	4.311	8.221	15.310	-

Table 16. Comparison of maximum stresses in the bifurcated elevated highways models

FIRST BEAM	LAST BEAM	INCREMENT	FLEXURAL RIGIDITY ($KN-MM^2$)	BREDT TORSIONAL RIGIDITY ($KN-MM^2$)	EFFECTIVE SHEAR RIGIDITY (KN)	R (EQN 3.21)	R (EQN 3.1) FOR FULL GJ ANALYSIS	R (EQN 3.1) FOR GJ(RED) ANALYSIS
1	13	6	.8802E+10	.6157E+10	.1018E+08	17.4	17.2	25.1
2	5	1	.5840E+10	.4815E+10	.8588E+07	17.4	17.2	25.1
8	11	1	.5840E+10	.4815E+10	.8588E+07	17.4	17.2	25.1
14	17	1	.5840E+10	.4815E+10	.8588E+07	17.4	17.2	25.1
6	18	6	.8802E+10	.6157E+10	.1018E+08	17.4	17.2	25.1
19	27	1	.8802E+10	.6157E+10	.1018E+08	2.7	2.1	2.3
21	24	3	.6967E+10	.5489E+10	.9138E+07	2.7	2.1	2.3
25	-	-	.6967E+10	.5489E+10	.9138E+07	2.7	2.1	2.3
28	31	1	.6967E+10	.5489E+10	.9138E+07	2.7	2.1	2.3
32	34	2	.5991E+10	.4233E+10	.8067E+07	2.0	1.2	1.6
33	-	-	.1198E+11	.8466E+10	.1613E+08	-	-	-
36	-	-	.6967E+10	.5489E+10	.9138E+07	2.7	2.1	2.3
35	37	2	.8128E+10	.7038E+10	.1042E+08	3.7	3.0	3.2
38	40	1	.5911E+10	.4233E+10	.8067E+07	2.7	2.1	2.3
42	44	1	.5991E+10	.4233E+10	.8067E+07	2.7	2.1	2.3
41	45	4	.6814E+10	.4536E+10	.8529E+07	2.7	2.1	2.3
46	52	6	.6814E+10	.4536E+10	.8529E+07	-	-	-
47	50	1	.5099E+10	.3741E+10	.7615E+07	-	-	-
53	56	1	.5099E+10	.3741E+10	.7615E+07	-	-	-
51	57	6	.6814E+10	.4538E+10	.8529E+07	-	-	-
58	60	1	.8128E+10	.7038E+10	.1042E+08	3.7	3.0	3.2

- continued -

FIRST BEAM	LAST BEAM	INCREMENT	FLEXURAL RIGIDITY (KN-MM^2)	BREDT TORSIONAL RIGIDITY (KN-MM^2)	EFFECTIVE SHEAR RIGIDITY (KN)	R (EQN 3.21)	R (EQN 3.1) FOR FULL GJ ANALYSIS	R (EQN 3.1) FOR GJ(RED) ANALYSIS
62	64	1	.8128E+10	.7038E+10	.1042E+08	3.7	3.0	3.2
61	65	4	.1149E+11	.8246E+10	.1238E+08	3.7	3.0	3.2
66	72	6	.1149E+11	.8246E+10	.1238E+08	46.9	36.8	62.1
67	70	1	.6712E+10	.6132E+10	.9755E+07	46.9	36.8	62.1
73	76	1	.6712E+10	.6132E+10	.9755E+07	46.9	36.8	62.1
71	77	6	.1149E+11	.8246E+10	.1238E+08	46.9	36.8	62.1
78	87	1	.4450E+09	.1100E+08	.1336E+07	-	-	-
127	128	1	.4450E+09	.1100E+08	.1336E+07	-	-	-
88	126	1	.2130E+09	.2800E+08	.4208E+07	-	-	-

Table 17. Bifurcated Elevated Highways Model 4

Member properties for grid analysis

and torsional stiffness reduction

βL_D	DIAPHRAGM STIFFNESS q			
	for σ_{DW} (point load)	for σ_{DW} (udl)	for σ_{DB} (point load)	for σ_{DB} (udl)
3	*	*	1	1
2	*	*	5	20
1	10	100	50	500
.8	50	200	100	1000
.5	500	200	1000	10000
.3	2000	200	10000	20000

Table 18: Minimum diaphragm stiffness for spacing βL_D

* Diaphragms do not reduce stresses at midpanel for $\beta L_D > 1.6$

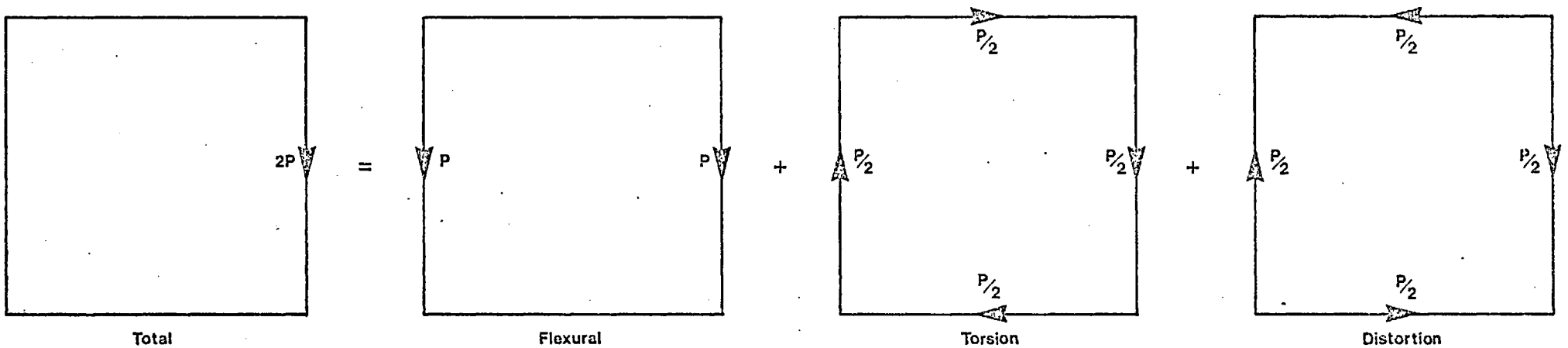
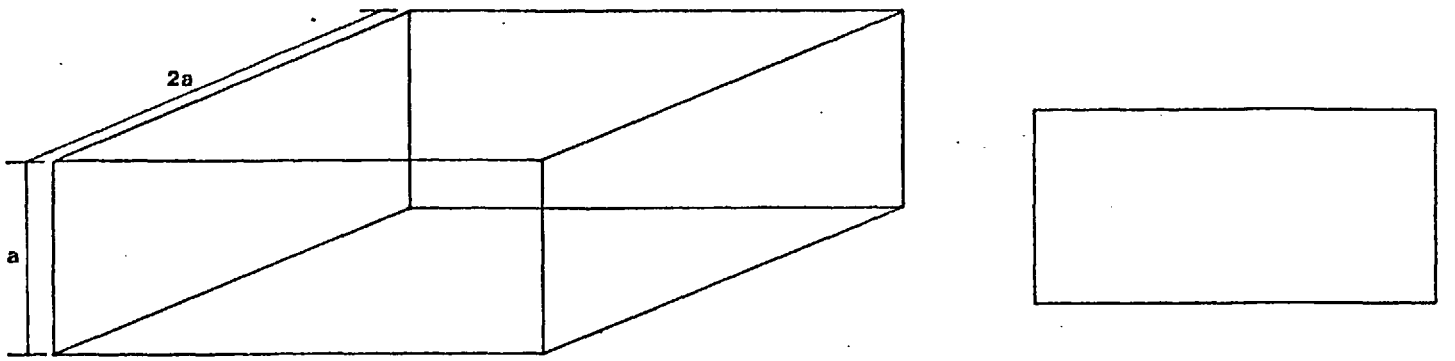
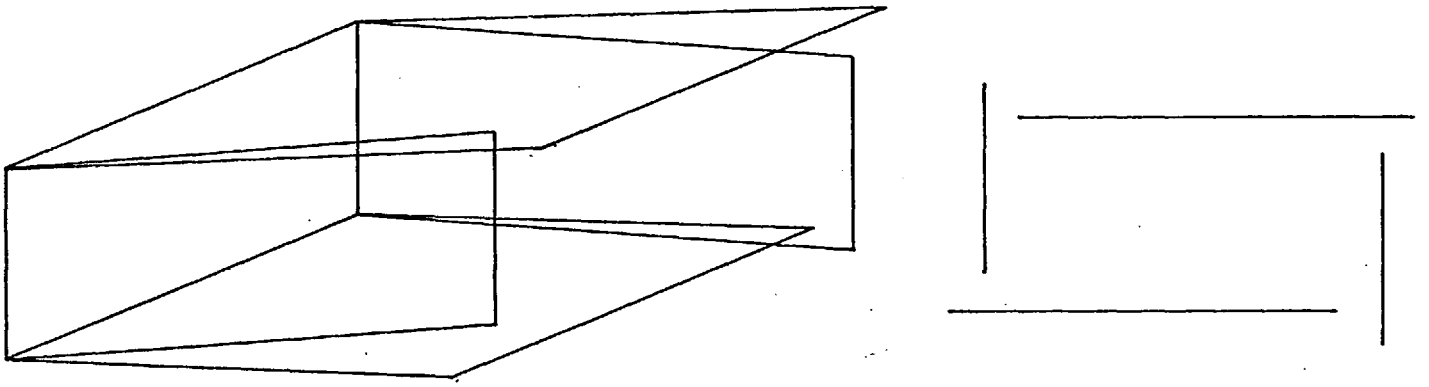


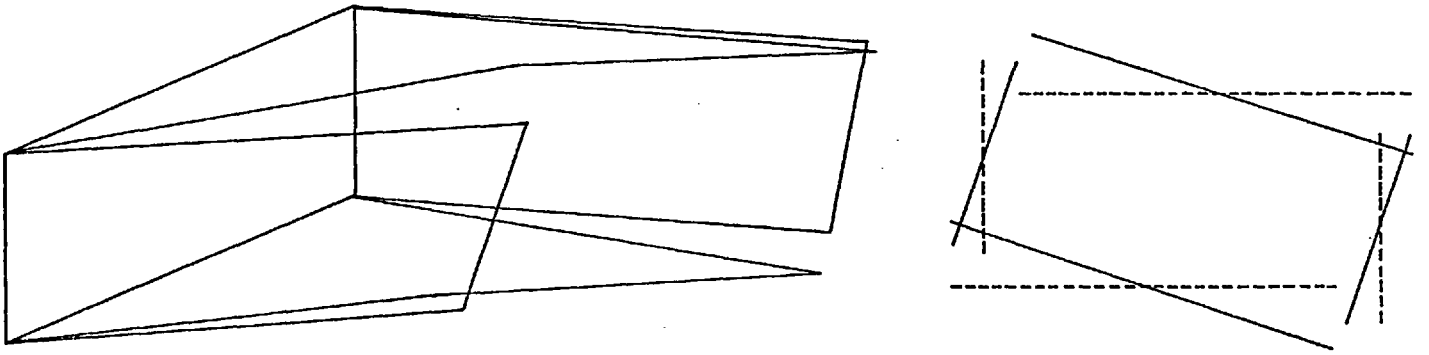
Fig.1 Components of an eccentric load



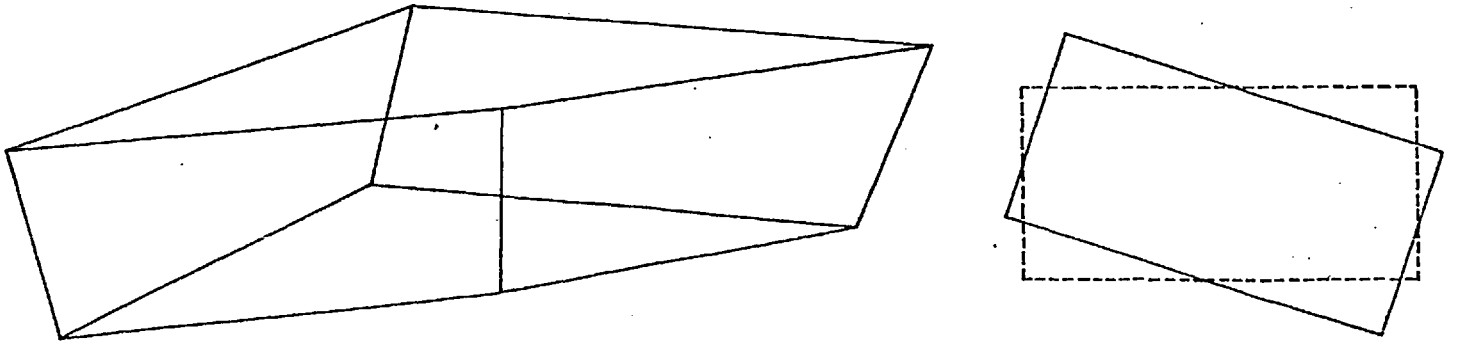
Undeformed state



Stage 1: Shearing of individual plates



Stage 2: Twisting of plates



Stage 3: In-plane body rotations of plates
to obtain compatability at box corners

Fig.2 Torsion of a rectangular box

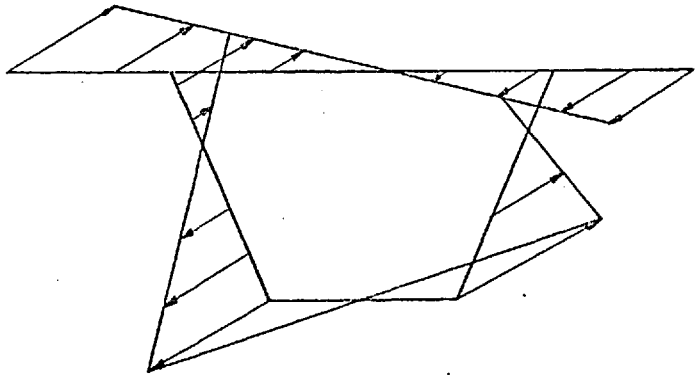
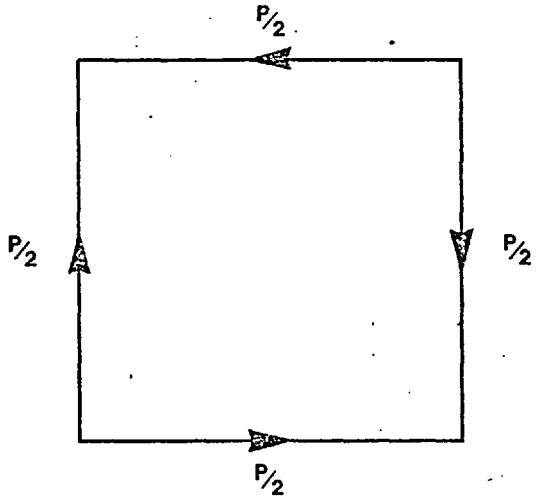
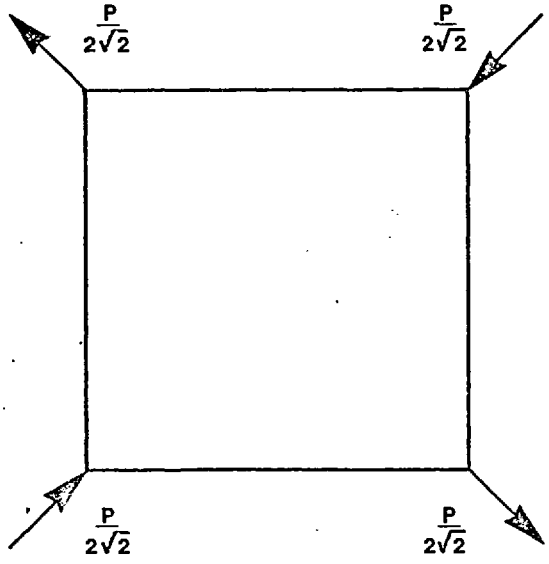


Fig.3 Cross sectional distribution of restrained warping stresses

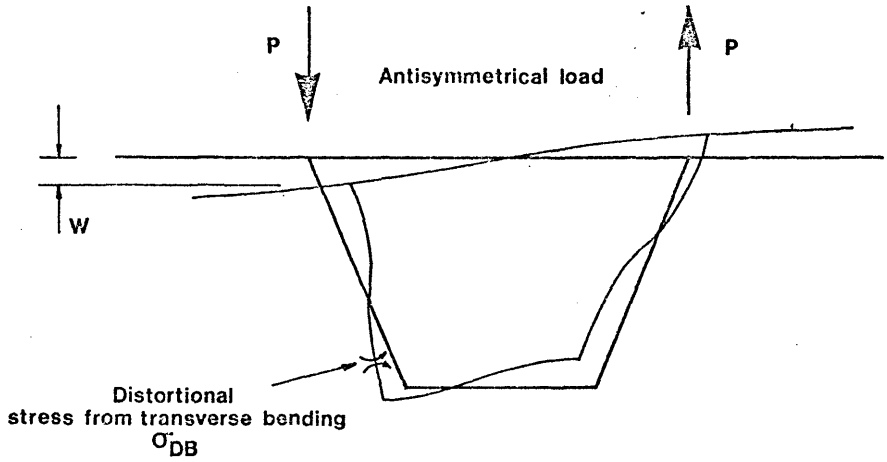


Distortional component from Figure.1

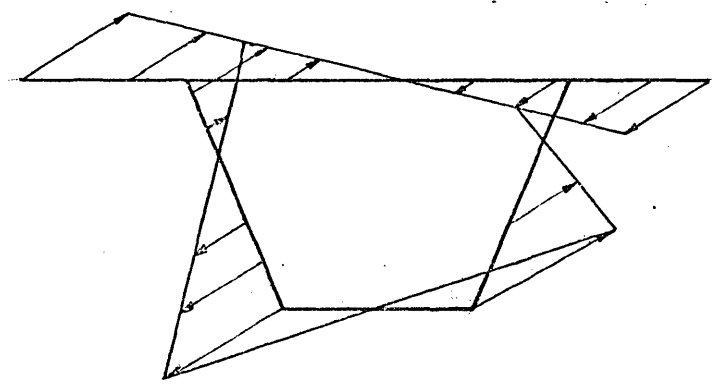


Distortional component resolved at Box corners

Fig.4



Deformation of cross section



Warping stress pattern
σ_{DW}

Fig.5 Effects of deformation of the cross section

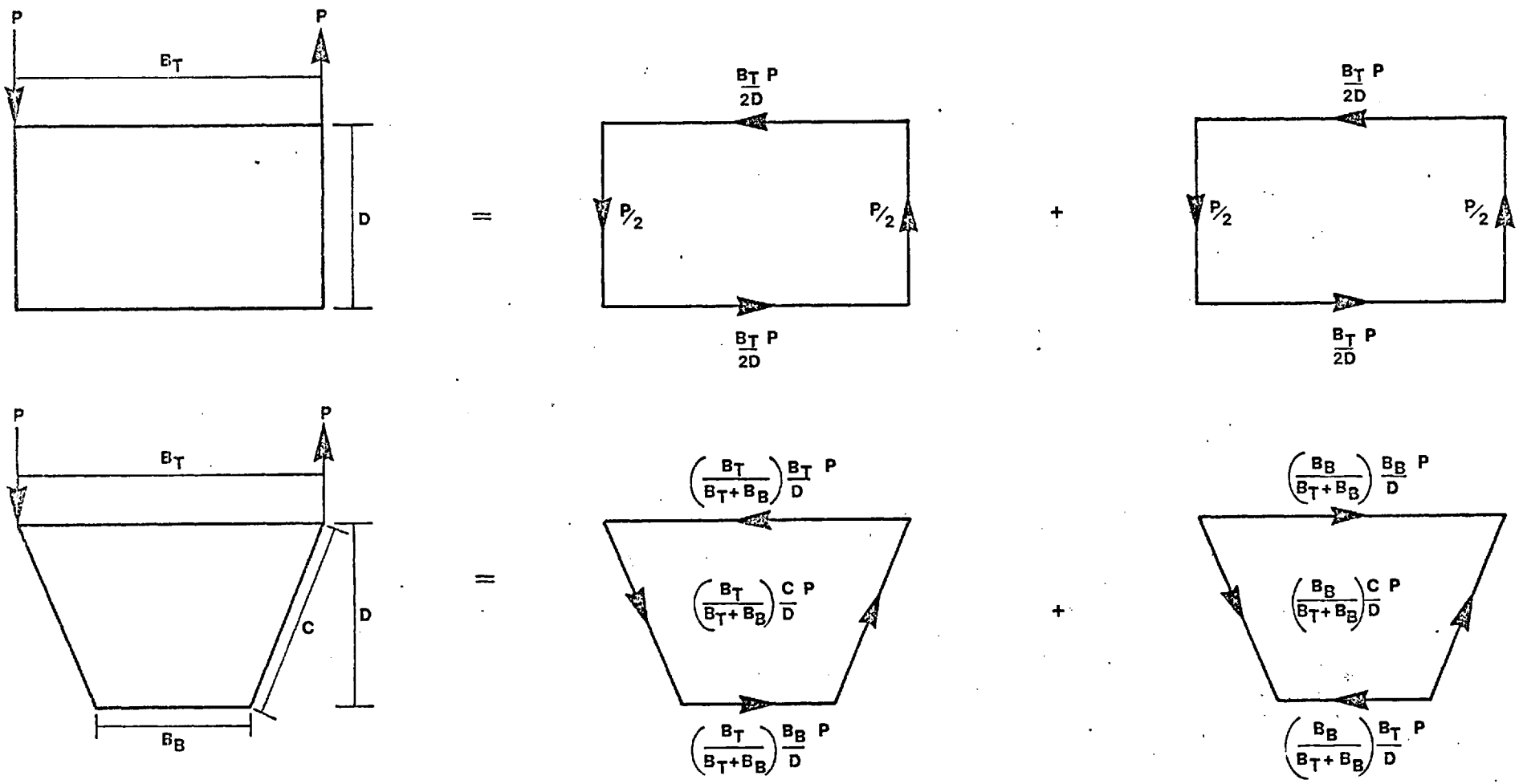
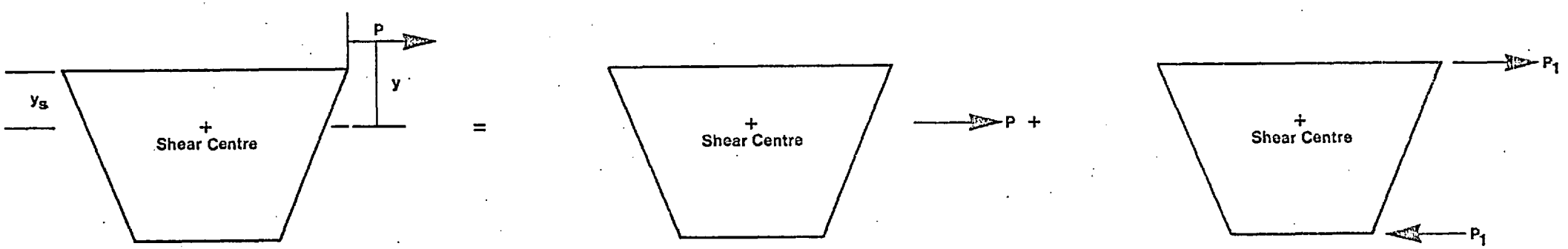


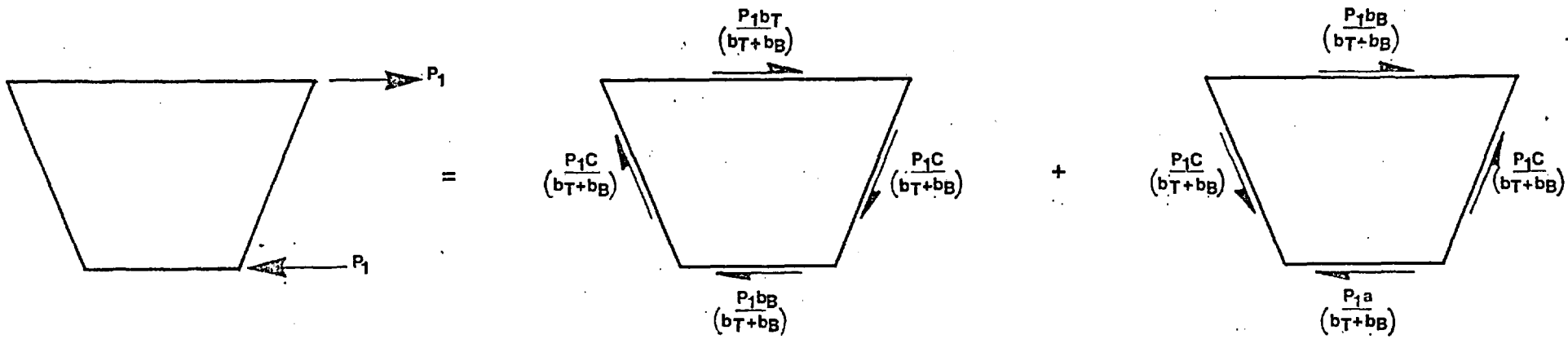
Fig.6a Components of antisymmetrical loading for rectangular and trapezoidal boxes



$$y_s = \frac{D}{I_y} \frac{\left[\frac{CB_B}{t_w} - \frac{B_B B_T}{2t_B} - \frac{B_T^2}{2t_T}\right]\left[(B_T+2B_B)\frac{Ct_w}{12} + \frac{B_B^2 t_B}{12}\right] + \frac{B_T}{6}(B_T+B_B)\left[C(B_T+B_B) - \frac{B_T^2}{6} + \frac{1}{2}(B_T+2B_P)^2 + \frac{B_B t_B}{3t_T}\right]}{\left[\frac{B_B}{2t_B} + \frac{B_T}{2t_T} + \frac{C}{t_w}\right]}$$

$$P_1 = \frac{Py}{D}$$

Fig.6b Symmetrical and antisymmetrical components of horizontal loading



Equivalent vertical distortional load

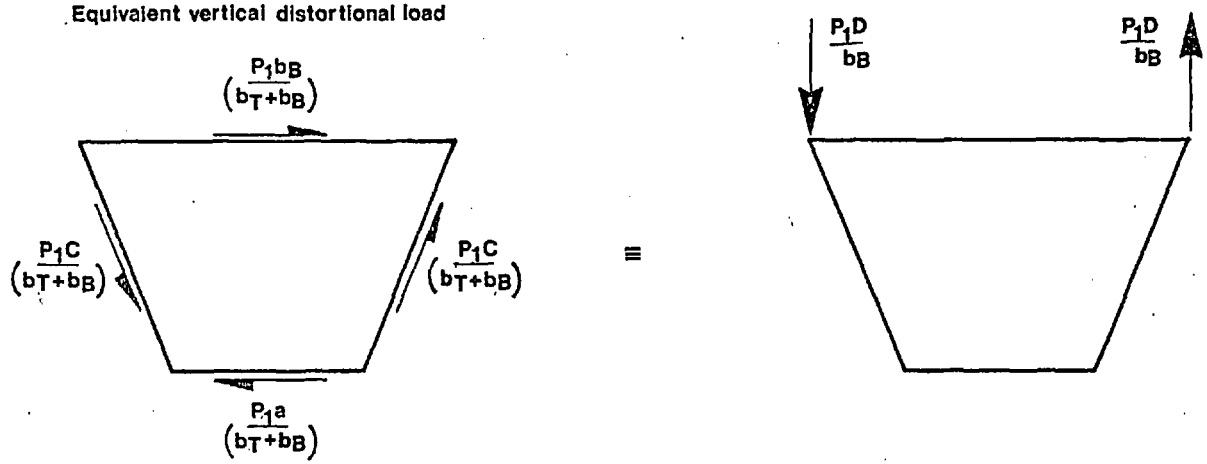


Fig.6c Components of horizontal antisymmetrical loading

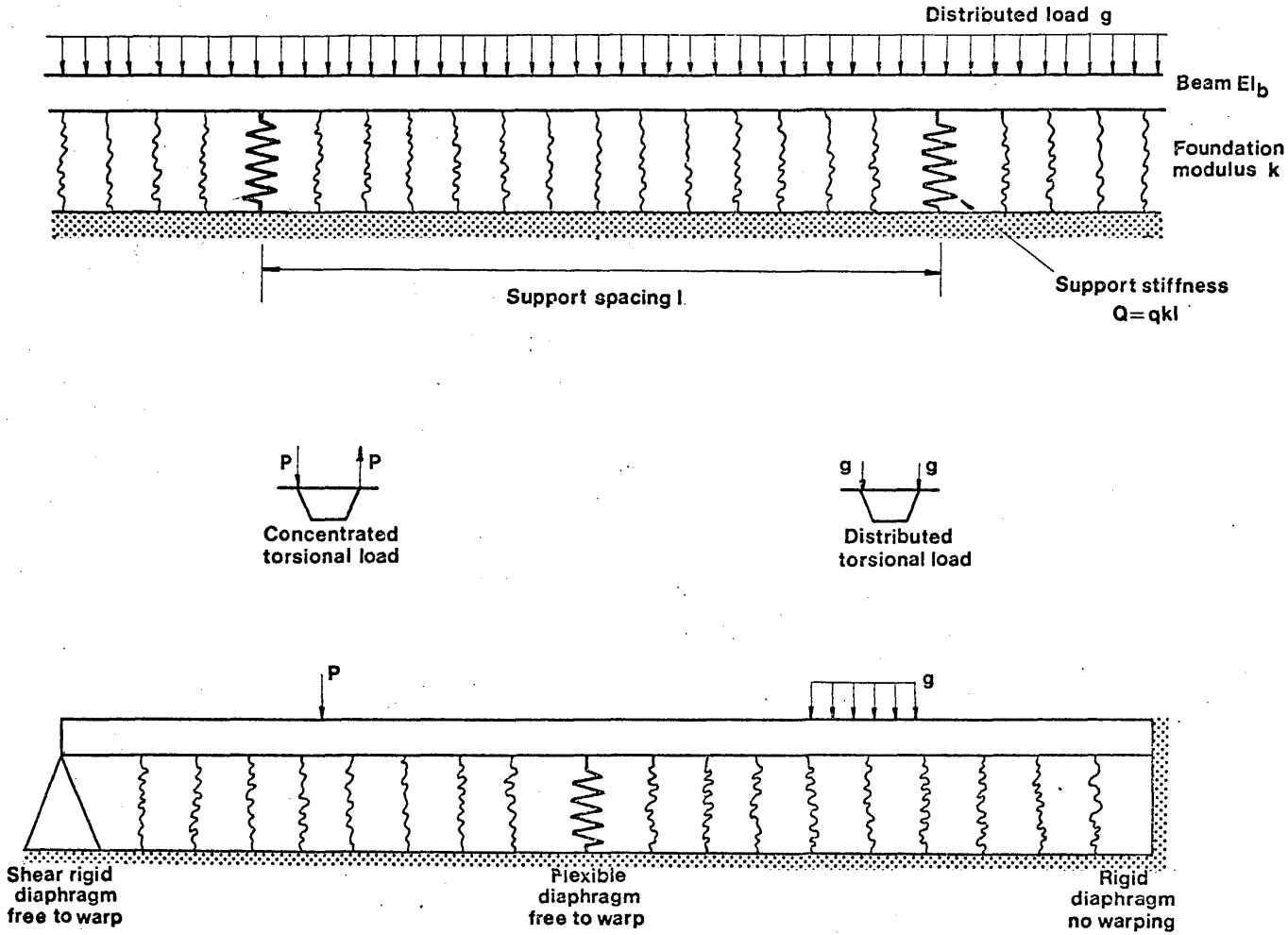
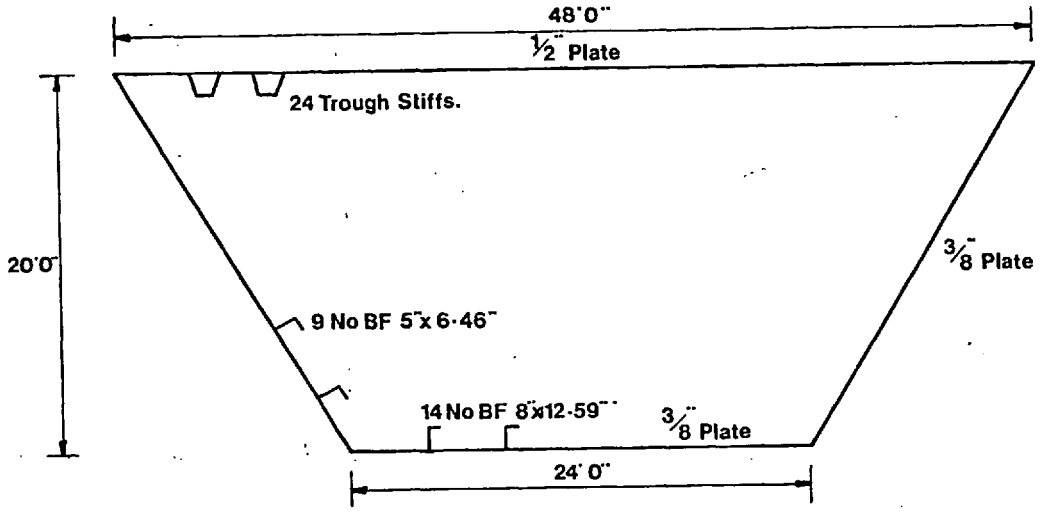


Fig.7 Analogy between Box Girder and B.E.F.



Cross frame at 15'0" c. c	Top Flange	15 x 3/8 plate
	Web	13 x 5/16 plate
	Bottom Flange	13 x 5/16 plate

Fig.8 Dimensions of Example 2

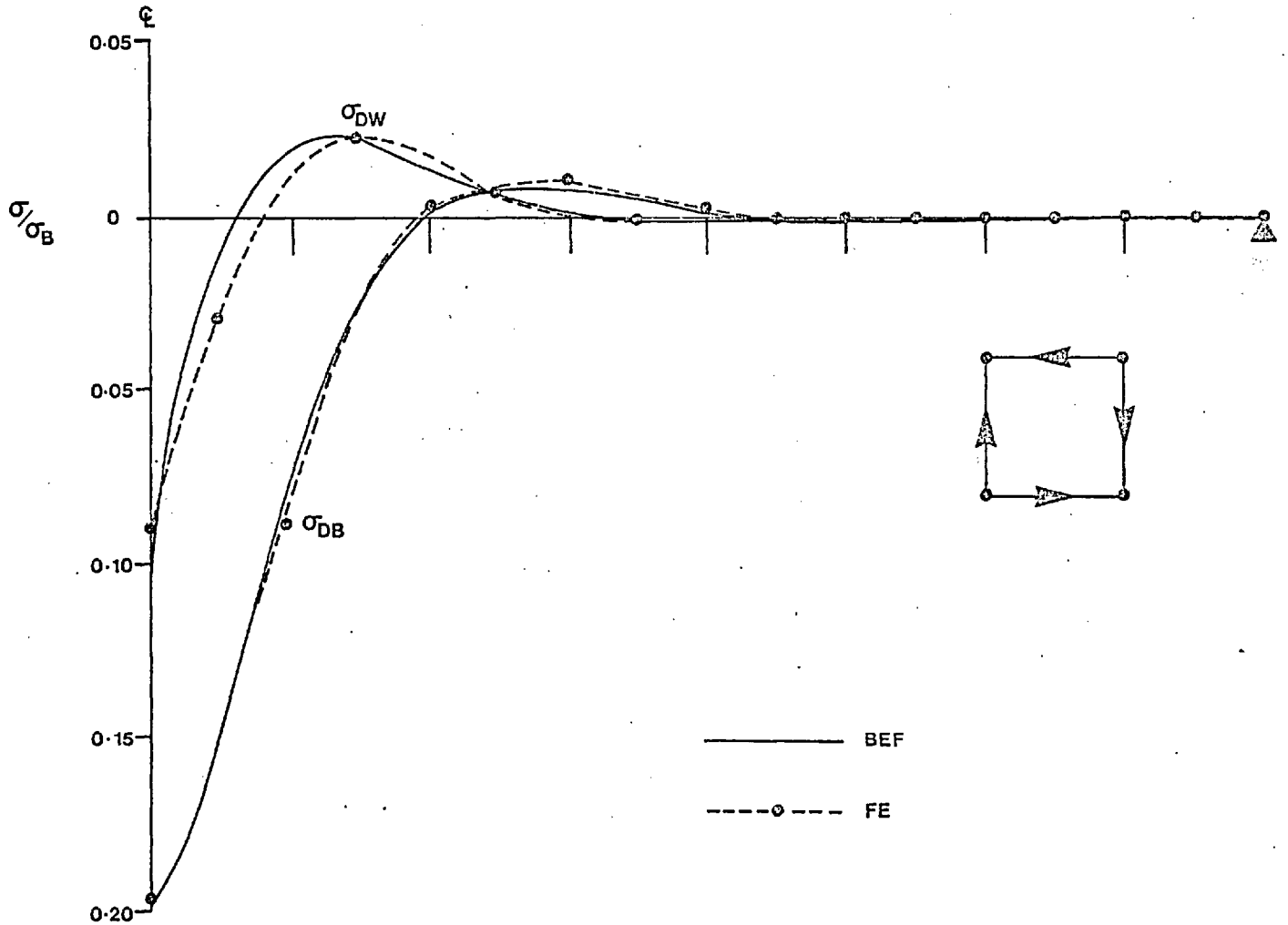


Fig.9 Longitudinal distribution of distortional stresses for 6ft x 6ft concrete box girder under distortional component of central point load

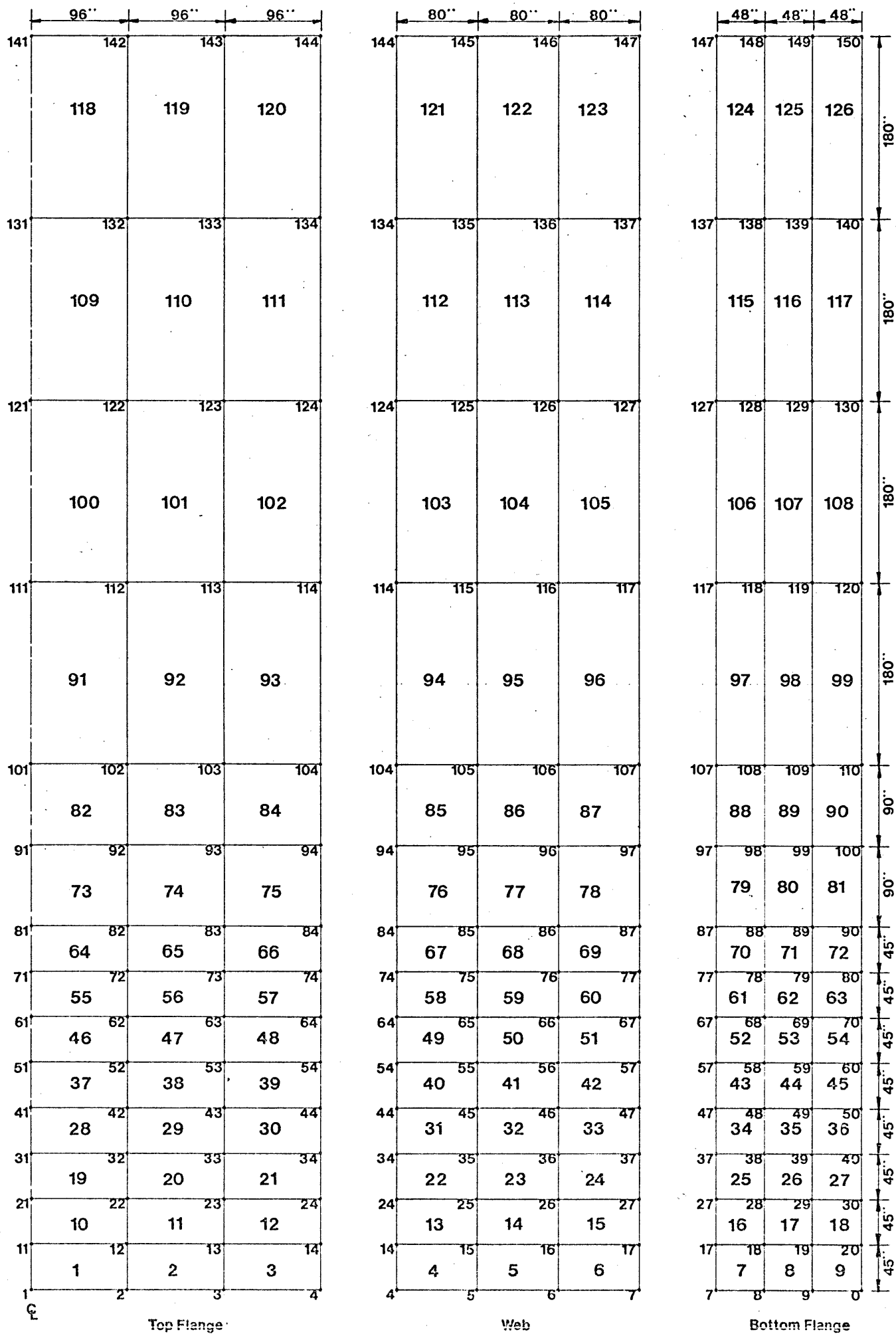


Fig.10 Finite element mesh for Example 2

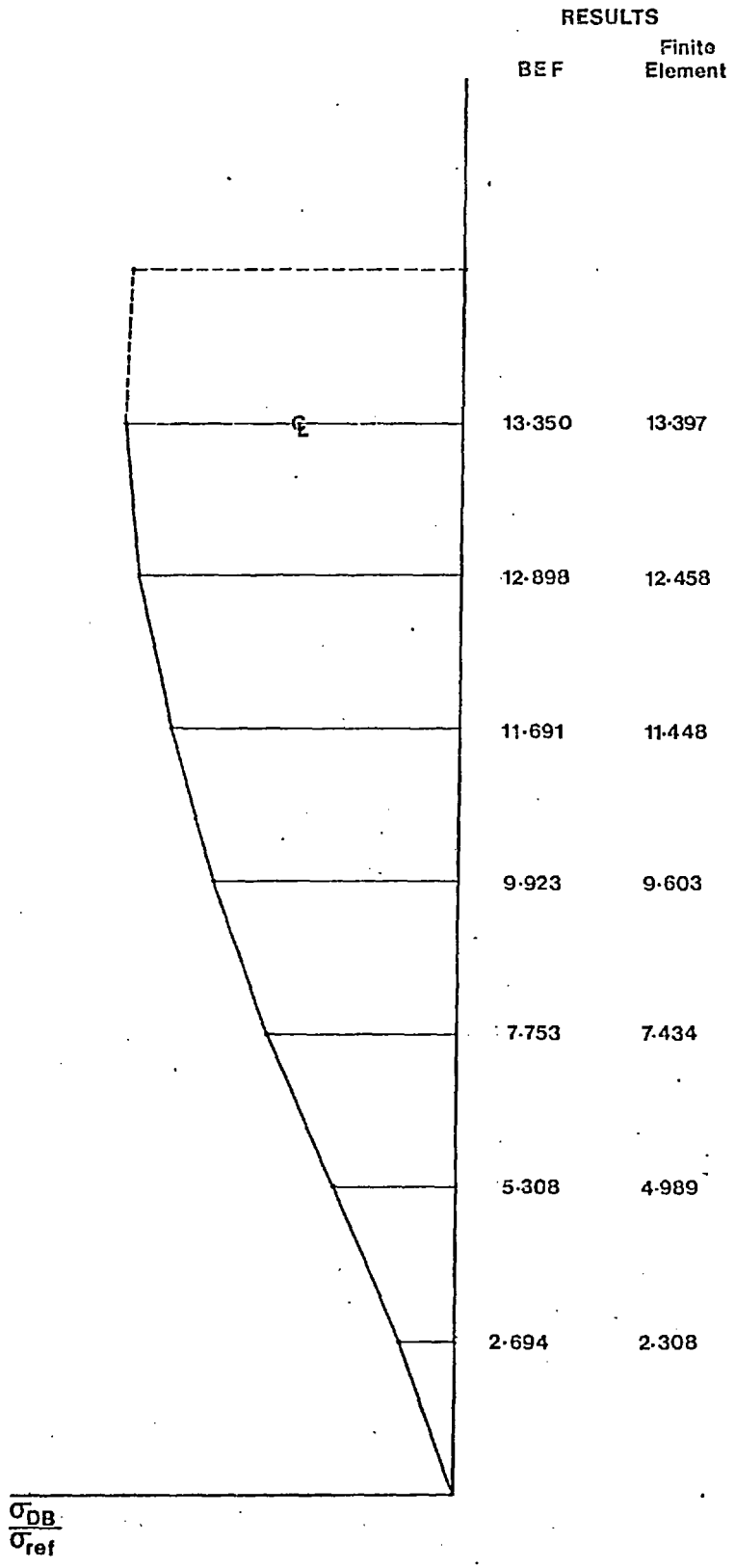


Fig.11 Longitudinal distribution of σ_{DB} for central concentrated load on Example 2, showing comparison of BEF and FE results

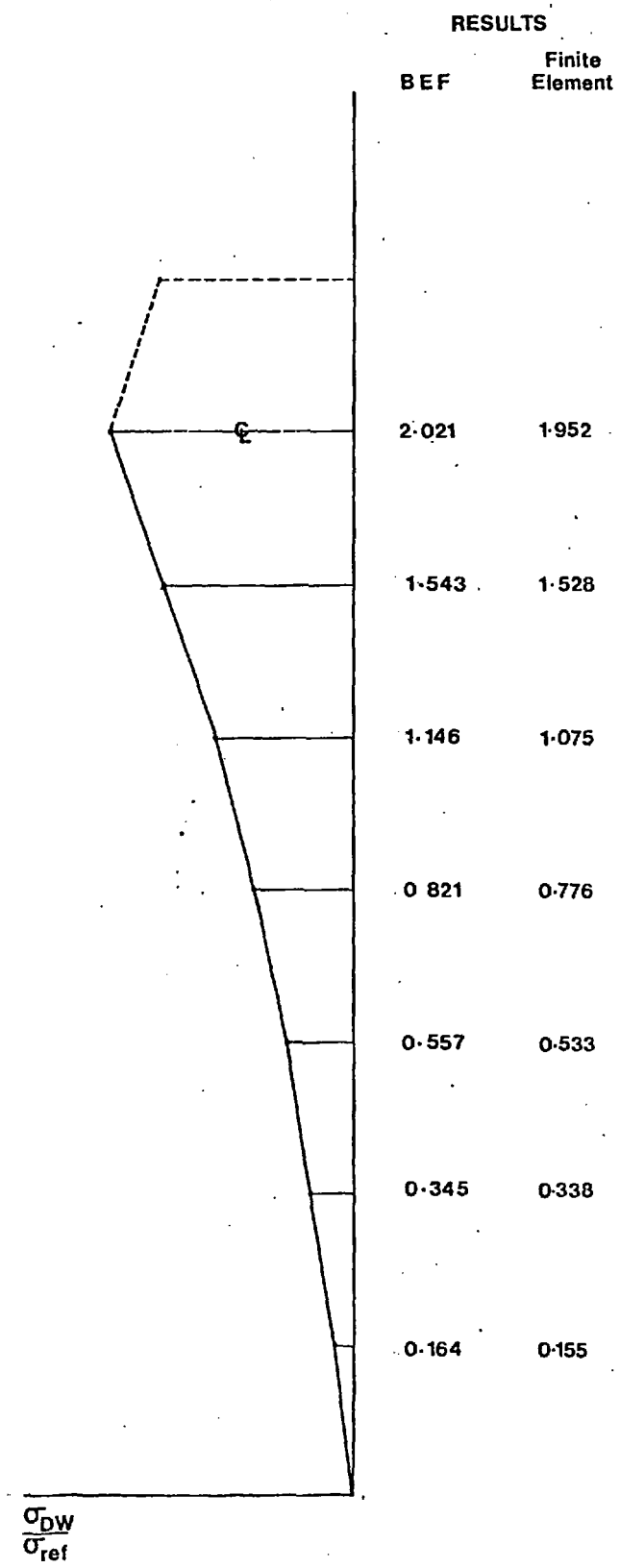


Fig.12 Longitudinal distribution of σ_{DW} for central concentrated load on Example 2, showing comparison of BEF and FE results

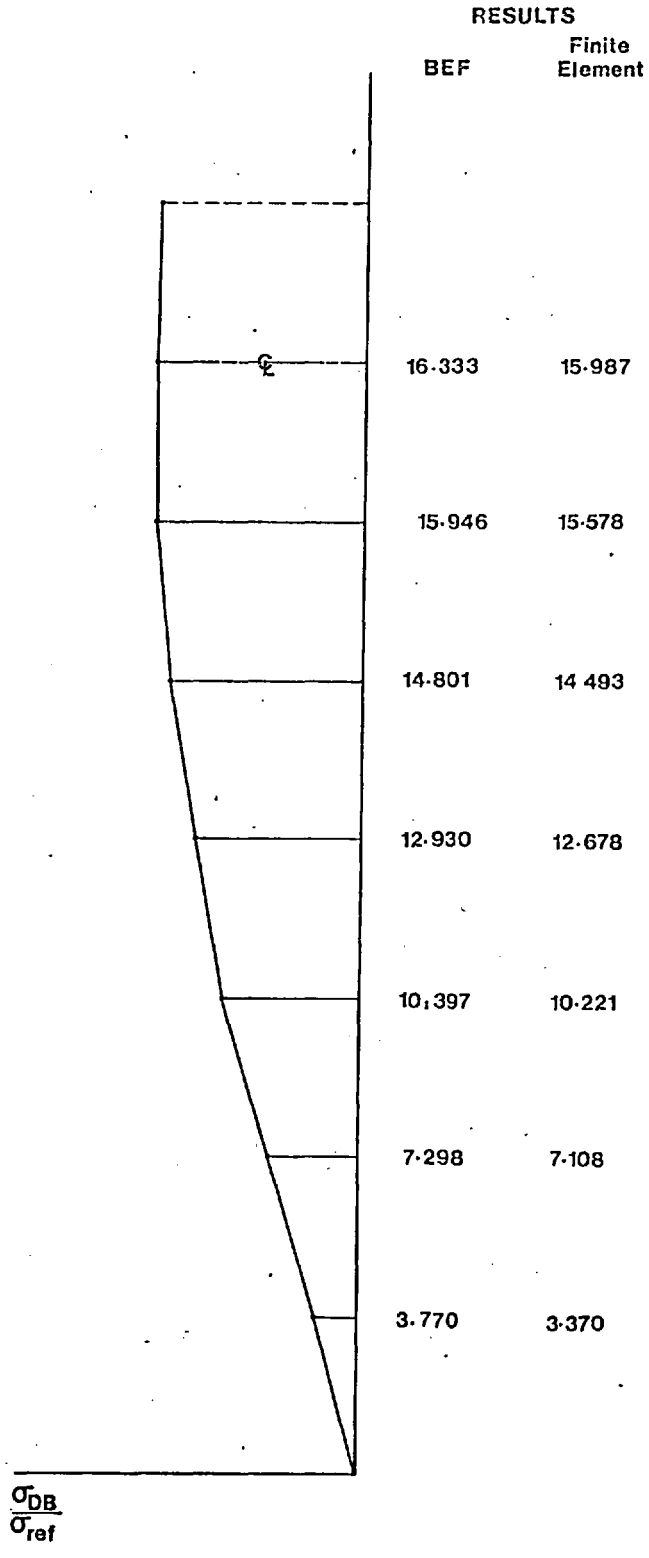


Fig.13 Longitudinal distribution of σ_{DB} for uniformly distributed load on Example 2, showing comparison of BEF and FE results

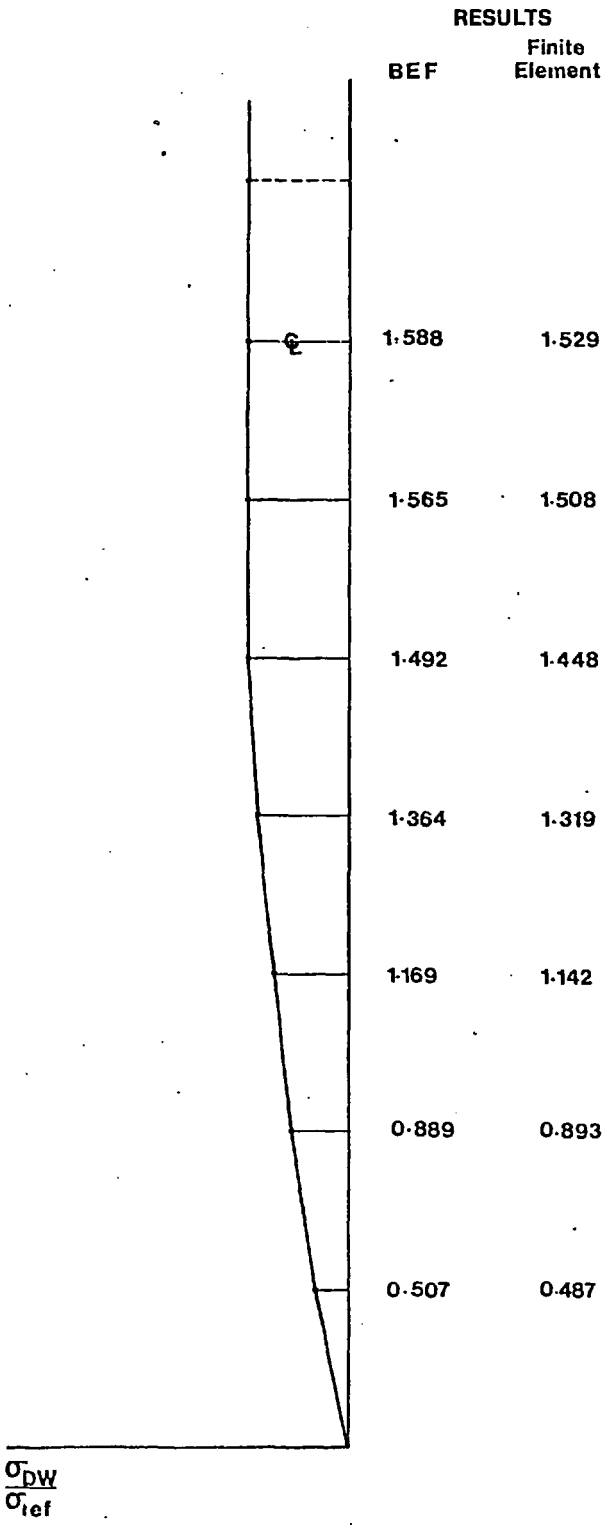
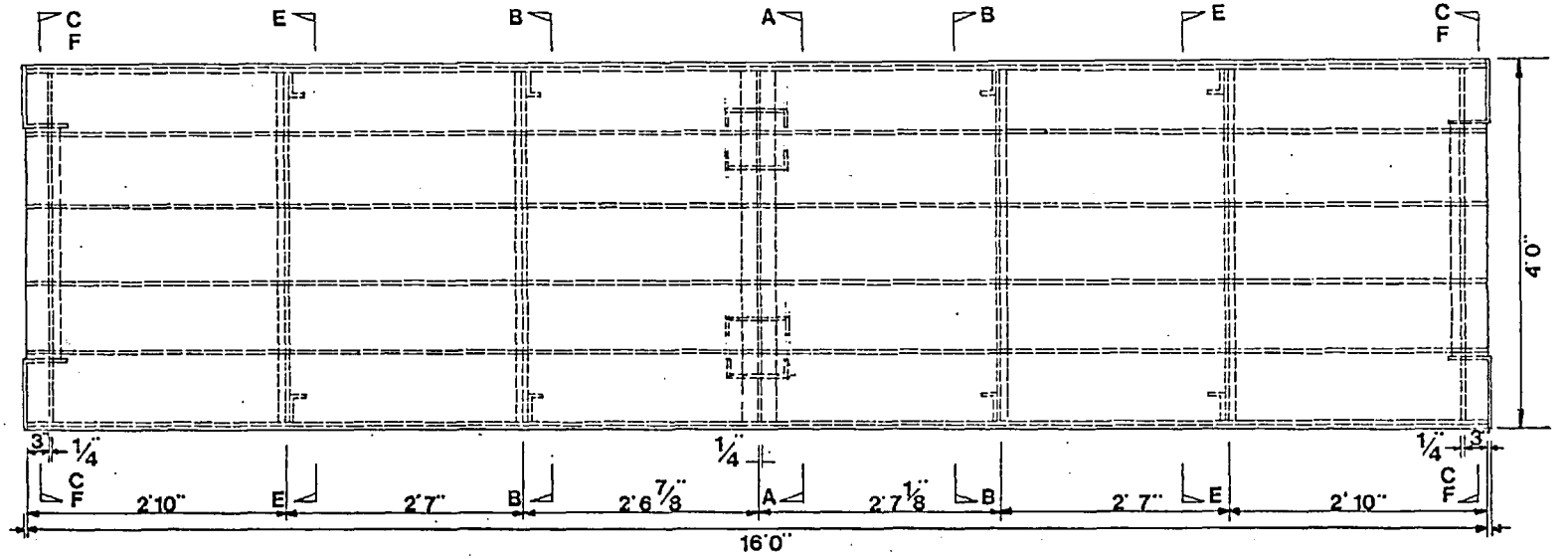
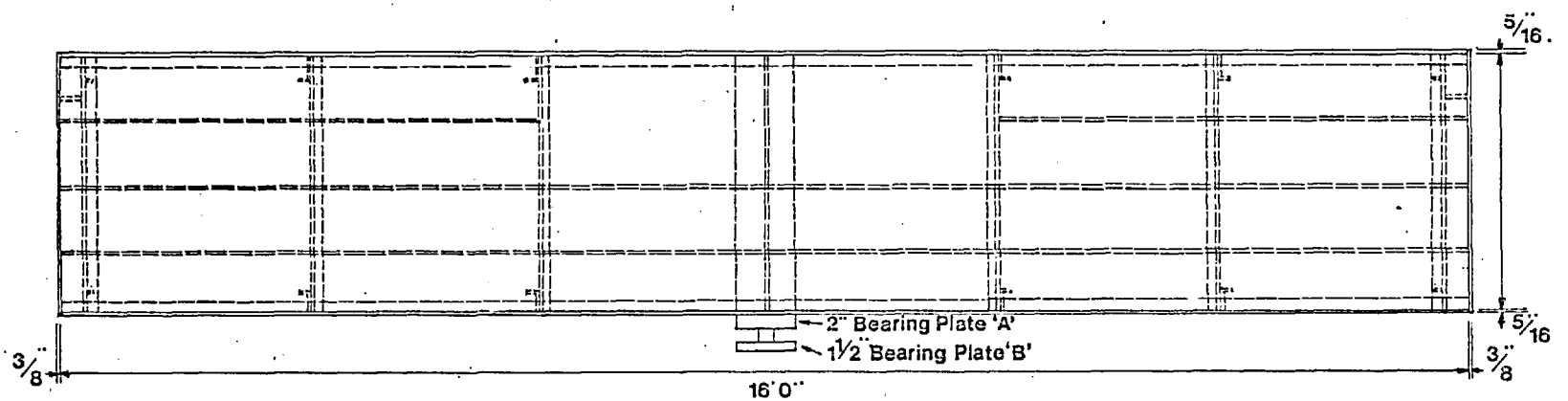


Fig.14 Longitudinal distribution of σ_{DW} for uniformly distributed load on Example 2, showing comparison of BEF and FE results

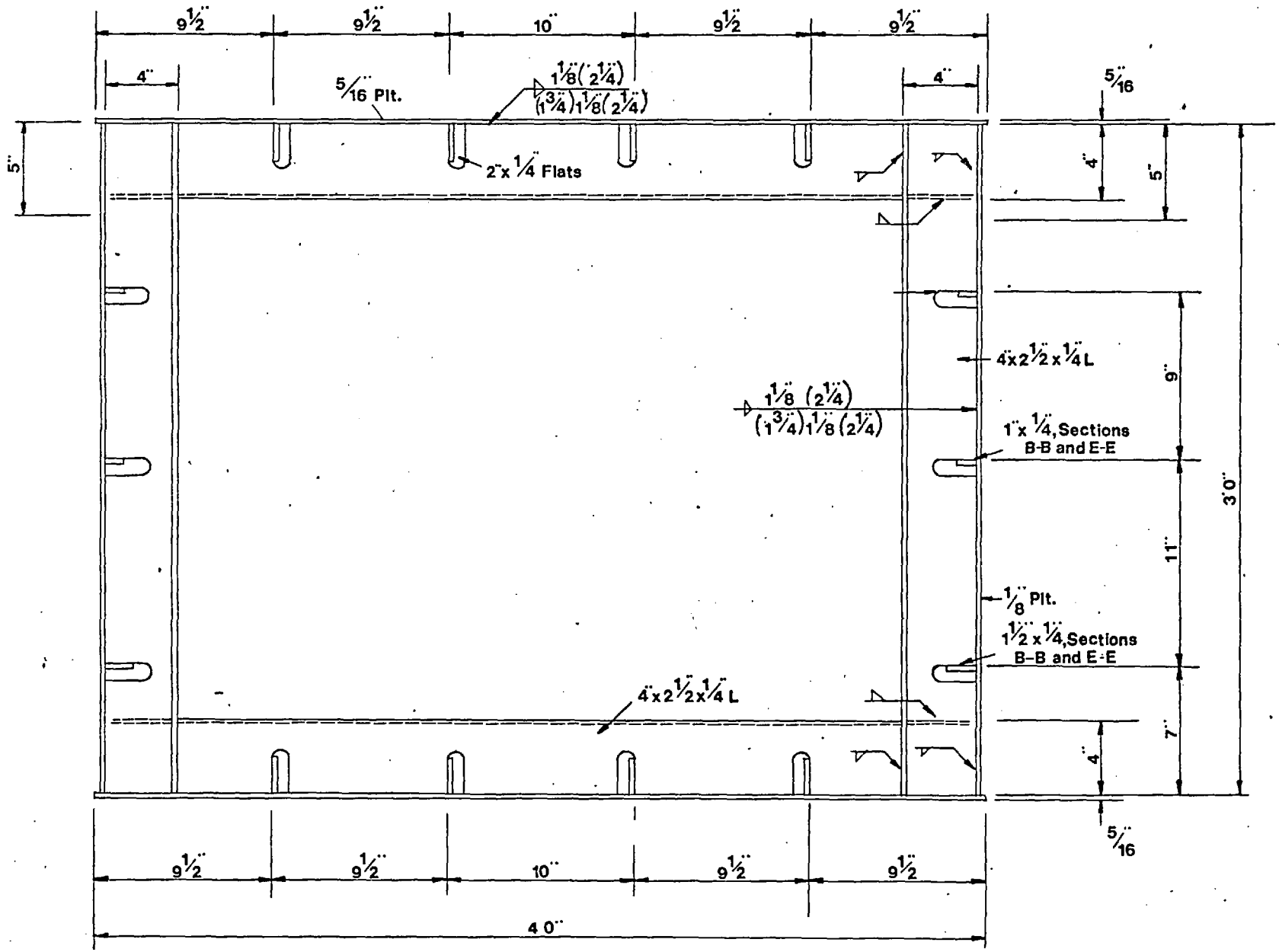


Plan on top



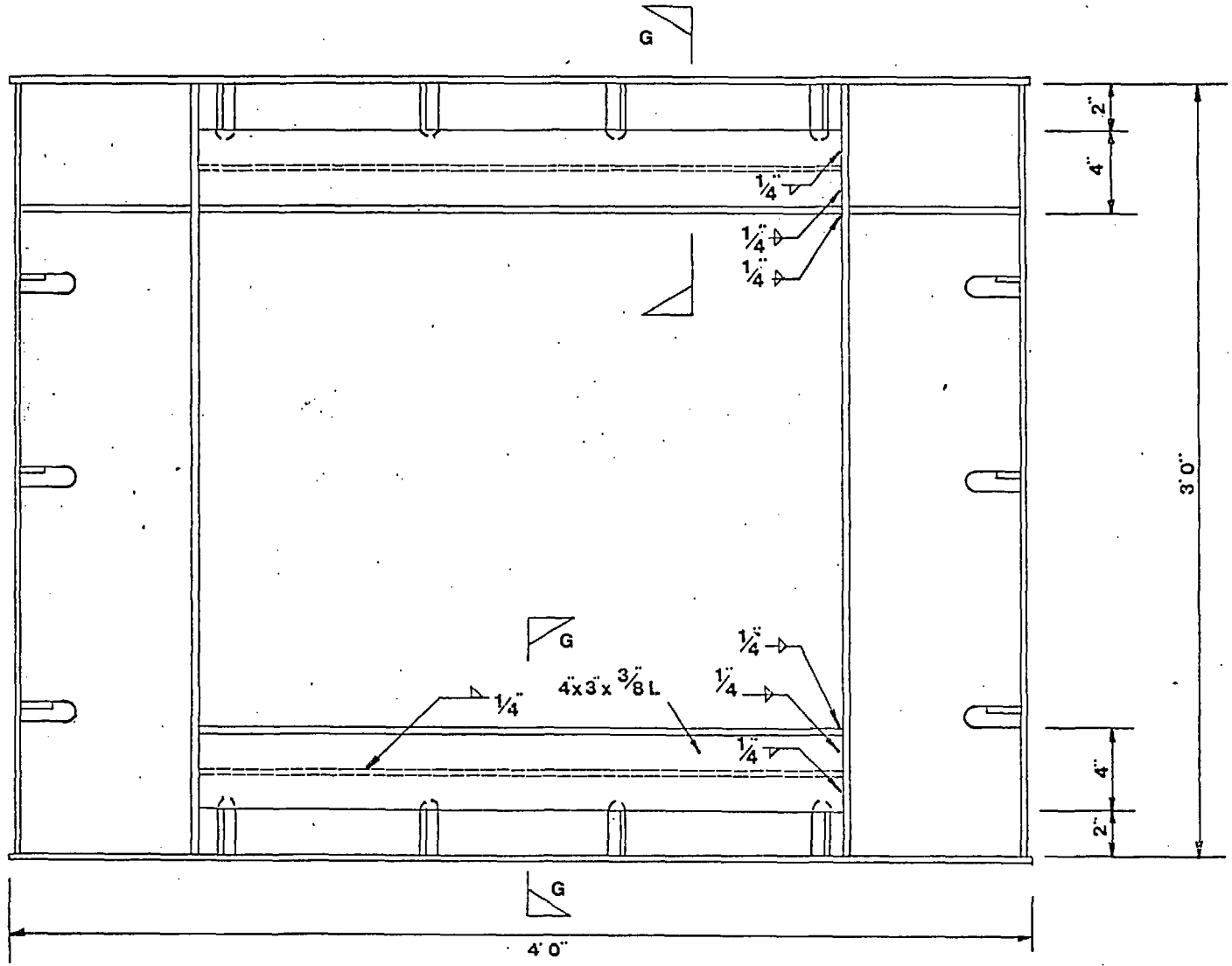
Side Elevation

Fig.15 Dimensions of Test Box 7



Section B-B

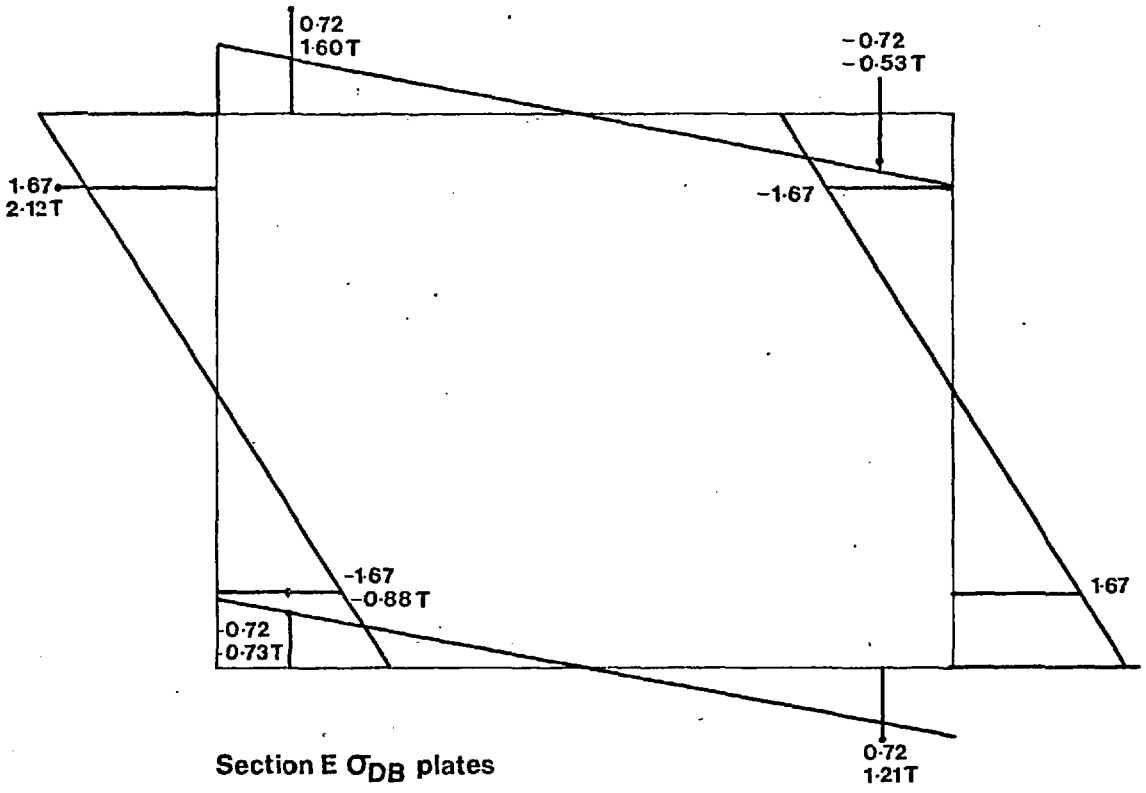
Fig.16 Details of internal ring stiffeners of Test Box 7



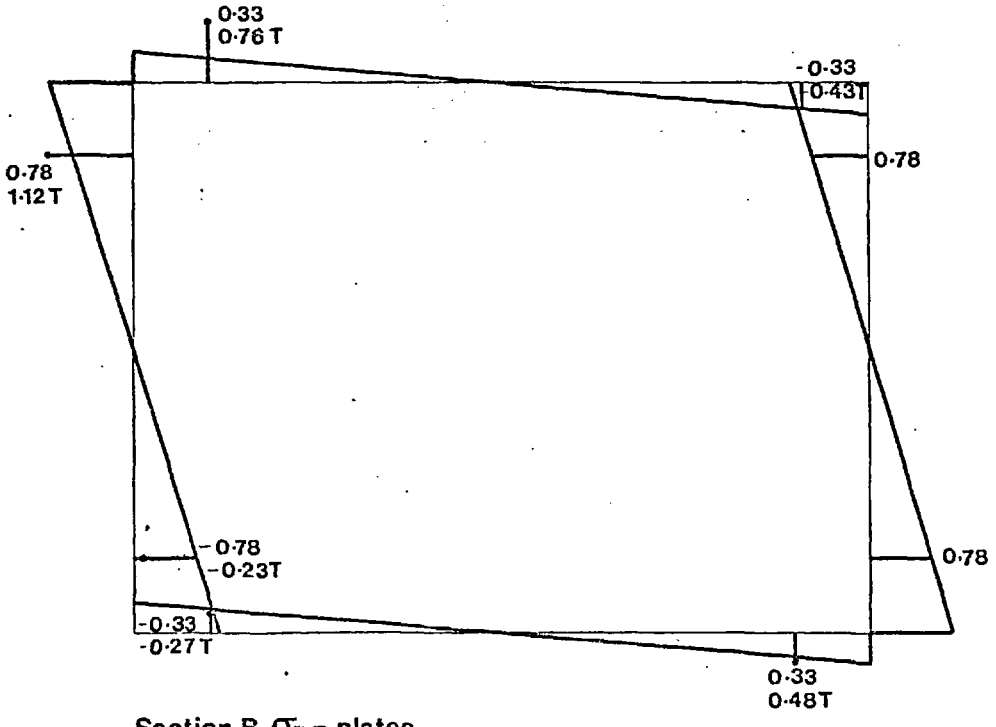
Section F-F

Fig.17. Details of end ring stiffeners of Test Box 7

T = Test result
Stresses in Tons/in^2

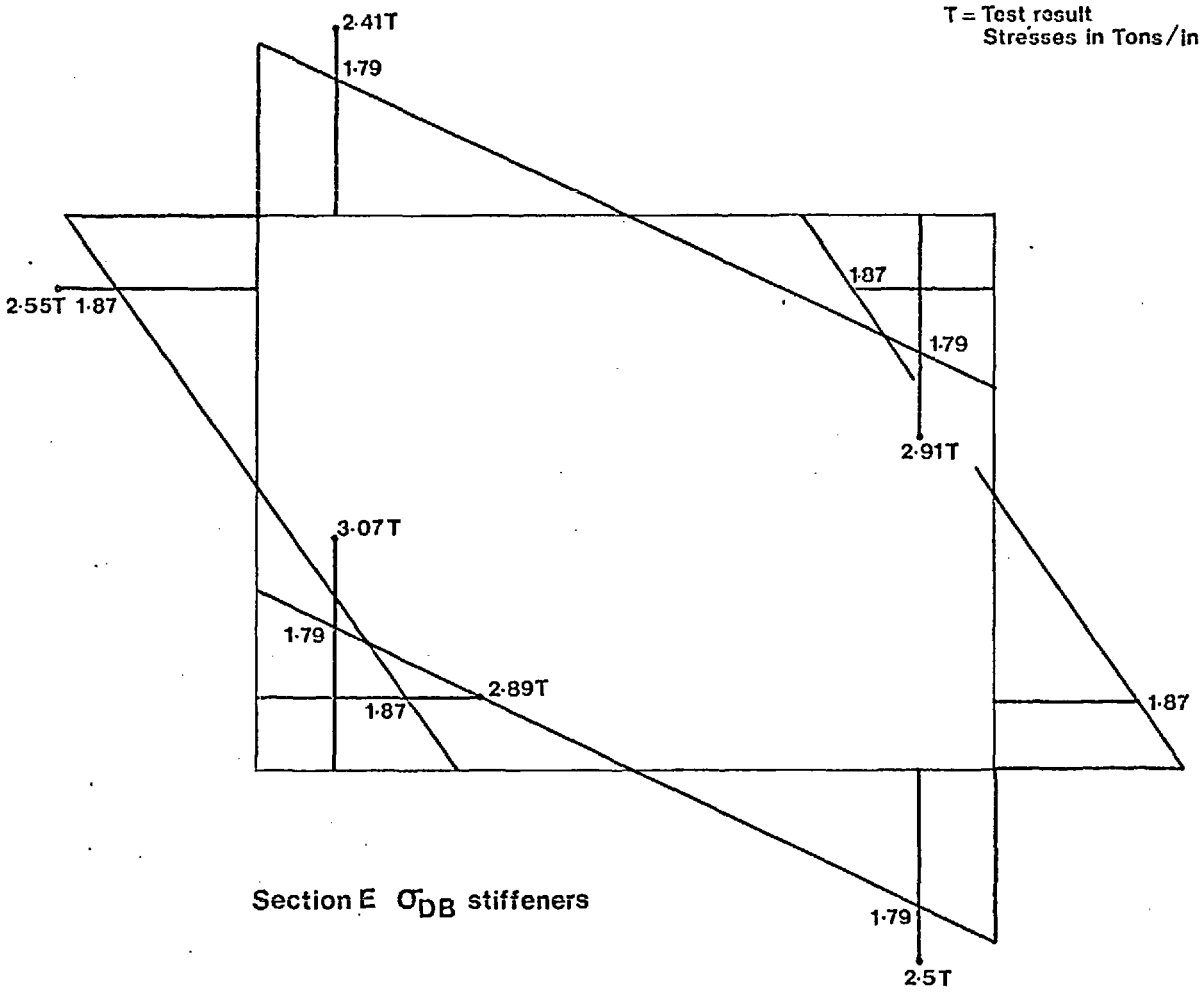


Section E σ_{DB} plates

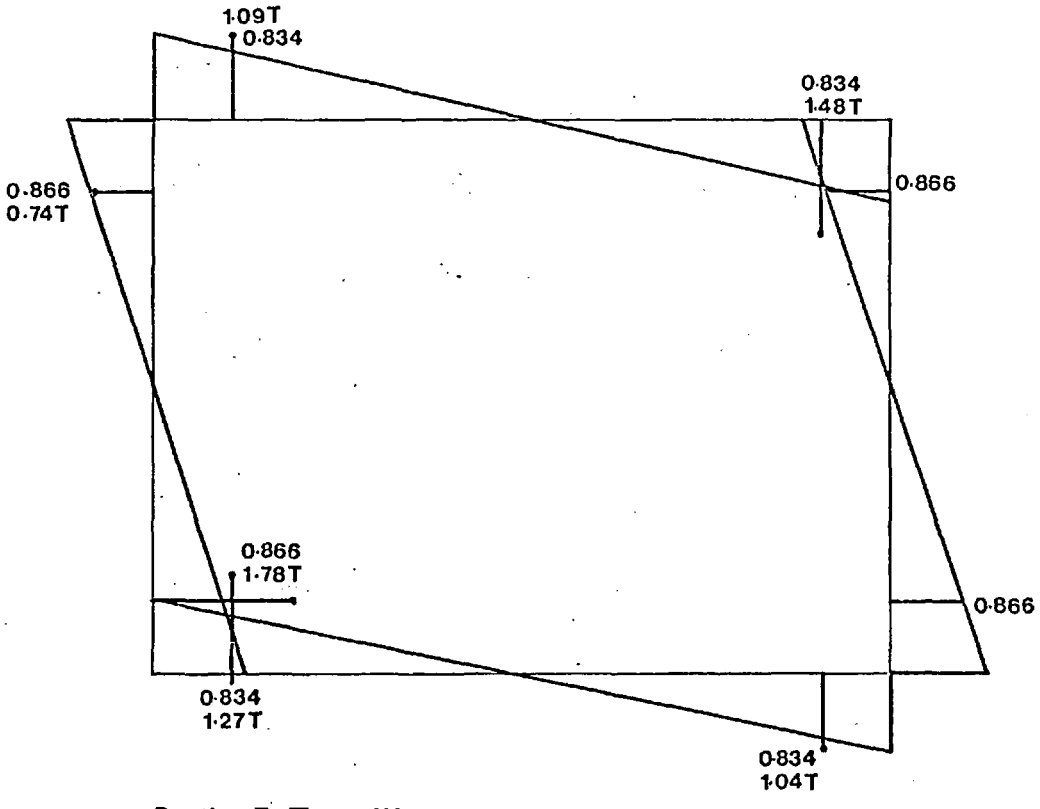


Section B σ_{DB} plates

Fig.18 B.E.F and model test results for Box7



Section E σ_{DB} stiffeners



Section B σ_{DB} stiffeners

Fig.19 B.E.F and model test results for Box 7

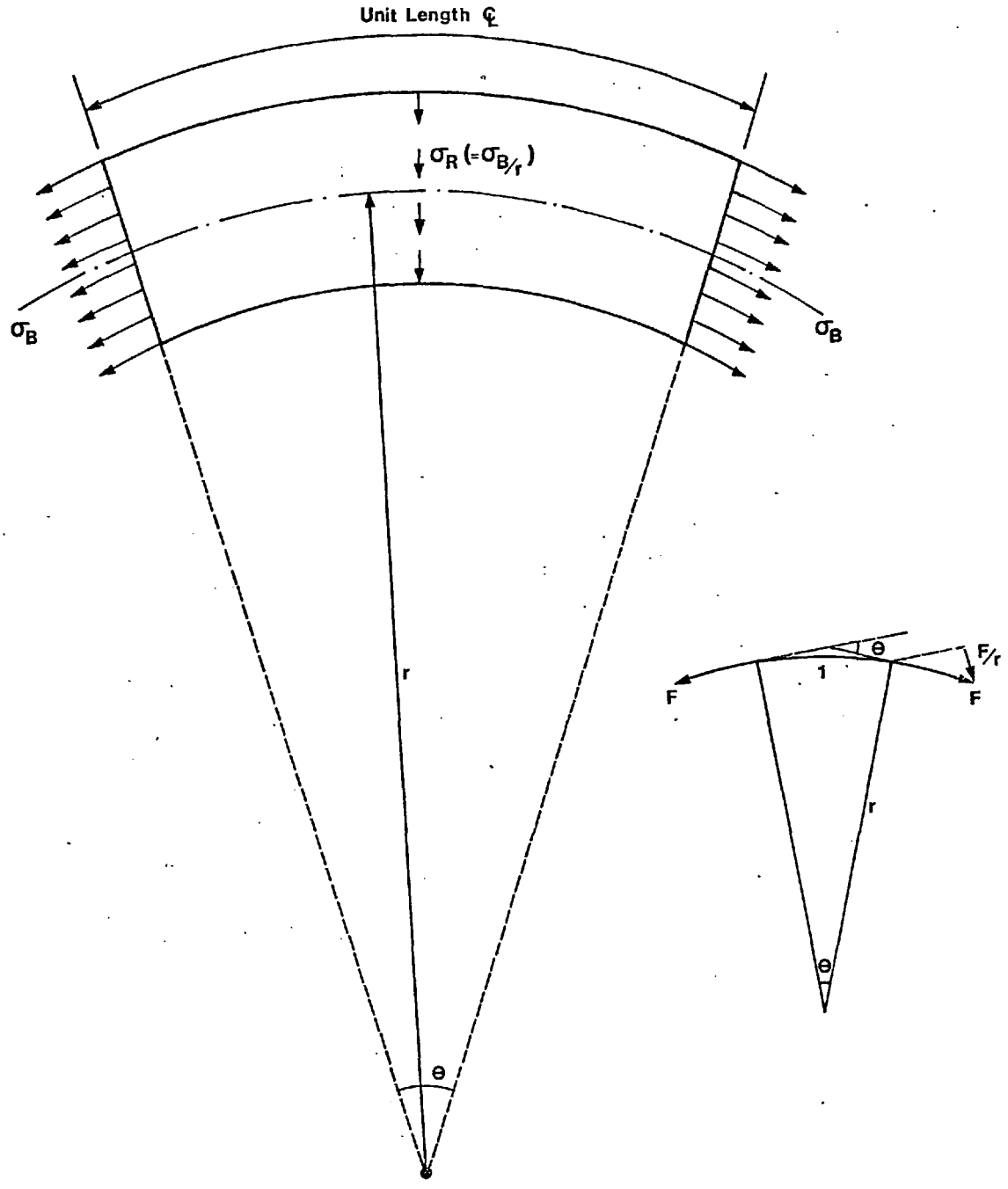


Fig.20 Radial component of longitudinal bending stresses

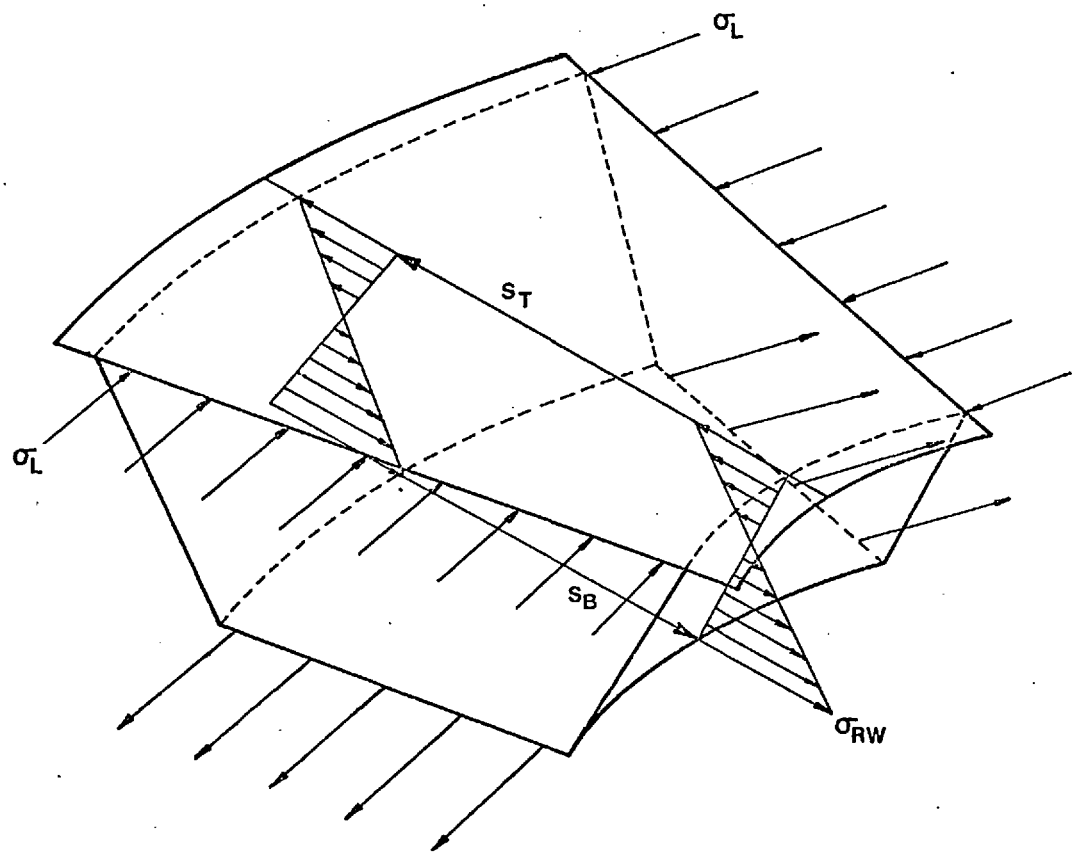
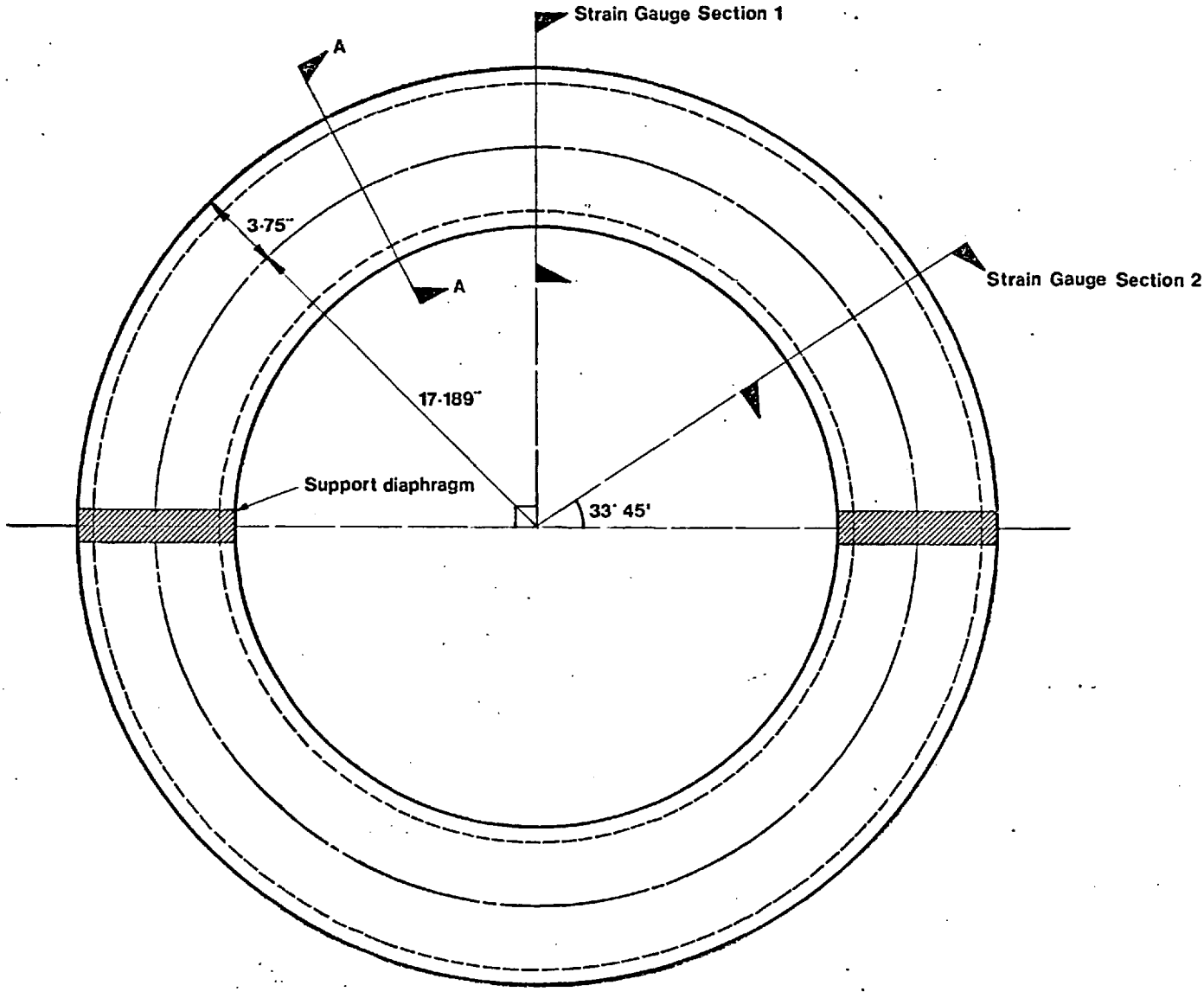
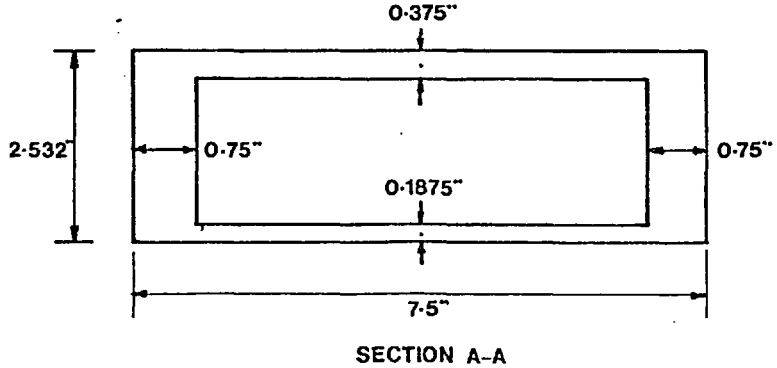


Fig.21 Distortional forces due to bending moments in curved boxes





SECTION A–A

Fig. 22 Dimensions of curved box model

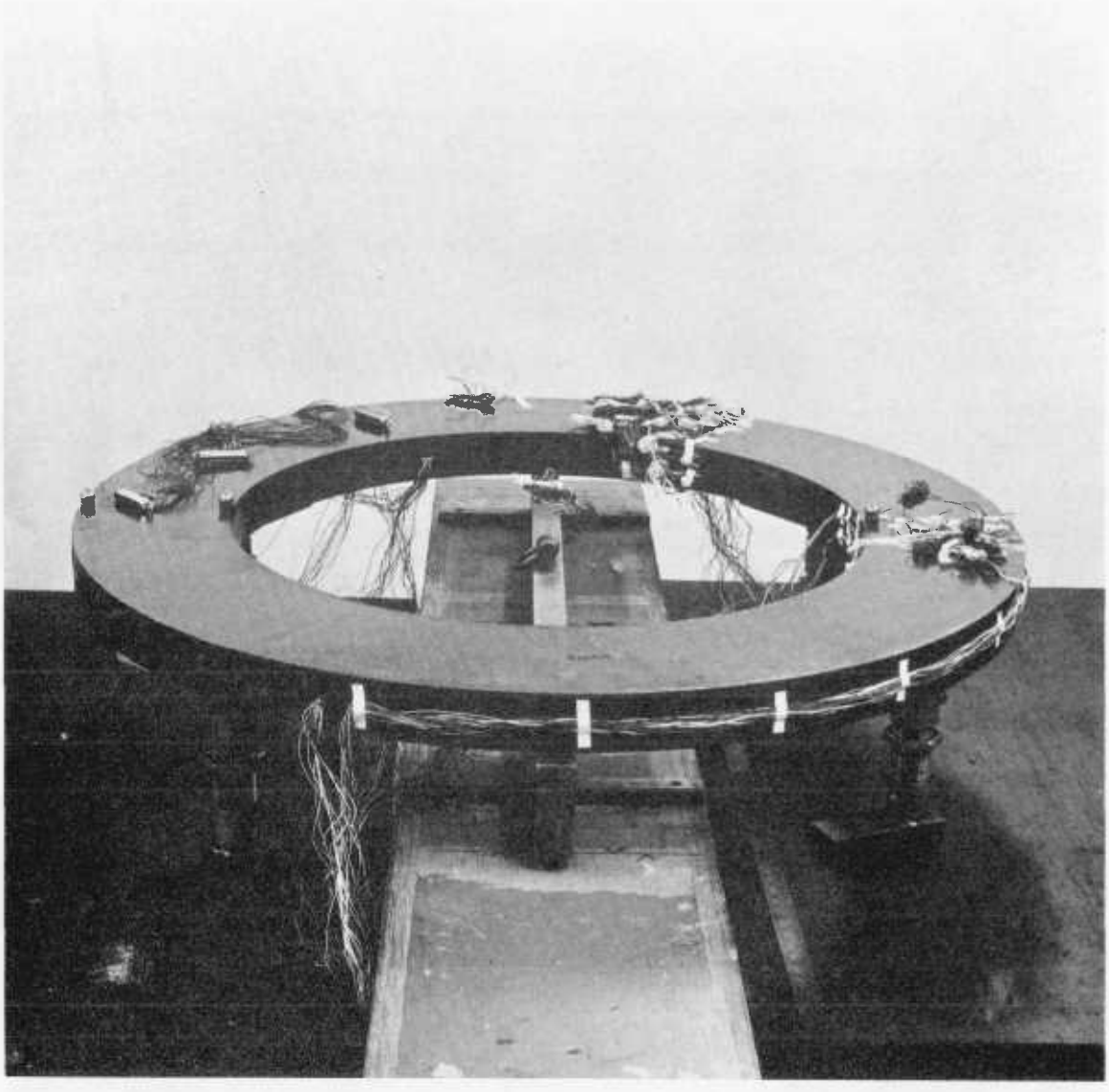


Fig. 23 Curved box model

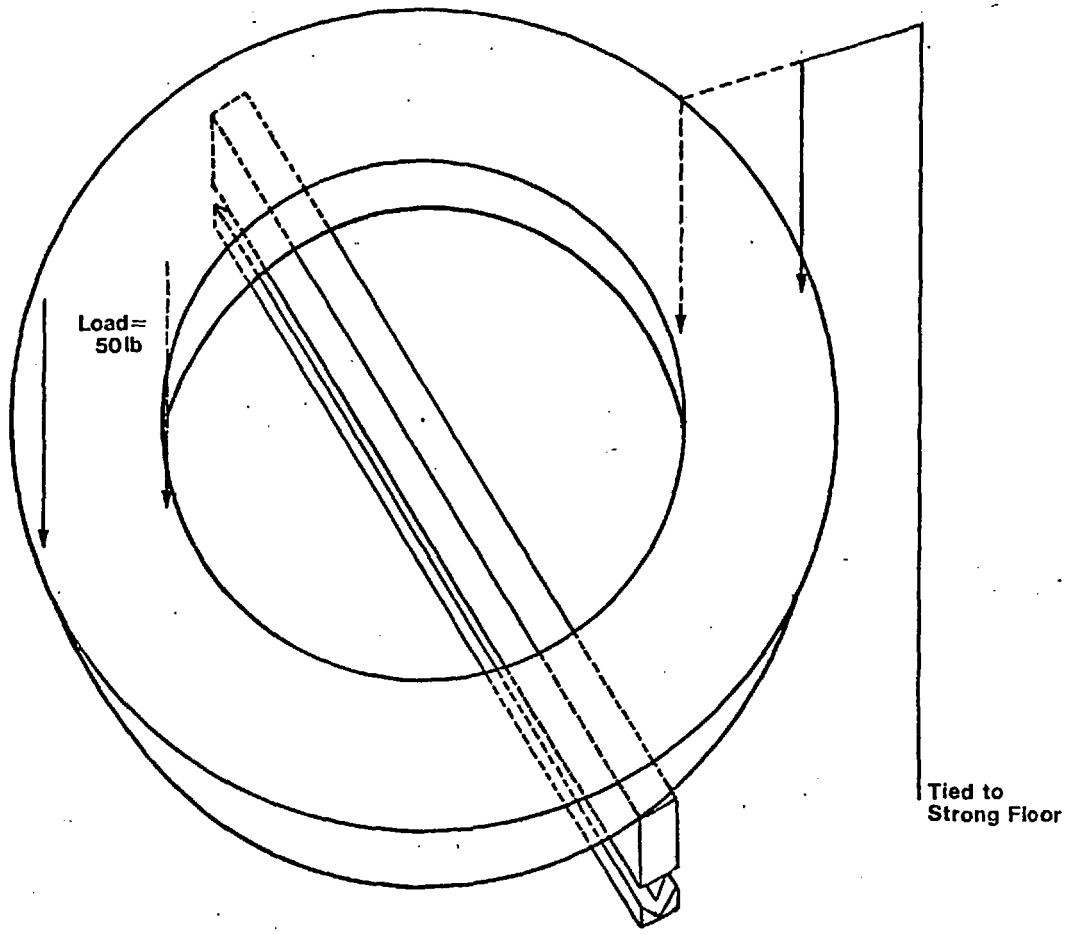


Fig.24 Loading and support arrangement for curved box model

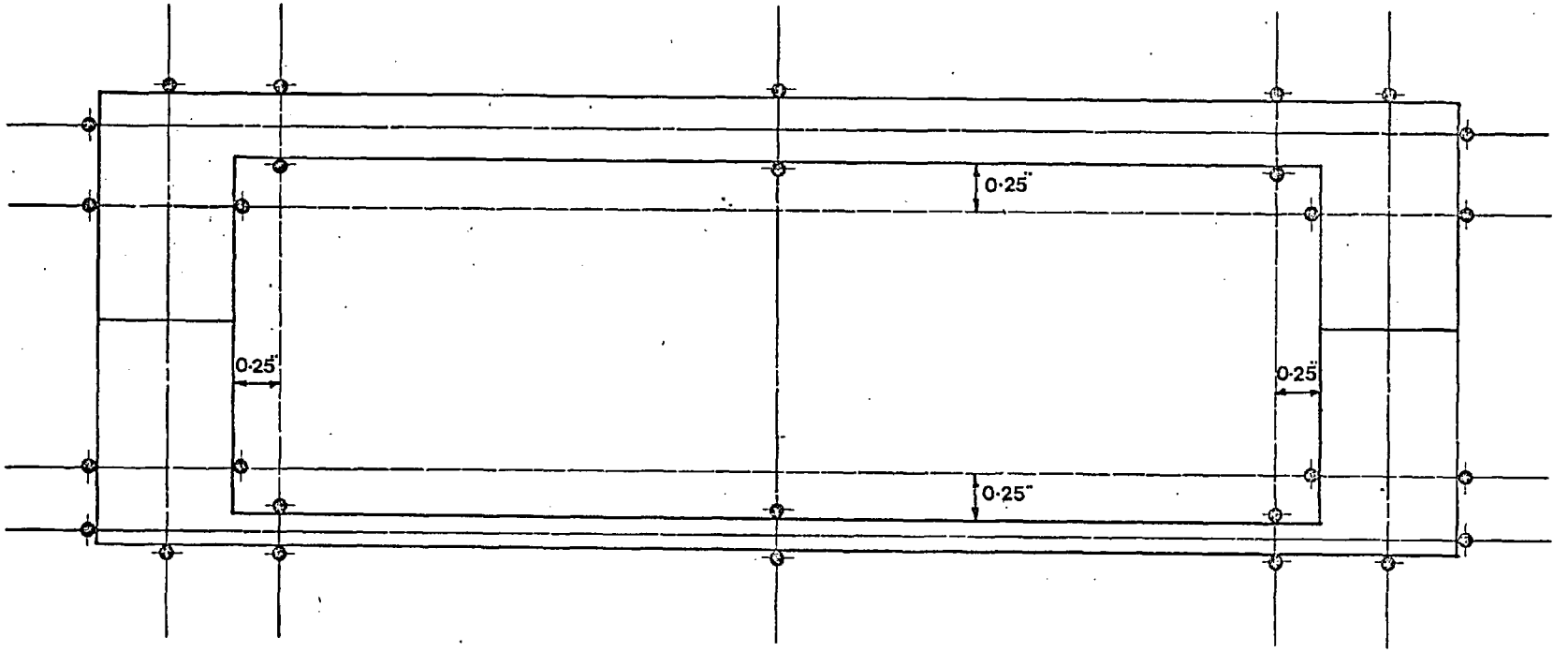


Fig.25 Strain gauge locations at Sections 1 and 2 of curved box model

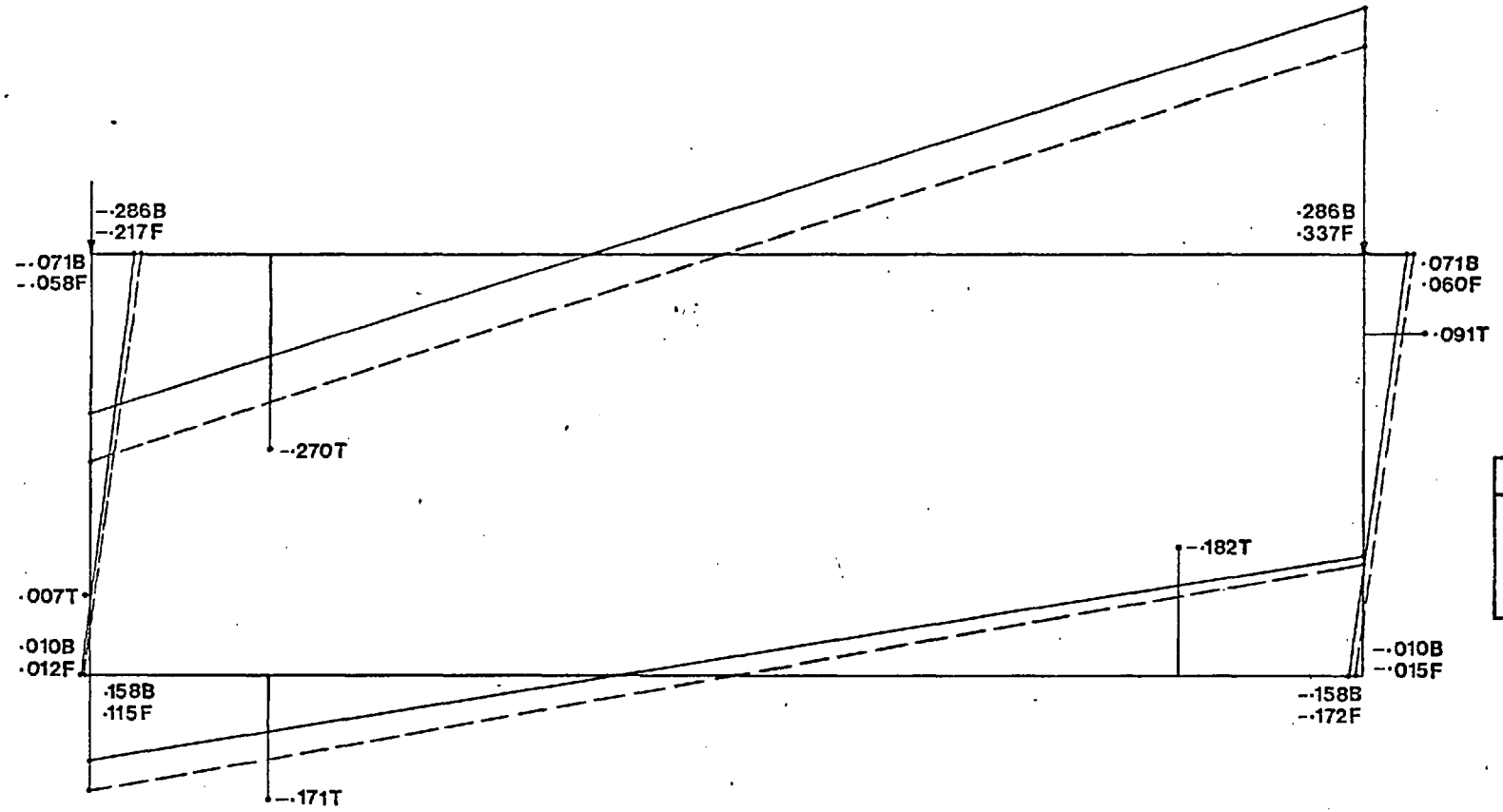


Fig.26 Curved box model; cross-sectional distribution of σ_{DB}/σ_B at midspan due to the symmetrical component of central point loading

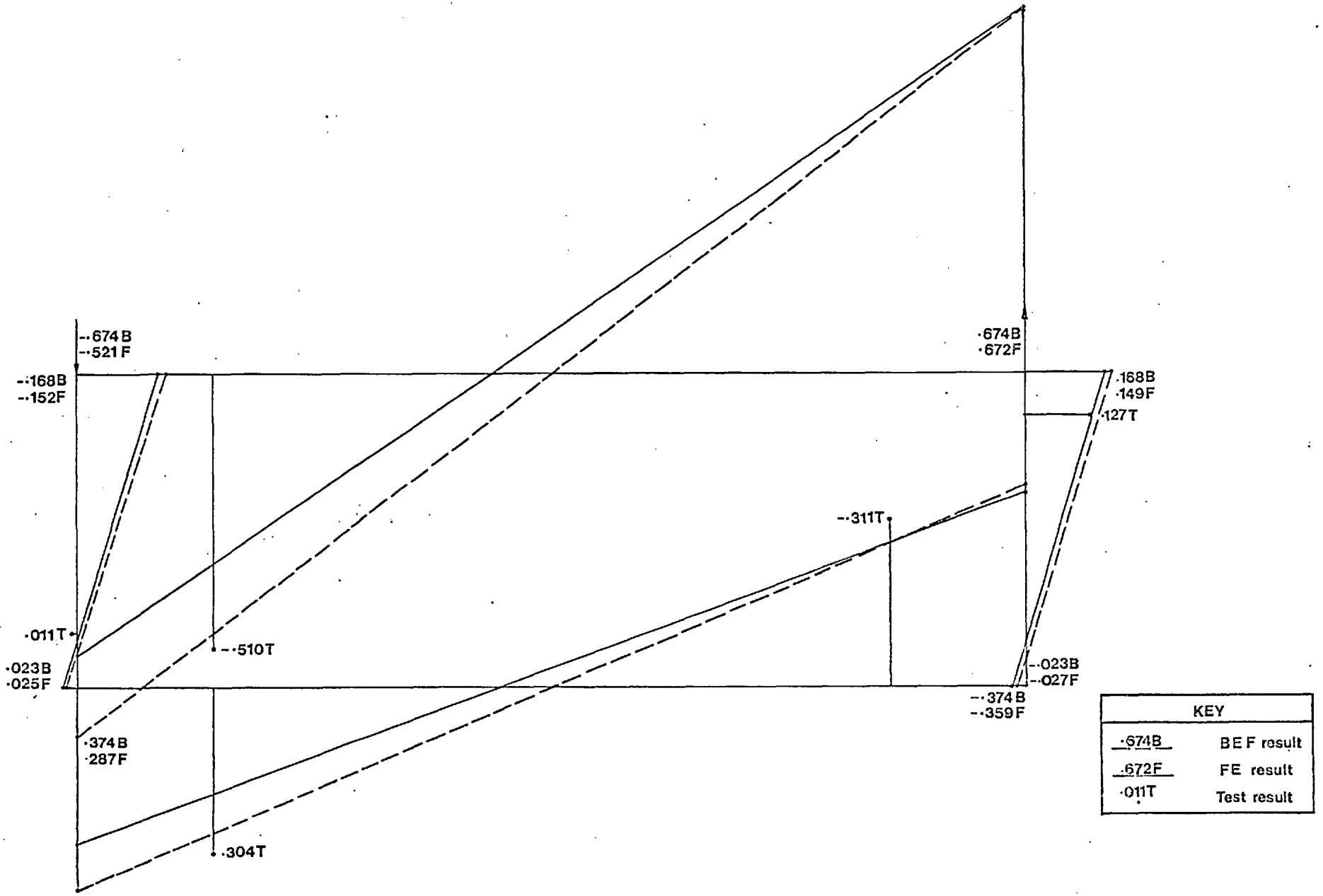


Fig.27 Curved box model;cross- sectional distribution of σ_{DB}/σ_B at midspan due to antisymmetrical component of central point loading

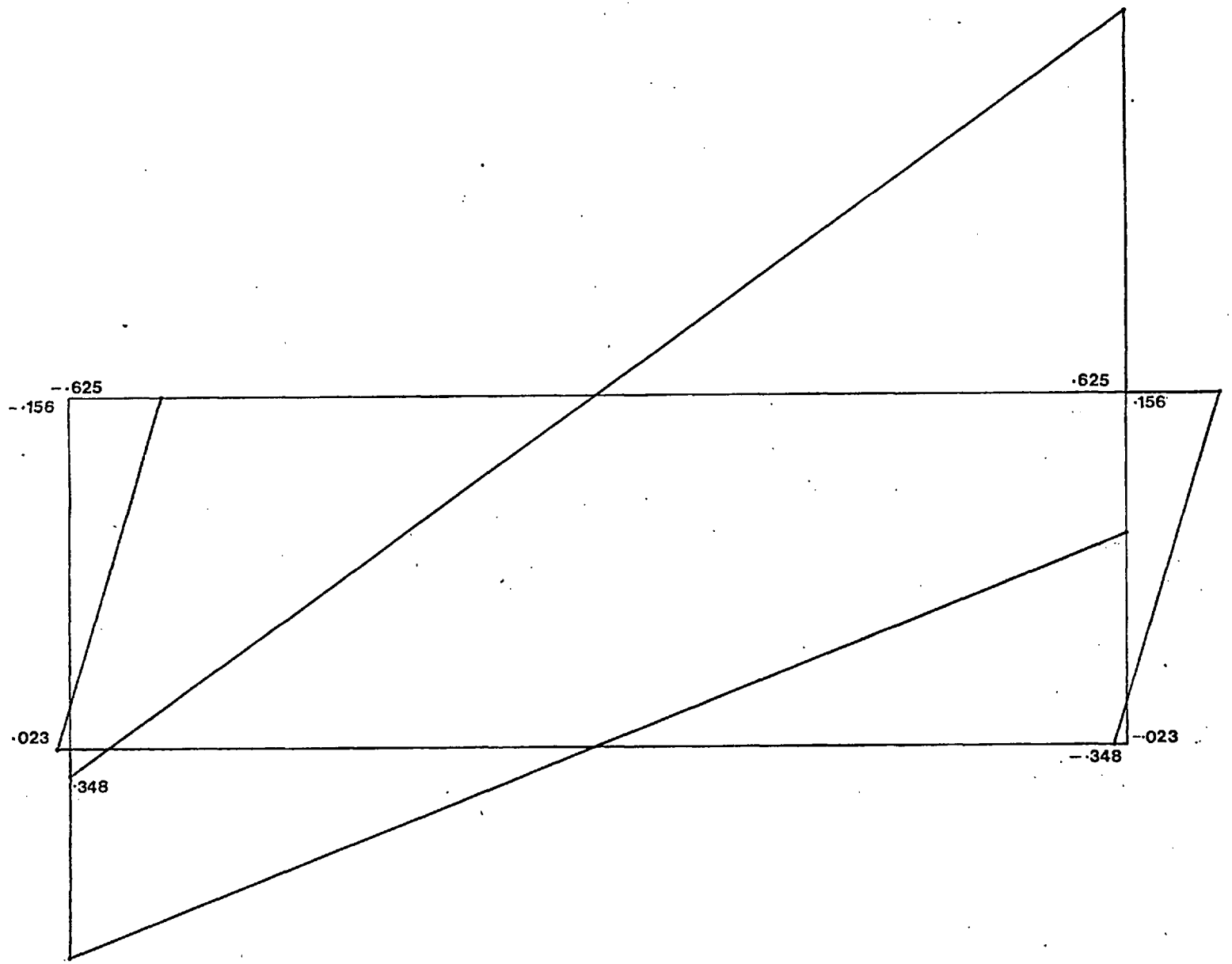


Fig.28 Curved box model; cross-sectional distribution of σ_{DB}/σ_B at midspan for antisymmetrical component of load applied to the equivalent straight bridge (F.E results)

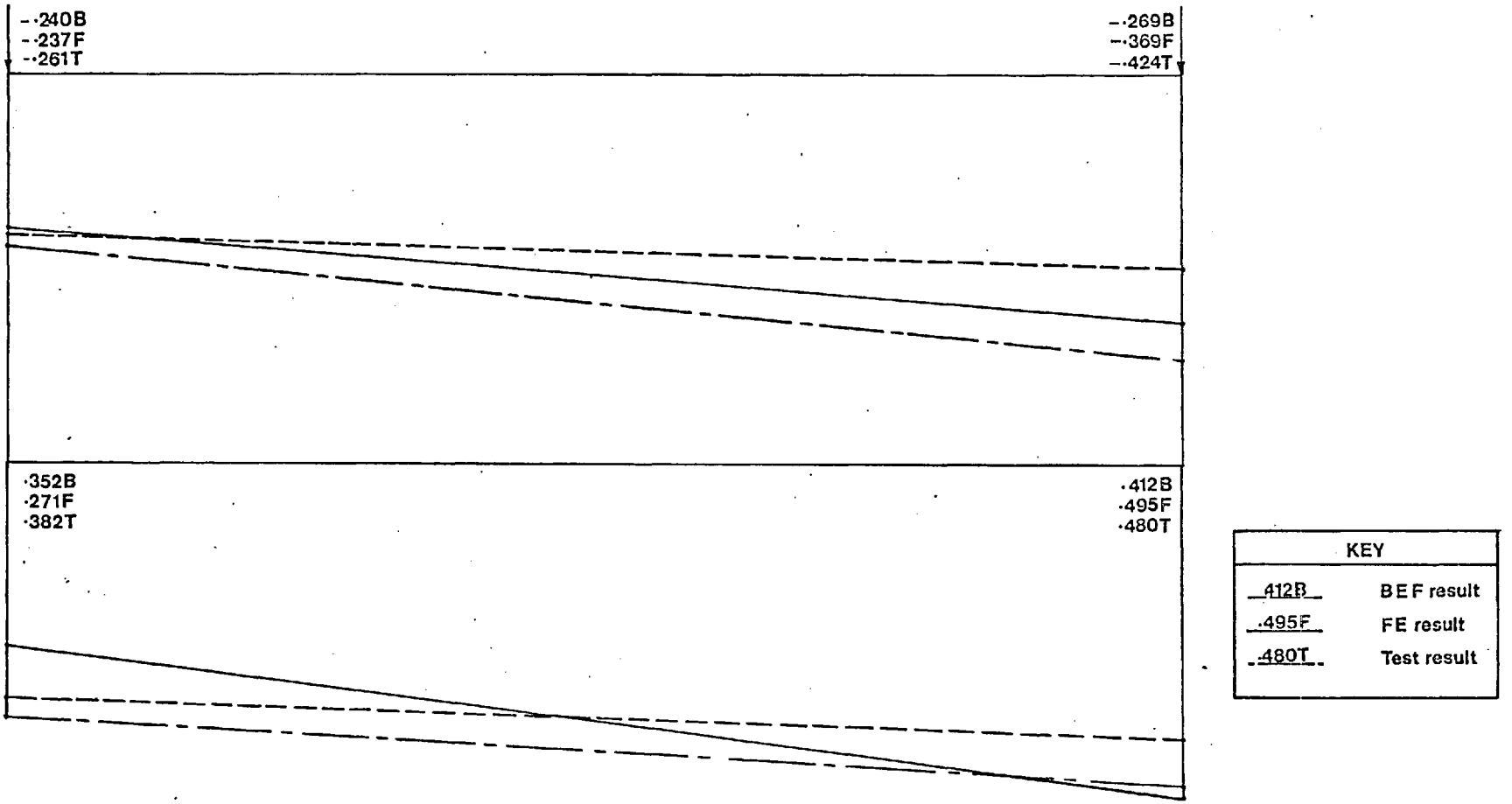


Fig.29 Curved box model; cross-sectional distribution of σ_L / σ_B at midspan due to the symmetrical component of central point loading

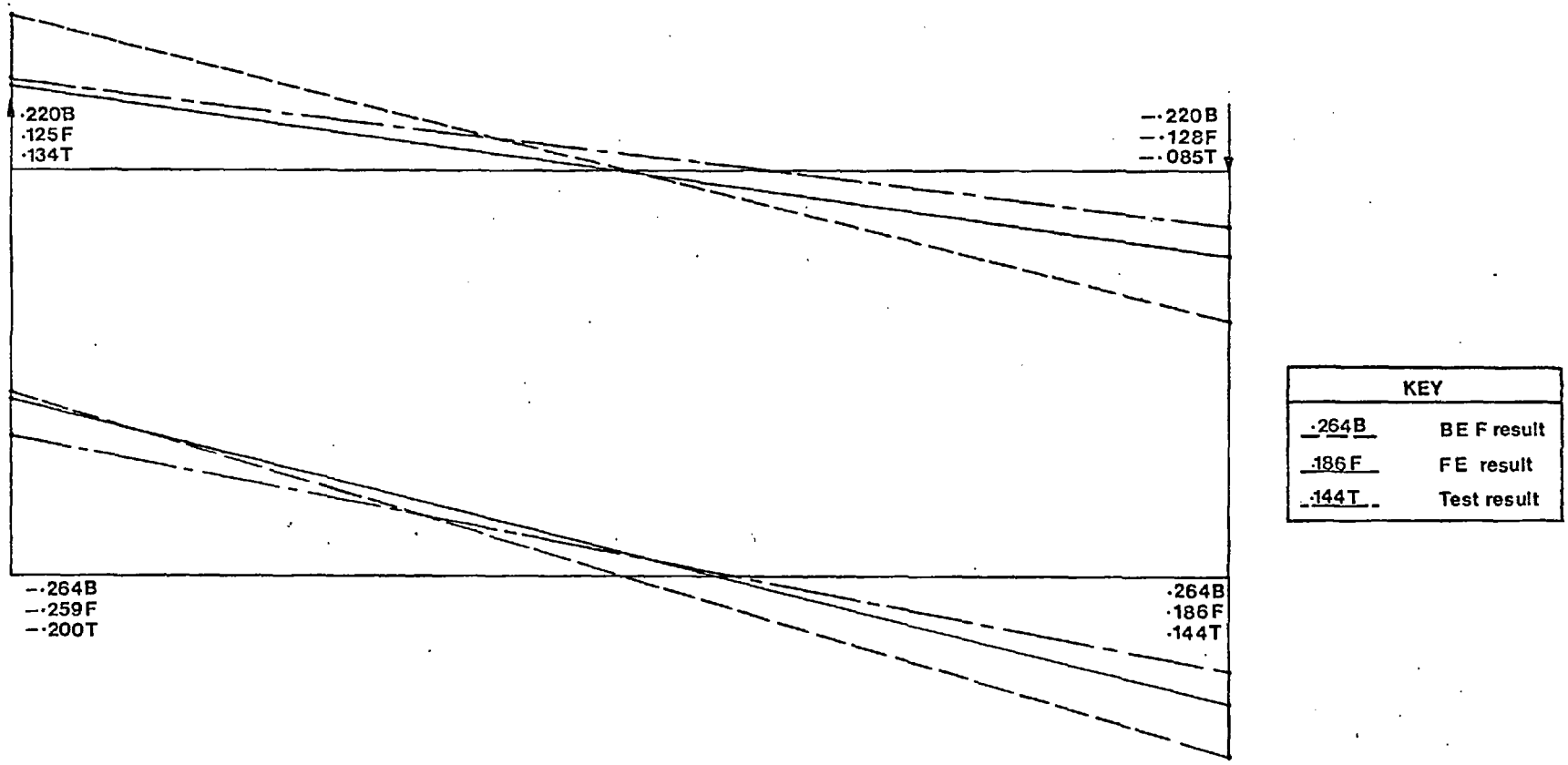


Fig.30 Curved box model;cross-sectional distribution of σ_L / σ_B at midspan due to the antisymmetrical component of central point loading

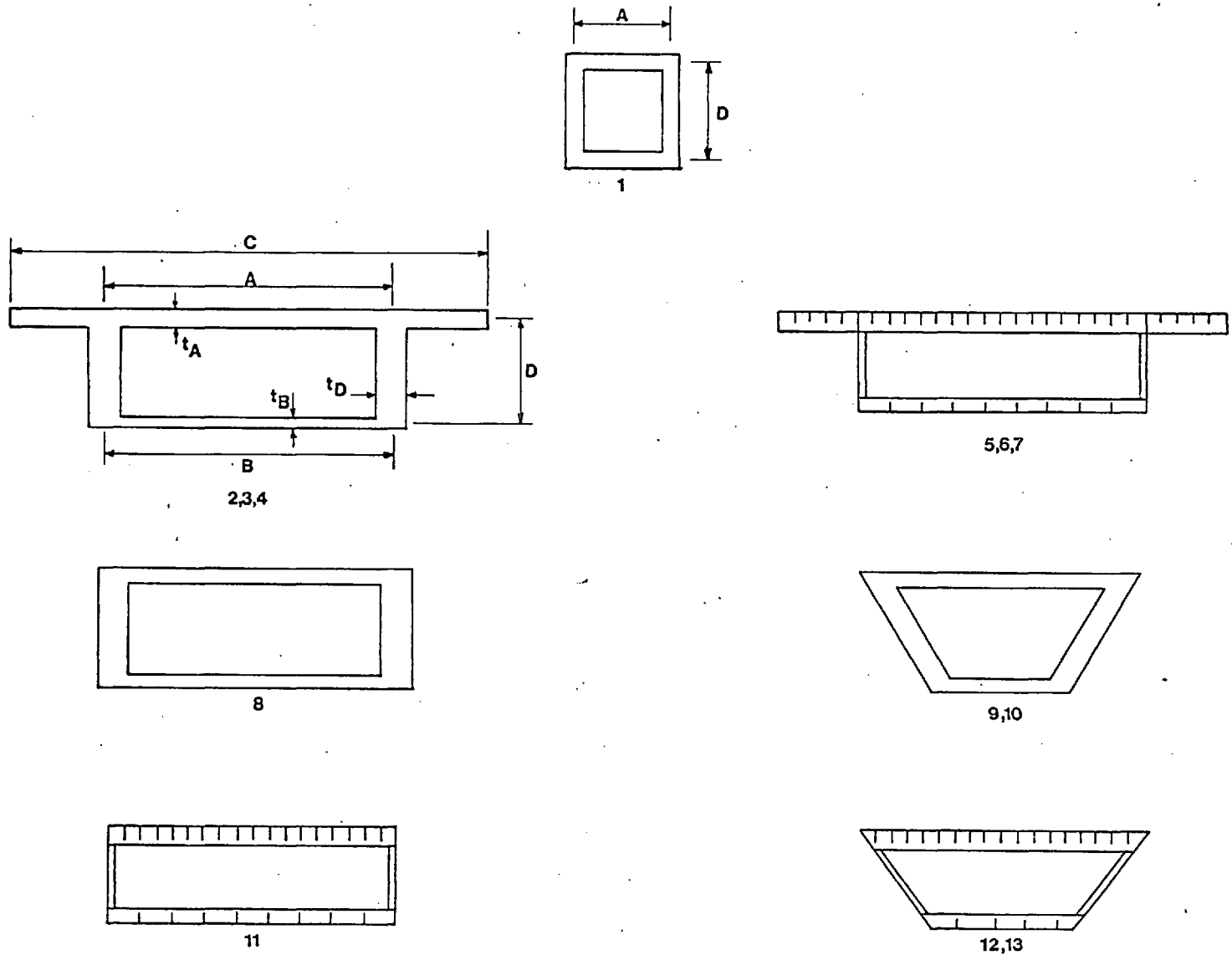


Fig.31 Bridge cross sections used in Section 2·5

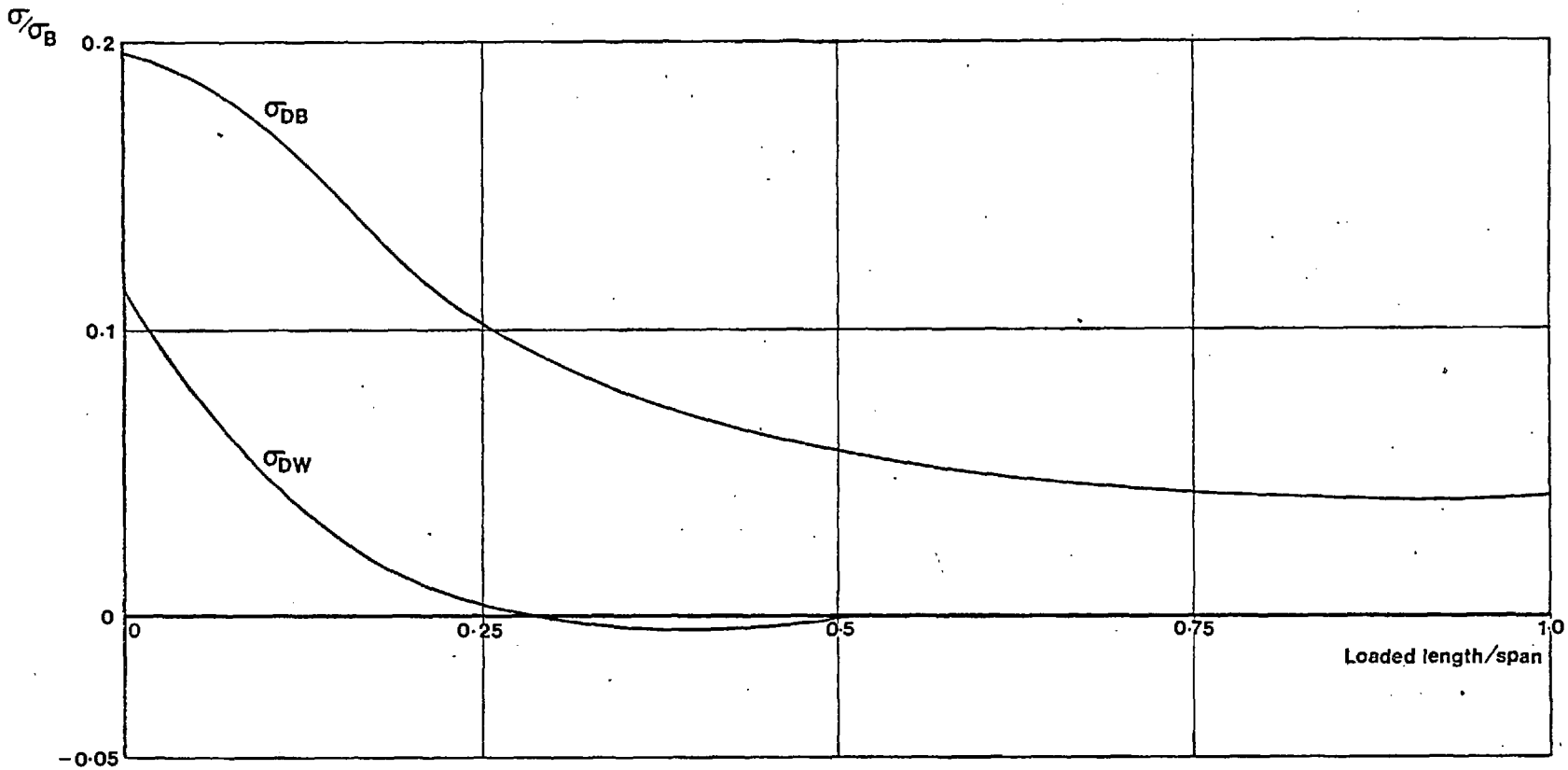


Fig.32 Variation of midspan distortional stresses for Section 1 under a fixed load distributed over an increasing length. (The stresses are non-dimensionalised with the central bending stress for the relevant loaded length)

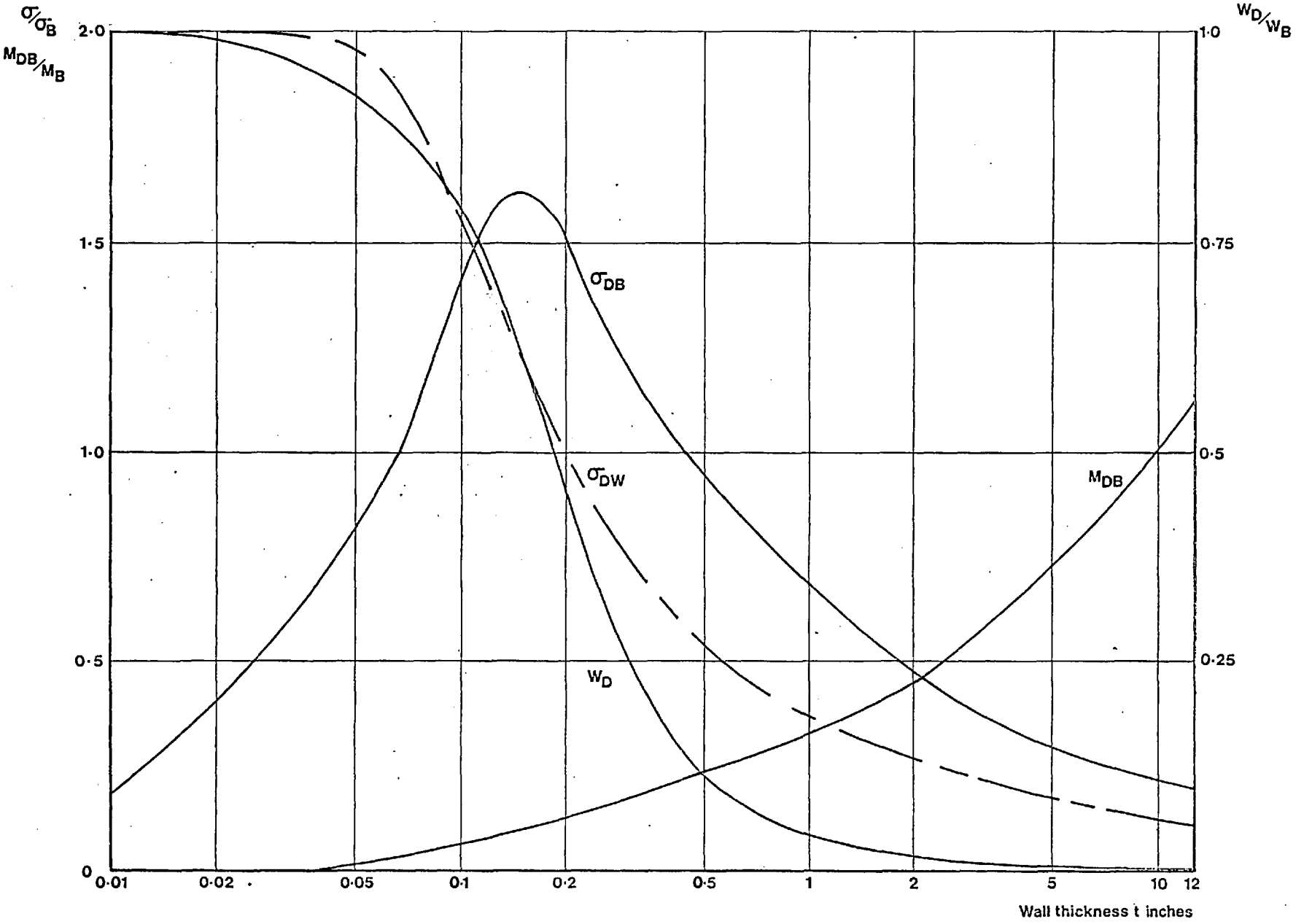


Fig.33 Variation of peak transverse distortional bending stress, distortional warping stress, distortional deflection, and transverse distortional moment with wall thickness for a 6ft x 6ft box girder under a central point load

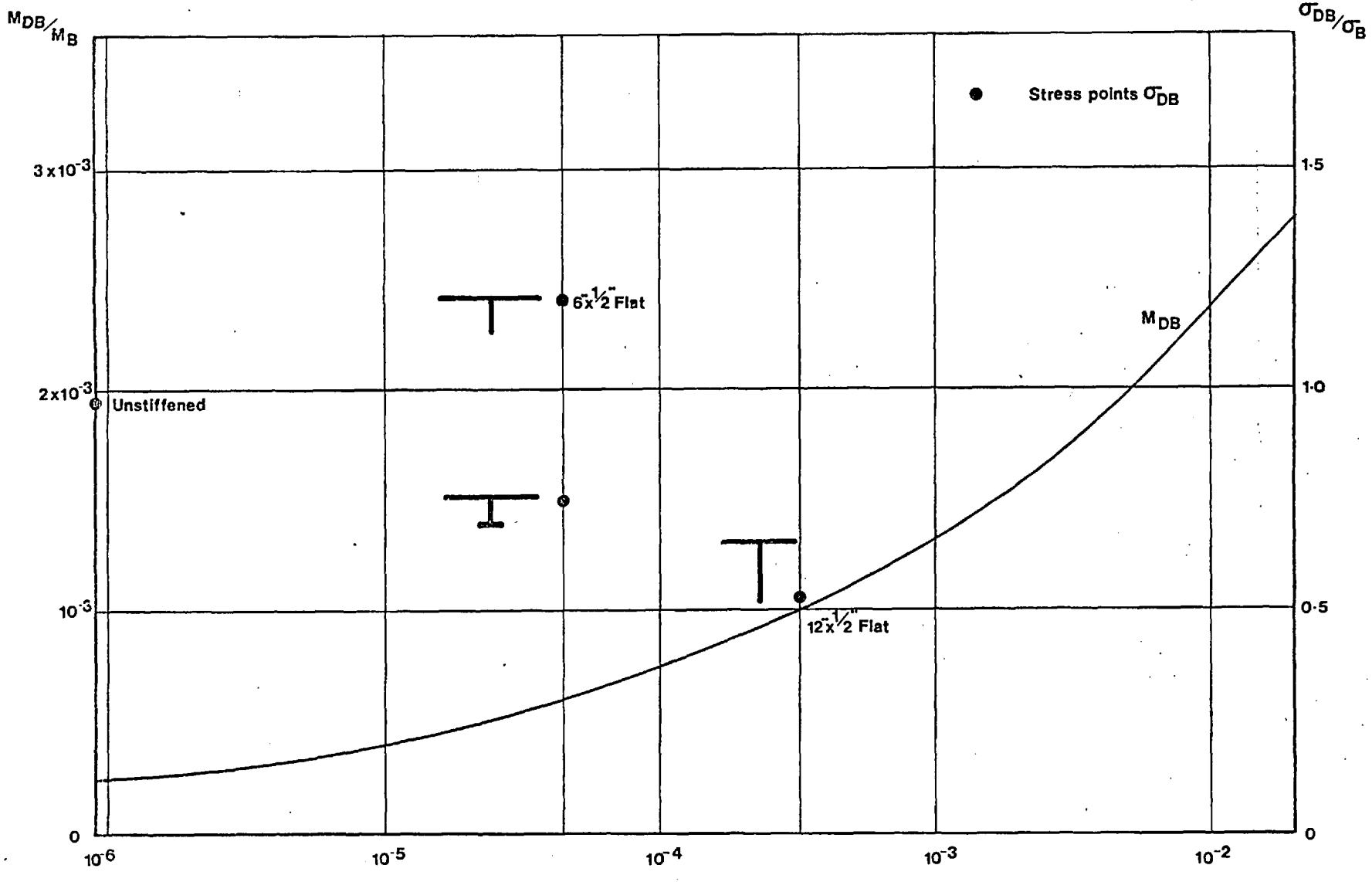
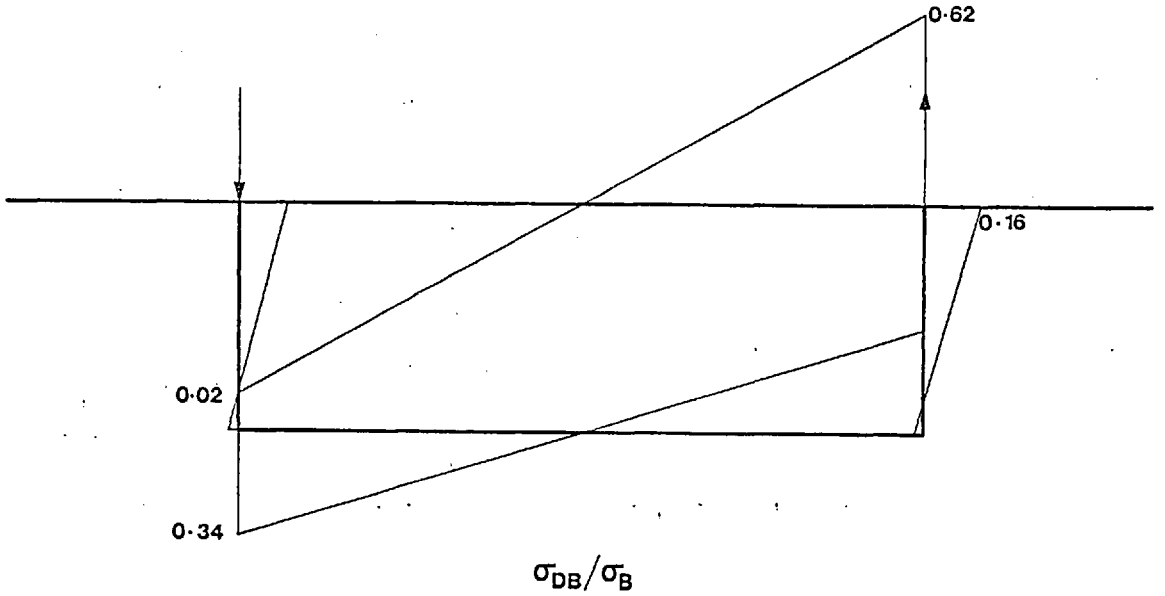


Fig.34 Variation of maximum transverse distortional moment and the corresponding transverse distortional stresses as the distortional stiffness of the section is increased while the warping stiffness is kept constant for a 6ft x 6ft box with ½ in plates under a central point load



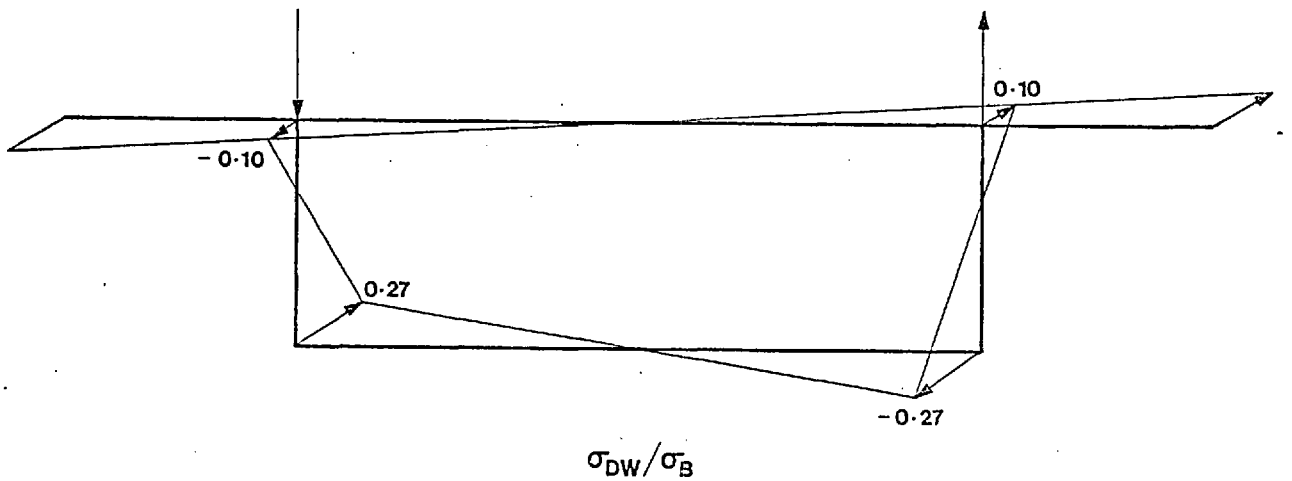


Fig.35 Cross sectional distribution of σ_{DB} and σ_{DW} for Section 3 under a central point load

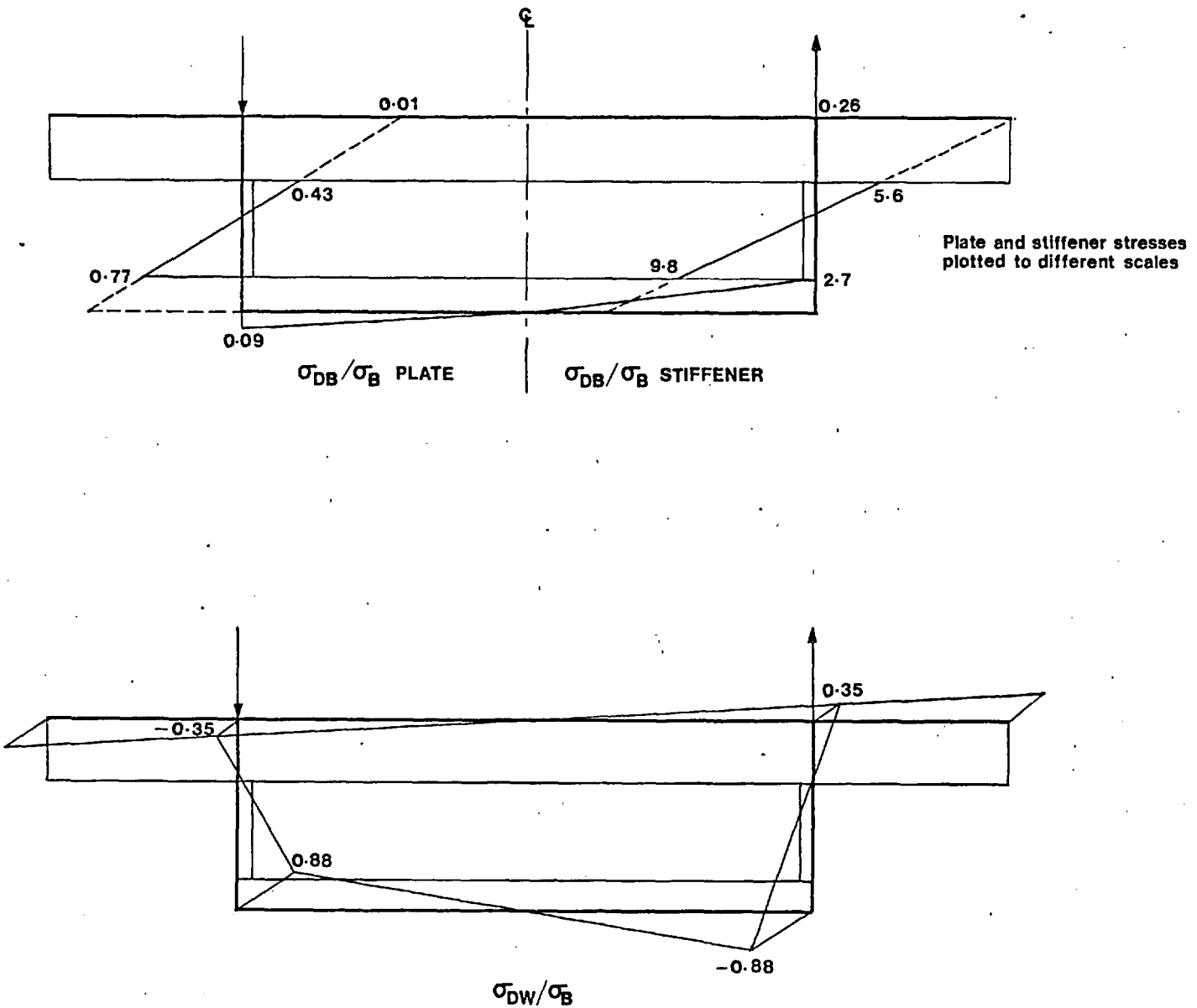


Fig.36 Cross sectional distribution of σ_{DB} and σ_{DW} for Section 6 under a central point load

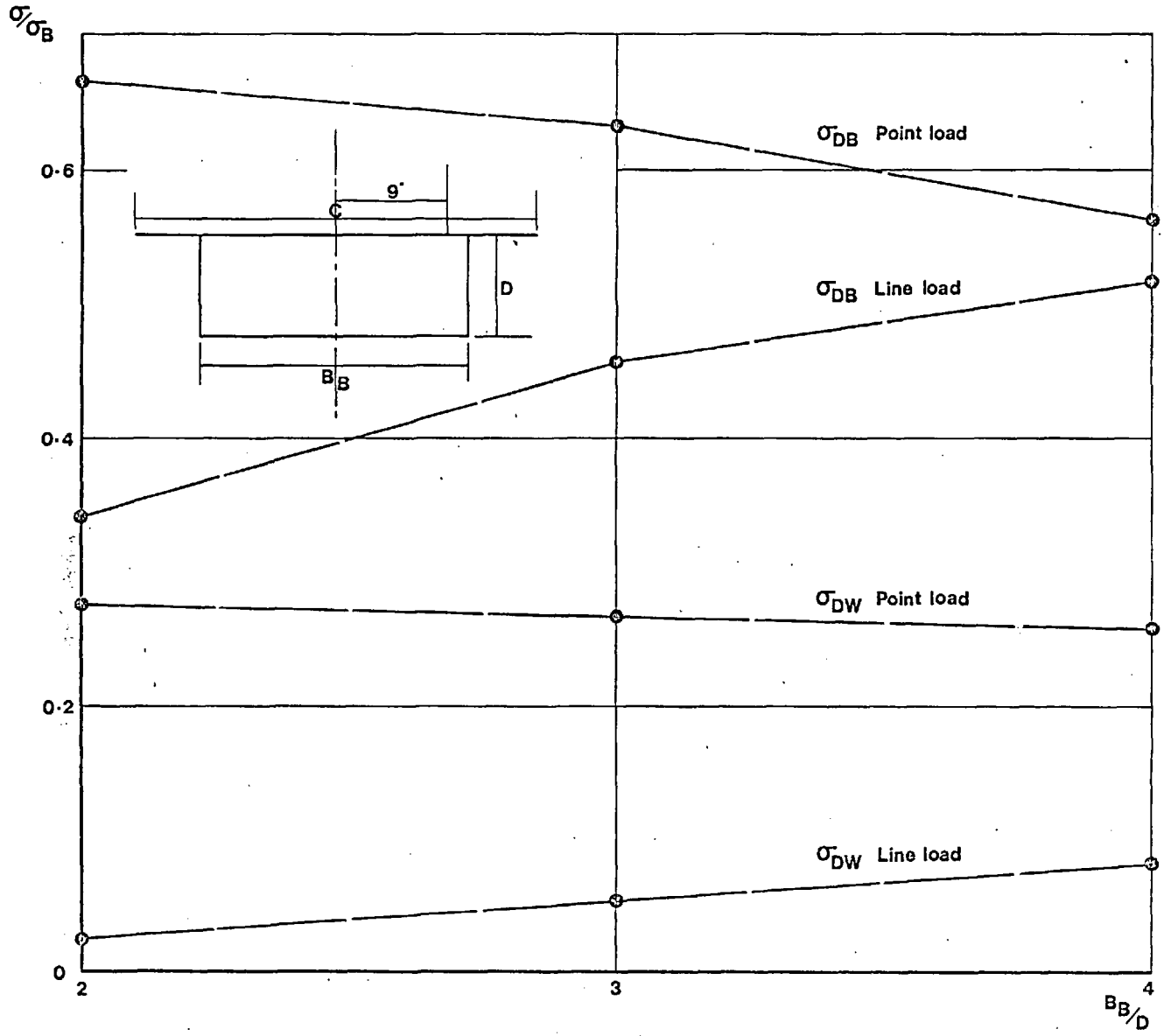


Fig.37 Maximum distortional stresses for Sections 2,3 and 4 under a central point load and a uniformly distributed line load

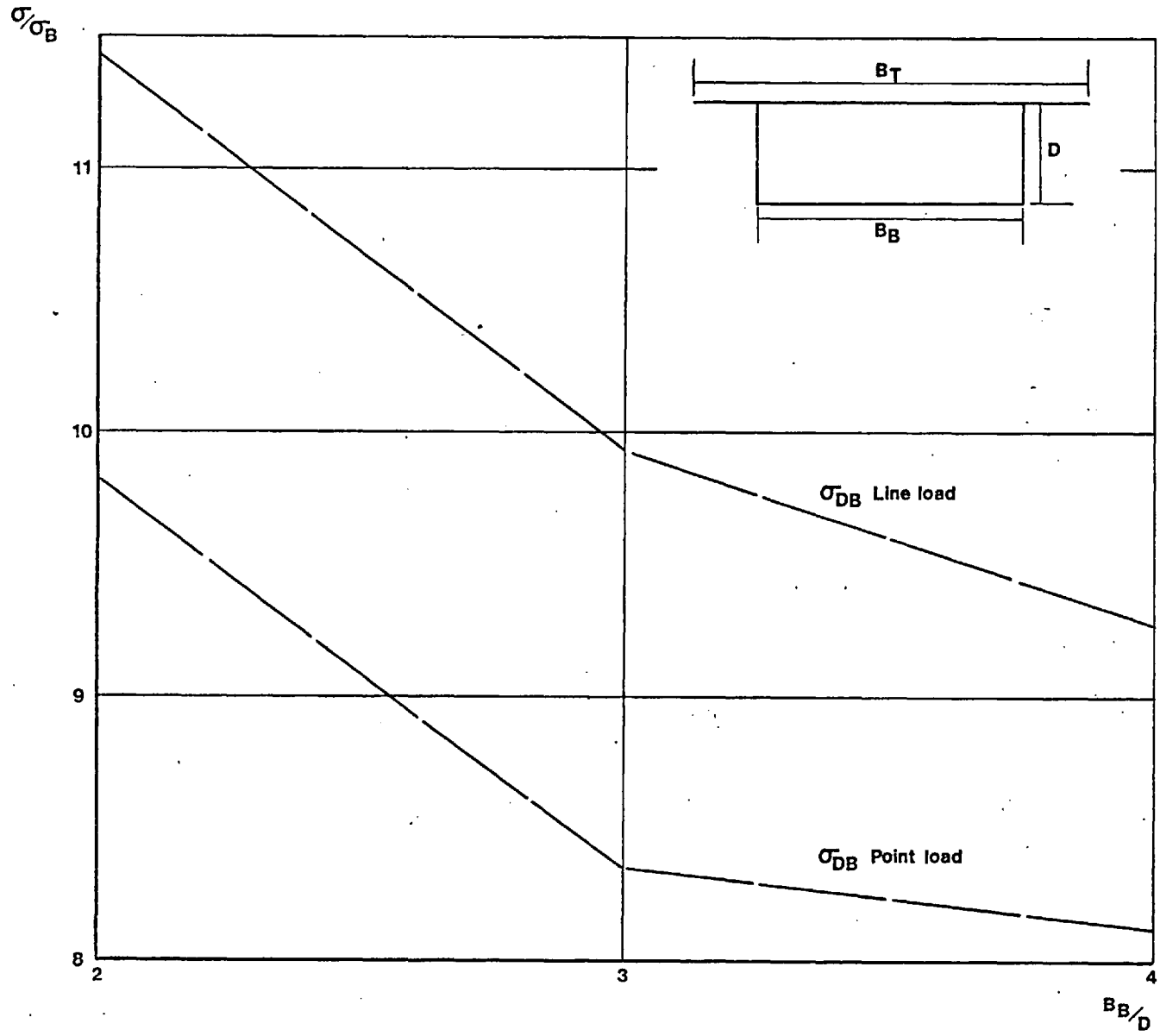


Fig.38 Maximum σ_{DB} for Sections 5,6 and 7 under a central point load and a uniformly distributed line load

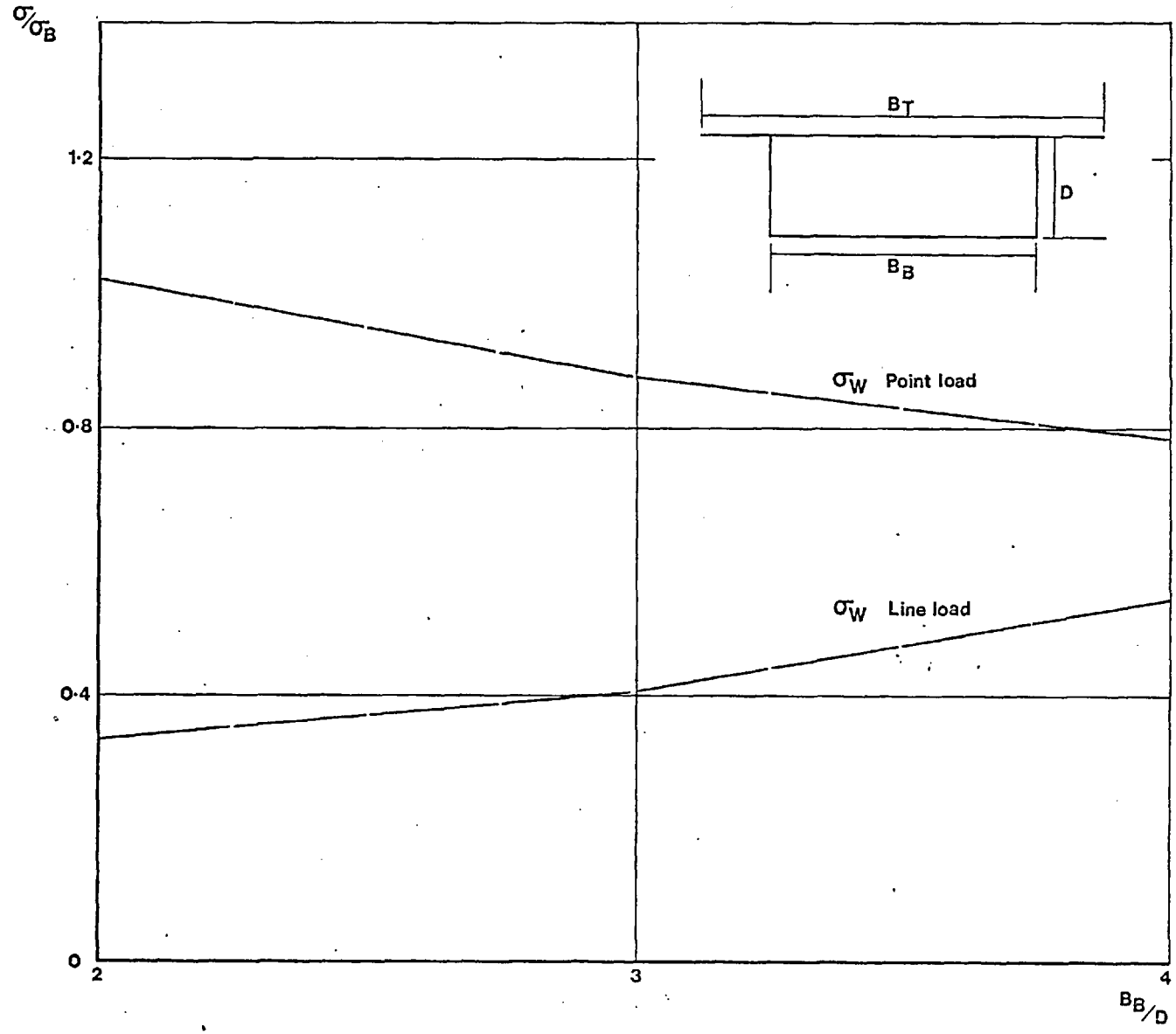


Fig.39 Maximum σ_{DW} for Sections 5,6 and 7 under a central point local and a uniformly distributed line load

334

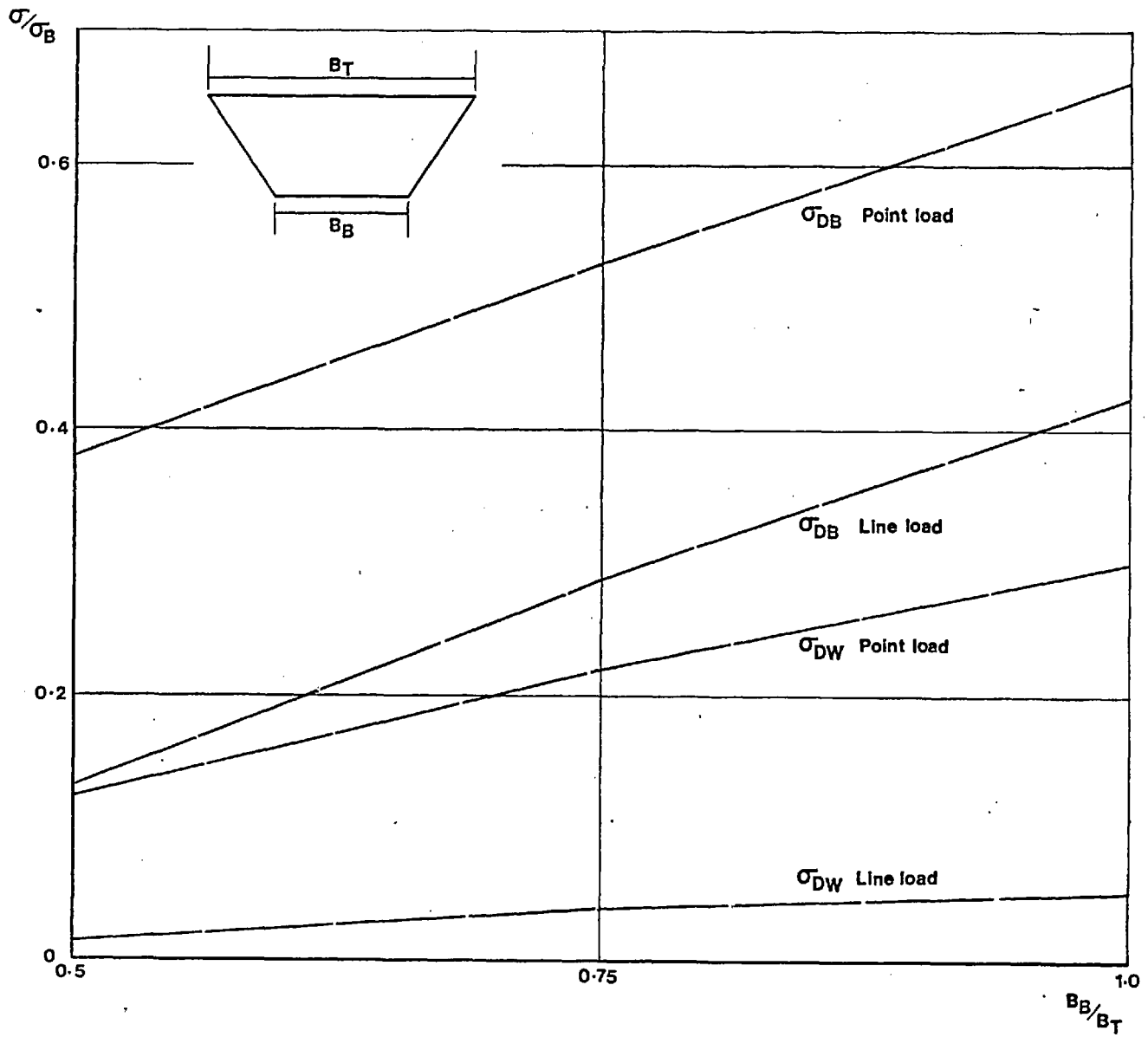


Fig.40 Maximum distortional stresses for Sections 8,9 and 10 under a central point load and a uniformly distributed line load

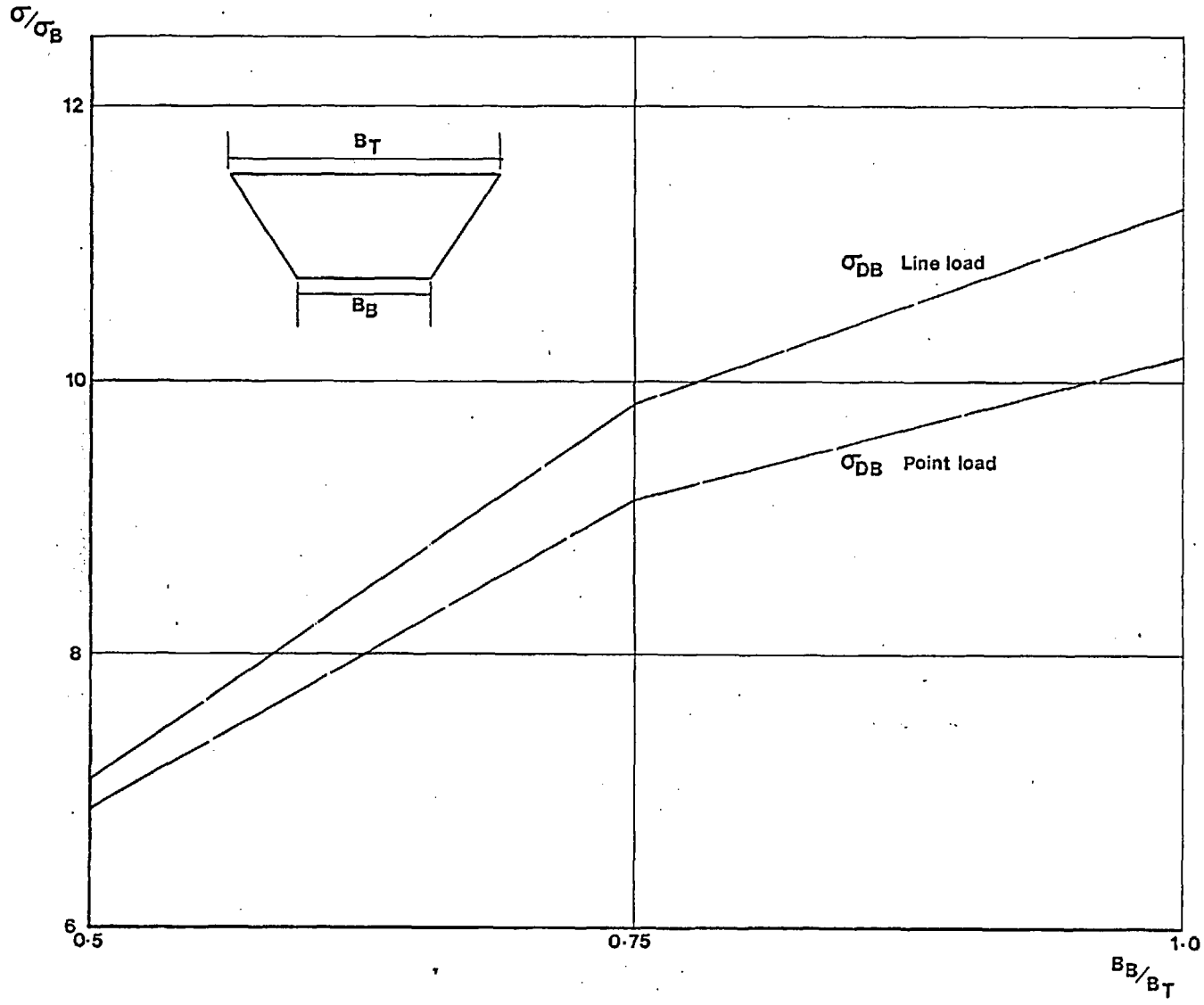


Fig.41 Maximum σ_{DB} for Sections 11,12 and 13 under a central point load and a uniformly distributed line load

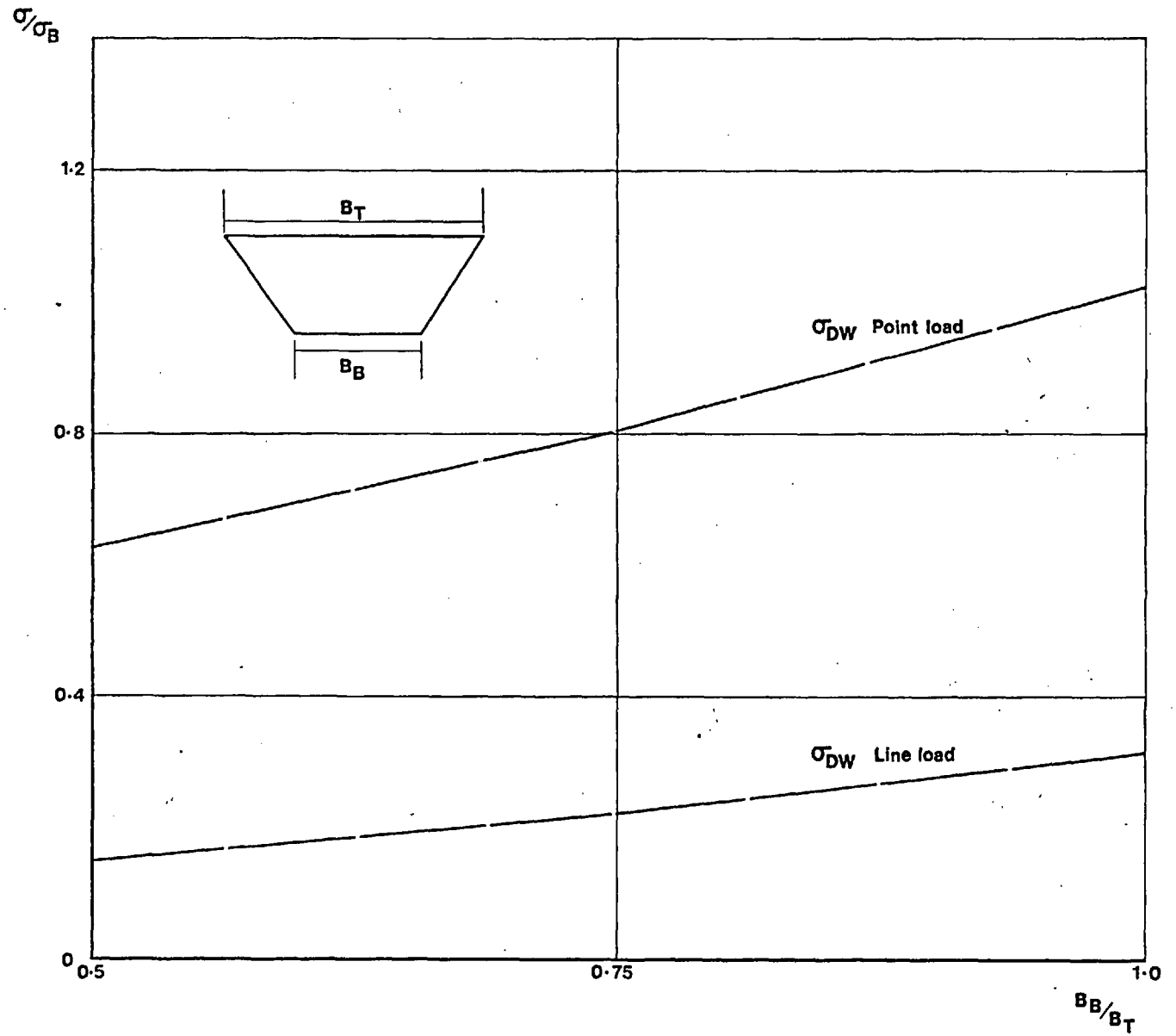


Fig.42 Maximum σ_{DW} for Sections 11,12 and 13 under a central point load and a uniformly distributed line load

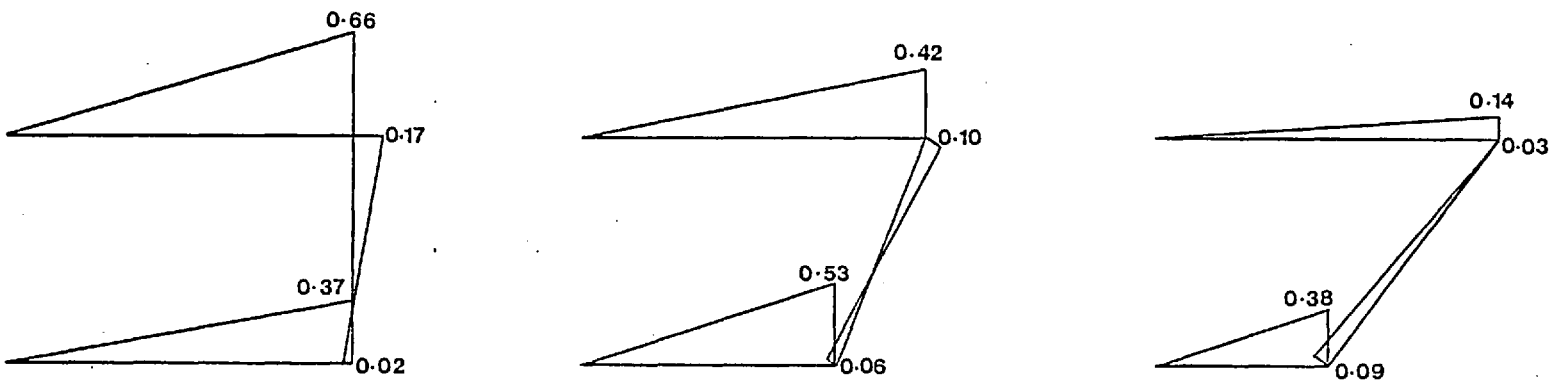
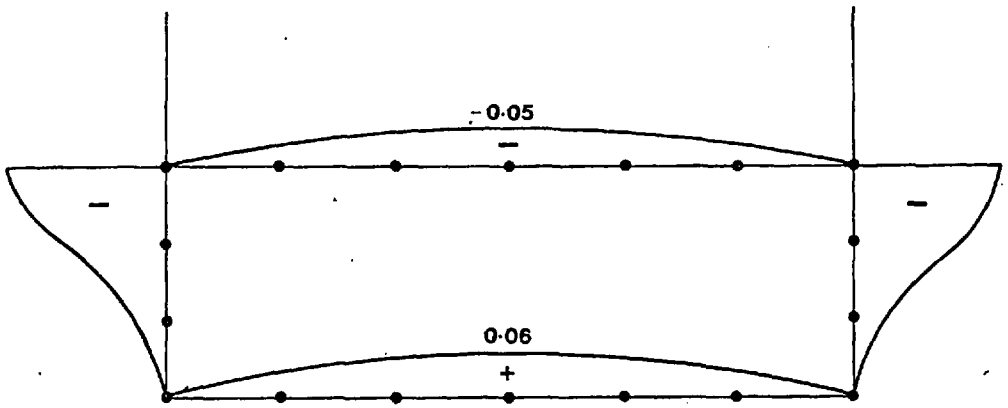
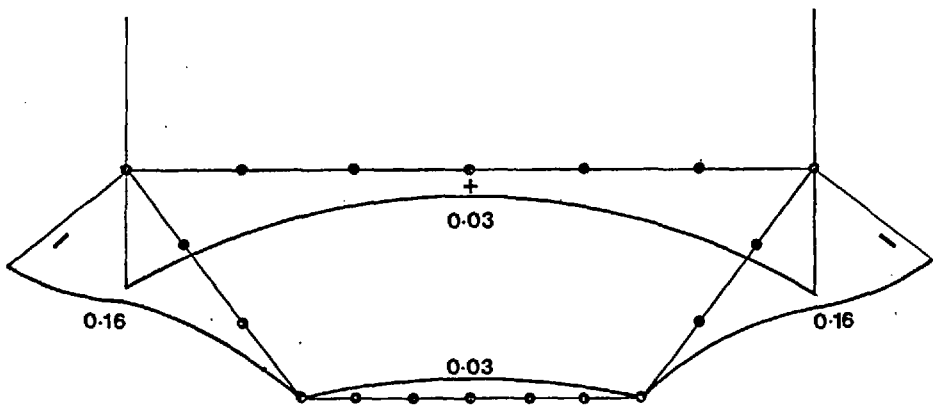


Fig.43 Cross sectional distribution of maximum σ_{DB}/σ_B for Sections 8,9 and 10 under a central point load



SECTION 8



SECTION 10

Fig.44

Distribution of transverse in-plane stresses σ/σ_B at midspan for Sections 8 and 10 under symmetrical central point load (FE mesh length = span/48)

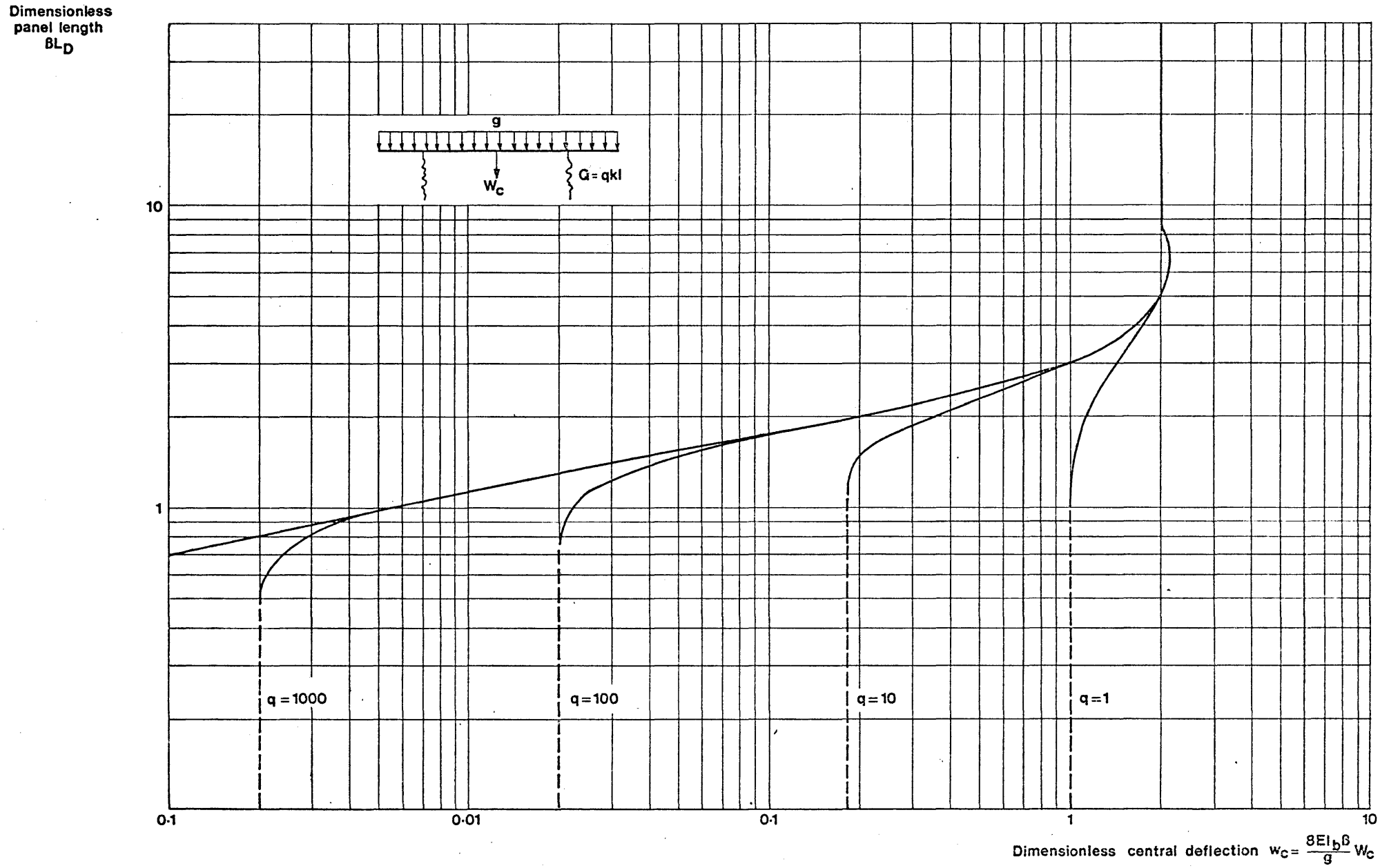


Fig.45 Dimensionless central deflection w_c the practical range of dimensionless panel lengths βL_D

340

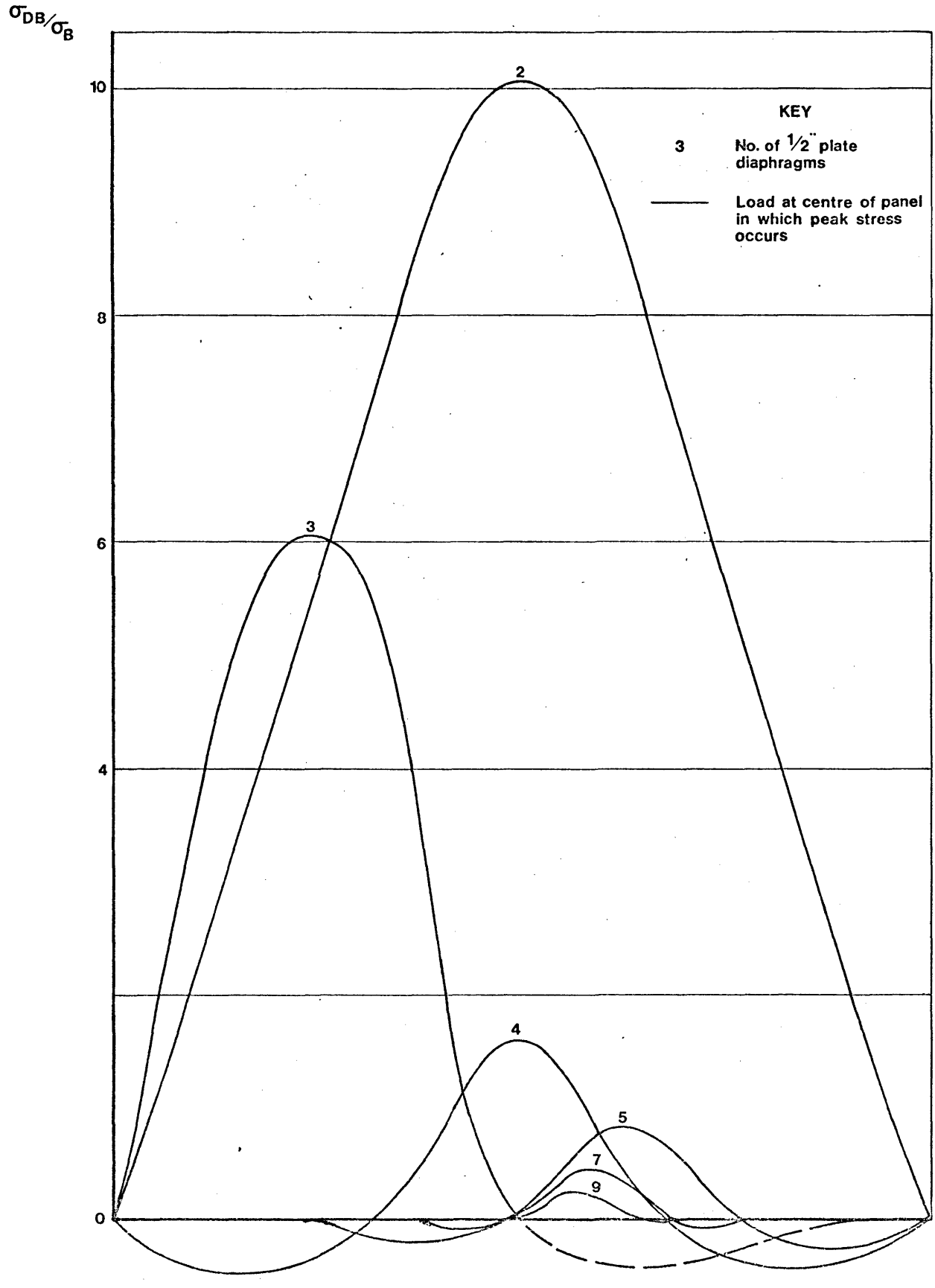


Fig.46 Longitudinal distribution of σ_{DB} for Section 11 with various numbers of equally spaced diaphragms

342

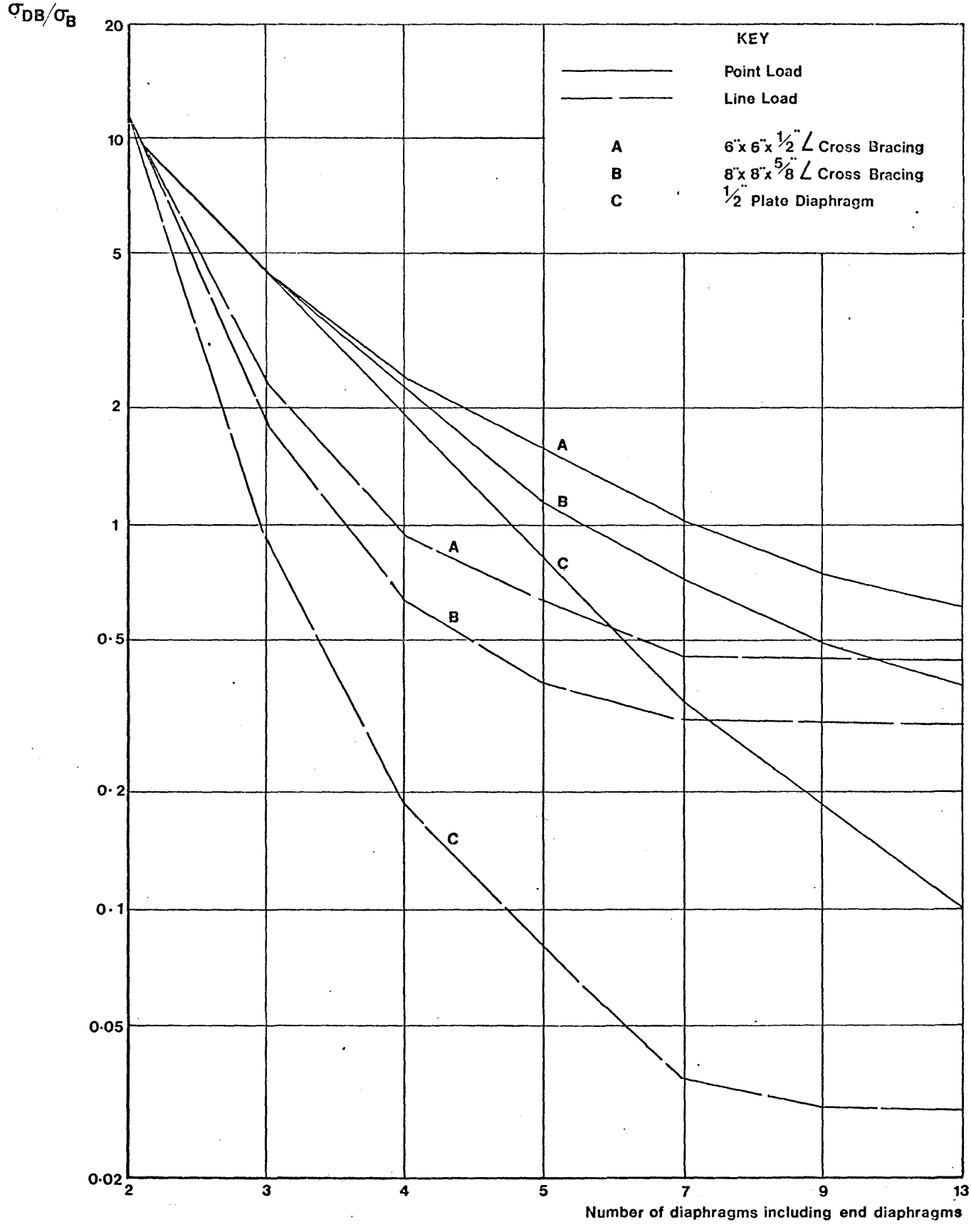


Fig.47 Effect of different numbers of alternative diaphragms on the maximum σ_{DB} for Section 11 (Point load at centre of panel nearest midspan)

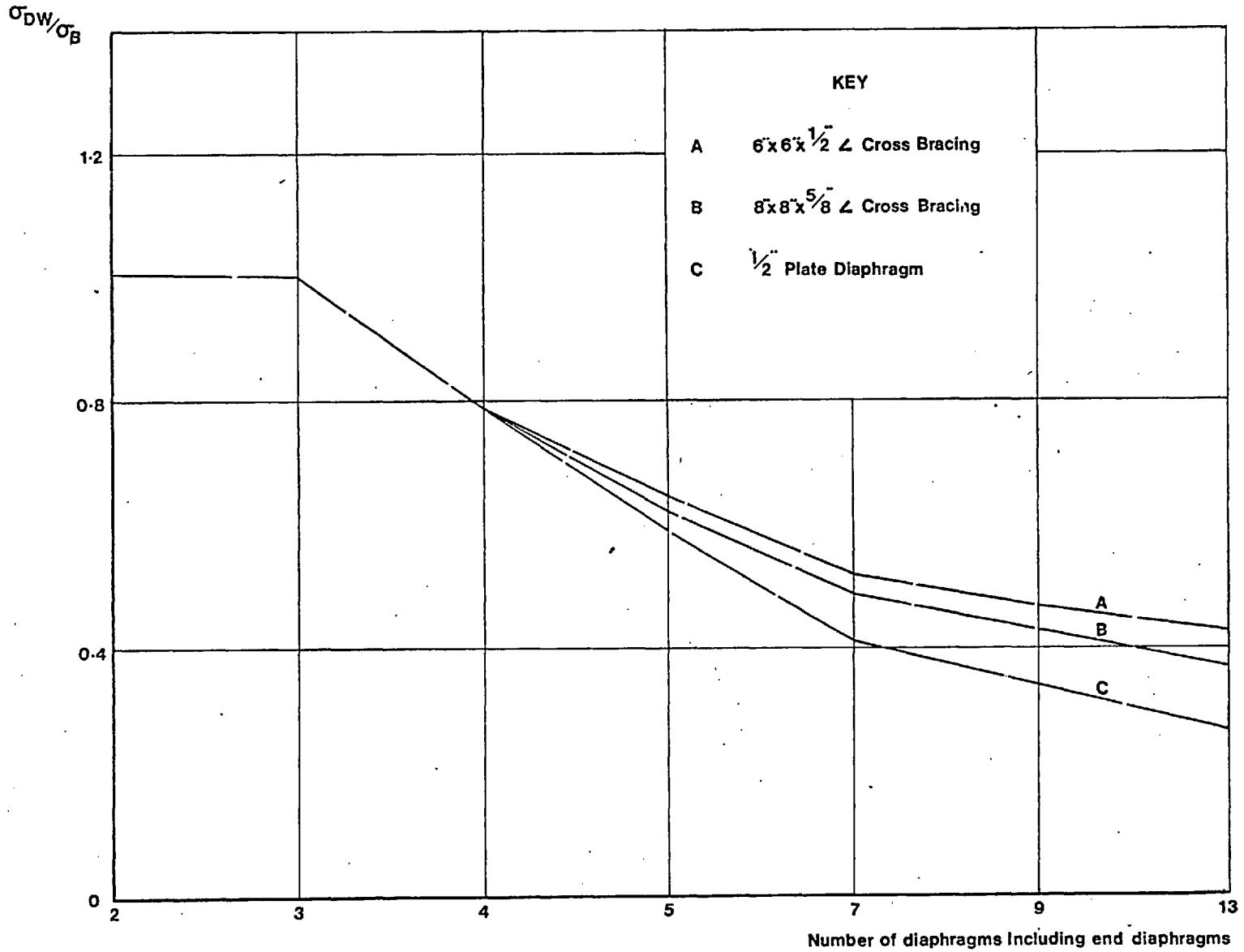


Fig.48 Effect of different numbers of alternative diaphragms on the maximum σ_{DW} for Section 11 (Point load at centre of panel nearest midspan)

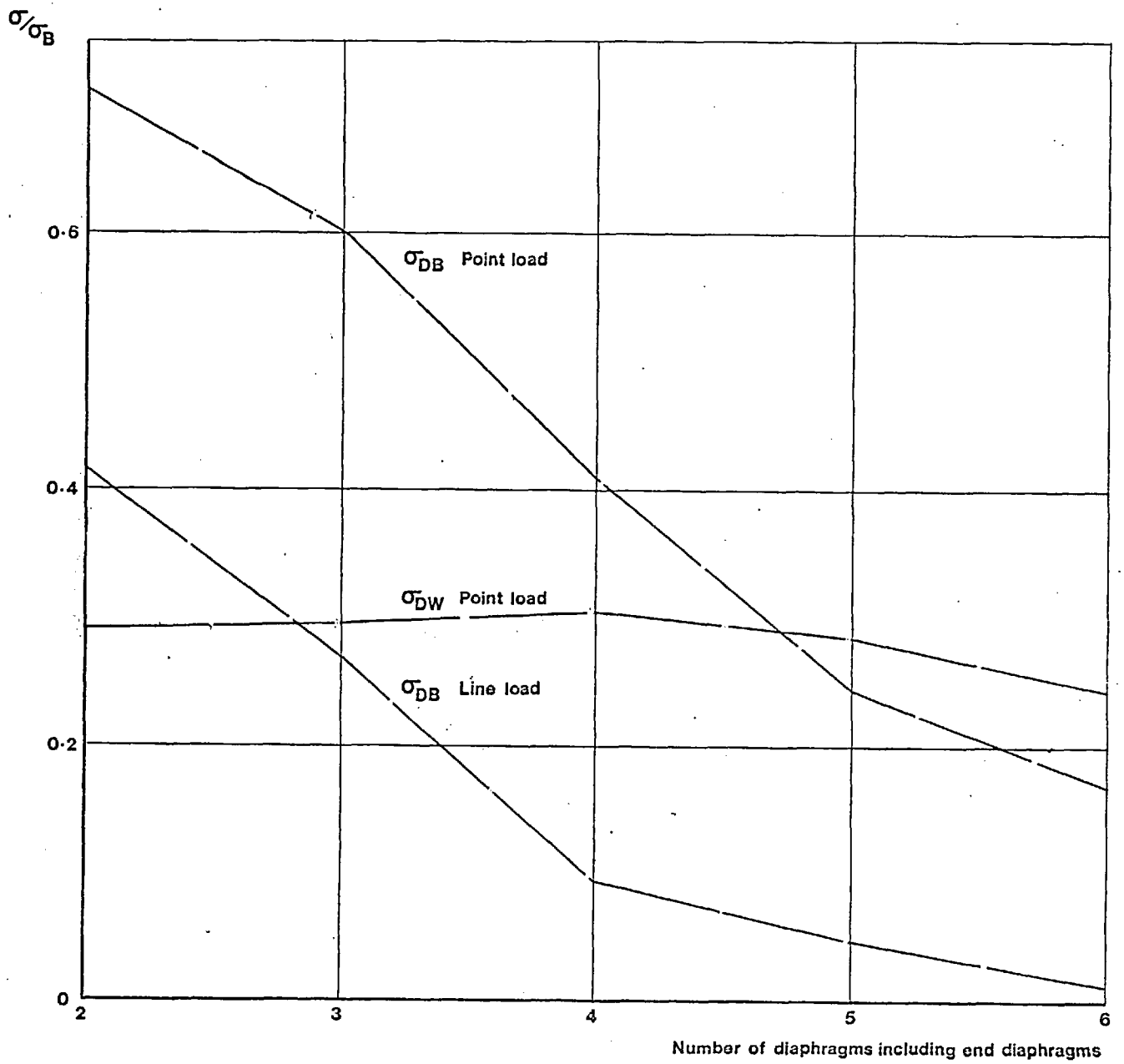
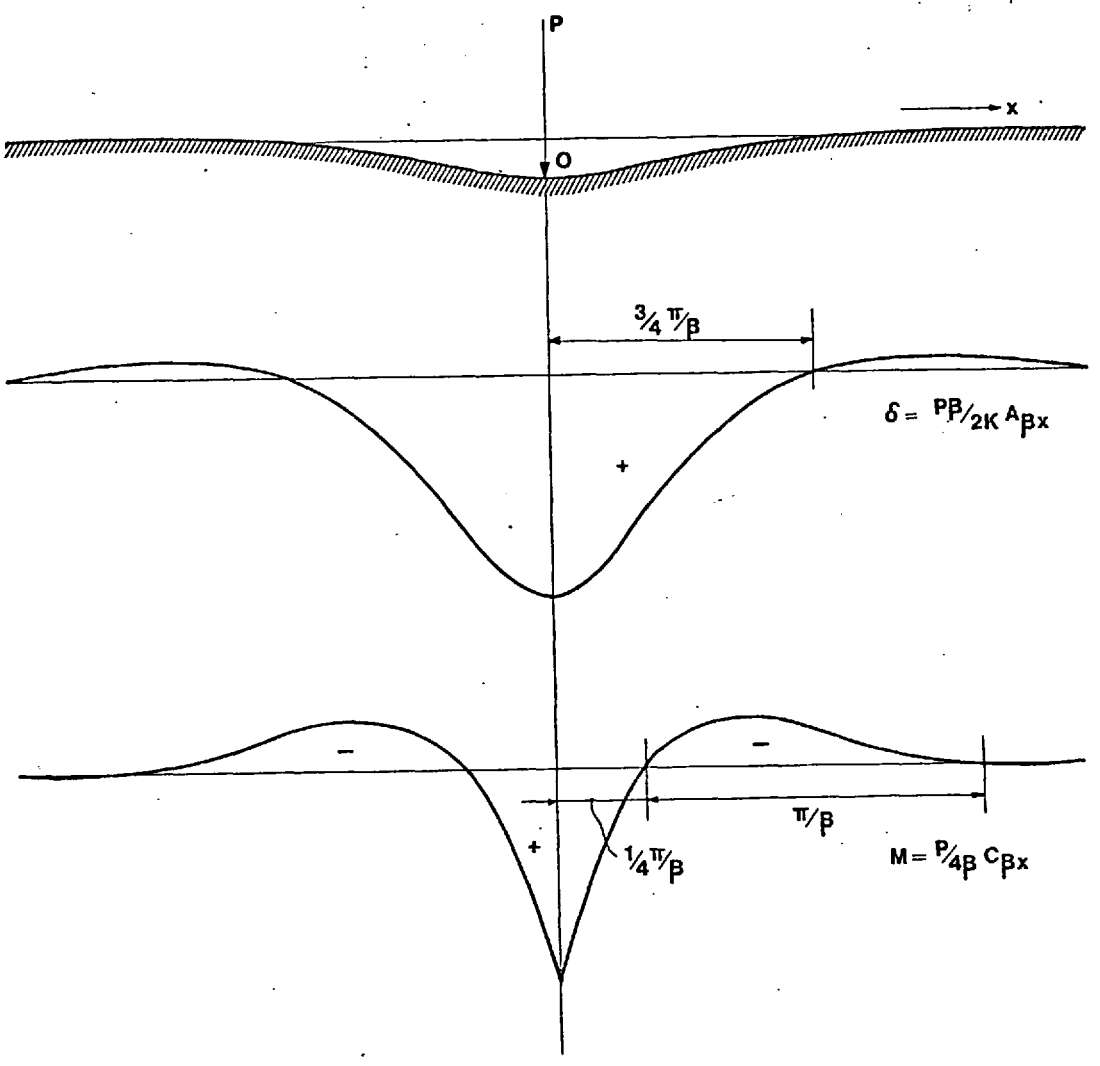


Fig.49 Effect of different members of 12" thick diaphragms on maximum σ_{DB} and σ_{DW} for Section 8

344



$A_{\beta x} = e^{-x}(\cos x + \sin x)$

$C_{\beta x} = e^{-x}(\cos x - \sin x)$

Fig.50 Response of an infinite BEF to a concentrated load

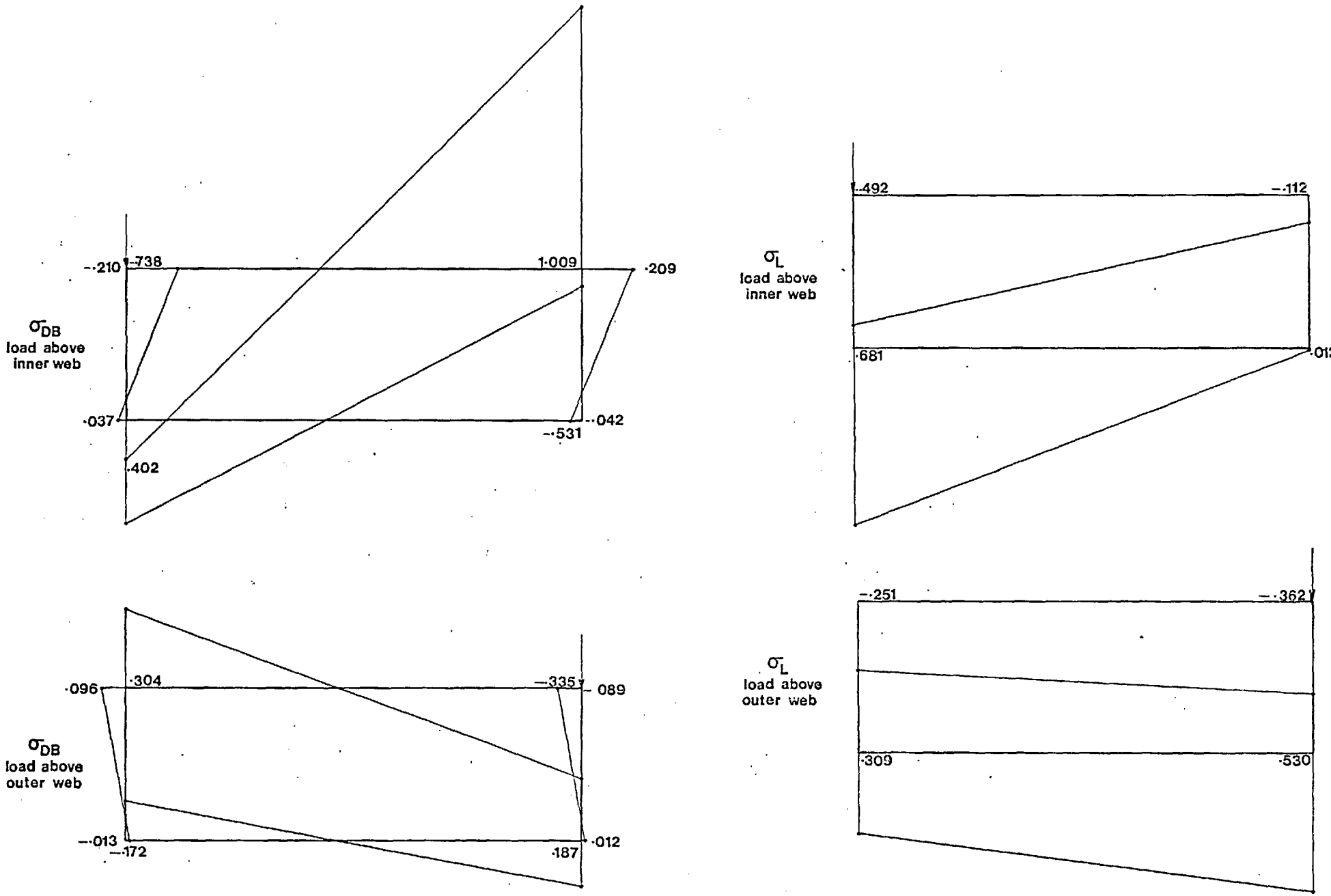


Fig.51 Curved box model - comparison of stress for load placed above inner and outer webs

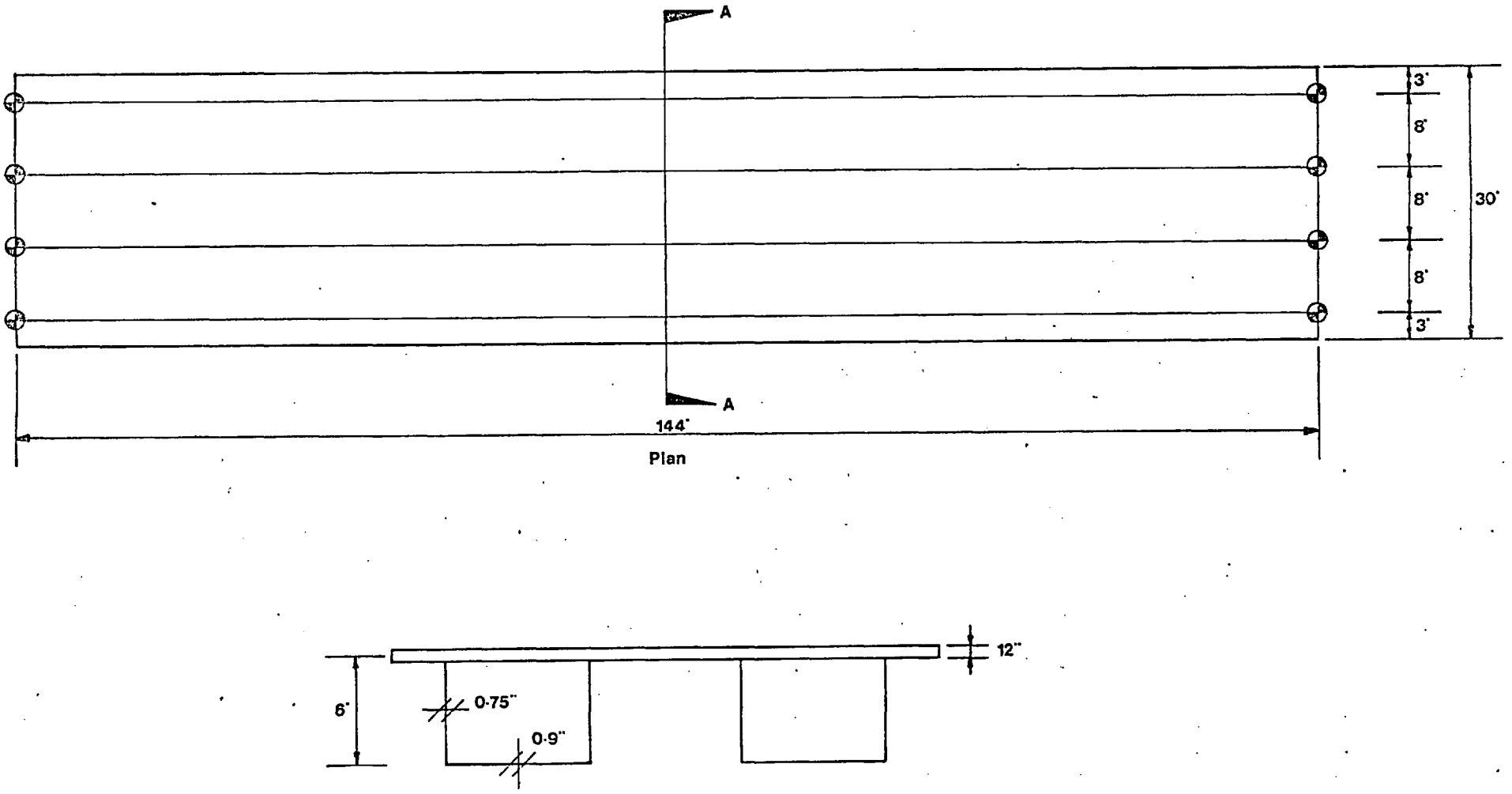


Fig.52 Dimensions of twin box example of Chapter 3

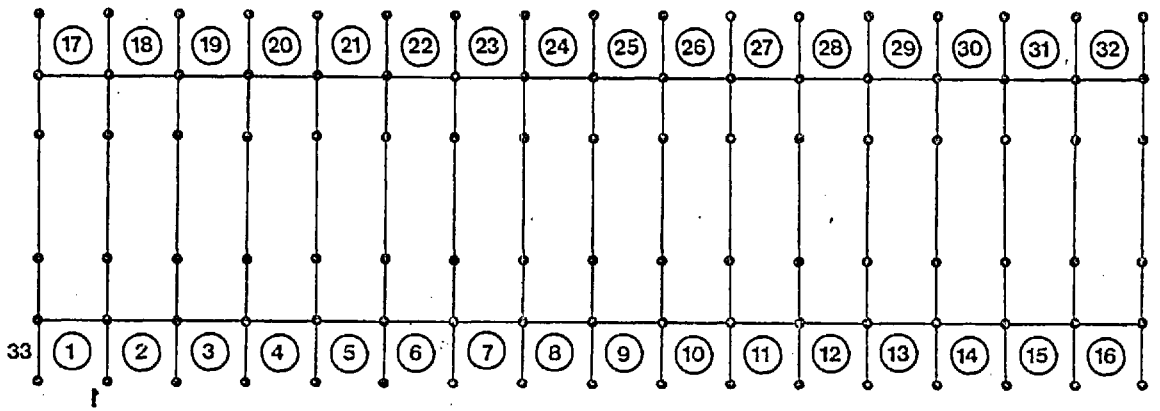


Fig.53 Grid for twin box example

348

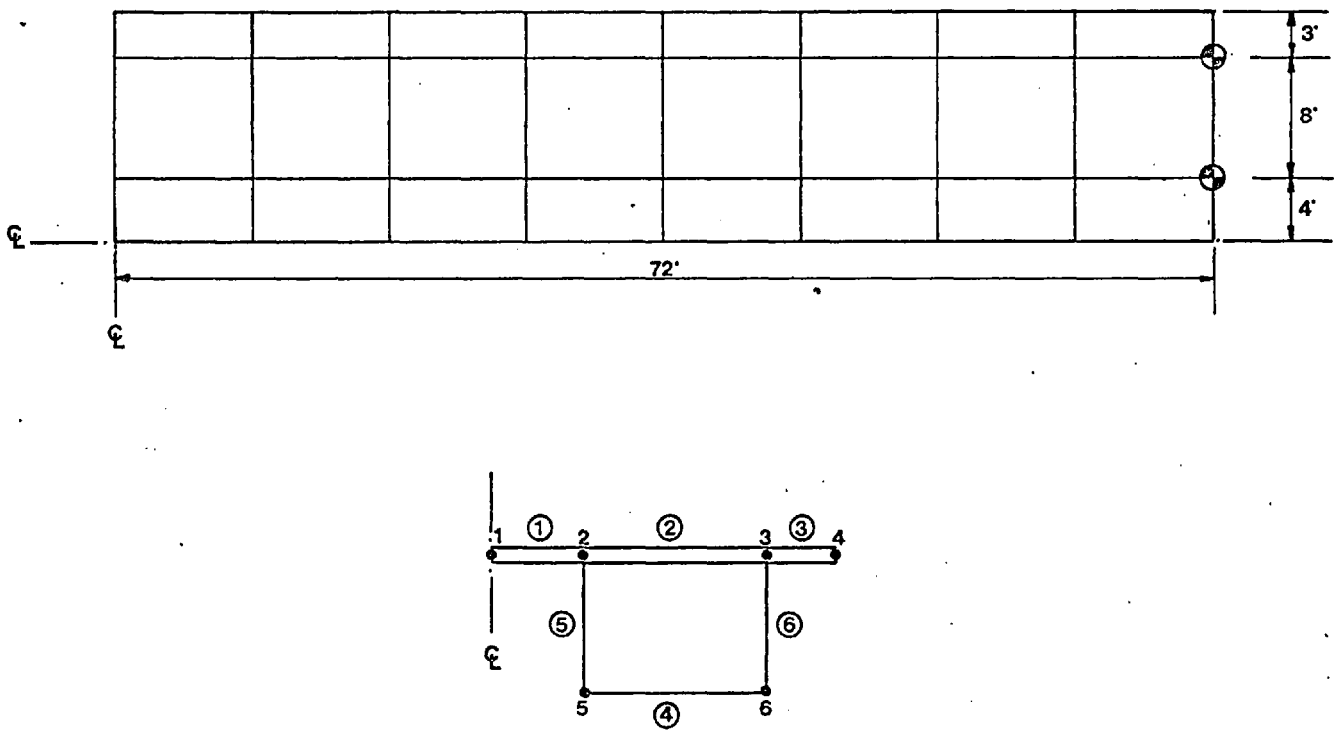


Fig.54 Finite element mesh for twin box example

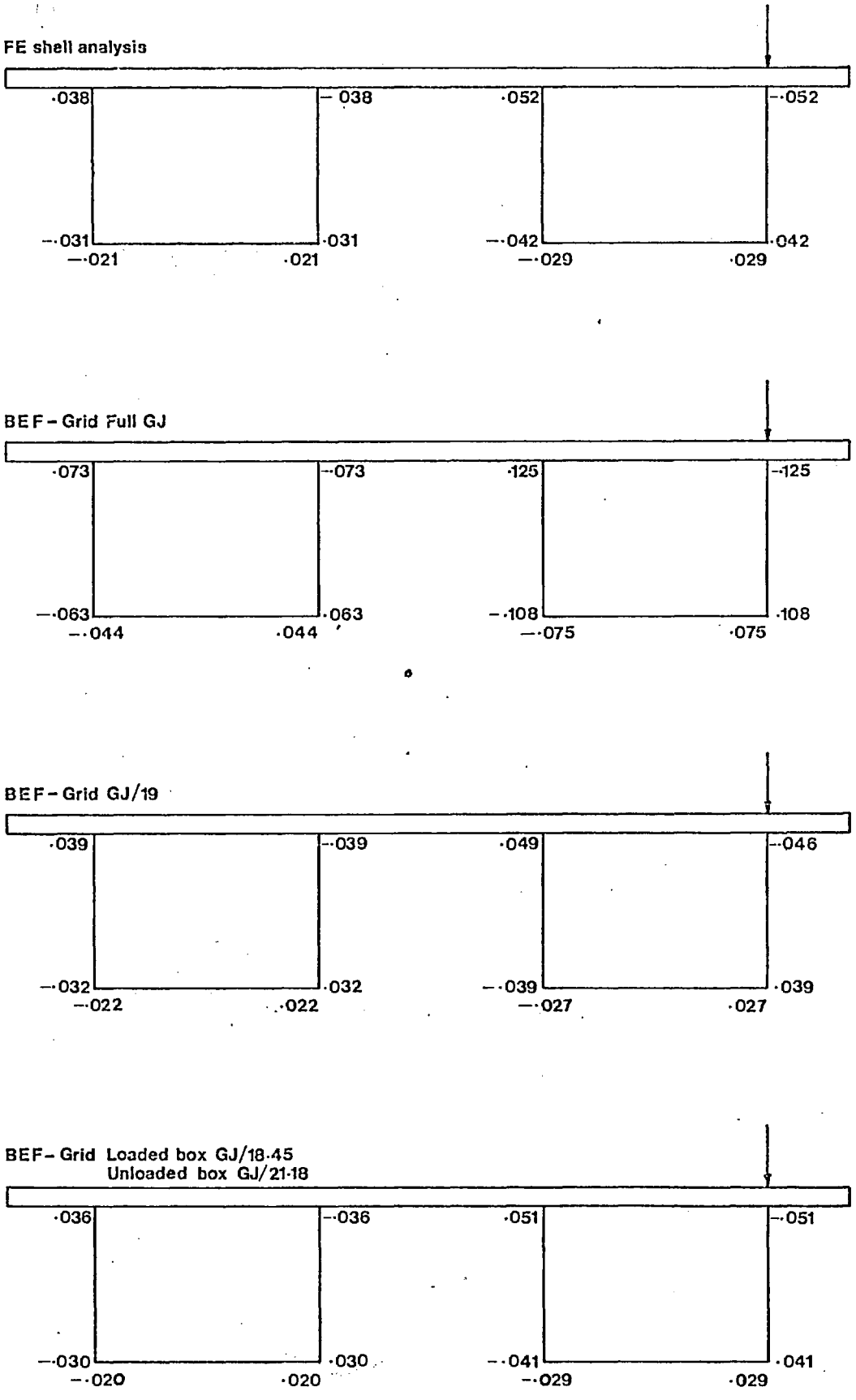


Fig.55 Comparison of cross sectional distributions of σ_{DB} in twin box example for a concentrated load applied above an outer web at midspan

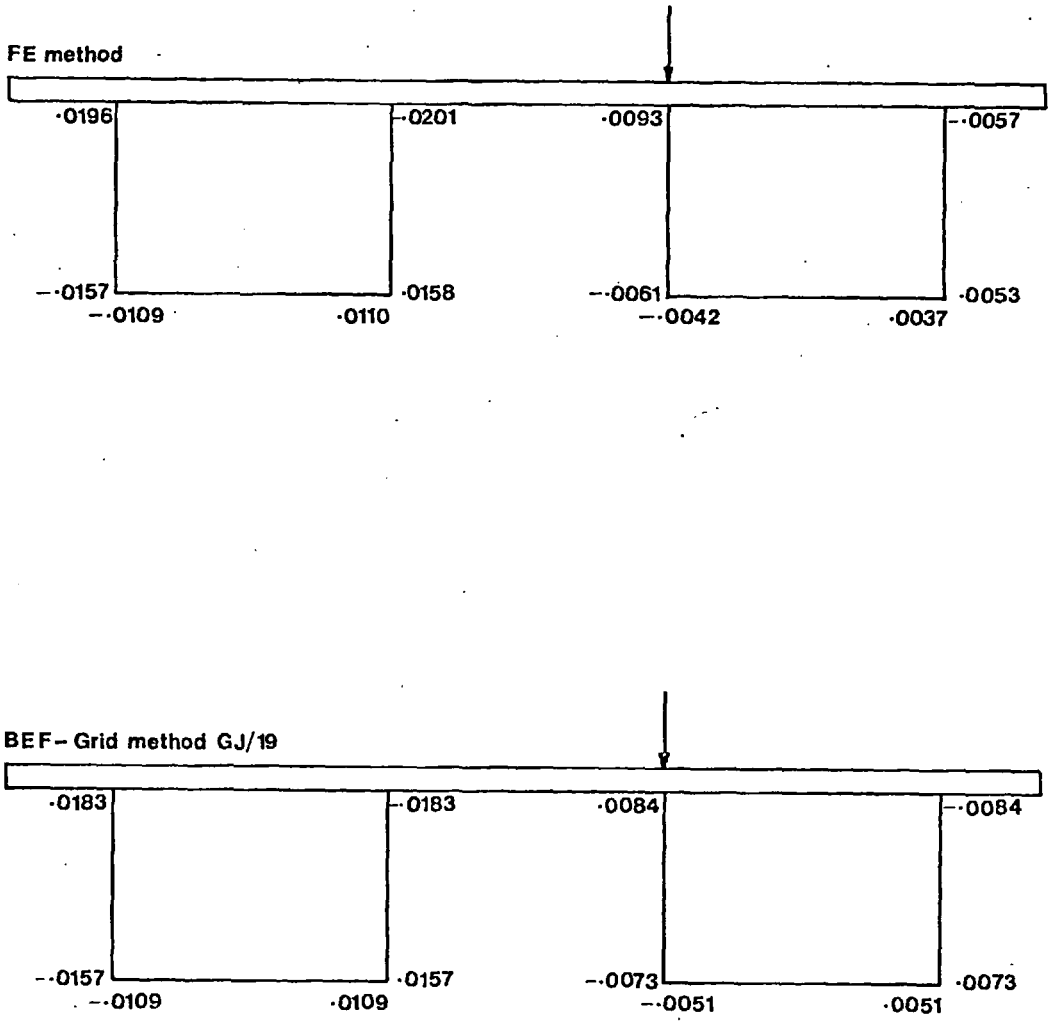


Fig.56 Comparison of cross sectional distributions of $\bar{\sigma}_{DB}$ in twin box example for a concentrated load applied above an inner web at midspan

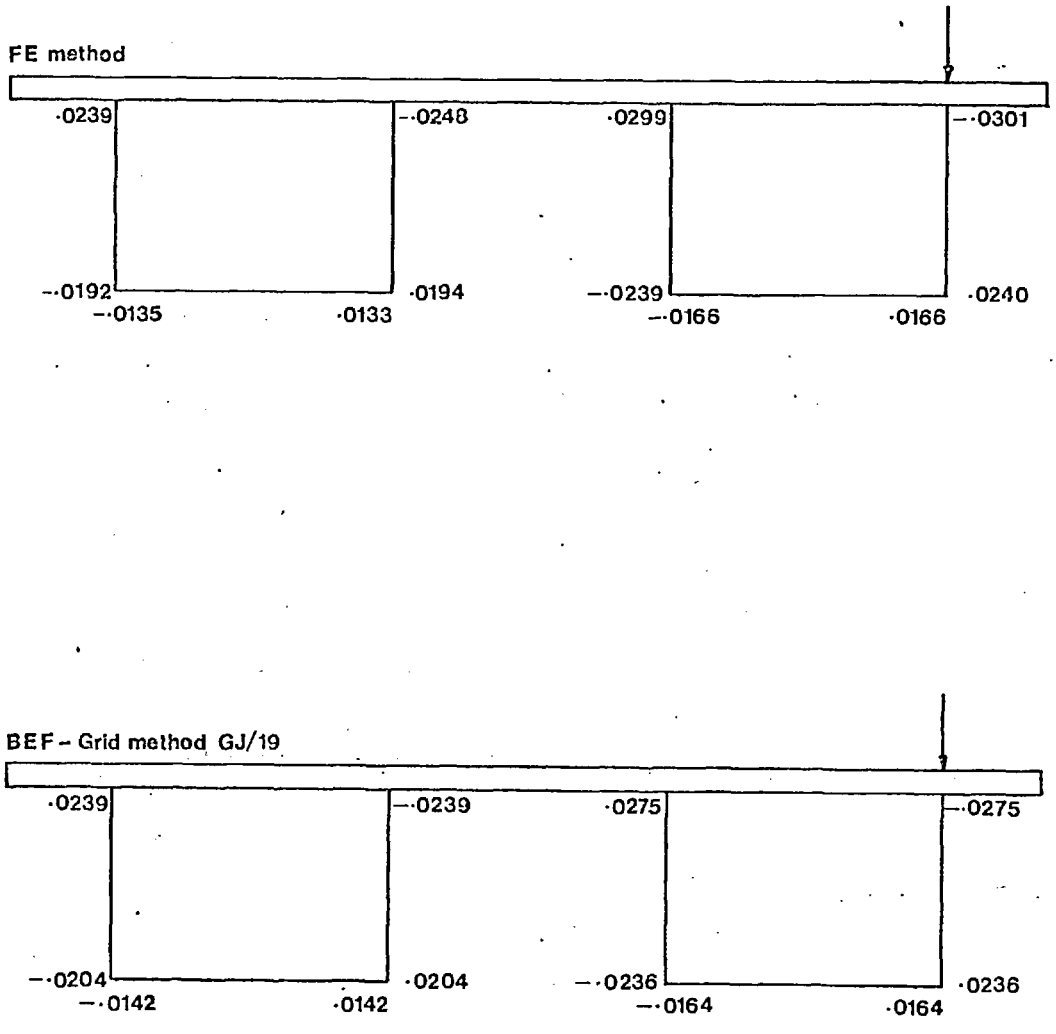


Fig.57 Comparison of cross sectional distributions of σ_{DB} in twin box example for a uniformly distributed line load above an outer web

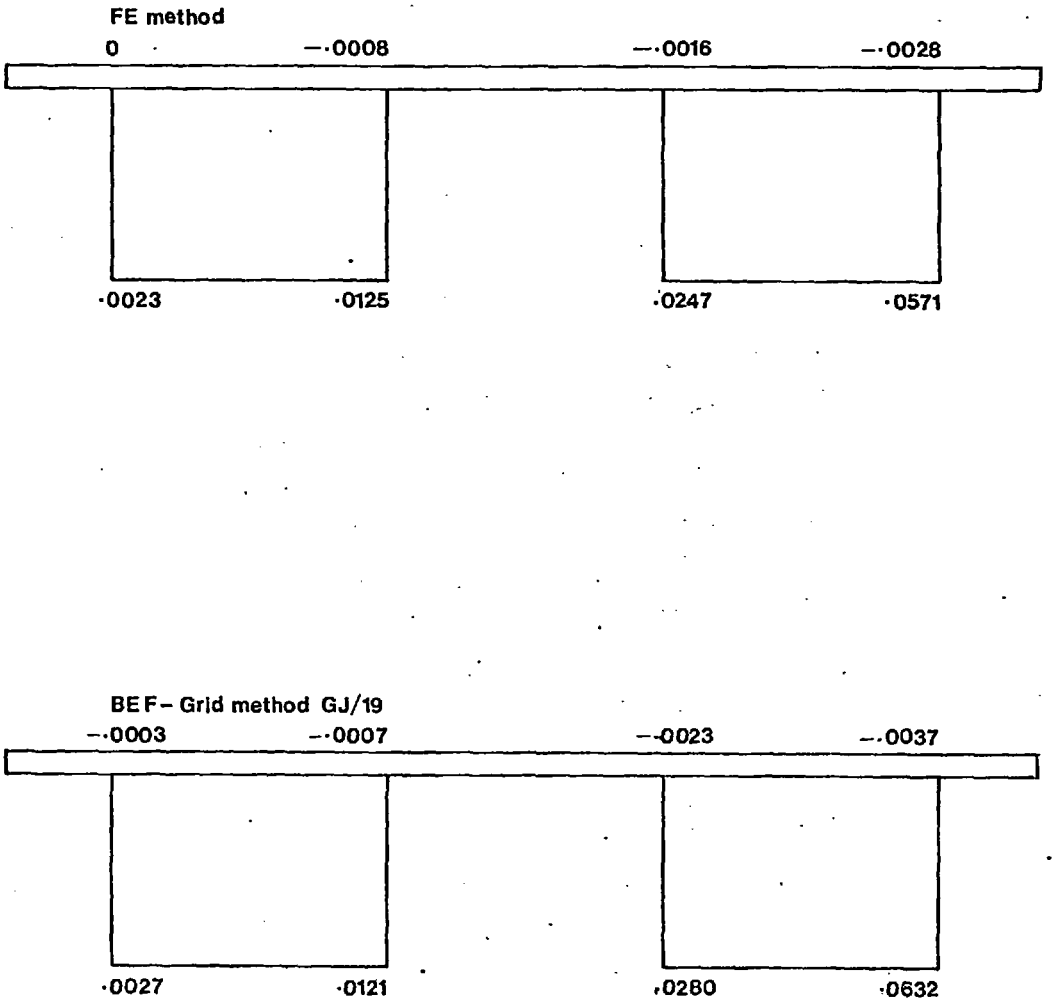


Fig.58 Comparison of longitudinal stresses in twin box example for a concentrated load applied above an outer web at midspan

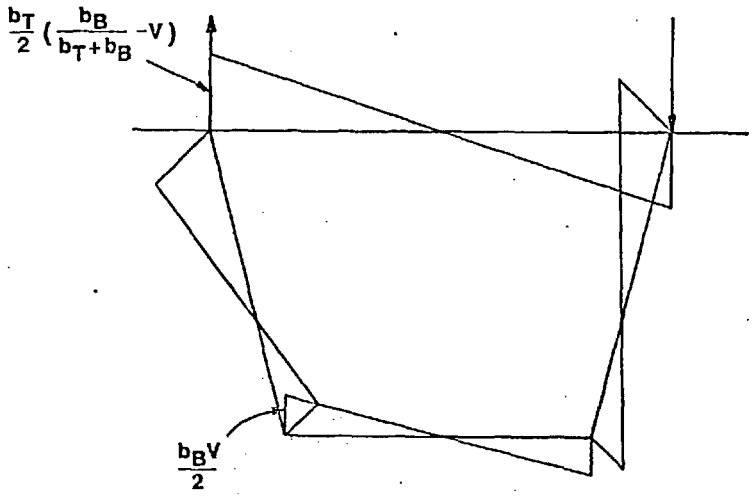


Fig.59 Transverse bending moment diagrams for a unit length of box subjected to unit antisymmetrical loading

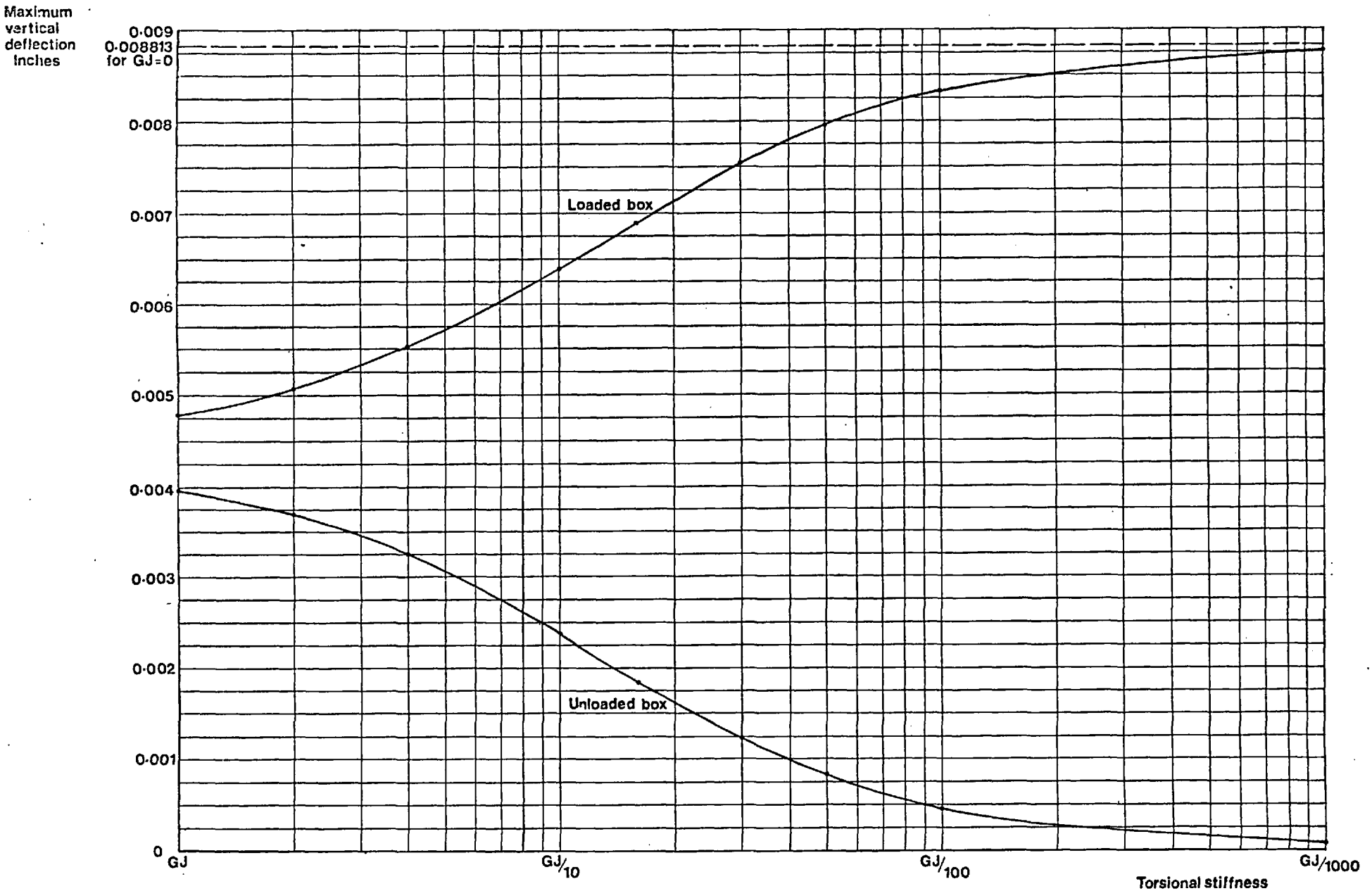


Fig.60 Twin box example – variation of maximum vertical deflation under the centre line of each box with a reducing torsional stiffness

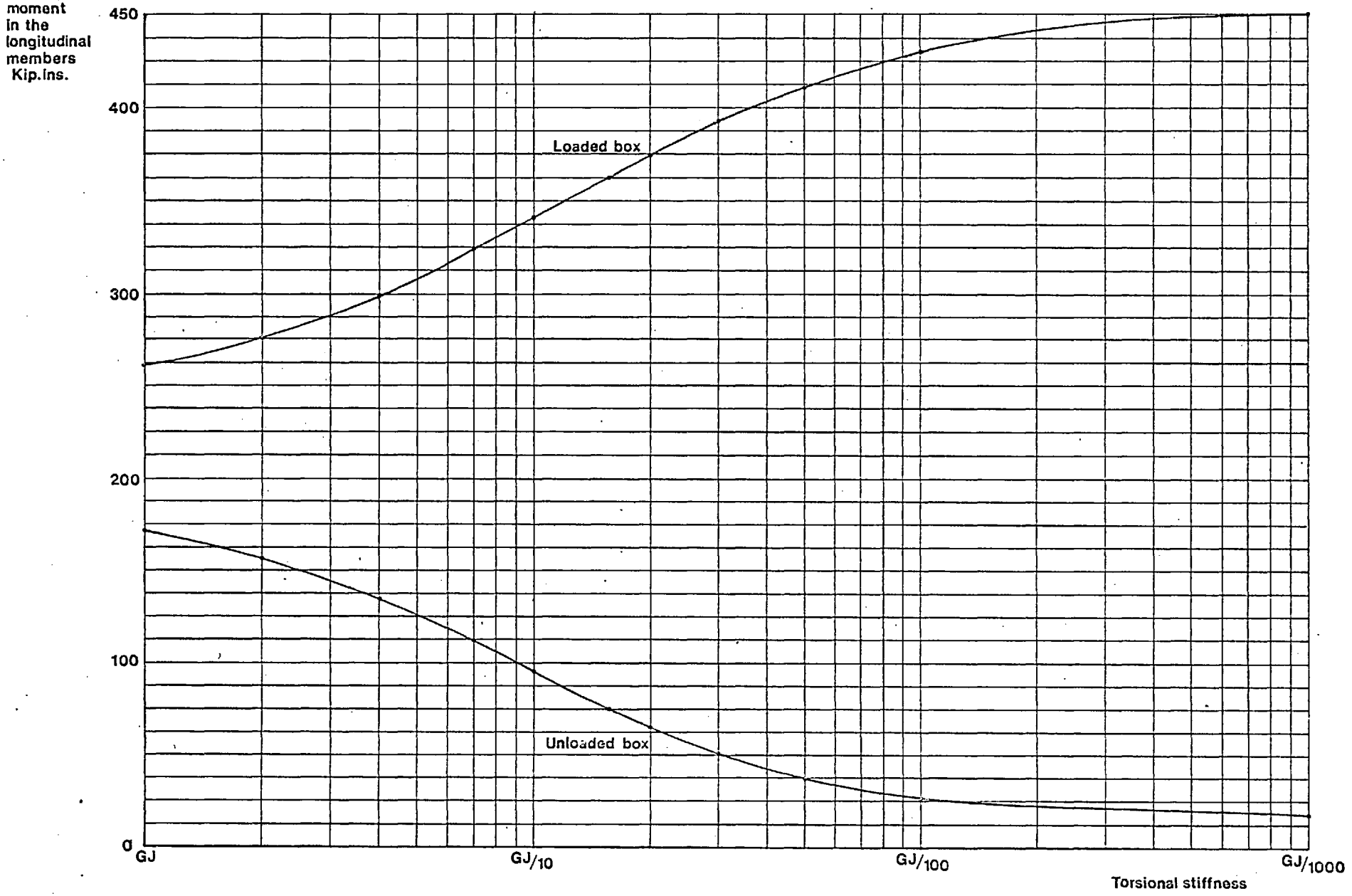


Fig.61 Twin box example – variation of maximum longitudinal bending moment in each box with a reducing torsional stiffness

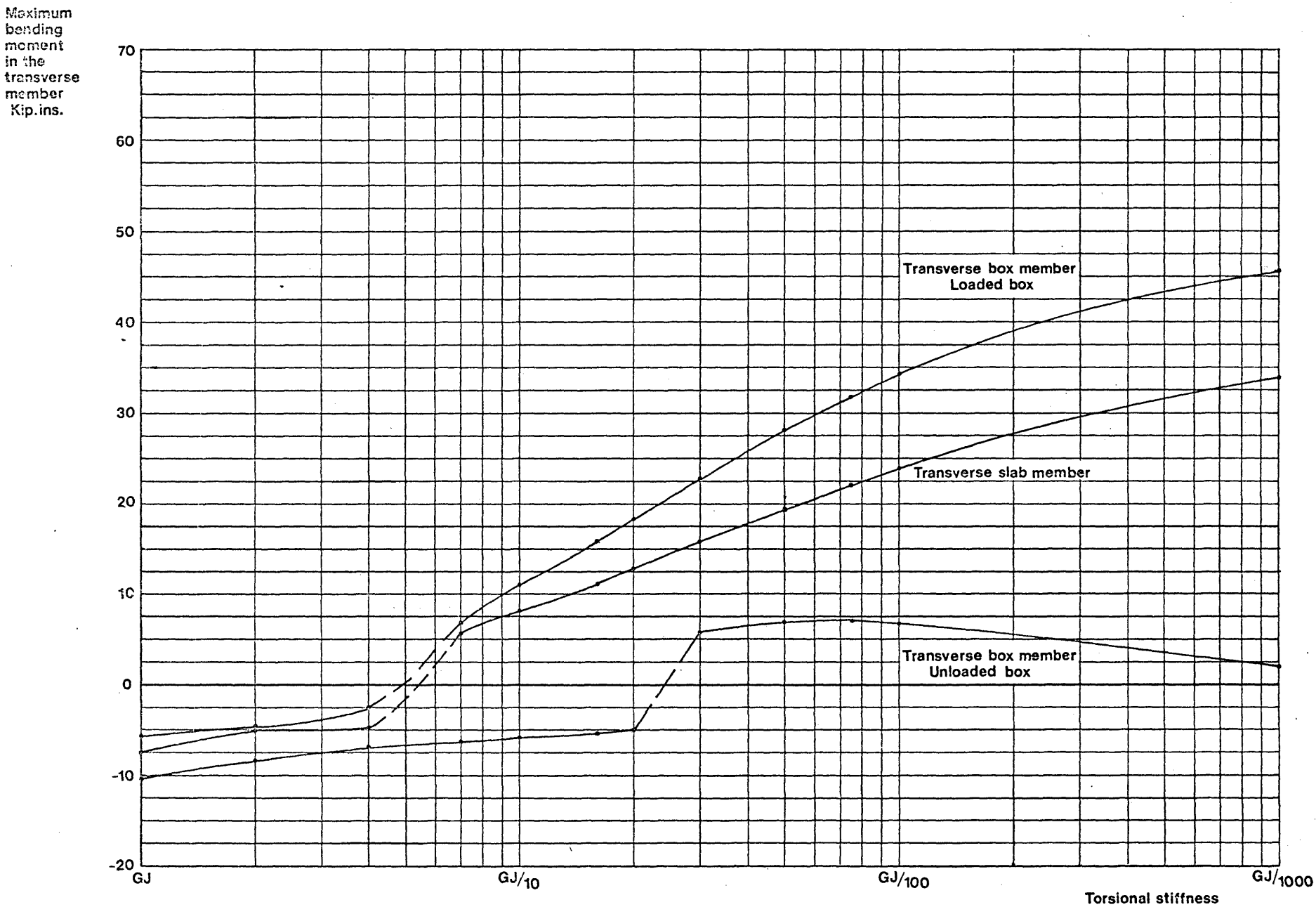


Fig.62 Twin box example – variation of maximum bending moment in the transverse members with a reducing torsional stiffness

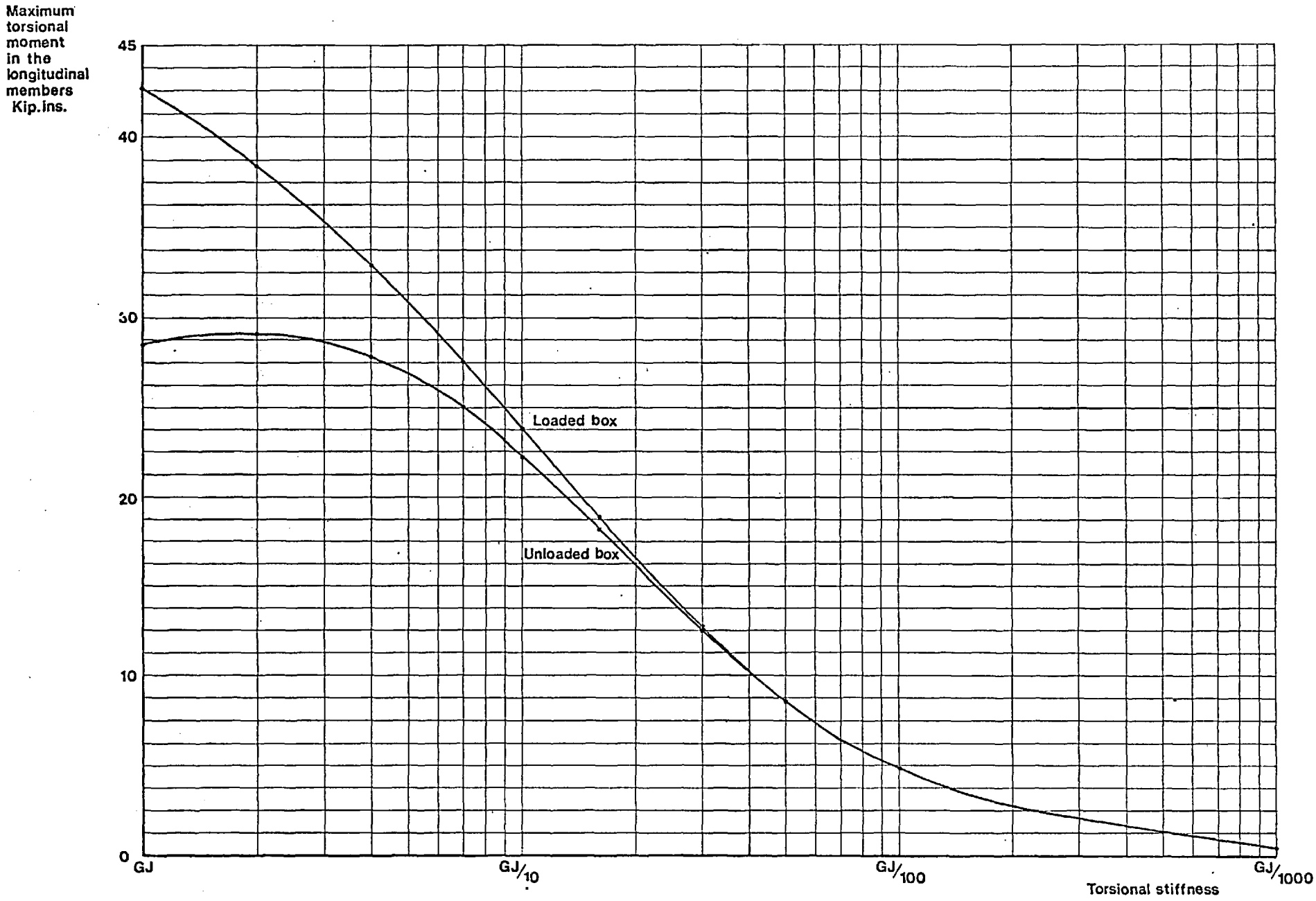


Fig.63 Twin box example – variation of maximum torsional moments in each box with a reducing torsional stiffness

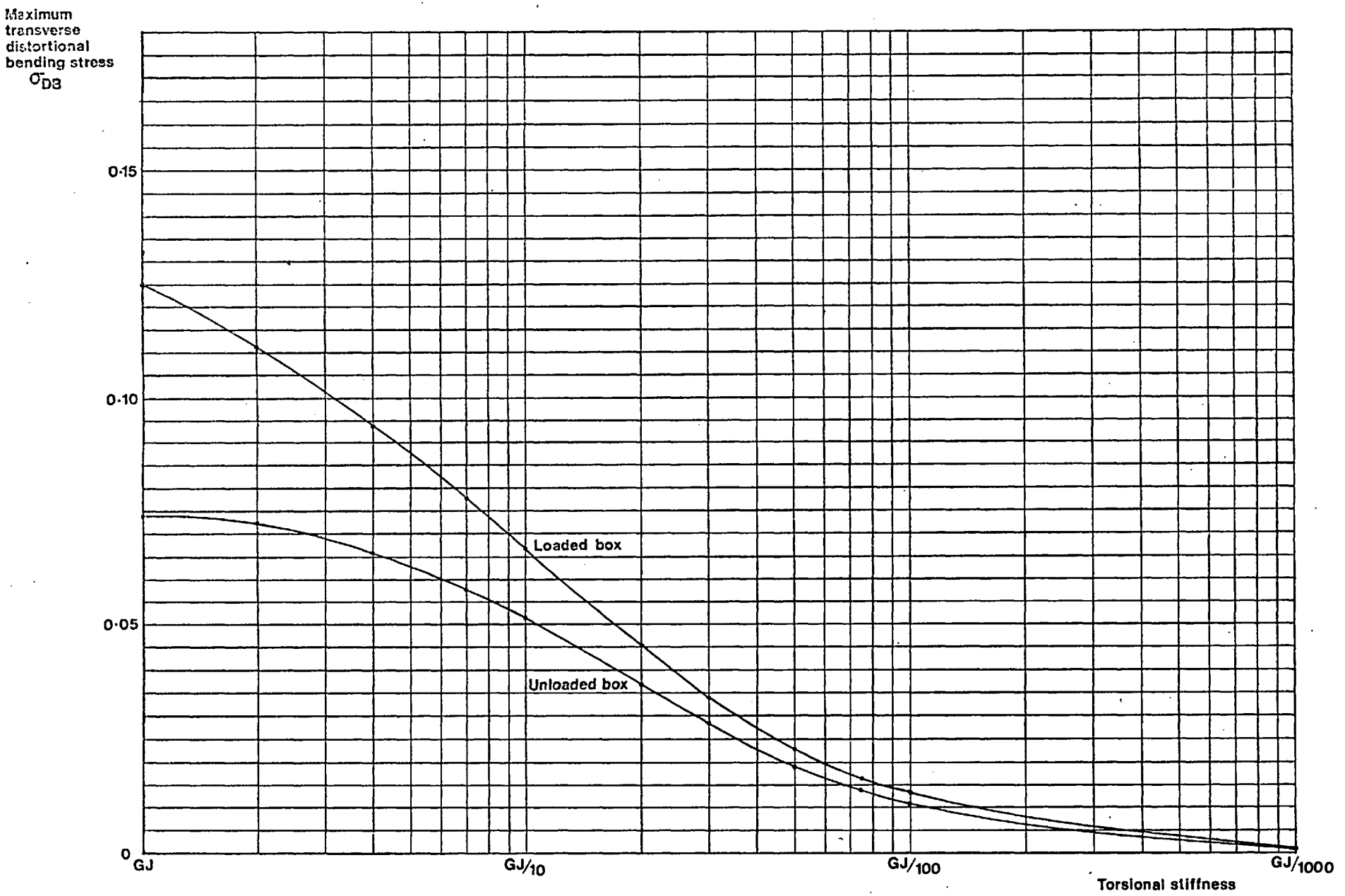


Fig.64 Twin box example – variation of maximum transverse distortional bending stresses in each box with a reducing torsional stiffness

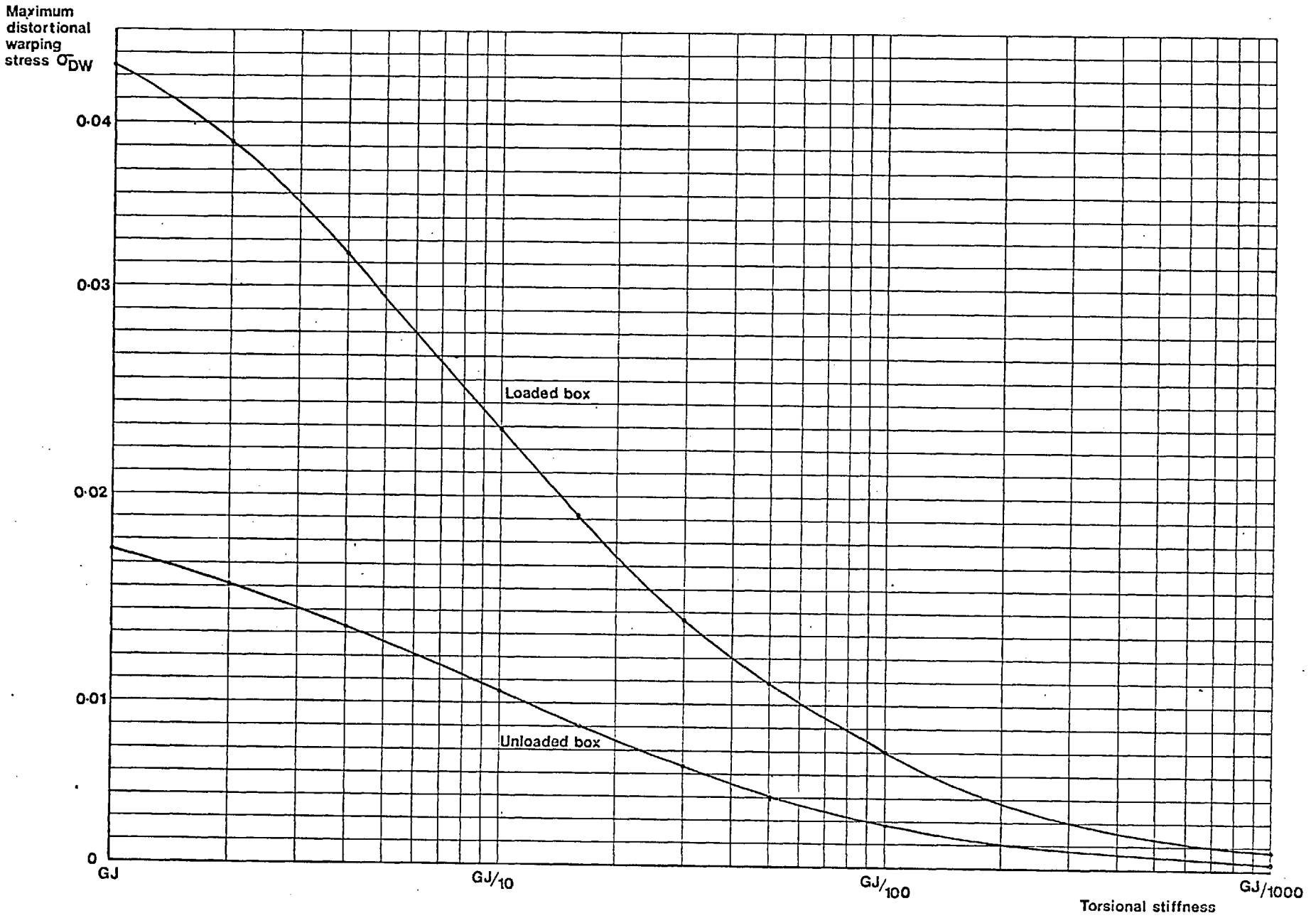


Fig.65 Twin box example – variation of maximum distortional warping stresses in each box with a reducing torsional stiffness

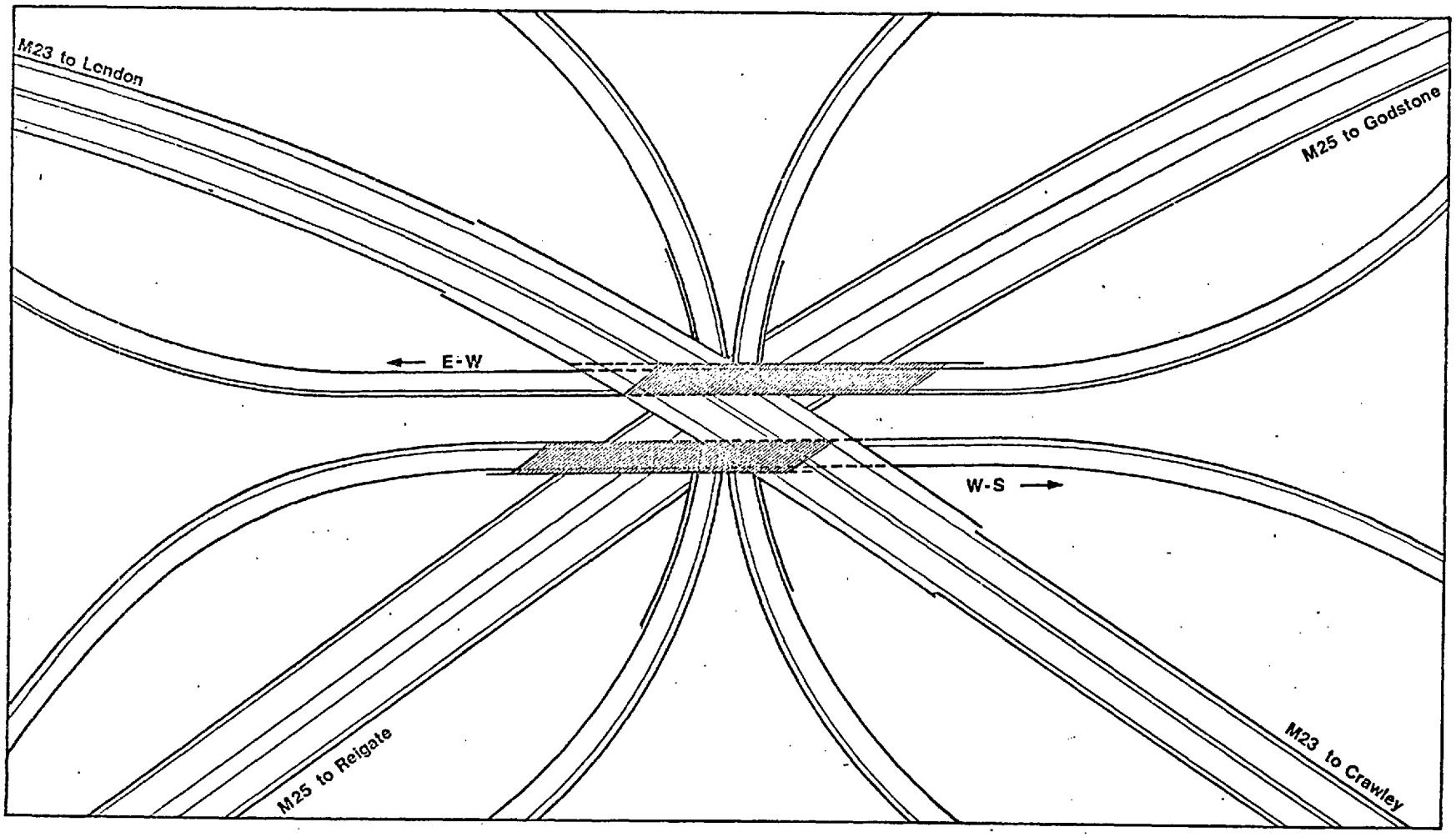
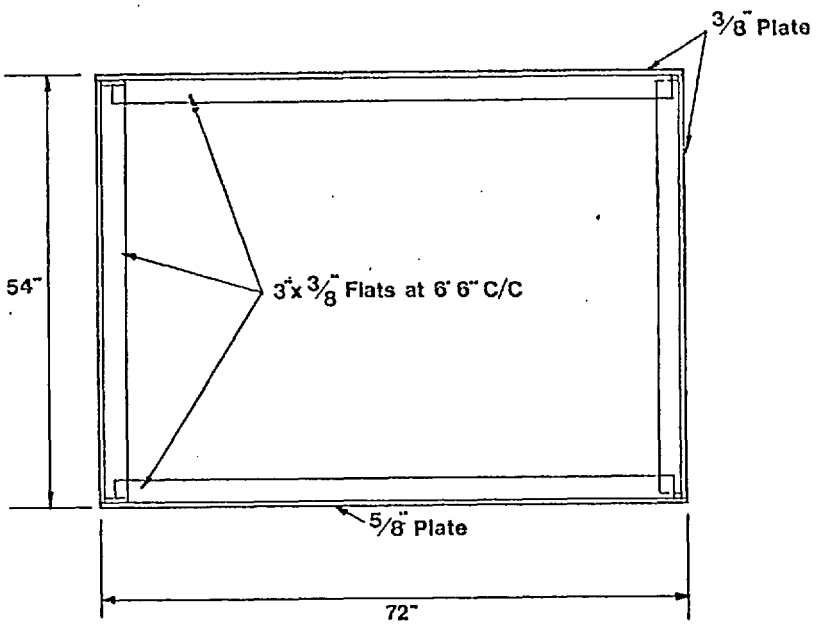
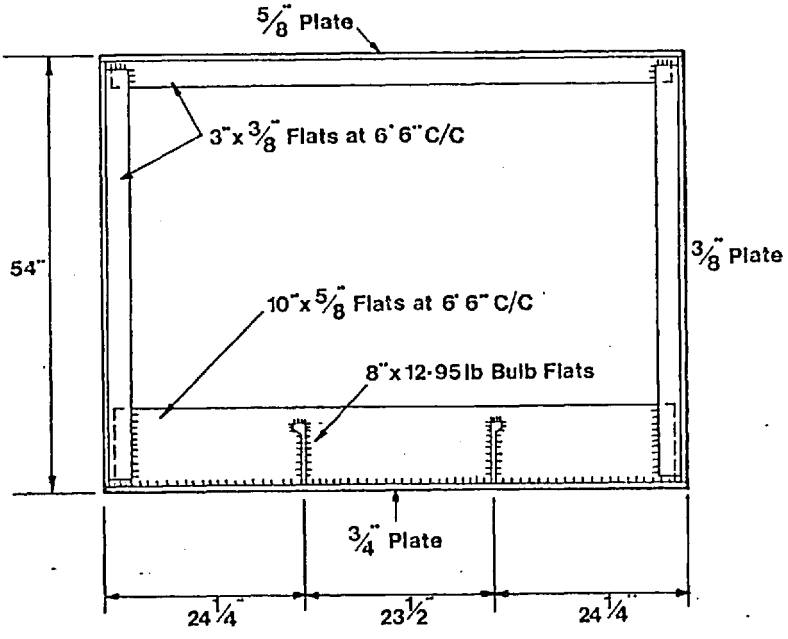


Fig.66 Layout of Merstham Interchange

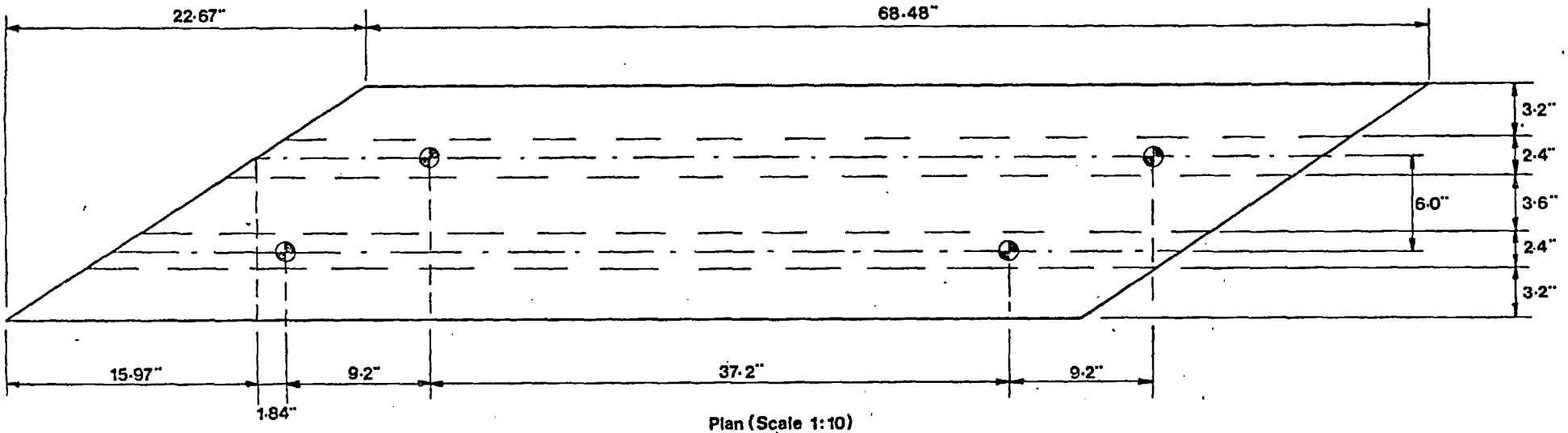


Midspan Section

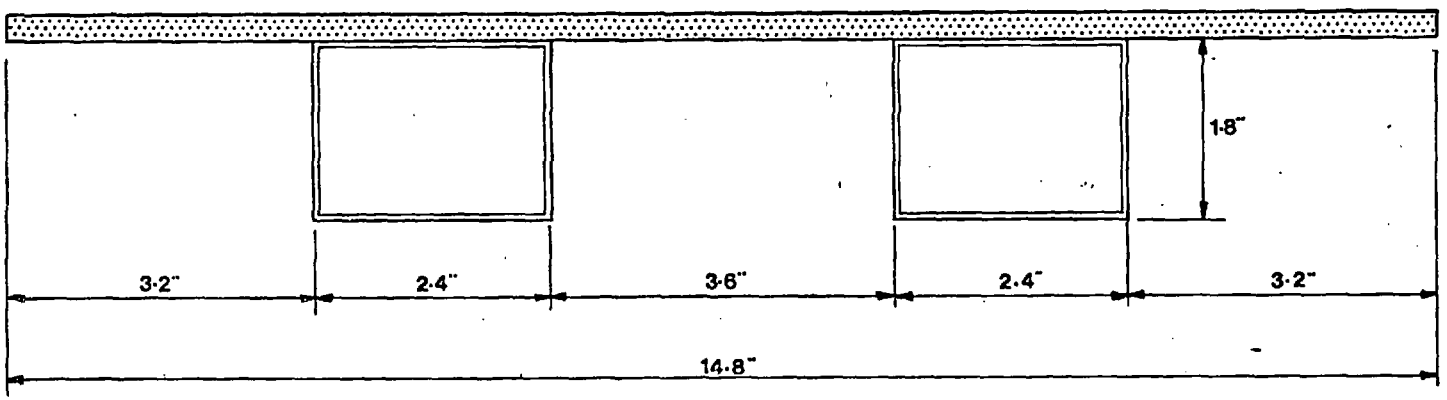


Support Section

Fig.67 . Details of full scale box girder stiffening for Merstham Interchange



Plan (Scale 1:10)



Section (Scale 1:2)

Fig.68 Merstham Interchange model dimensions

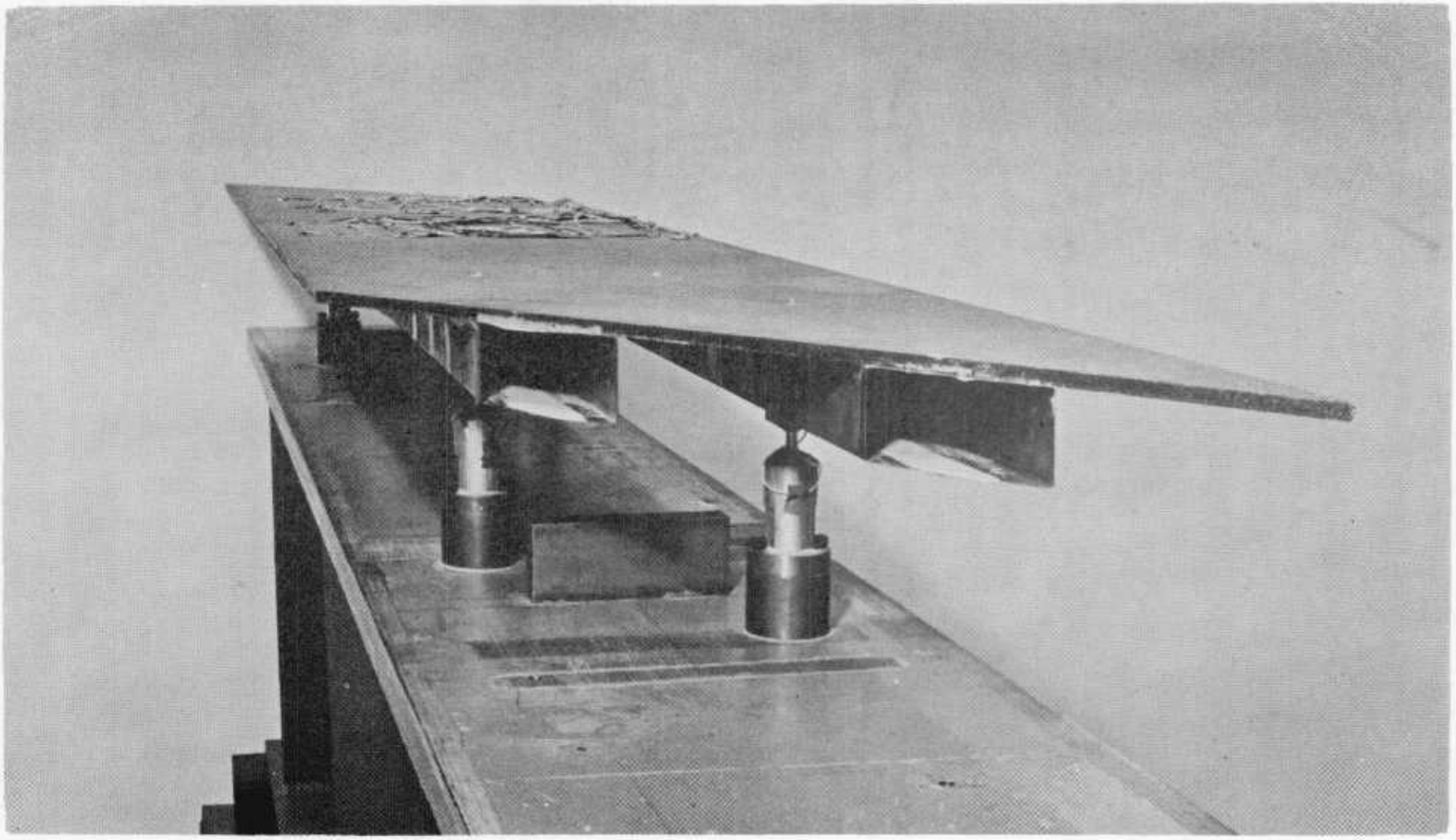


Fig.69 View of model showing the end cross section
MERSTHAM INTERCHANGE MODEL

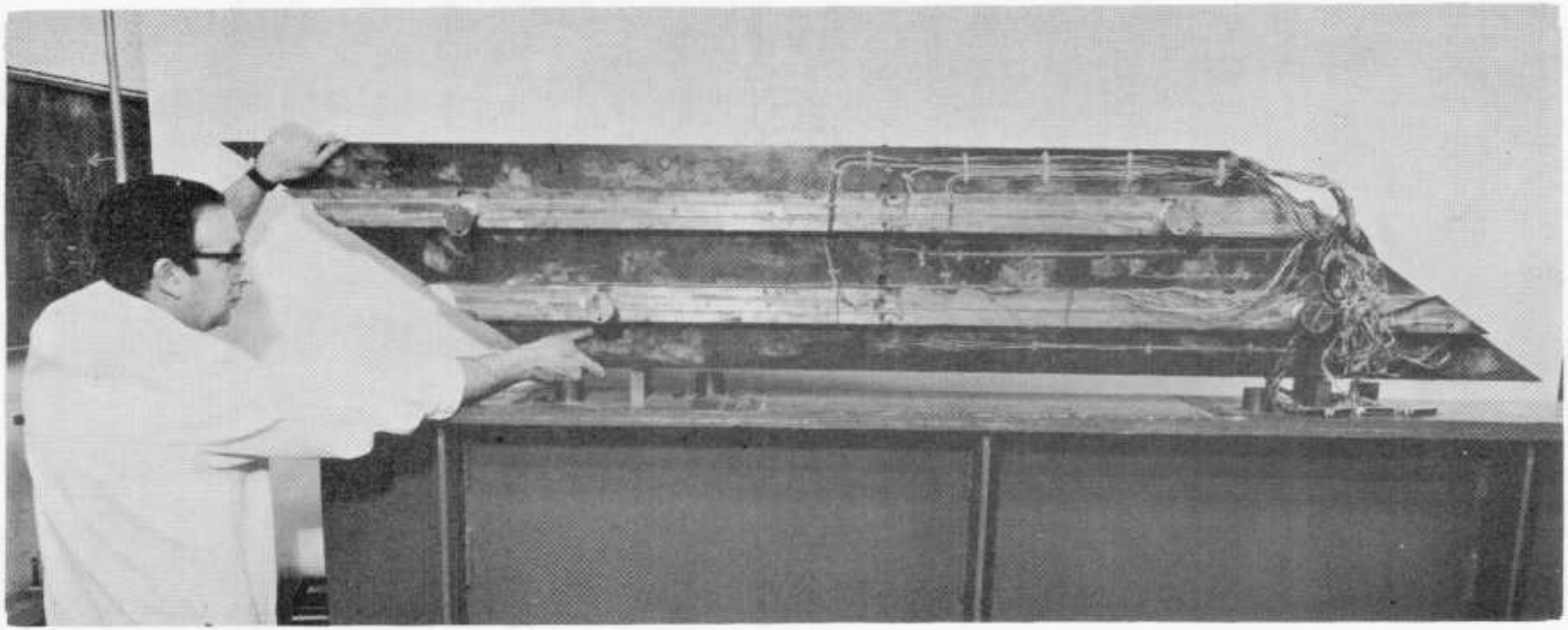


Fig.70 Underside of model
MERSTHAM INTERCHANGE MODEL

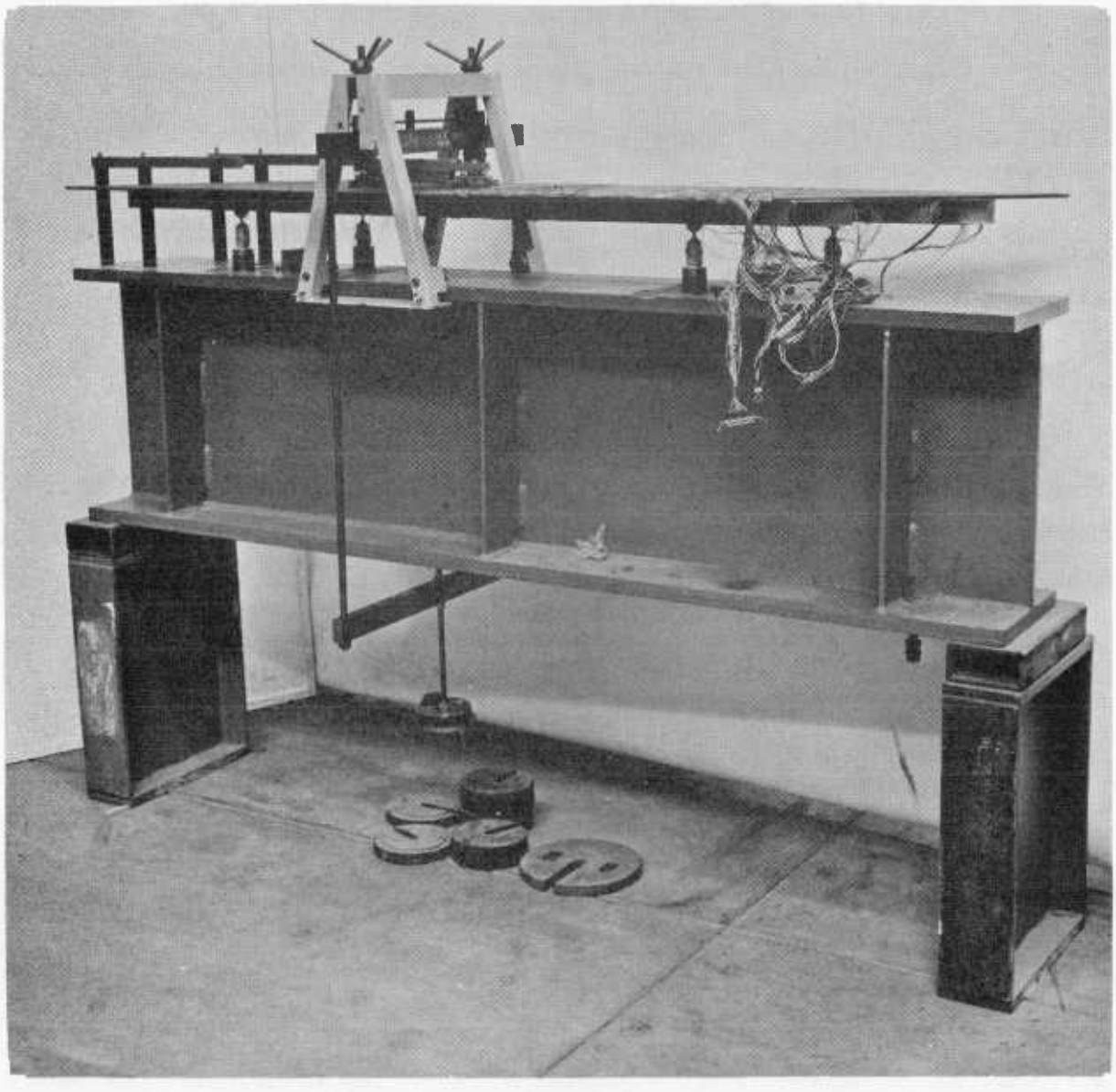
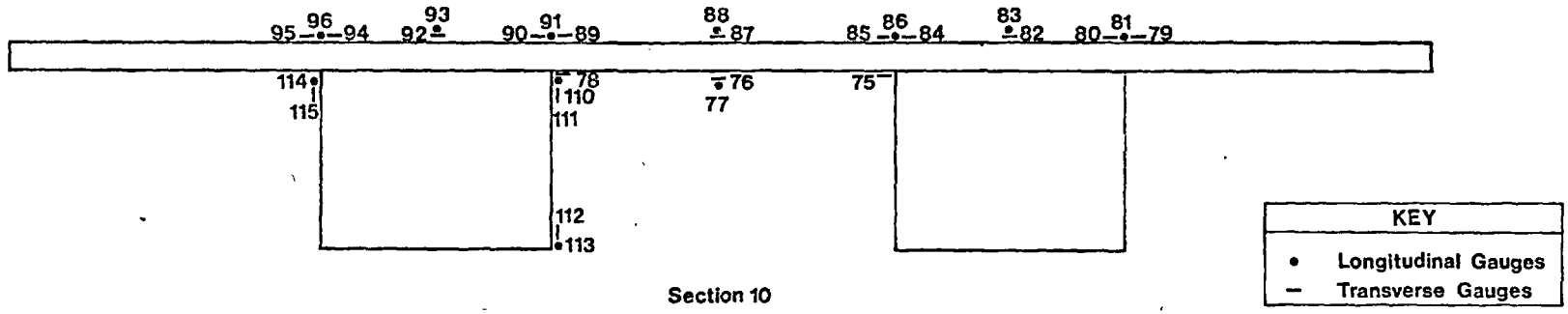
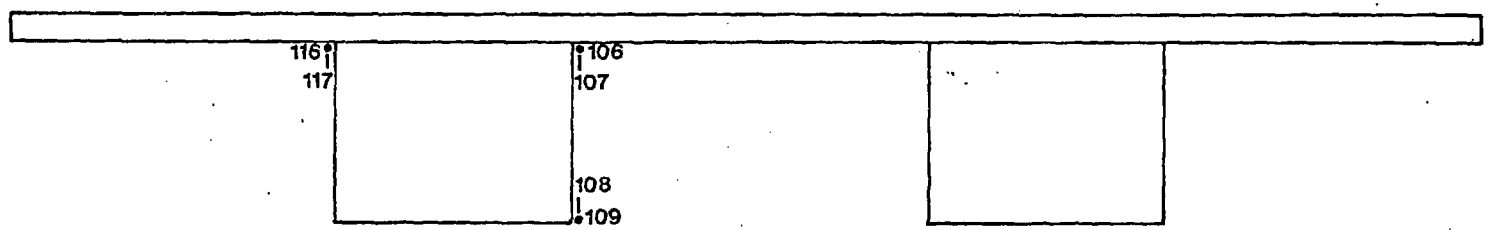


Fig.71 Model testing arrangement
MERSTHAM INTERCHANGE MODEL

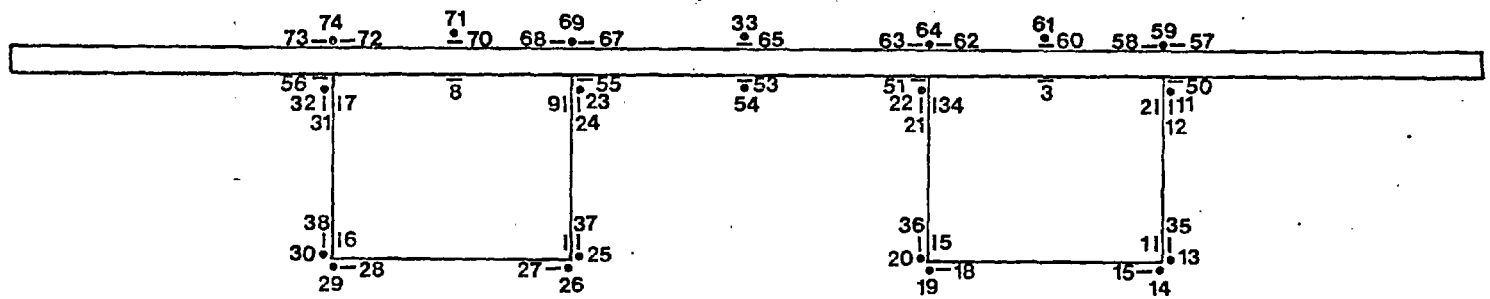
MERSTHAM INTERCHANGE MODEL



Section 10



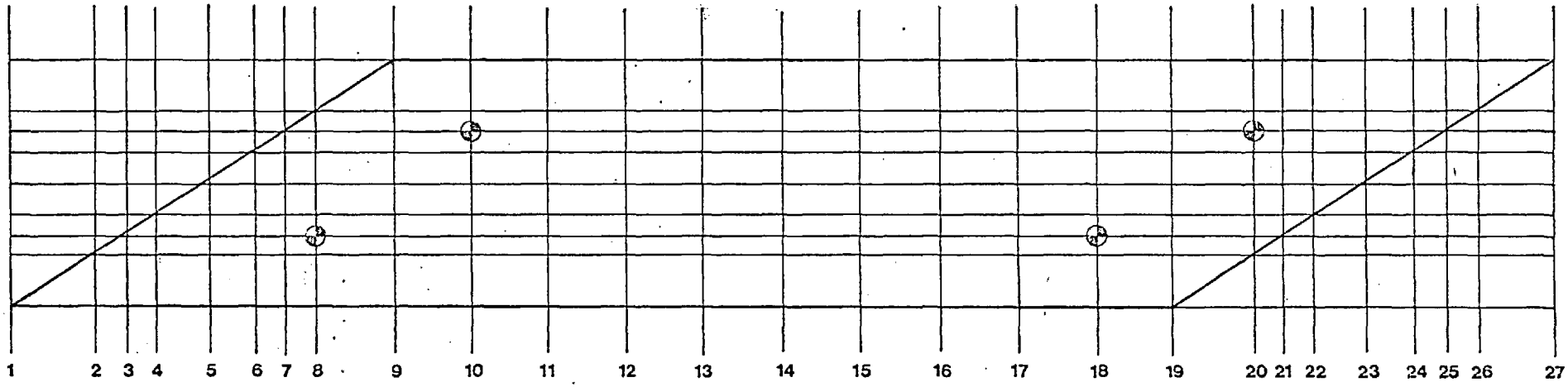
Section 12



Section 14

Fig.72 Strain gauge layout

MERSTHAM INTERCHANGE MODEL



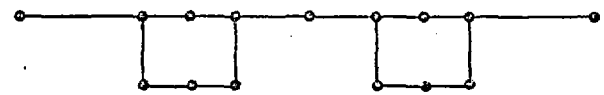


Fig.73 Finite element mesh

MERSTHAM INTERCHANGE MODEL

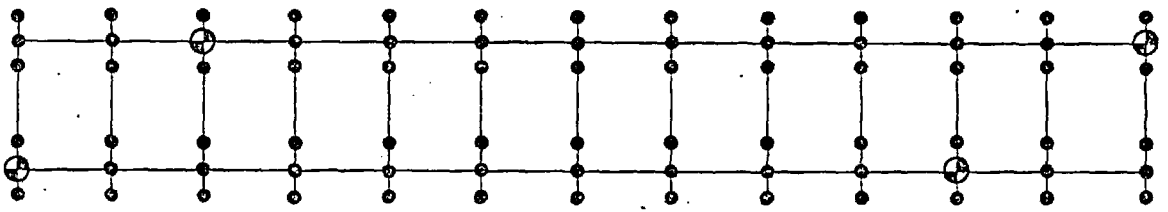
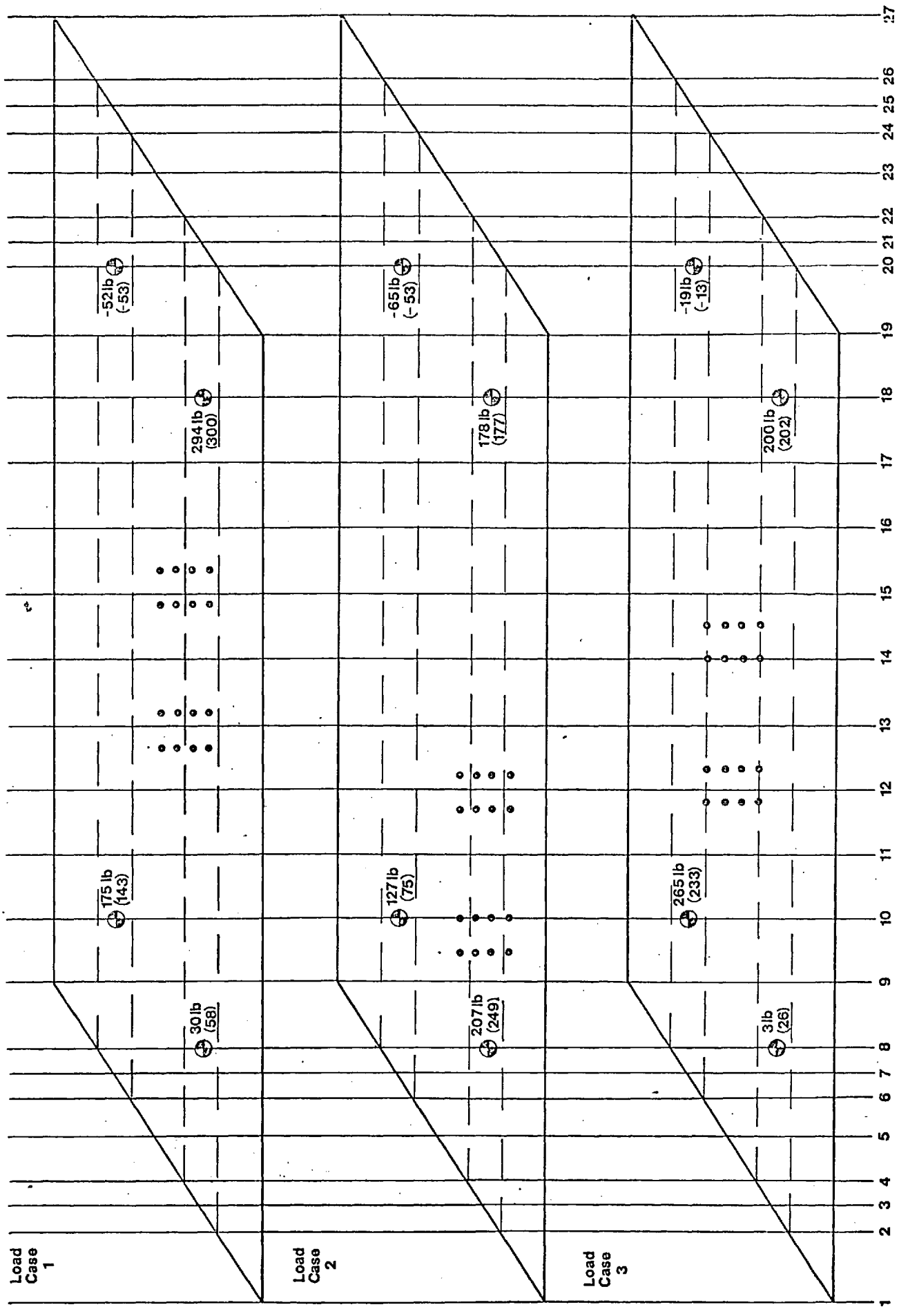


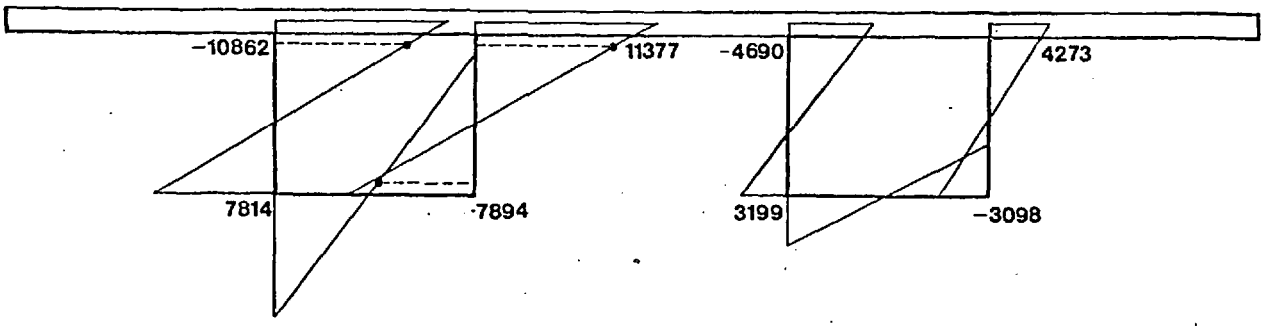
Fig.74 Grillage



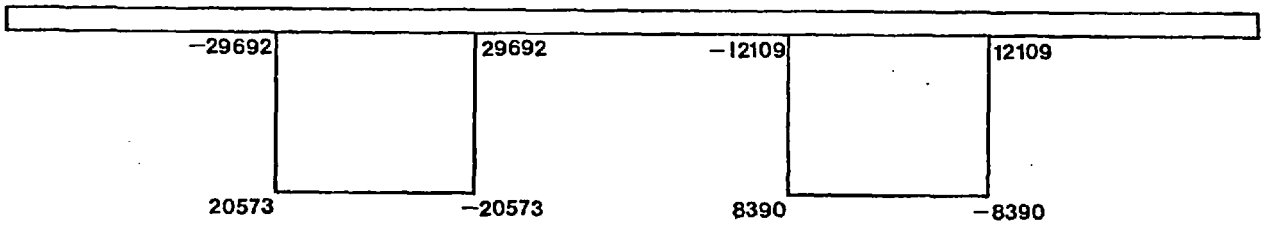
MERSTHAM INTERCHANGE MODEL

Fig.75 Positions of 448lb HB vehicle for Load Cases 1–3. The F.E. support reactions are shown together with the model reactions which are in parentheses

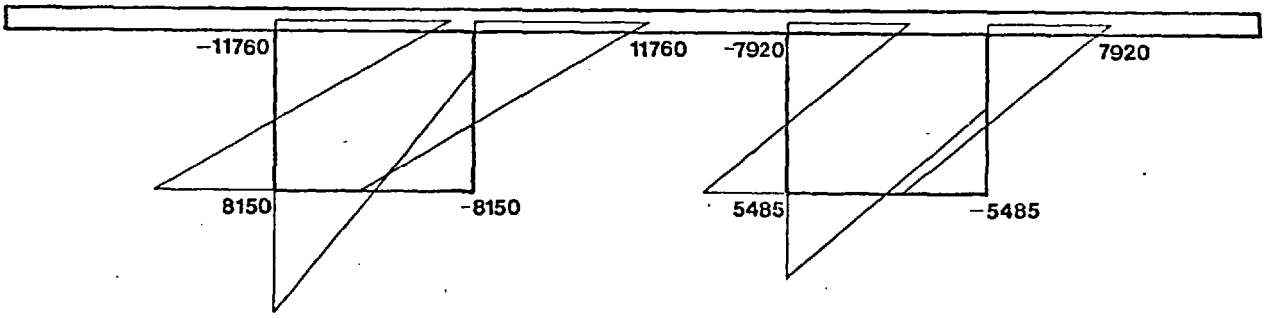
FE shell analysis and model analysis



Grillage - BEF method. Full GJ



Grillage - BEF method.GJ/16



Grillage - BEF method. Loaded box GJ/16
Unloaded box GJ/25

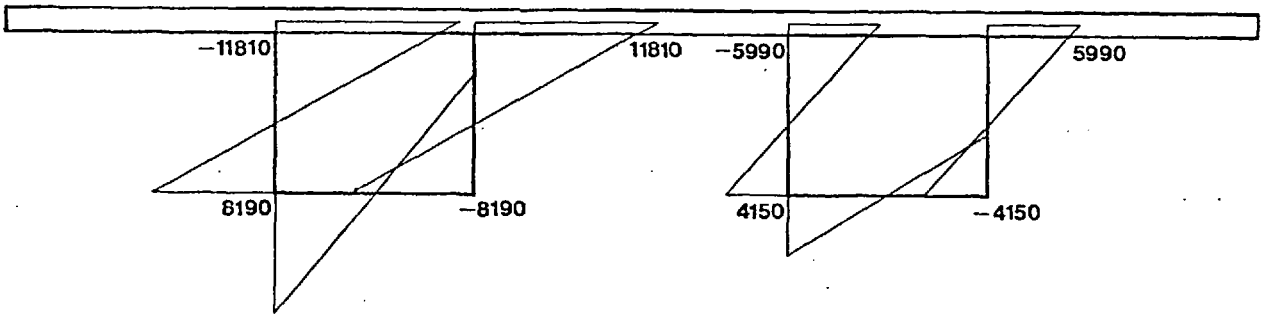
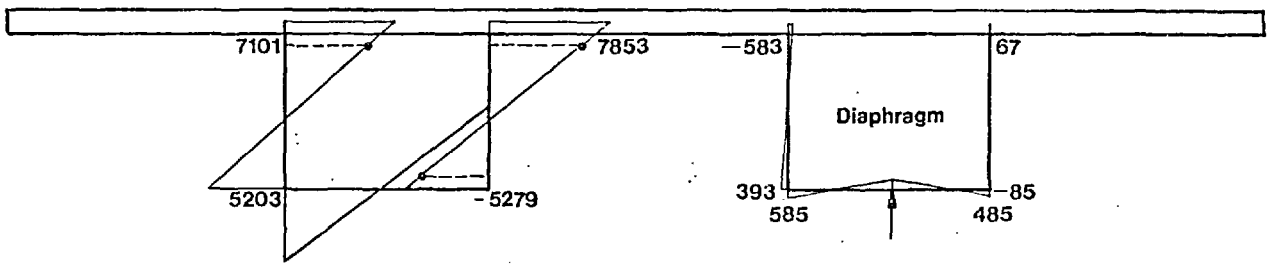


Fig.76 Comparison of transverse distortional bending stresses at Section 12

MERSTHAM INTERCHANGE MODEL

FE shell analysis and model analysis



Grillage - BEF method. Loaded box GJ/16 -
Unloaded box GJ/25

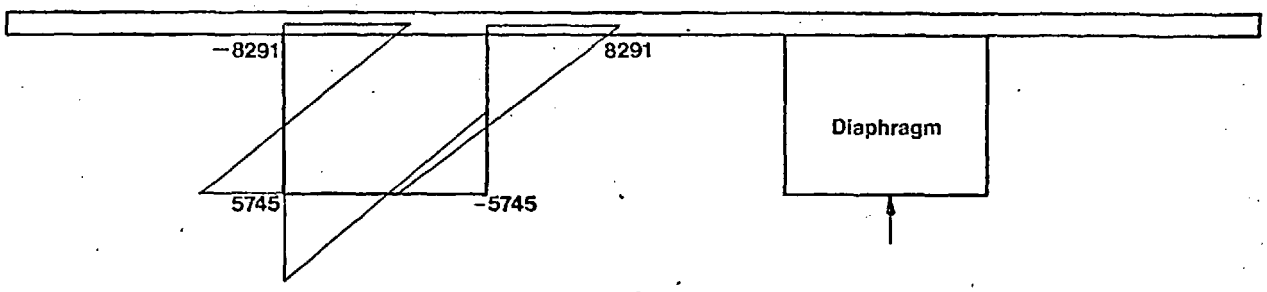
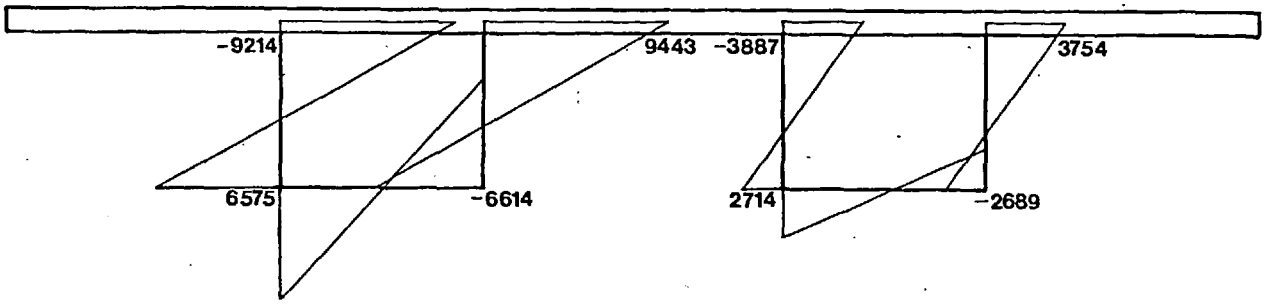


Fig.77 Comparison of transverse distortional bending stresses at Section 10

MERSTHAM INTERCHANGE MODEL

FE shell analysis



Grillage - BEF method. Loaded box GJ/16
Unloaded box GJ/25

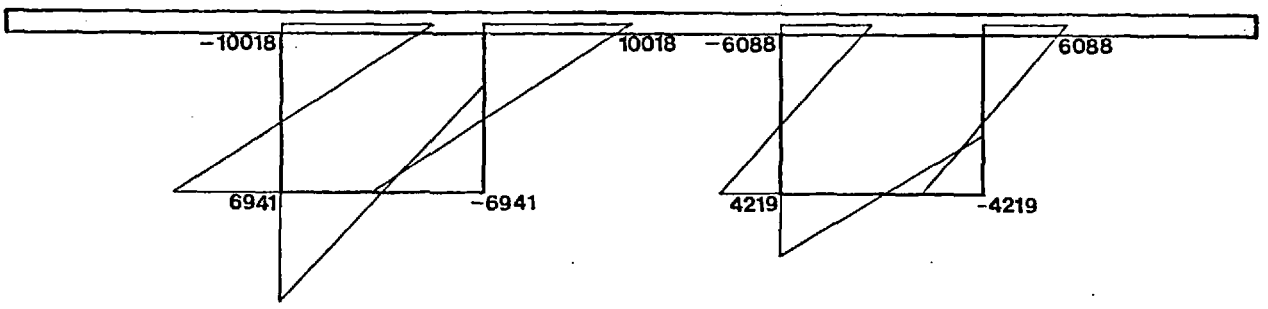


Fig.78 Comparison of transverse distortional bending stresses at Section 14

MERSTHAM INTERCHANGE MODEL

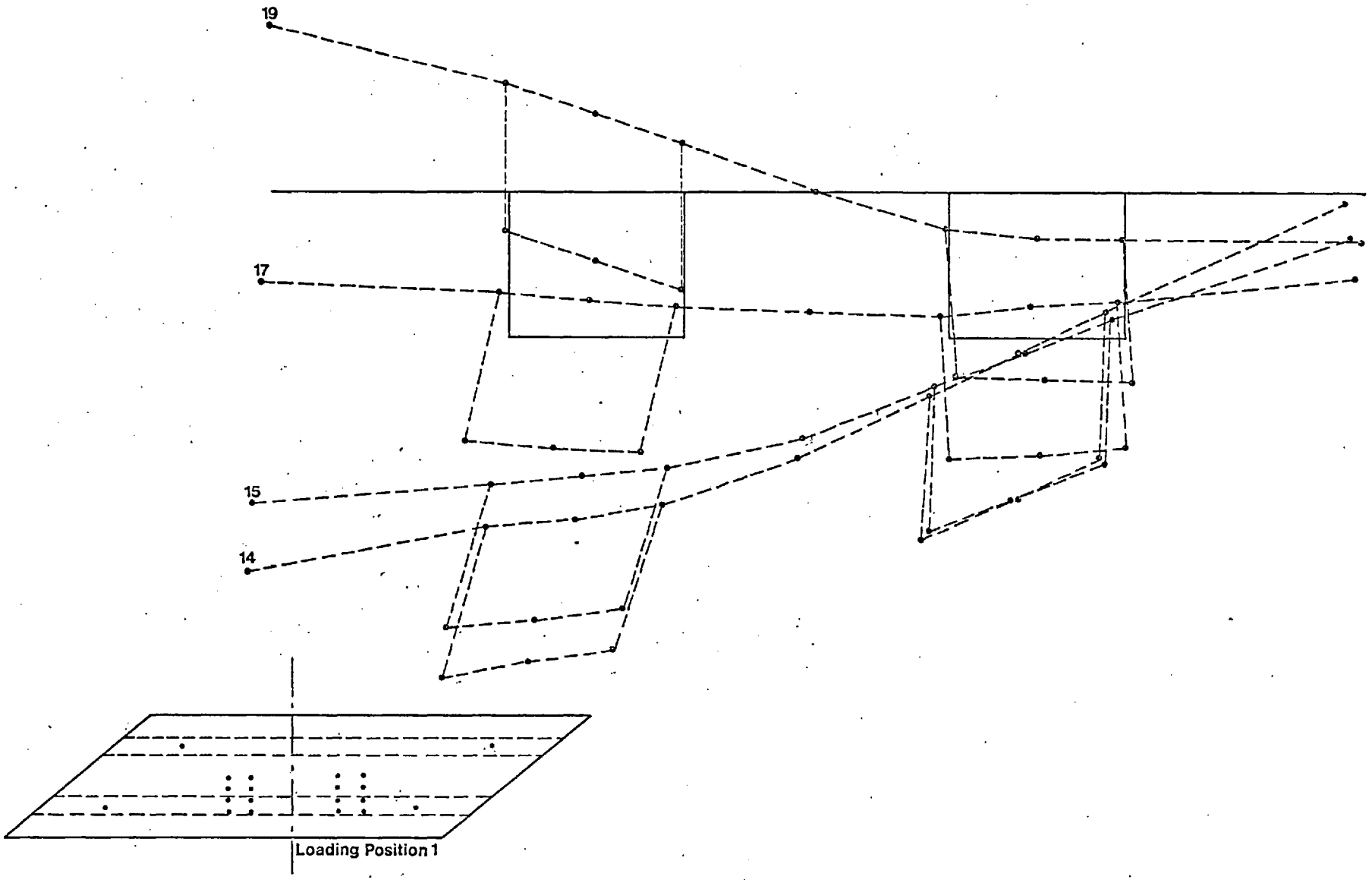


Fig.79a Finite element deflections for Load Case 1

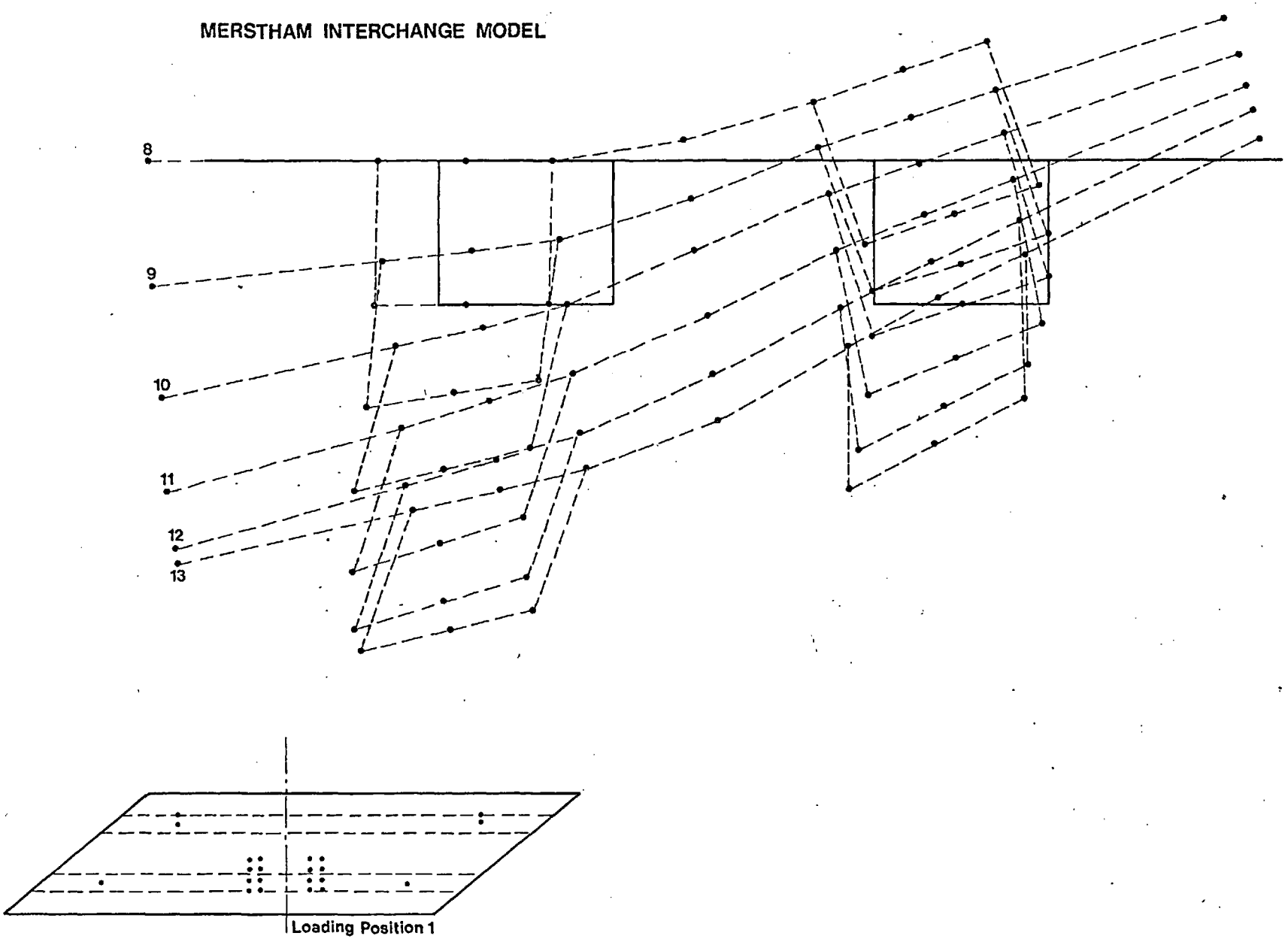


Fig.79b Finite element deflections for Load Case 1

MERSTHAM INTERCHANGE MODEL

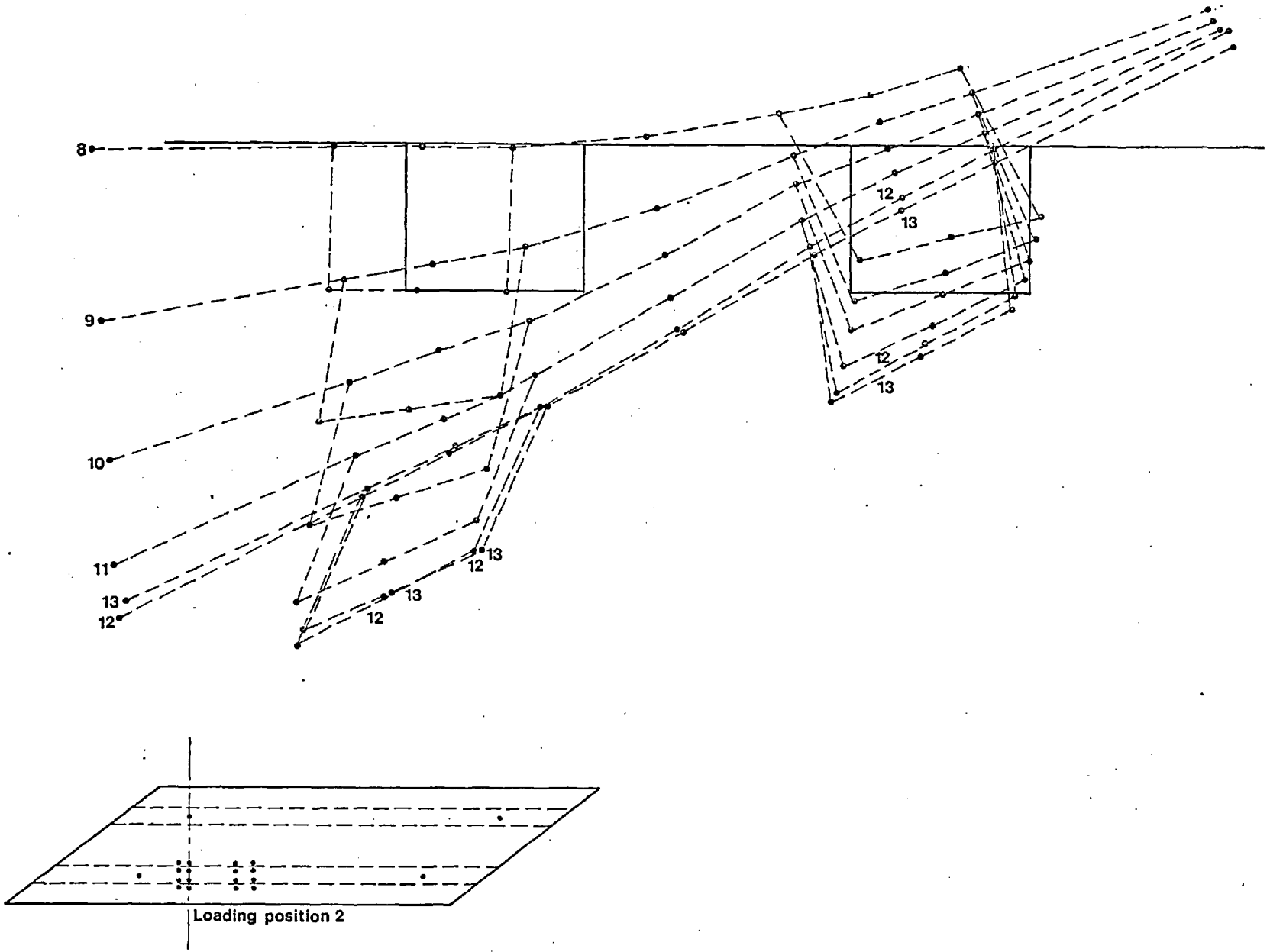


Fig.80a Finite element deflections for Load Case 2

MERSTHAM INTERCHANGE MODEL

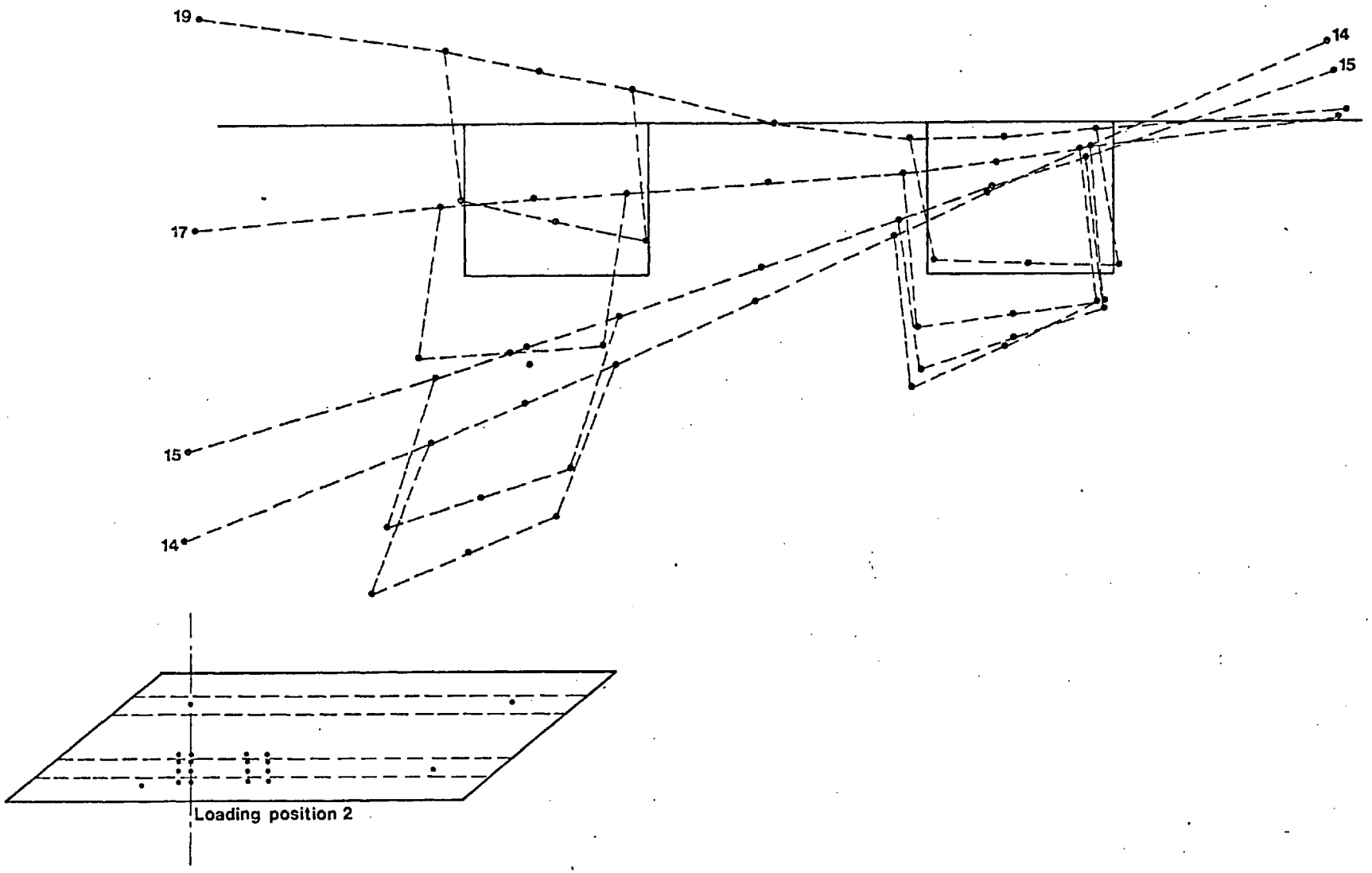


Fig.80b Finite element deflections for Load Case 2

MERSTHAM INTERCHANGE MODEL

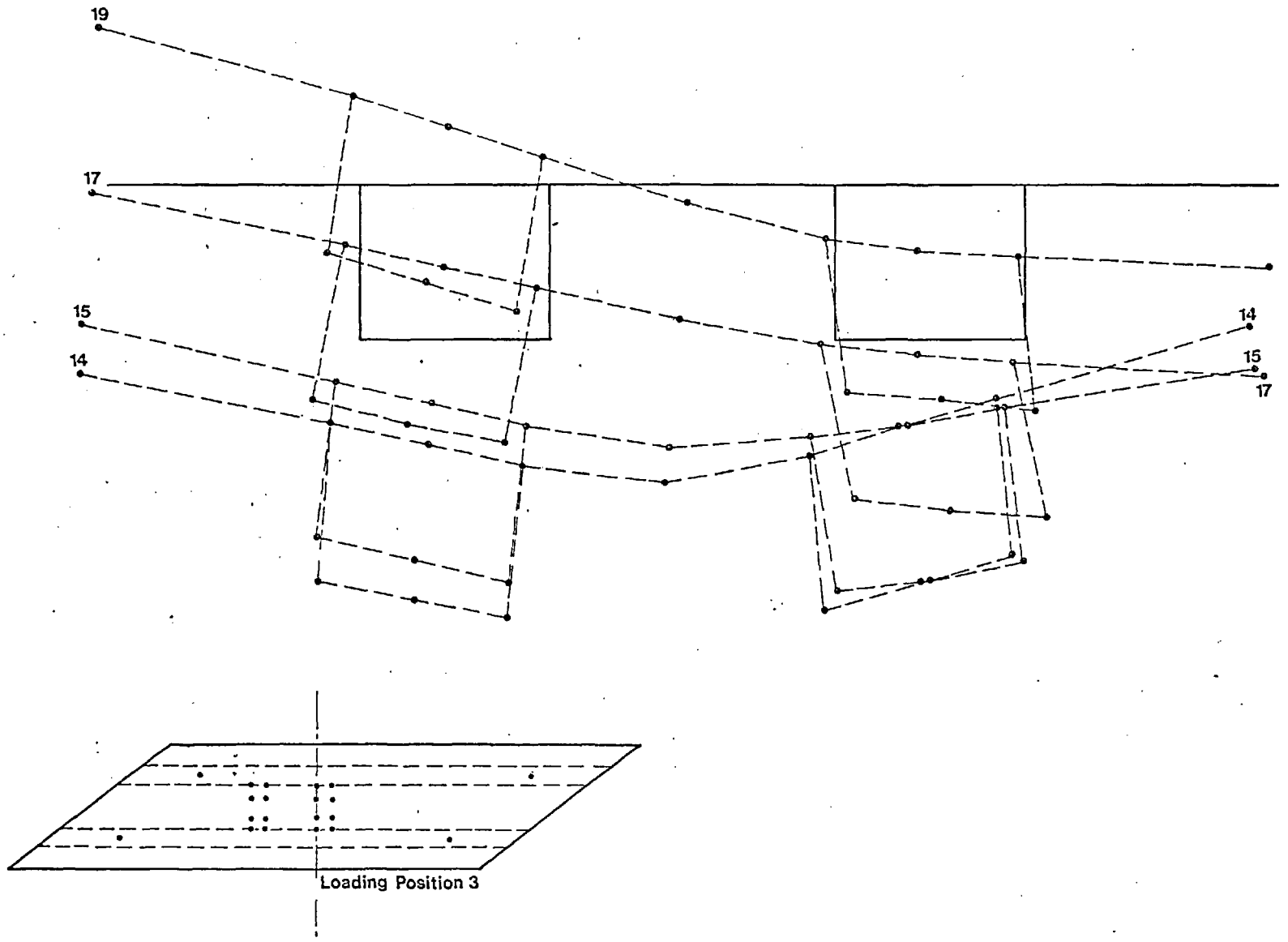


Fig.81a Finite element deflections for Load Case 3

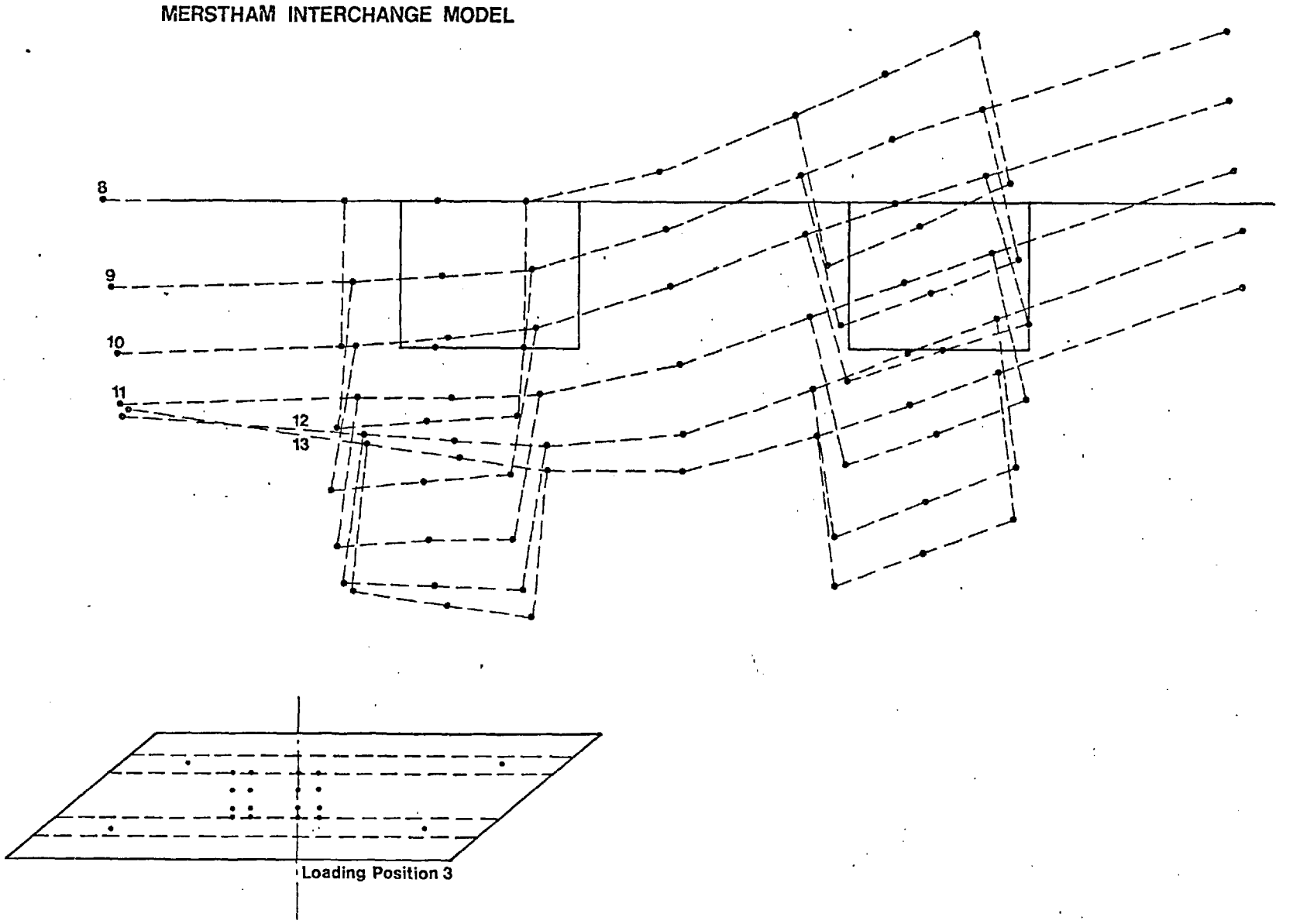


Fig.81b Finite element deflections for Load Case 3

MERSTHAM INTERCHANGE MODEL

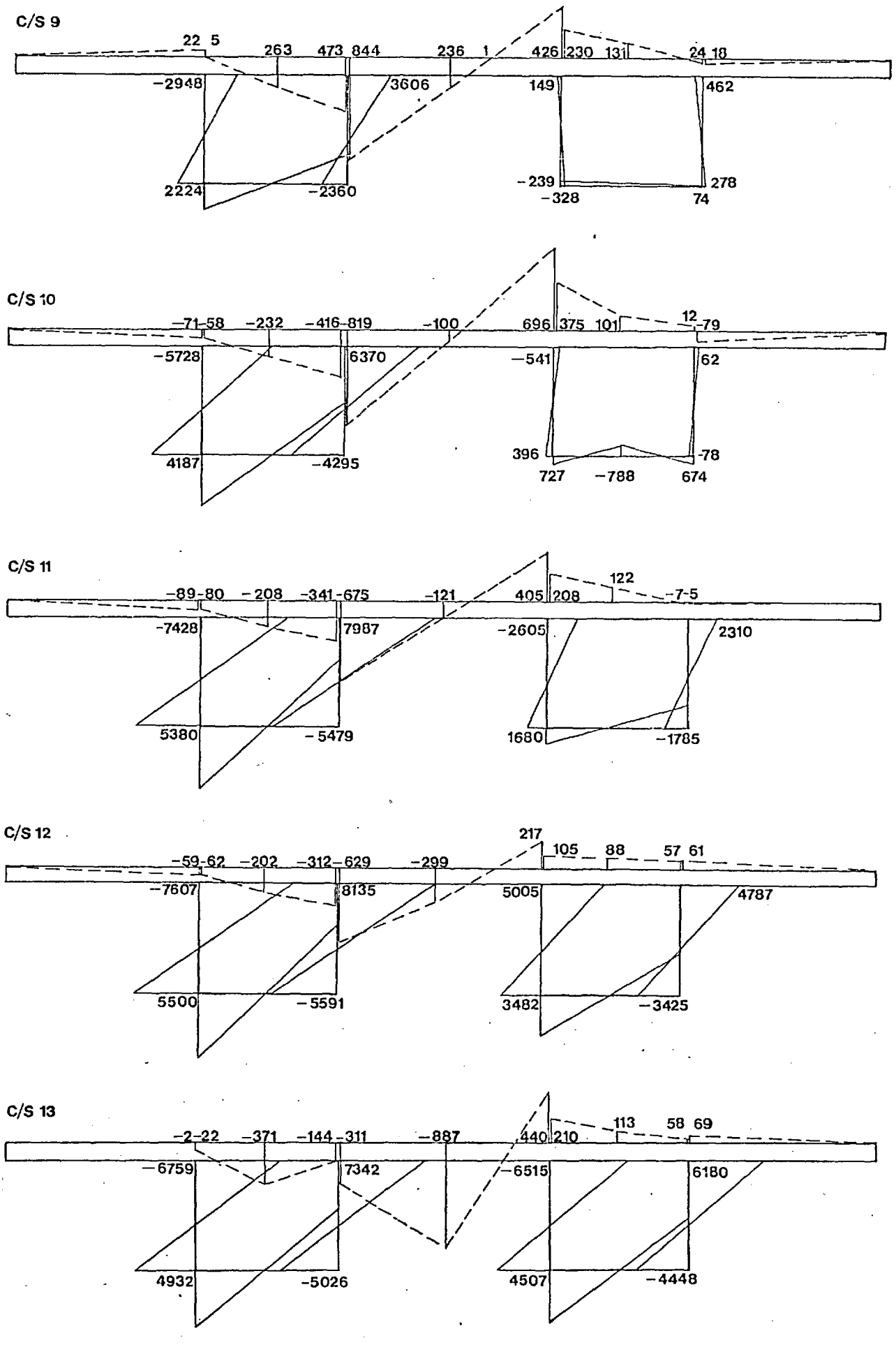


Fig.82a Finite element transverse stresses for Load Case 1

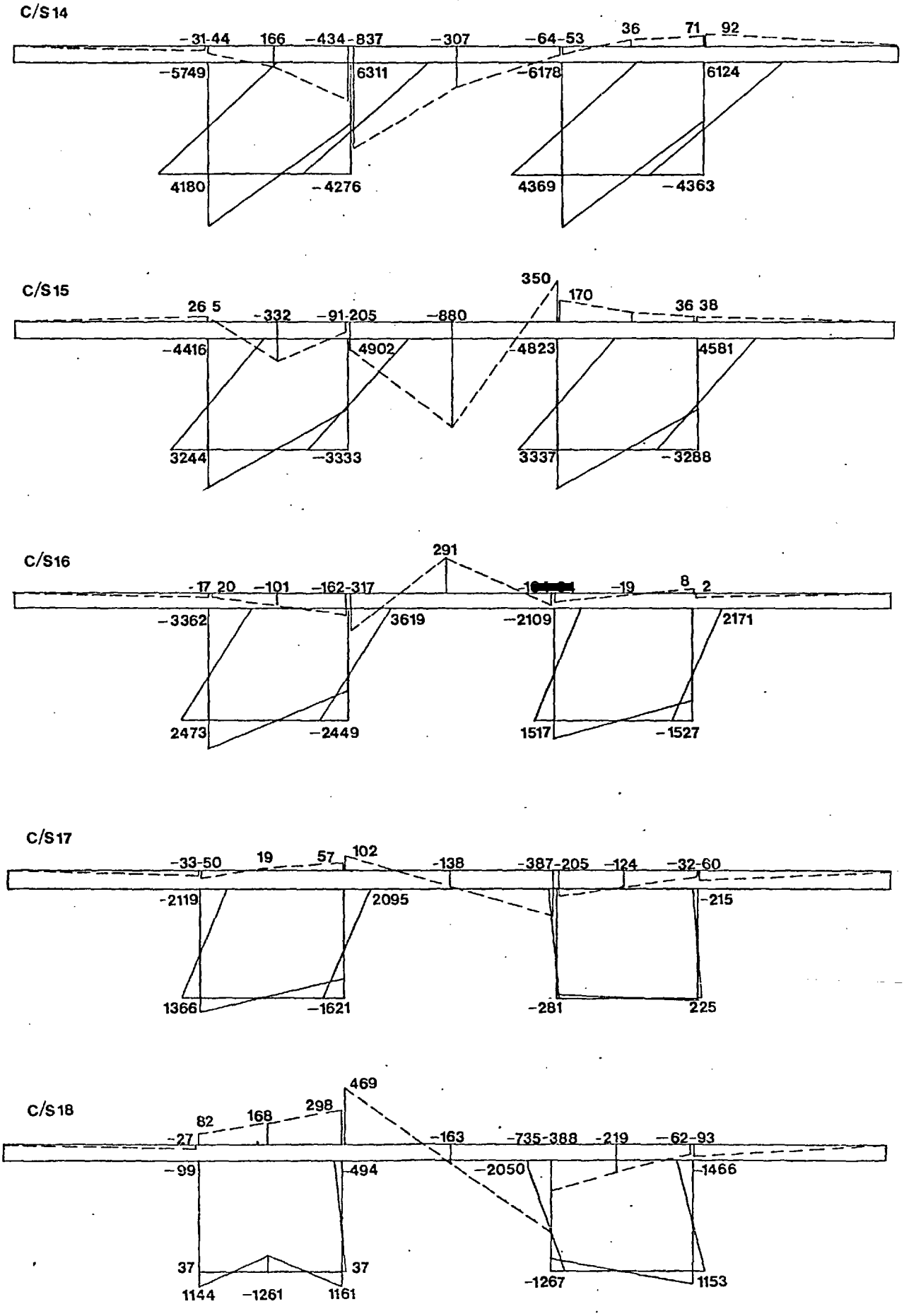


Fig.82b Finite element transverse stresses for Load Case 1

MERSTHAM INTERCHANGE MODEL

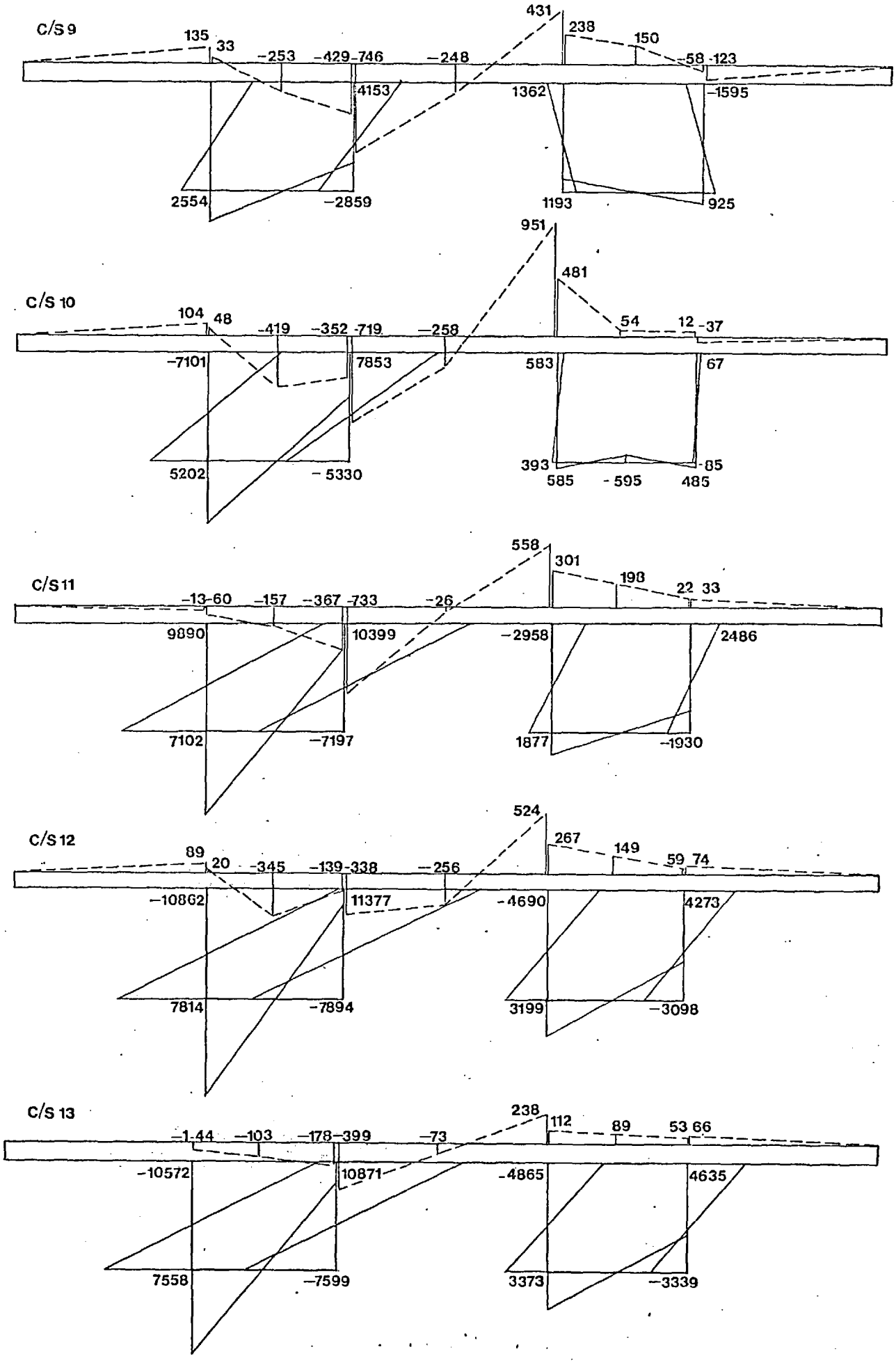


Fig.83a Finite element transverse stresses for Load Case 2

MERSTHAM INTERCHANGE MODEL

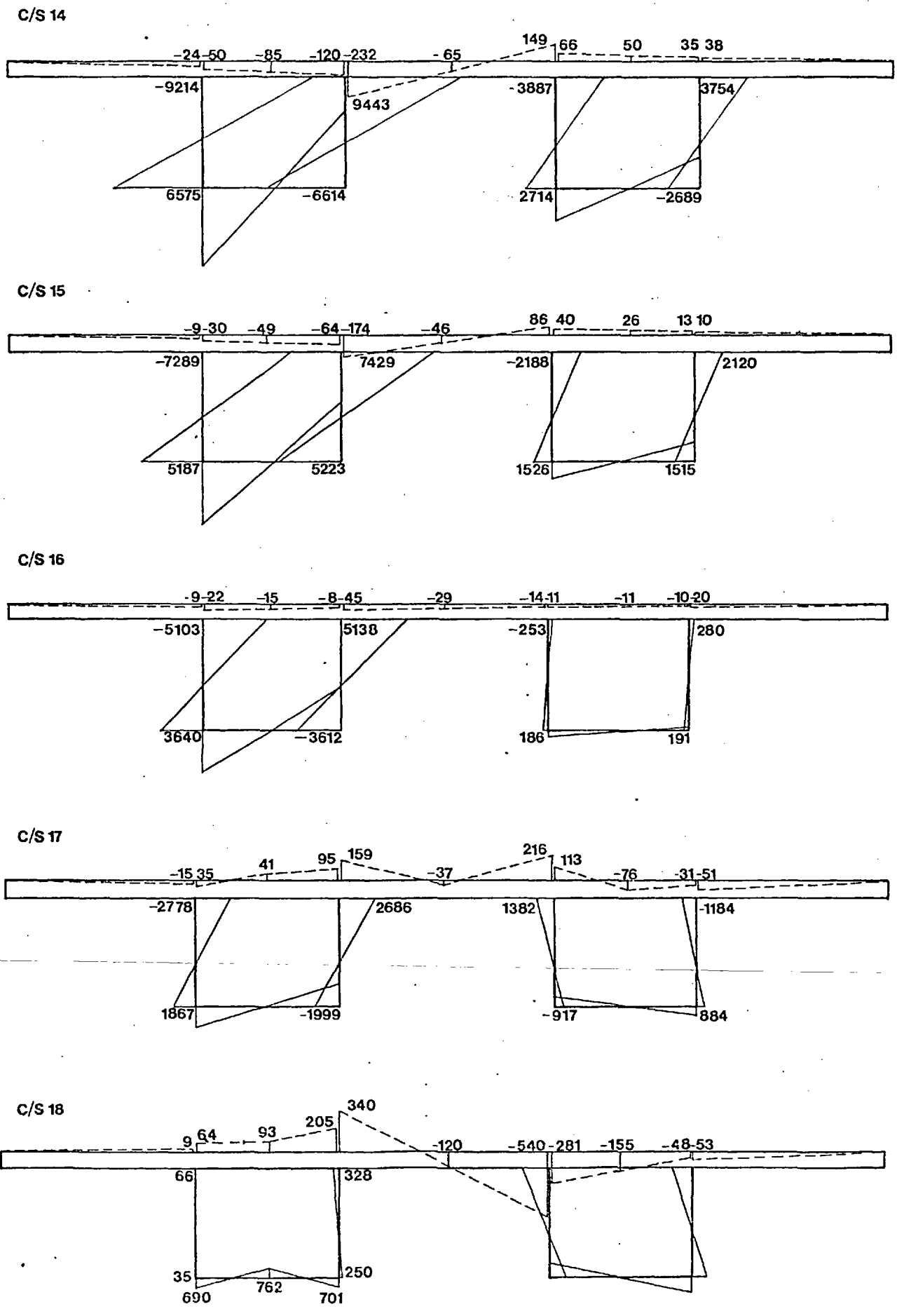


Fig.83b Finite element transverse stresses for Load Case 2

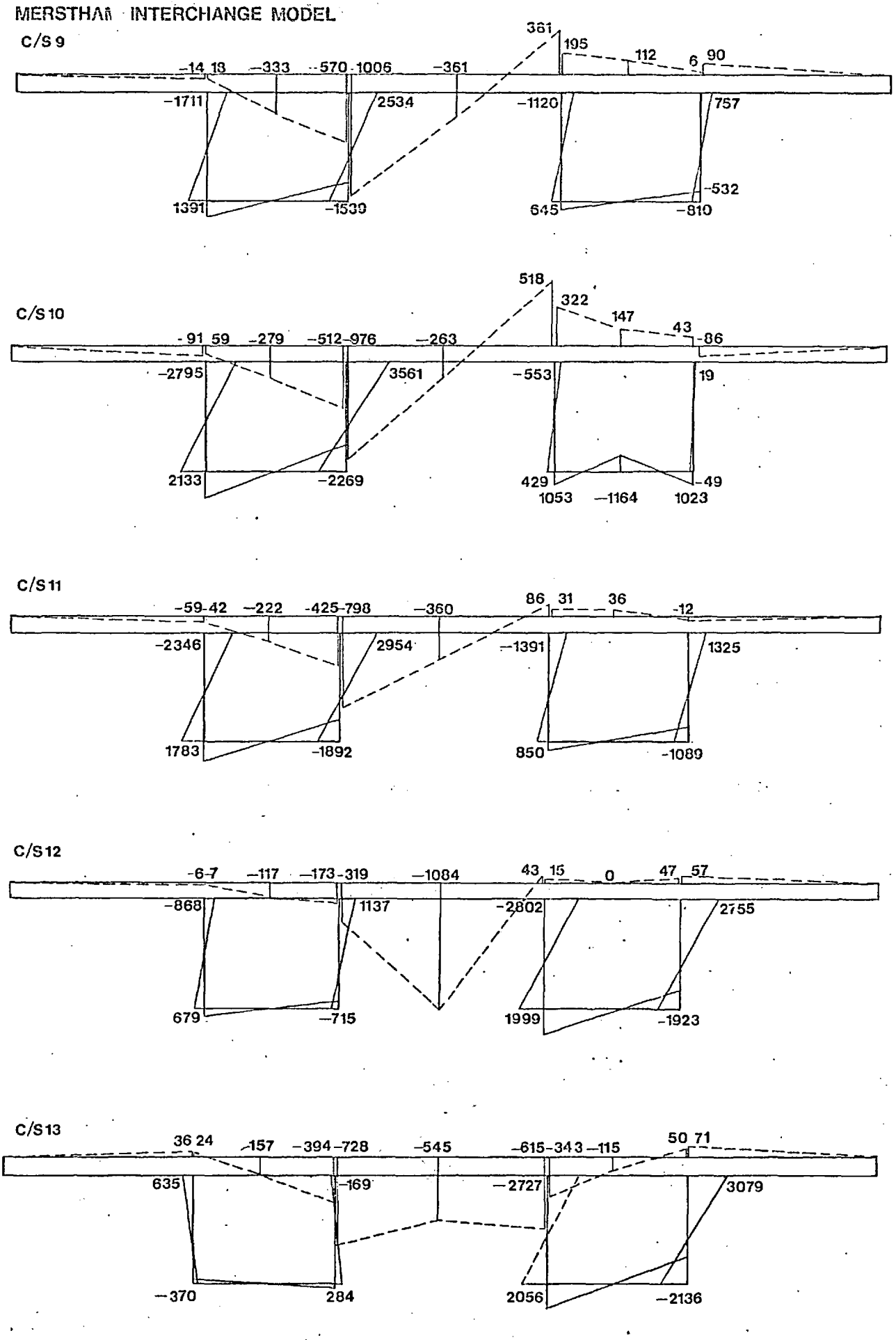


Fig.84a Finite element transverse stresses for Load Case 3

MERSTHAM INTERCHANGE MODEL

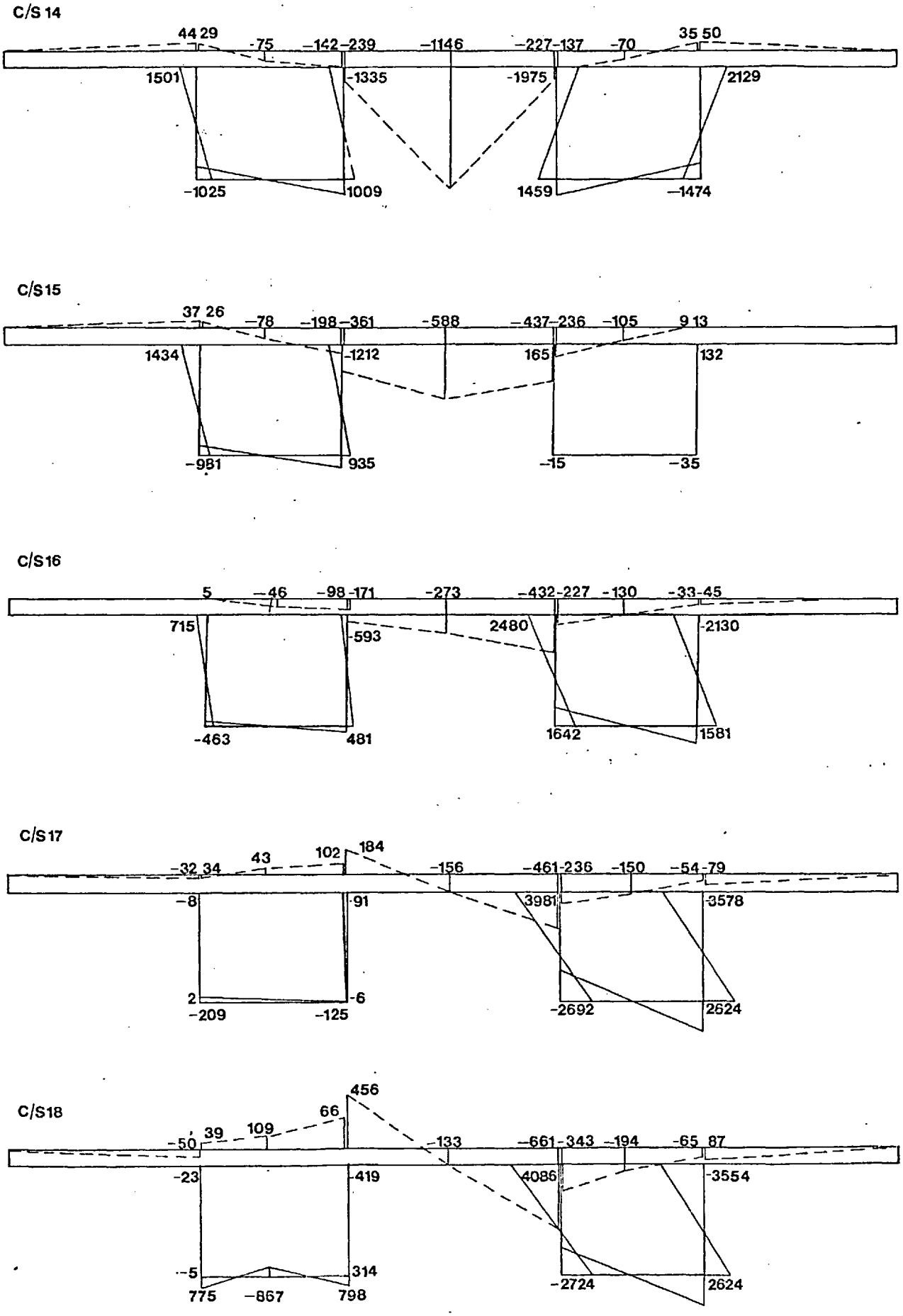
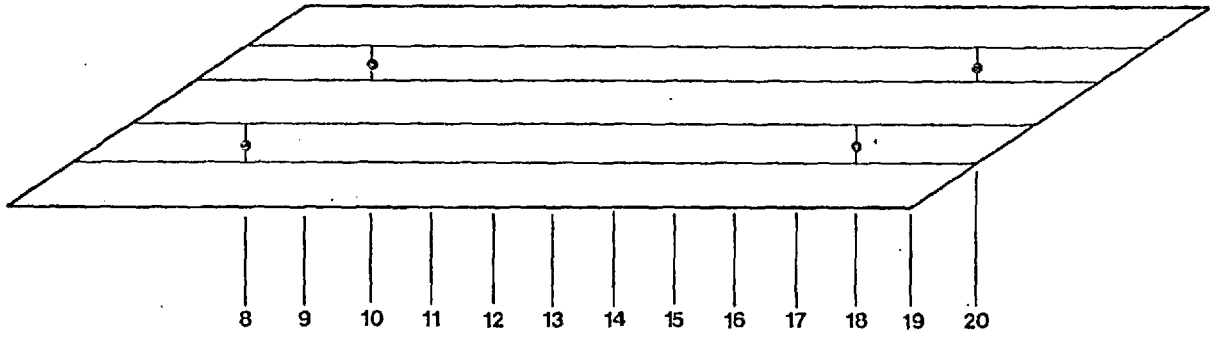
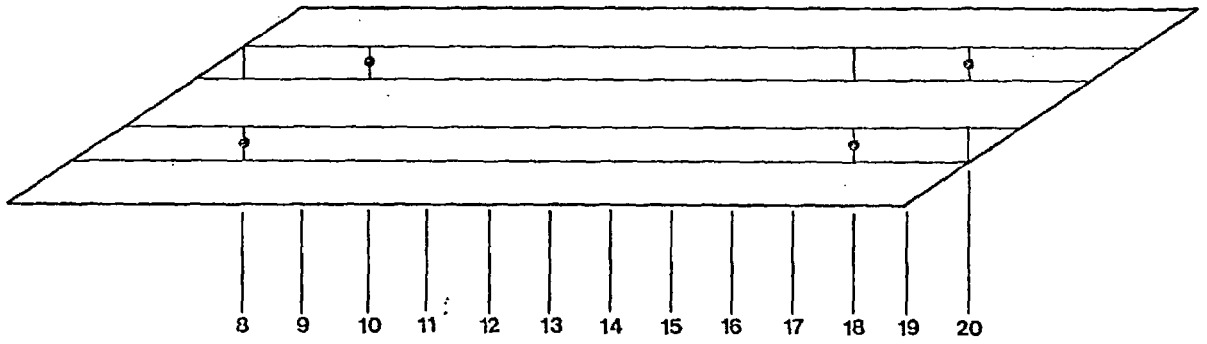


Fig.84b Finite element transverse stresses for Load Case 3

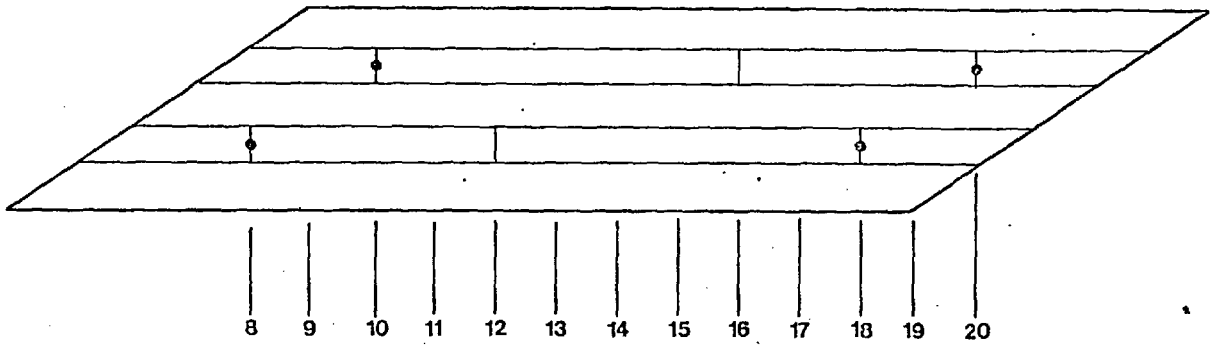
MERSTHAM INTERCHANGE MODEL



Diaphragm layout 1—undiaphragmed model



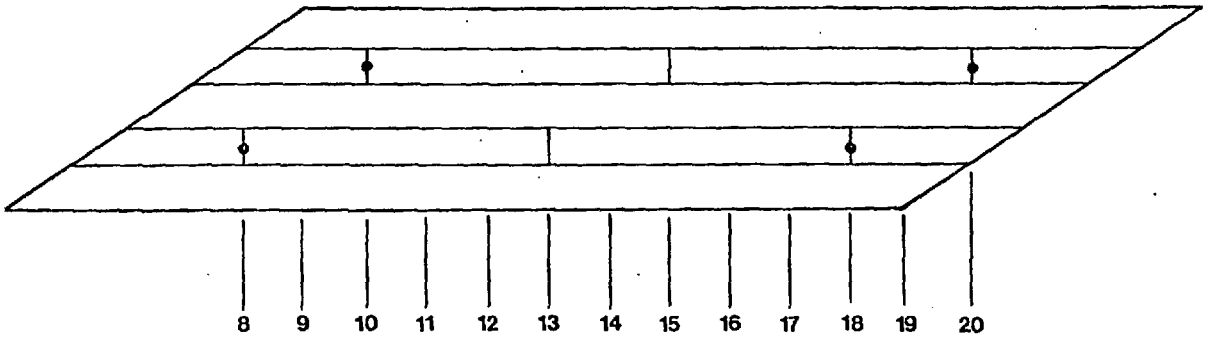
Diaphragm layout 2—internal bracing at Sections 10 and 18



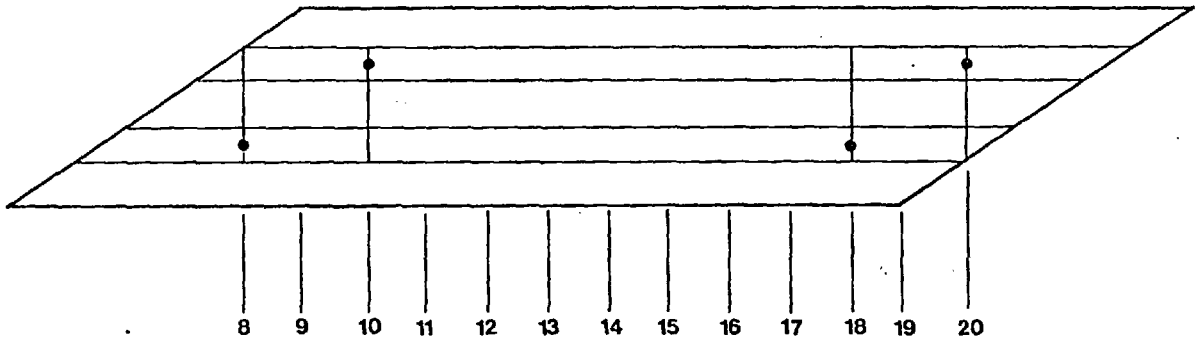
Diaphragm layout 3 — internal bracing at Sections 12 and 16

Fig.85a Diaphragm layouts 1–3

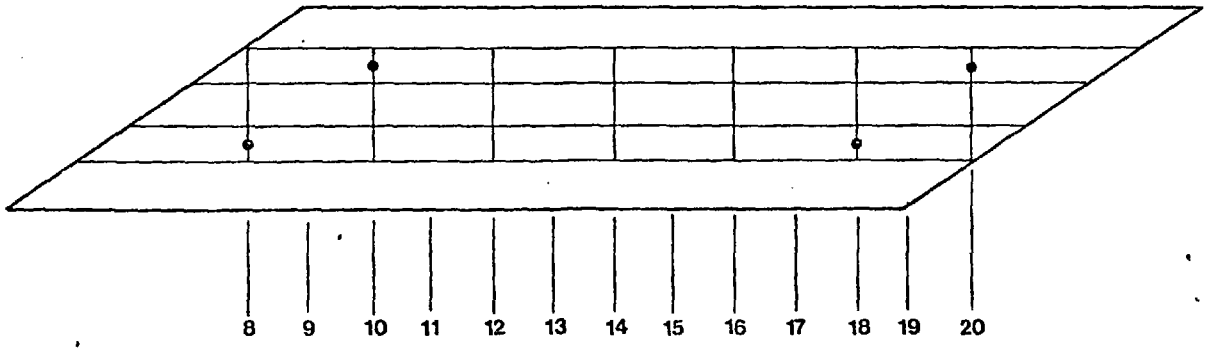
MERSTHAM INTERCHANGE MODEL



Diaphragm layout 4 – internal bracing at Sections 13 and 15



Diaphragm layout 5 – bracing in and between boxes at Sections 10 and 18



Diaphragm layout 6 – fully diaphragmed model

Fig.85b Diaphragm layouts 4–6

MERSTHAM INTERCHANGE MODEL

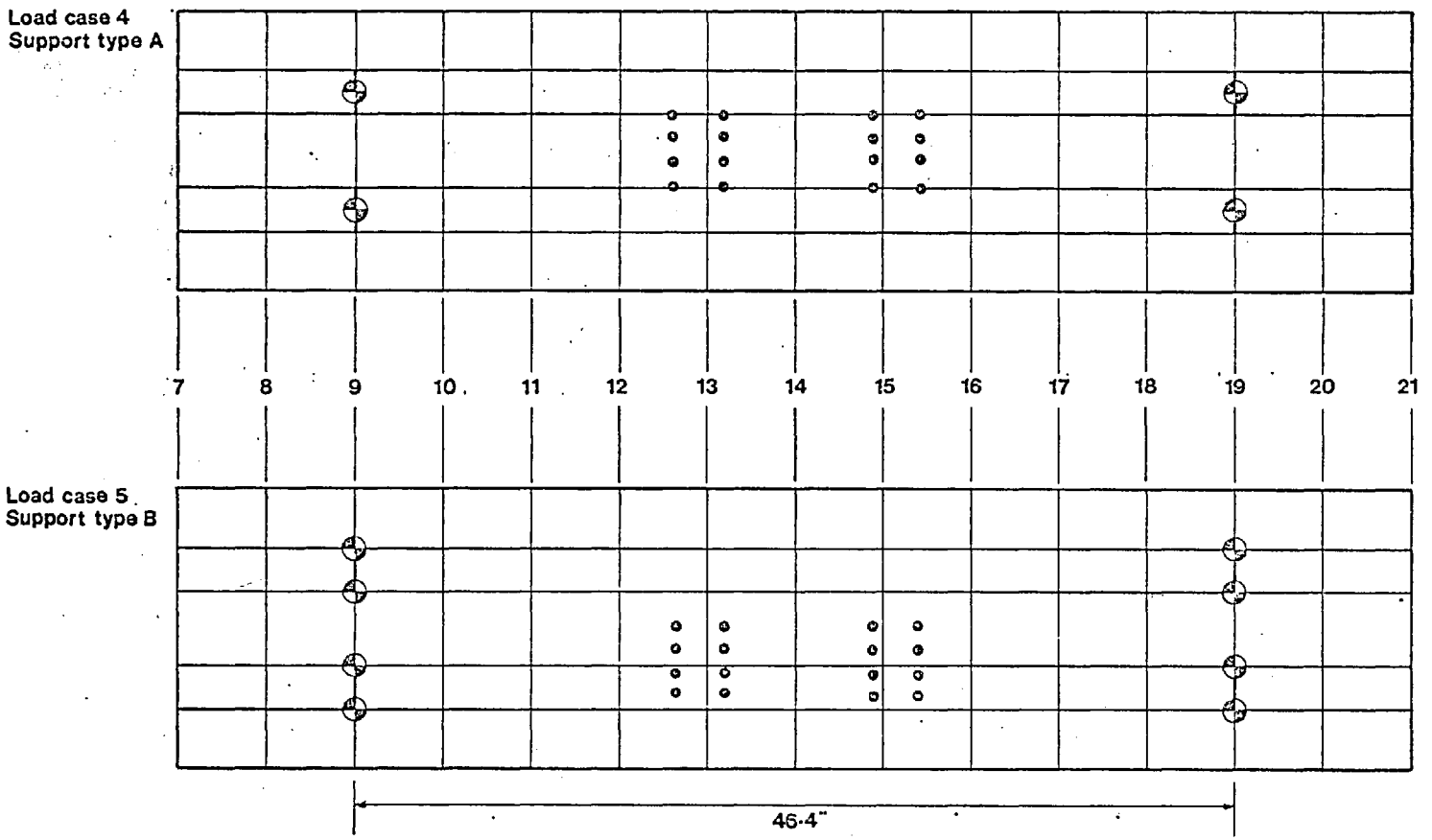


Fig.86 Equivalent right bridge structures showing loading positions 4 and 5 and alternative support arrangements. The Section numbers have been chosen to coincide with those of the skew structure.

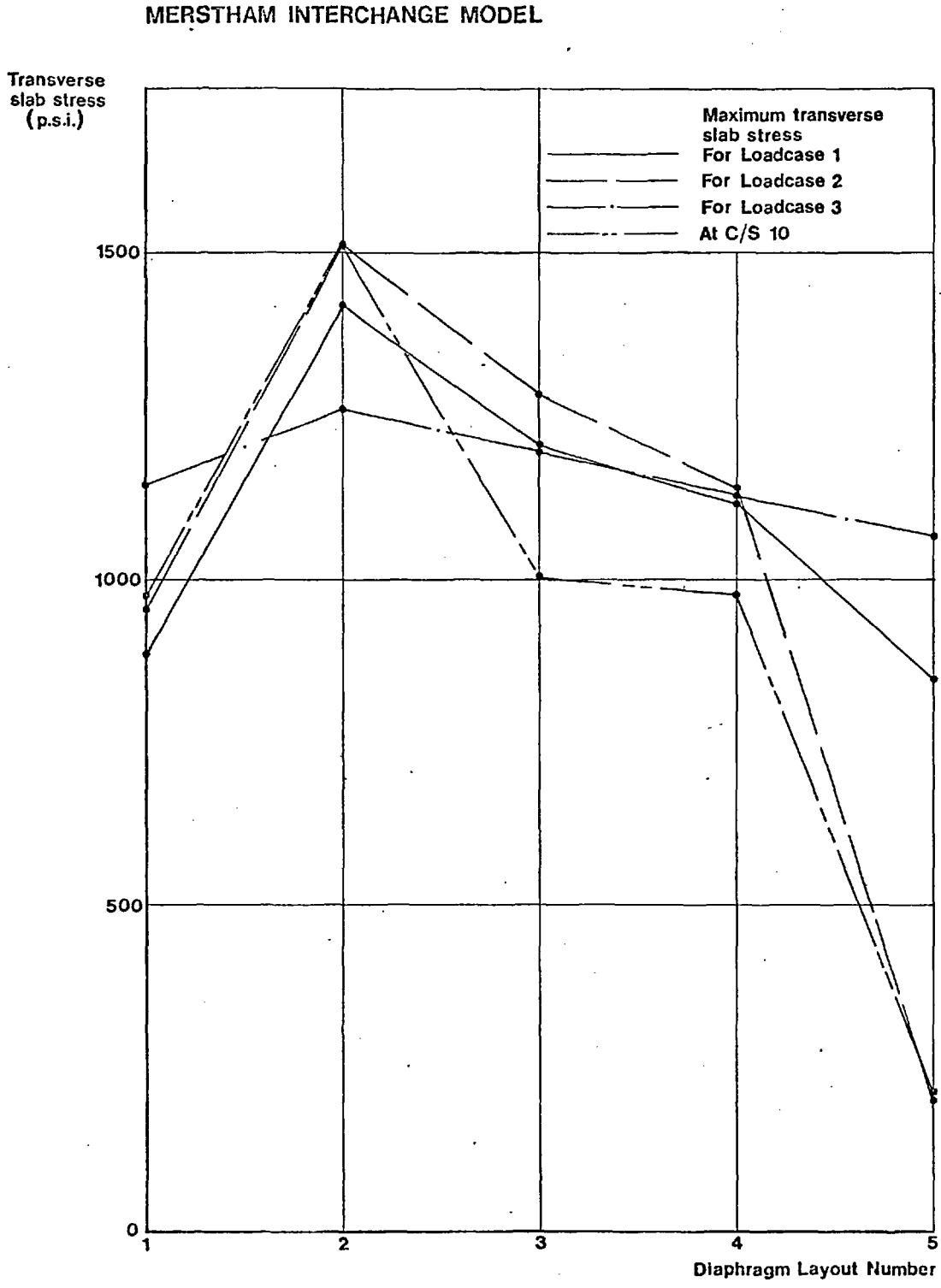


Fig.87 Summary of maximum transverse slab stresses for Diaphragm layouts 1–5

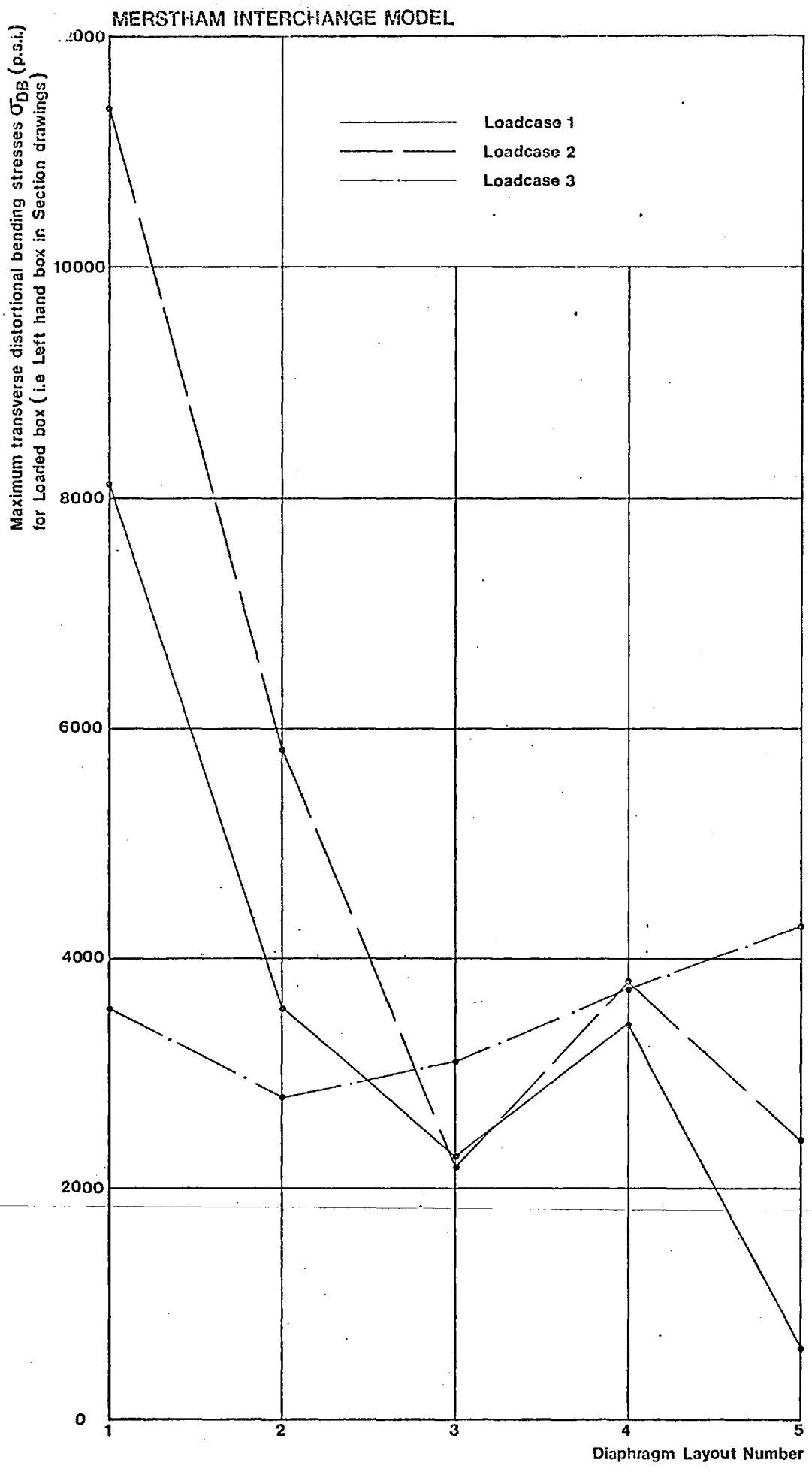


Fig.88 Summary of maximum transverse distortional stresses σ_{DB} in loaded box for Diaphragm layout 1–5

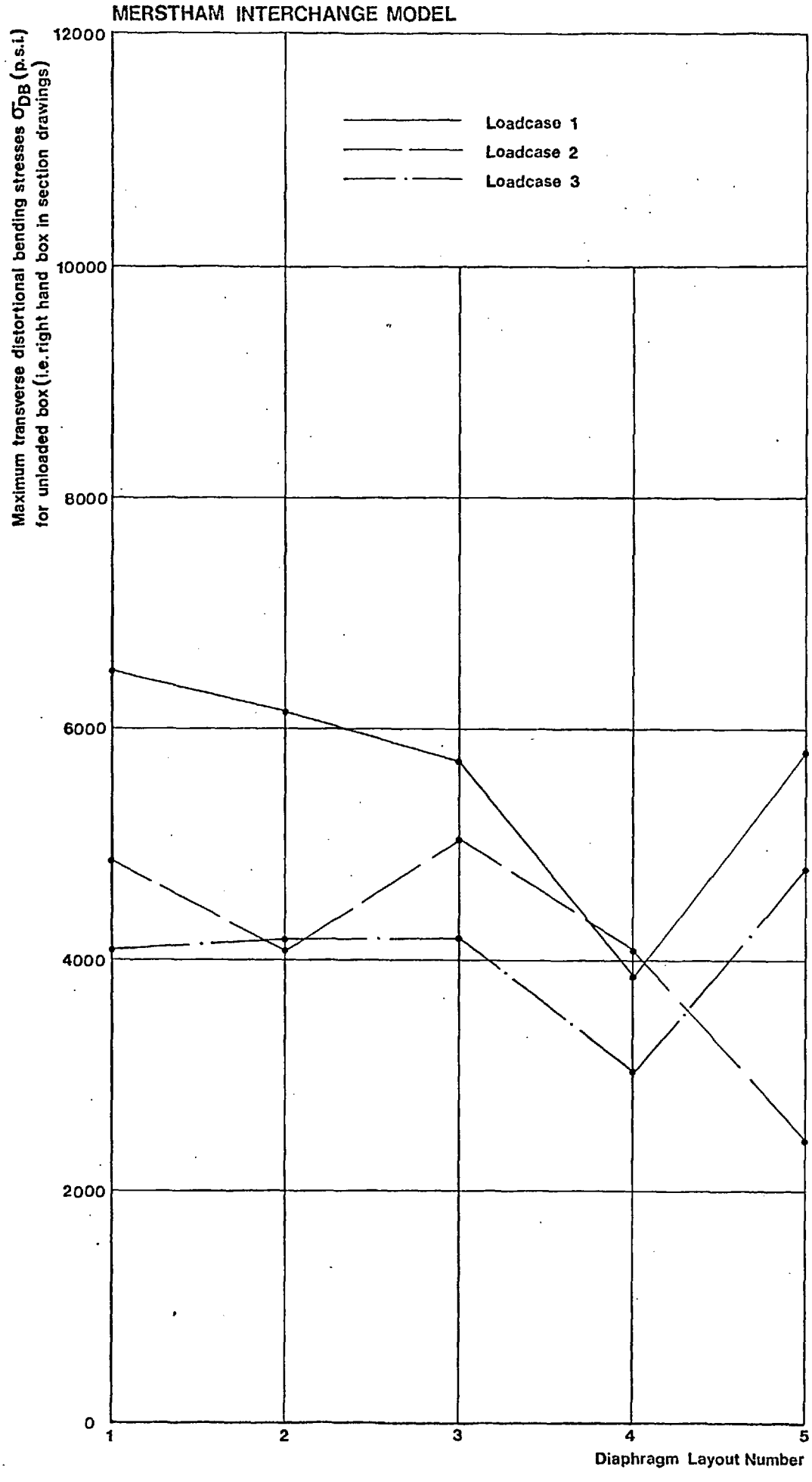


Fig.89 Summary of maximum transverse distortional stresses O_{DB} in unloaded box for Diaphragm layouts 1-5

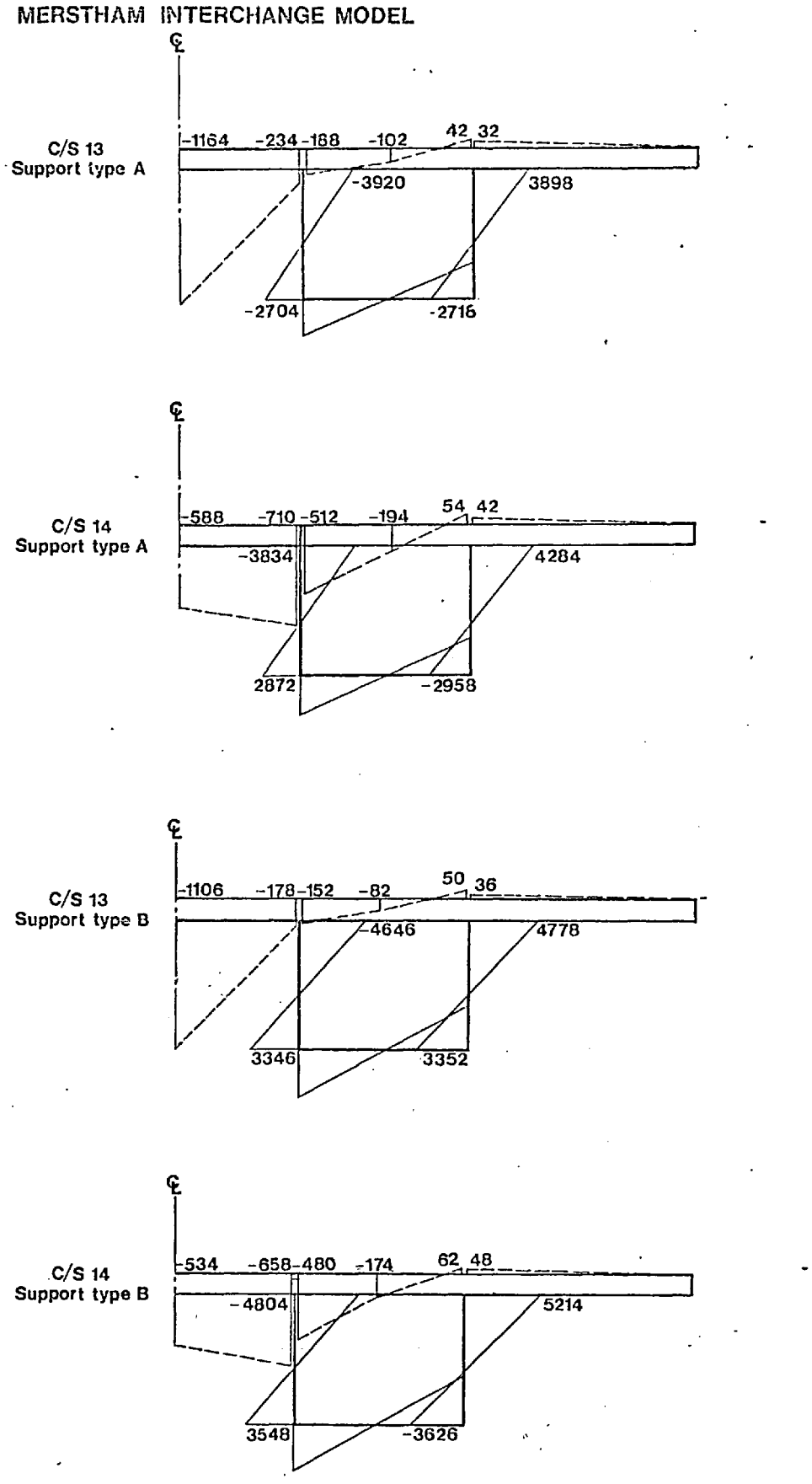
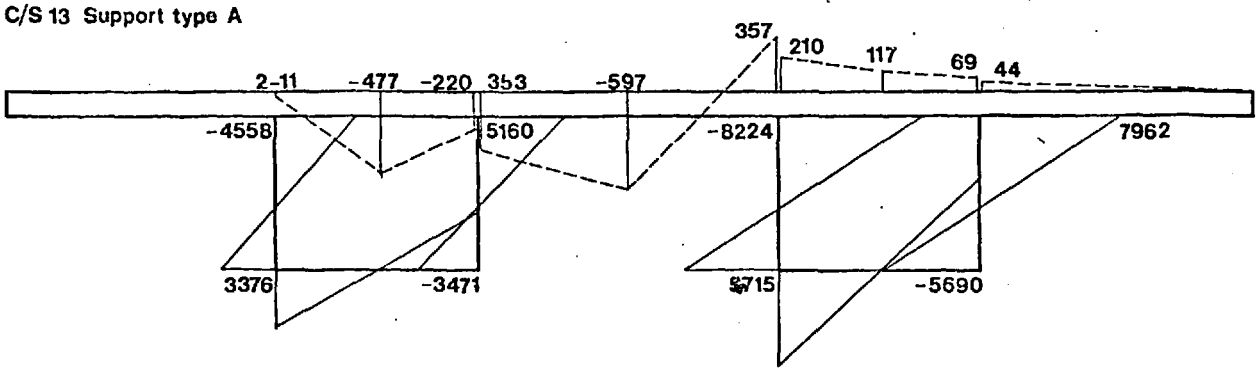


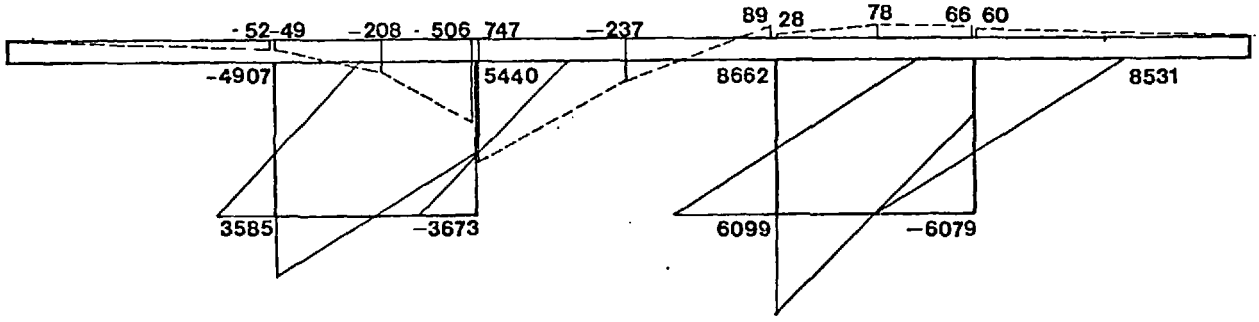
Fig.90 Right bridge structure – transverse flexural stresses for Load case 4

MERSTHAM INTERCHANGE MODEL

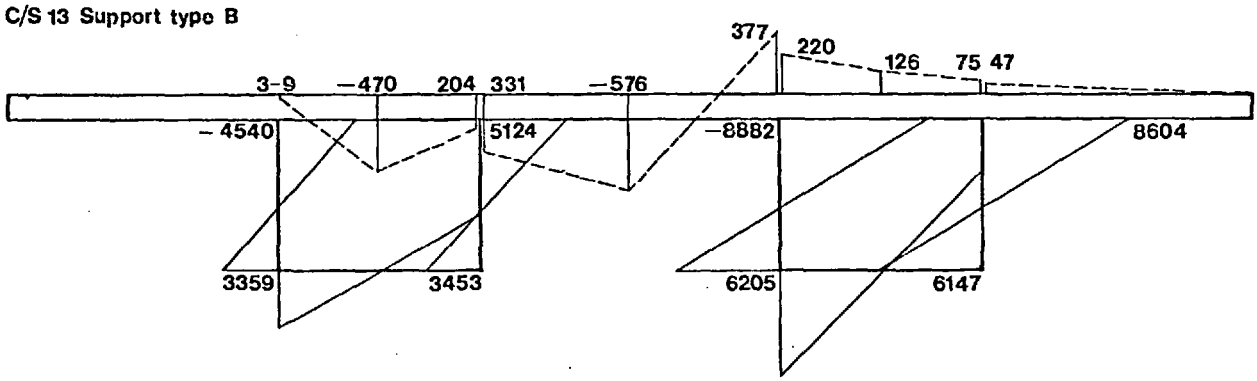
C/S 13 Support type A



C/S 14 Support type A



C/S 13 Support type B



C/S 14 Support type B

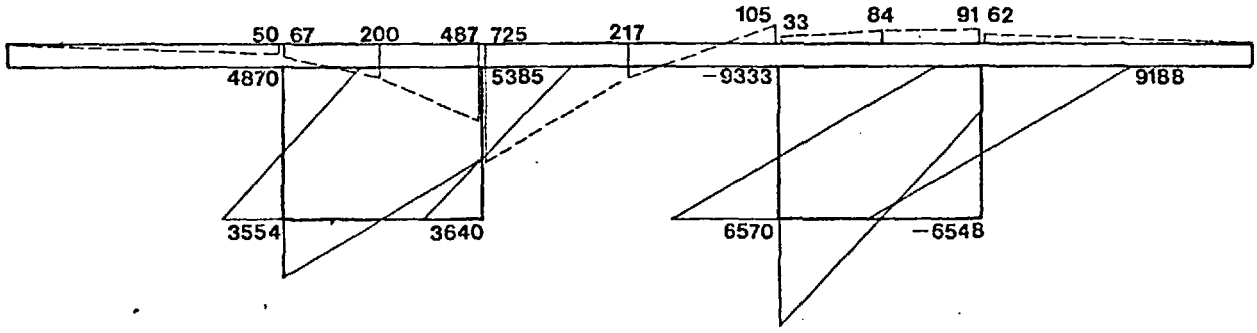


Fig.91 Right bridge structure - transverse flexural stresses for Load Case 5

BIFURCATED ELEVATED HIGHWAYS MODELS

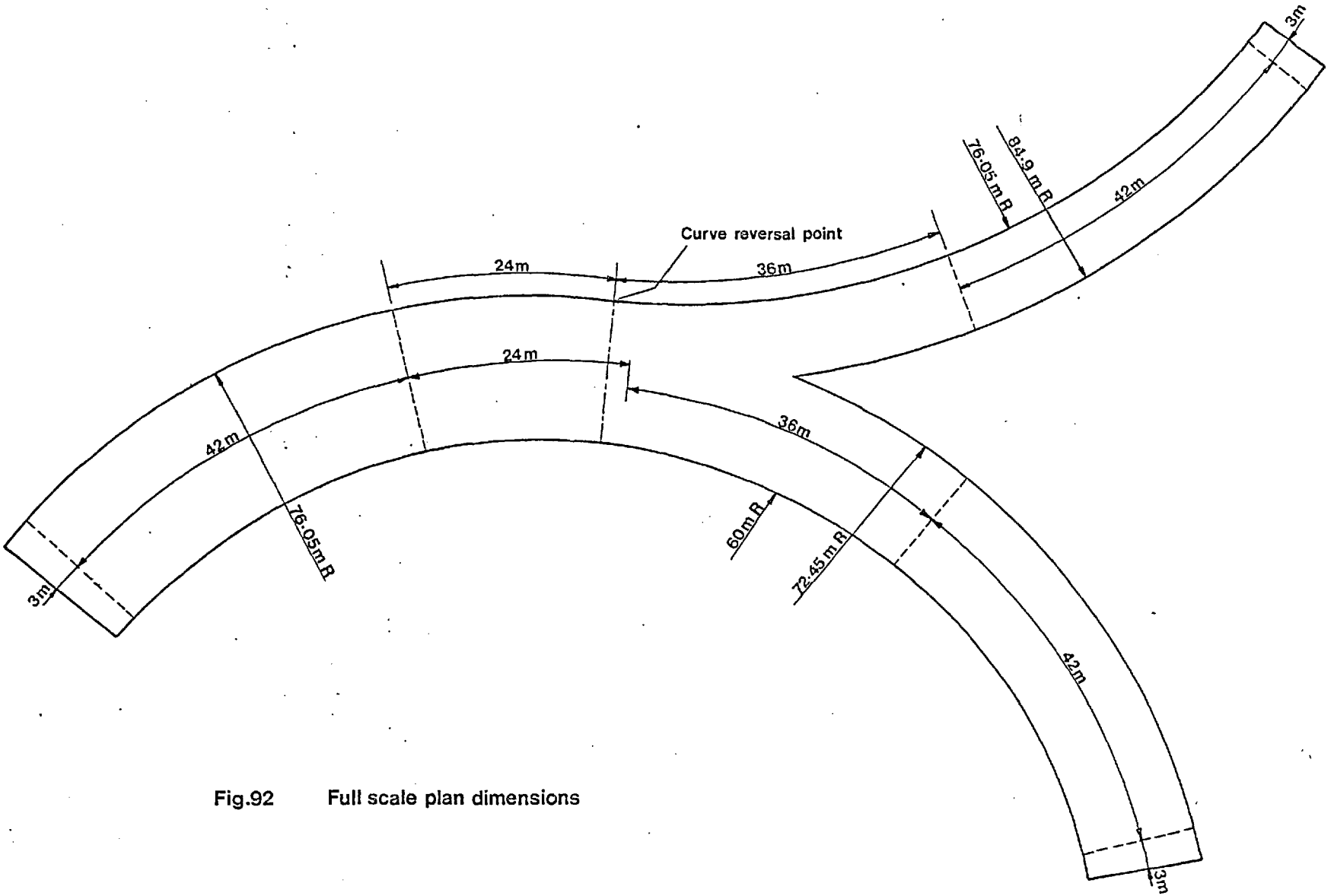


Fig.92 Full scale plan dimensions

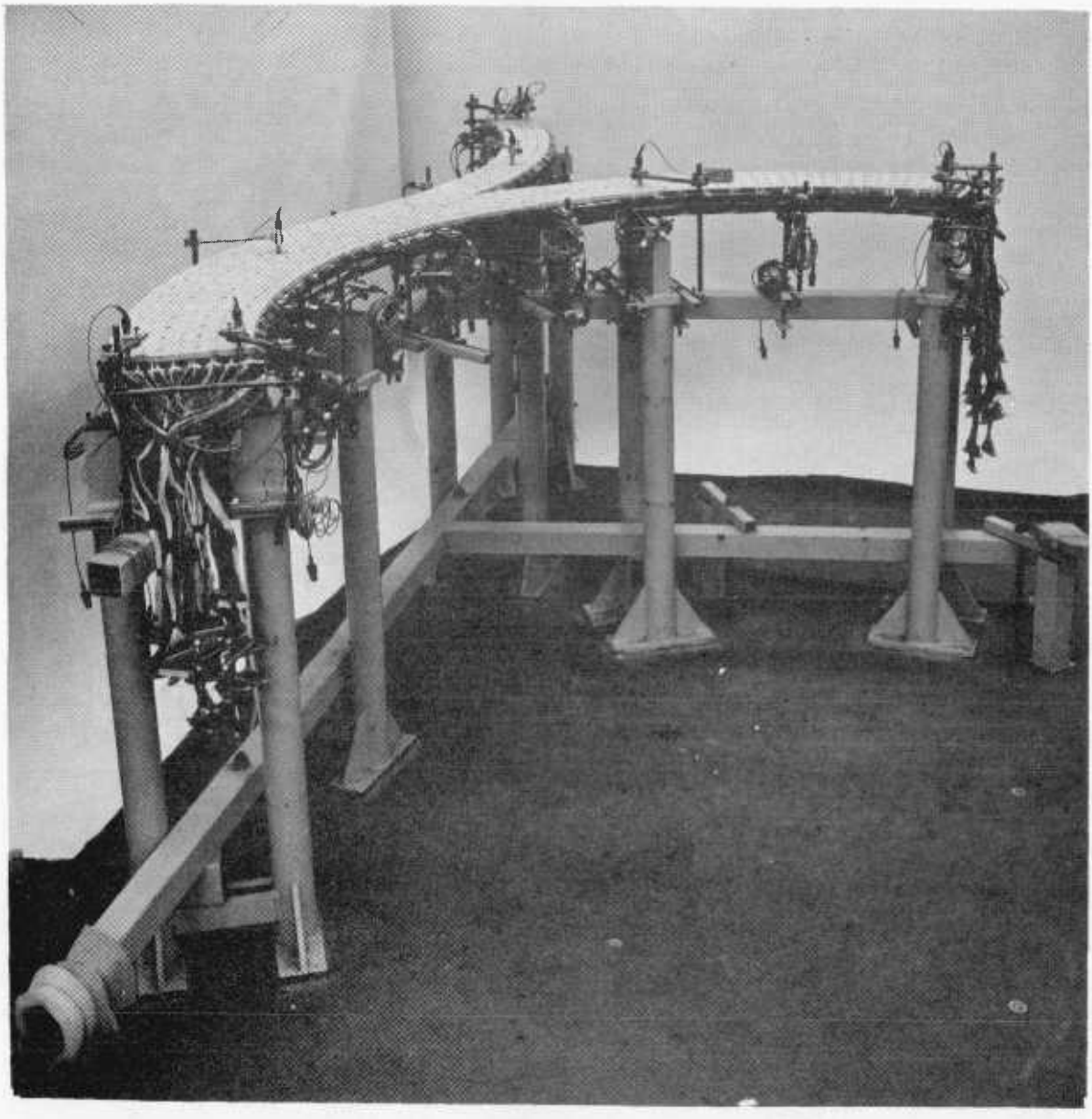


Fig.93 General view of support and deflection rig with Model 2 in position
BIFURCATED ELEVATED HIGHWAYS MODELS

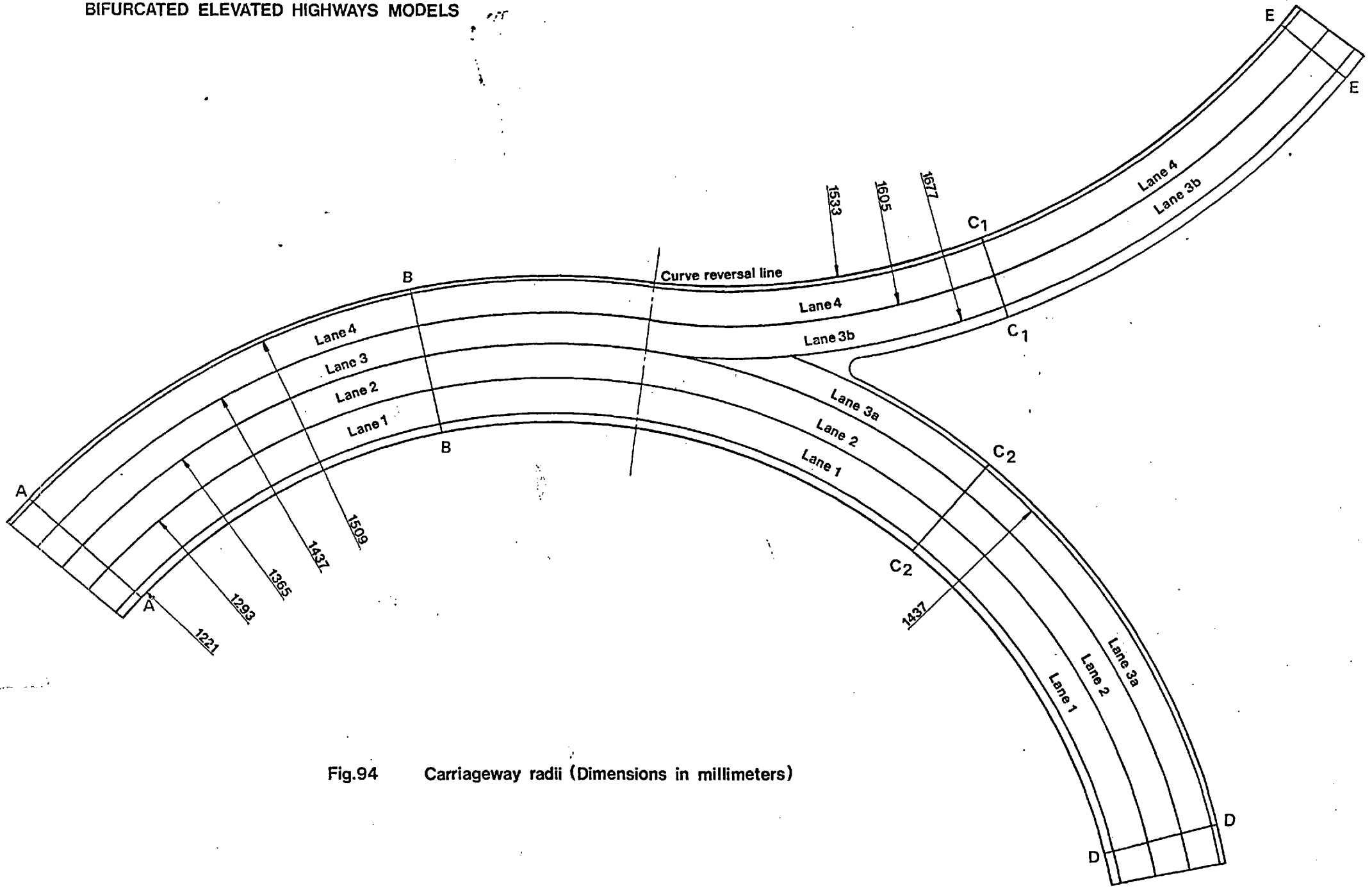


Fig.94 Carriageway radii (Dimensions in millimeters)

BIFURCATED ELEVATED HIGHWAYS MODELS

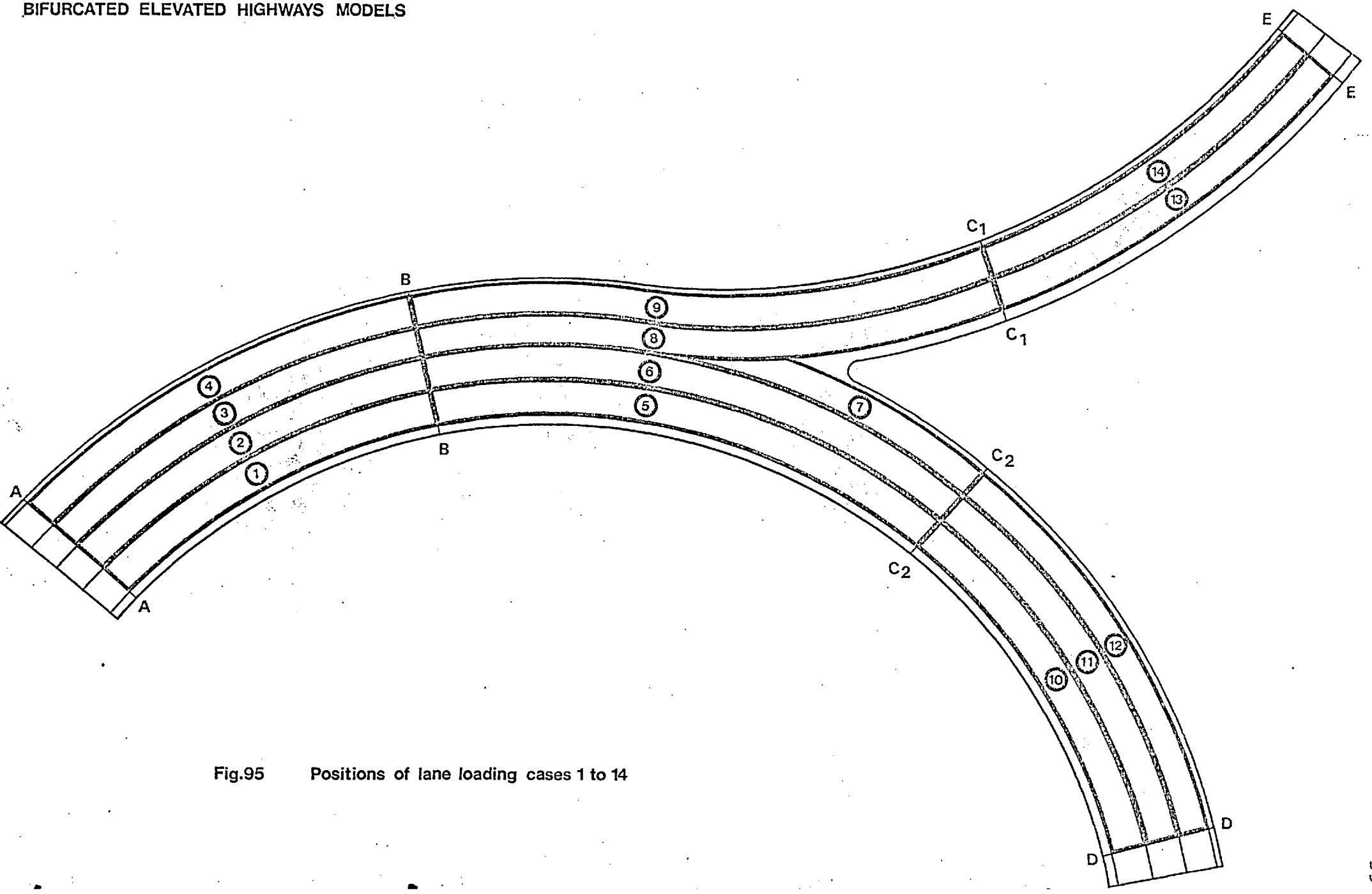


Fig.95 Positions of lane loading cases 1 to 14

BIFURCATED ELEVATED HIGHWAYS MODELS

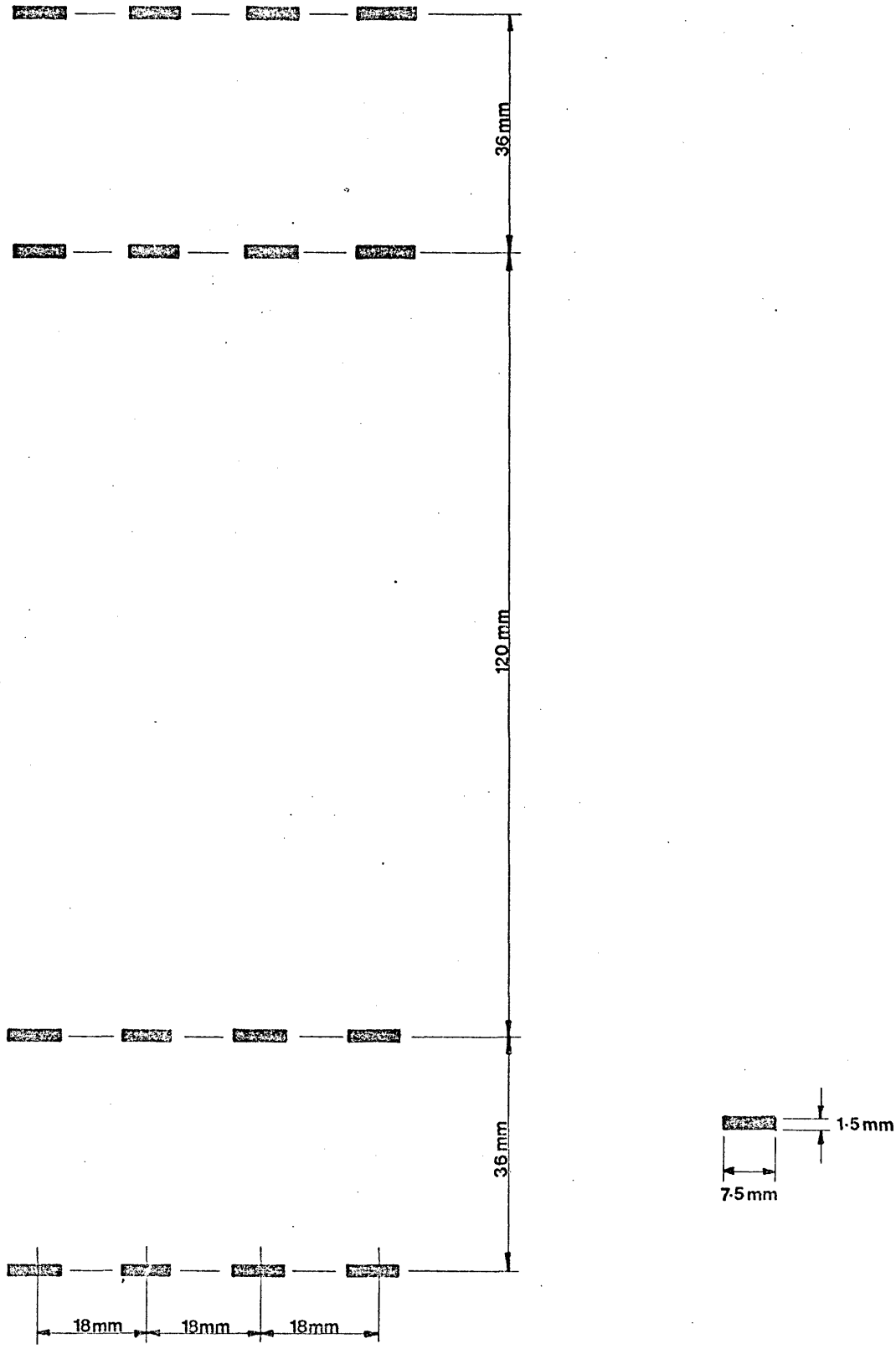


Fig.96 Dimensions of HB vehicle

BIFURCATED ELEVATED HIGHWAYS MODELS

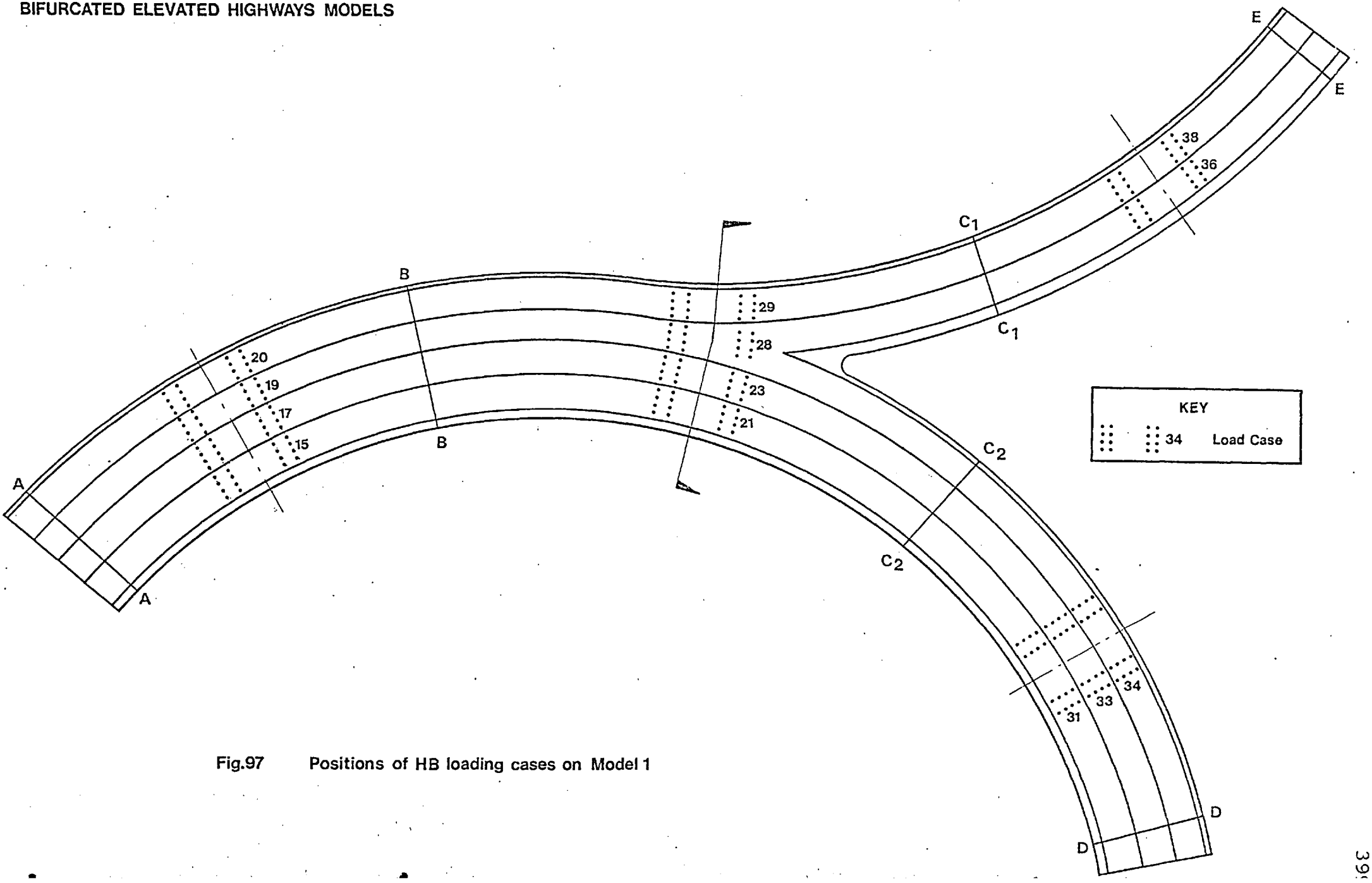


Fig.97 Positions of HB loading cases on Model 1

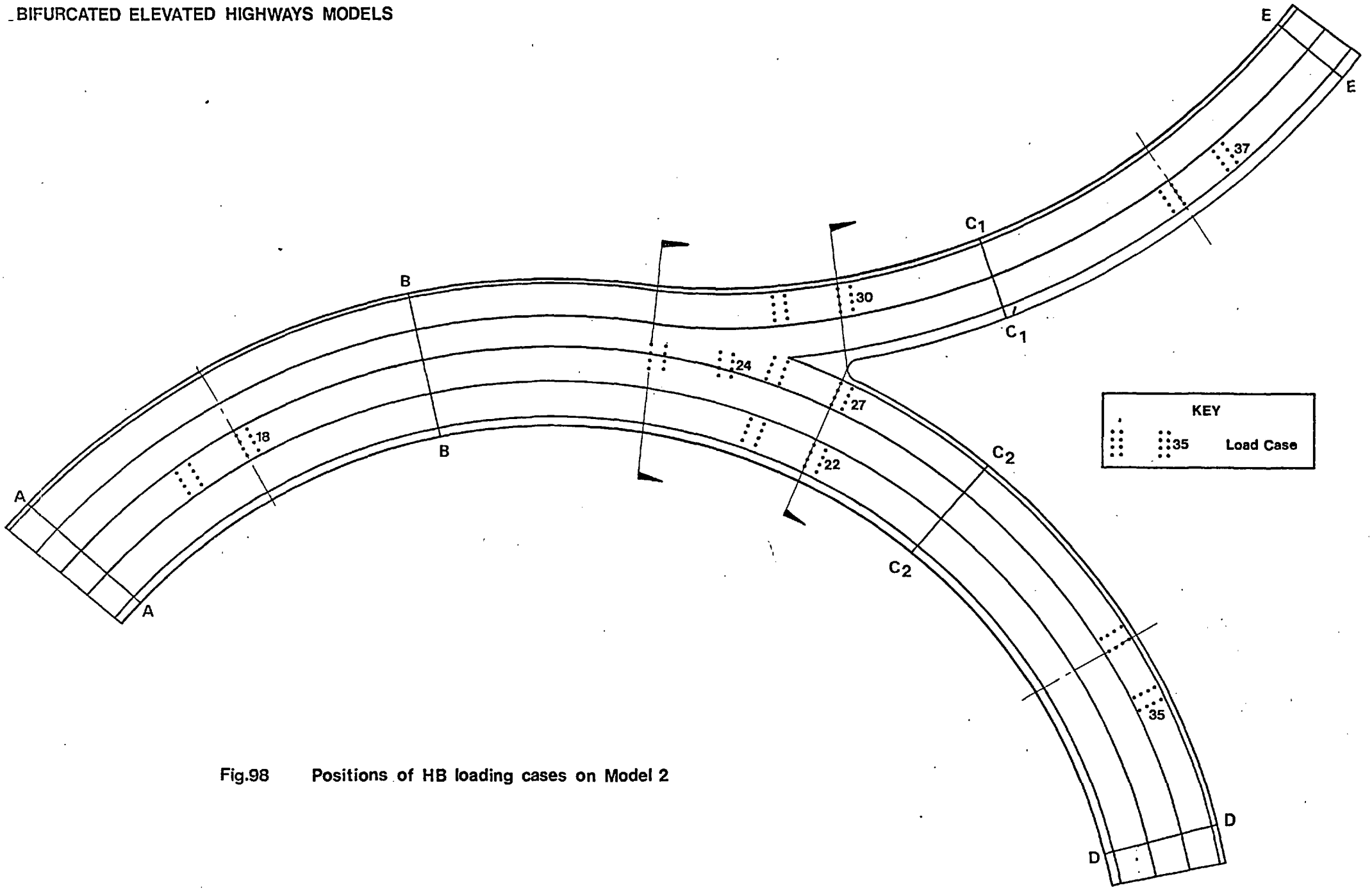


Fig.98 Positions of HB loading cases on Model 2

BIFURCATED ELEVATED HIGHWAYS MODELS

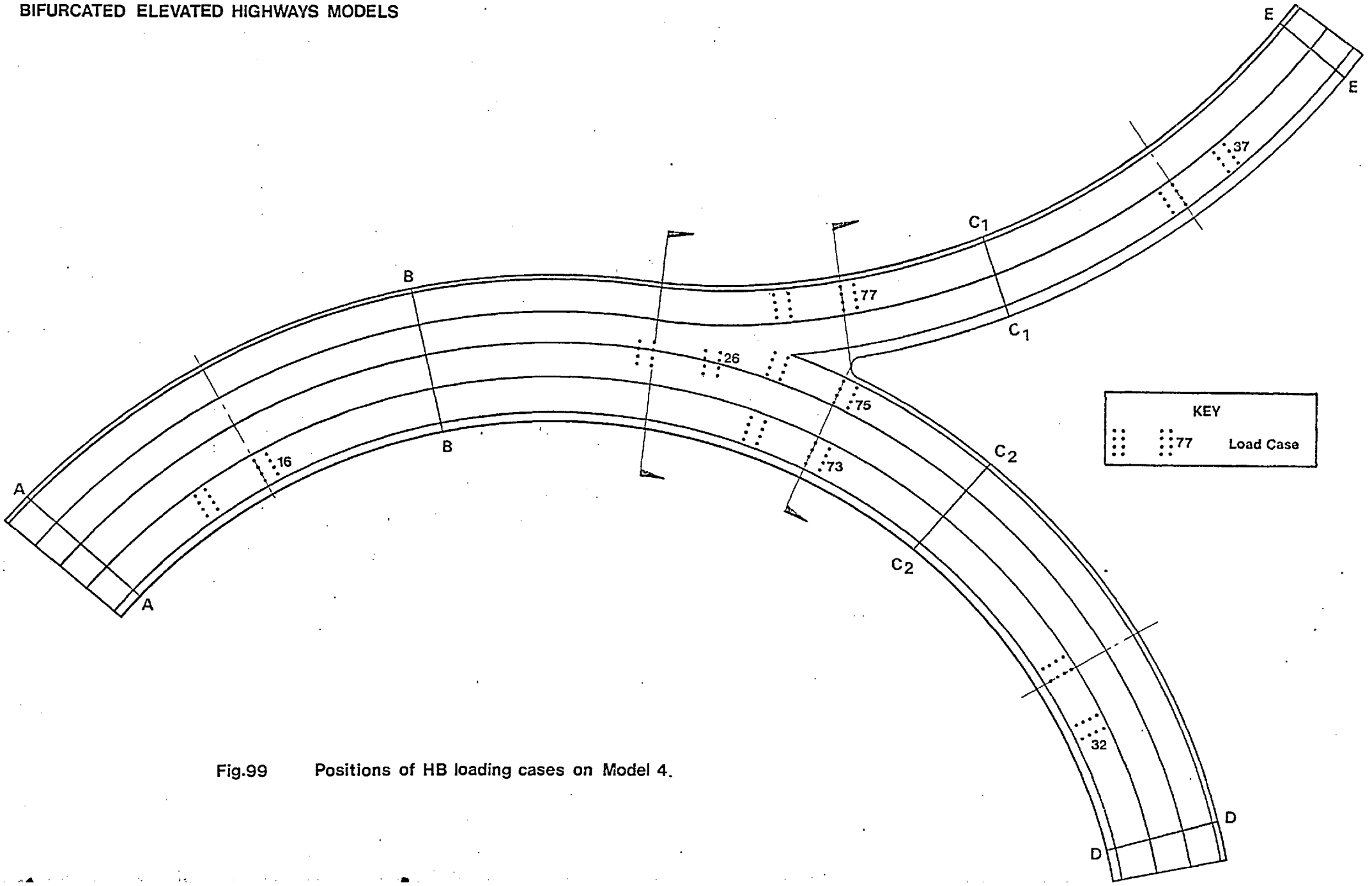


Fig.99 Positions of HB loading cases on Model 4.

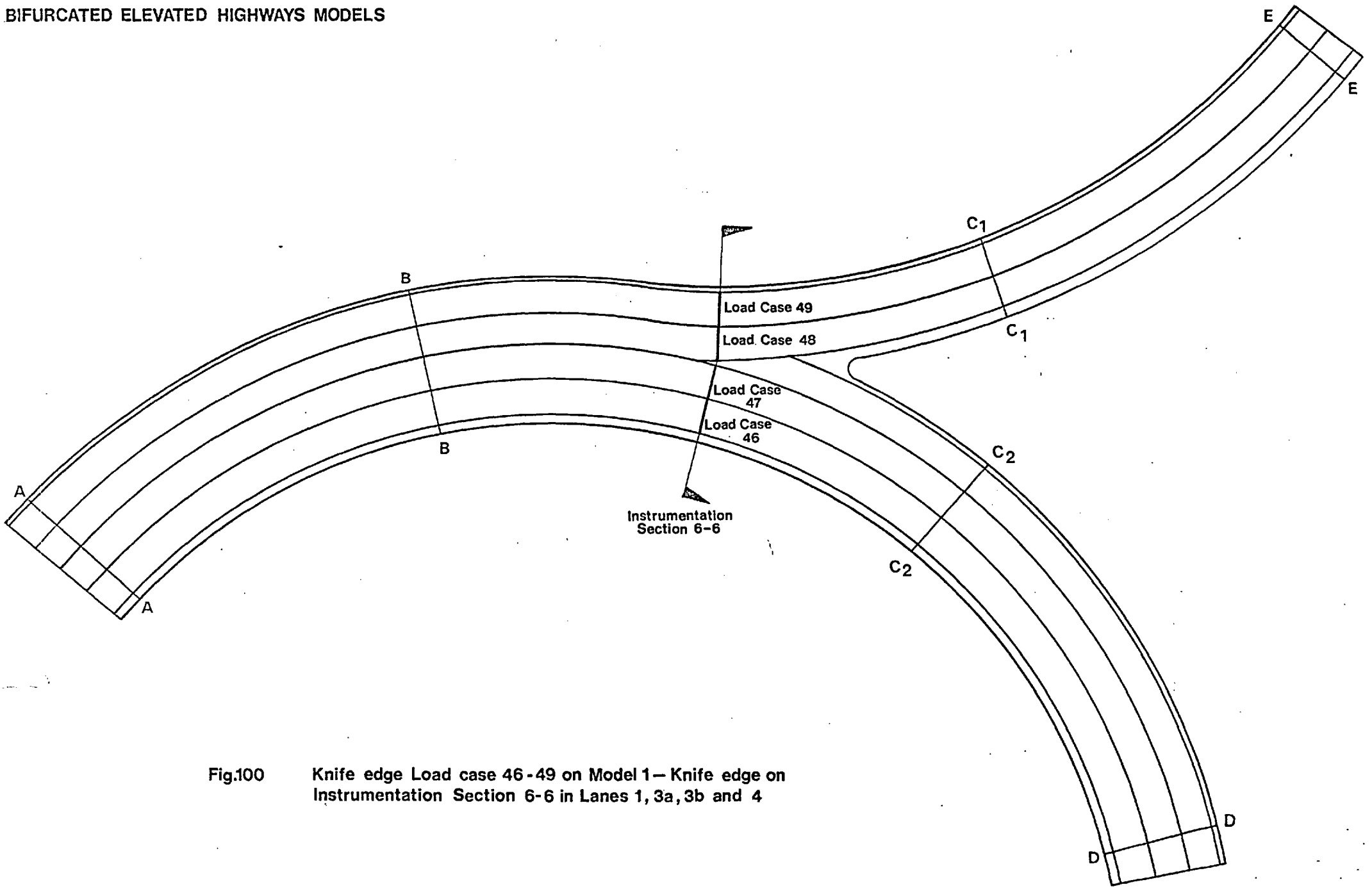


Fig.100 Knife edge Load case 46 - 49 on Model 1 — Knife edge on Instrumentation Section 6-6 in Lanes 1, 3a, 3b and 4

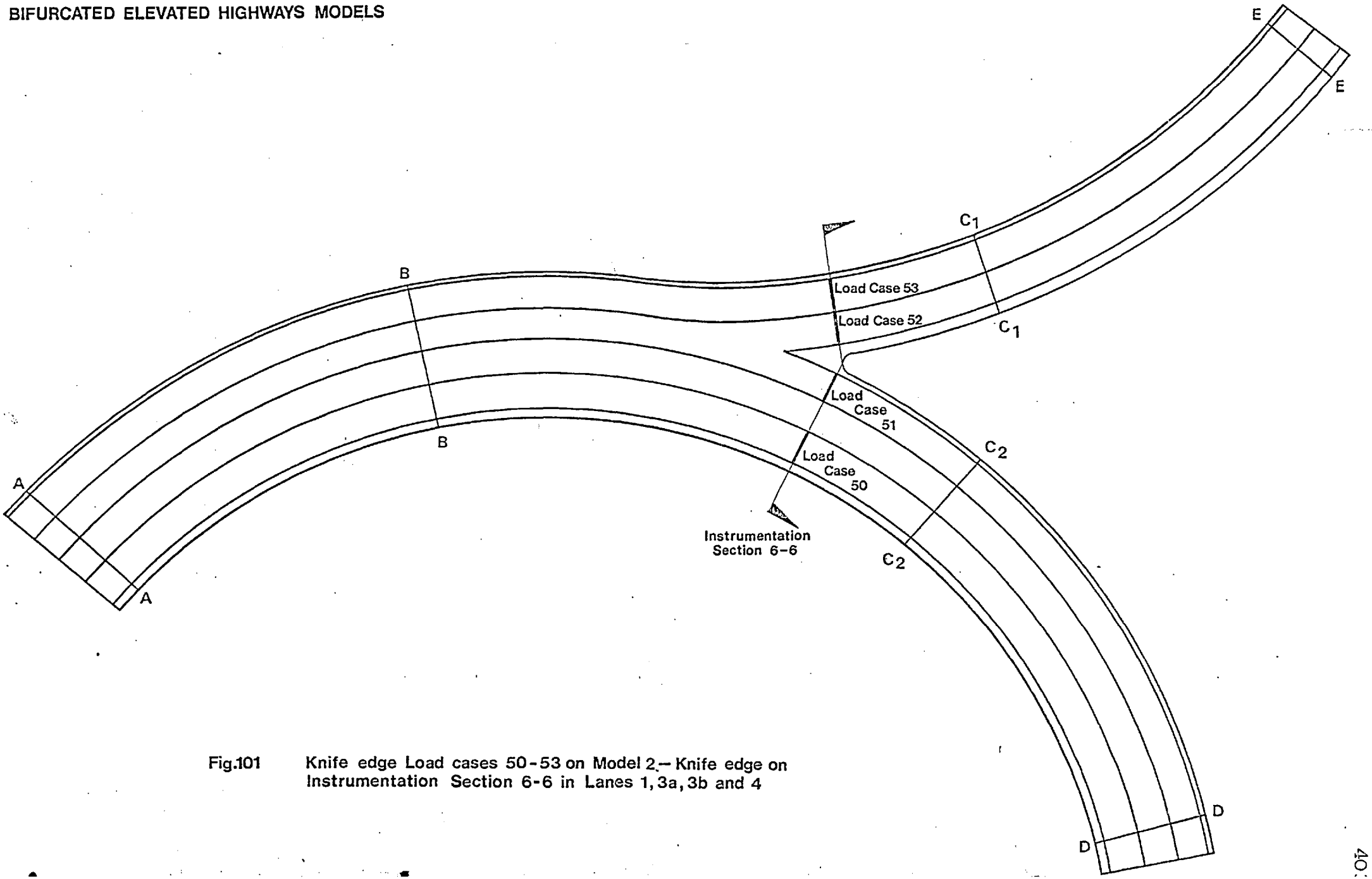


Fig.101 Knife edge Load cases 50-53 on Model 2.– Knife edge on Instrumentation Section 6-6 in Lanes 1, 3a, 3b and 4

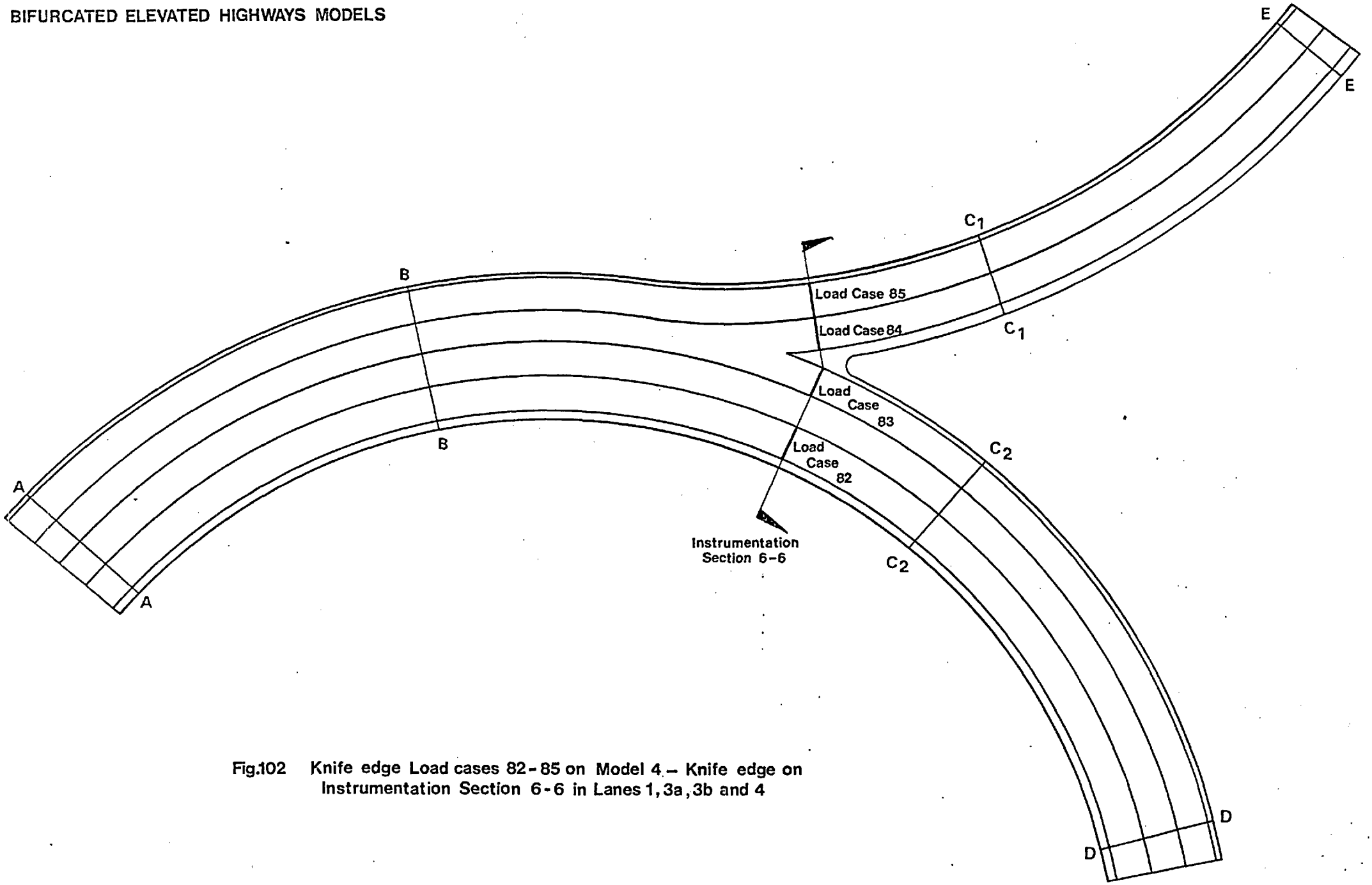


Fig.102 Knife edge Load cases 82-85 on Model 4 – Knife edge on Instrumentation Section 6-6 in Lanes 1, 3a, 3b and 4

BIFURCATED ELEVATED HIGHWAYS MODELS

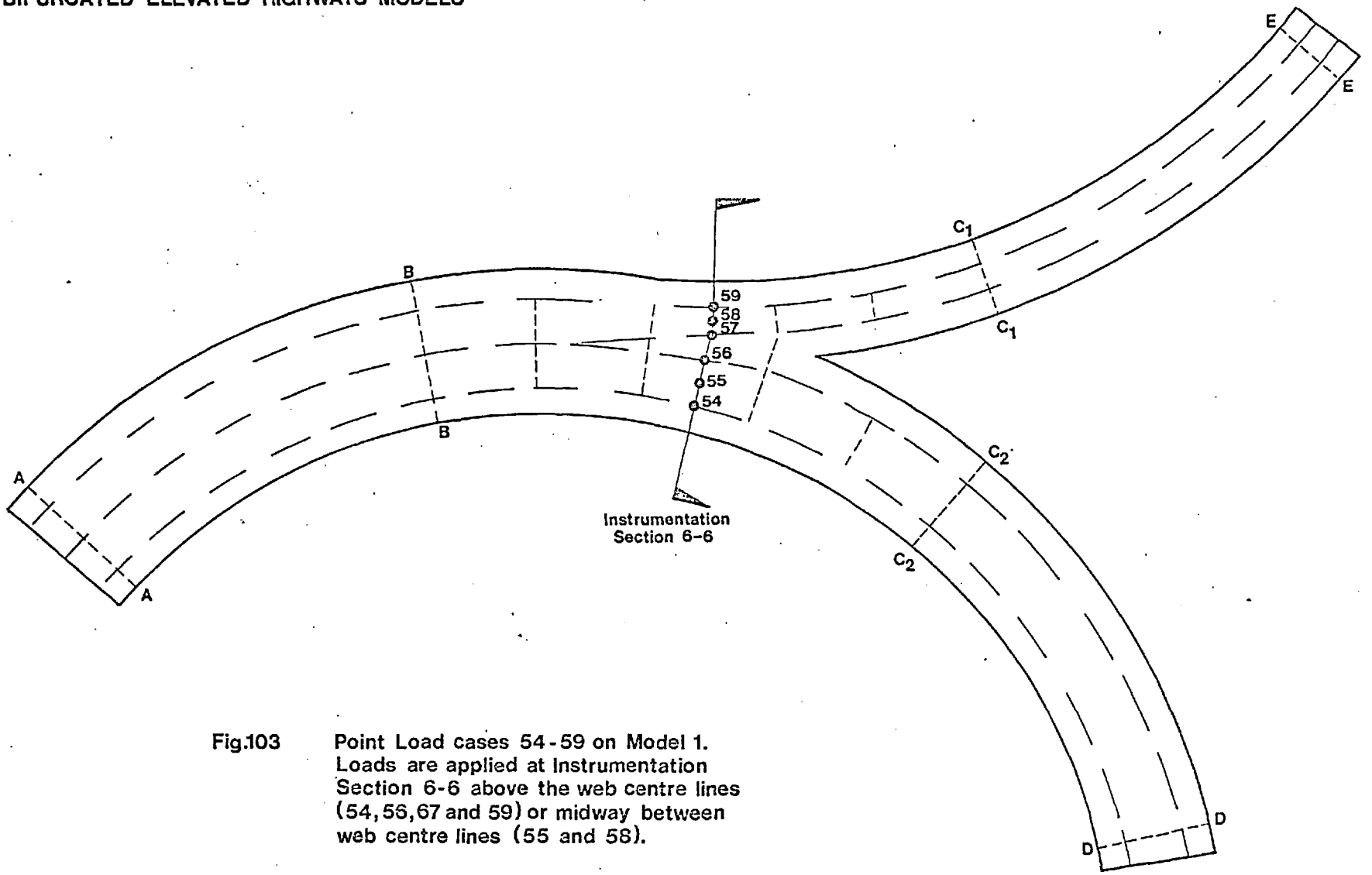


Fig.103 Point Load cases 54 - 59 on Model 1. Loads are applied at Instrumentation Section 6-6 above the web centre lines (54, 56, 67 and 59) or midway between web centre lines (55 and 58).

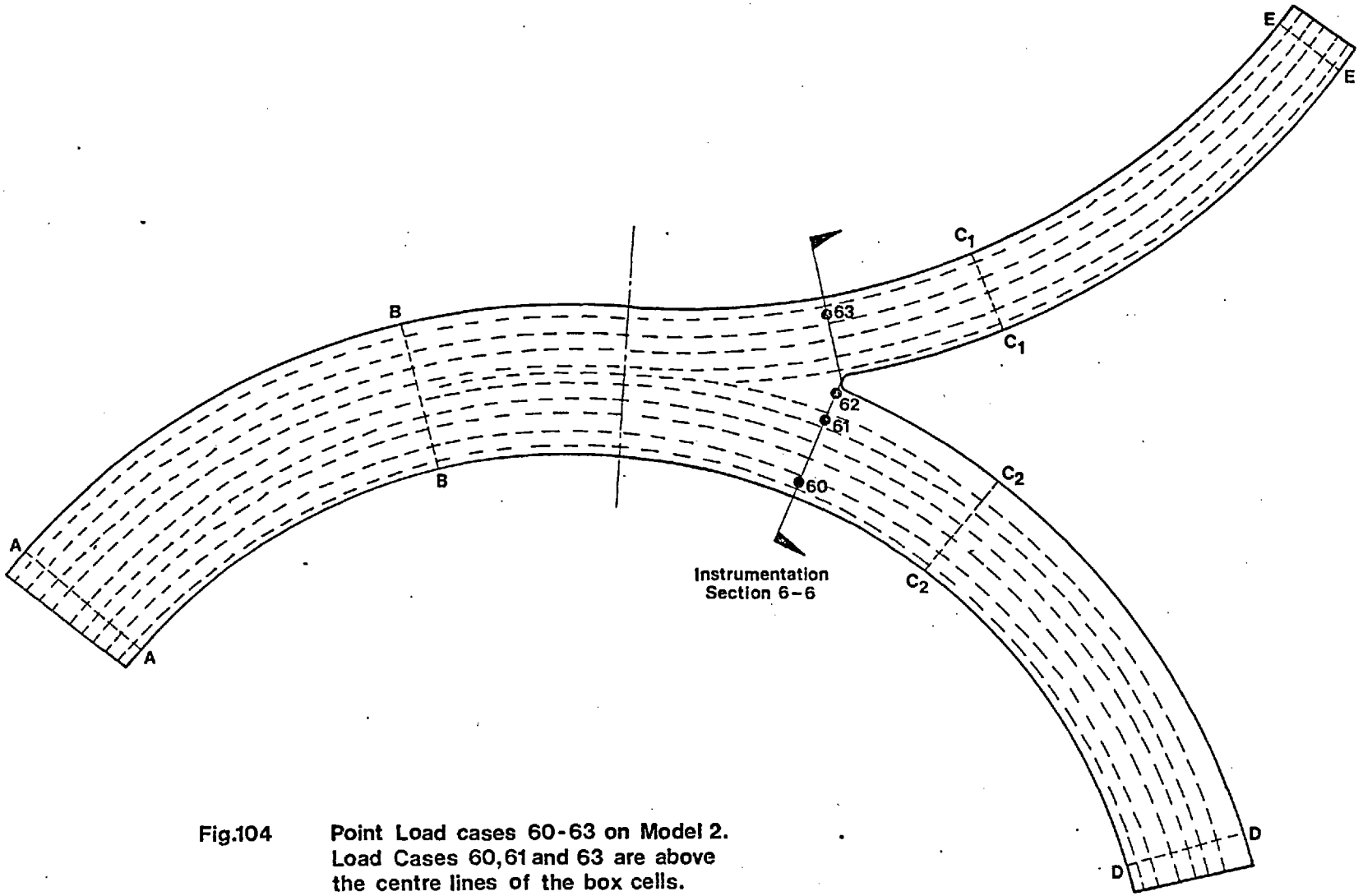


Fig.104 Point Load cases 60-63 on Model 2.
Load Cases 60,61 and 63 are above
the centre lines of the box cells.
Load 62 is above the edge of Lane 3a.
(on radius 1437mm)

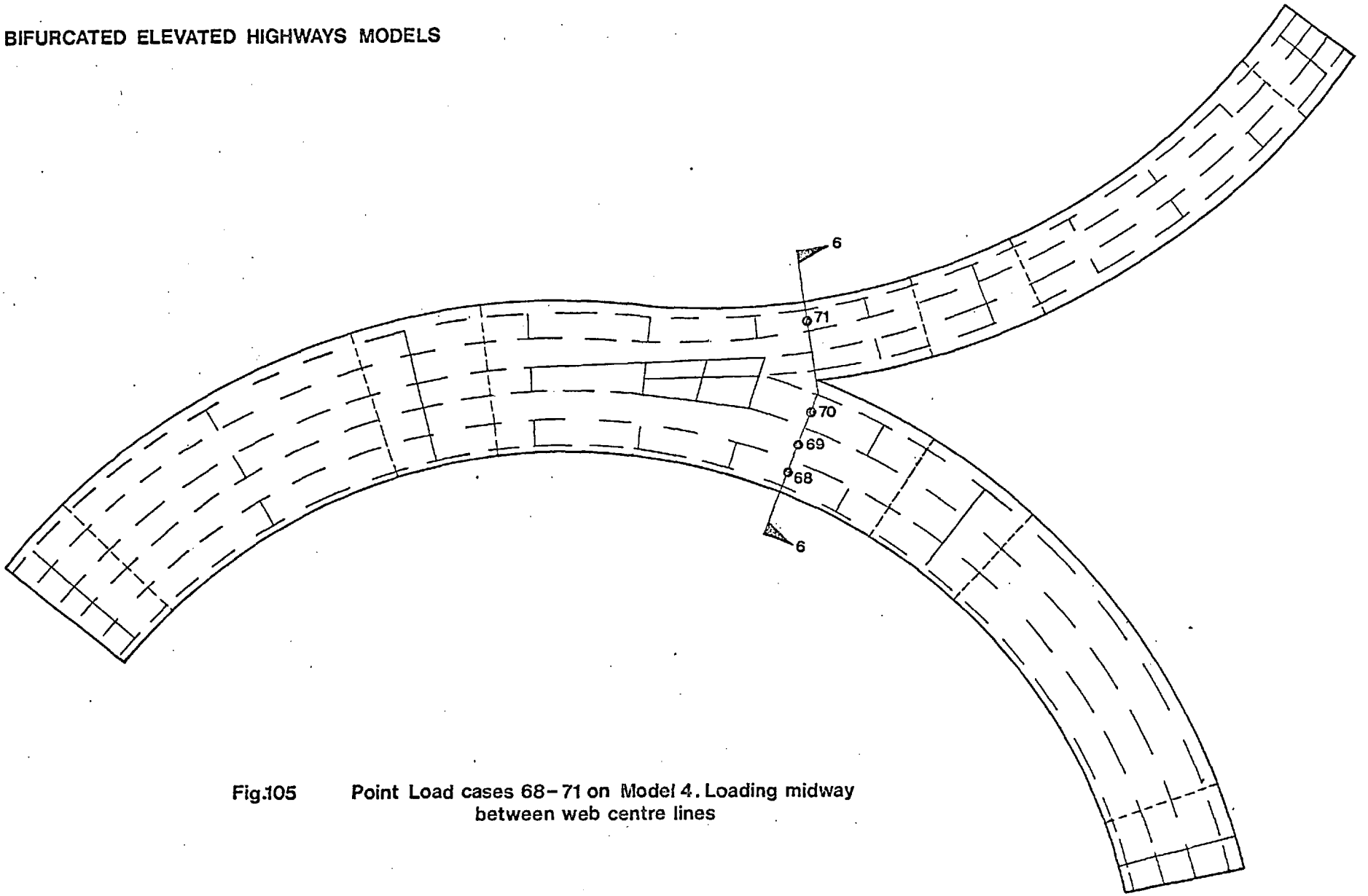


Fig.105 Point Load cases 68–71 on Model 4. Loading midway between web centre lines

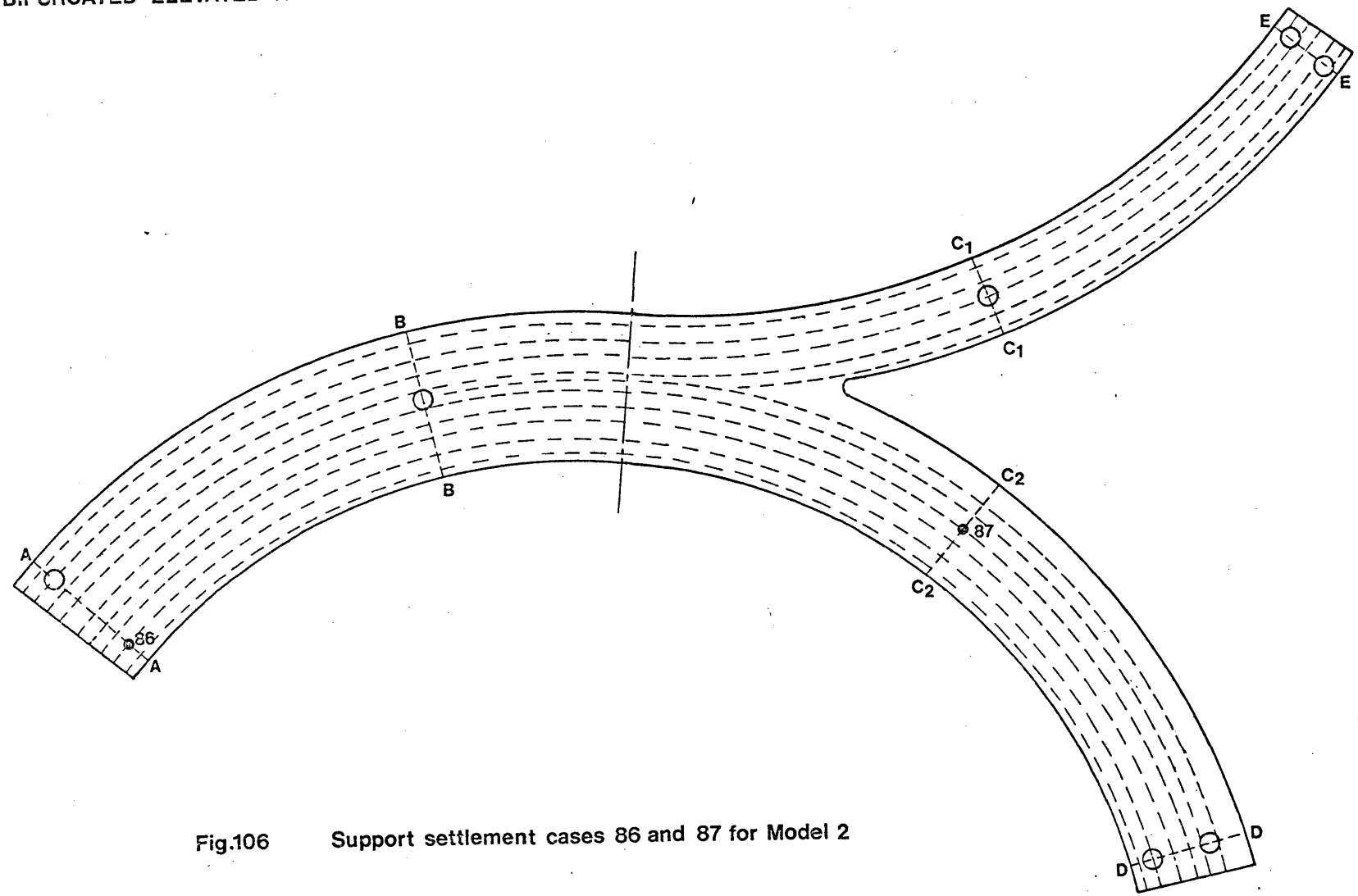


Fig.106 Support settlement cases 86 and 87 for Model 2

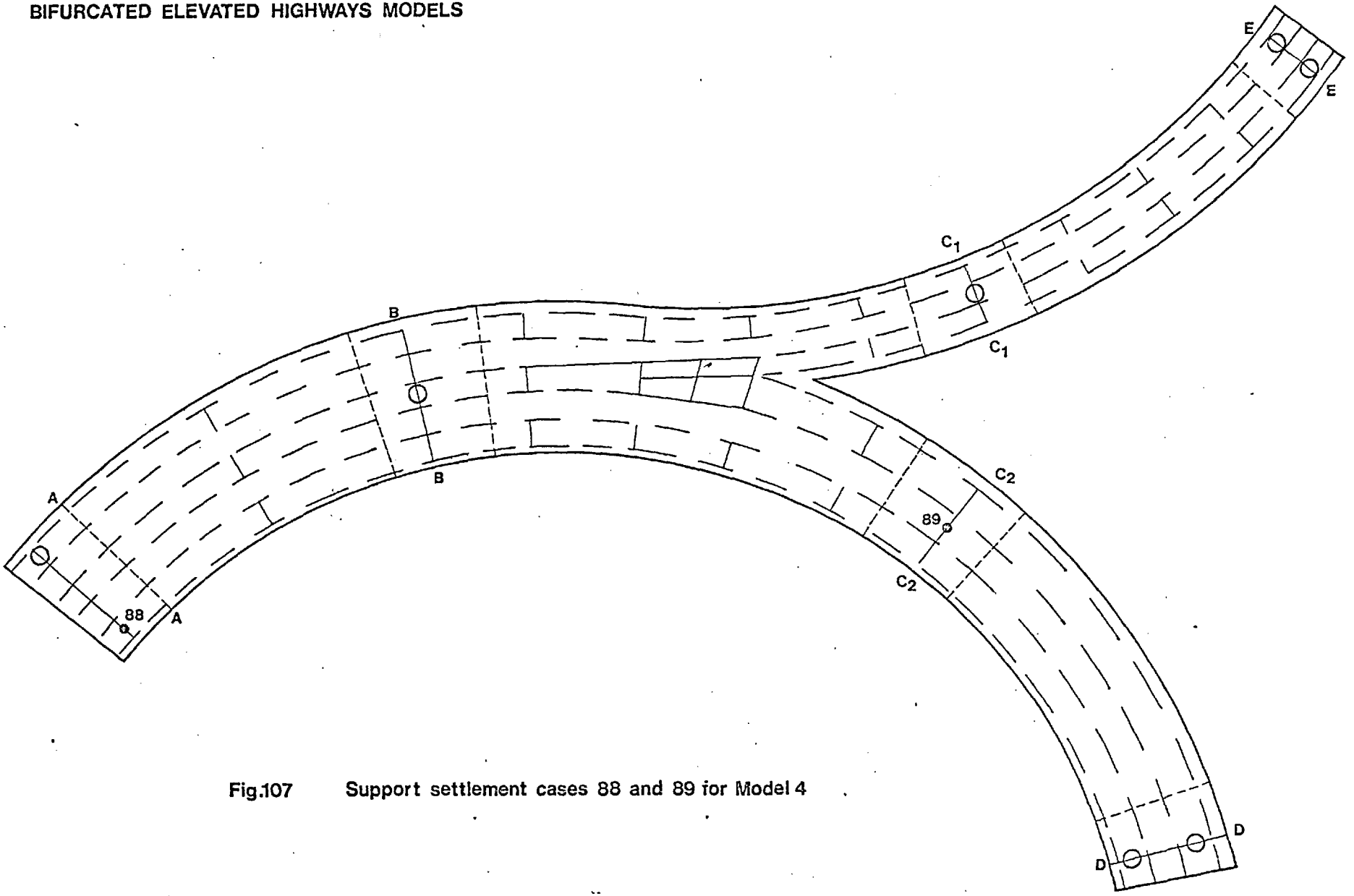


Fig.107 Support settlement cases 88 and 89 for Model 4

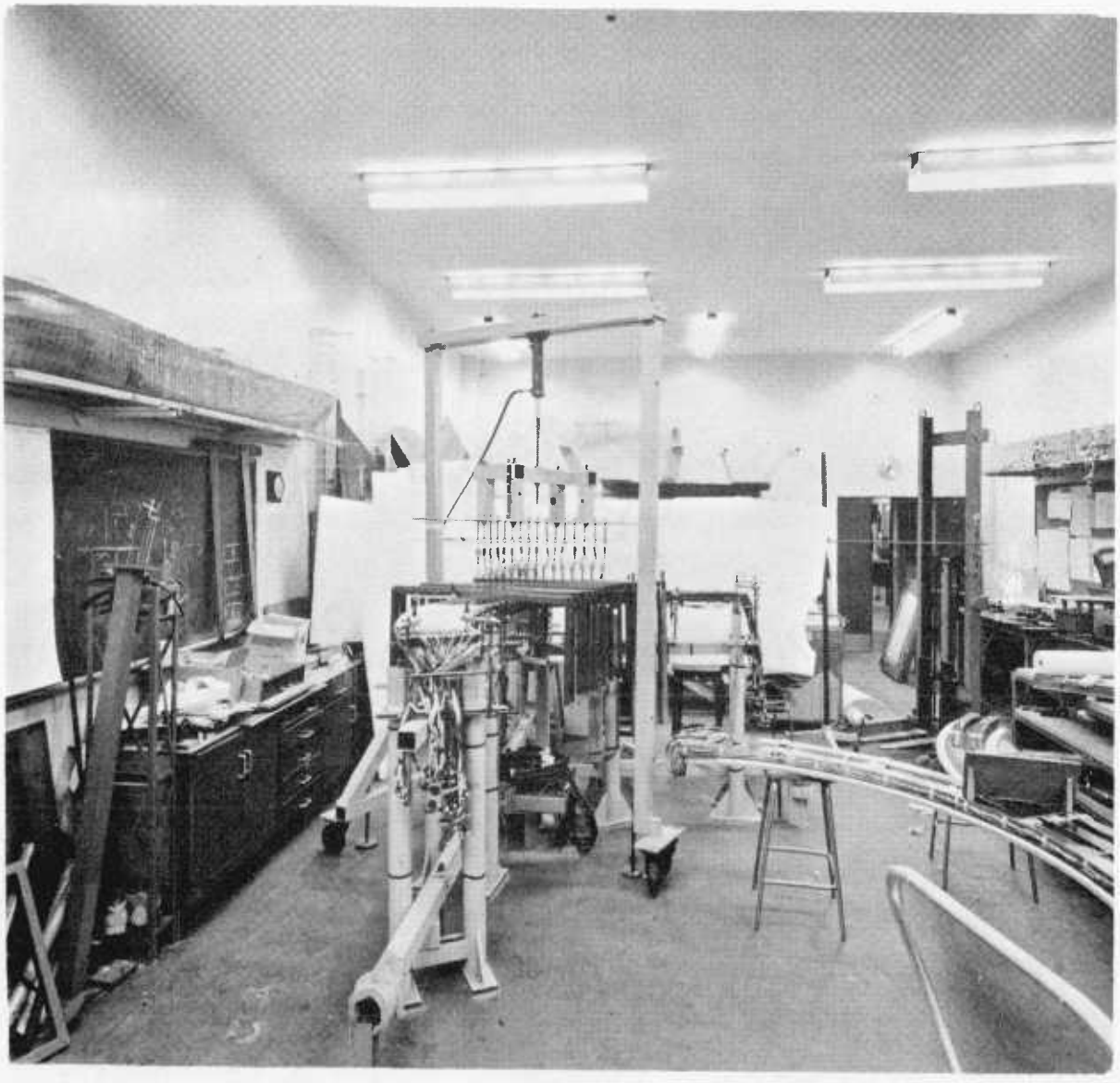


Fig.108 General view of testing arrangement
BIFURCATED ELEVATED HIGHWAYS MODELS

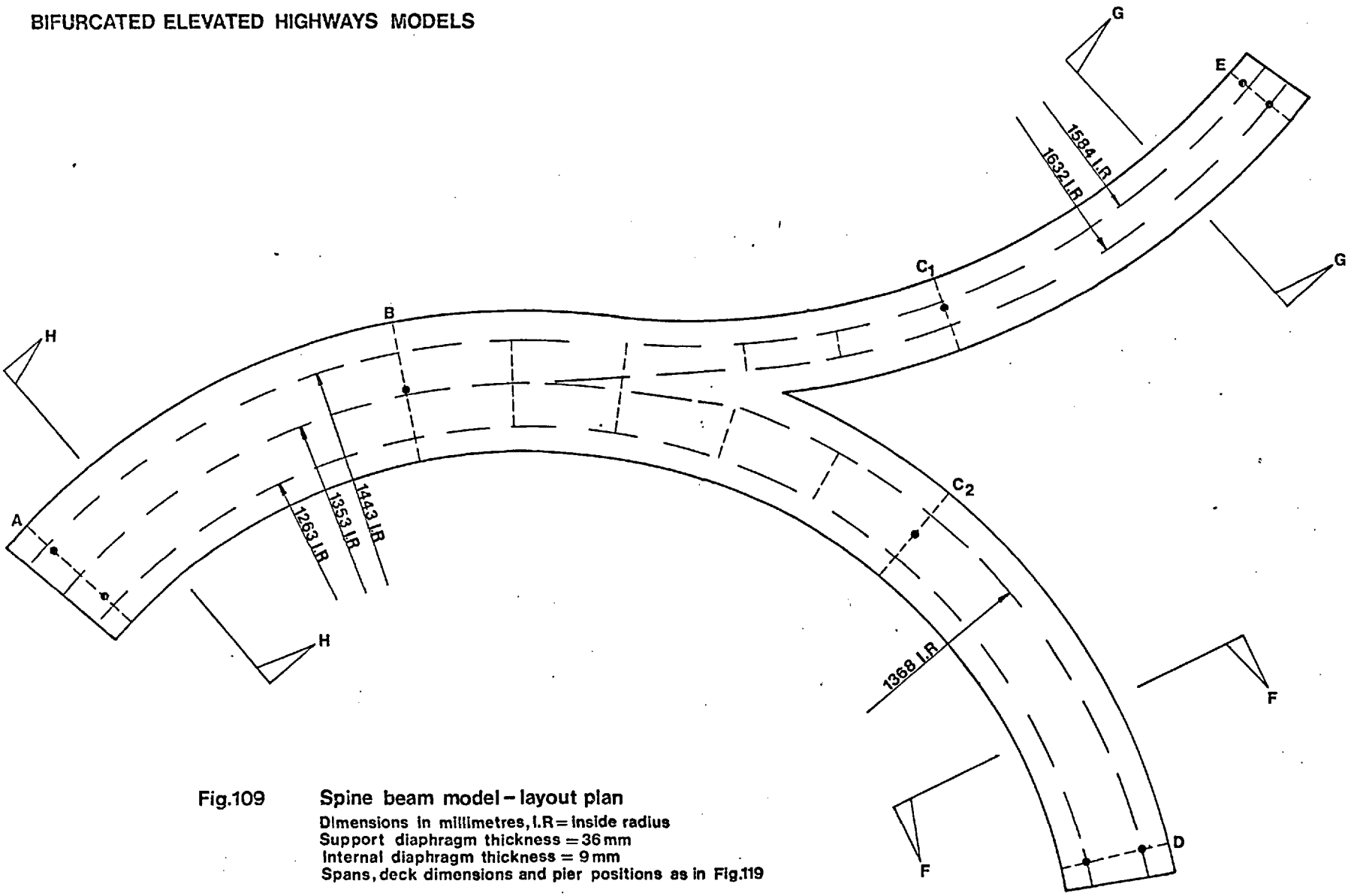


Fig.109 **Spine beam model – layout plan**

Dimensions in millimetres, I.R = inside radius
Support diaphragm thickness = 36 mm
Internal diaphragm thickness = 9 mm
Spans, deck dimensions and pier positions as in Fig.119

BIFURCATED ELEVATED HIGHWAYS MODELS

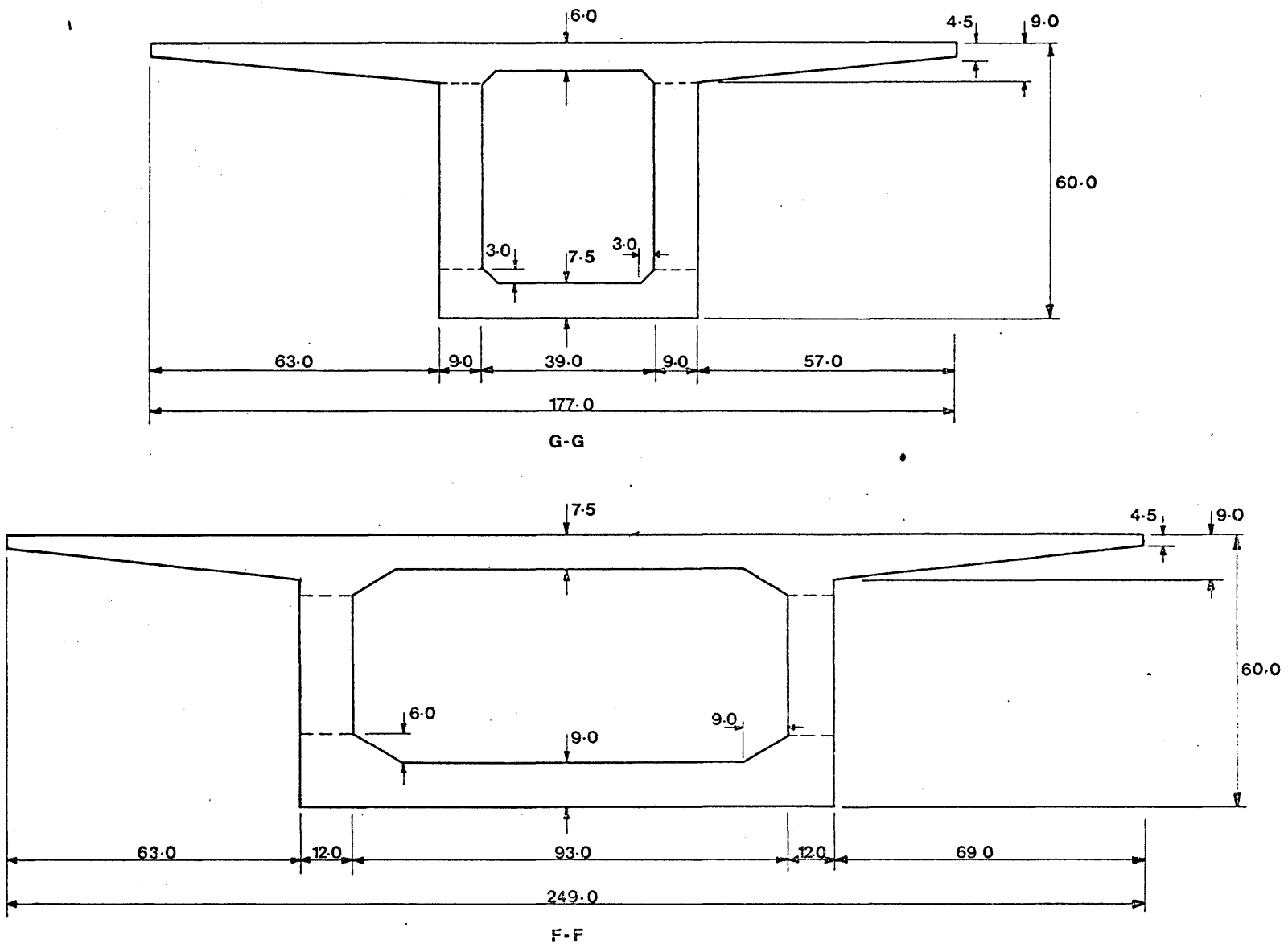


Fig.110 Spine beam model - Cross Sections F-F and G-G (Dimensions in millimeters)

BIFURCATED ELEVATED HIGHWAYS MODELS

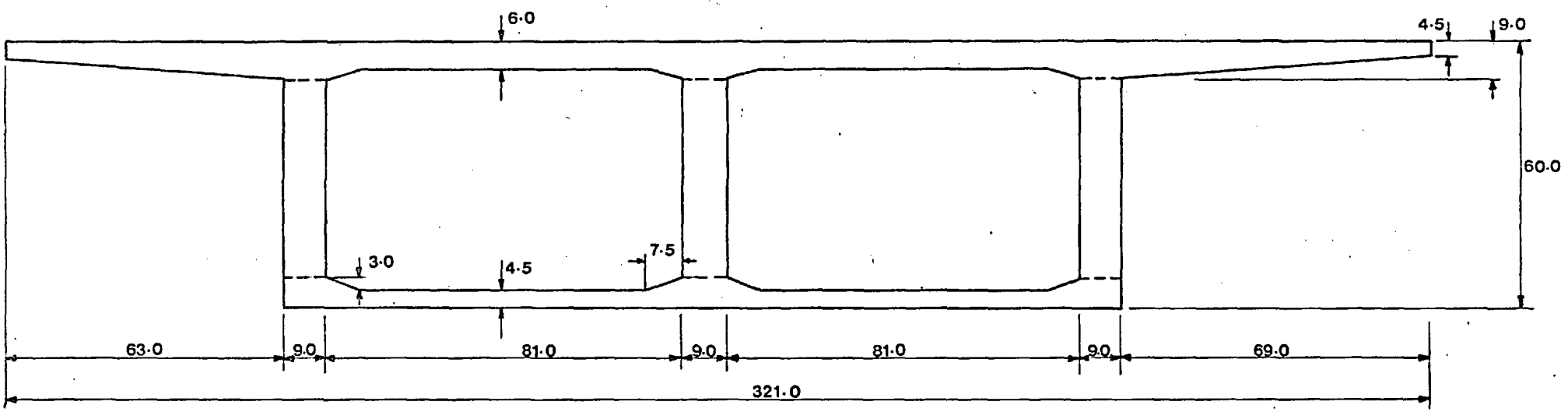


Fig.111 Spine beam model - Cross Section H-H (Dimensions in millimetres)

BIFURCATED ELEVATED HIGHWAYS MODELS

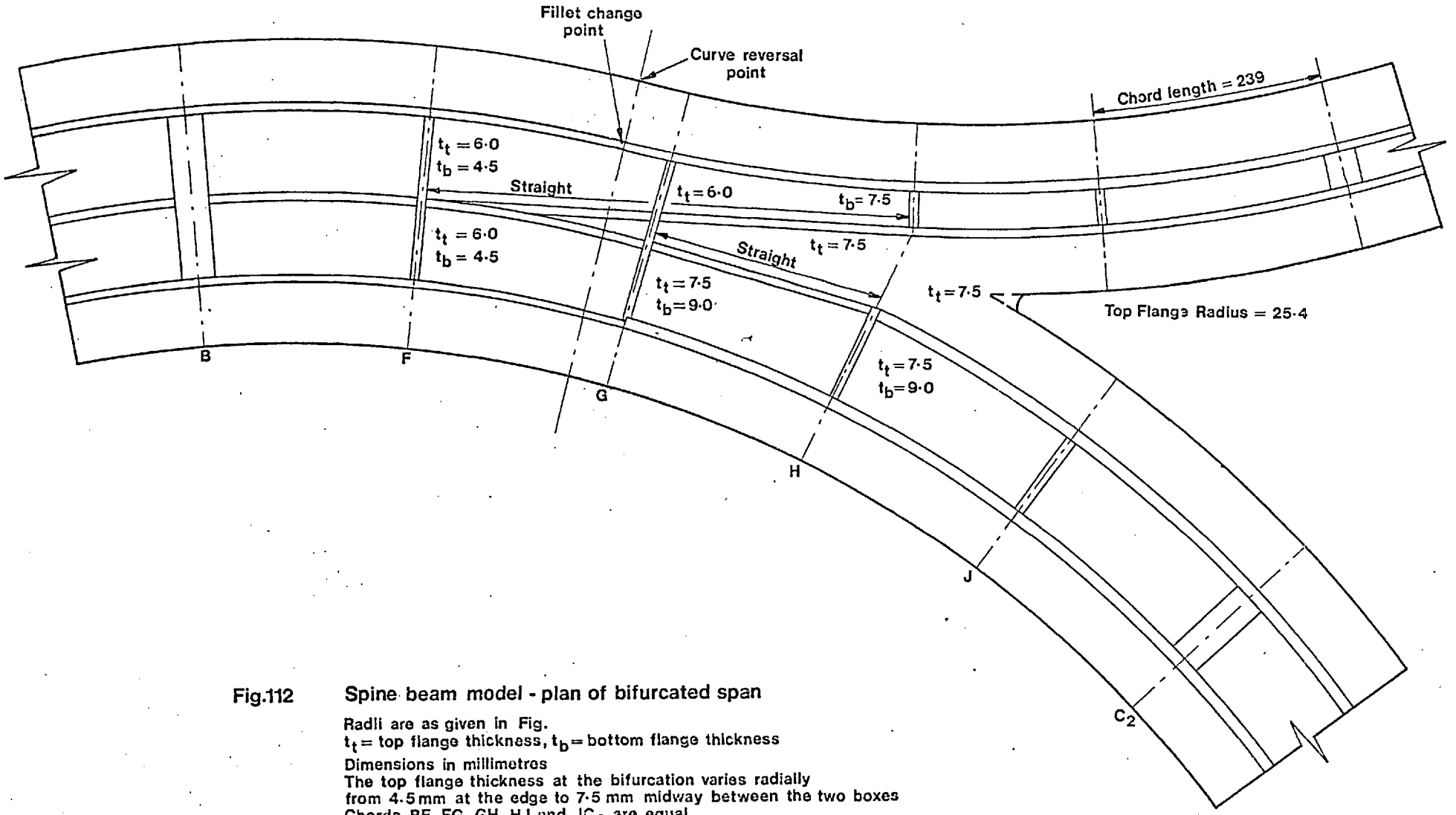


Fig.112 Spine beam model - plan of bifurcated span

Radii are as given in Fig.
t_t = top flange thickness, t_b = bottom flange thickness
Dimensions in millimetres
The top flange thickness at the bifurcation varies radially from 4·5 mm at the edge to 7·5 mm midway between the two boxes
Chords BF, FG, GH, HJ and JC_2 are equal

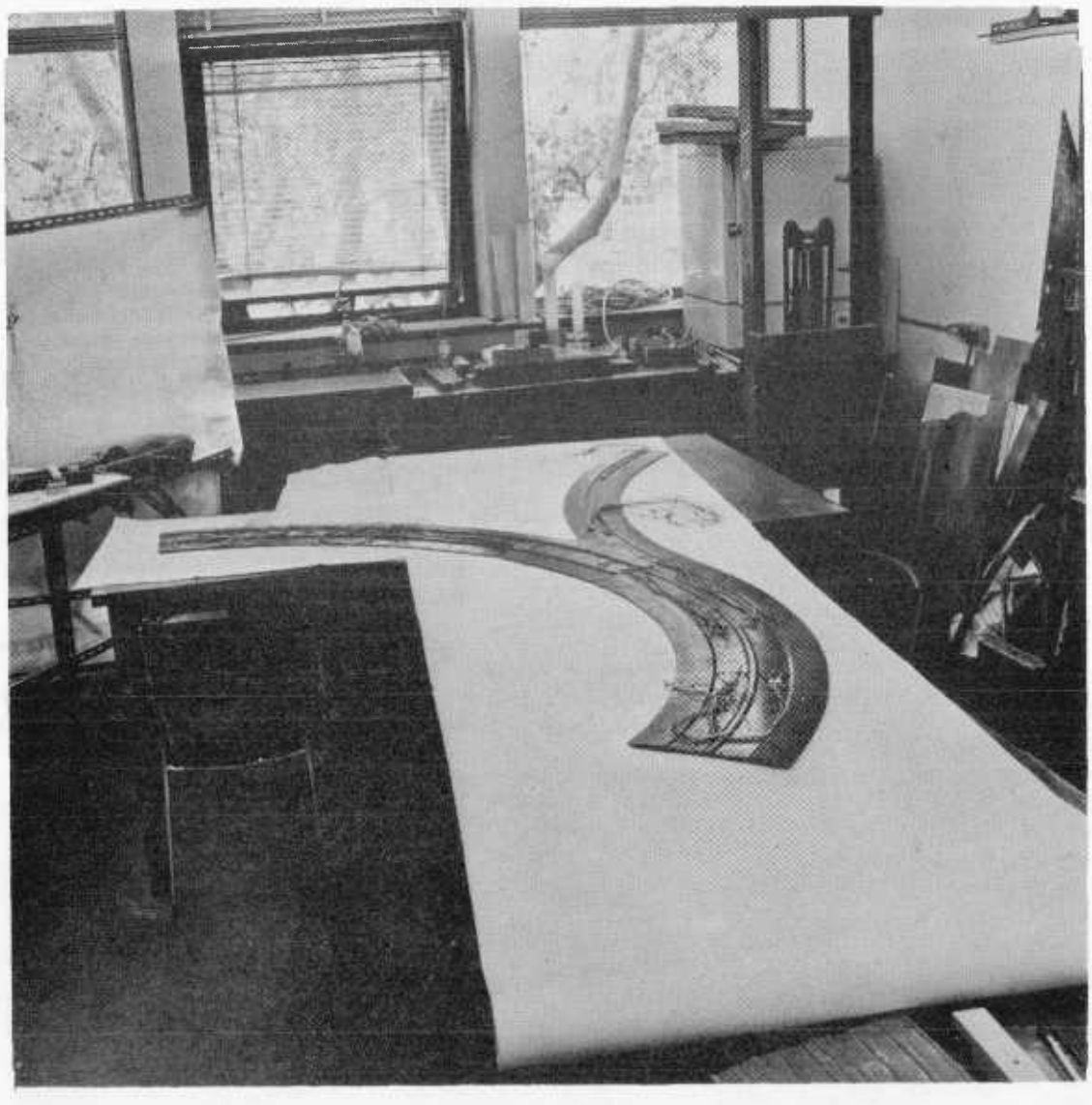


Fig.113 Model 1 - underside of instrumented top flange casting

BIFURCATED ELEVATED HIGHWAYS MODELS

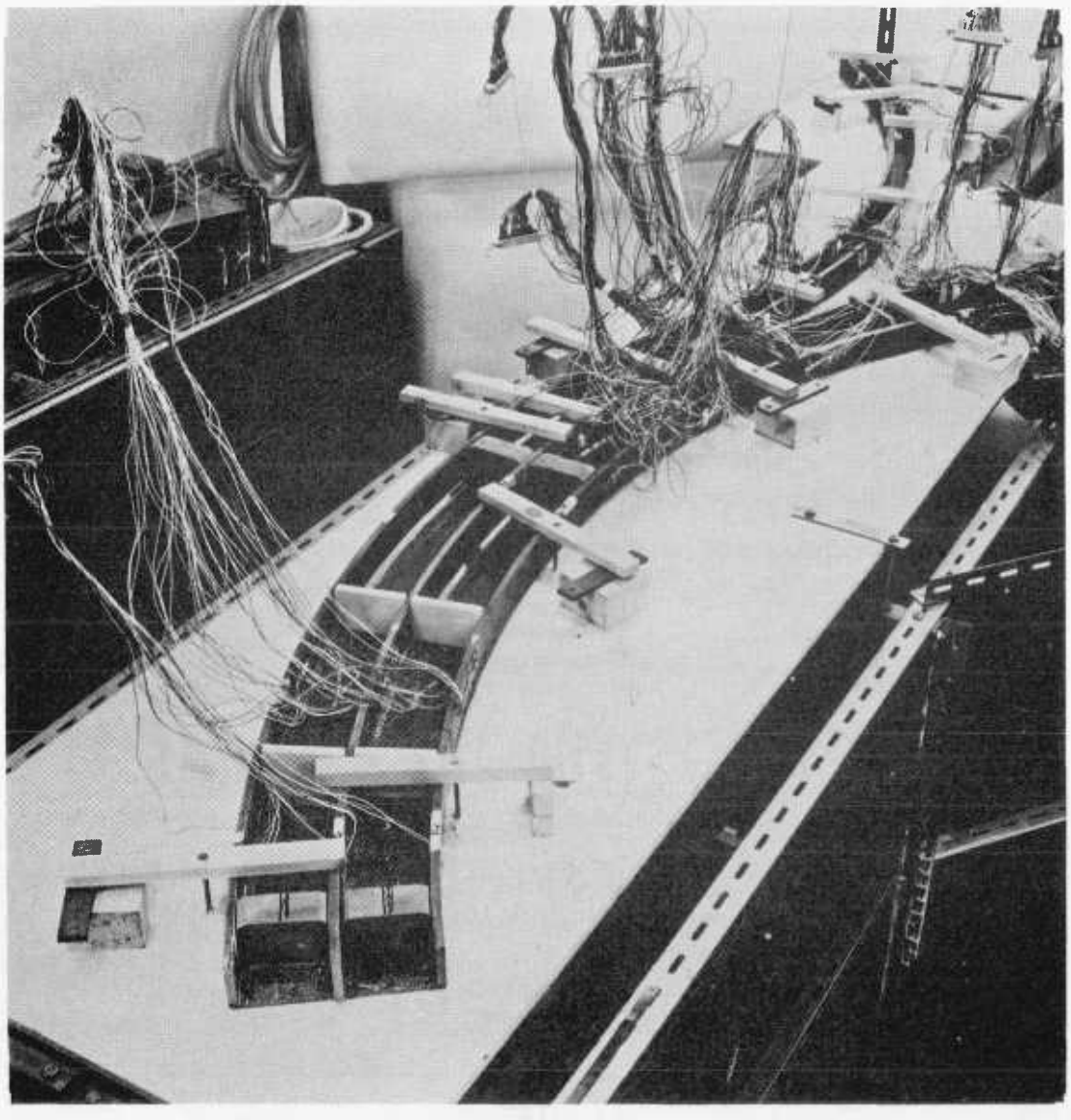


Fig.114 Model 1 during assembly. At this stage the webs are being bonded to the bottom flange. The wooden spaces and clamps are removed after glueing.

BIFURCATED ELEVATED HIGHWAYS MODELS

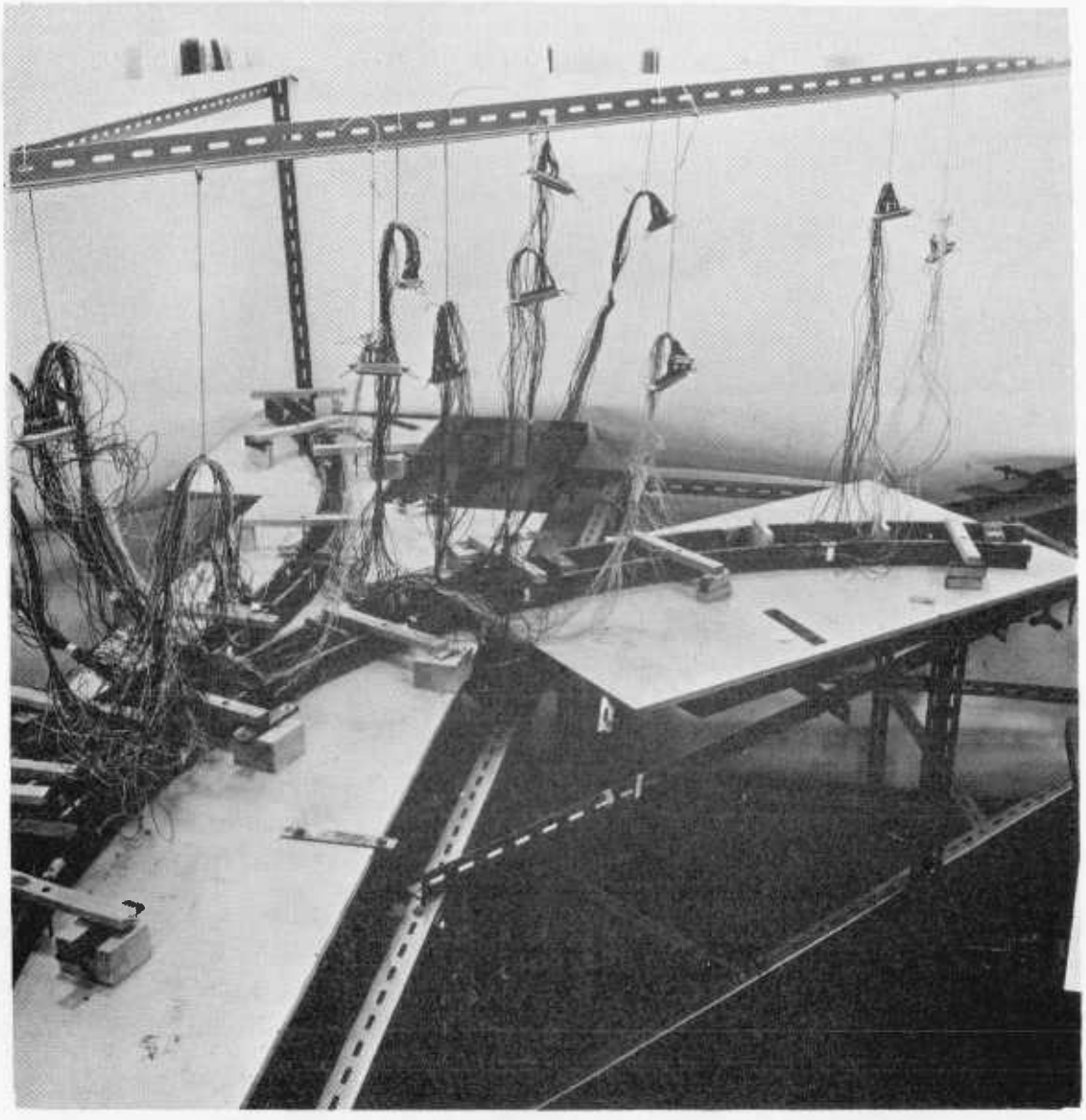


Fig.115 Model 1 during assembly
BIFURCATED ELEVATED HIGHWAYS MODELS

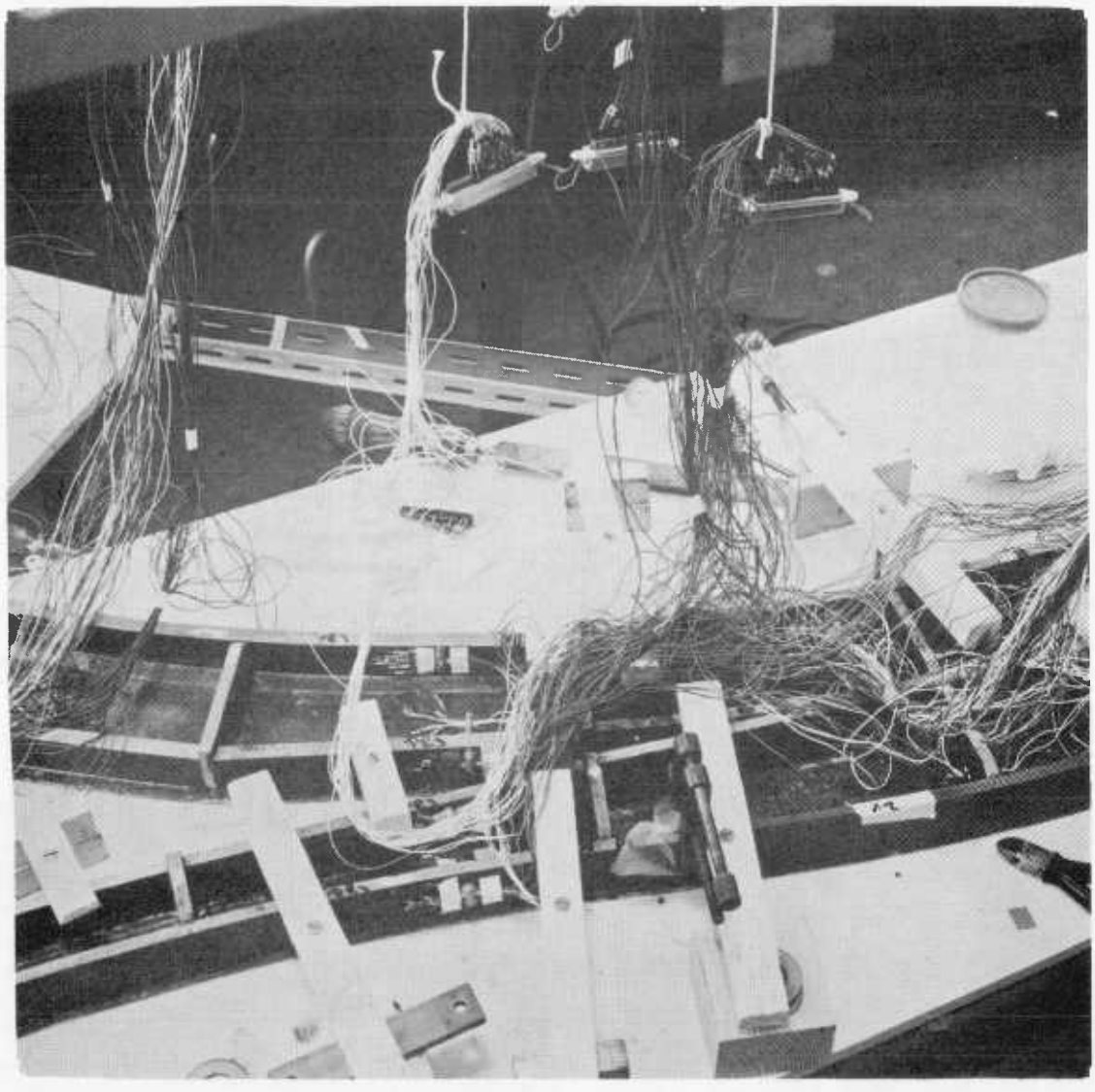


Fig.116 Model 1 during assembly, showing bifurcation
BIFURCATED ELEVATED HIGHWAYS MODELS

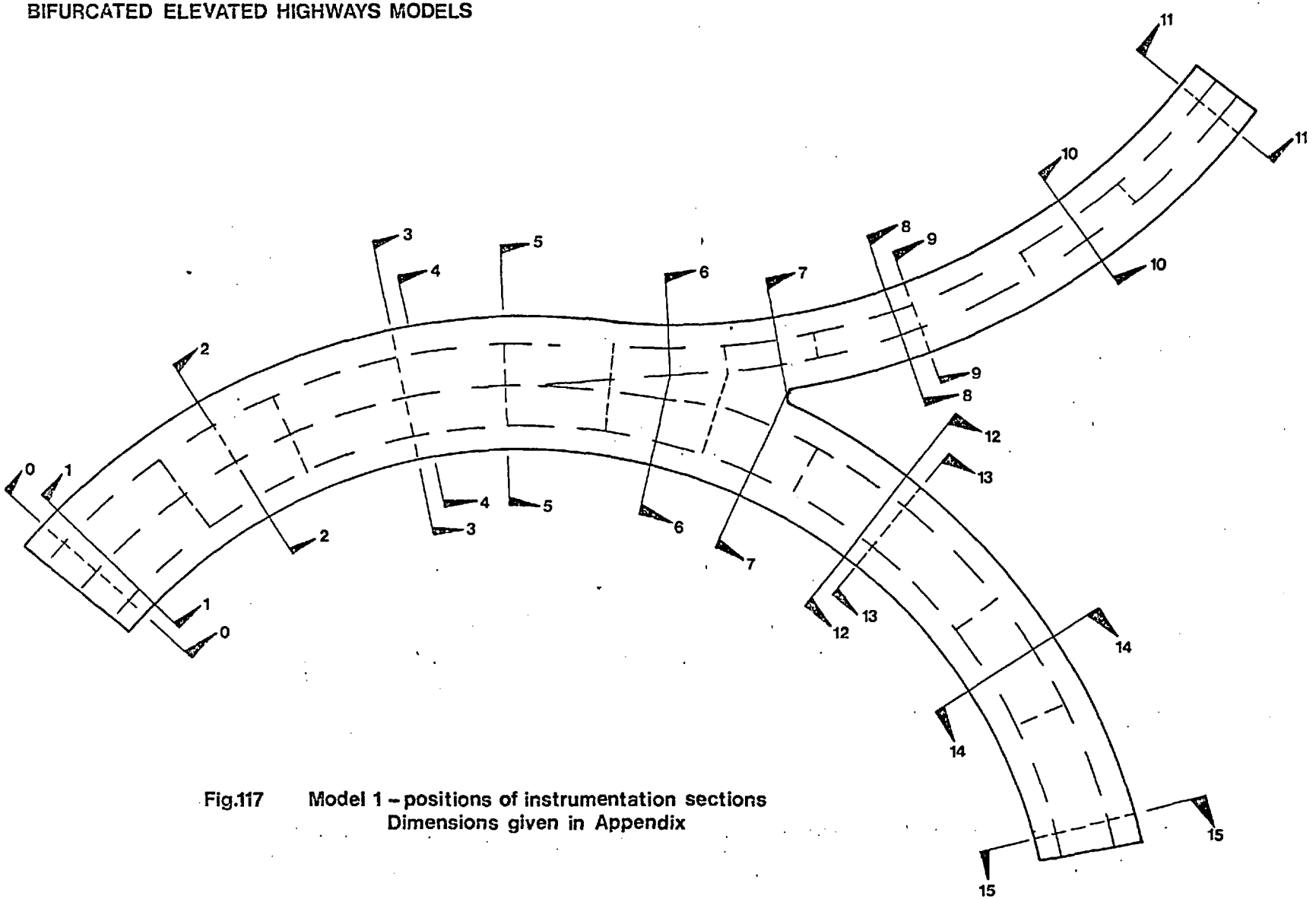


Fig.117 Model 1 – positions of instrumentation sections
Dimensions given in Appendix

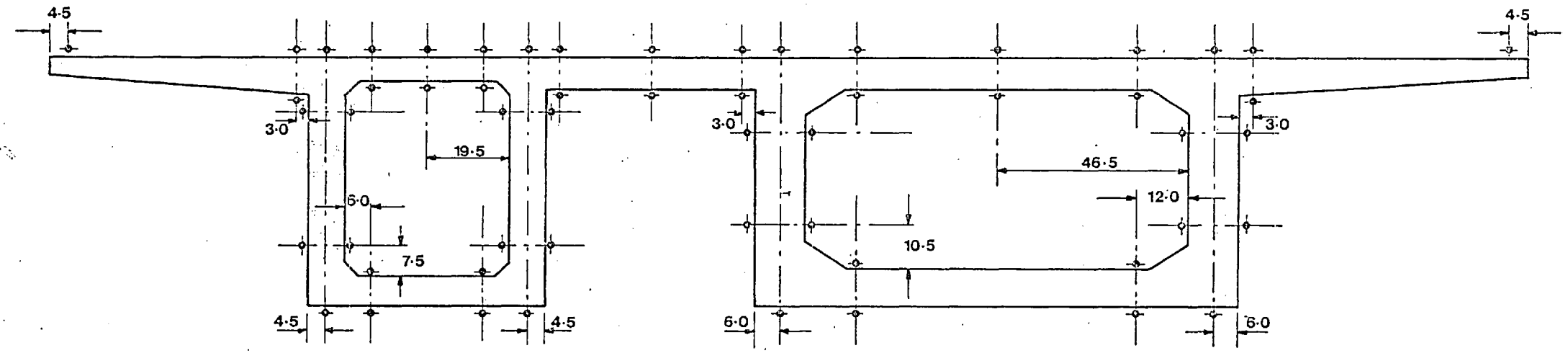


Fig.118 Longitudinal strain gauge element positions and numbering at Instrumentation Section 6-6

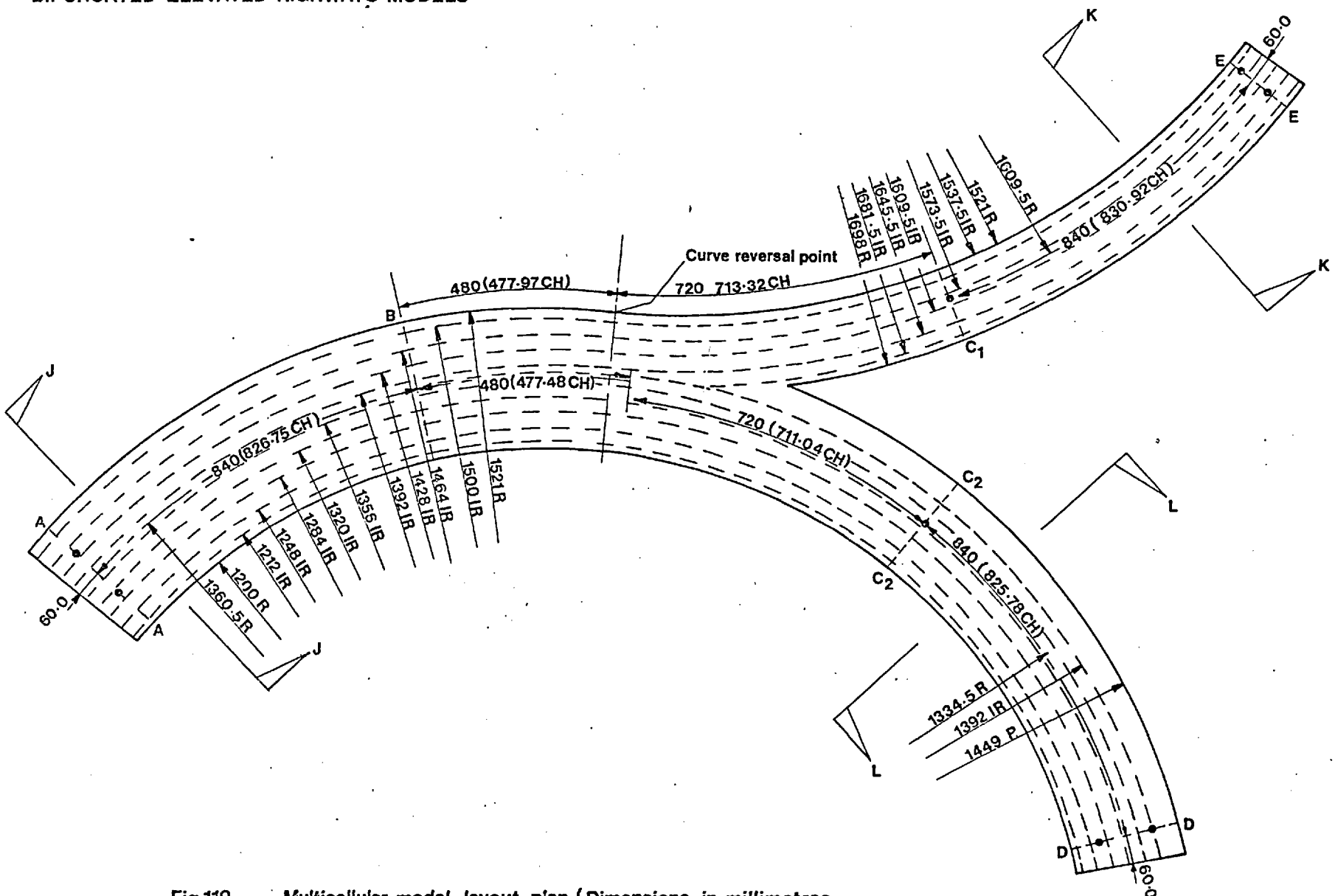
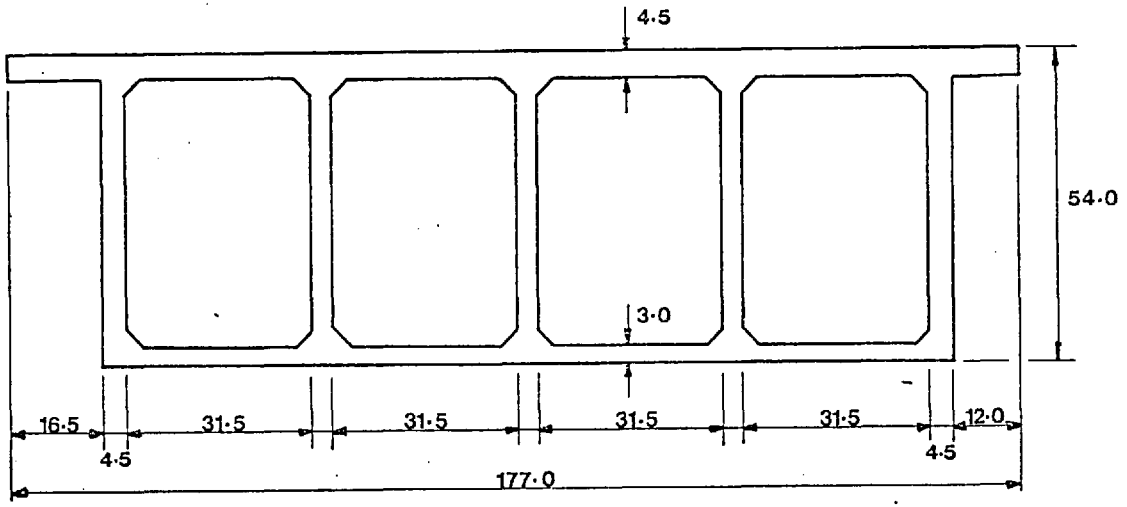
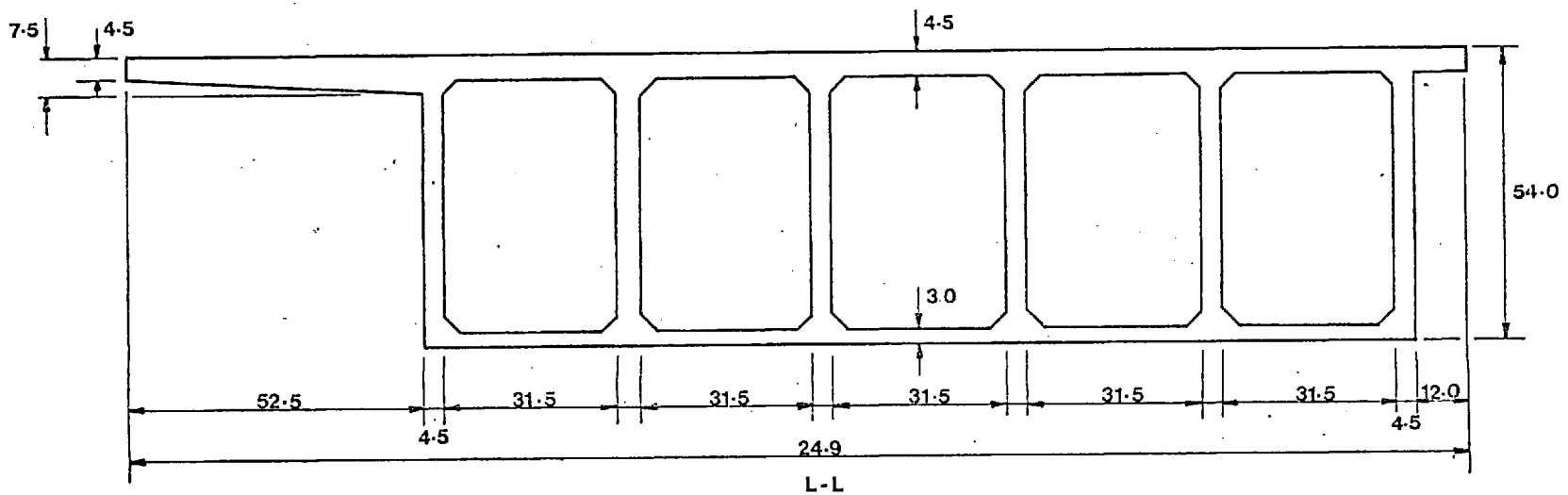


Fig.119 Multicellular model layout plan (Dimensions in millimetres, I.R.= inside radius). Support diaphragm thickness=36mm

BIFURCATED ELEVATED HIGHWAYS MODELS



K-K



L-L

Fig. 4.25 11 Hinged model - Cross Sections K-K and L-L (Dimensions in millimetres)

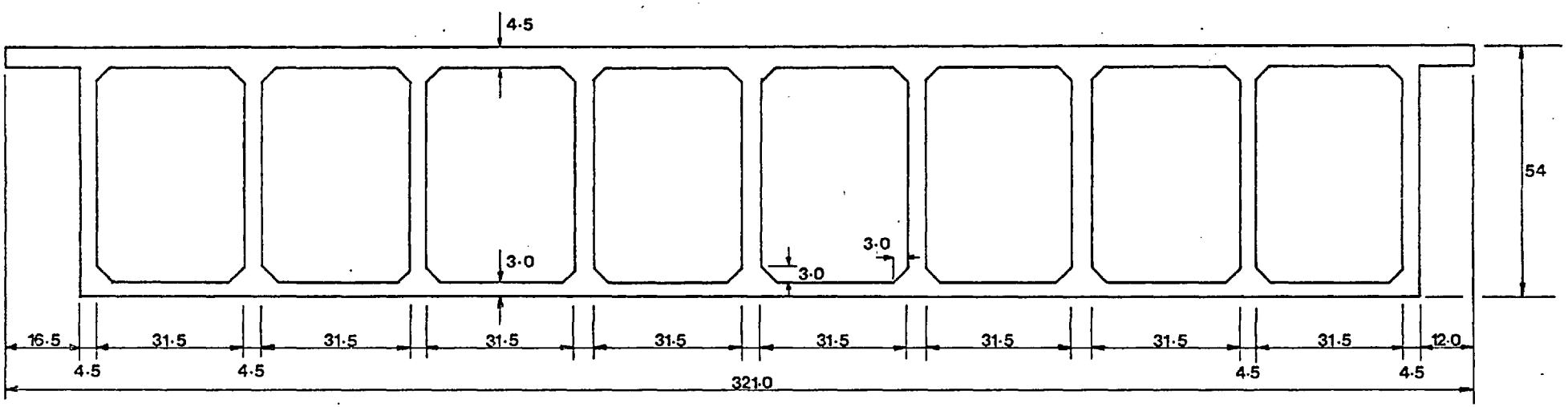
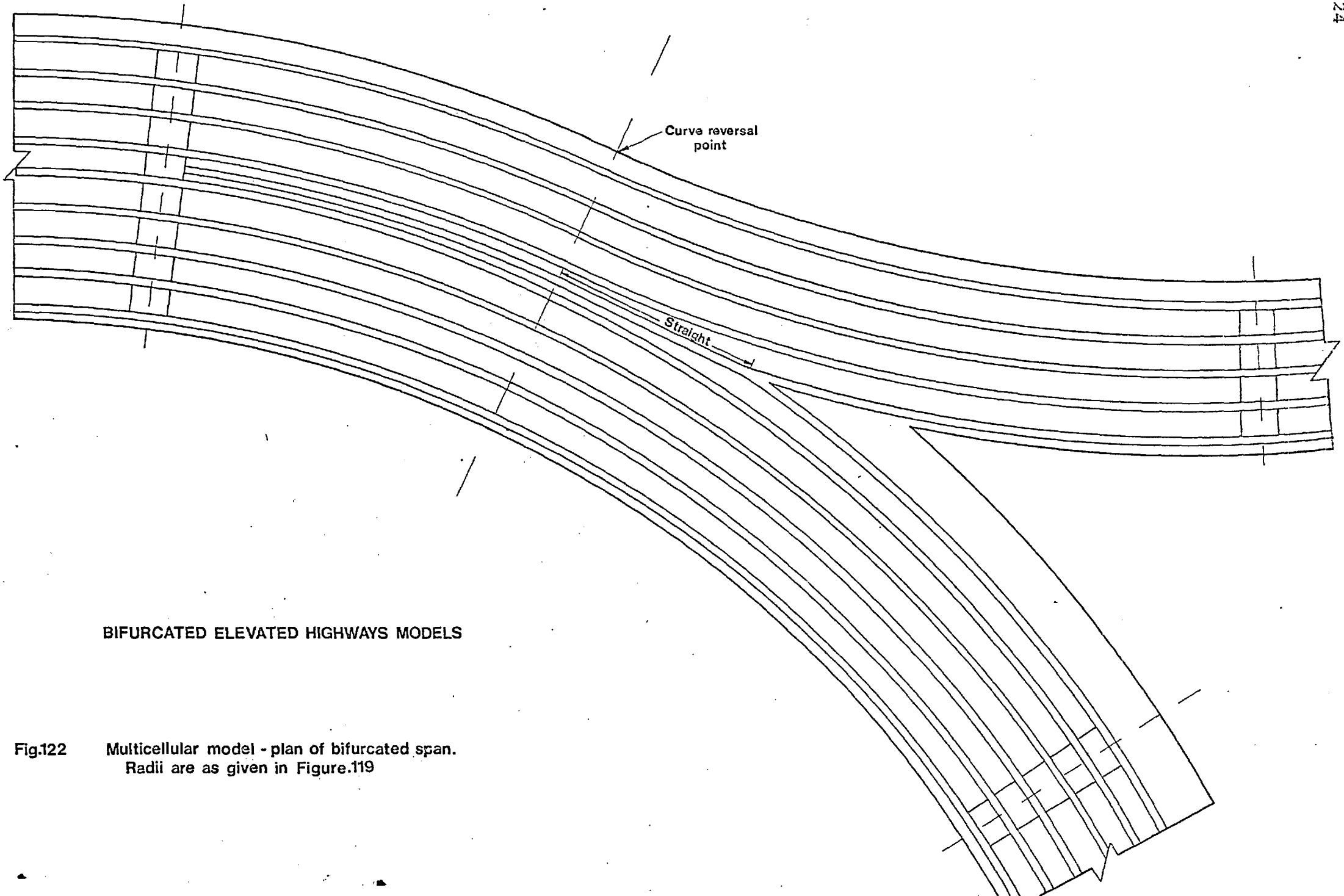


Fig.121 Multicellular model - Cross Section J-J (Dimensions in millimetres)



BIFURCATED ELEVATED HIGHWAYS MODELS

Fig.122 Multicellular model - plan of bifurcated span. Radii are as given in Figure.119

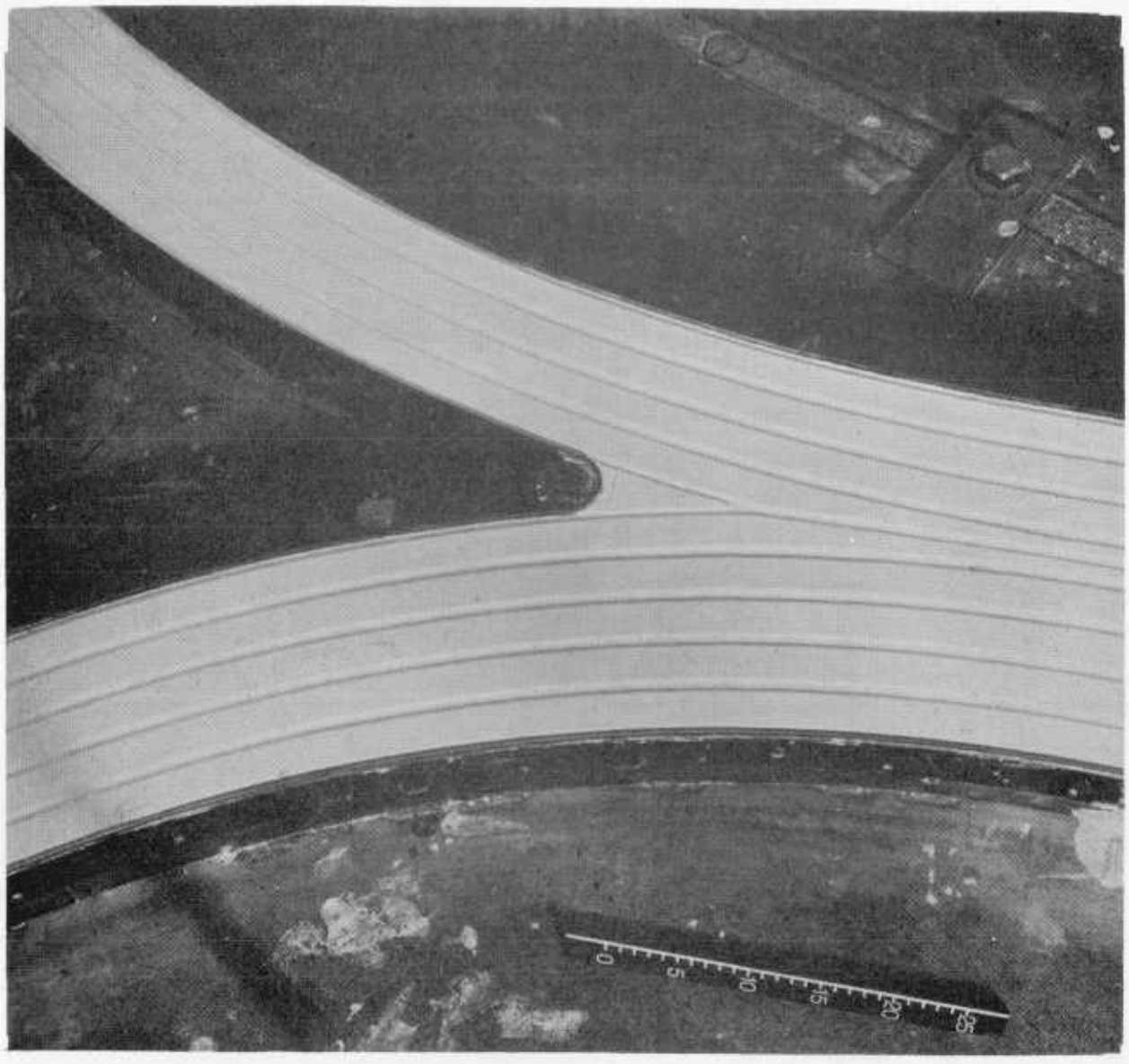


Fig.123 Multicellular model - bottom flange mould at bifurcation
BIFURCATED ELEVATED HIGHWAYS MODELS



Fig.124 Casting multicellular model
BIFURCATED ELEVATED HIGHWAYS MODELS



Fig.125 Casting multicellular model
BIFURCATED ELEVATED HIGHWAYS MODELS

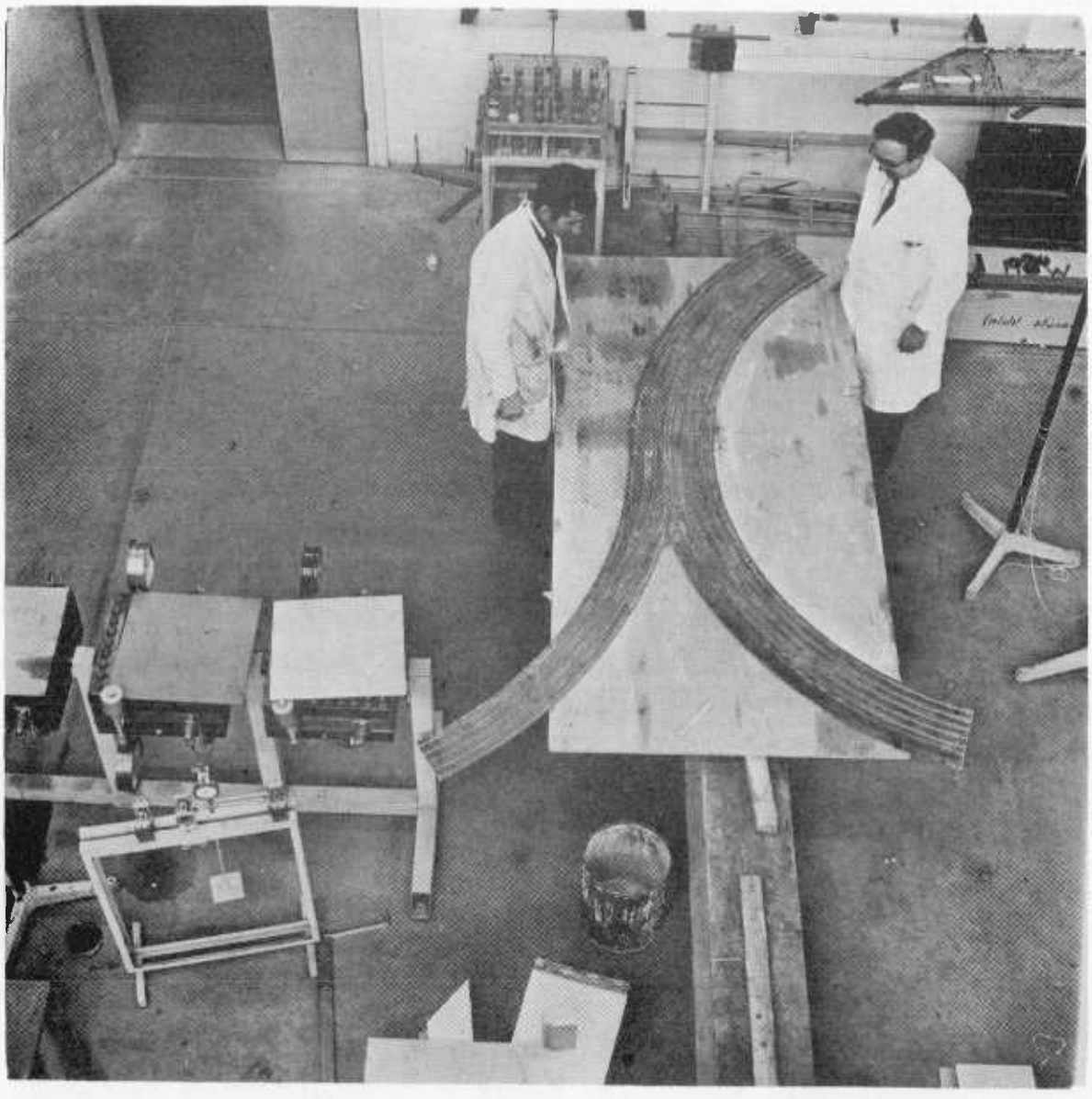


Fig.126 Multicellular model - underside of top flange casting
BIFURCATED ELEVATED HIGHWAYS MODELS

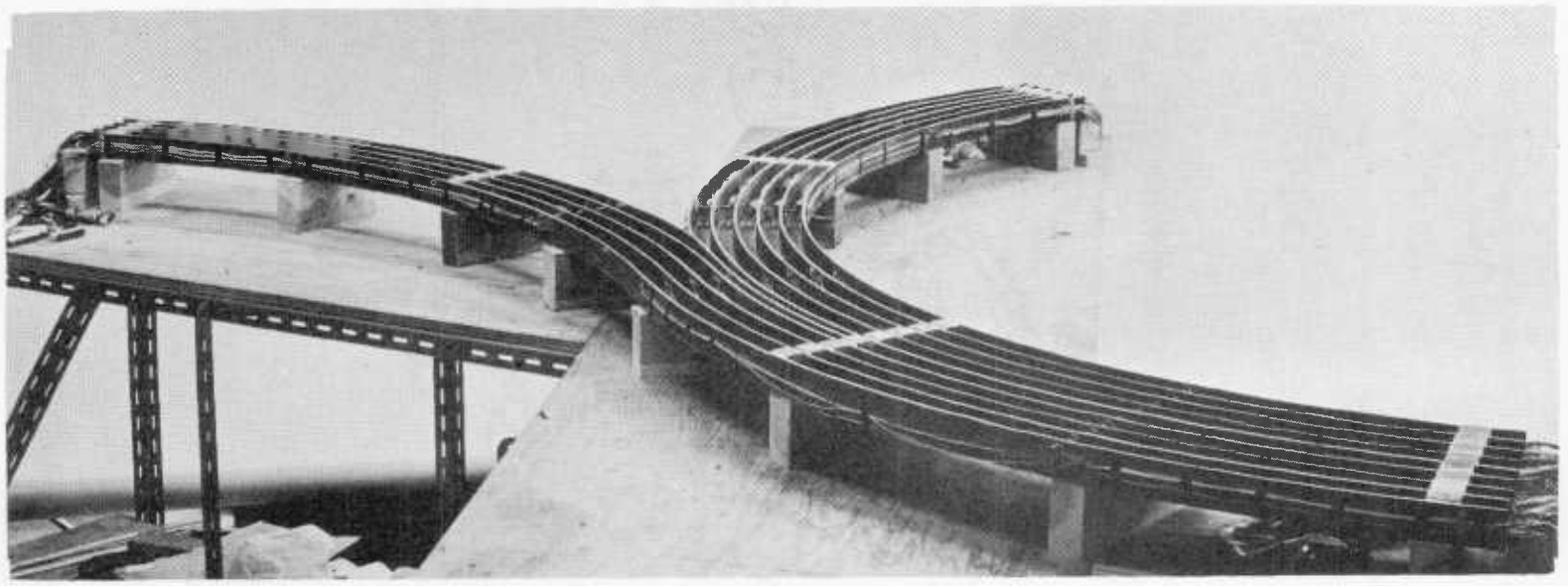


Fig.127 Model 2 during assembly
BIFURCATED ELEVATED HIGHWAYS MODELS

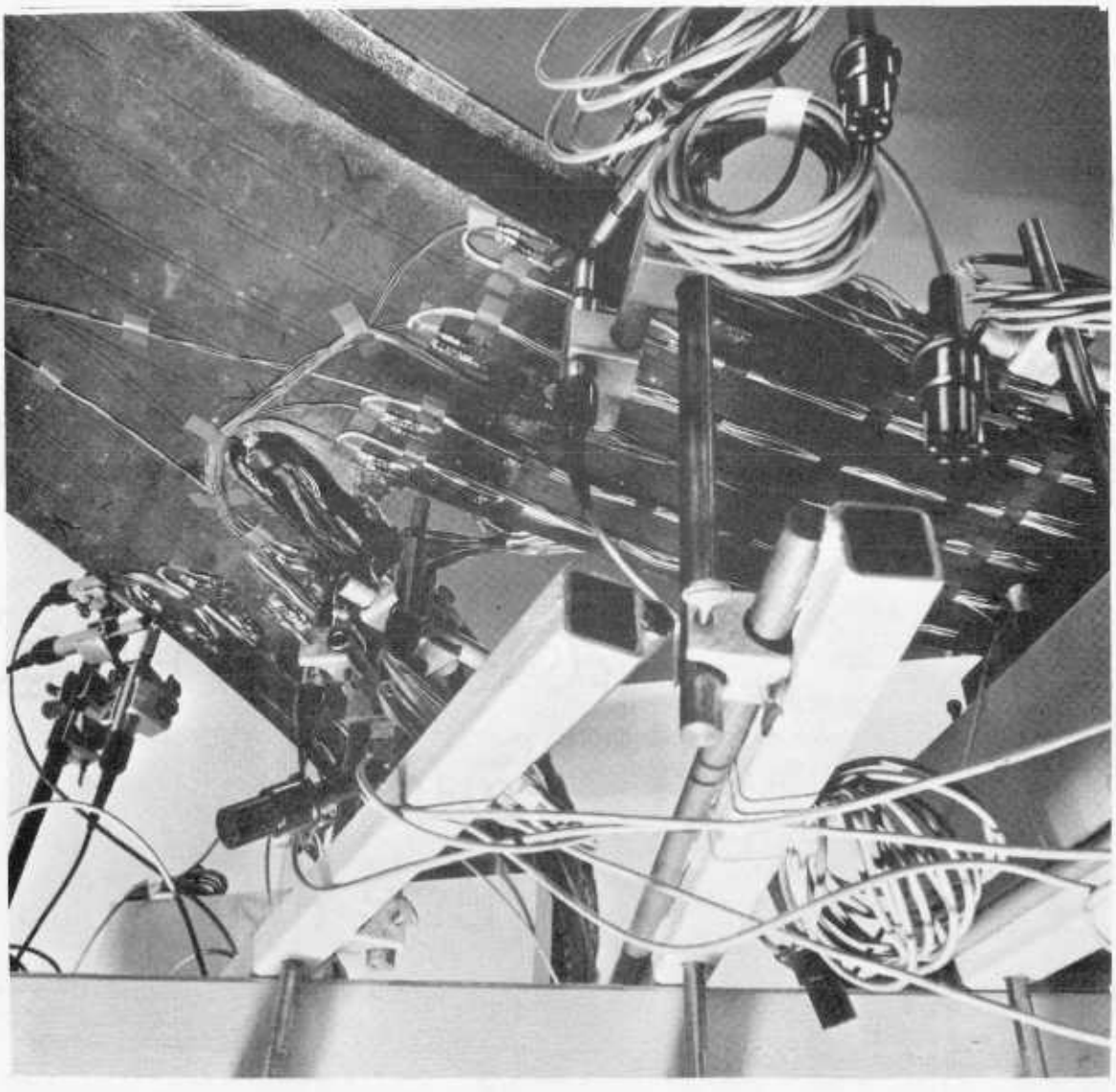


Fig.128 Model 2 from underside at bifurcation, showing Instrumentation at Section 6-6
BIFURCATED ELEVATED HIGHWAYS MODELS

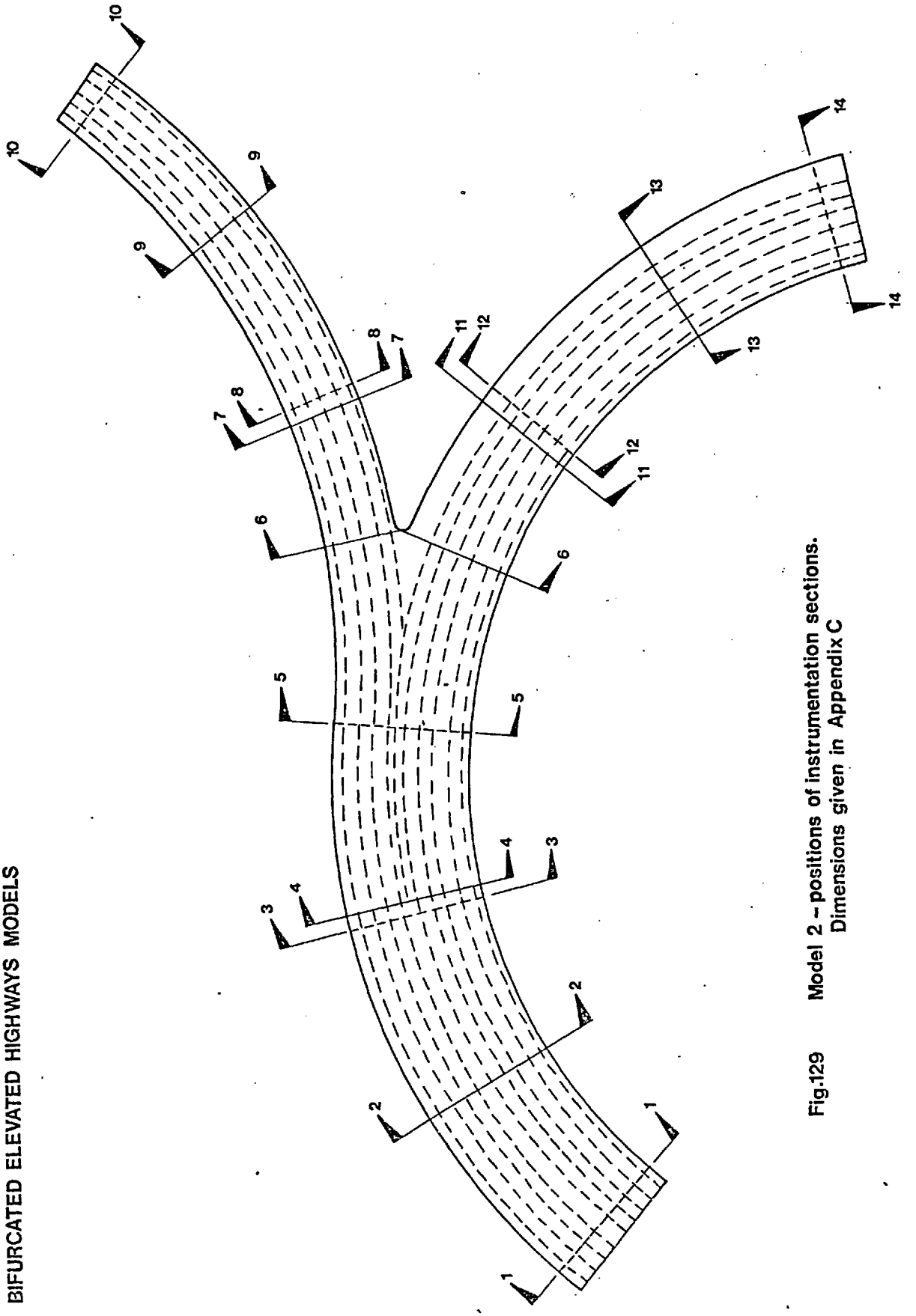


Fig.129 Model 2 – positions of instrumentation sections.
Dimensions given in Appendix C

BIFURCATED ELEVATED HIGHWAYS MODELS

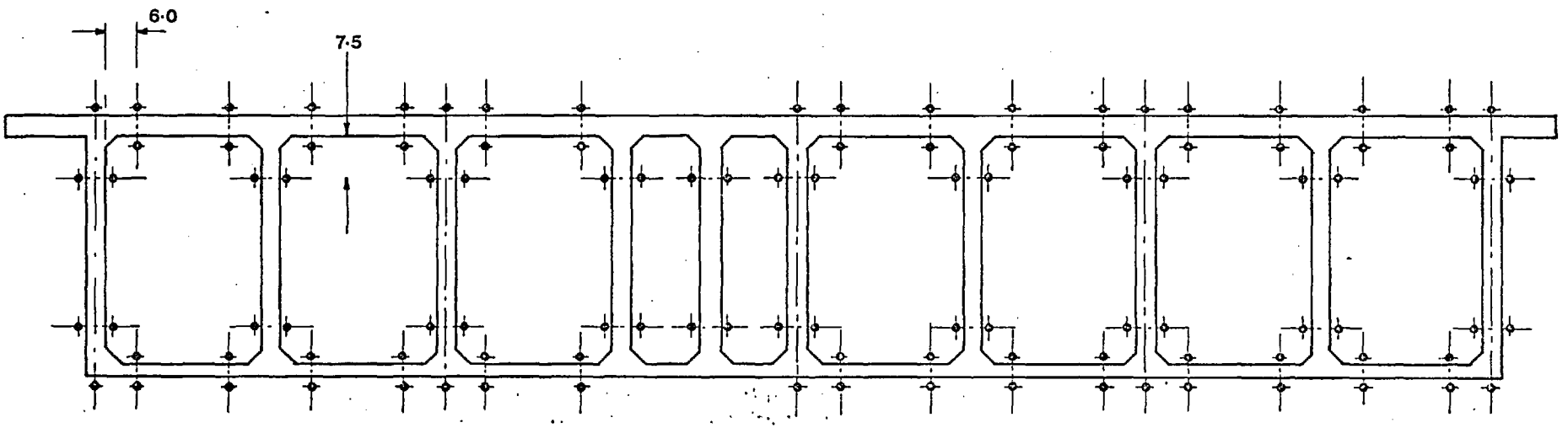


Fig.130 Model 2 - Typical layout of strain gauges at midspan section

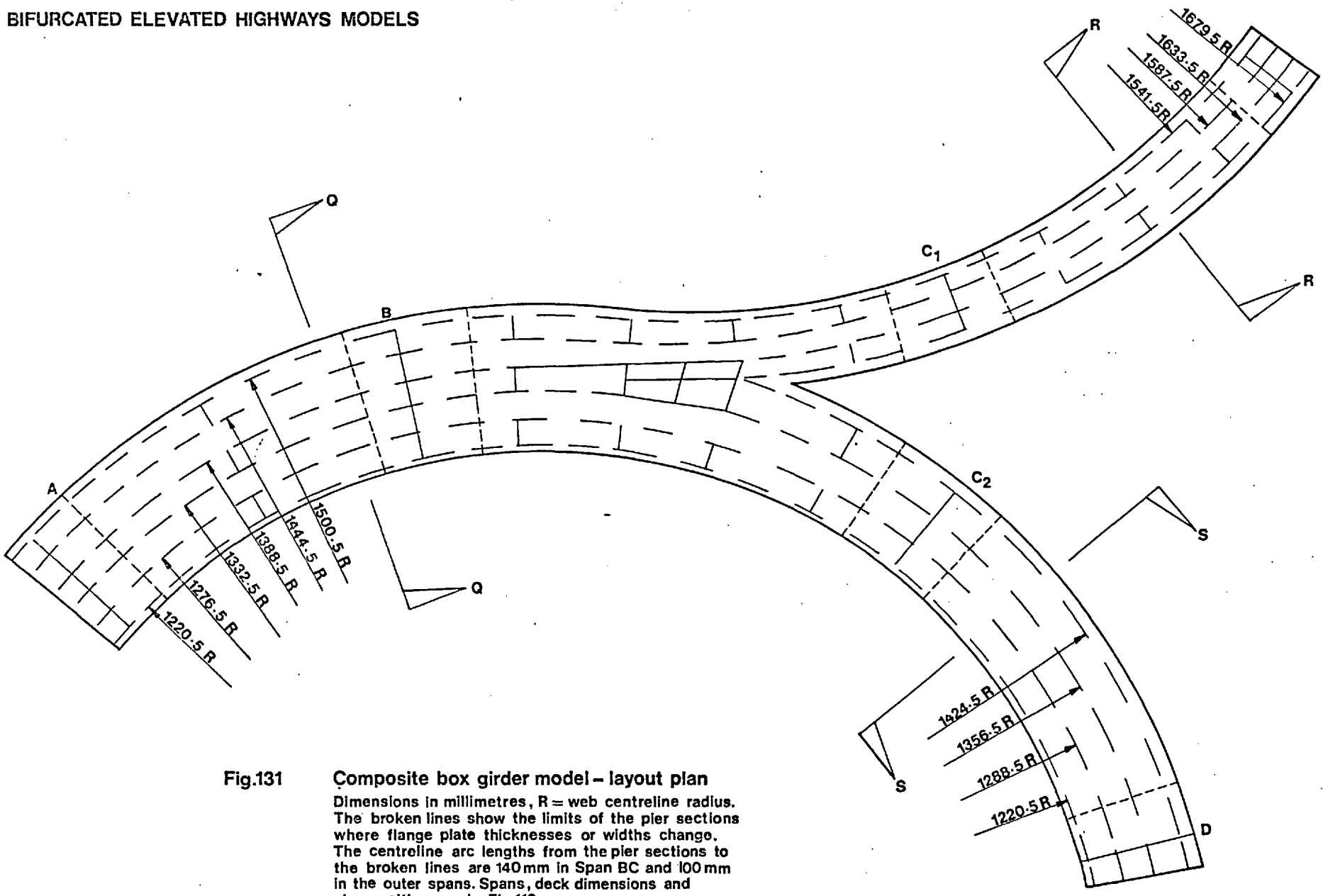
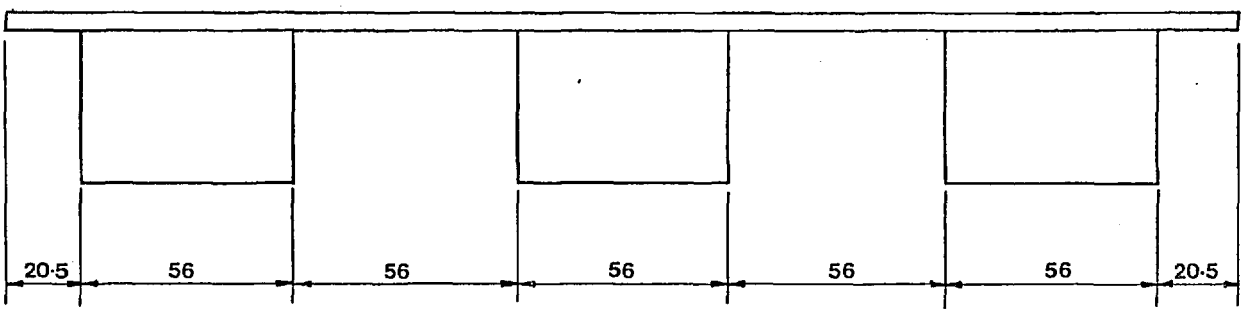


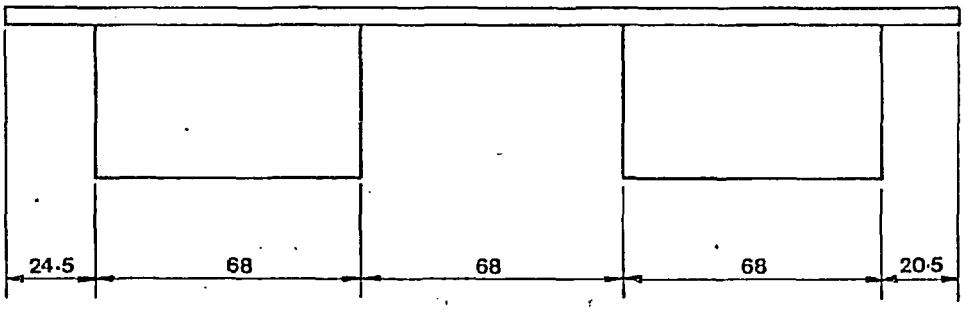
Fig.131 **Composite box girder model – layout plan**

Dimensions in millimetres, R = web centreline radius. The broken lines show the limits of the pier sections where flange plate thicknesses or widths change. The centreline arc lengths from the pier sections to the broken lines are 140 mm in Span BC and 100 mm in the outer spans. Spans, deck dimensions and pier positions as in Fig.119

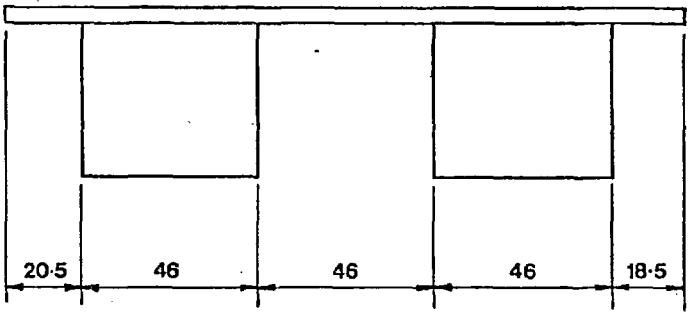
BIFURCATED ELEVATED HIGHWAYS MODELS



Section Q–Q



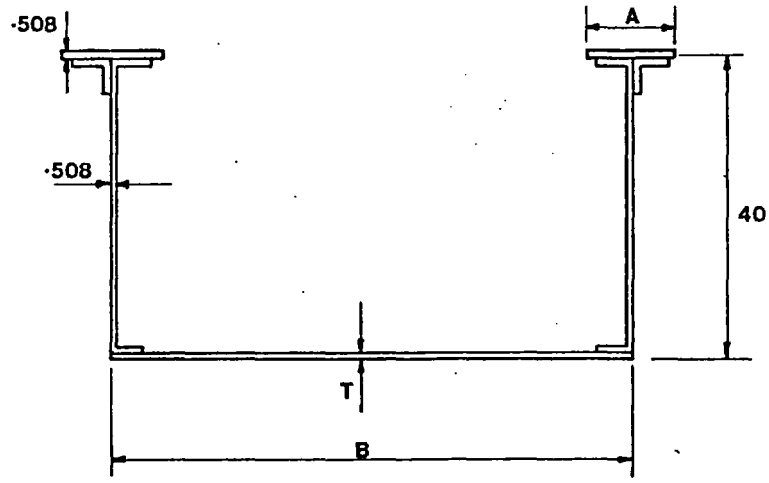
Section R–R



Section S–S

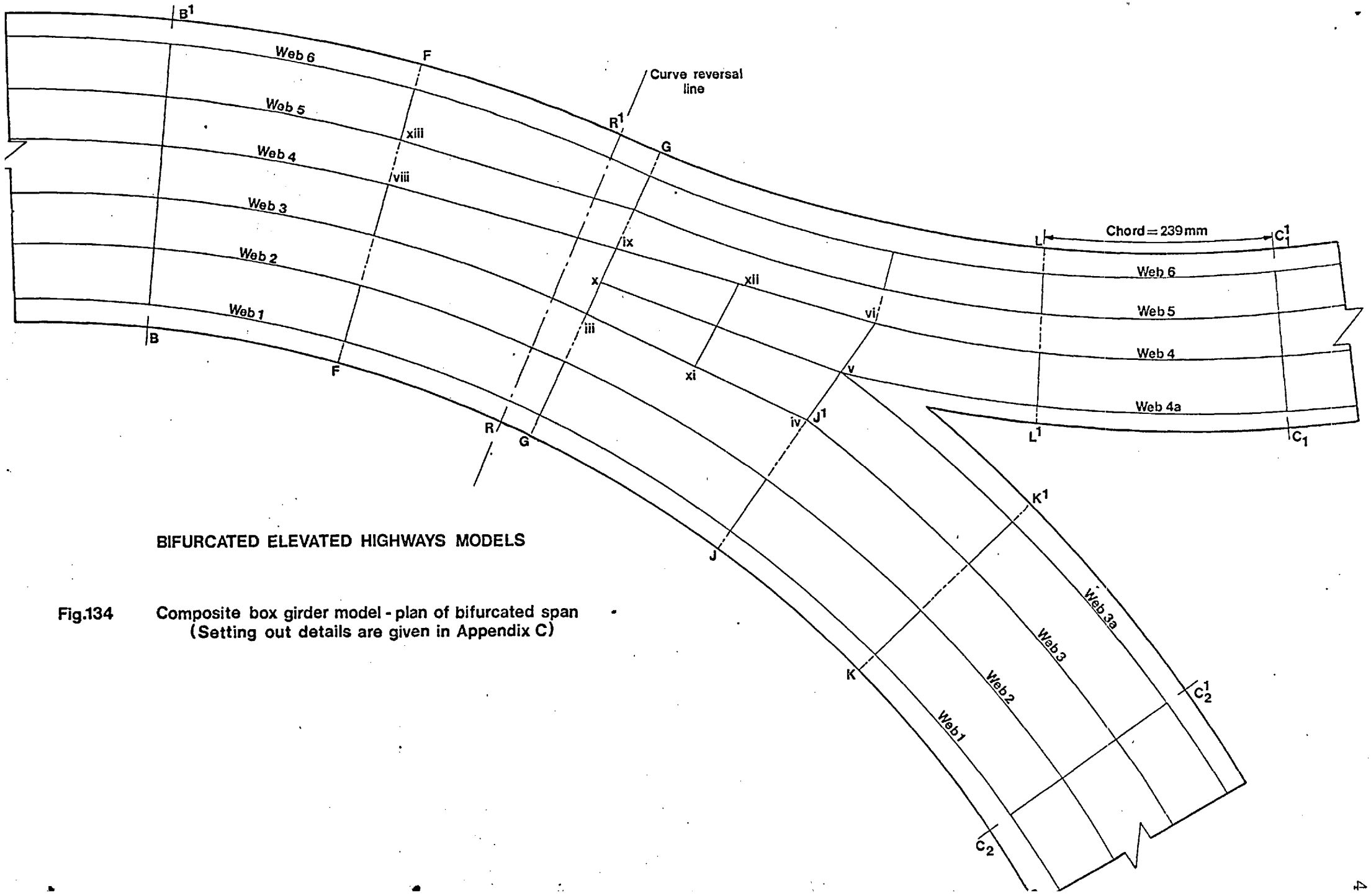
Fig.132 Composite box girder model– Sections ,Q-Q , R-R , S-S

BIFURCATED ELEVATED HIGHWAYS MODELS



LOCATION	A	B	T
Pier A	13	56	·622
Pier B	13	56	·622
Pier C_1	13	46	·511
Pier E	11	46	·511
Pier C_2D	16	68	·755
Span AB	13	56	·254
Span BC_1	13	56 → 46	·381
Span BC_2	13	56 → 68	·381
Span C_1D	11	46	·254
Span C_2D	16	68	·254

Fig.133 Composite box girder model - details of boxes and table of flange plate sizes



BIFURCATED ELEVATED HIGHWAYS MODELS

Fig.134 Composite box girder model - plan of bifurcated span
(Setting out details are given in Appendix C)

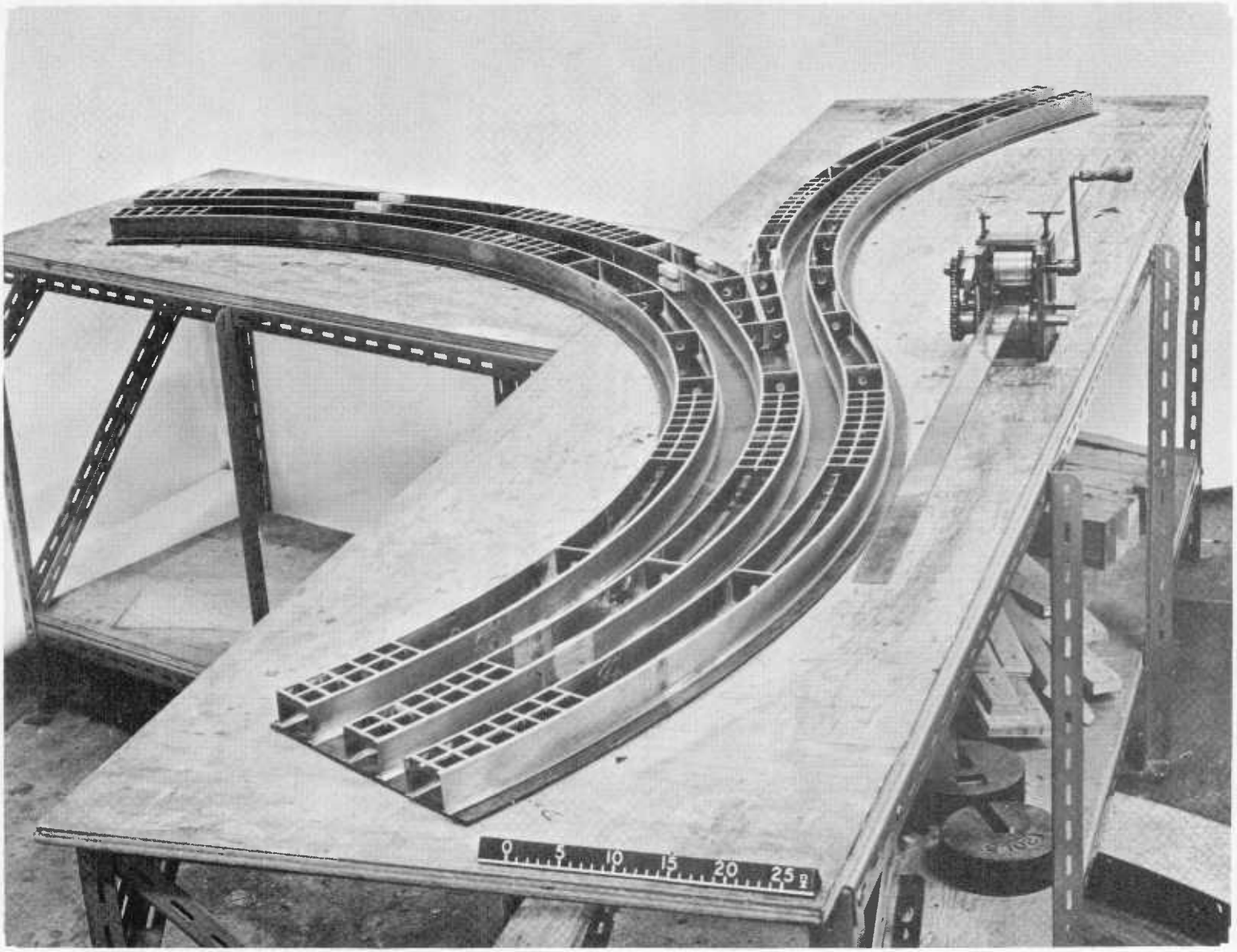


Fig.135 Underside of Model 4 during fabrication before fixing bottom flange plates

BIFURCATED ELEVATED HIGHWAYS MODELS

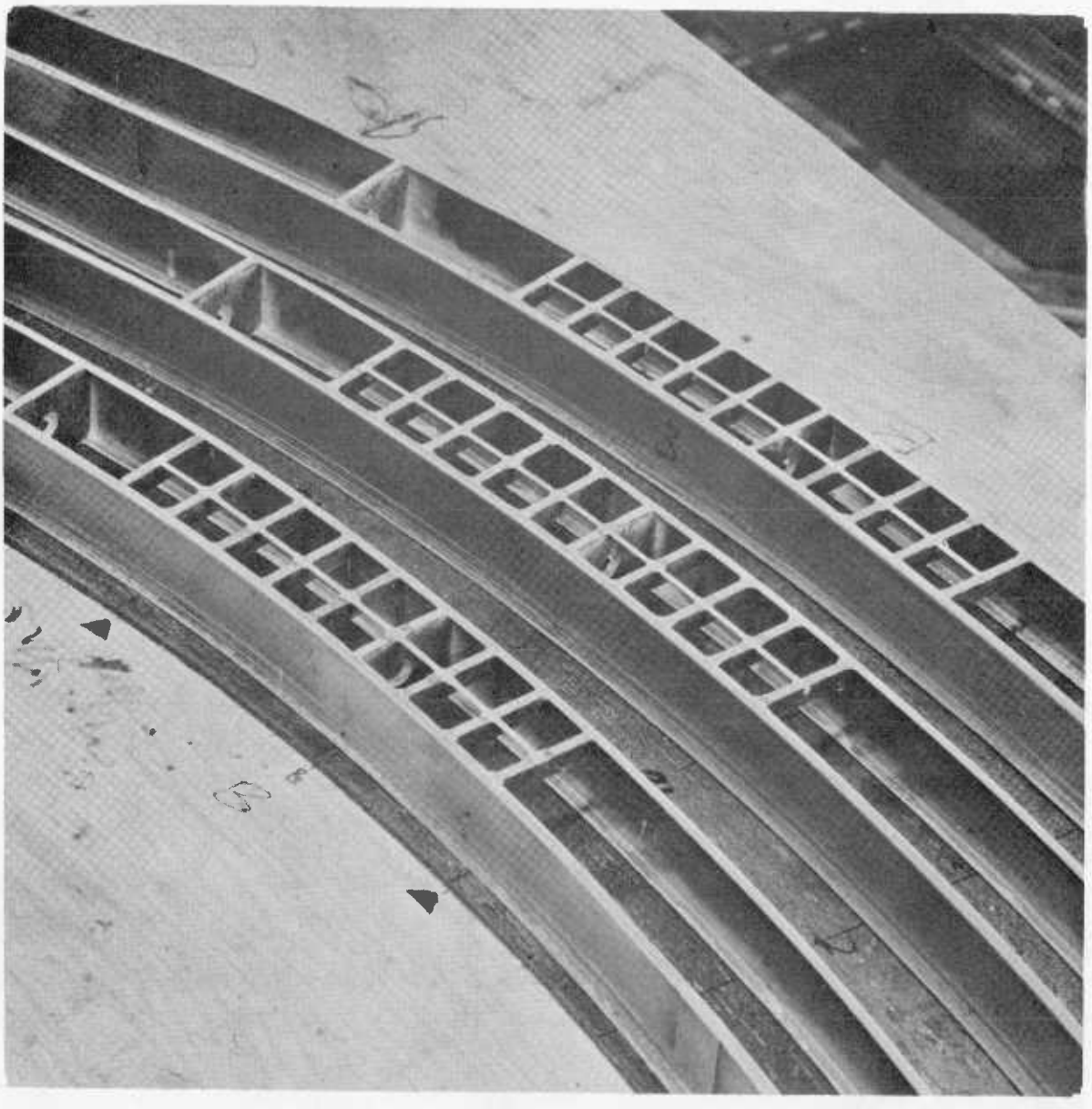


Fig.136 Underside of Pier Section B-B showing bottom flange stiffening
BIFURCATED ELEVATED HIGHWAYS MODELS

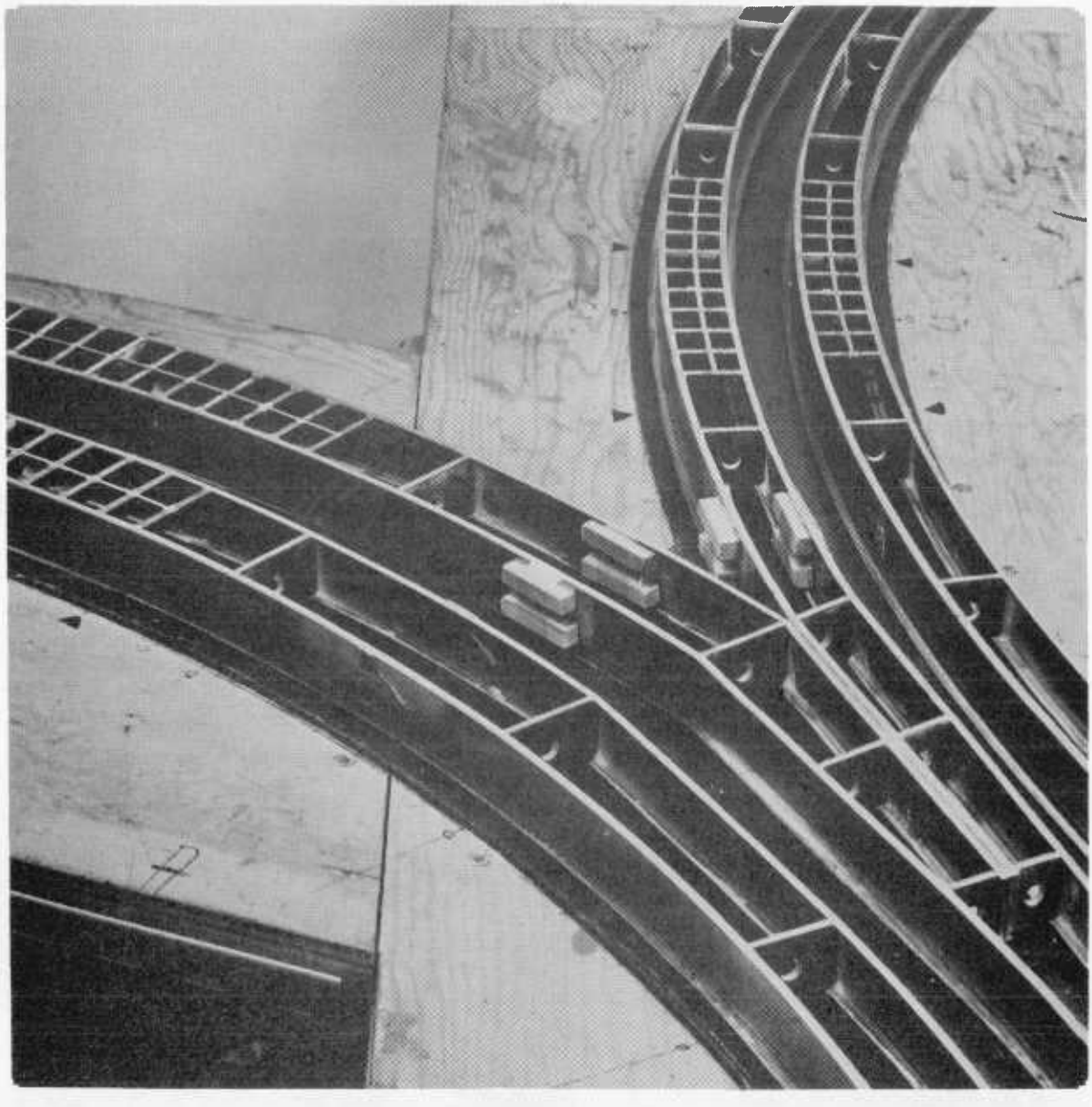


Fig.137 Underside of Model 4 during fabrication showing diaphragming at bifurcation

BIFURCATED ELEVATED HIGHWAYS MODELS

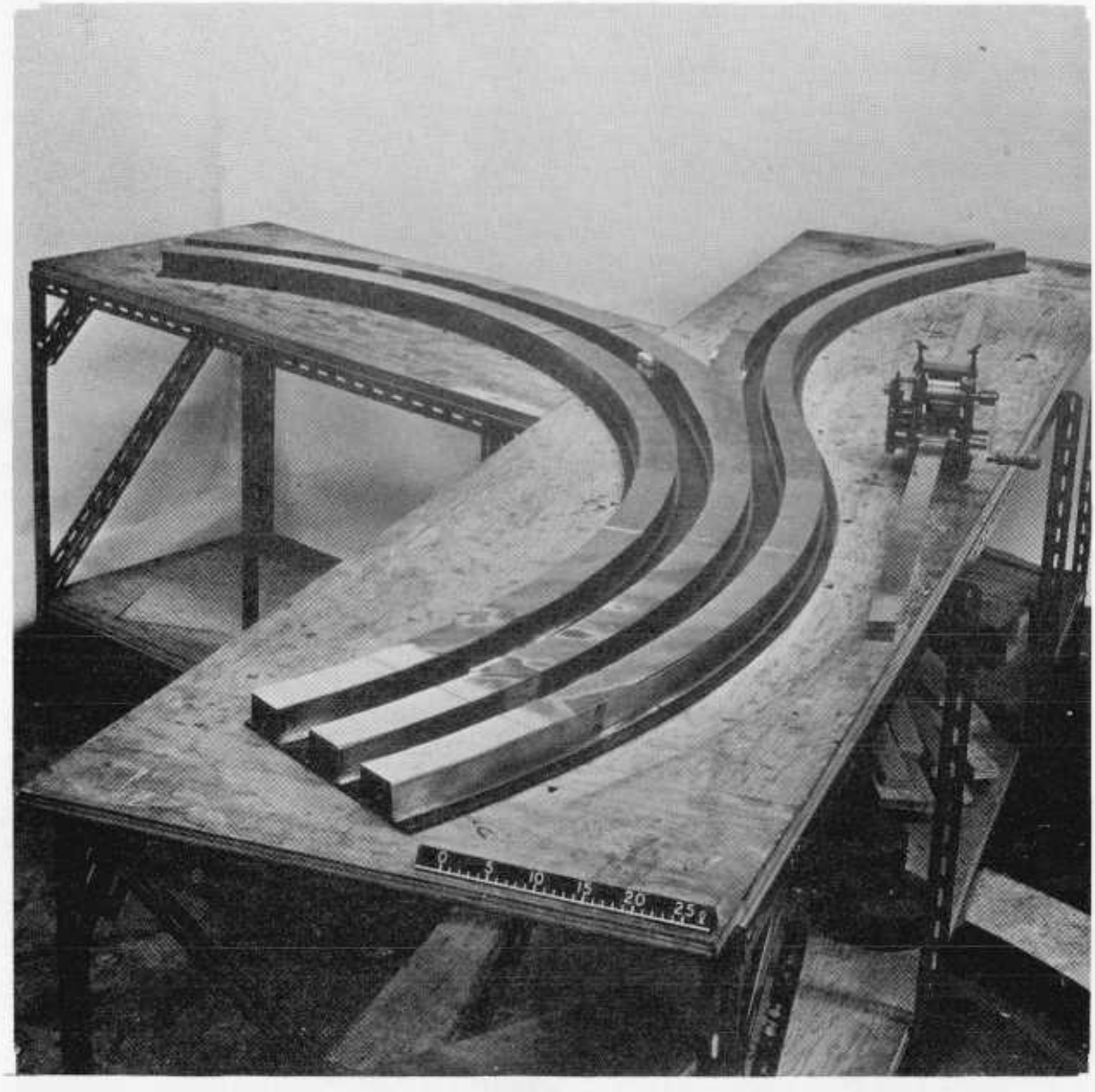


Fig.138 Underside of Model 4 with flange plates laid in position
BIFURCATED ELEVATED HIGHWAYS MODELS

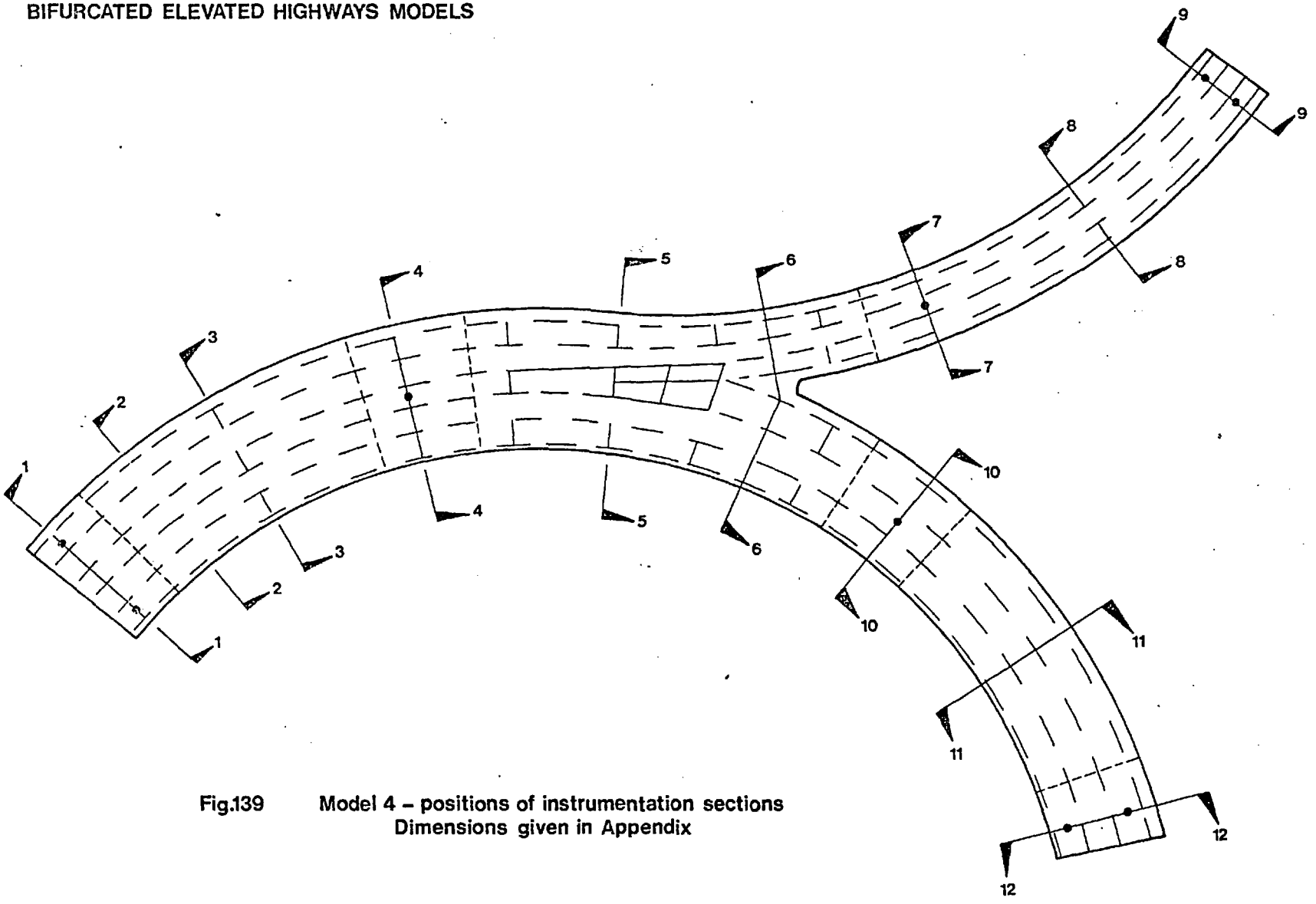


Fig.139 Model 4 – positions of instrumentation sections
Dimensions given in Appendix

BIFURCATED ELEVATED HIGHWAYS MODELS

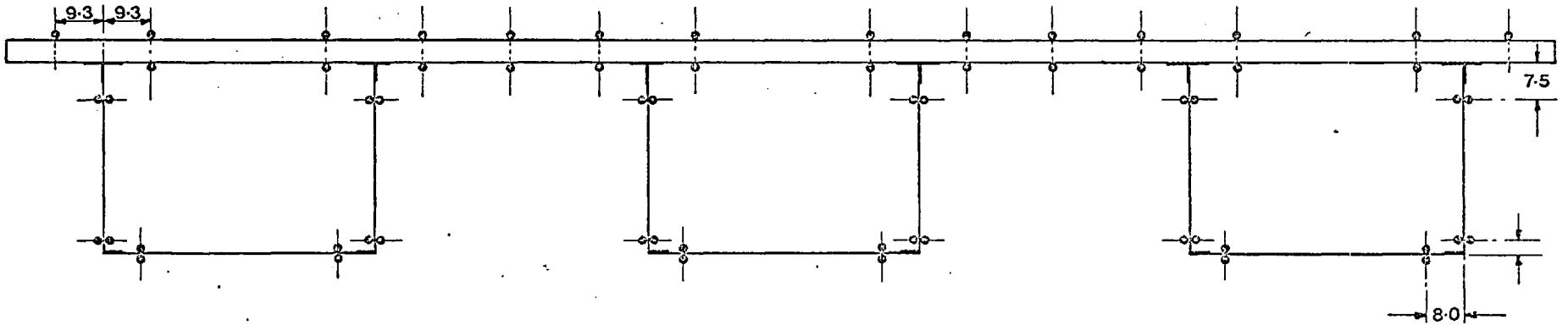


Fig.140 Model 4 - Typical layout of strain gauges at midspan section

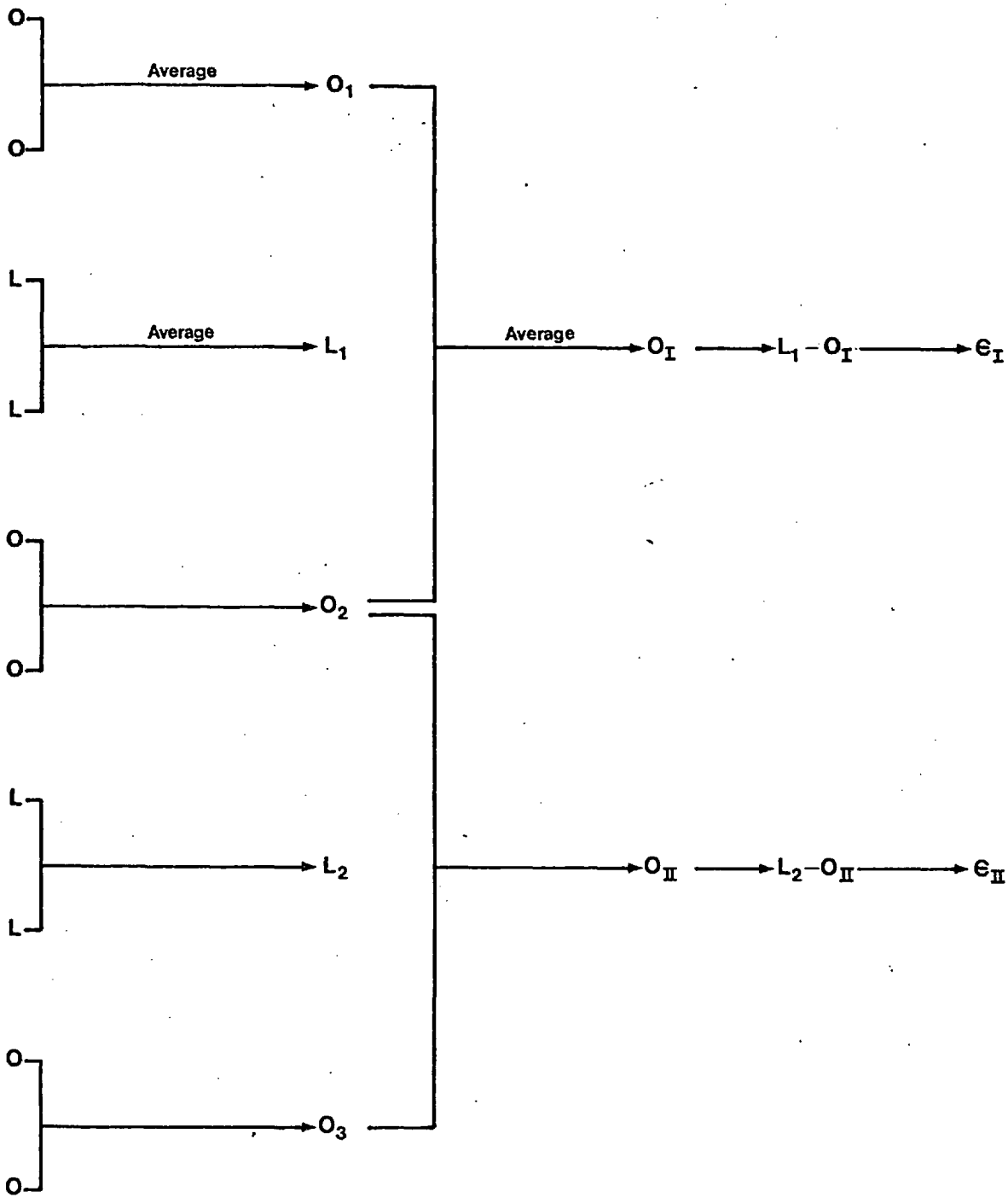


Fig.141 Conversion of strain gauge readings to real strains

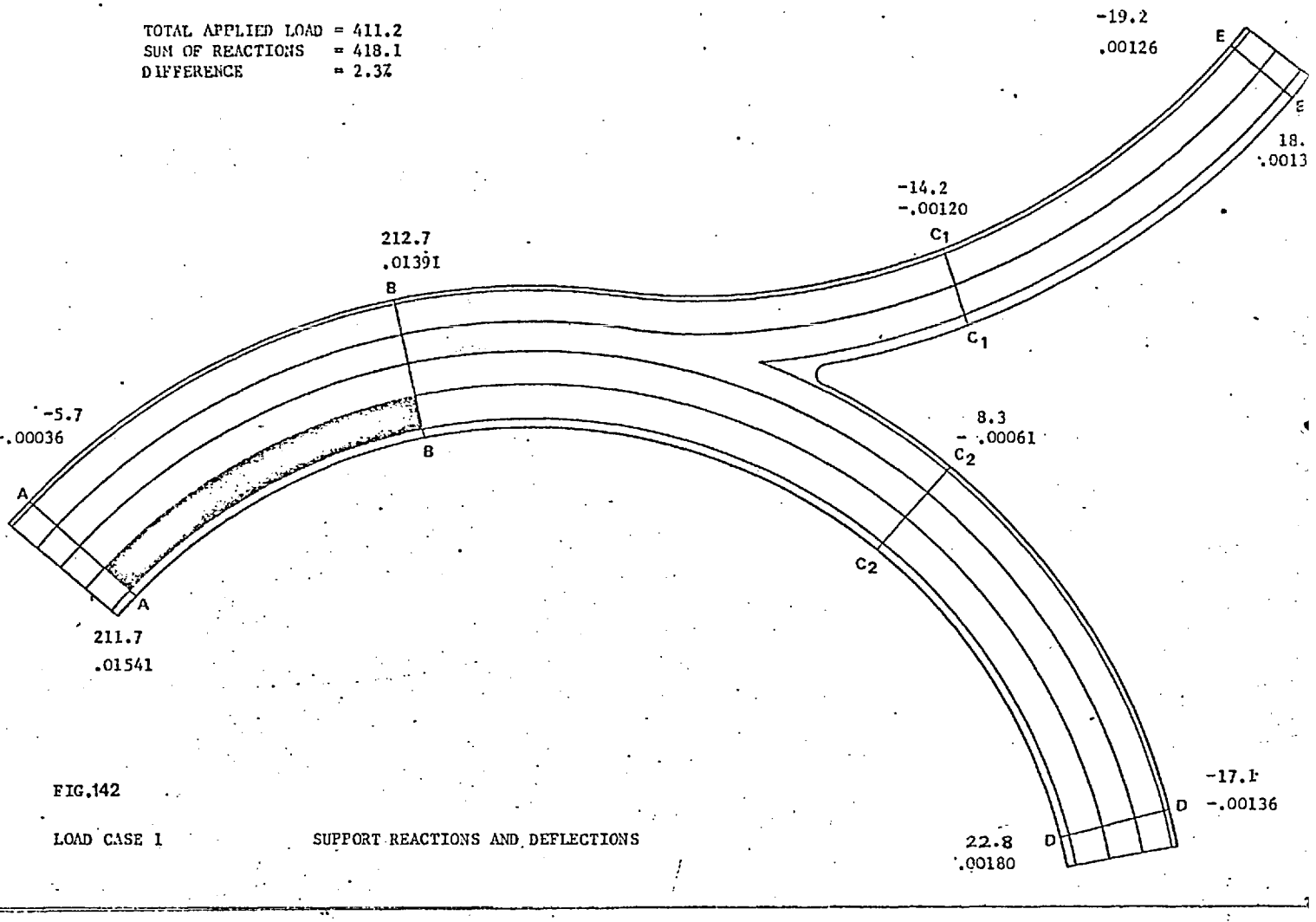


FIG.142

LOAD CASE 1 SUPPORT REACTIONS AND DEFLECTIONS

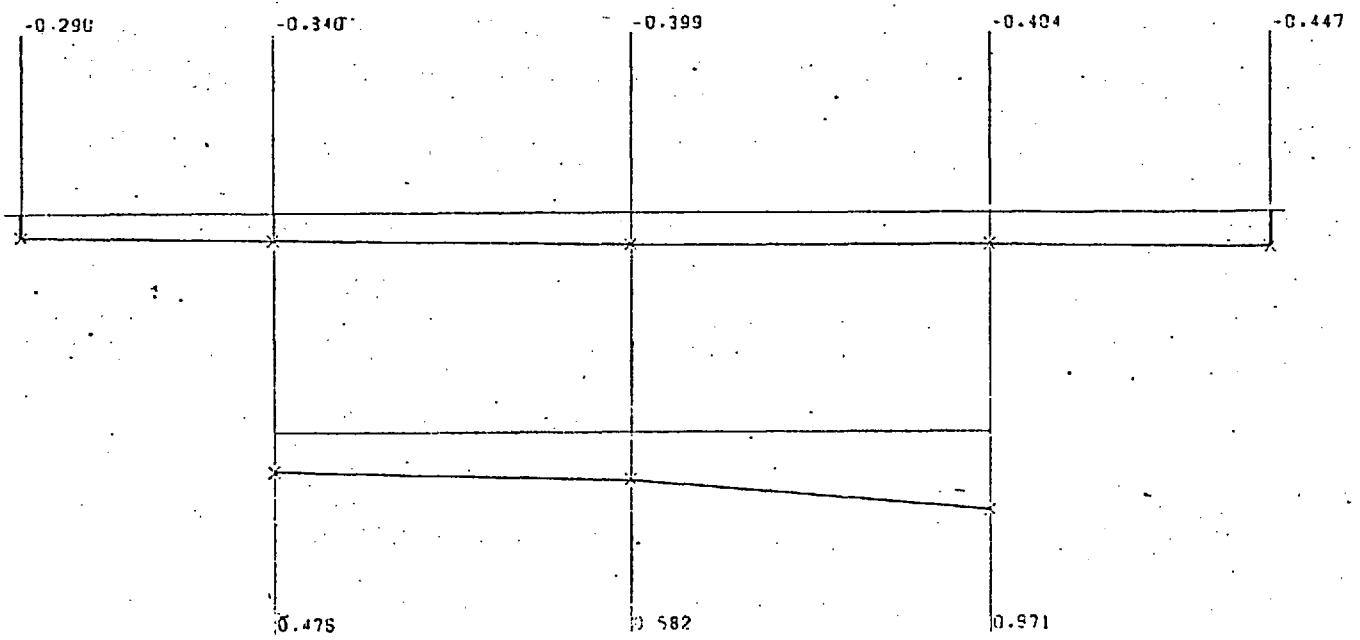


FIG 143

LOAD CASE 1 SECTION 1-1 MAIN STRESS GAUGES
LONGITUDINAL STRESSES AT EXTREME FIBRES

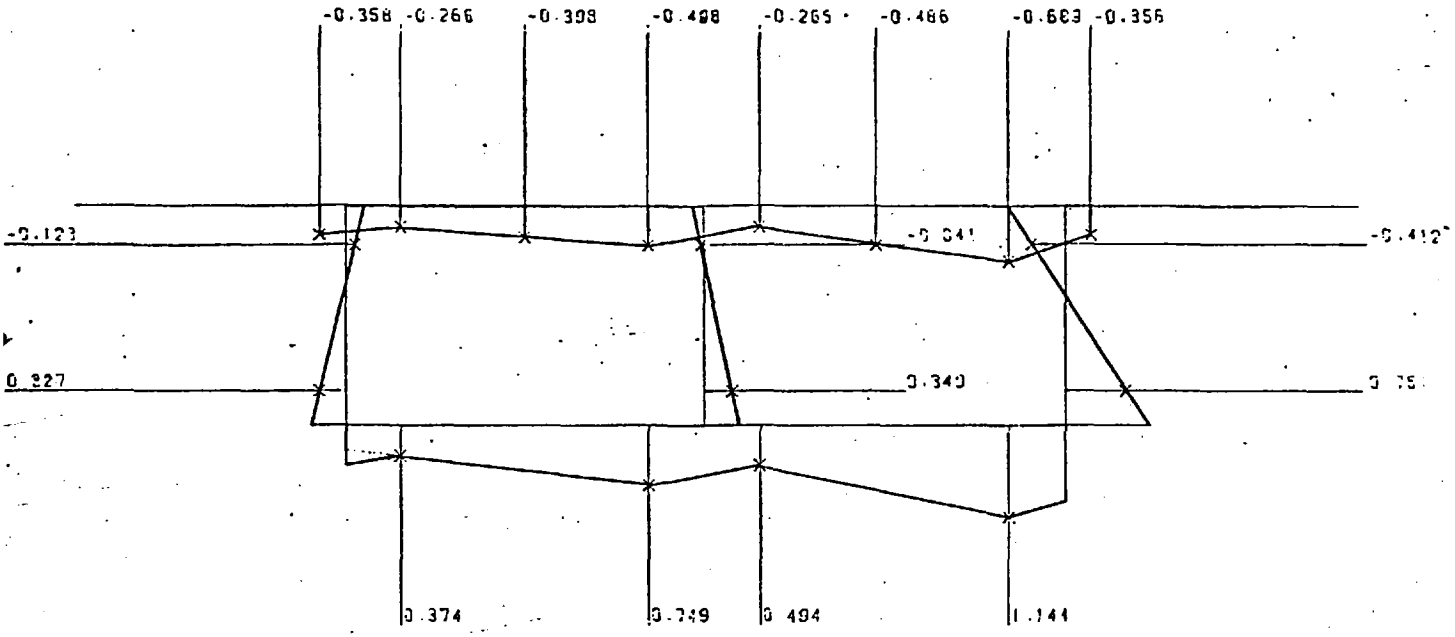


FIG 144

LOAD CASE 1 SECTION 1-1 SECONDARY STRESS GAUGES
LONGITUDINAL STRESSES AT EXTREME FIBRES

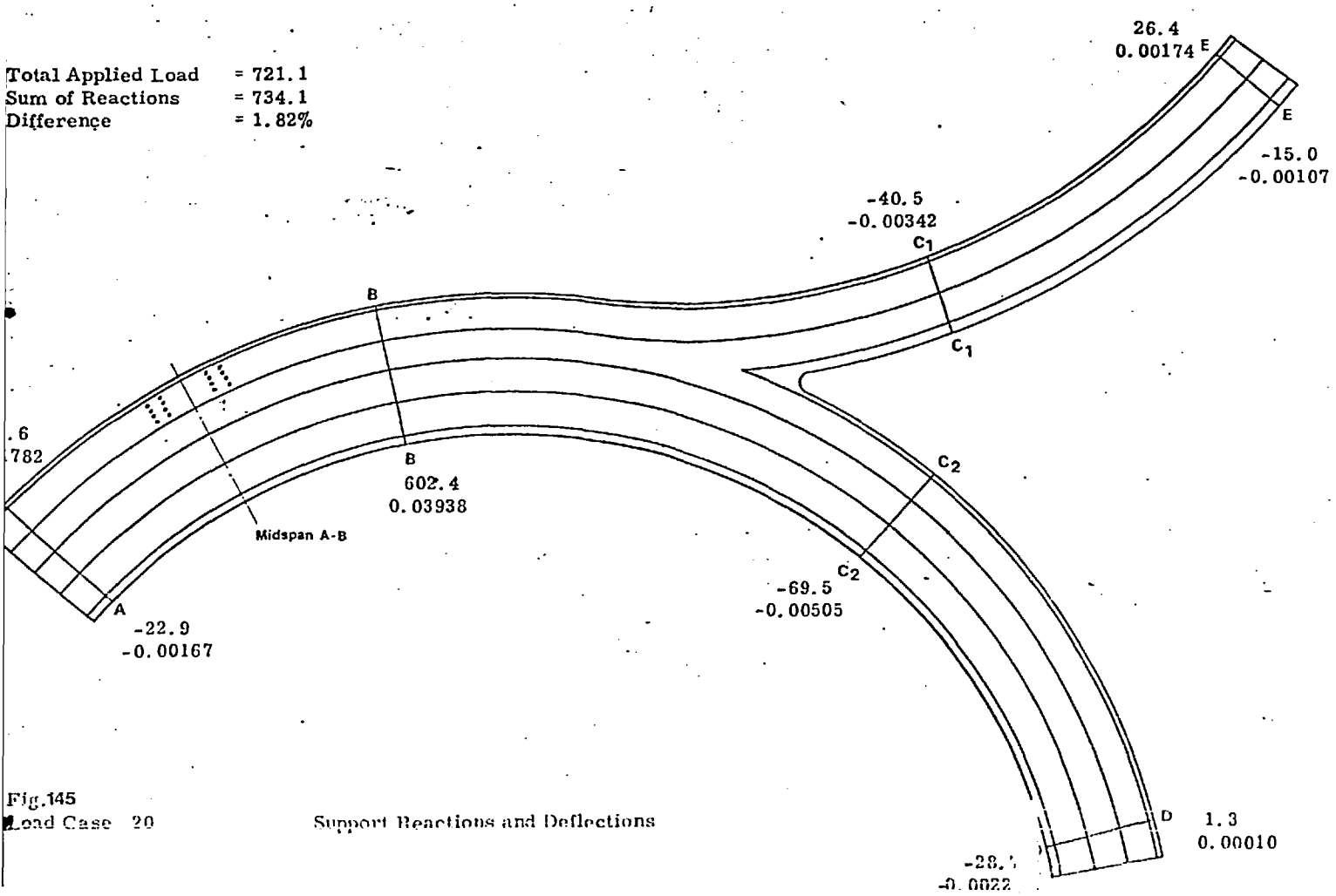


Fig.145
Load Case 20 Support Reactions and Deflections

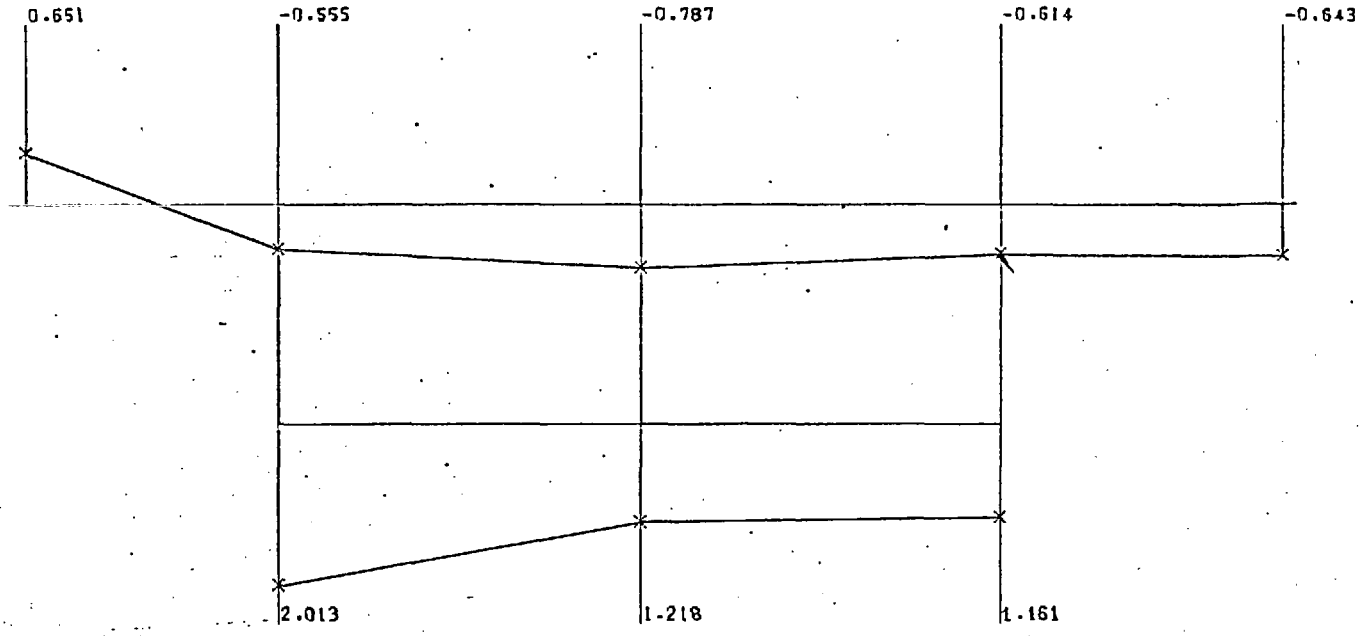


FIG 146

LOAD CASE 20 SECTION 1-1 MAIN STRESS GAUGES
LONGITUDINAL STRESSES AT EXTREME FIBRES

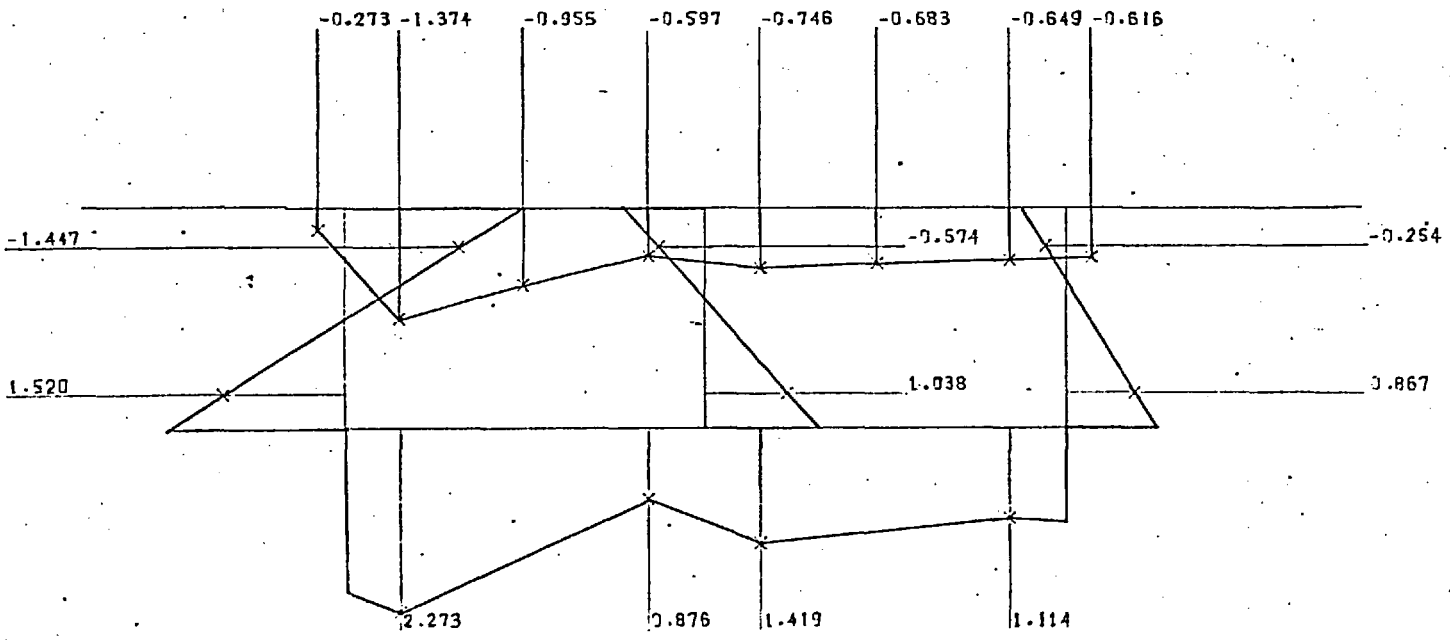


FIG 147

LOAD CASE 20 SECTION 1-1 SECONDARY STRESS GAUGES
LONGITUDINAL STRESSES AT EXTREME FIBRES

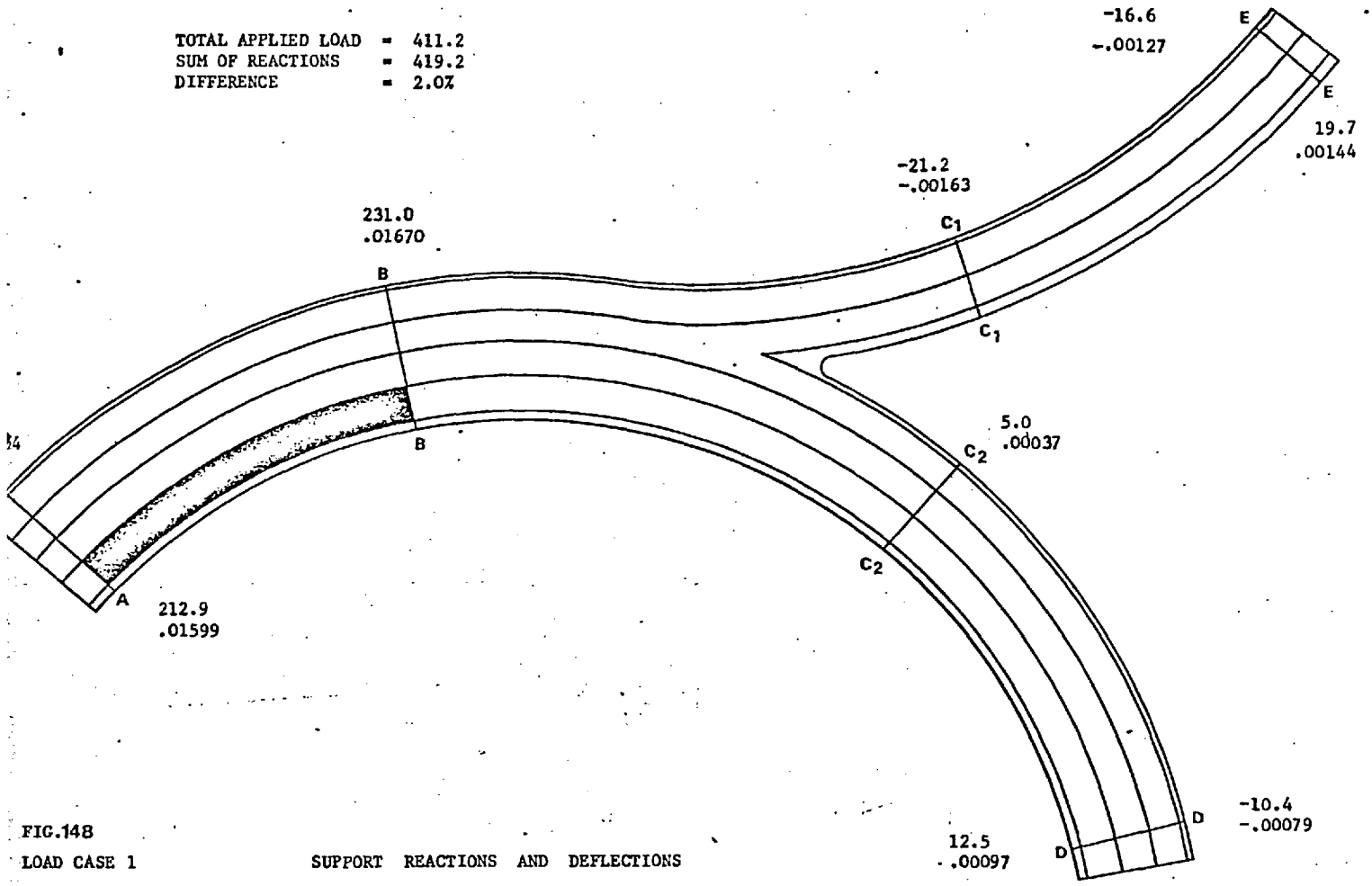


FIG.148
LOAD CASE 1 SUPPORT REACTIONS AND DEFLECTIONS

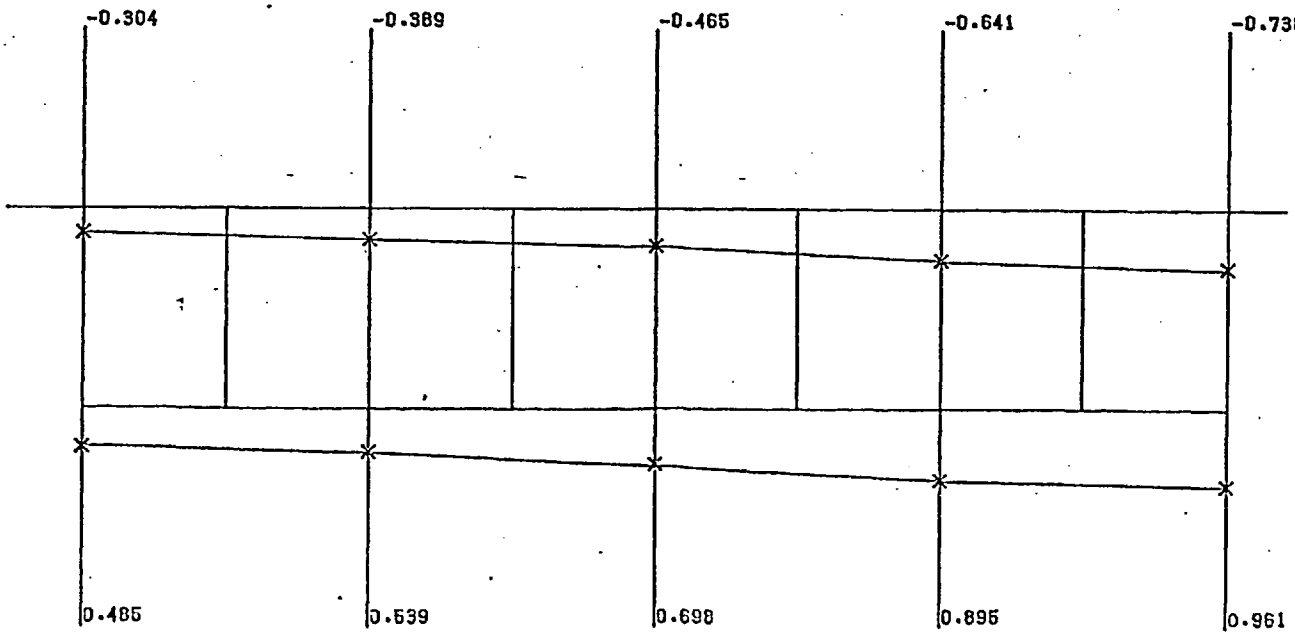


FIG 149

LOAD CASE 1 SECTION 2-2 MAIN STRESS GAUGES
LONGITUDINAL STRESSES AT EXTREME FIBRES

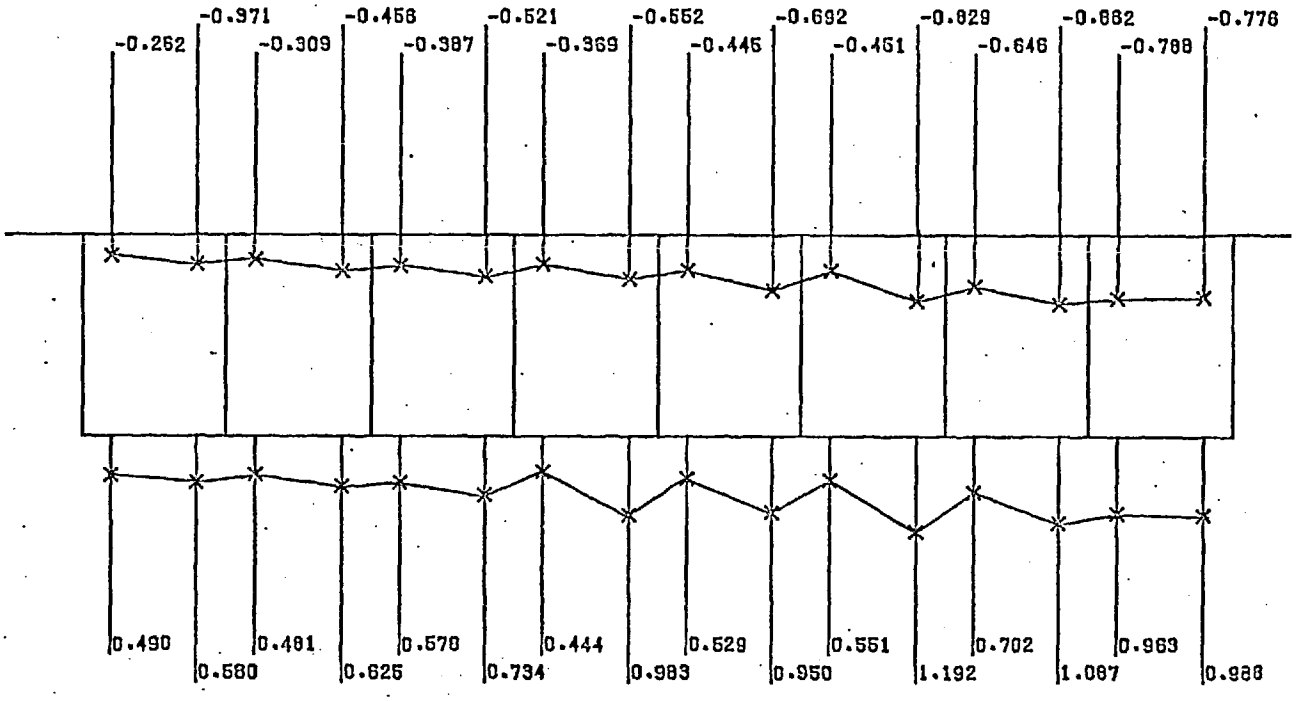


FIG 150

LOAD CASE 1 SECTION 2-2 SECONDARY STRESS GAUGES
LONGITUDINAL STRESSES AT EXTREME FIBRES

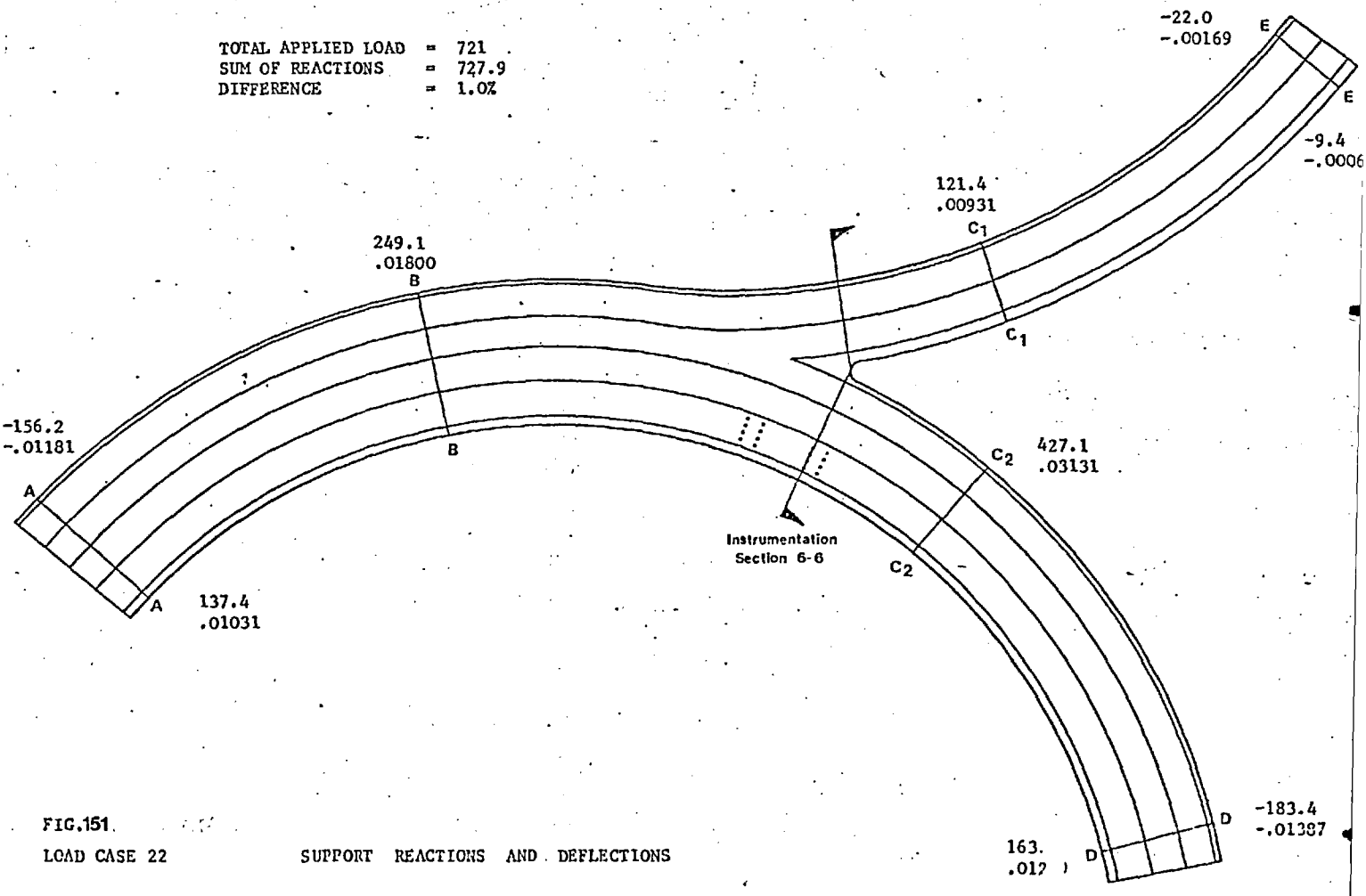


FIG.151.

LOAD CASE 22 SUPPORT REACTIONS AND DEFLECTIONS

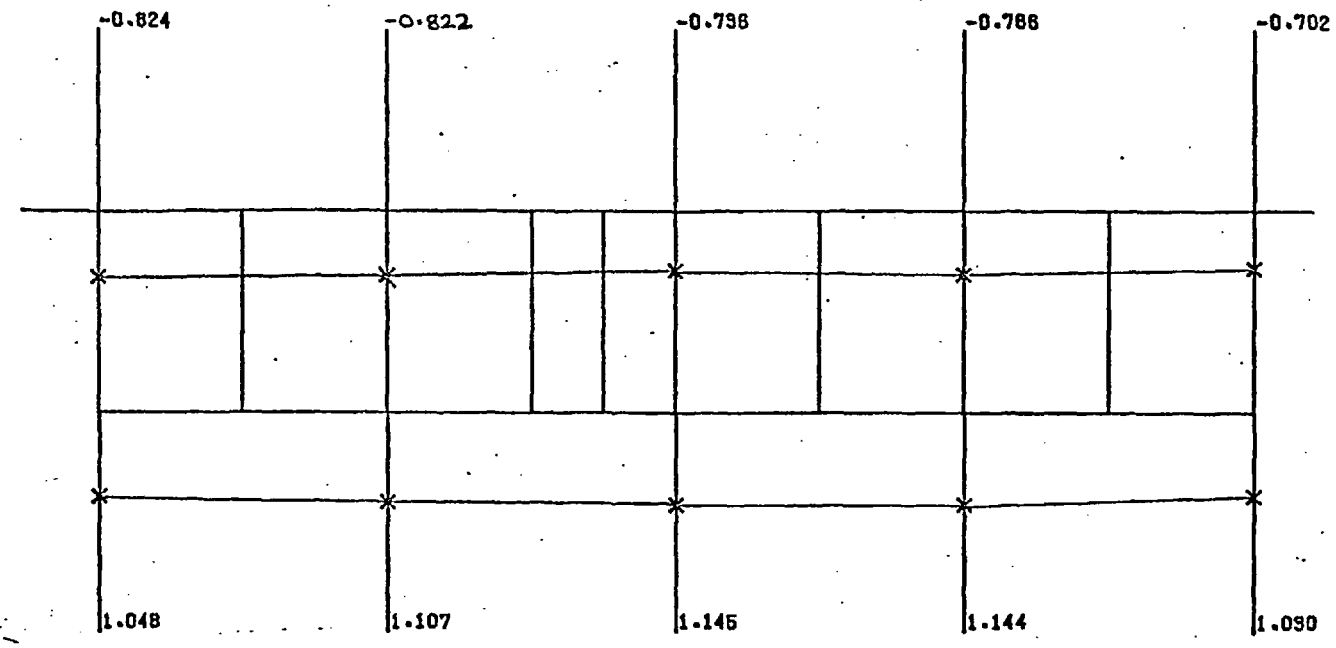


FIG 152

LOAD CASE 22 SECTION 5-5 MAIN STRESS GAUGES
LONGITUDINAL STRESSES AT EXTREME FIBRES

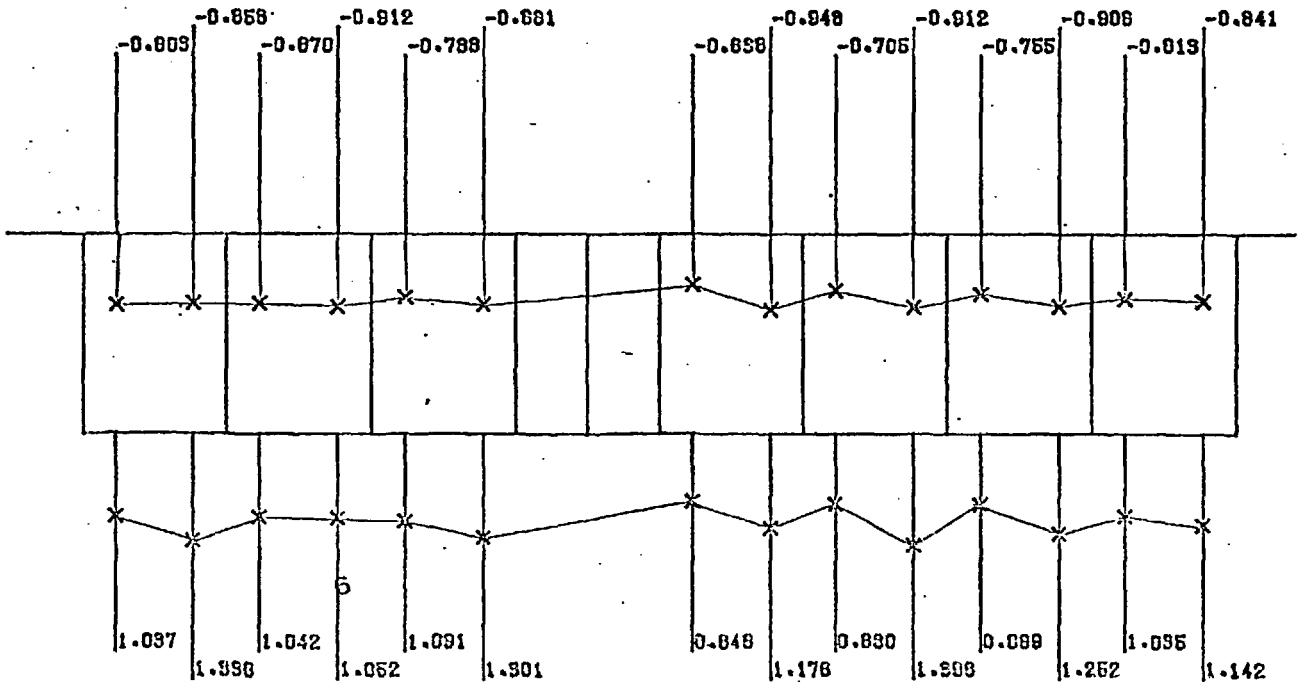


FIG 153

LOAD CASE 22 SECTION 5-5 SECONDARY STRESS GAUGES
LONGITUDINAL STRESSES AT EXTREME FIBRES

TOTAL APPLIED LOAD = 411.2
SUM OF REACTIONS = 420.7
DIFFERENCE = 2.3%

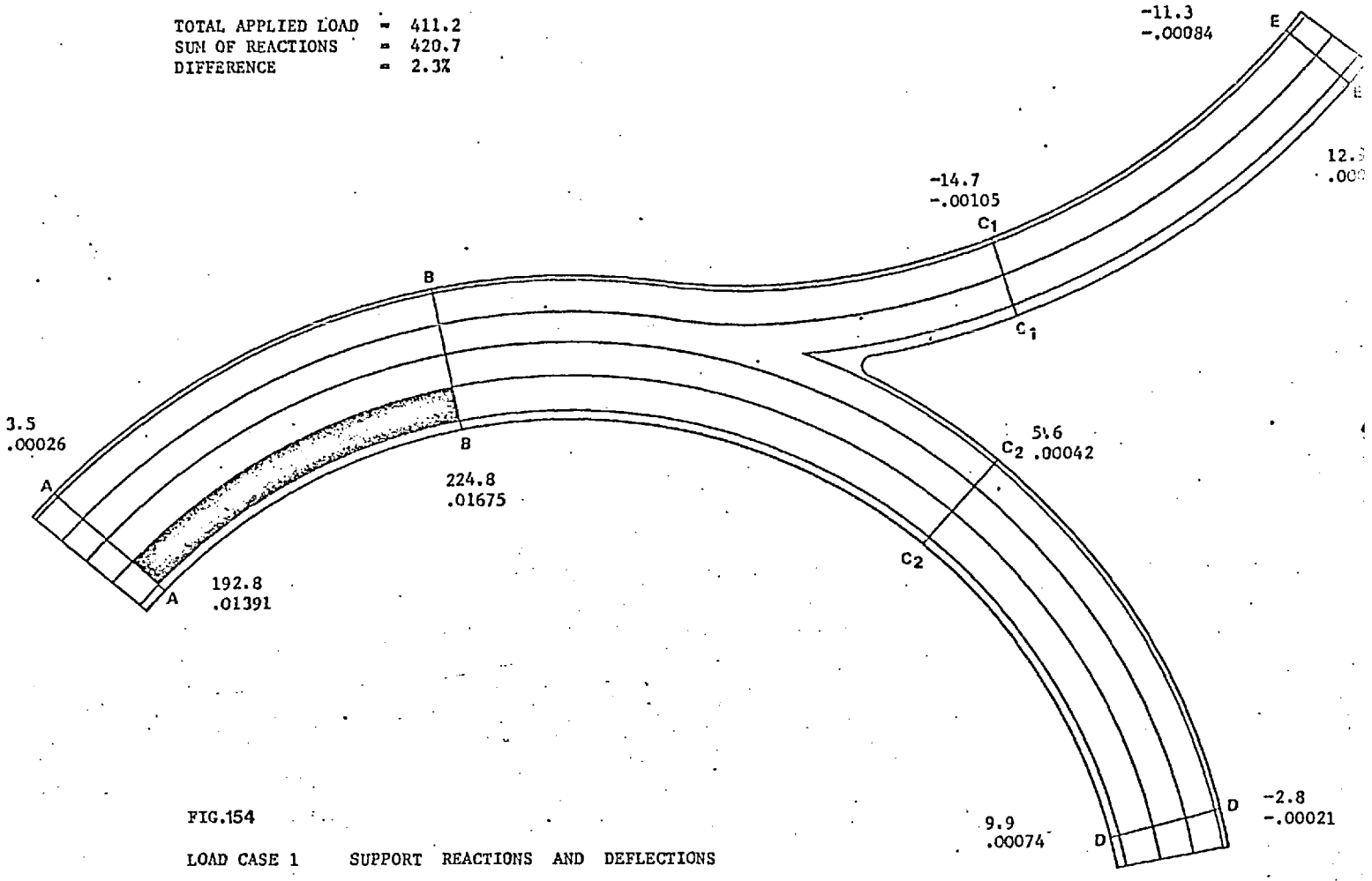


FIG.154

LOAD CASE 1 SUPPORT REACTIONS AND DEFLECTIONS

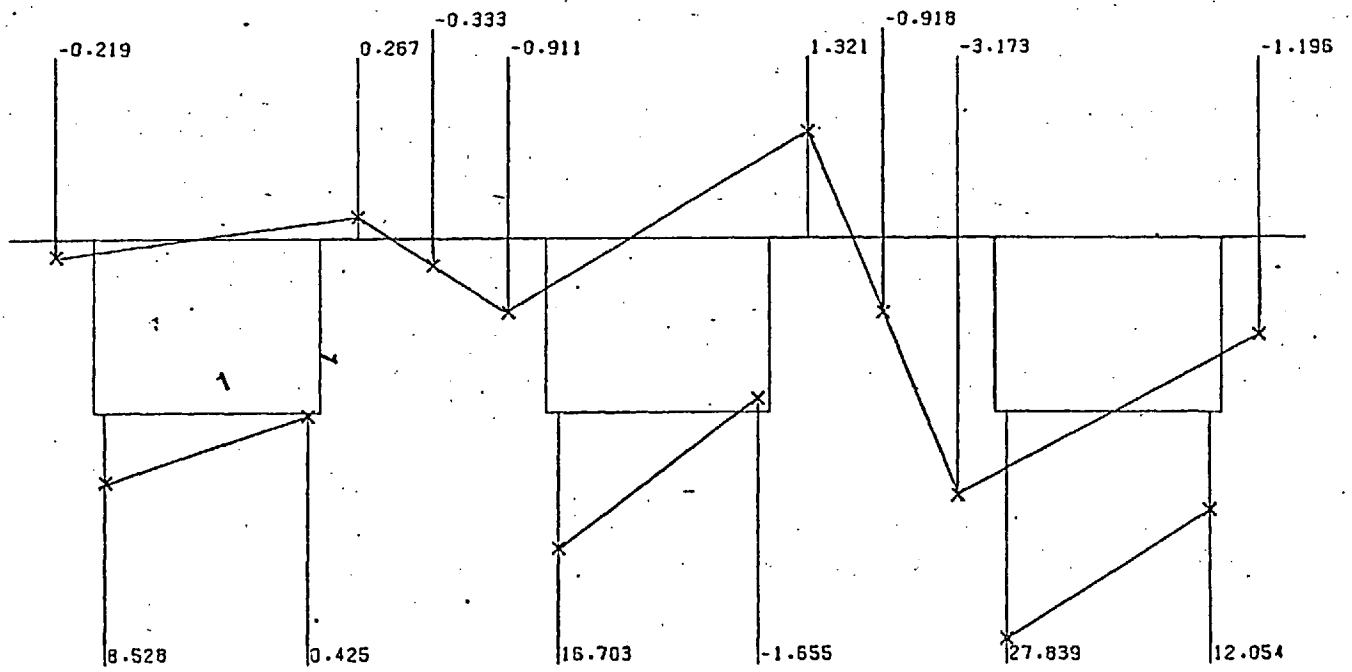


FIG 155

LOAD CASE 1 SECTION 3-3 SECONDARY STRESS GAUGES
LONGITUDINAL STRESSES AT EXTREME FIBRES

TOTAL APPLIED LOAD = 721
SUM OF REACTIONS = 716.6
DIFFERENCE = 0.6%

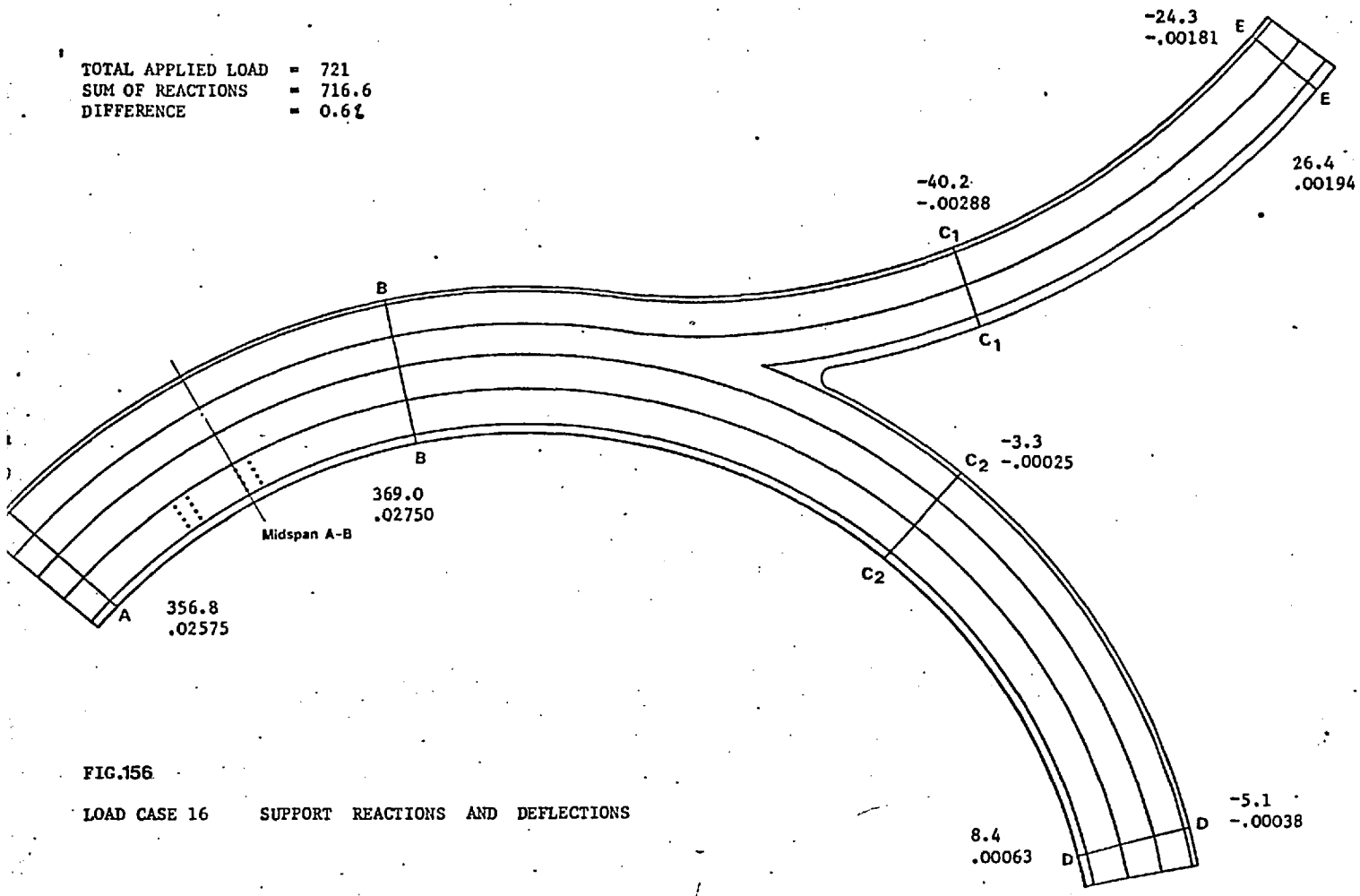


FIG.156

LOAD CASE 16 SUPPORT REACTIONS AND DEFLECTIONS

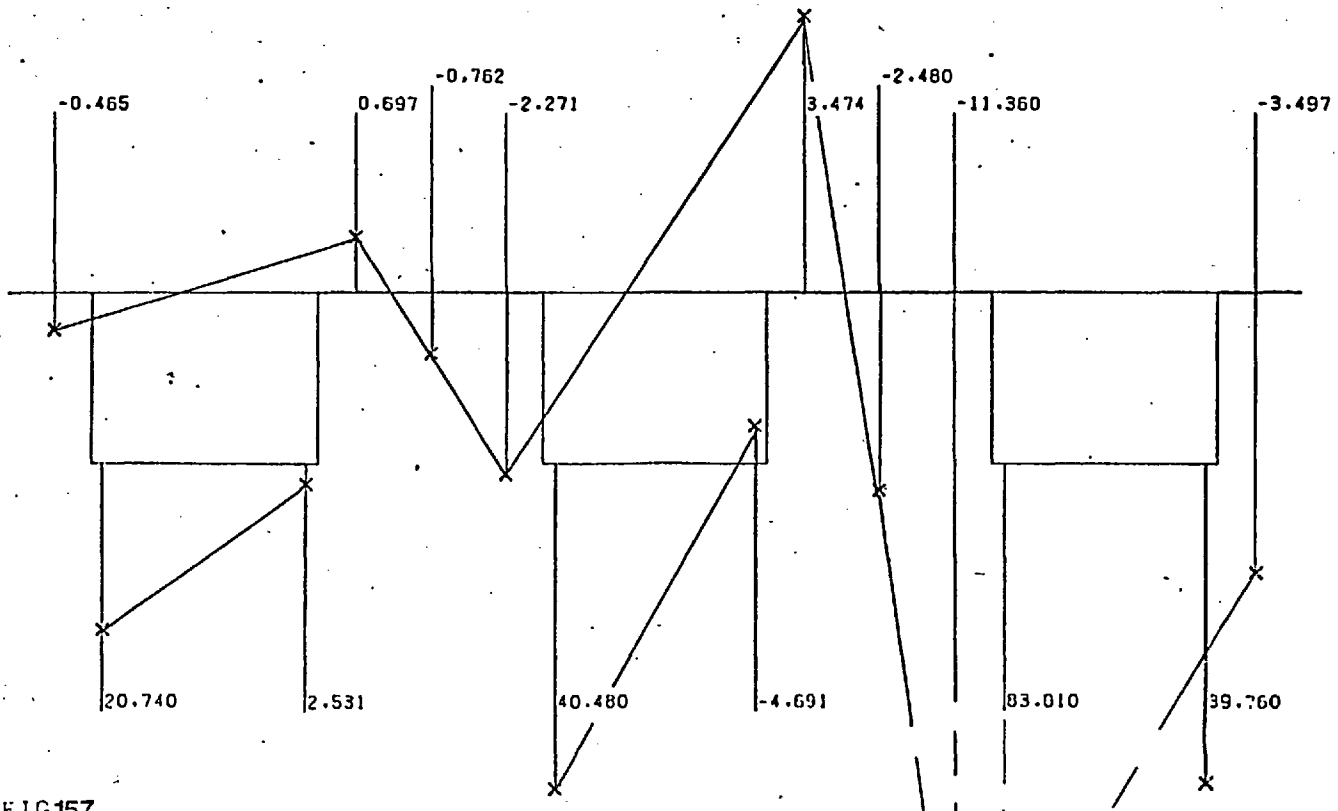


FIG157

LOAD CASE 16 SECTION 3-3 SECONDARY STRESS GAUGES
LONGITUDINAL STRESSES AT EXTREME FIBRES

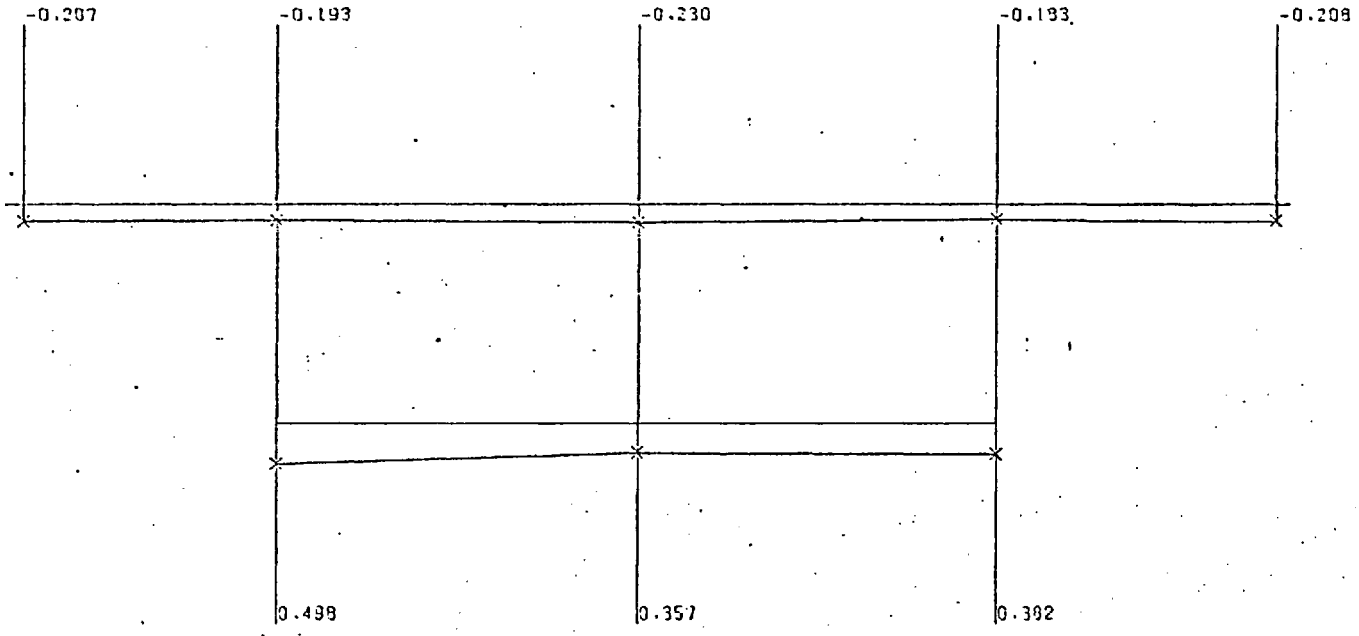


FIG158

LOAD CASE 4 SECTION 1-1 MAIN STRESS GAUGES
LONGITUDINAL STRESSES AT EXTREME FIBRES

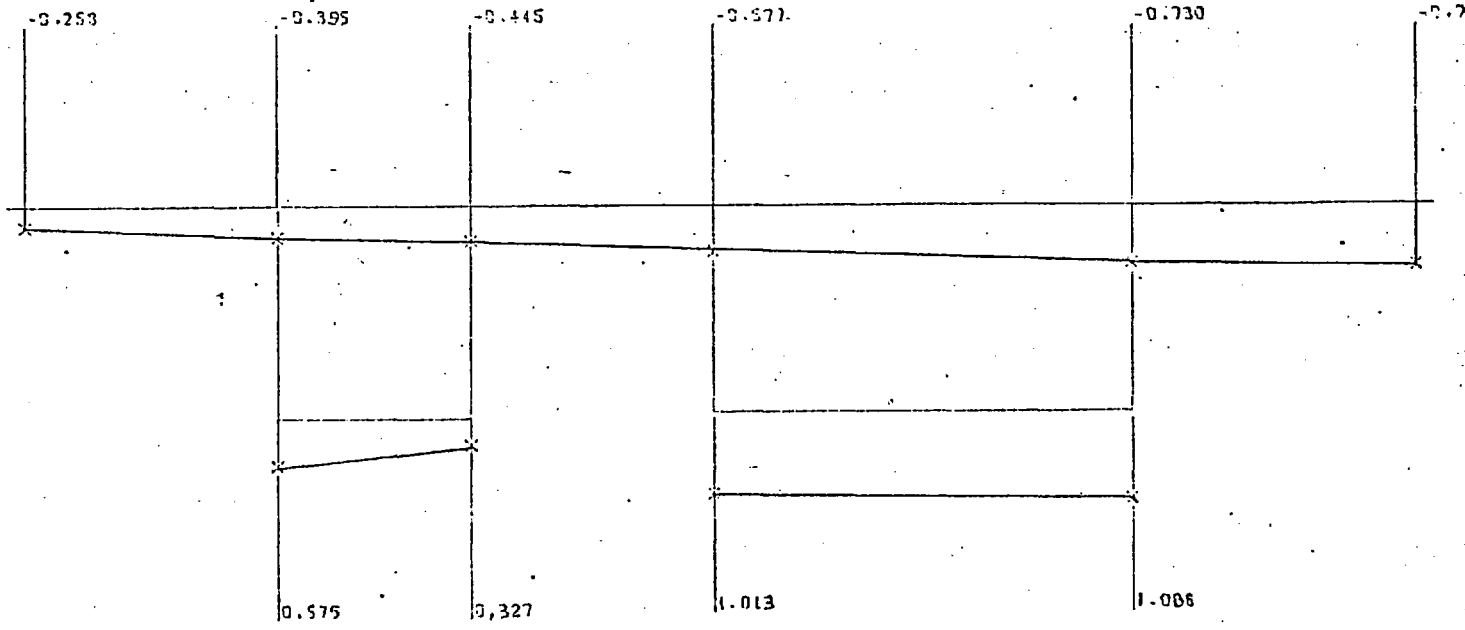


FIG159

LOAD CASE 5 SECTION S-S MAIN STRESS GAUGES
LONGITUDINAL STRESSES AT EXTREME FIBRES

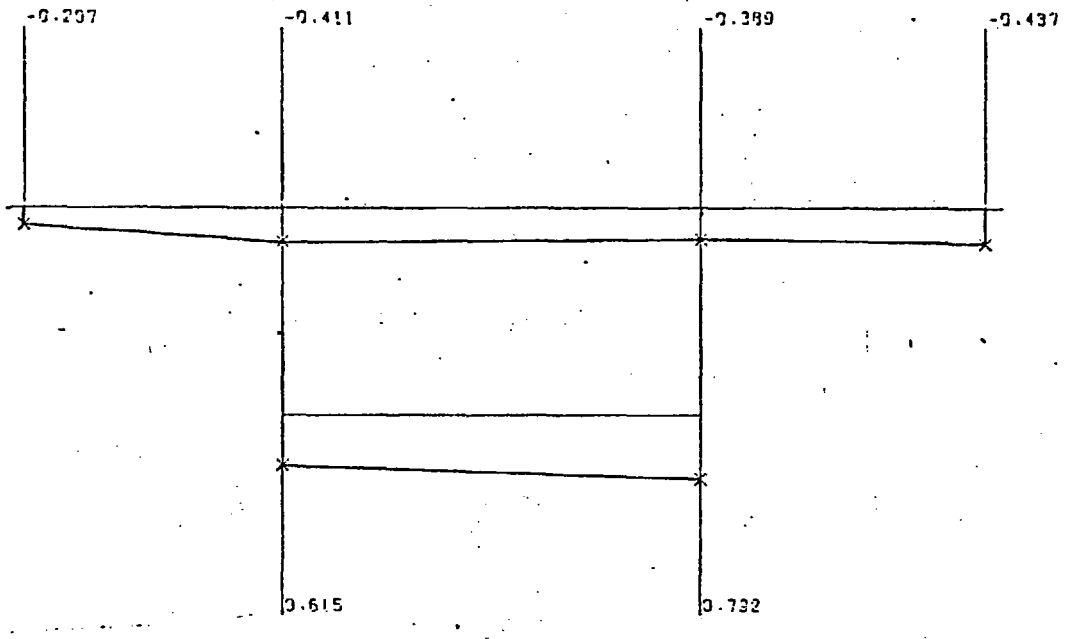


FIG160

LOAD CASE 10 SECTION 12-12 MAIN STRESS GAUGES
LONGITUDINAL STRESSES AT EXTREME FIBRES

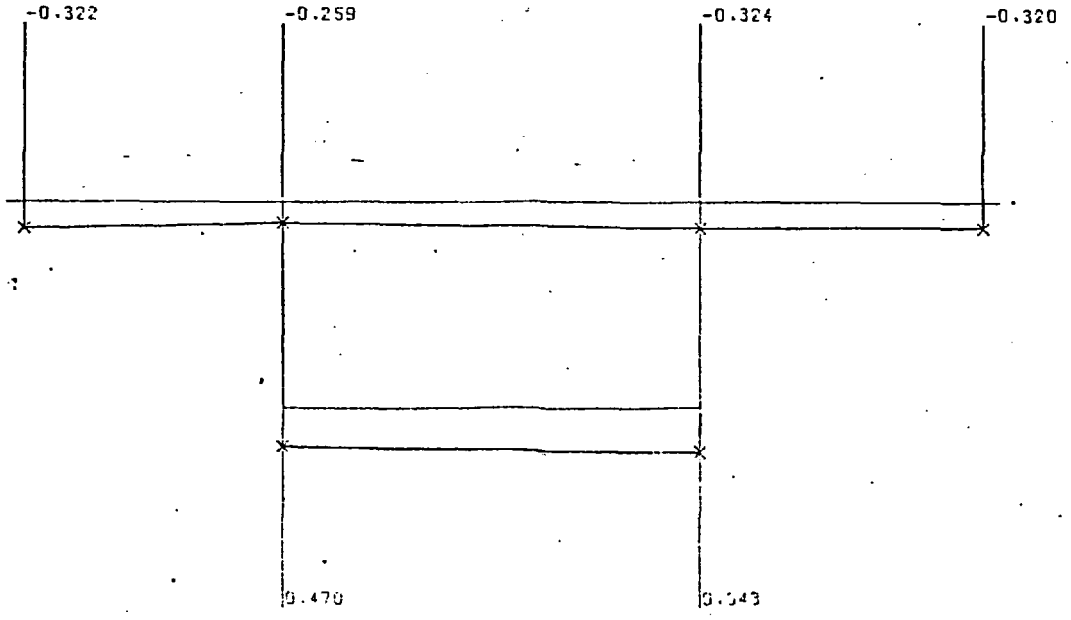


FIG161

LOAD CASE 12 SECTION 12-12 MAIN STRESS GAUGES
LONGITUDINAL STRESSES AT EXTREME FIBRES

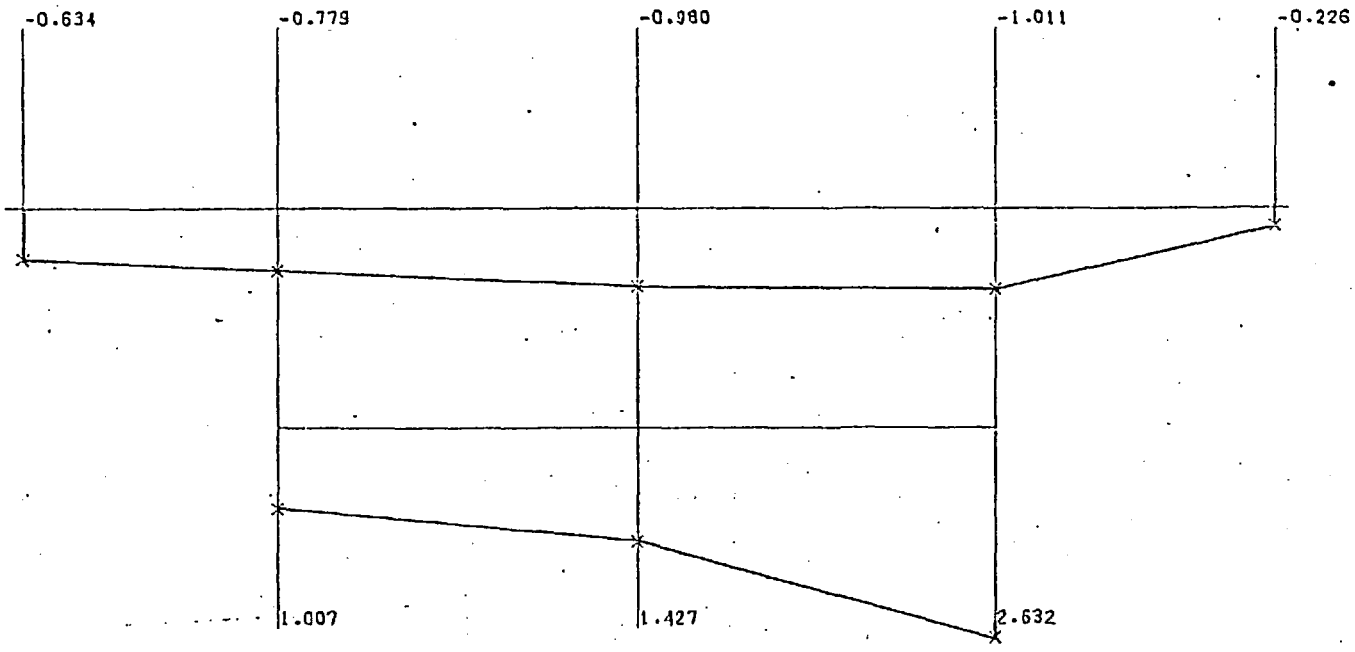


FIG 162

LOAD CASE 15 SECTION 1-1 MAIN STRESS GAUGES
LONGITUDINAL STRESSES AT EXTREME FIBRES

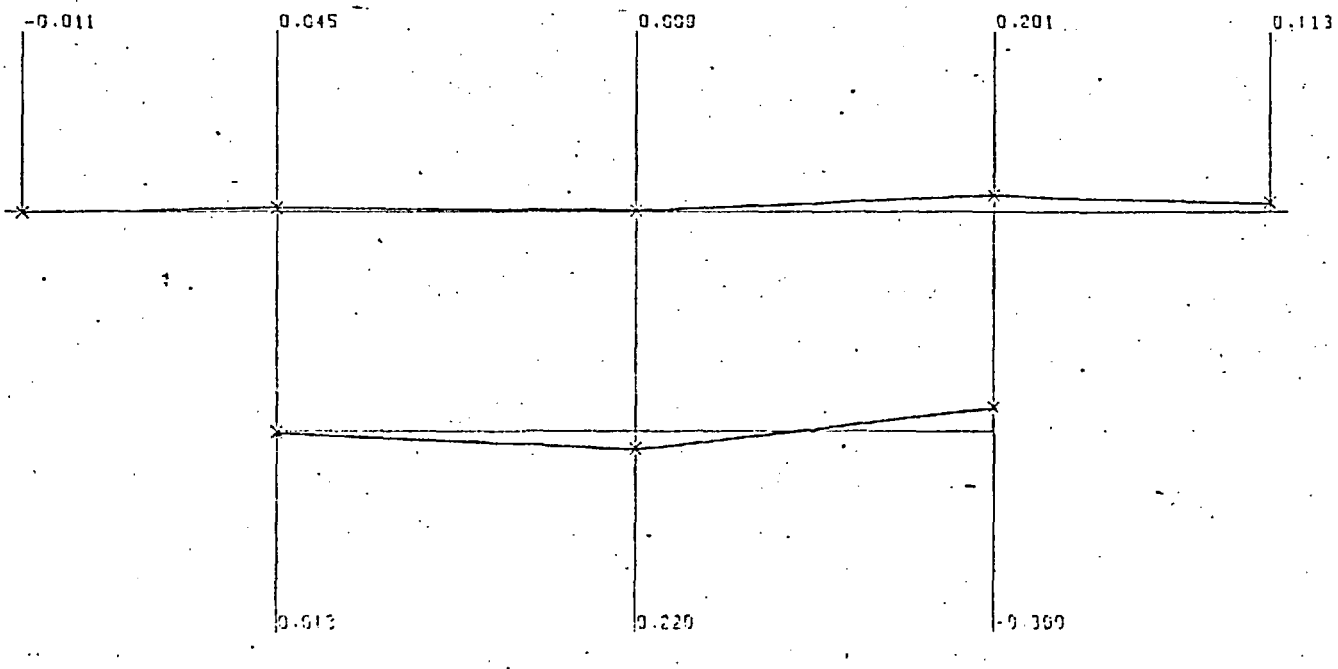


FIG 163

LOAD CASE 1 SECTION 2-2 MAIN STRESS GAUGES
LONGITUDINAL STRESSES AT EXTREME FIBRES

455

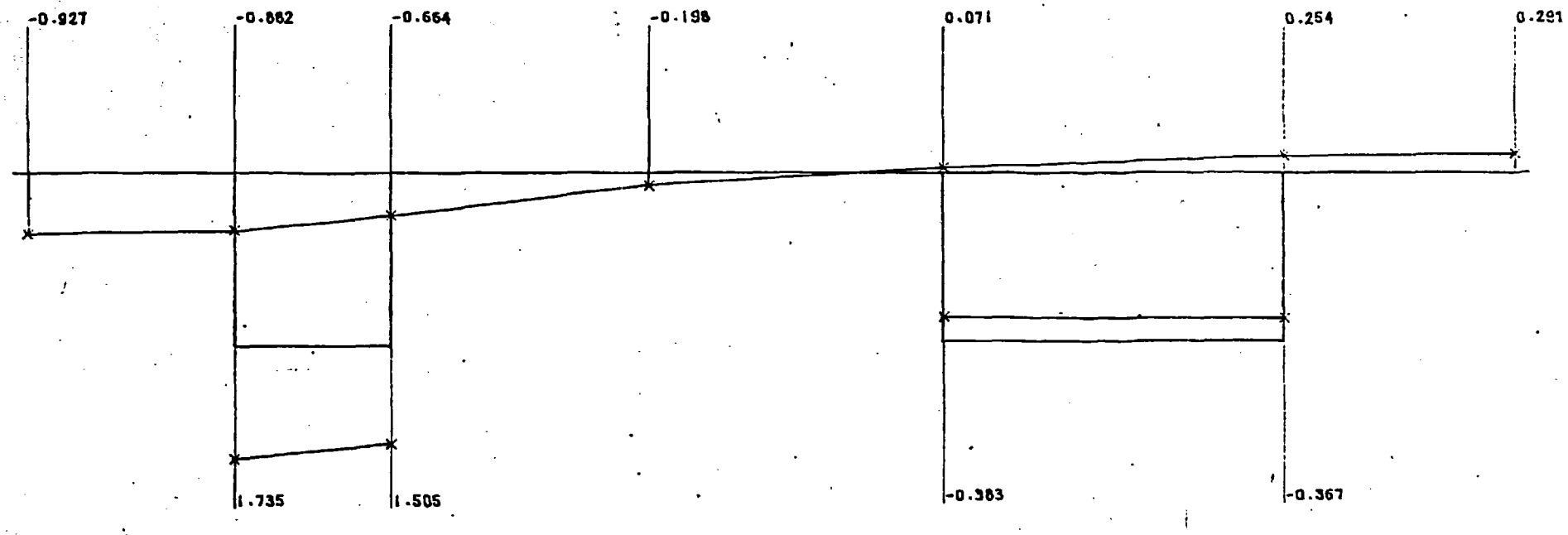


FIG164

LOAD CASE 9 SECTION 6-6 MAIN STRESS GAUGES
LONGITUDINAL STRESSES AT EXTREME FIBRES

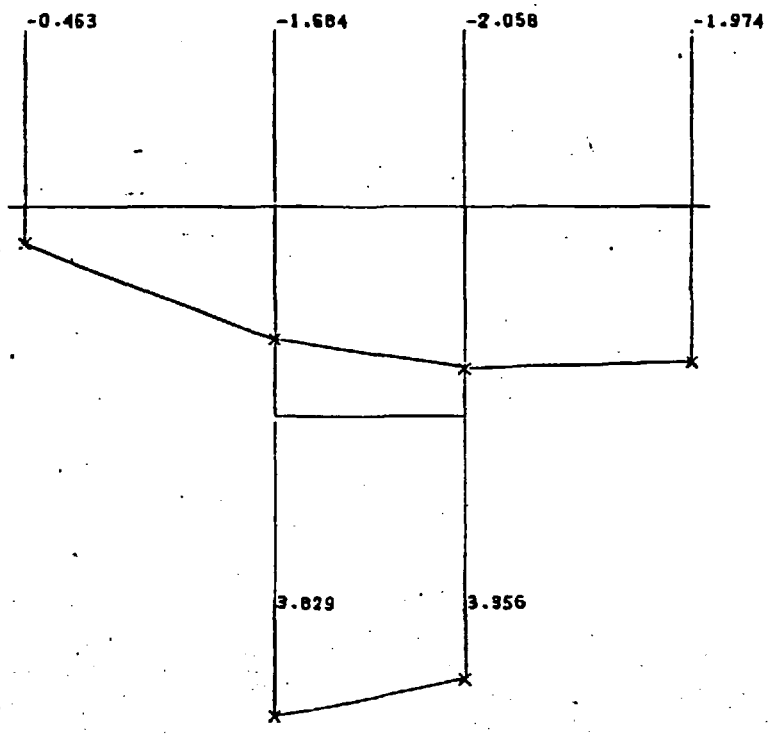


FIG165

LOAD CASE 30 SECTION 9-9 MAIN STRESS GAUGES
LONGITUDINAL STRESSES AT EXTREME FIBRES

456

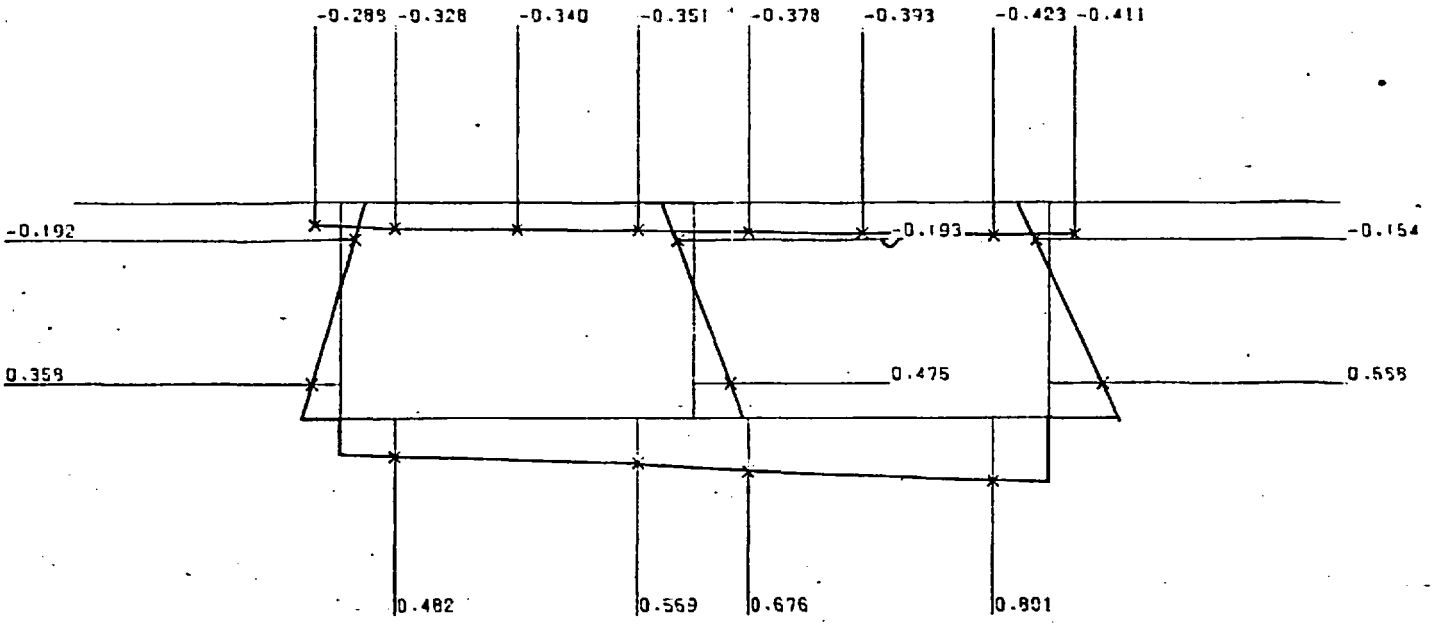


FIG166

LOAD CASE 1 SECTION 1-1 SECONDARY STRESS GAUGES
IN PLANE COMPONENT OF LONGITUDINAL STRESS

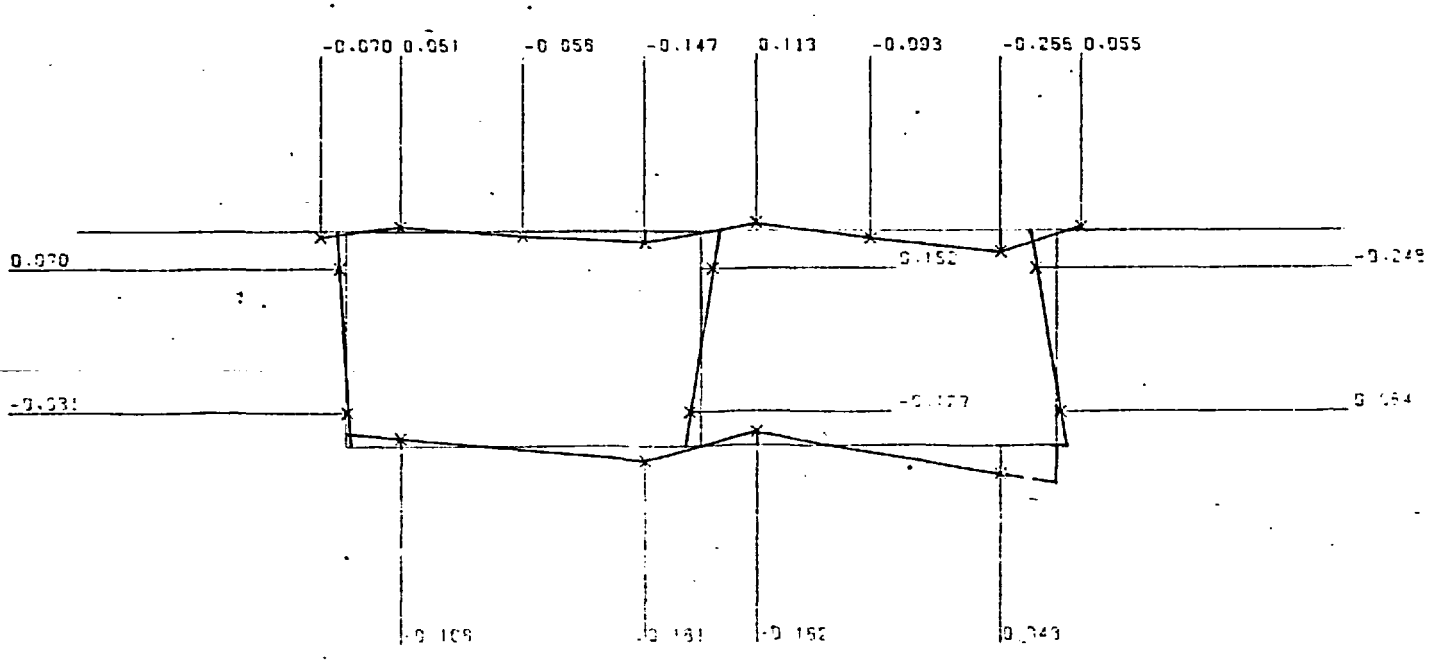


FIG167

LOAD CASE 1 SECTION 1-1 SECONDARY STRESS GAUGES

457

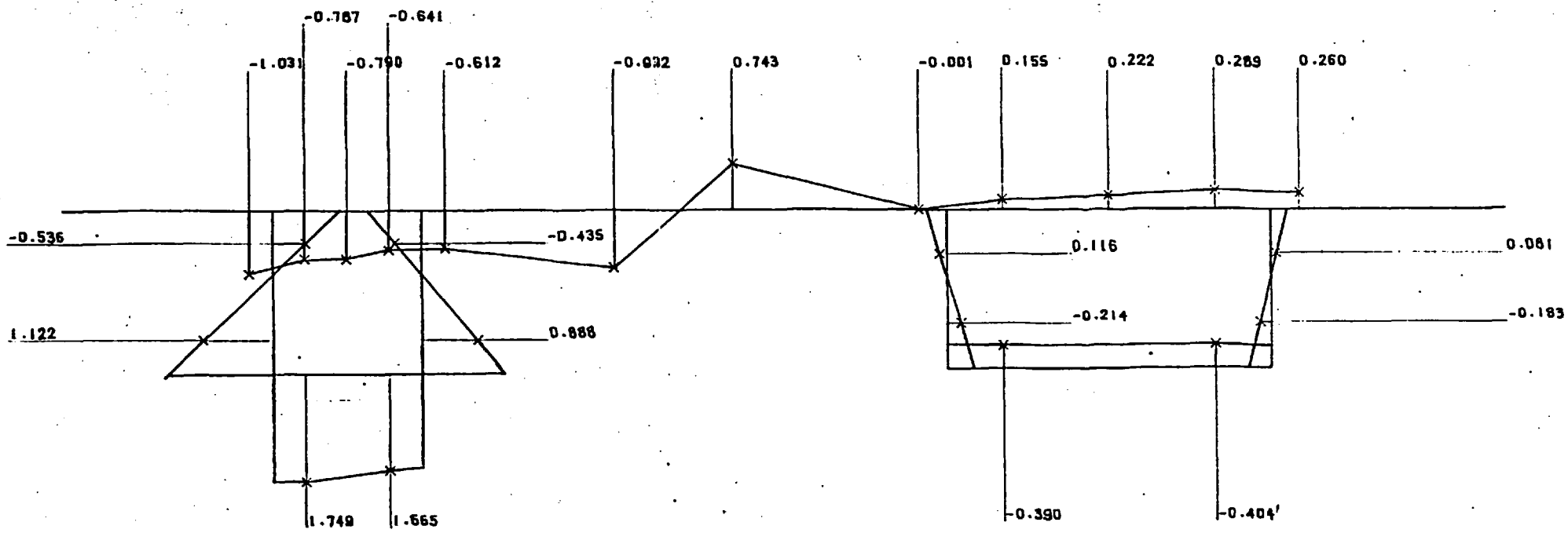


FIG 168

LOAD CASE 9 SECTION 6-6 SECONDARY STRESS GAUGES
LONGITUDINAL STRESSES AT EXTREME FIBRES

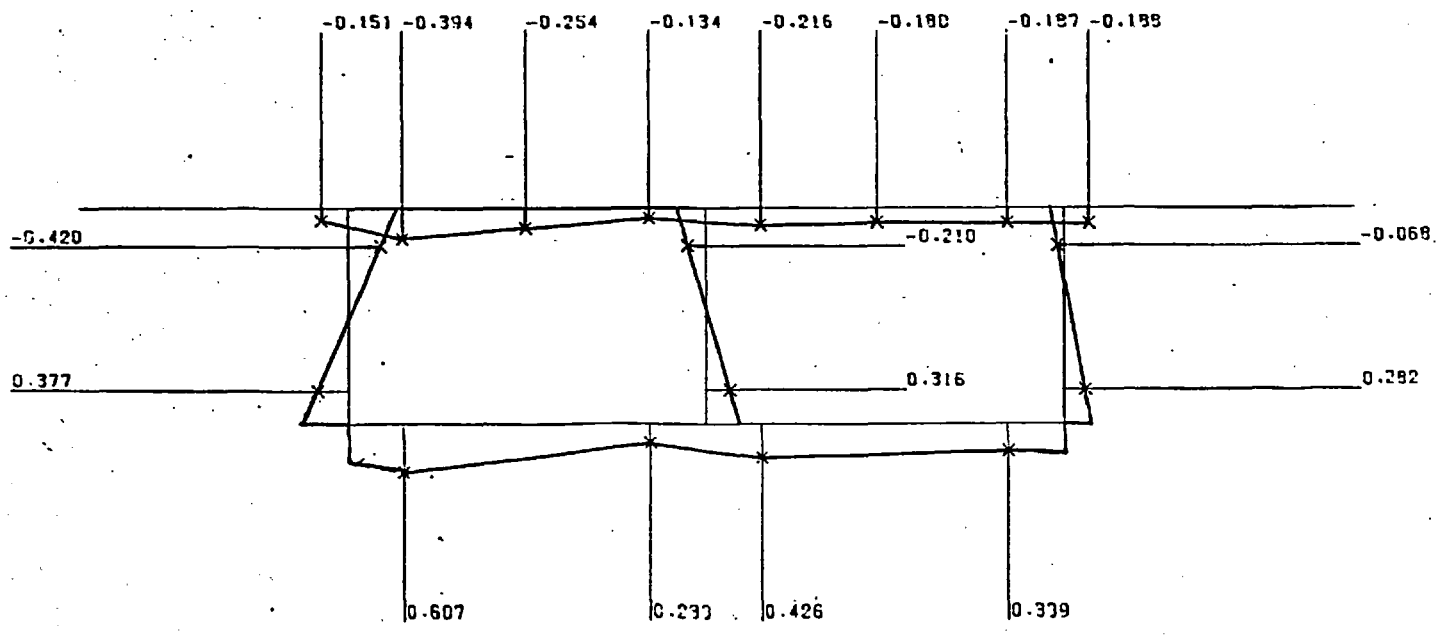


FIG 169

LOAD CASE 4 SECTION 1-1 SECONDARY STRESS GAUGES
LONGITUDINAL STRESSES AT EXTREME FIBRES

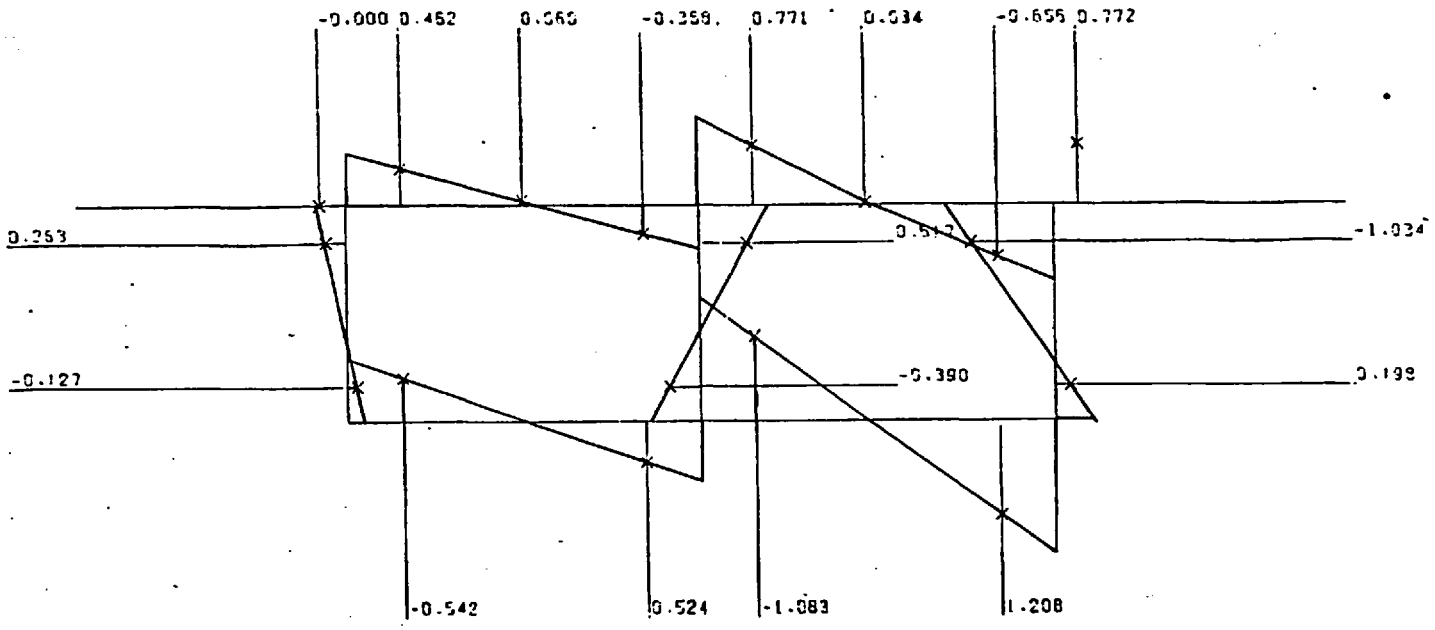


FIG170

LOAD CASE 1 SECTION 1-1 SECONDARY STRESS GAUGES
FLEXURAL COMPONENT OF TRANSVERSE STRESS

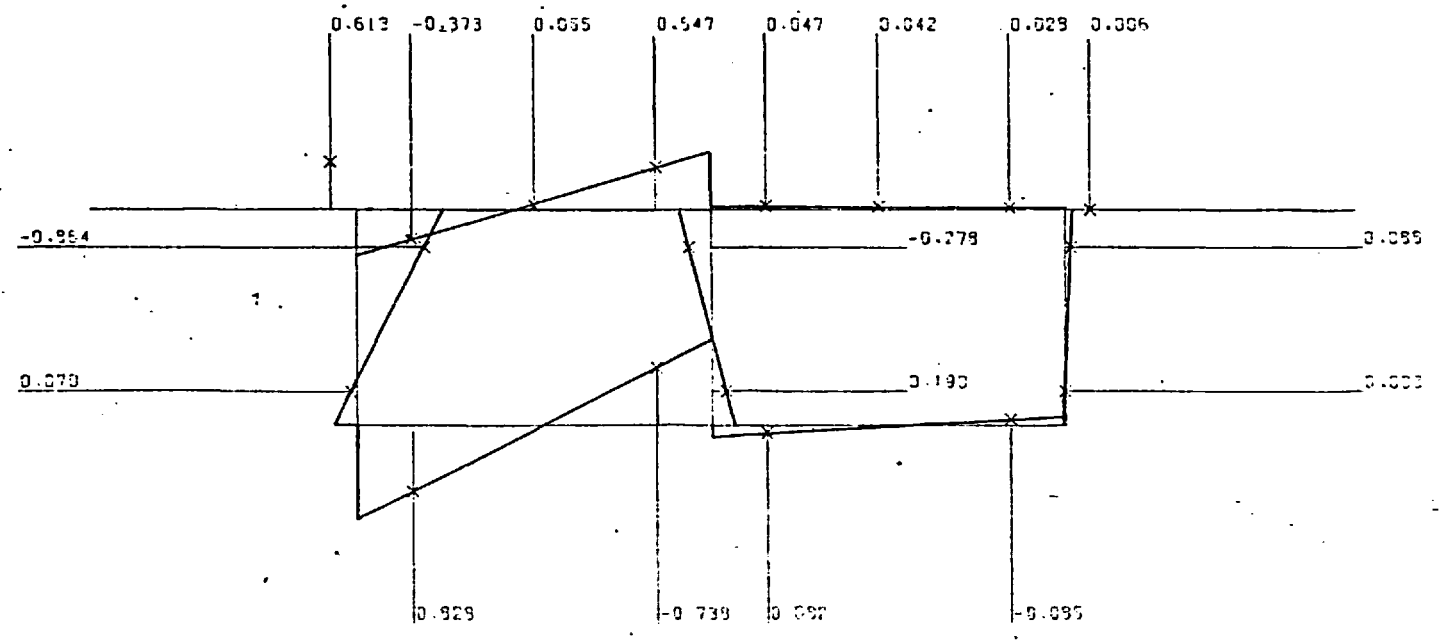


FIG171

LOAD CASE 4 SECTION 1-1 SECONDARY STRESS GAUGES
FLEXURAL COMPONENT OF TRANSVERSE STRESS

459

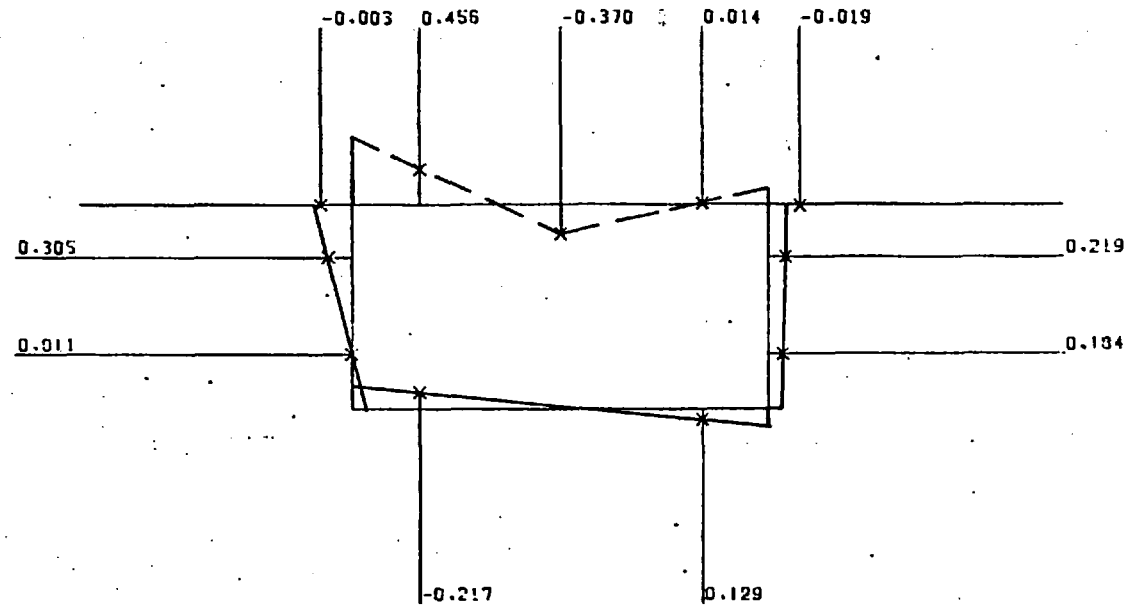


FIG172

LOAD CASE 11 SECTION 12-12 SECONDARY STRESS GAUGES
FLEXURAL COMPONENT OF TRANSVERSE STRESS

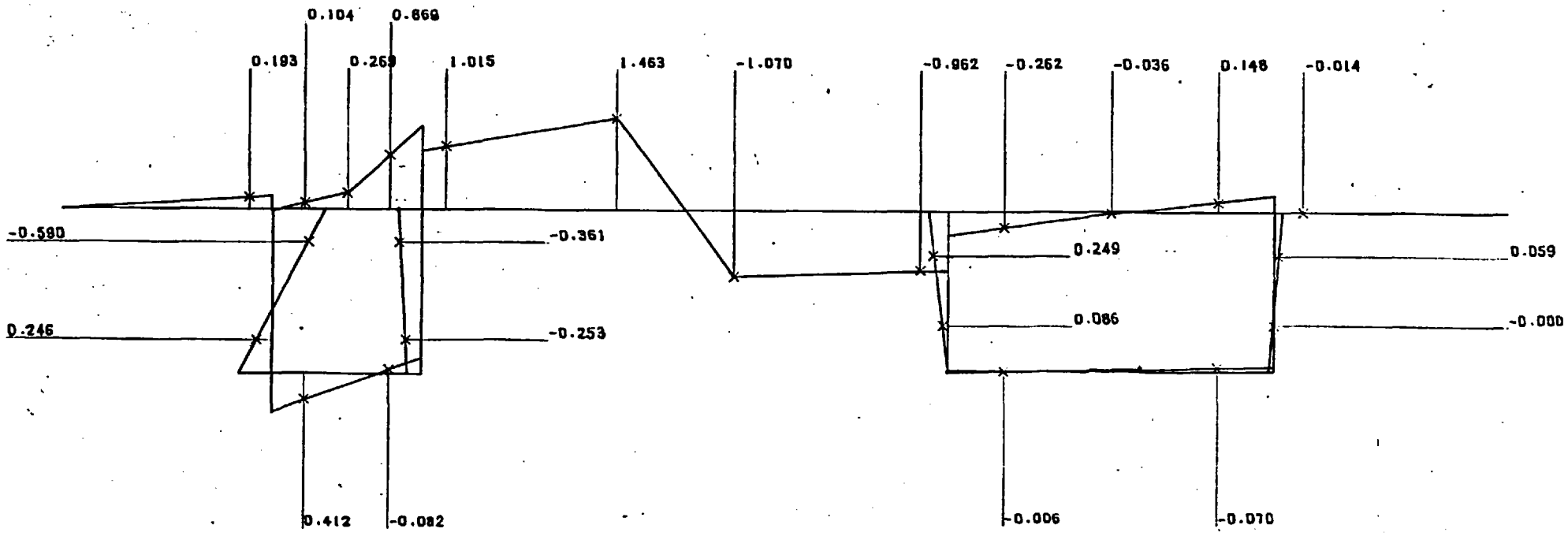


FIG173

LOAD CASE 9 SECTION 6-6 SECONDARY STRESS GAUGES
FLEXURAL COMPONENT OF TRANSVERSE STRESS

460

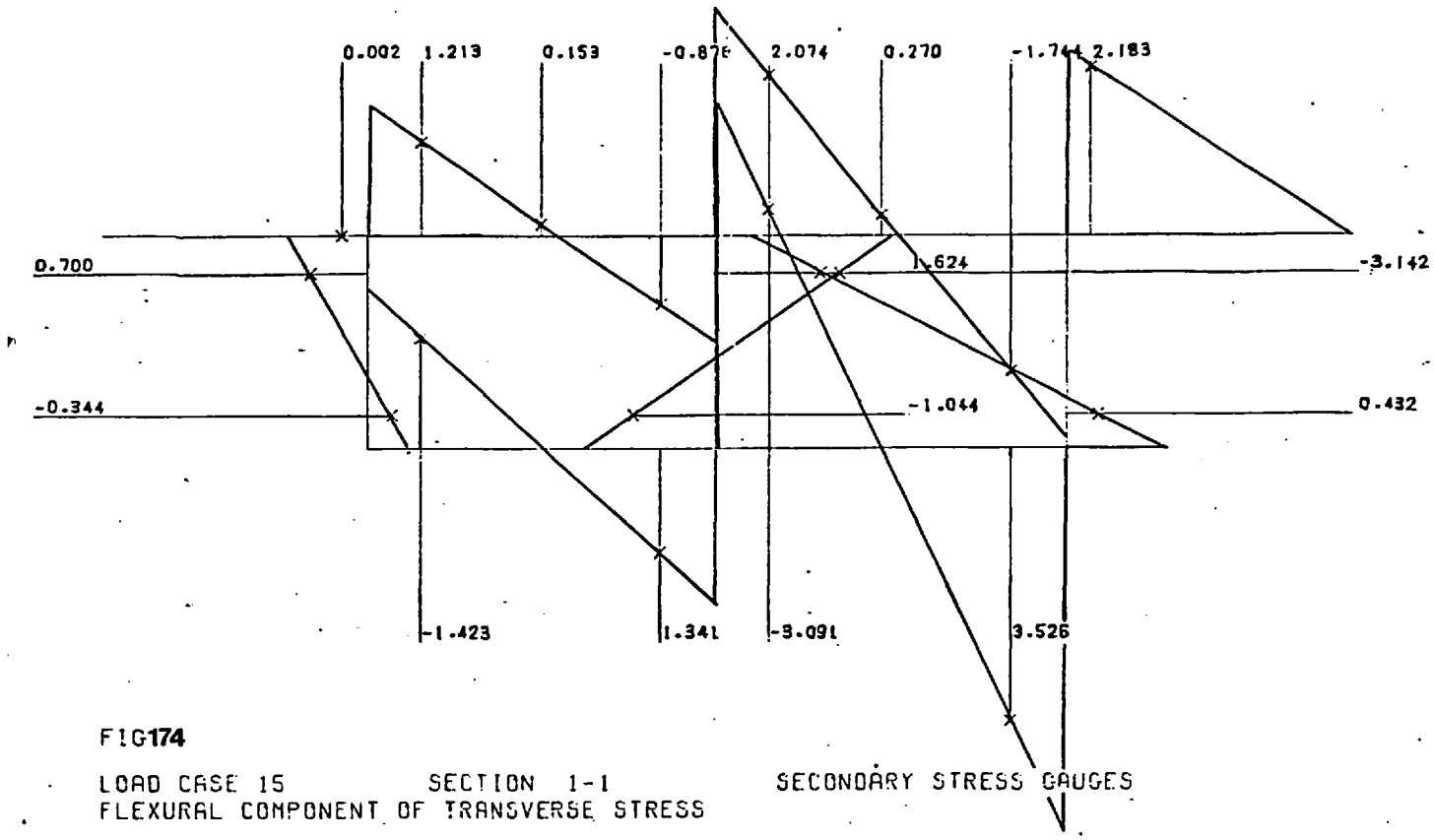


FIG**174**

LOAD CASE 15 SECTION 1-1 SECONDARY STRESS GAUGES
FLEXURAL COMPONENT OF TRANSVERSE STRESS

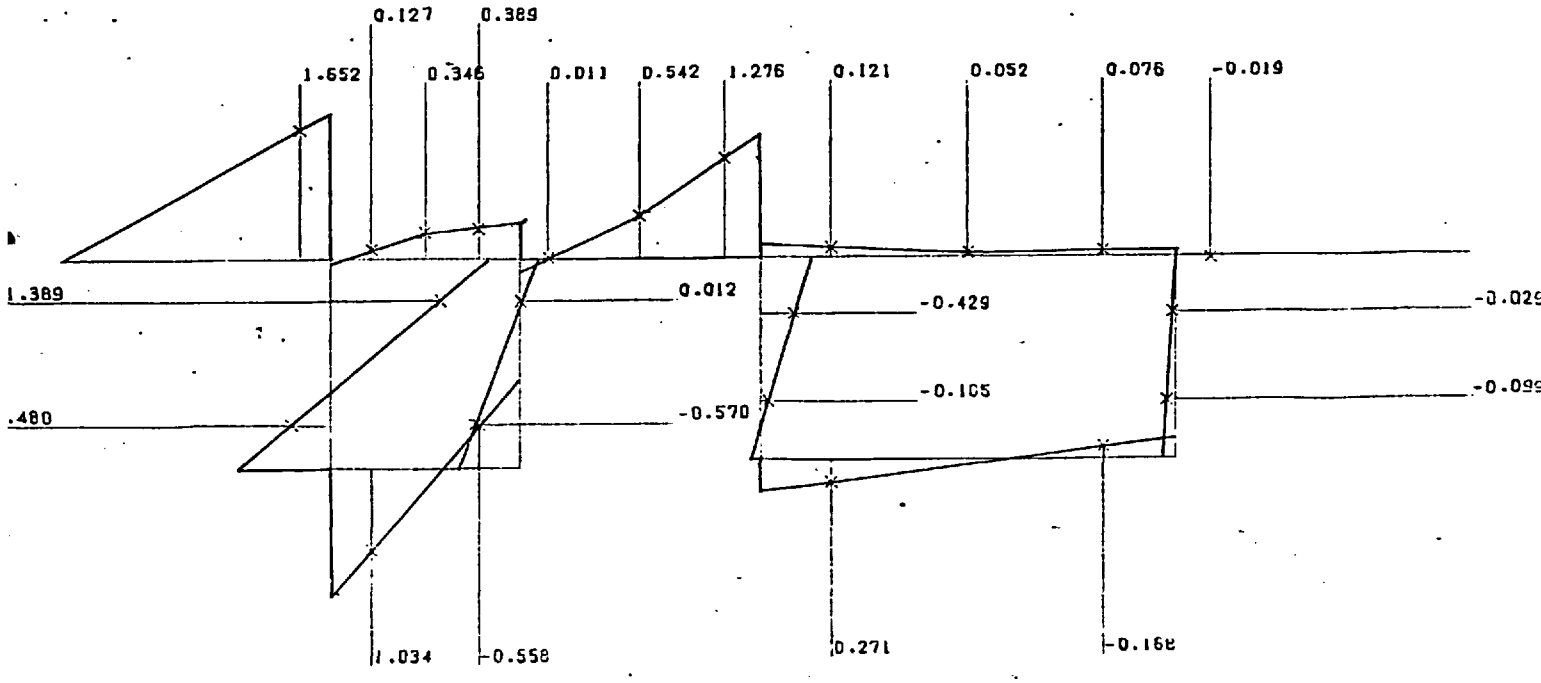


FIG**175**

LOAD CASE 29 SECTION 5-5 SECONDARY STRESS GAUGES
FLEXURAL COMPONENT OF TRANSVERSE STRESS

461

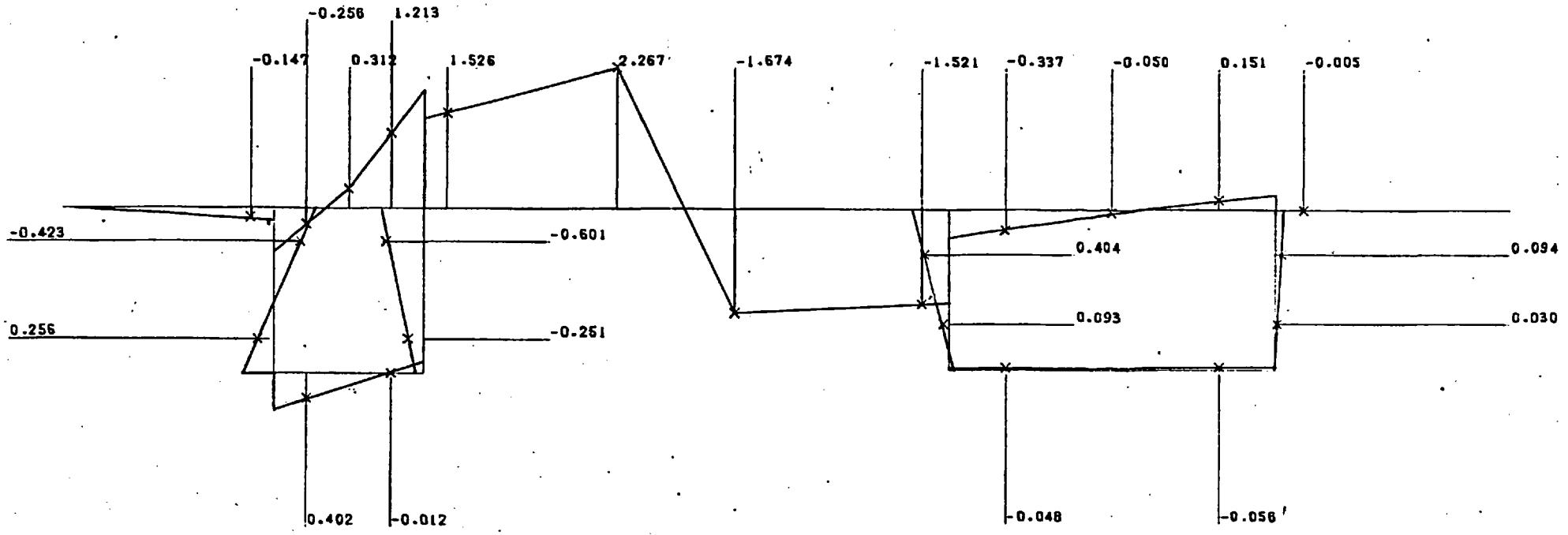


FIG176

LOAD CASE 29 SECTION 6-6 SECONDARY STRESS GAUGES
FLEXURAL COMPONENT OF TRANSVERSE STRESS

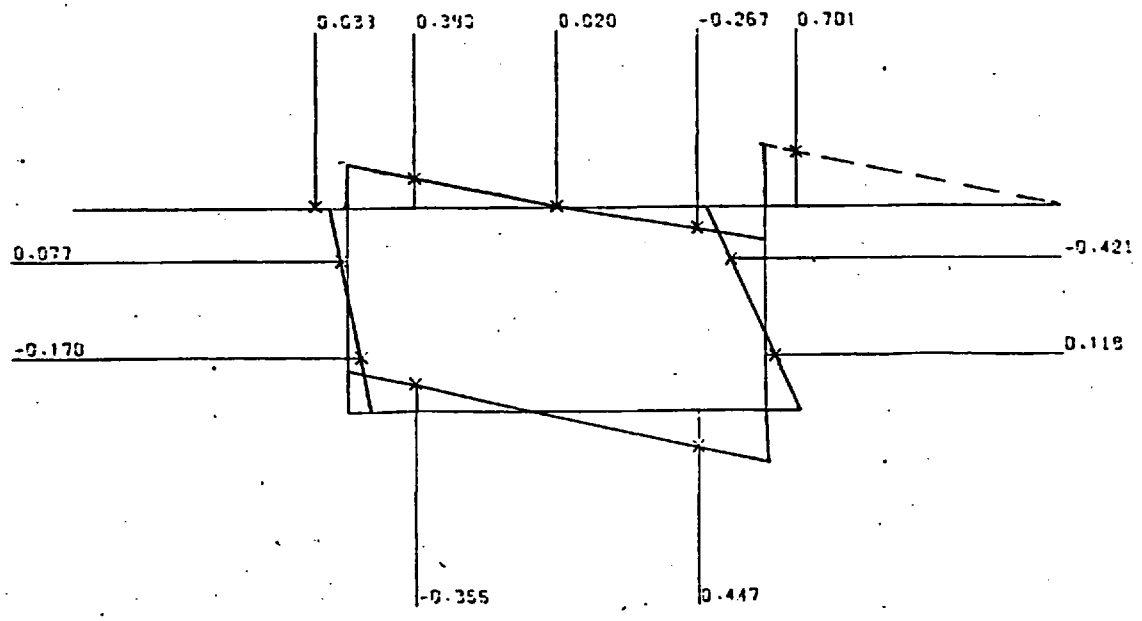


FIG177

LOAD CASE 10 SECTION 12-12 SECONDARY STRESS GAUGES
FLEXURAL COMPONENT OF TRANSVERSE STRESS

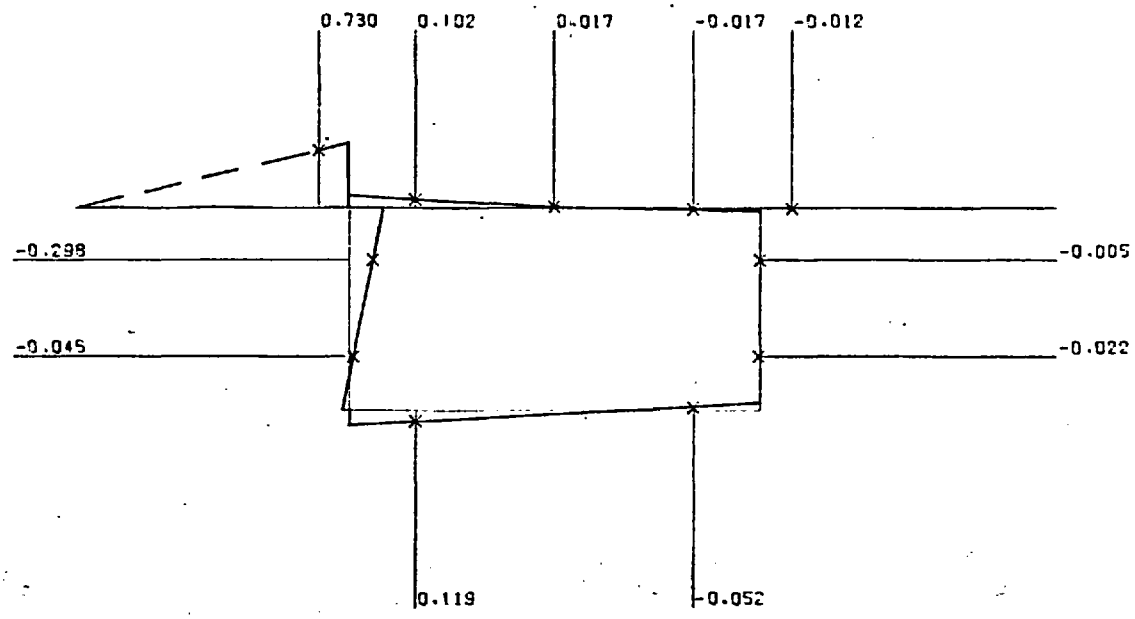


FIG178

LOAD CASE 12 SECTION 12-12 SECONDARY STRESS GAUGES
FLEXURAL COMPONENT OF TRANSVERSE STRESS

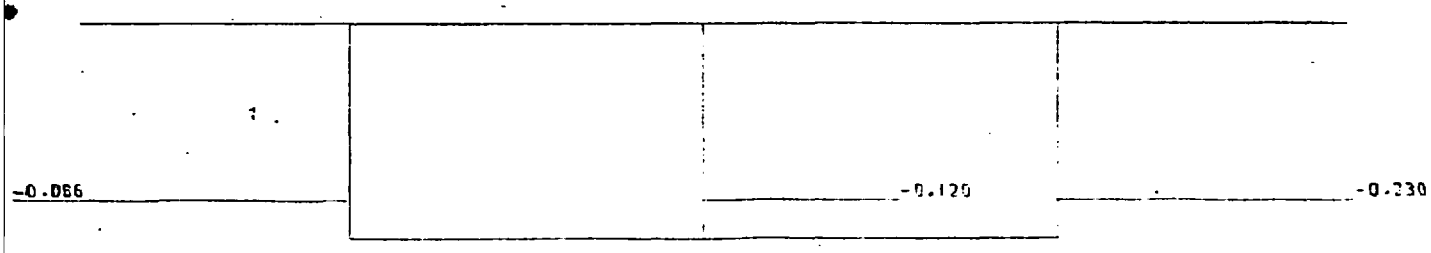


FIG179

LOAD CASE 5 SECTION 3-3 SECONDARY STRESS GAUGES
VERTICAL SHEAR STRESS IN WEB

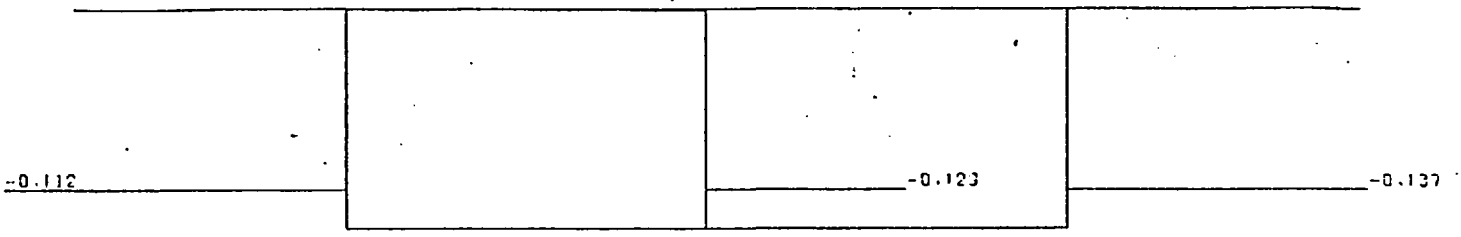


FIG180

LOAD CASE 9 SECTION 3-3 SECONDARY STRESS GAUGES
VERTICAL SHEAR STRESS IN WEBS

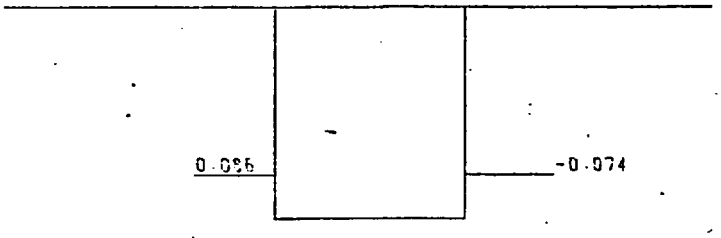


FIG181

LOAD CASE 5 SECTION 7-7 SECONDARY STRESS GAUGES
VERTICAL SHEAR STRESS IN WEBS

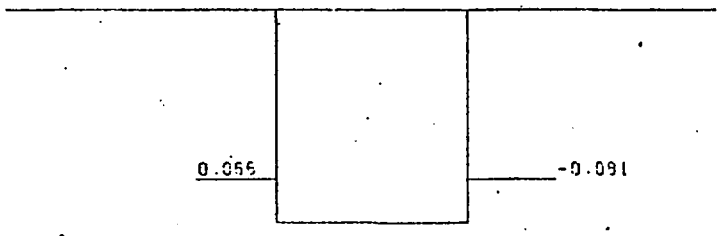


FIG182

LOAD CASE 6 SECTION 7-7 SECONDARY STRESS GAUGES
VERTICAL SHEAR STRESS IN WEBS

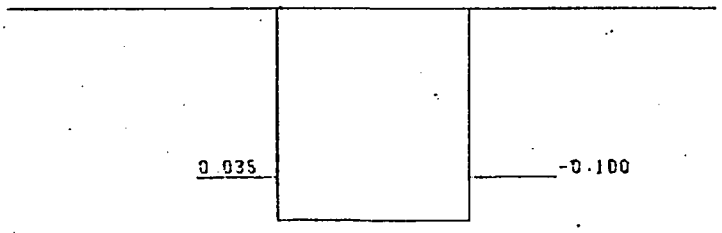


FIG183

LOAD CASE 7 SECTION 7-7 SECONDARY STRESS GAUGES
VERTICAL SHEAR STRESS IN WEBS

465

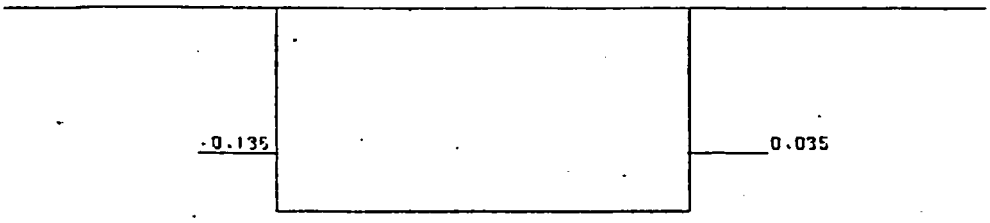


FIG184

LOAD CASE 9 SECTION 10-10 SECONDARY STRESS GAUGES
VERTICAL SHEAR STRESS IN WEBS

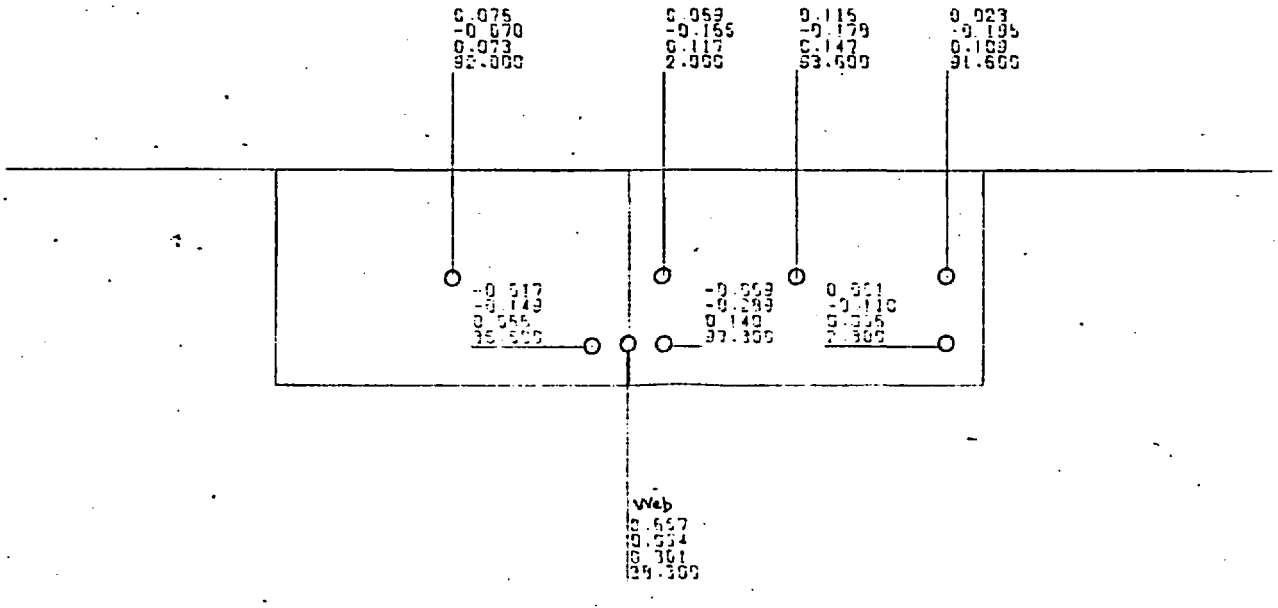


FIG185

LOAD CASE 5 SECTION 4-4 SECONDARY STRESS GAUGES
PRINCIPAL STRESSES, MAX. SHEAR, DIRECTION

466

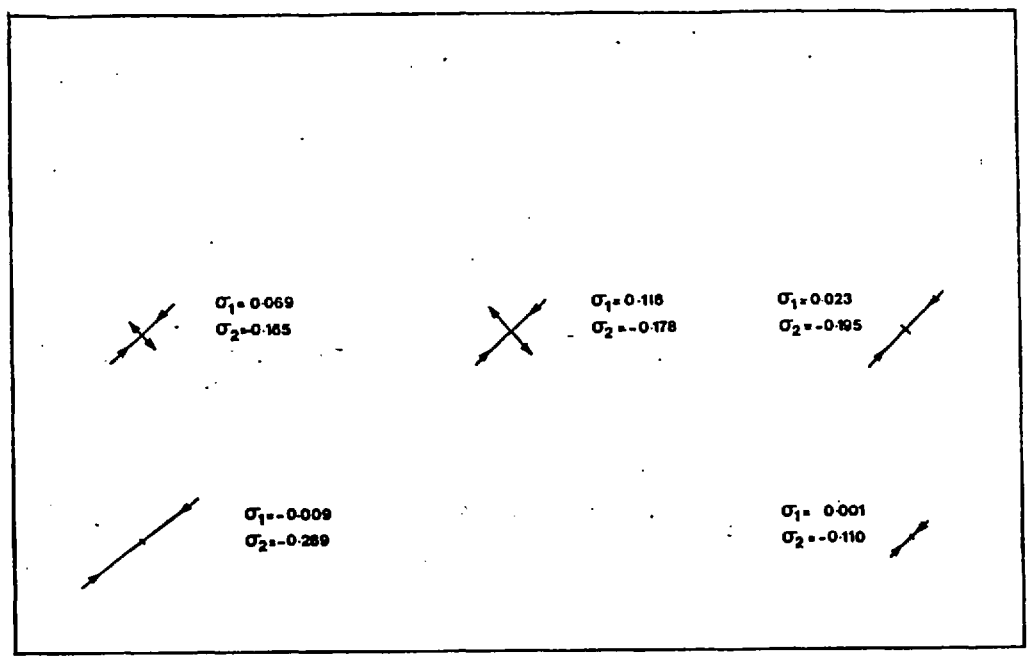


Fig.186 Principal stresses from Fig.185 plotted to scale in correct direction

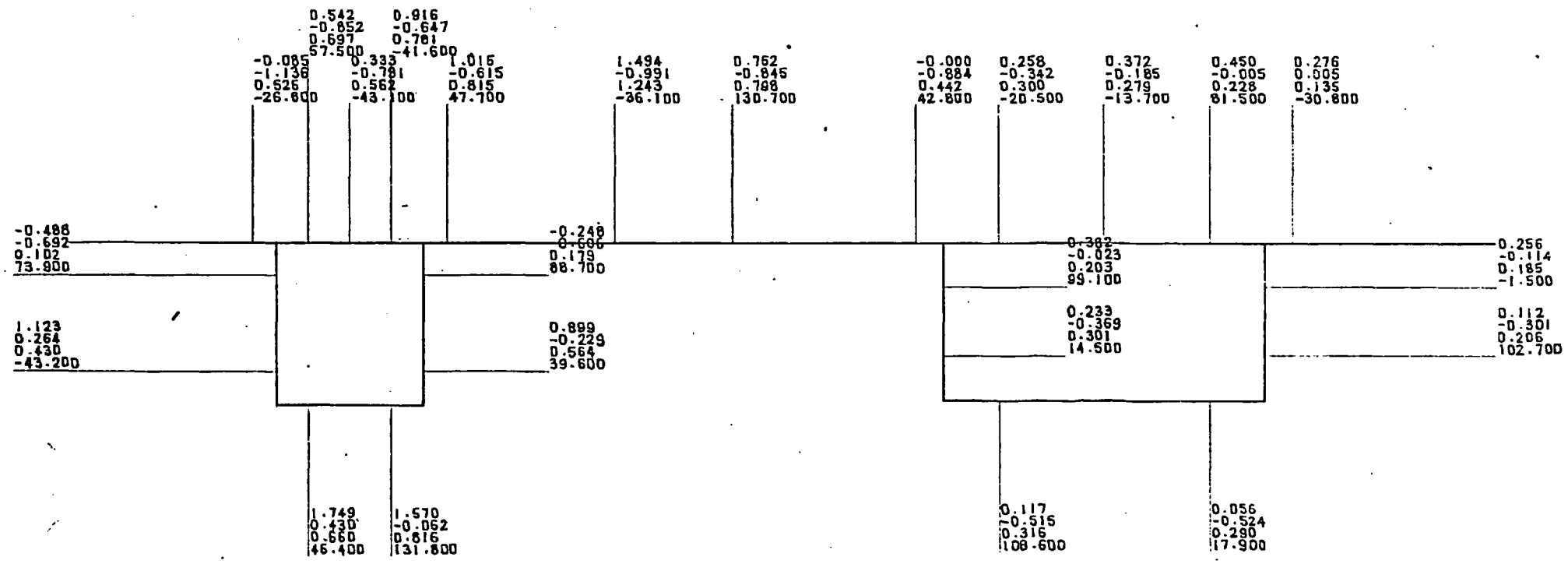


FIG 187

LOAD CASE 9 SECTION 6-6 SECONDARY STRESS GAUGES
PRINCIPAL STRESSES, MAX. SHEAR, DIRECTION

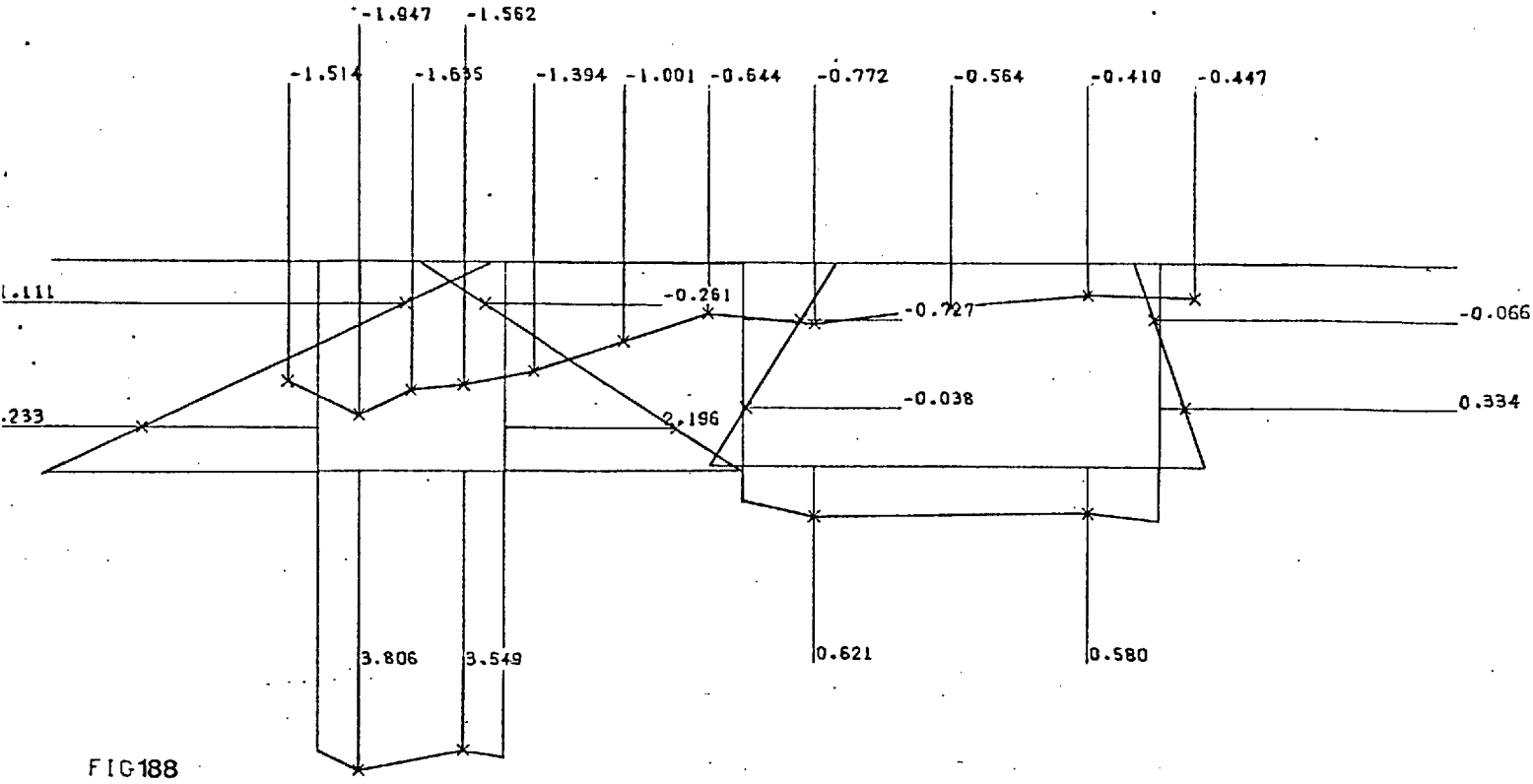


FIG188

LOAD CASE 29 SECTION 5-5 SECONDARY STRESS GAUGES
LONGITUDINAL STRESSES AT EXTREME FIBRES

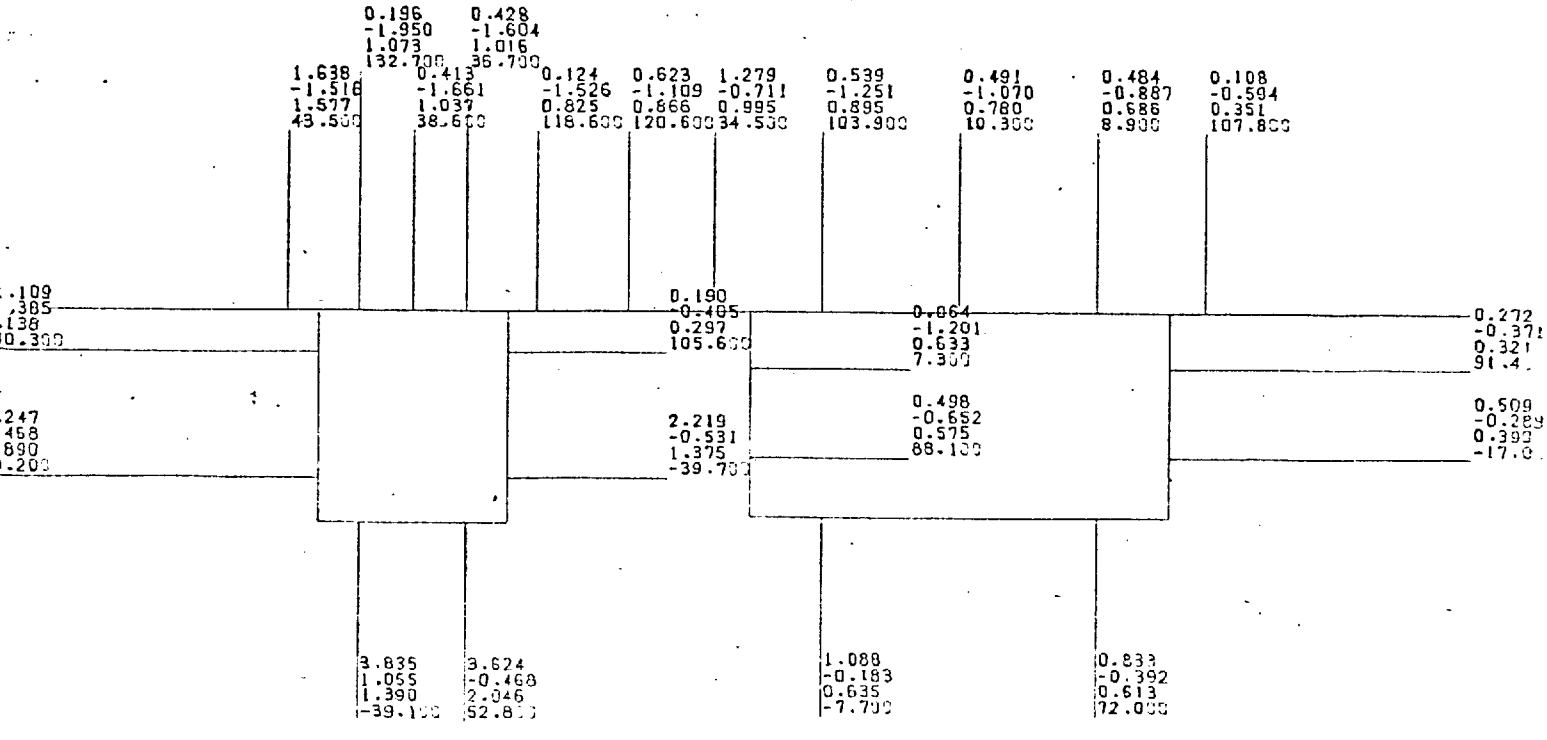


FIG189

LOAD CASE 29 SECTION 5-5 SECONDARY STRESS GAUGES
PRINCIPAL STRESSES MAX. SHEAR DIRECTION

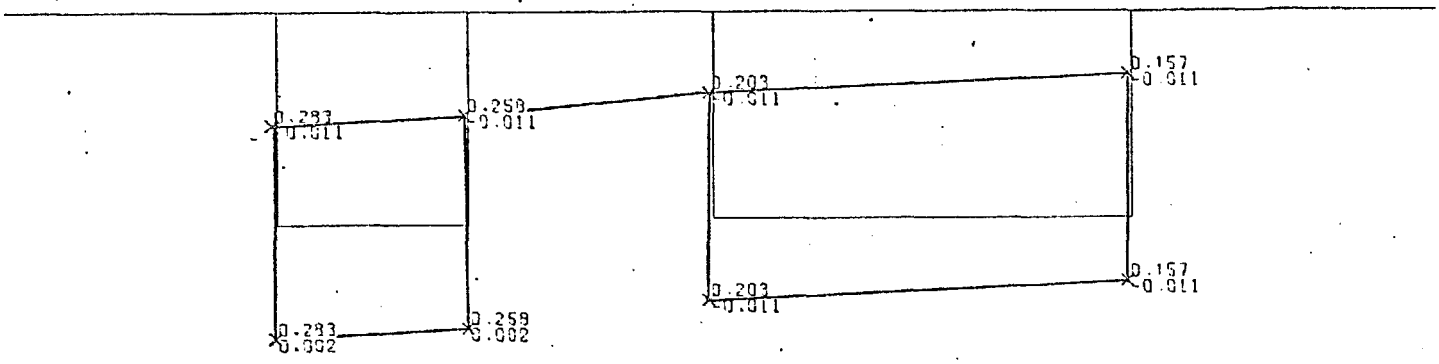


FIG 190

LOAD CASE 8 SECTION 5-5
DEFLECTIONS

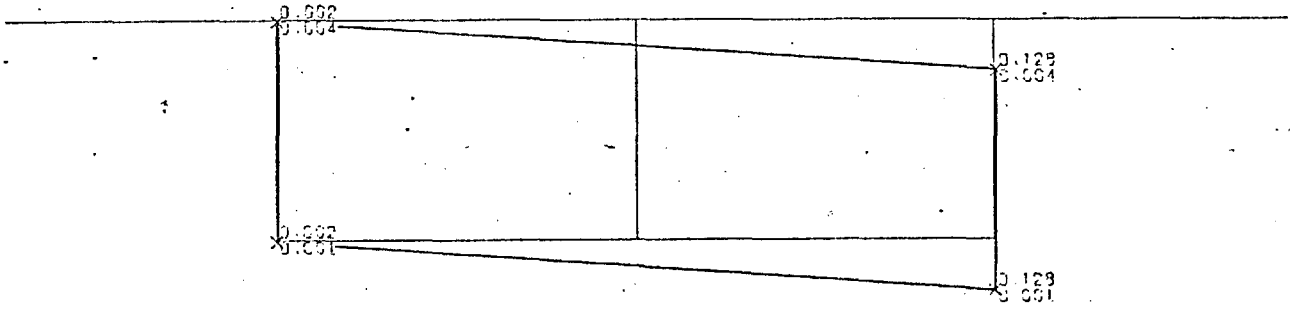


FIG 191

LOAD CASE 1 SECTION 1-1
DEFLECTIONS

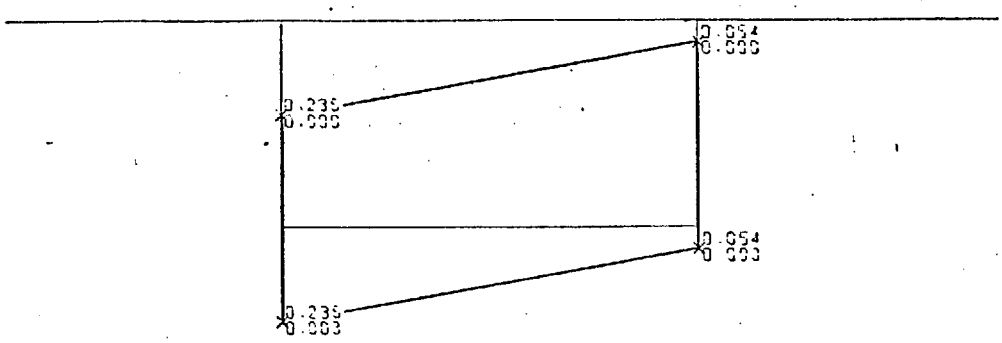


FIG192

LOAD CASE 12 SECTION 12-12
DEFLECTIONS

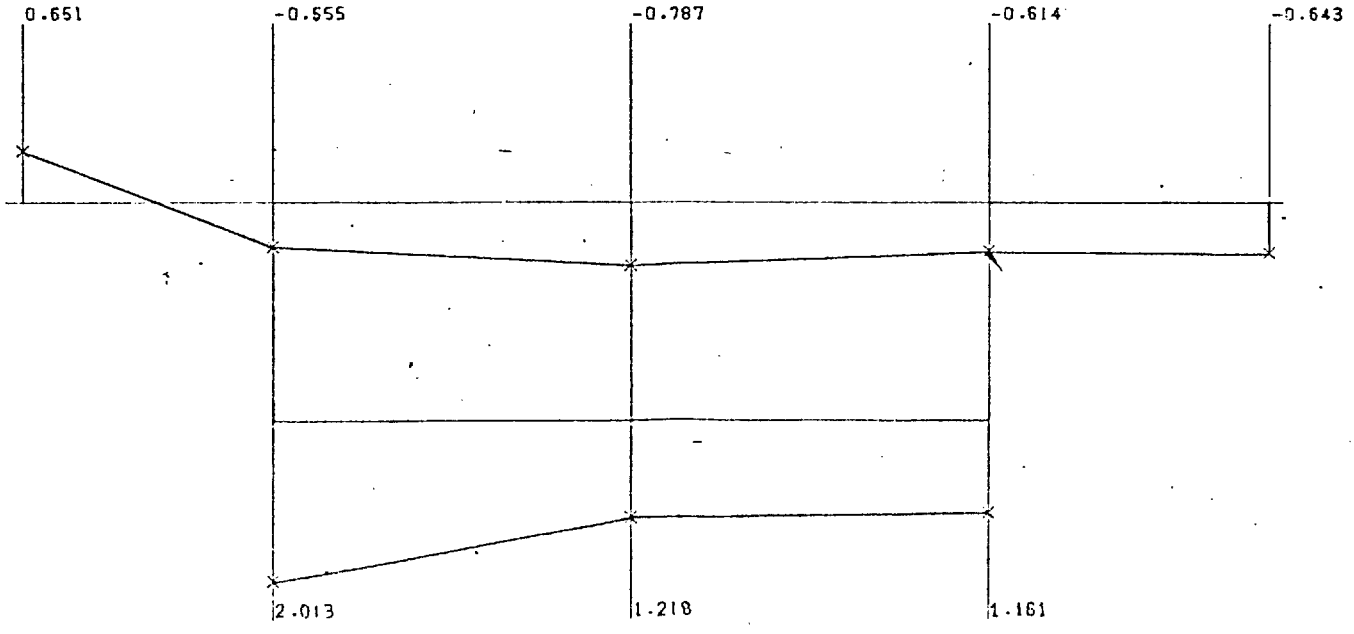


FIG193

LOAD CASE 20 SECTION 1-1 MAIN STRESS CAUSES
LONGITUDINAL STRESSES AT EXTREME FIBRES

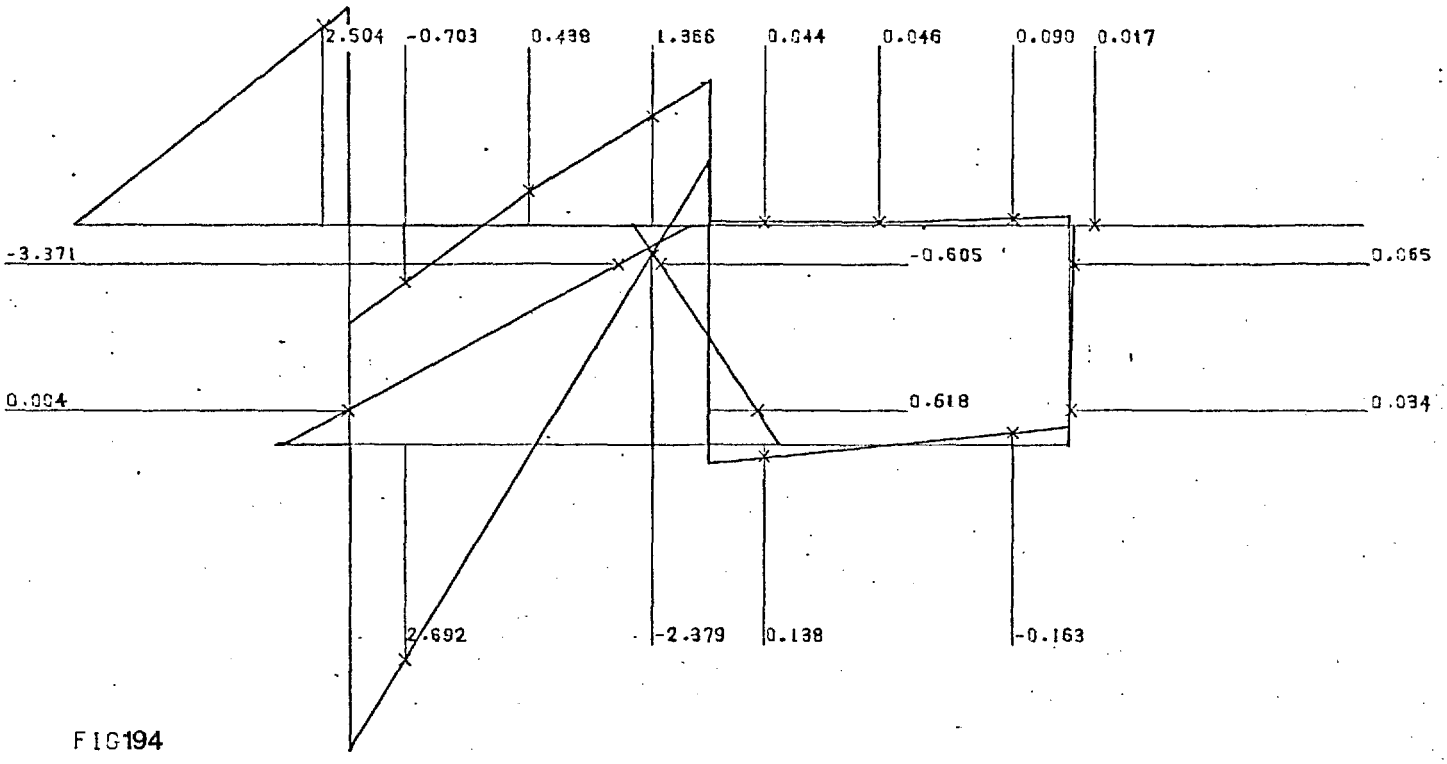


FIG194

LOAD CASE 20 SECTION 1-1 SECONDARY STRESS CAUSES
FLEXURAL COMPONENT OF TRANSVERSE STRESS

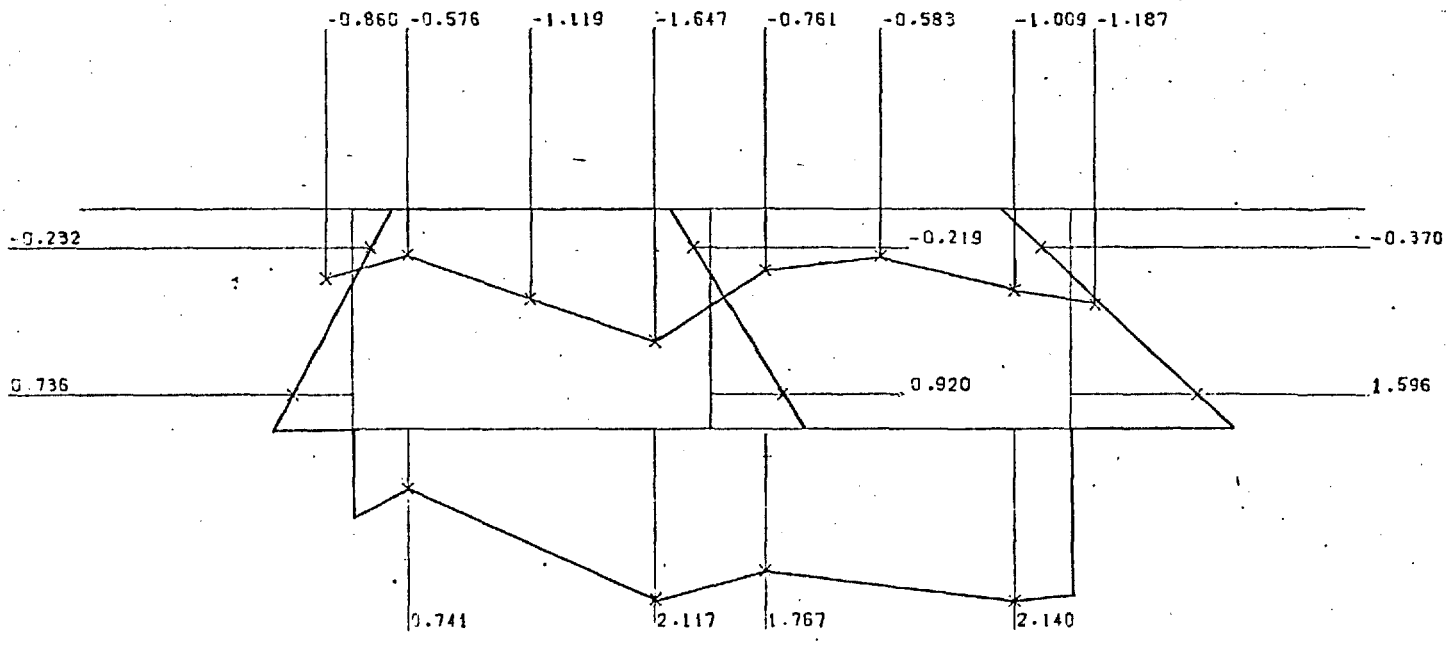


FIG195

LOAD CASE 17 SECTION 1-1 SECONDARY STRESS CAUSES
LONGITUDINAL STRESSES AT EXTREME FIBRES

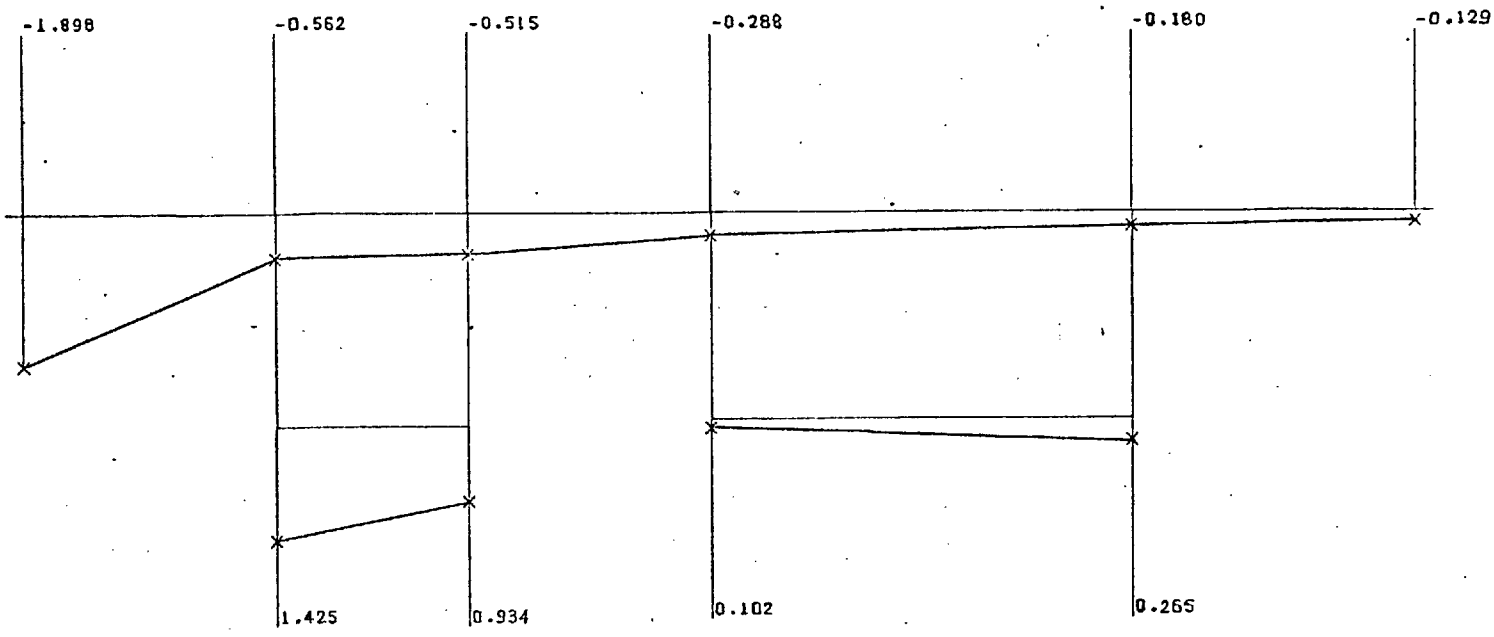


FIG196

LOAD CASE 49 SECTION 5-5 MAIN STRESS GAUGES
LONGITUDINAL STRESSES AT EXTREME FIBRES

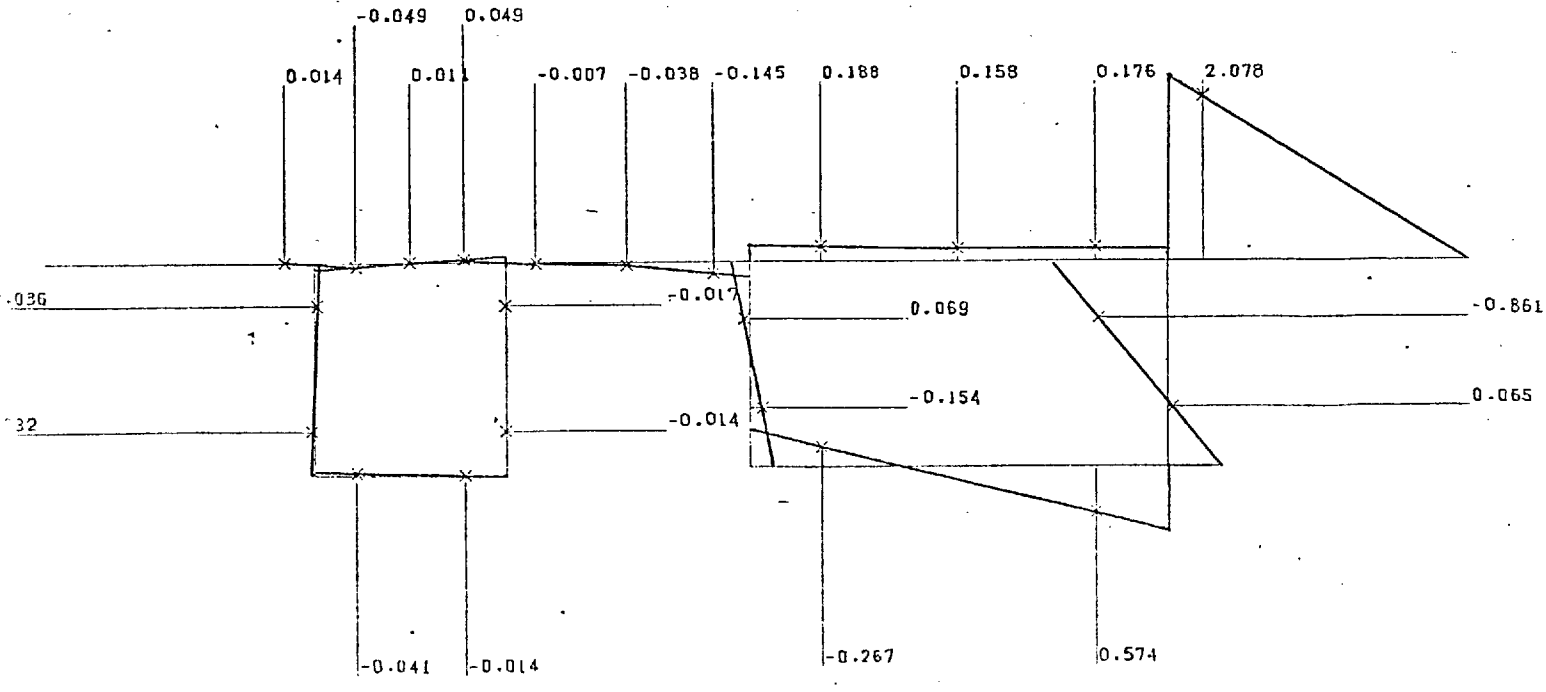


FIG197

LOAD CASE 46 SECTION 5-5 SECONDARY STRESS GAUGES
FLEXURAL COMPONENT OF TRANSVERSE STRESS

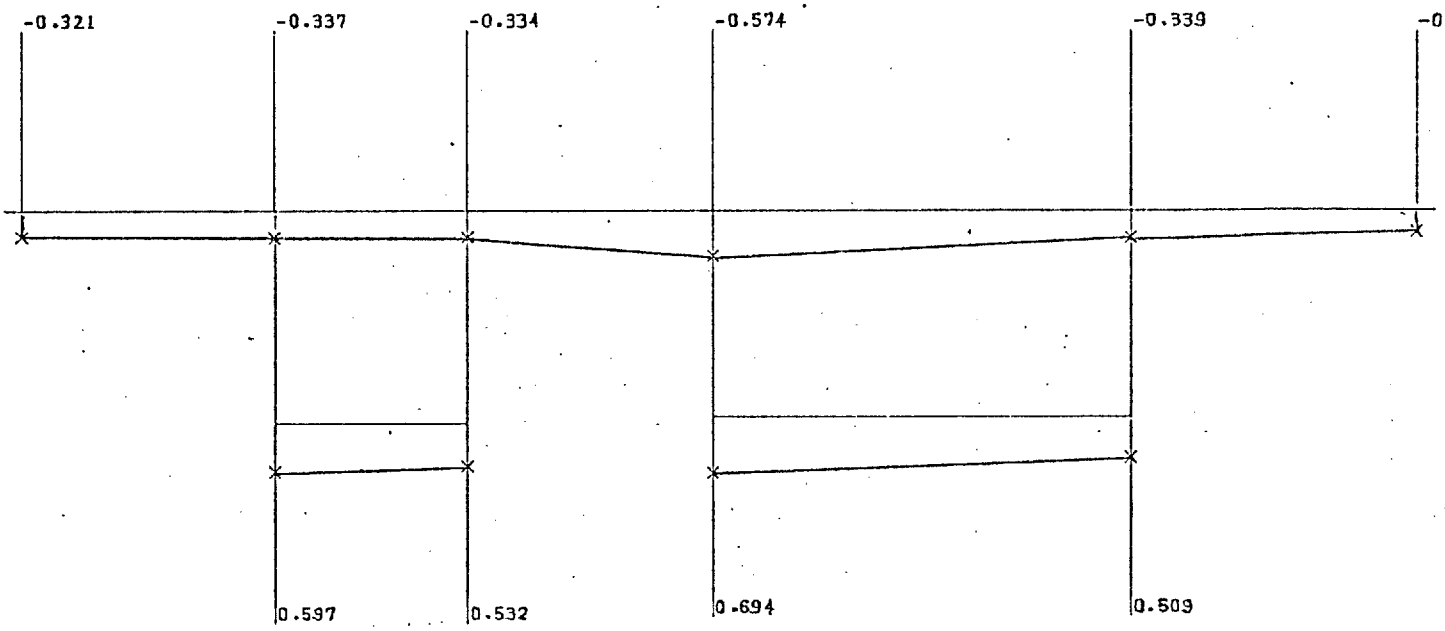


FIG198

LOAD CASE 56 SECTION 5-5 MAIN STRESS GAUGES
LONGITUDINAL STRESSES AT EXTREME FIBRES

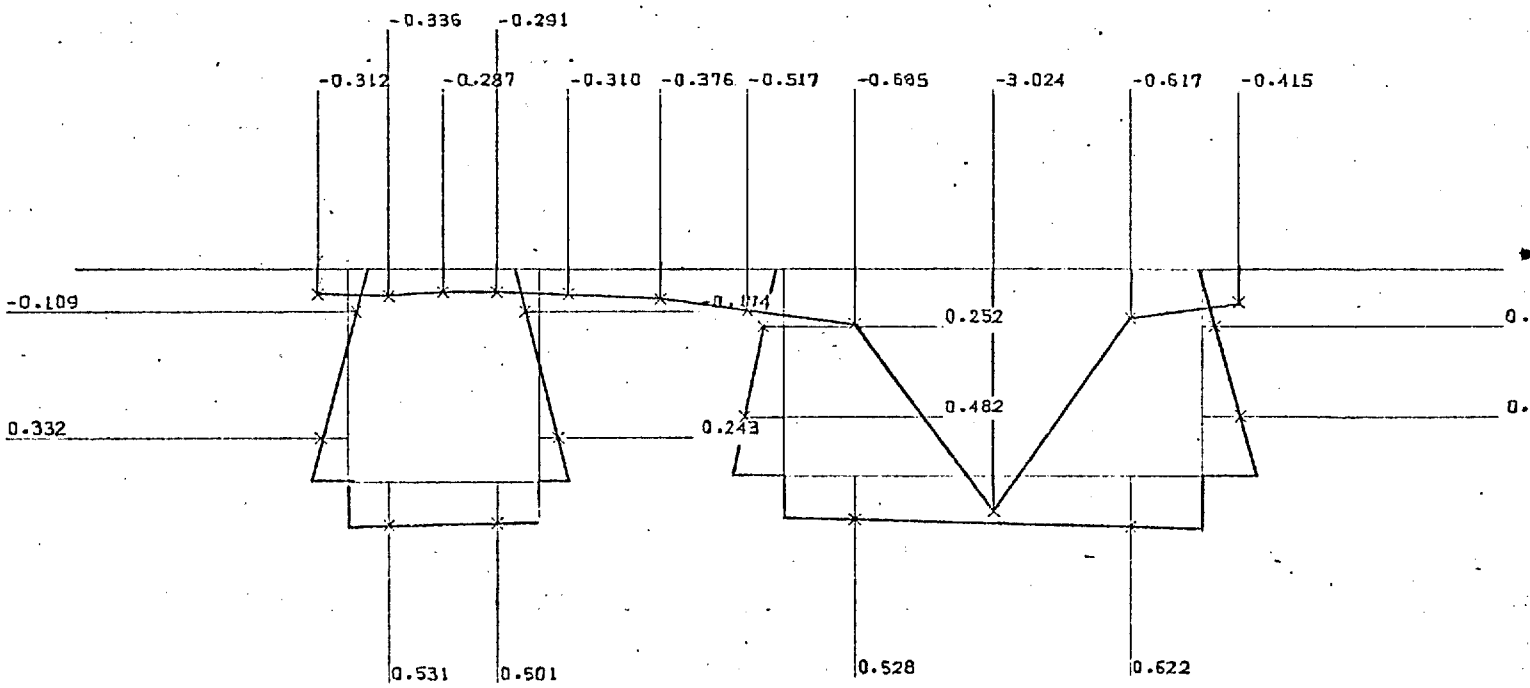


FIG199

LOAD CASE 55 SECTION 5-5 SECONDARY STRESS GAUGES
LONGITUDINAL STRESSES AT EXTREME FIBRES

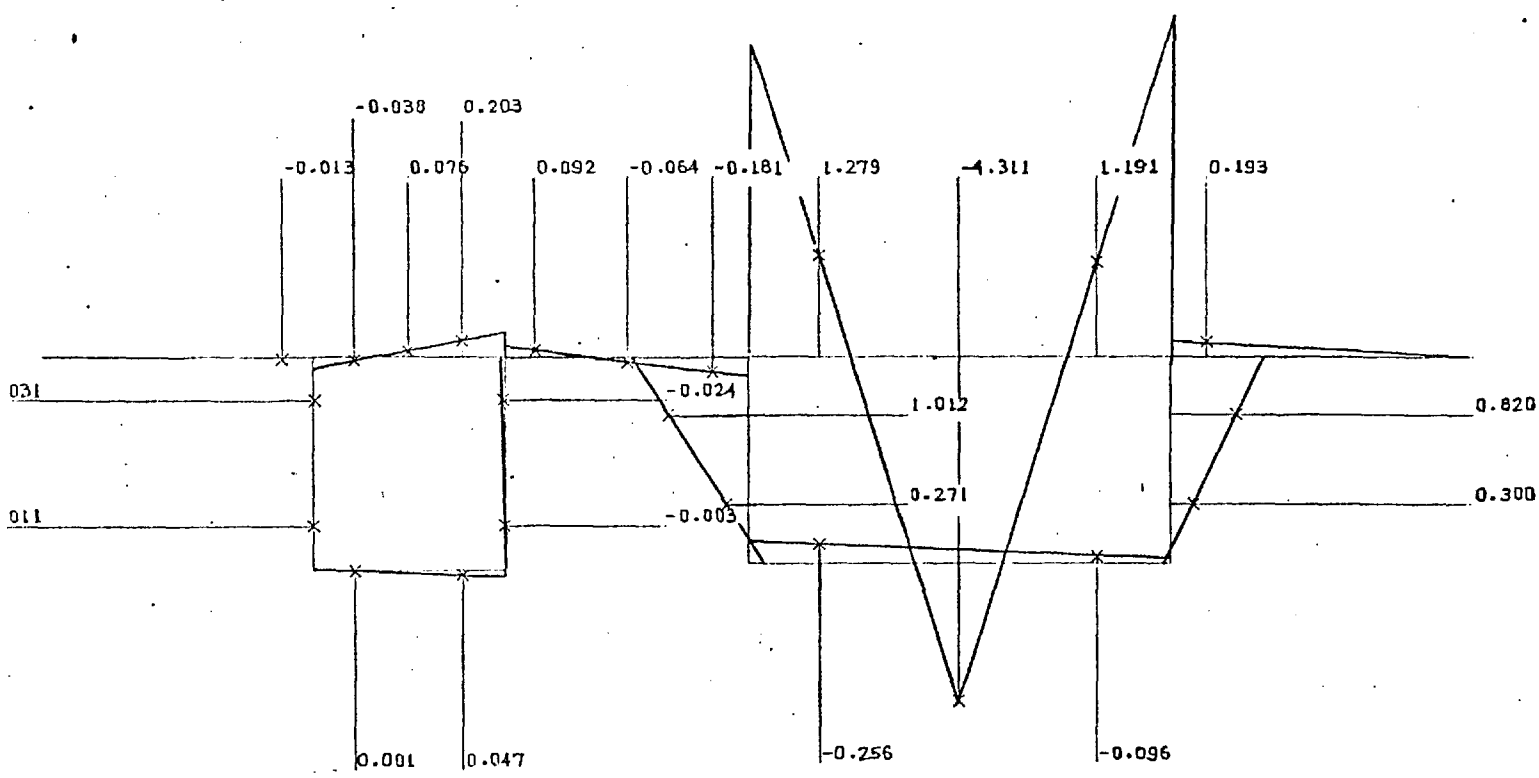


FIG 200

LOAD CASE 55 SECTION 5-5 SECONDARY STRESS GAUGES
FLEXURAL COMPONENT OF TRANSVERSE STRESS

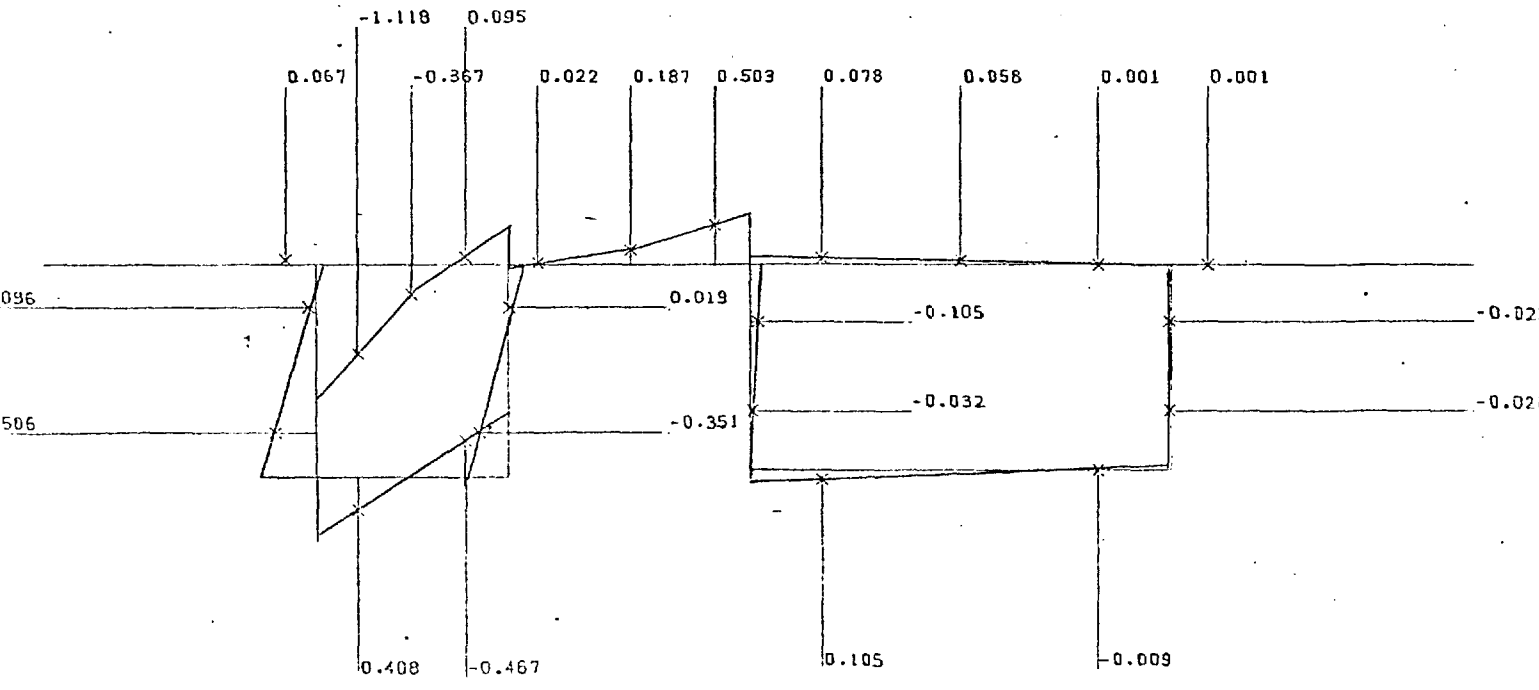


FIG 201

LOAD CASE 56 SECTION 5-5 SECONDARY STRESS GAUGES
FLEXURAL COMPONENT OF TRANSVERSE STRESS

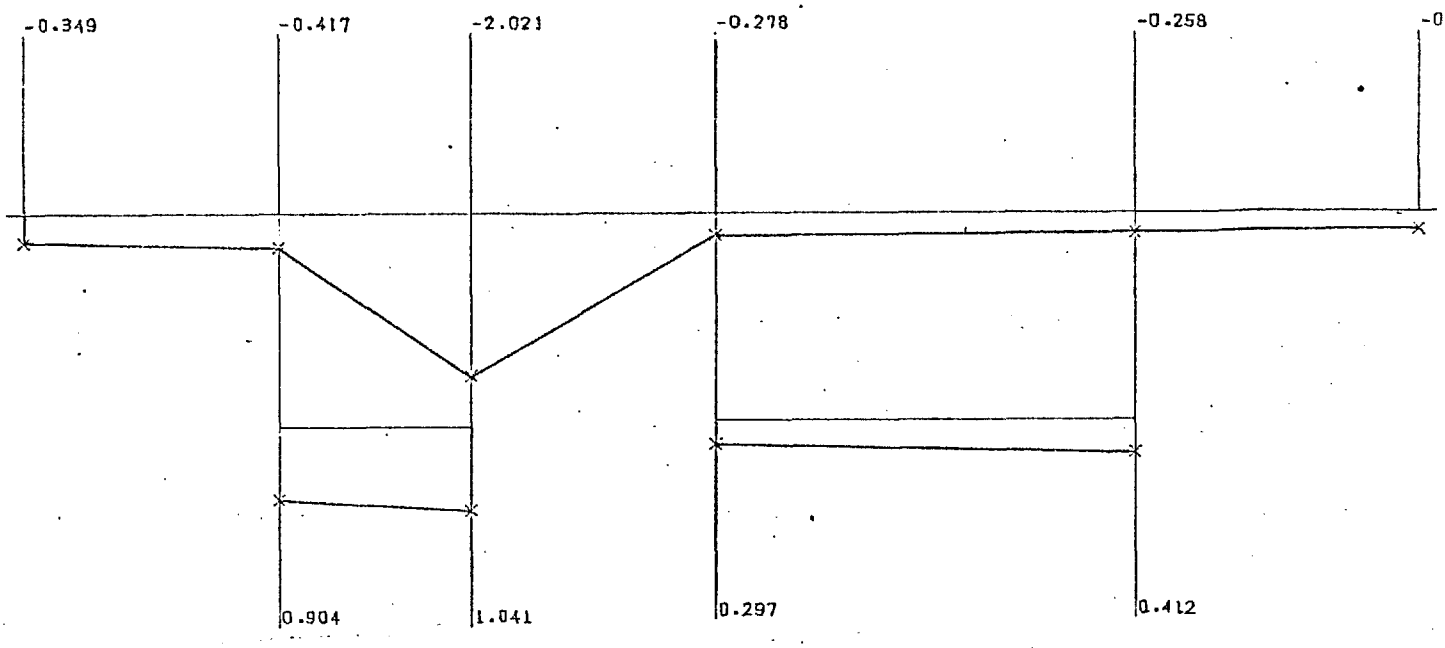


FIG 202

LOAD CASE 57 SECTION 5-5 MAIN STRESS GAUGES
LONGITUDINAL STRESSES AT EXTREME FIBRES

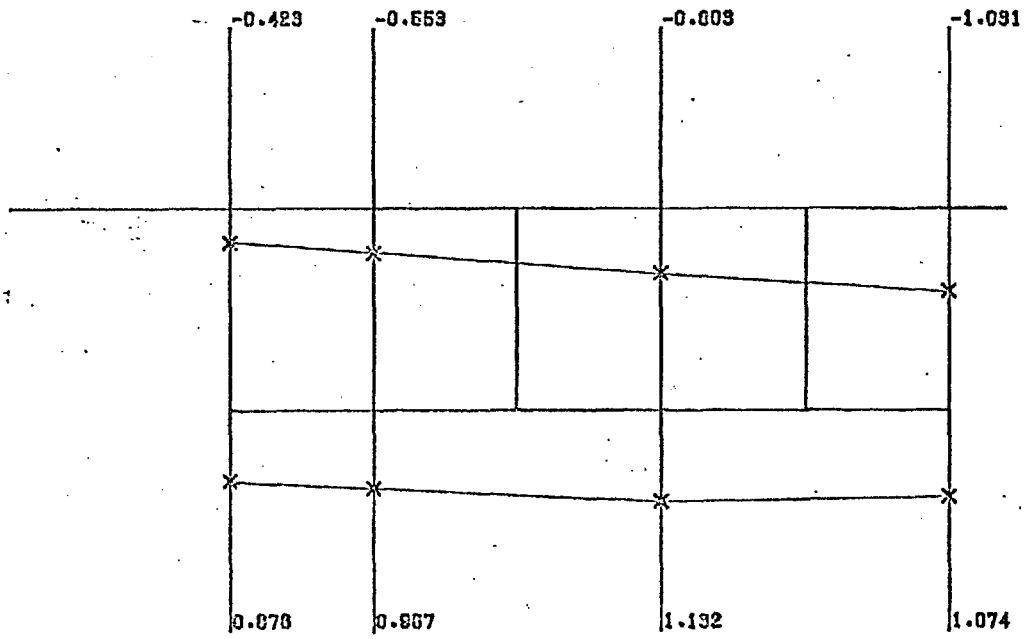


FIG 203

LOAD CASE 10 SECTION 13-13 MAIN STRESS GAUGES
LONGITUDINAL STRESSES AT EXTREME FIBRES

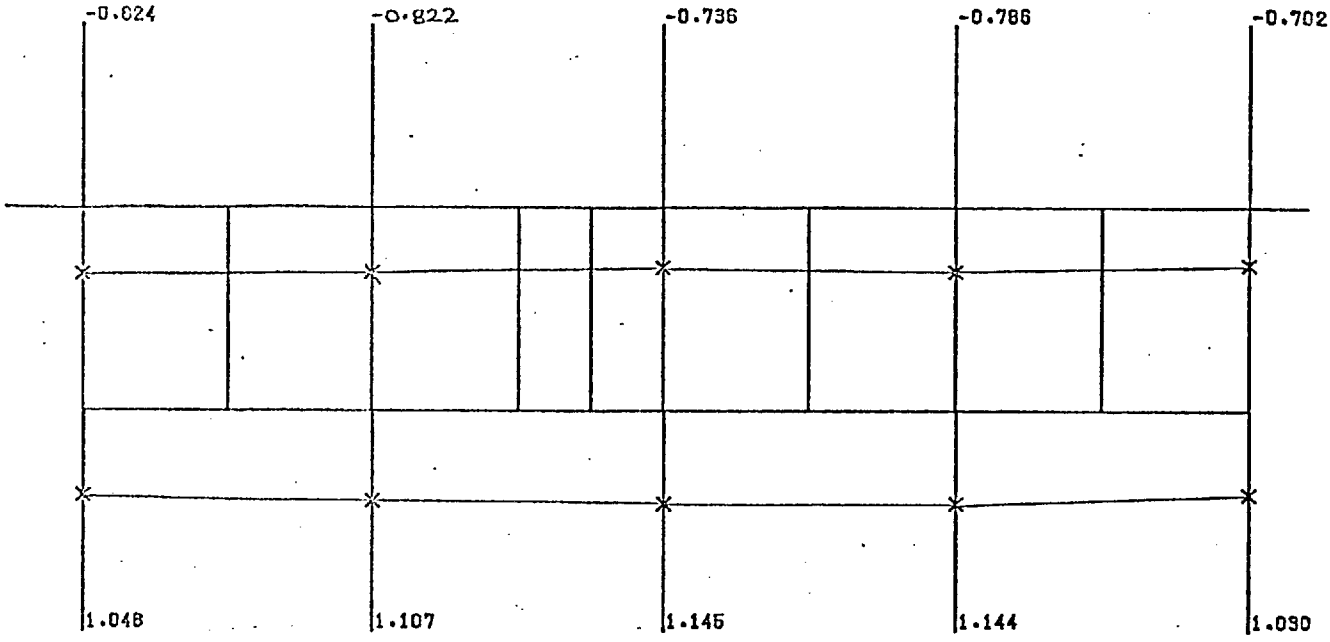


FIG 204

LOAD CASE 22 SECTION 5-5 MAIN STRESS GAUGES
LONGITUDINAL STRESSES AT EXTREME FIBRES

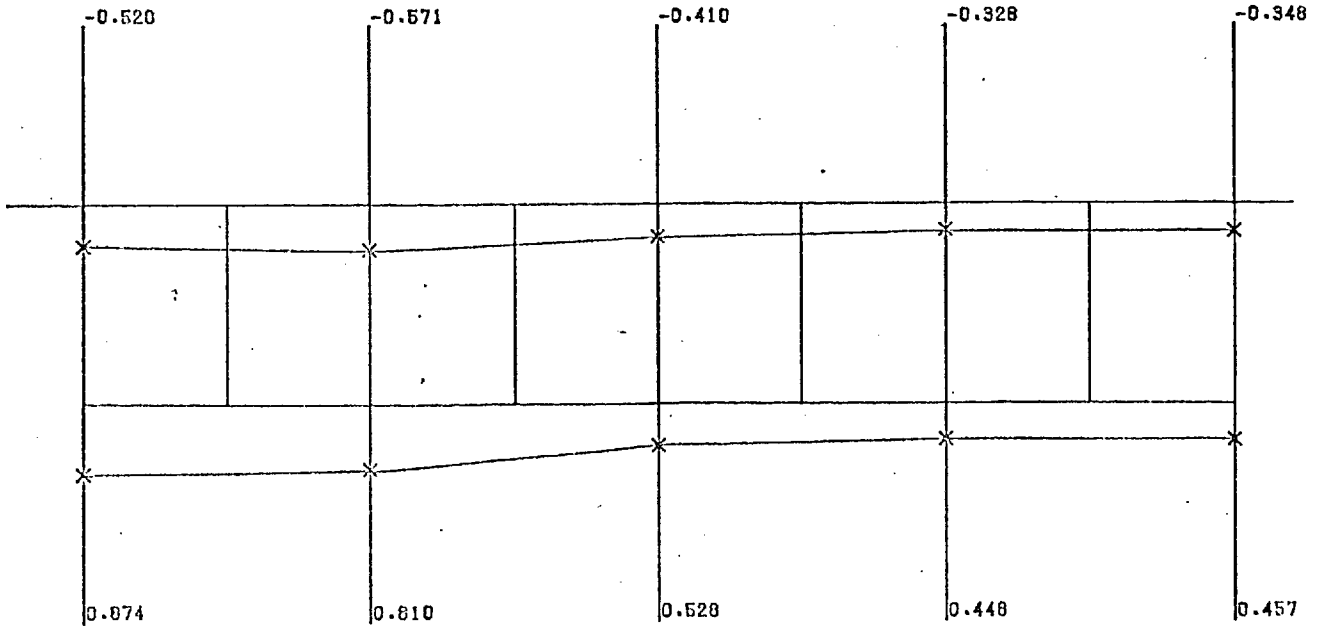


FIG 205

LOAD CASE 4 SECTION 2-2 MAIN STRESS GAUGES
LONGITUDINAL STRESSES AT EXTREME FIBRES

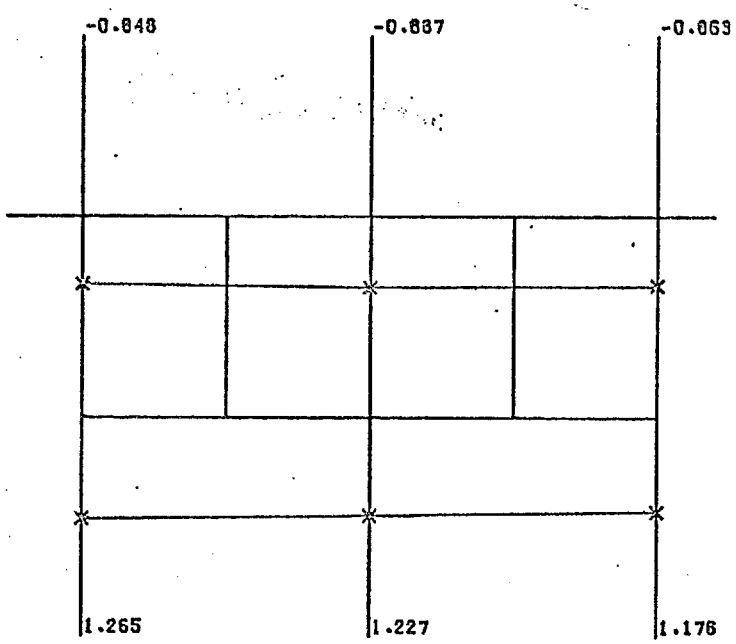


FIG206

LOAD CASE 13 SECTION 9-9 MAIN STRESS GAUGES
LONGITUDINAL STRESSES AT EXTREME FIBRES

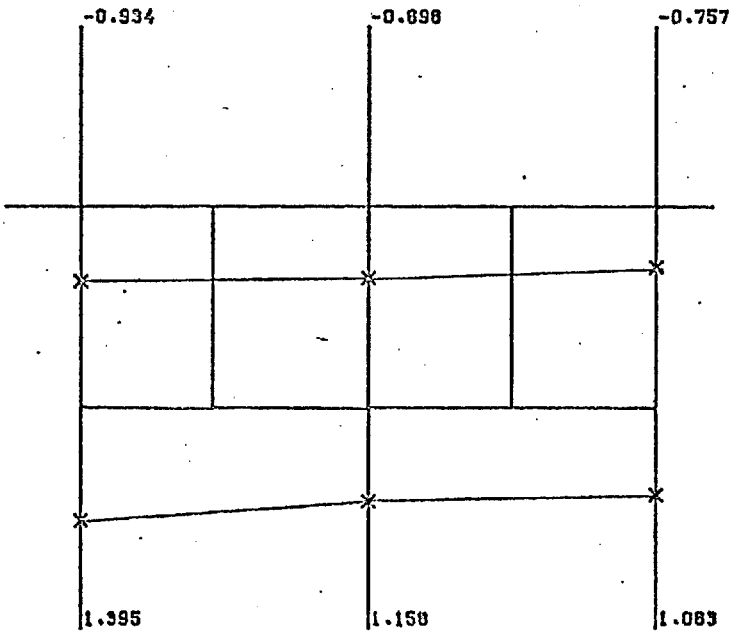


FIG207

LOAD CASE 14 SECTION 9-9 MAIN STRESS GAUGES
LONGITUDINAL STRESSES AT EXTREME FIBRES

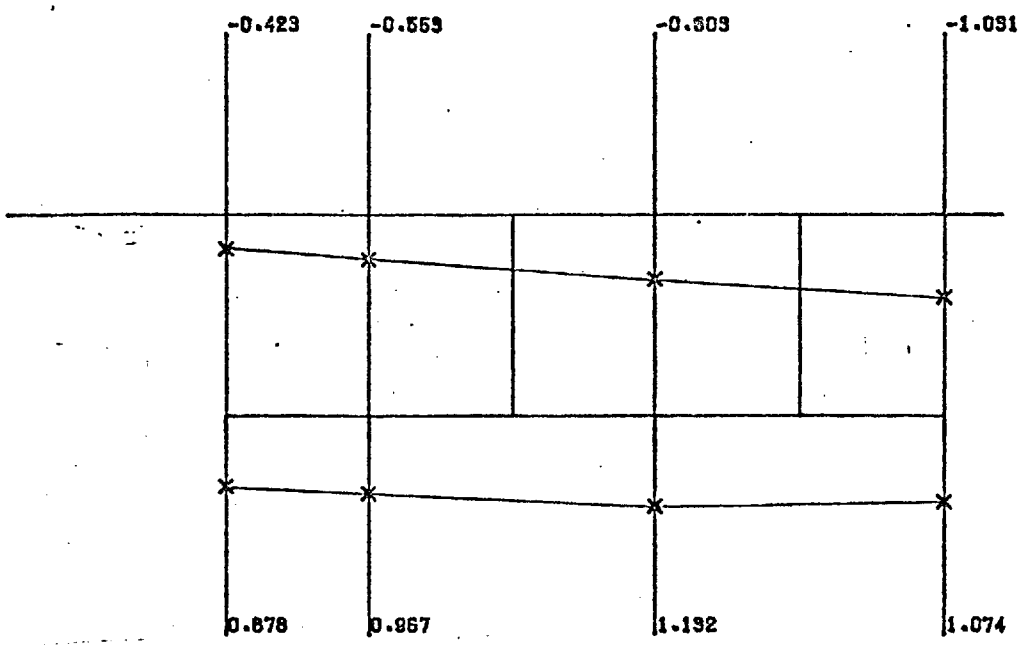


FIG 208

LOAD CASE 10 SECTION 13-13 MAIN STRESS GAUGES
LONGITUDINAL STRESSES AT EXTREME FIBRES

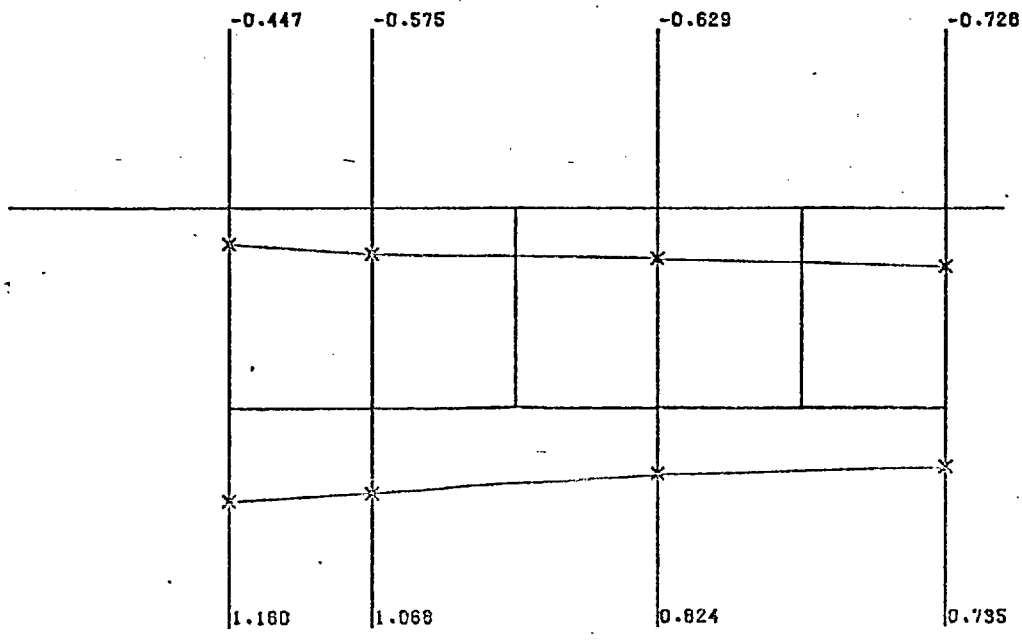


FIG 209

LOAD CASE 12 SECTION 13-13 MAIN STRESS GAUGES
LONGITUDINAL STRESSES AT EXTREME FIBRES

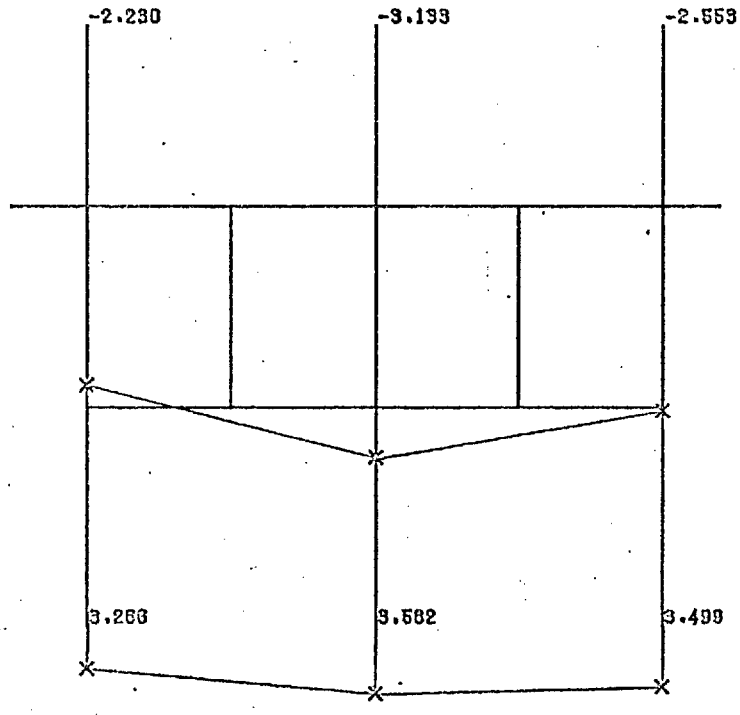


FIG210

LOAD CASE 37 SECTION 9-9 MAIN STRESS GAUGES
LONGITUDINAL STRESSES AT EXTREME FIBRES

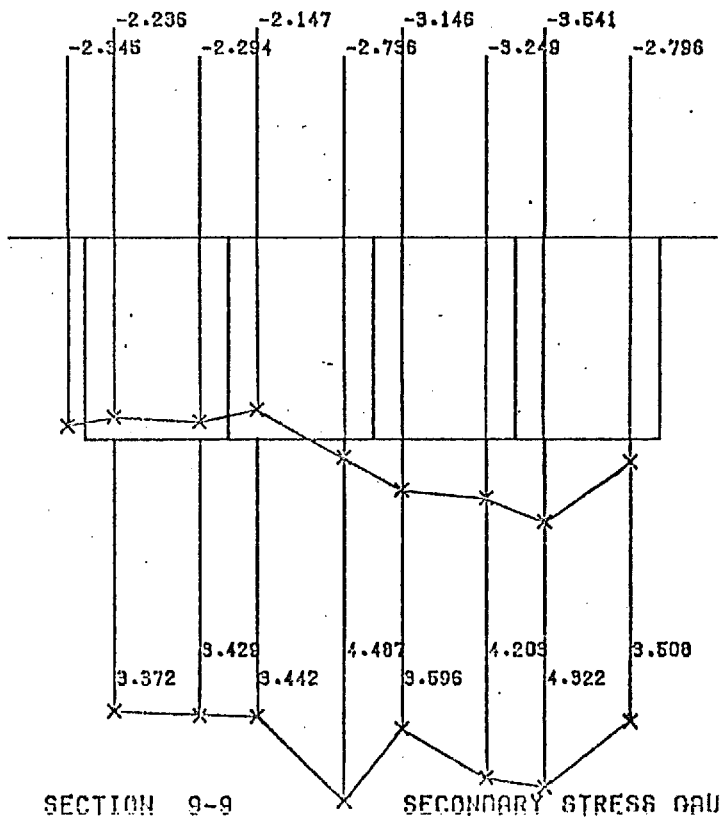


FIG211

LOAD CASE 37 SECTION 9-9 SECONDARY STRESS GAUGES
LONGITUDINAL STRESSES AT EXTREME FIBRES

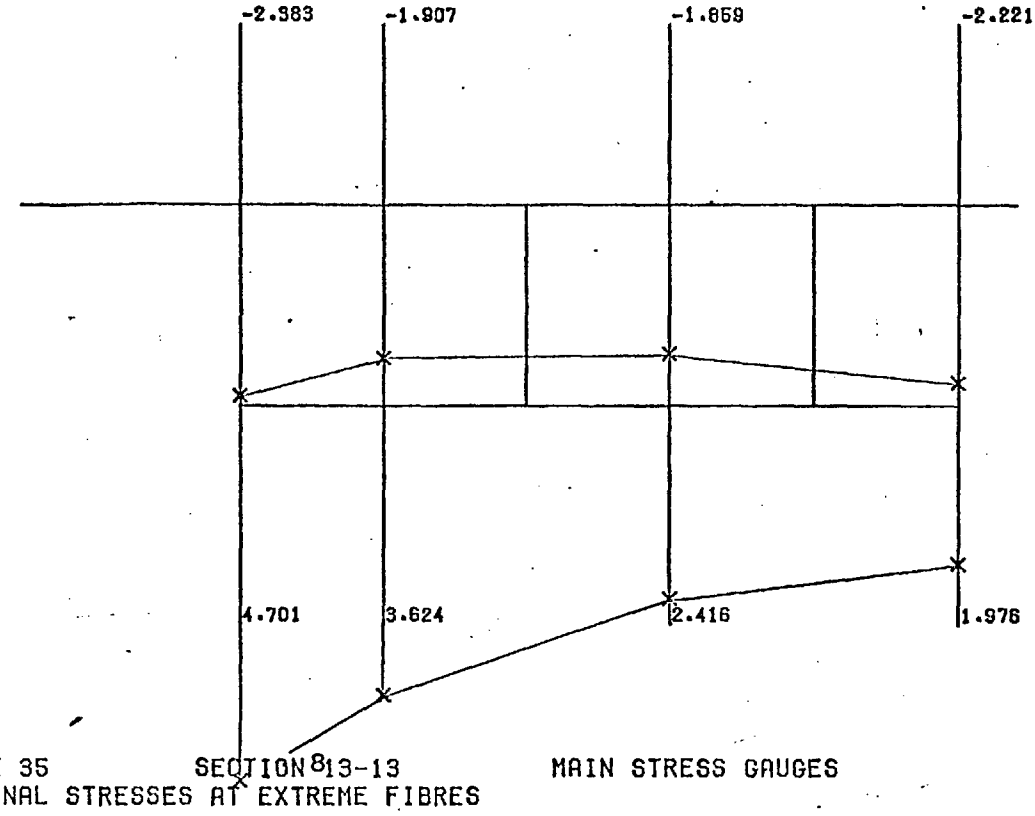


FIG212

LOAD CASE 35 SECTION 13-13 MAIN STRESS GAUGES
LONGITUDINAL STRESSES AT EXTREME FIBRES

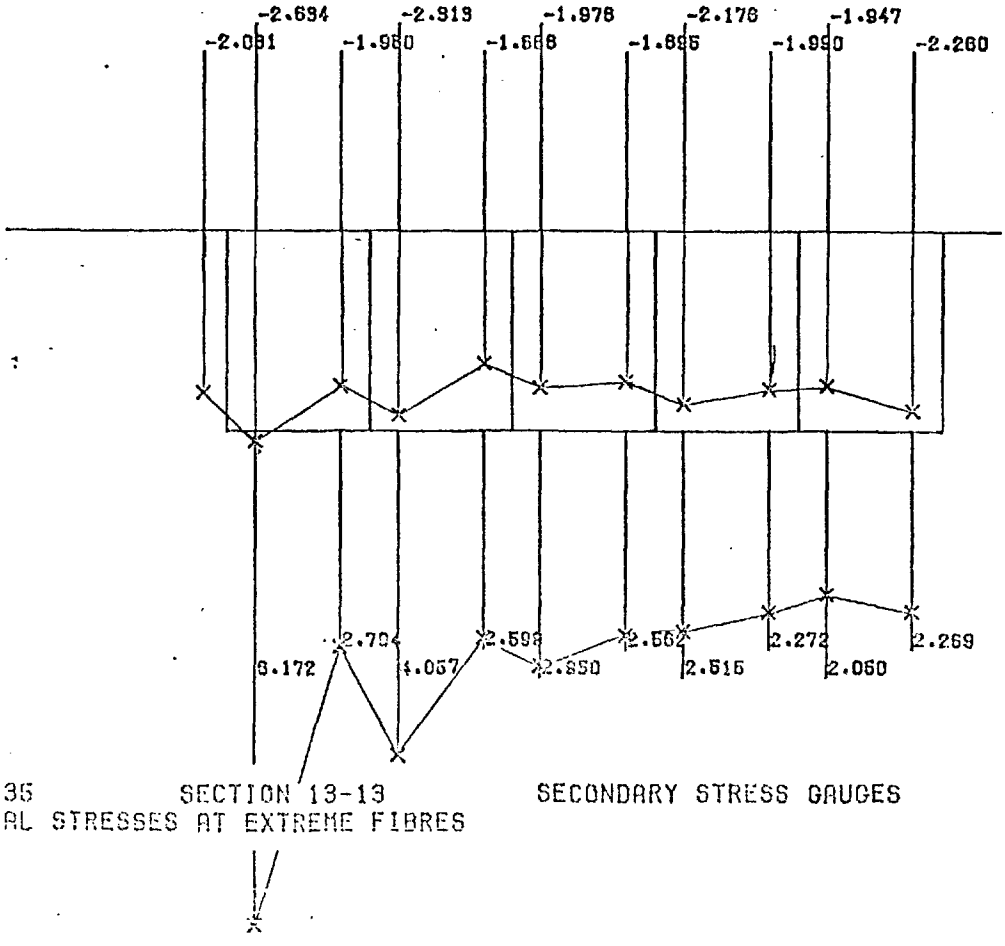


FIG213

LOAD CASE 35 SECTION 13-13 SECONDARY STRESS GAUGES
LONGITUDINAL STRESSES AT EXTREME FIBRES

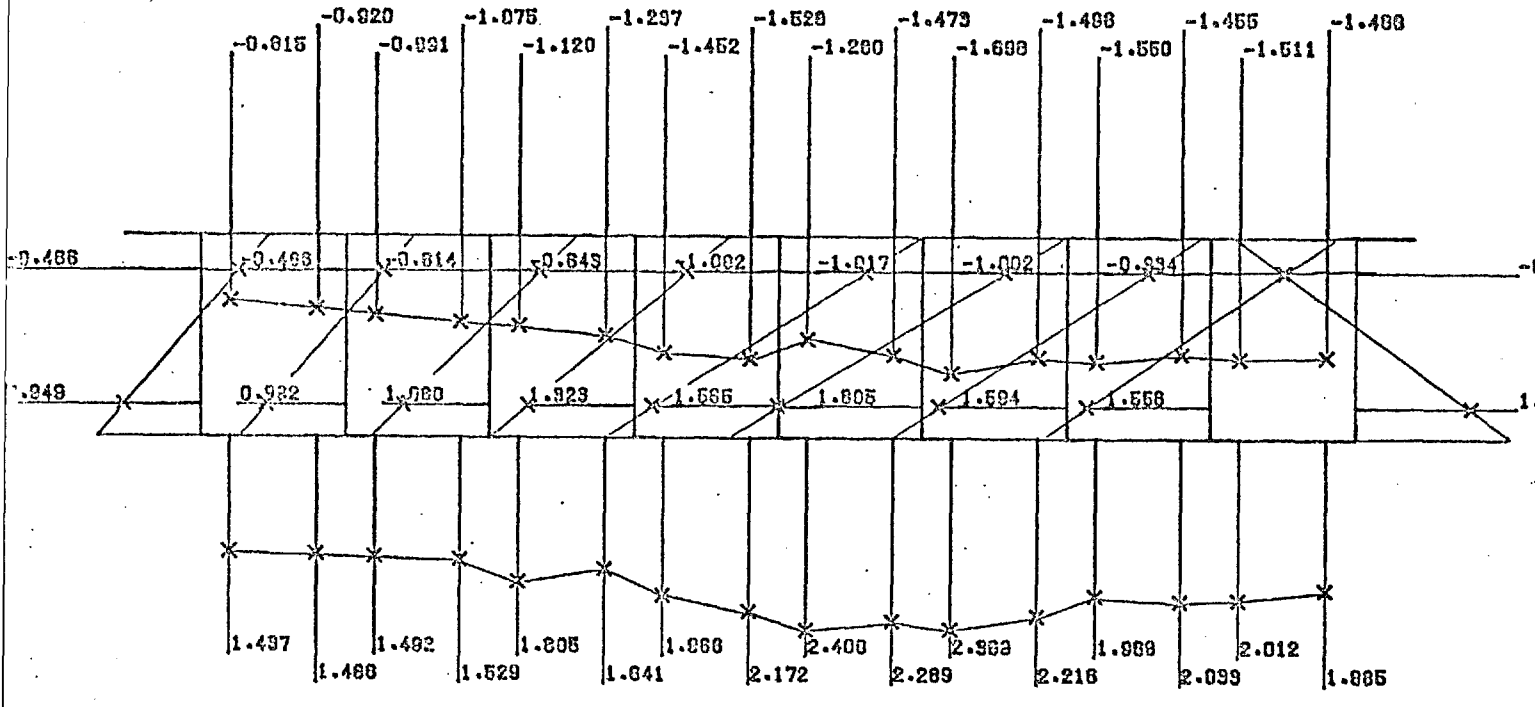


FIG 214

LOAD CASE 18 SECTION 2-2 SECONDARY STRESS GAUGES
IN PLANE COMPONENT OF LONGITUDINAL STRESS

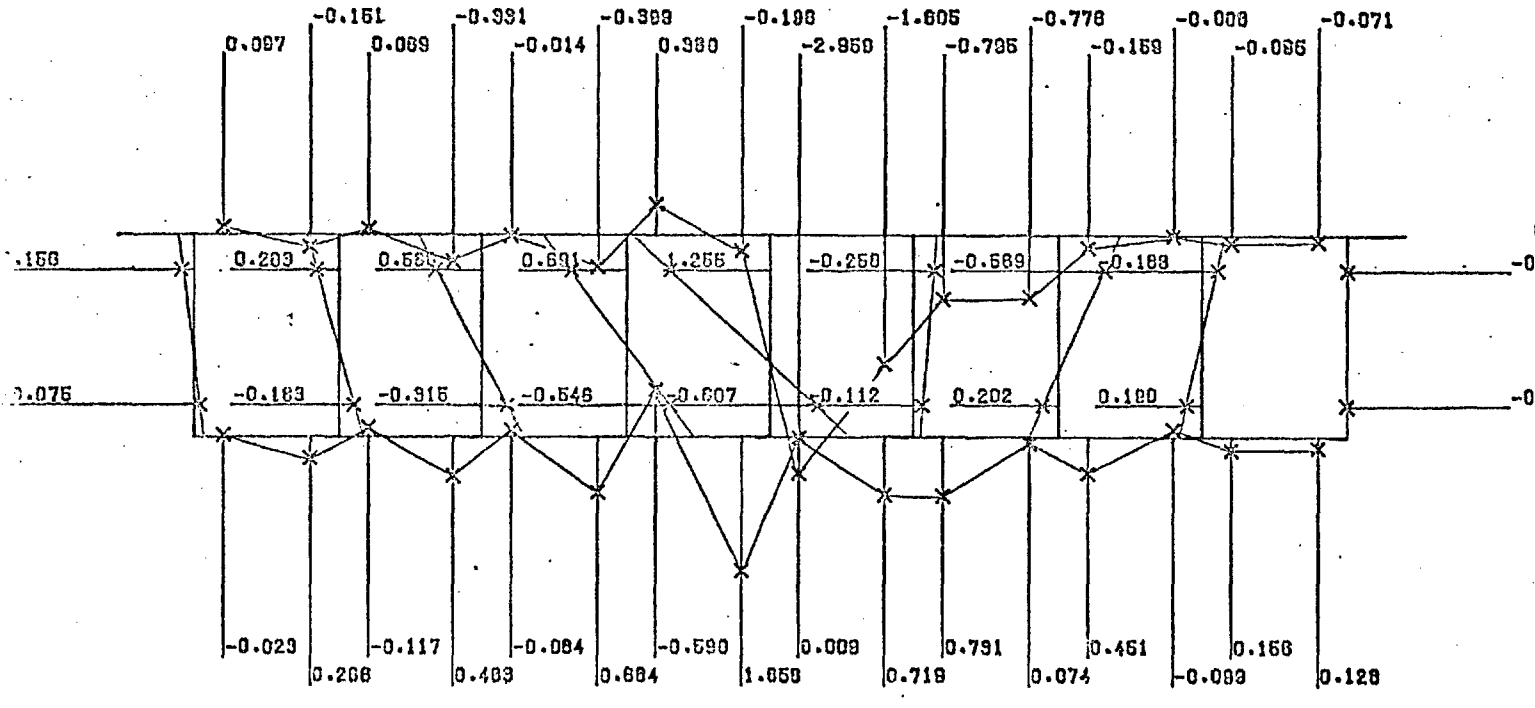


FIG 215

LOAD CASE 18 SECTION 2-2 SECONDARY STRESS GAUGES
FLEXURAL COMPONENT OF LONGITUDINAL STRESS

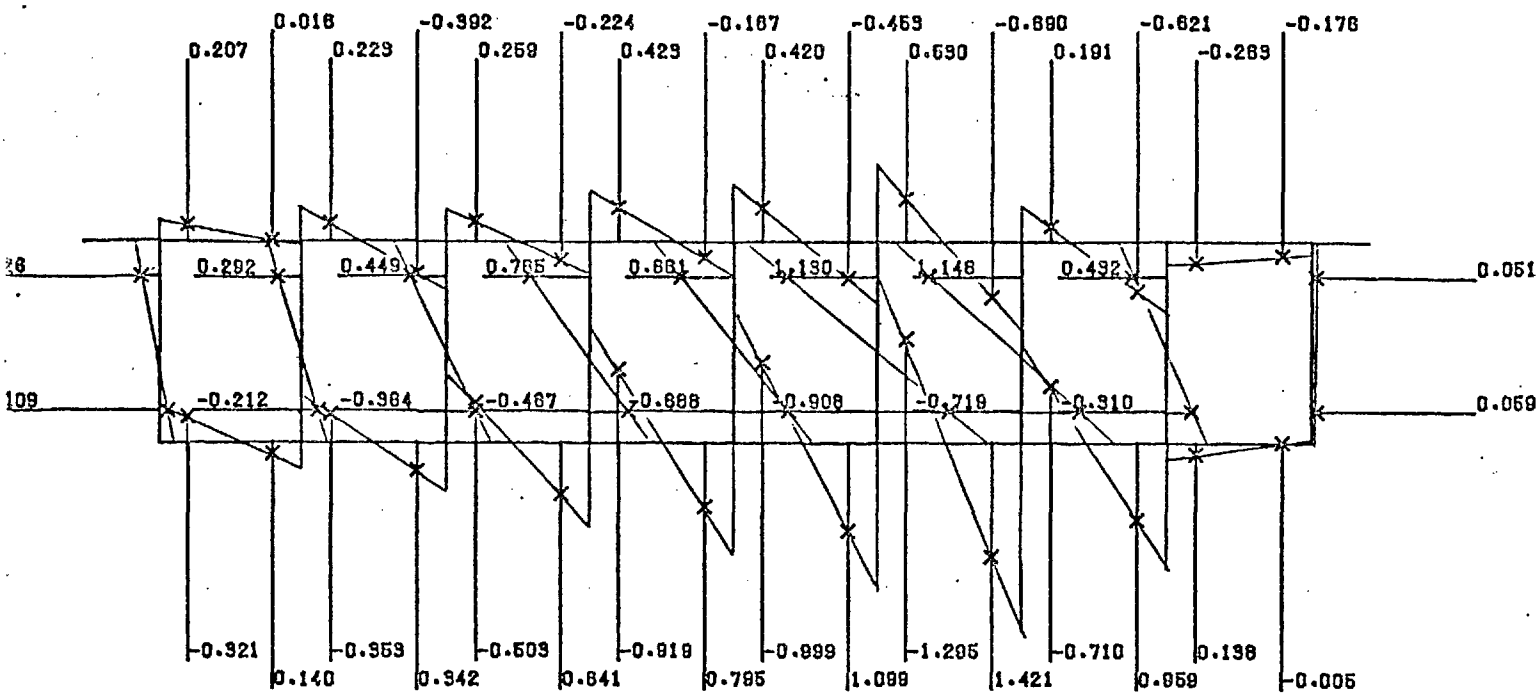


FIG 216

LOAD CASE 1 SECTION 2-2 SECONDARY STRESS GAUGES
FLEXURAL COMPONENT OF TRANSVERSE STRESS

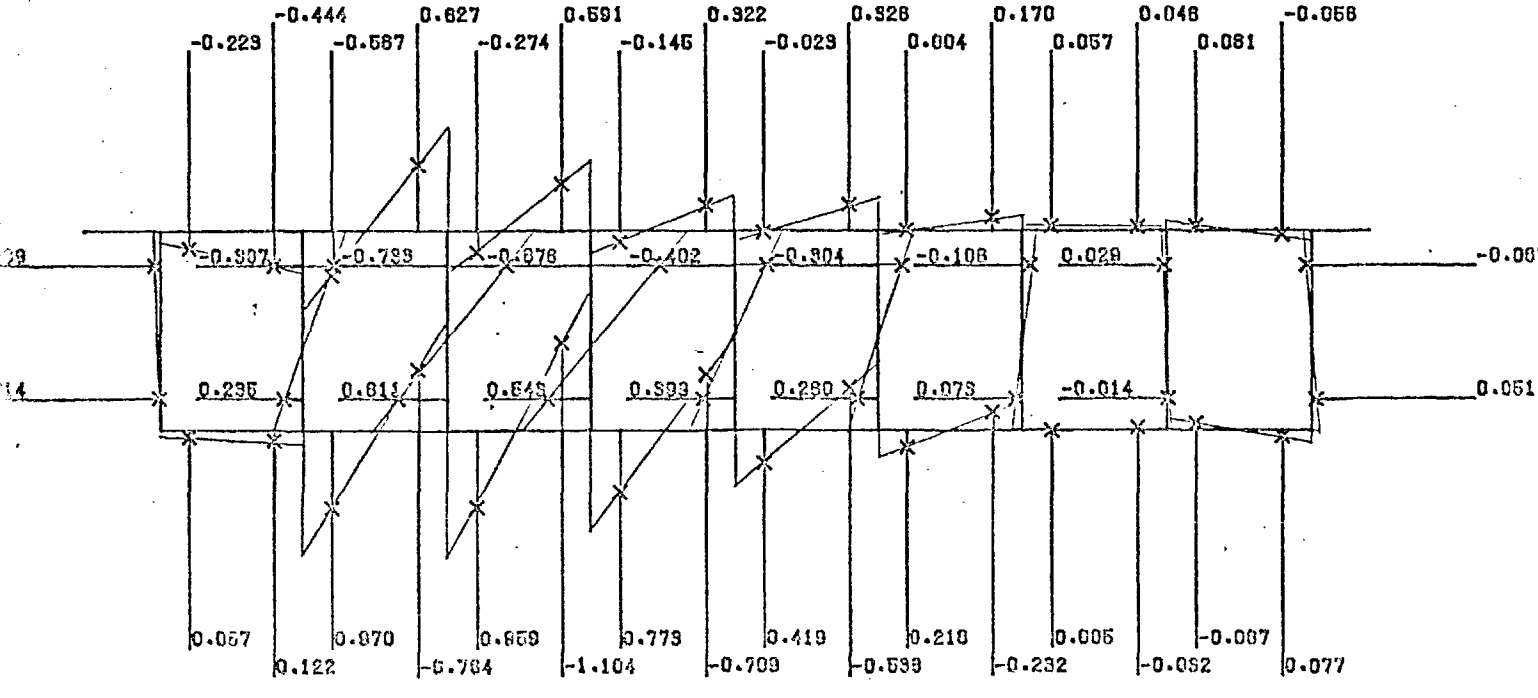


FIG 217

LOAD CASE 4 SECTION 2-2 SECONDARY STRESS GAUGES
FLEXURAL COMPONENT OF TRANSVERSE STRESS

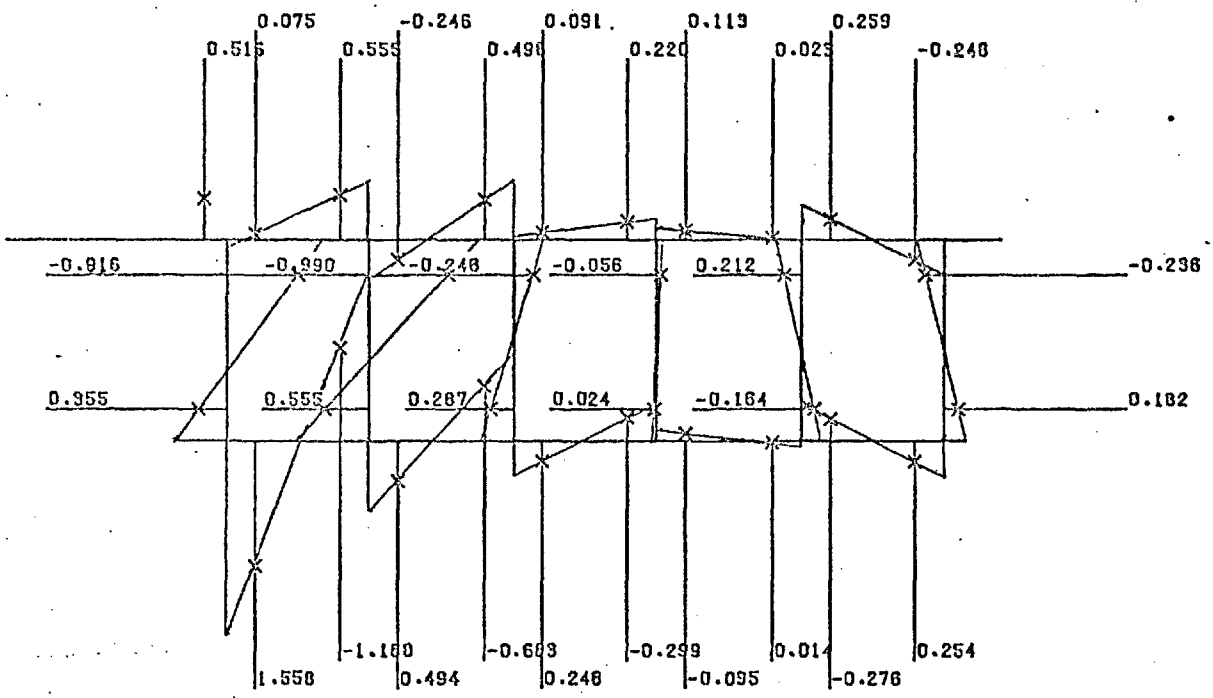


FIG 218

LOAD CASE 12 SECTION 13-13 SECONDARY STRESS GAUGES
FLEXURAL COMPONENT OF TRANSVERSE STRESS

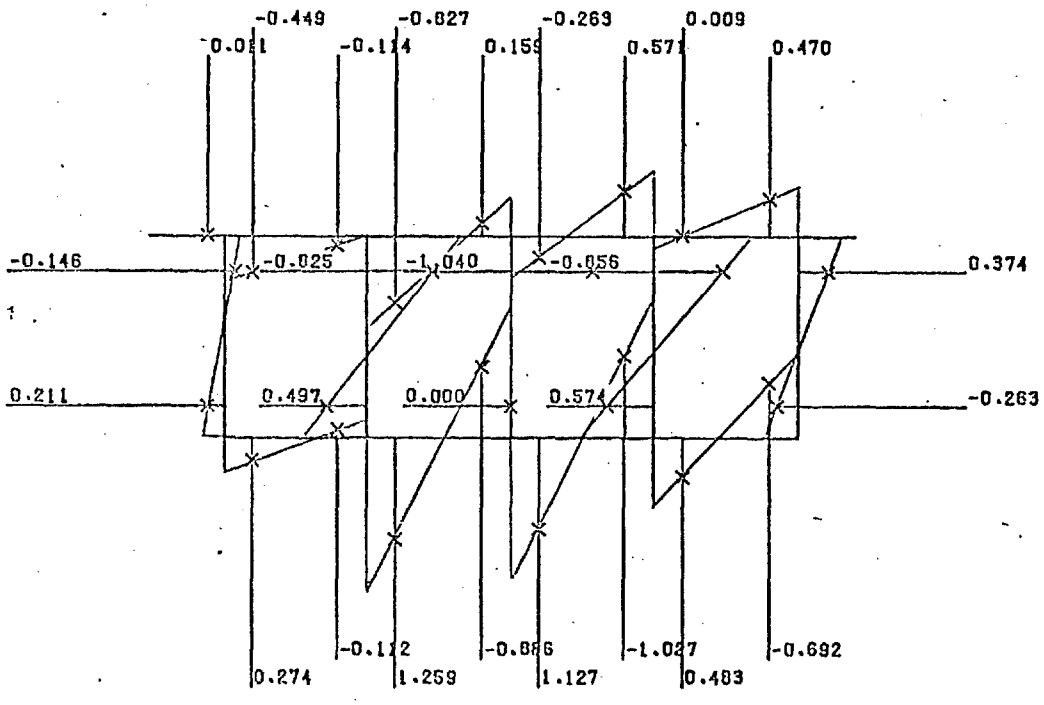


FIG 219

LOAD CASE 14 SECTION 9-9 SECONDARY STRESS GAUGES
FLEXURAL COMPONENT OF TRANSVERSE STRESS

483

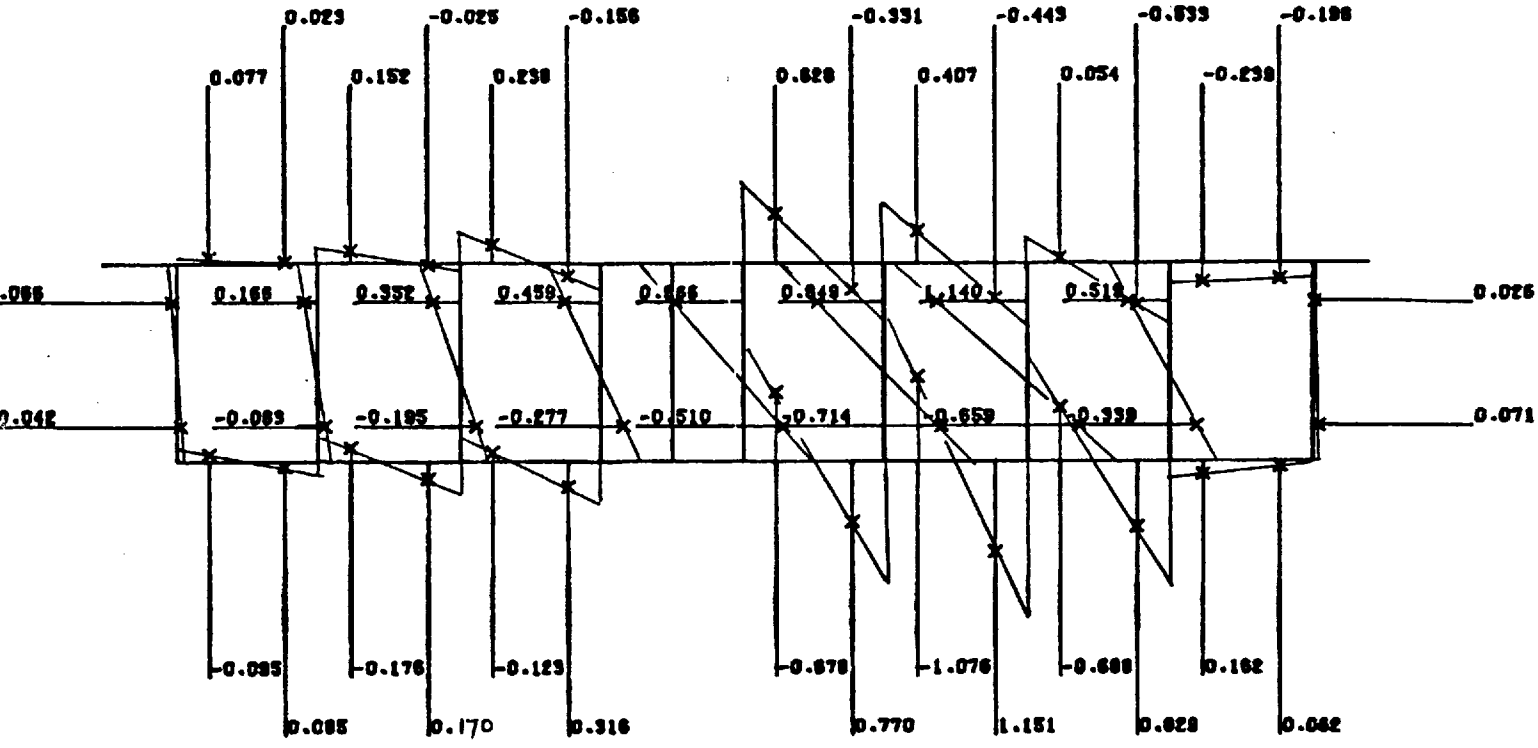


FIG 220

LOAD CASE 5 SECTION 5-5 SECONDARY STRESS GAUGES
FLEXURAL COMPONENT OF TRANSVERSE STRESS

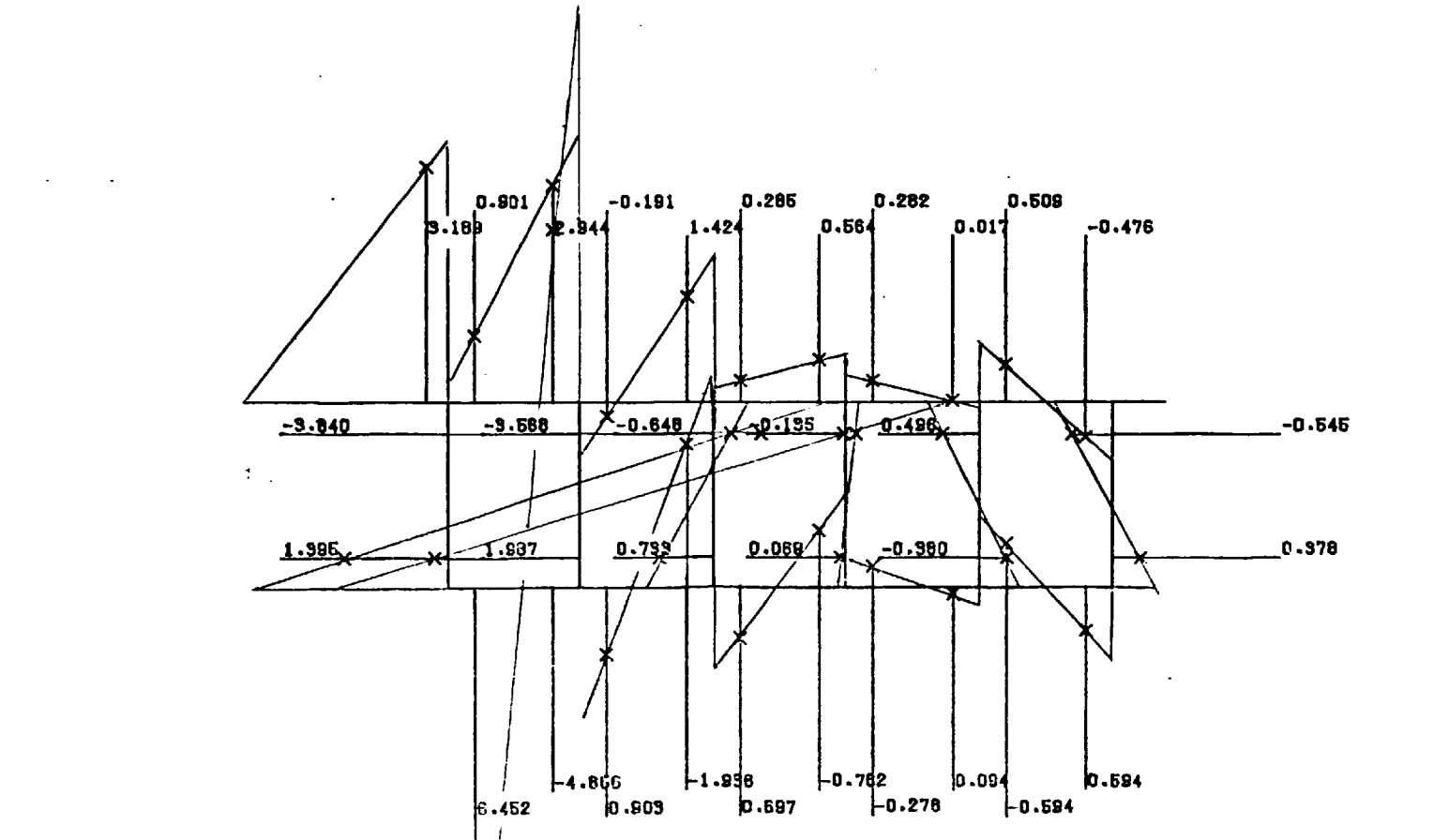


FIG 221

LOAD CASE 35 SECTION 13-13 SECONDARY STRESS GAUGES
FLEXURAL COMPONENT OF TRANSVERSE STRESS

484

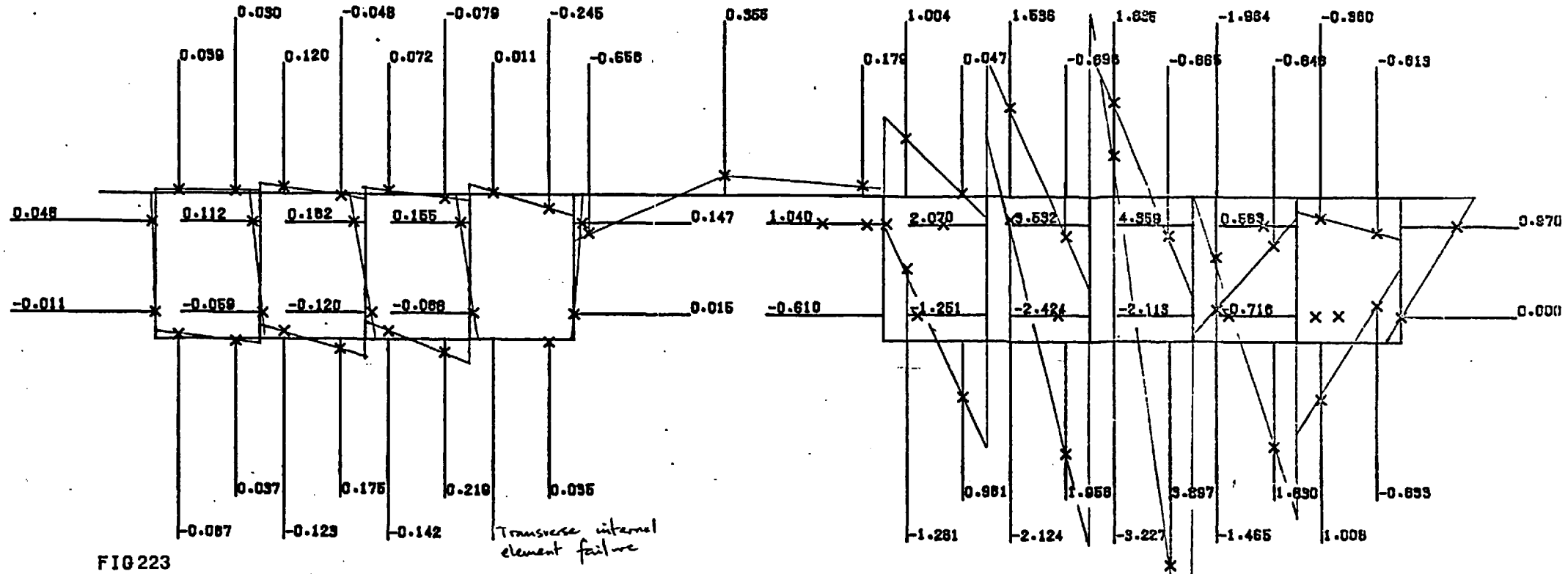


FIG 223

LOAD CASE 22 SECTION 6-6 SECONDARY STRESS GAUGES
FLEXURAL COMPONENT OF TRANSVERSE STRESS

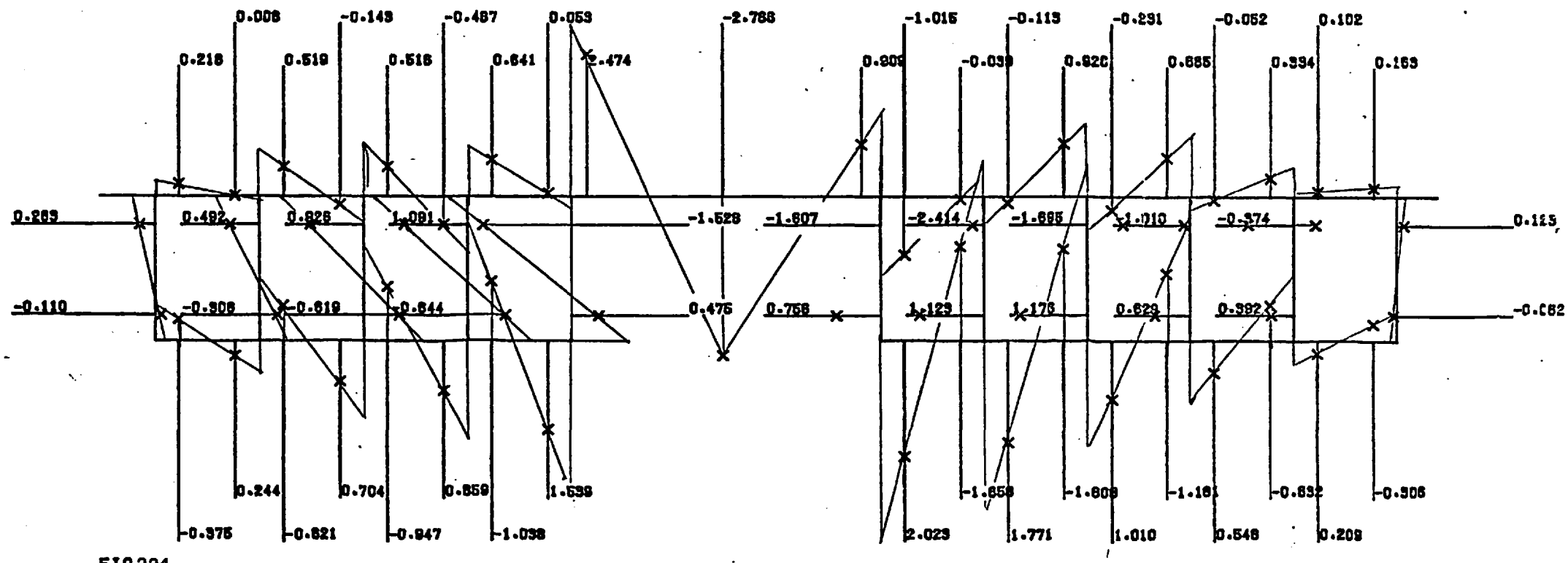


FIG 224

LOAD CASE 27 SECTION 6-6 SECONDARY STRESS GAUGES
FLEXURAL COMPONENT OF TRANSVERSE STRESS

485

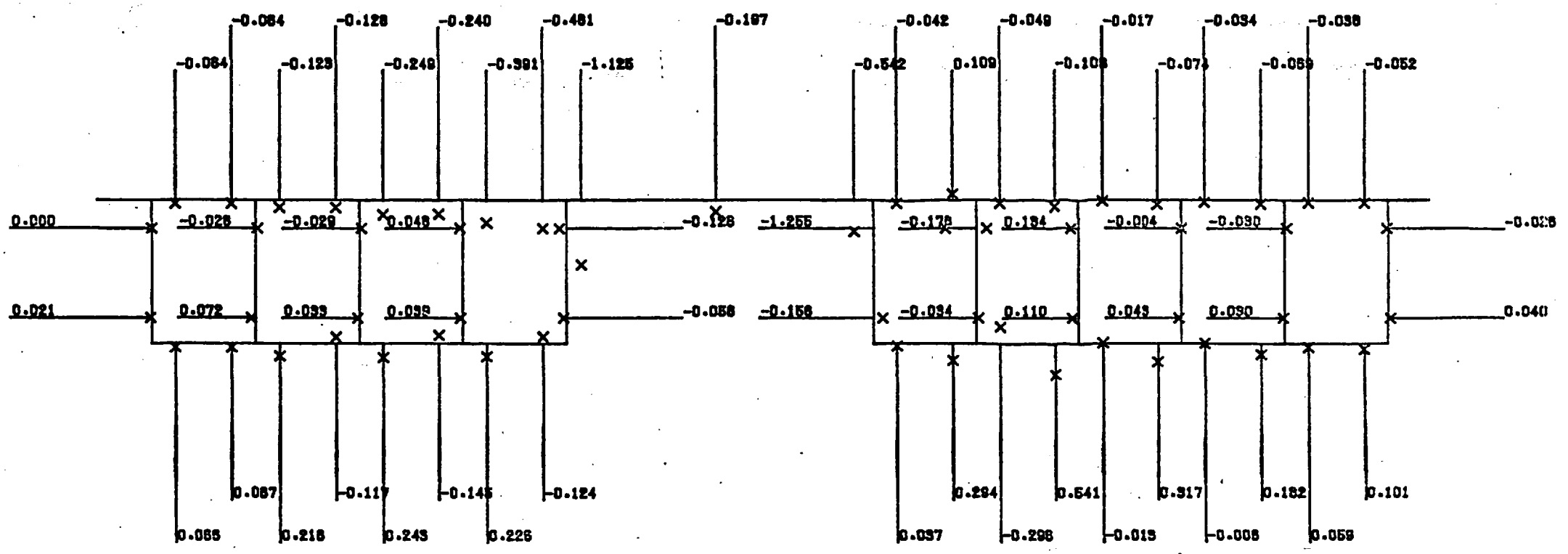


FIG225

LOAD CASE 27 SECTION 6-6 SECONDARY STRESS GAUGES
IN-PLANE COMPONENT OF TRANSVERSE STRESS

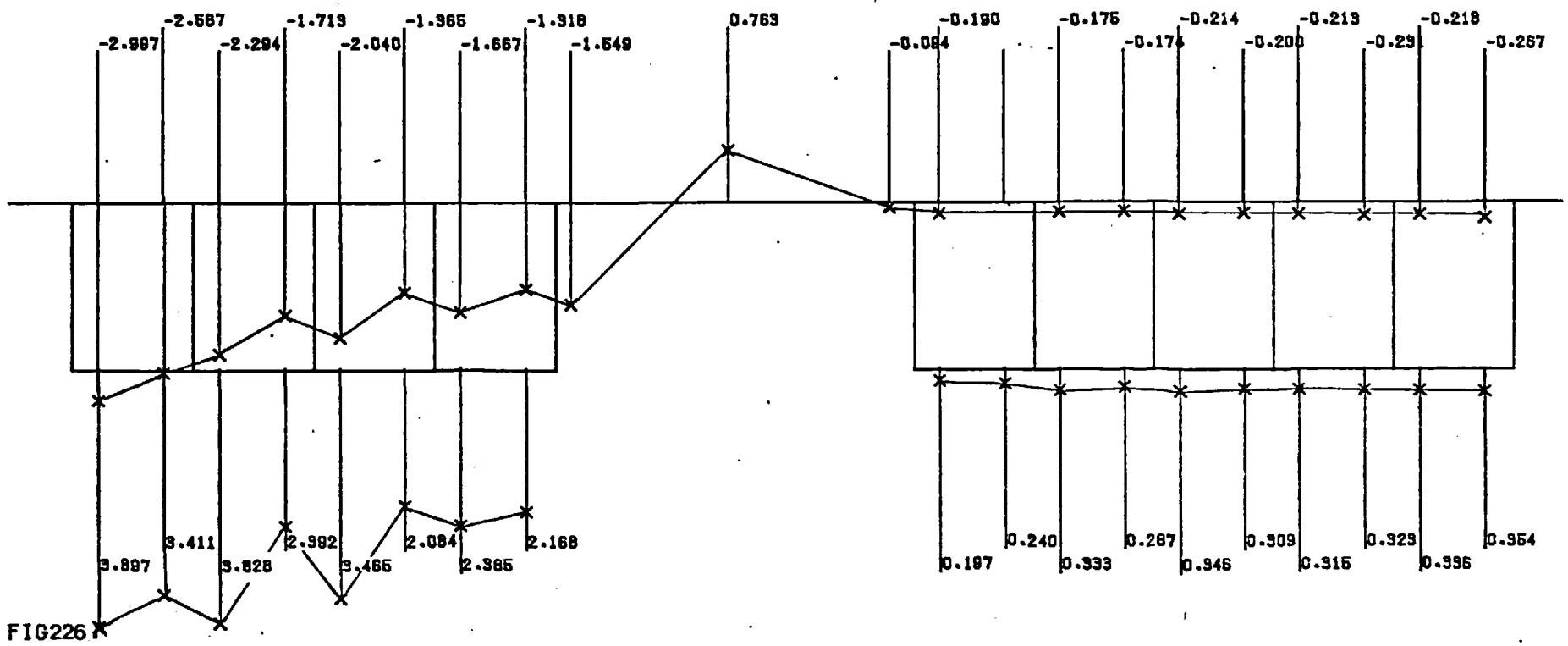


FIG226

LOAD CASE 30 SECTION 6-6 SECONDARY STRESS GAUGES
LONGITUDINAL STRESSES AT EXTREME FIBRES

486

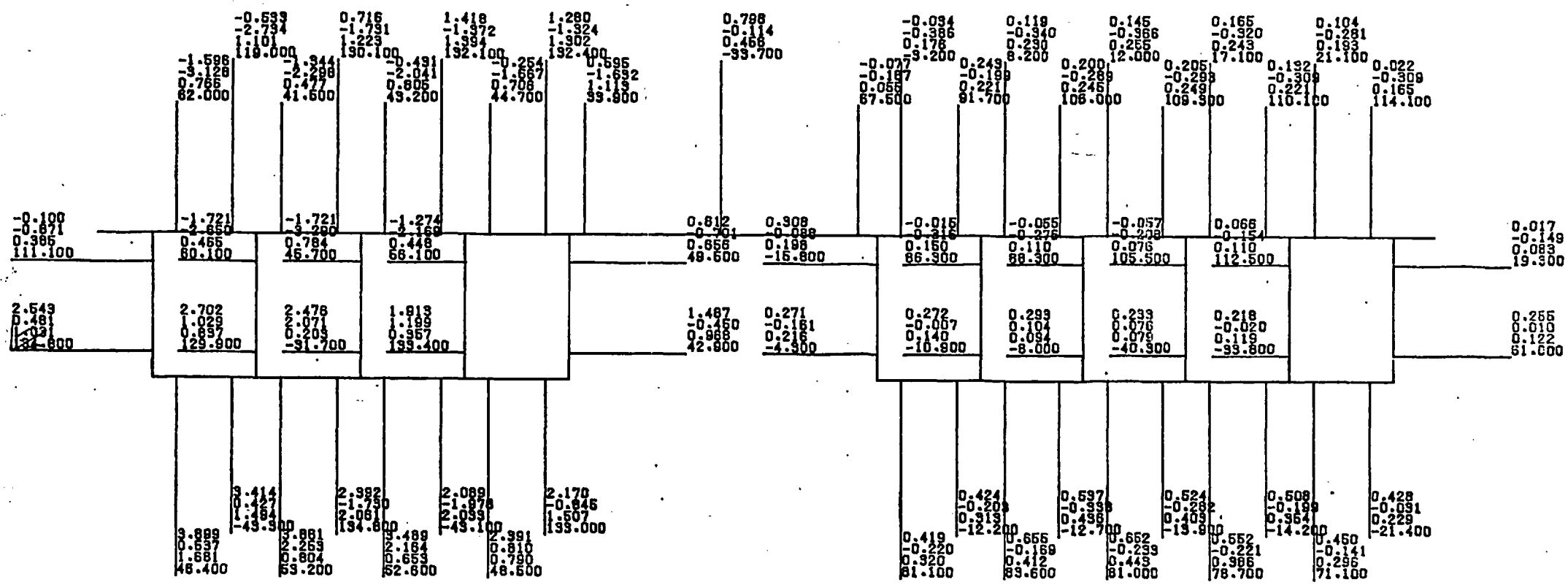


FIG227

LOAD CASE 30 SECTION 6-6 SECONDARY STRESS GAUGES
PRINCIPAL STRESSES.MAX. SHEAR.DIRECTION

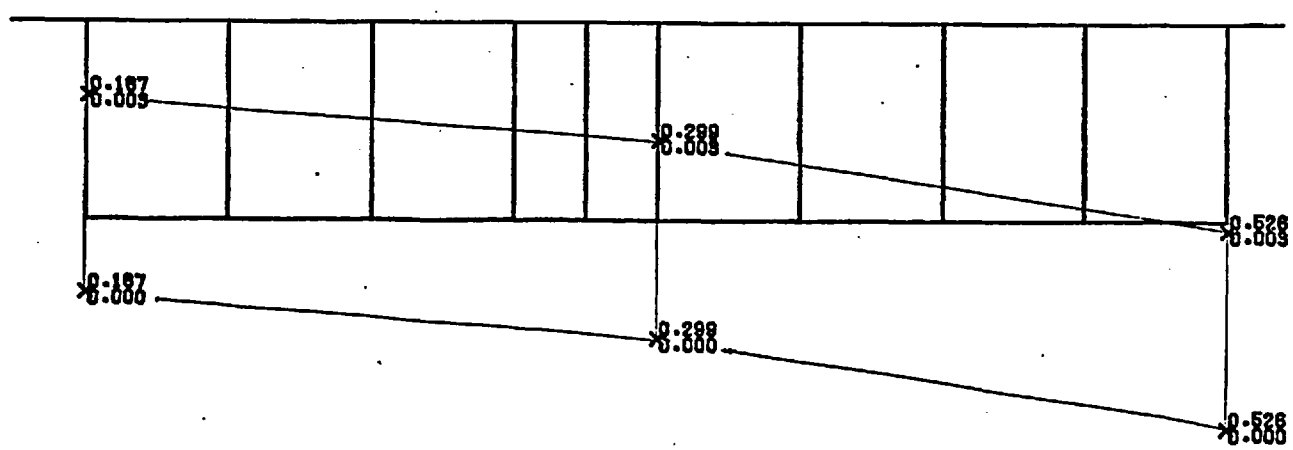


FIG228

LOAD CASE 22 SECTION 5-5
DEFLECTIONS

487

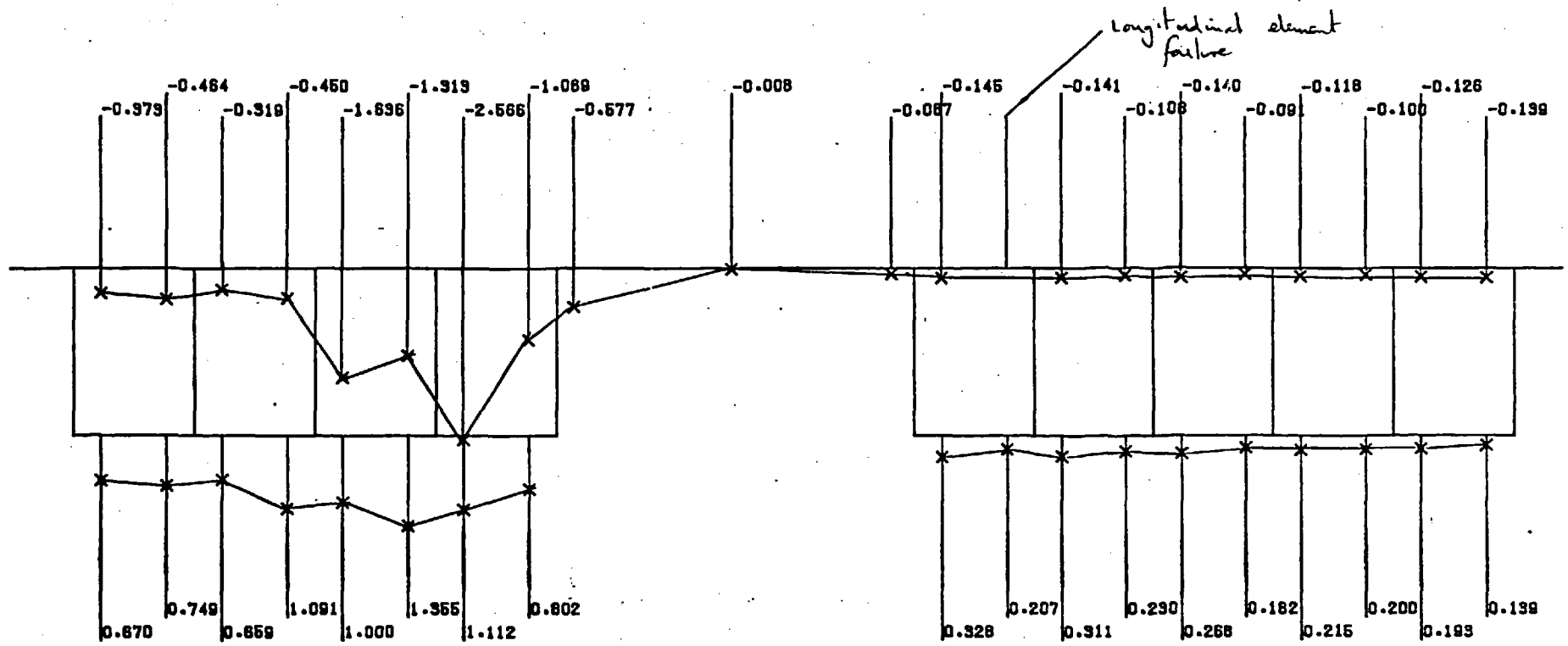


FIG229

LOAD CASE 52 SECTION 6-6 SECONDARY STRESS GAUGES
LONGITUDINAL STRESSES AT EXTREME FIBRES

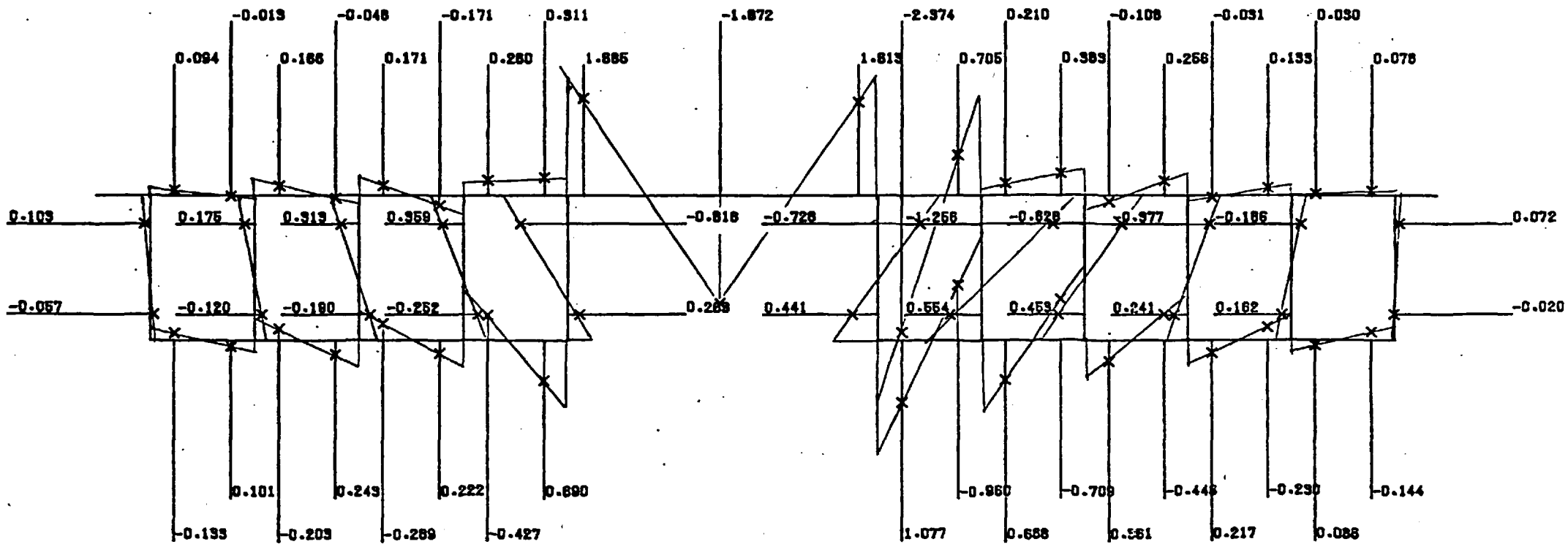


FIG230

LOAD CASE 51 SECTION 6-6 SECONDARY STRESS GAUGES
FLEXURAL COMPONENT OF TRANSVERSE STRESS

488

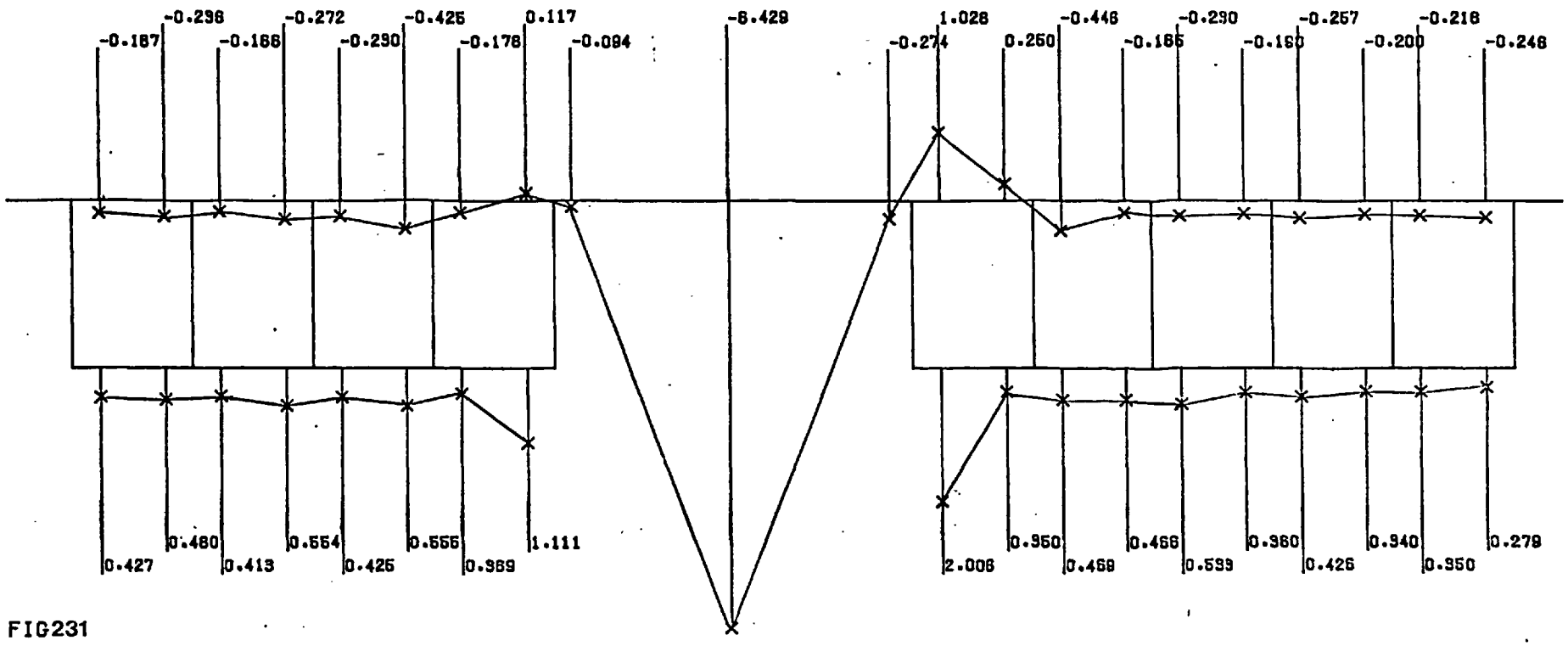


FIG231

LOAD CASE 62 SECTION 6-6 SECONDARY STRESS GAUGES
LONGITUDINAL STRESSES AT EXTREME FIBRES

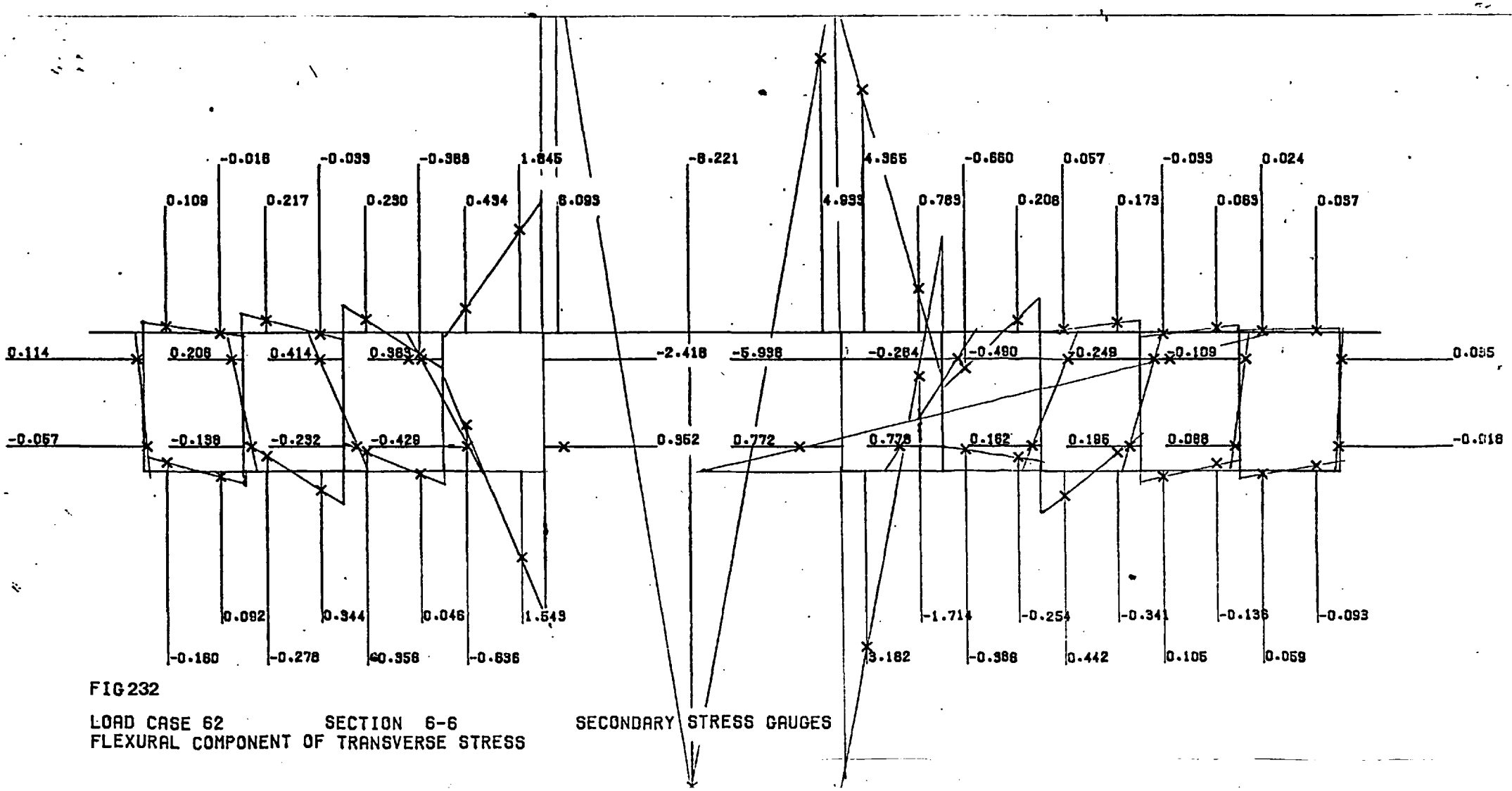


FIG232

LOAD CASE 62 SECTION 6-6 SECONDARY STRESS GAUGES
FLEXURAL COMPONENT OF TRANSVERSE STRESS

489

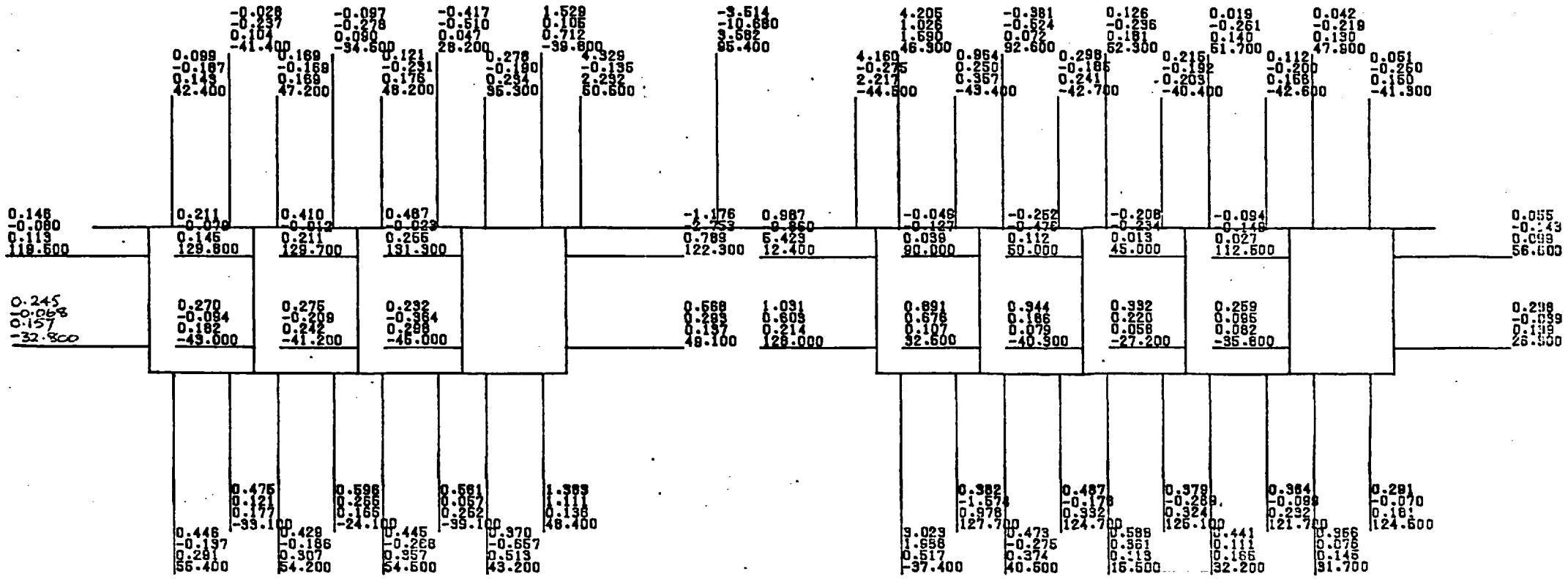


FIG233

LOAD CASE 62 SECTION 6-6 SECONDARY STRESS GAUGES
PRINCIPAL STRESSES,MAX. SHEAR,DIRECTION

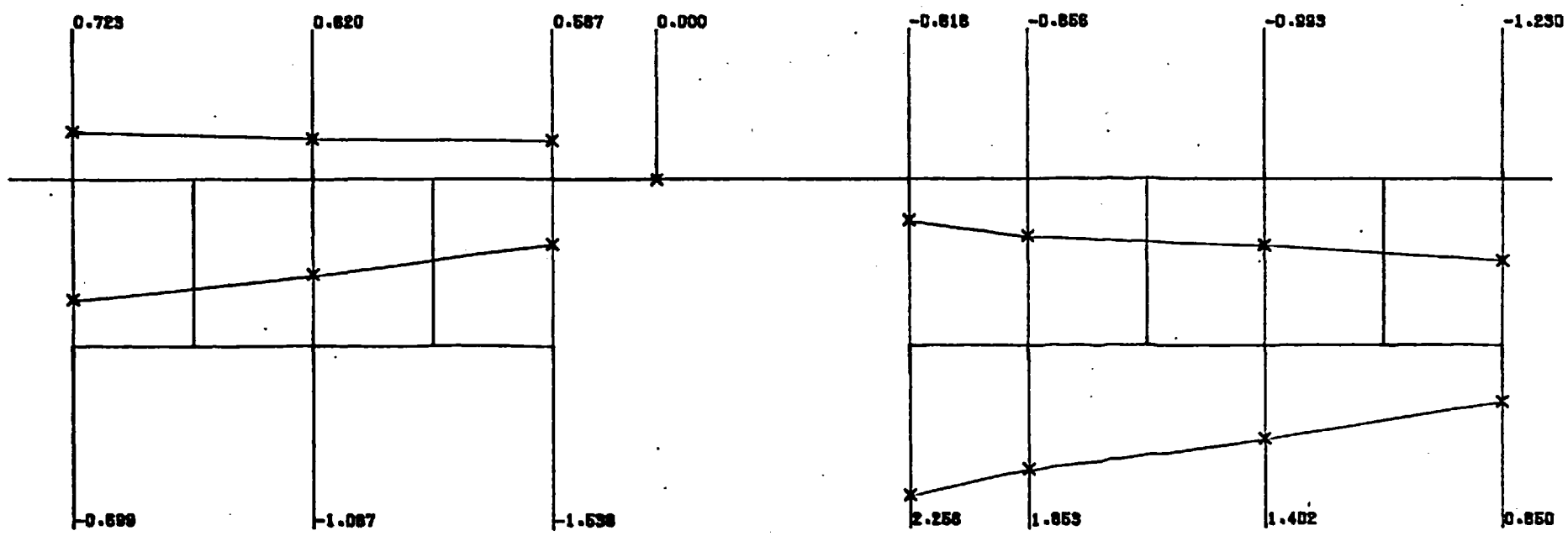


FIG234

LOAD CASE 86 SECTION 6-6 MAIN STRESS GAUGES
LONGITUDINAL STRESSES AT EXTREME FIBRES

490

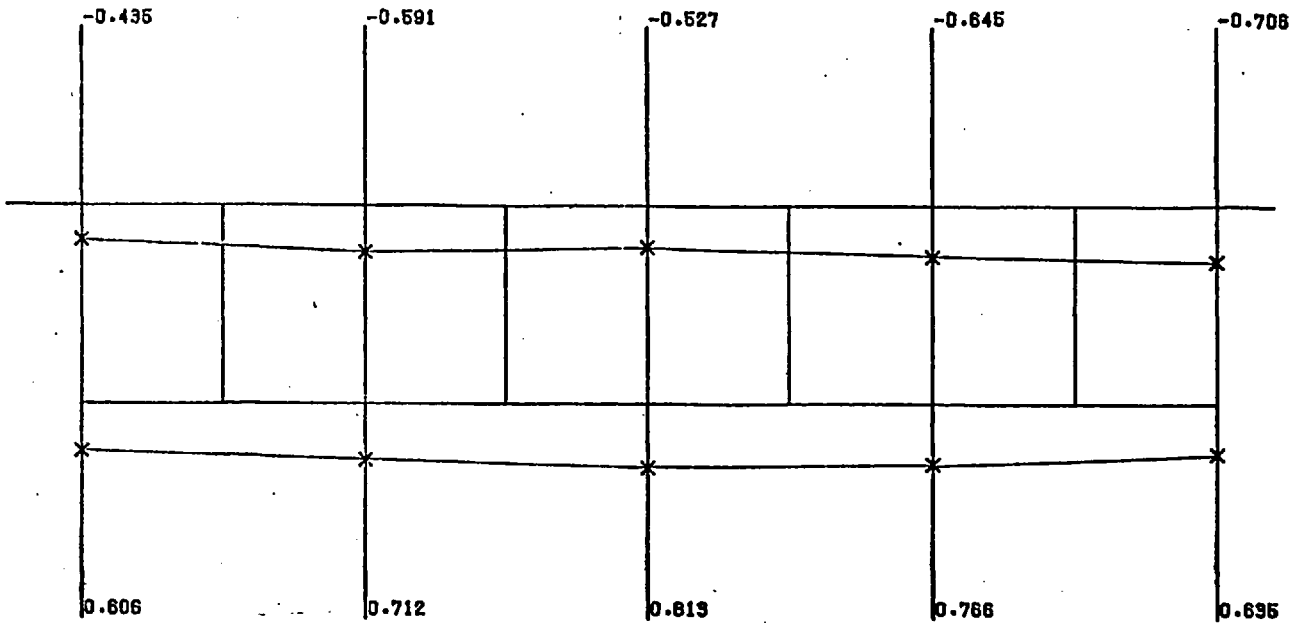


FIG235

LOAD CASE 86 SECTION 2-2 MAIN STRESS GAUGES
LONGITUDINAL STRESSES AT EXTREME FIBRES

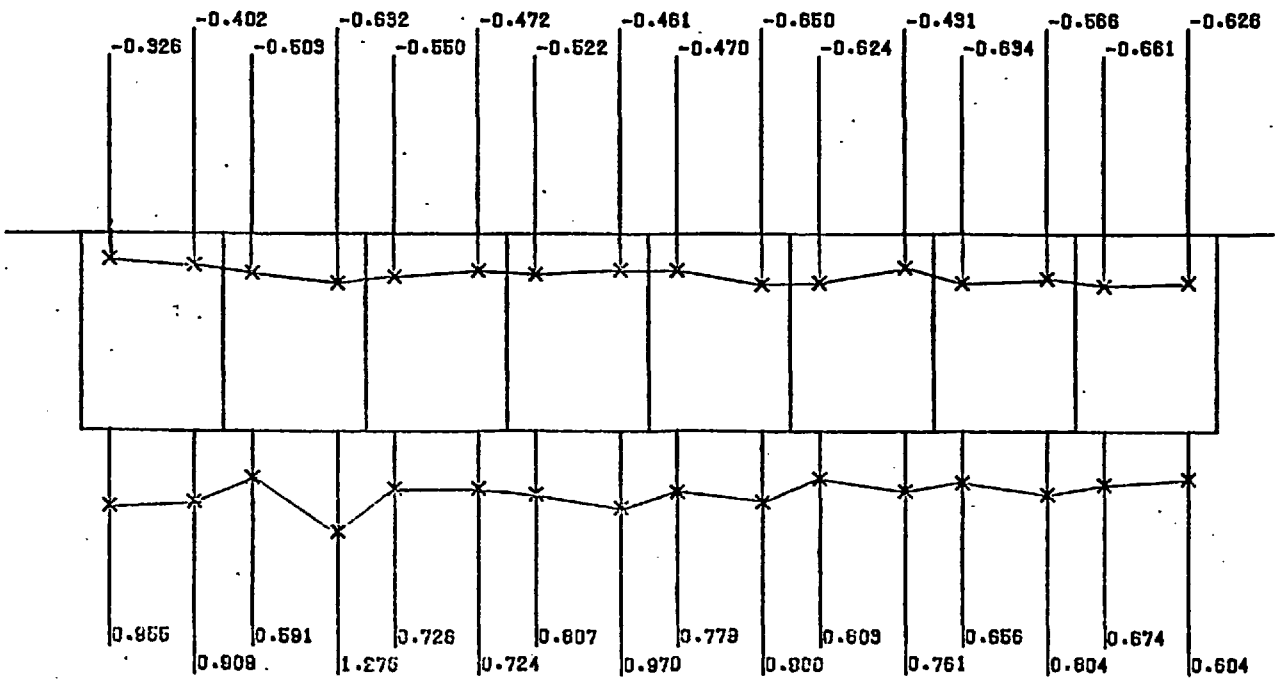


FIG236

LOAD CASE 86 SECTION 2-2 SECONDARY STRESS GAUGES
LONGITUDINAL STRESSES AT EXTREME FIBRES

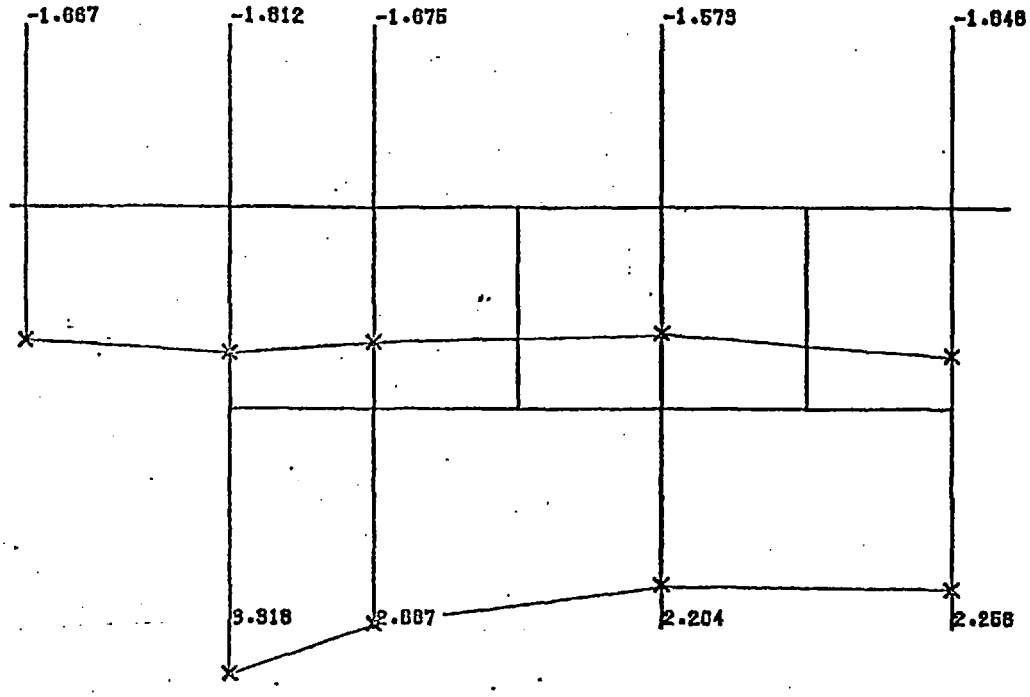
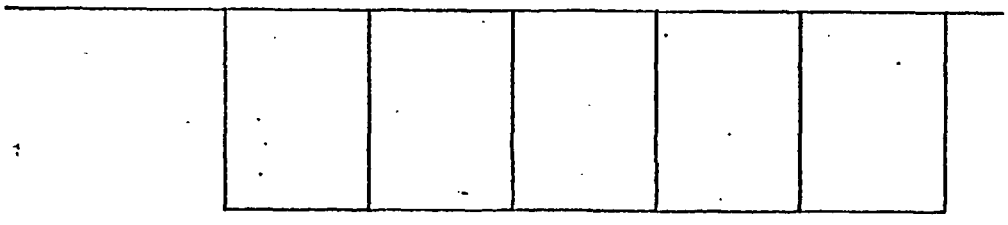


FIG237

LOAD CASE 87 SECTION 12-12 MAIN STRESS GAUGES
LONGITUDINAL STRESSES AT EXTREME FIBRES



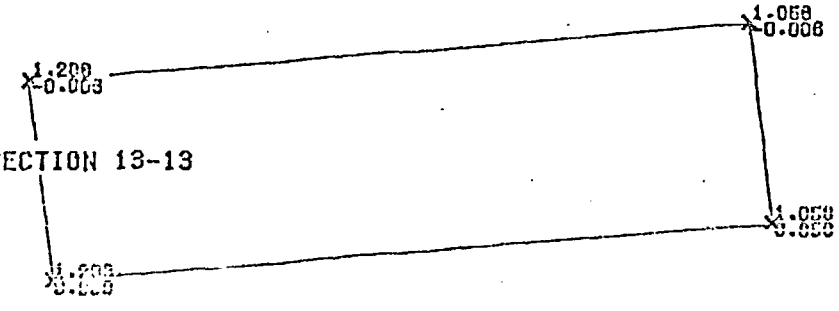


FIG238

LOAD CASE 87 SECTION 13-13
DEFLECTIONS

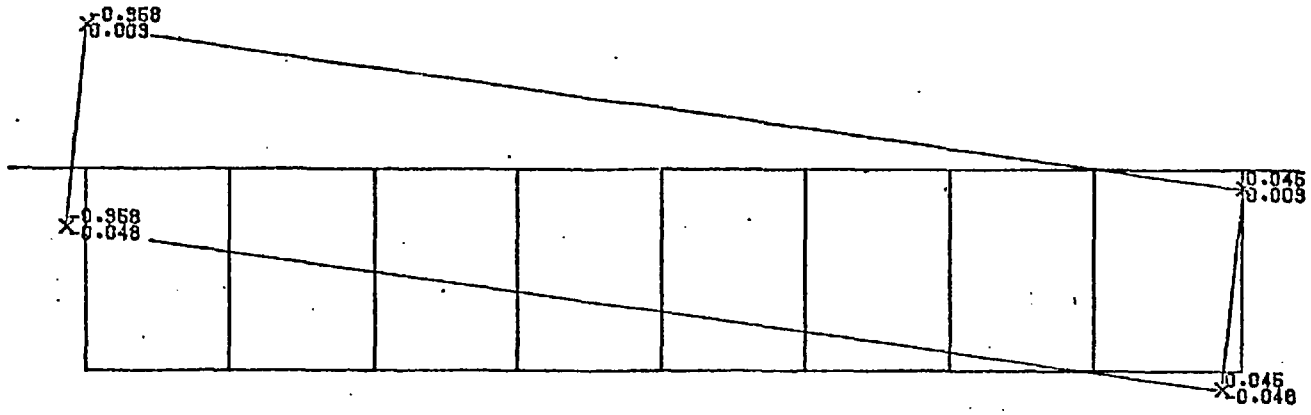


FIG239

LOAD CASE 87 SECTION 2-2
DEFLECTIONS

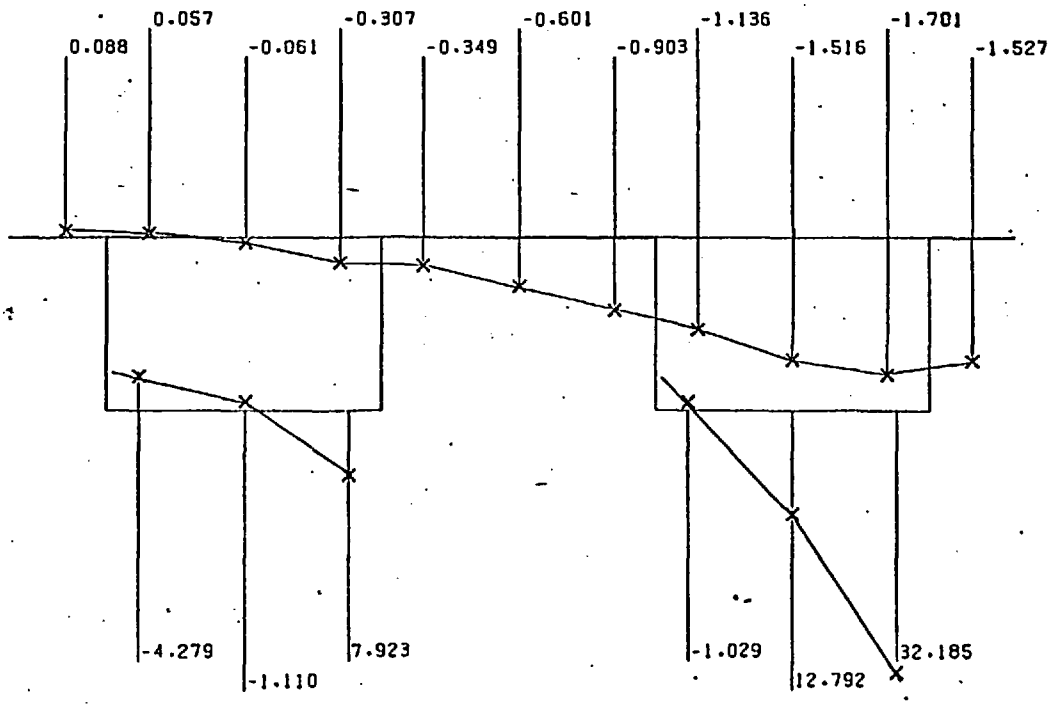


FIG240

LOAD CASE 10 SECTION 11-11 SECONDARY STRESS GAUGES
LONGITUDINAL STRESSES AT EXTREME FIBRES

493

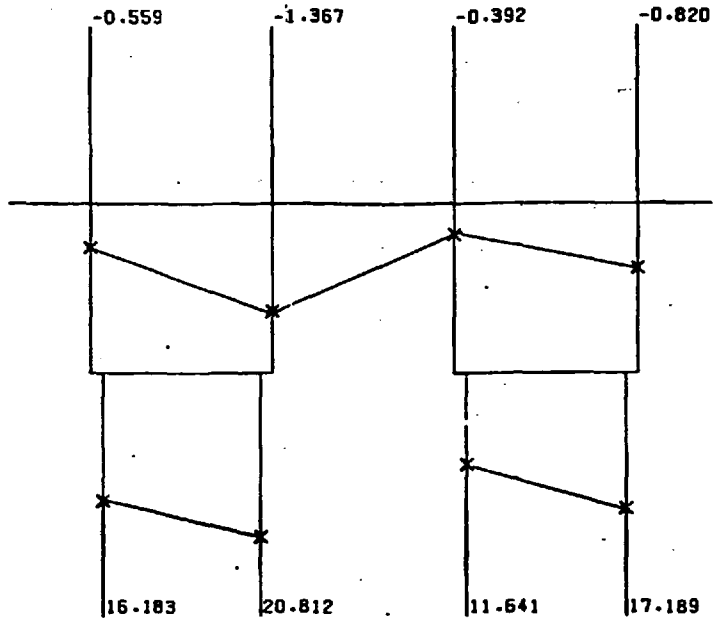


FIG241

LOAD CASE 14 SECTION 8-8 MAIN STRESS GAUGES
LONGITUDINAL STRESSES AT EXTREME FIBRES

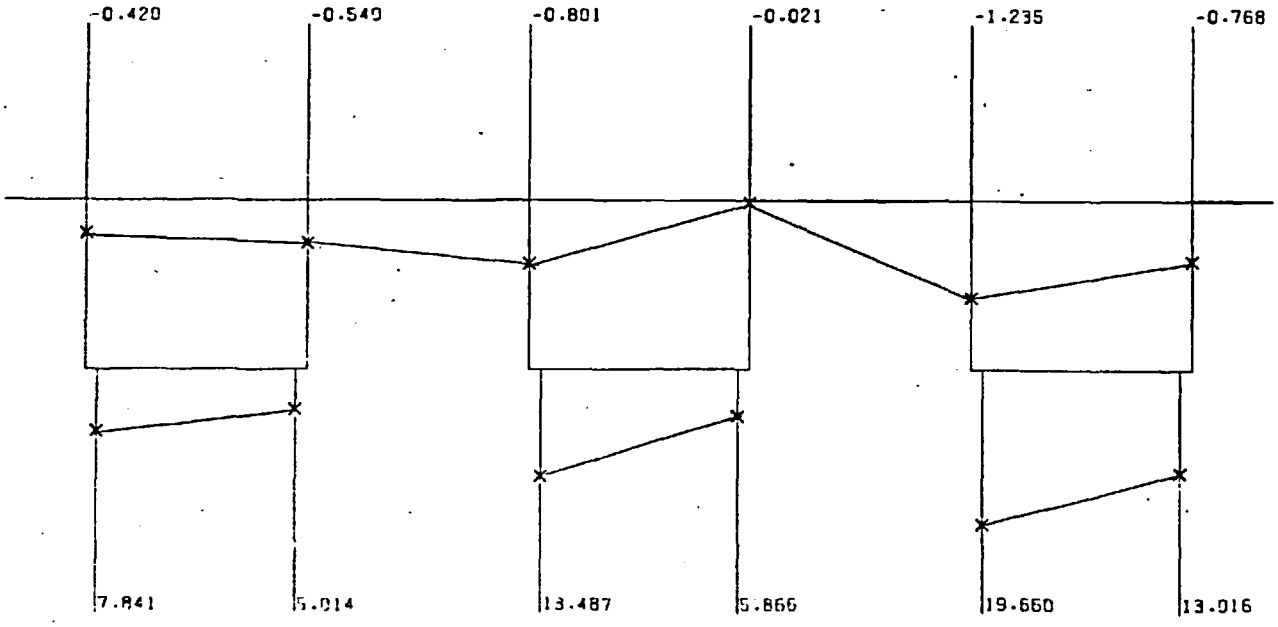


FIG242

LOAD CASE 5 SECTION 5-5 MAIN STRESS GAUGES
LONGITUDINAL STRESSES AT EXTREME FIBRES

494

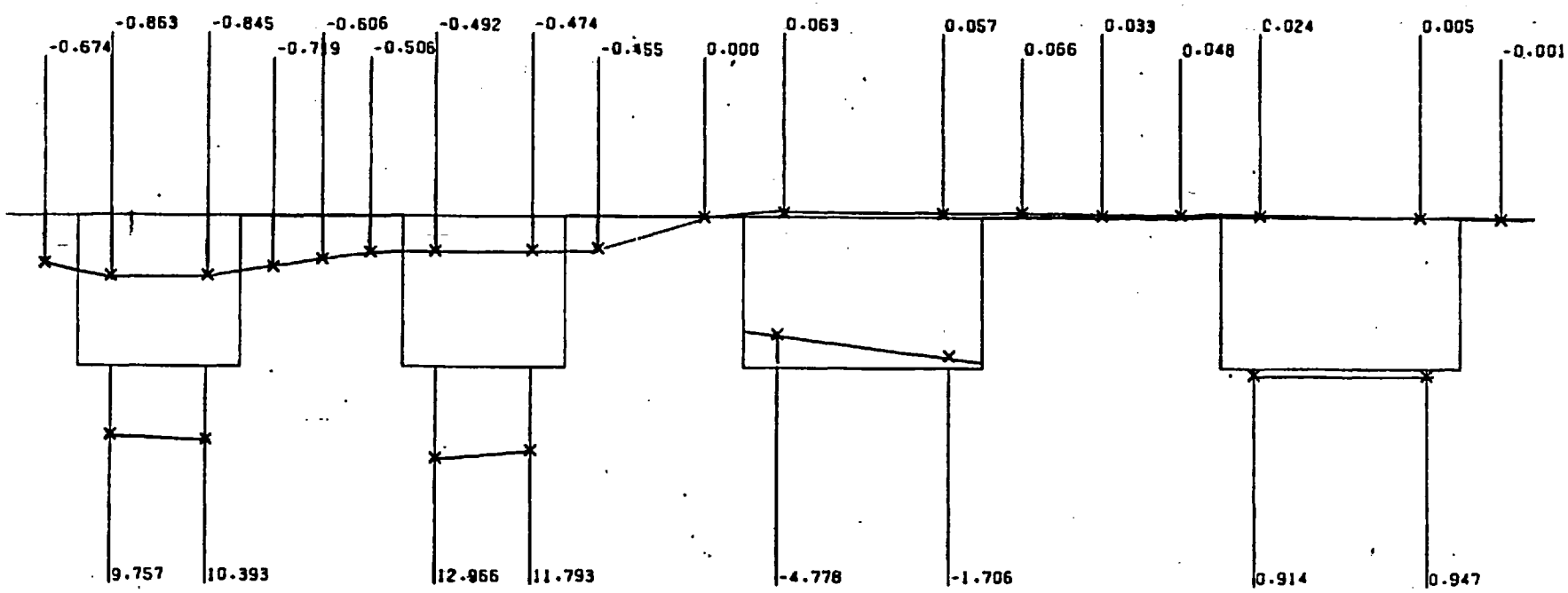


FIG243

LOAD CASE 9 SECTION 6-6 SECONDARY STRESS GAUGES
LONGITUDINAL STRESSES AT EXTREME FIBRES

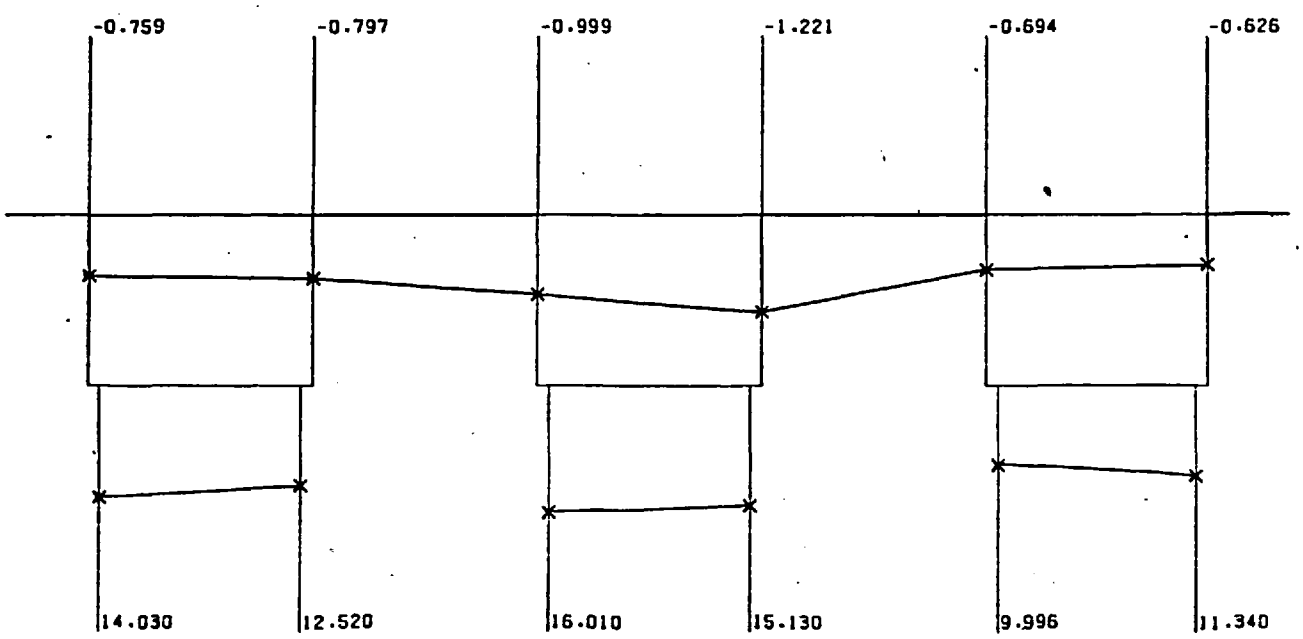


FIG244

LOAD CASE 75 SECTION 5-5 MAIN STRESS GAUGES
LONGITUDINAL STRESSES AT EXTREME FIBRES

495

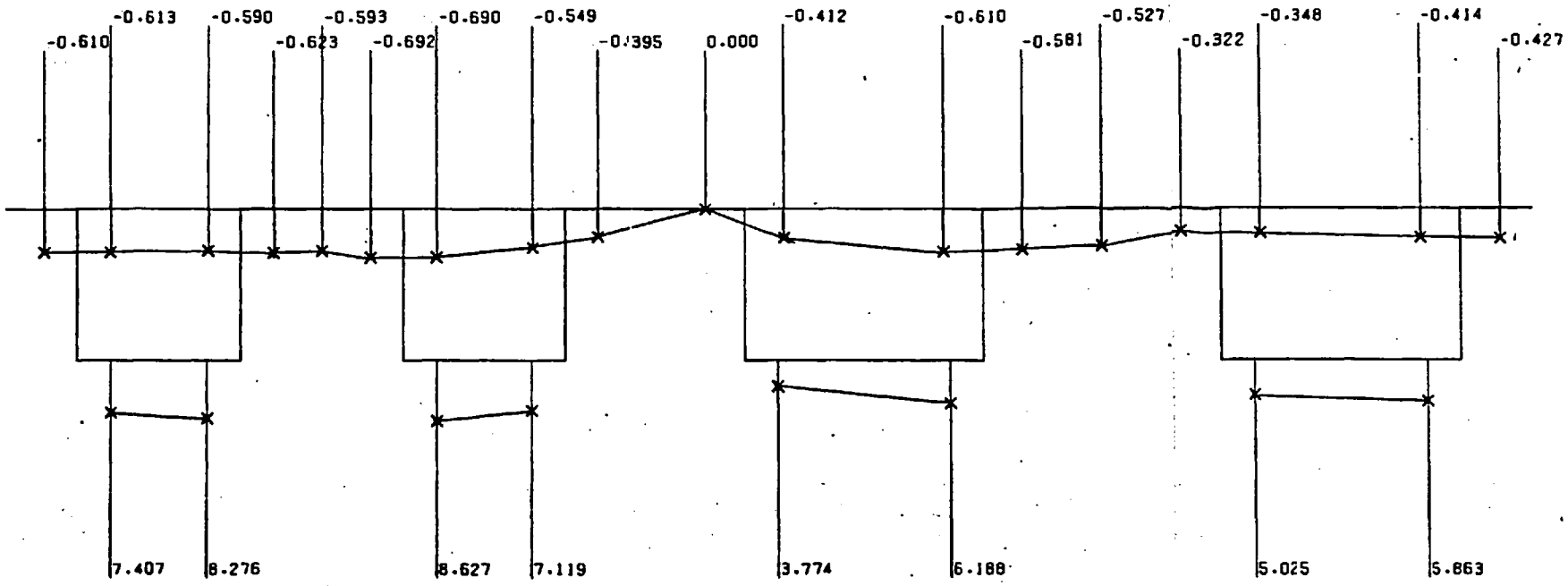


FIG245

LOAD CASE 26 SECTION 6-6 SECONDARY STRESS GAUGES
LONGITUDINAL STRESSES AT EXTREME FIBRES

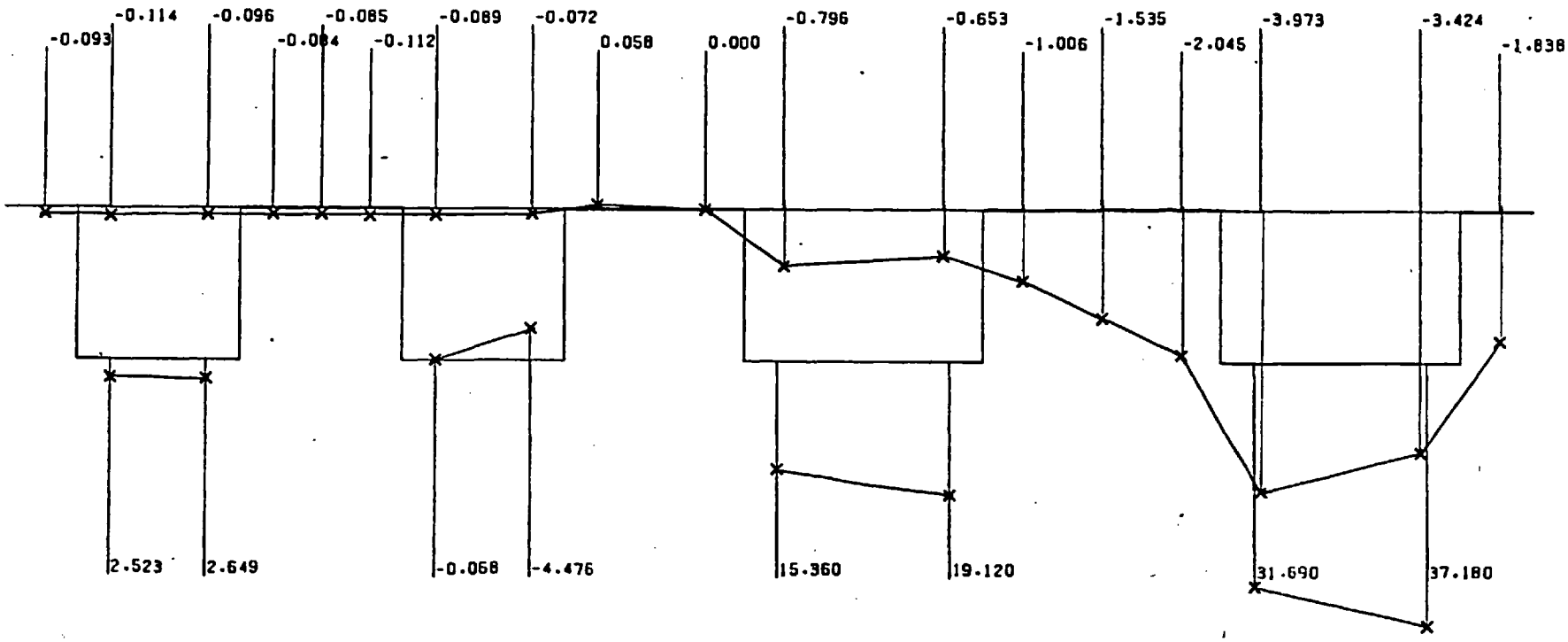


FIG246

LOAD CASE 73 SECTION 6-6 SECONDARY STRESS GAUGES
LONGITUDINAL STRESSES AT EXTREME FIBRES

496

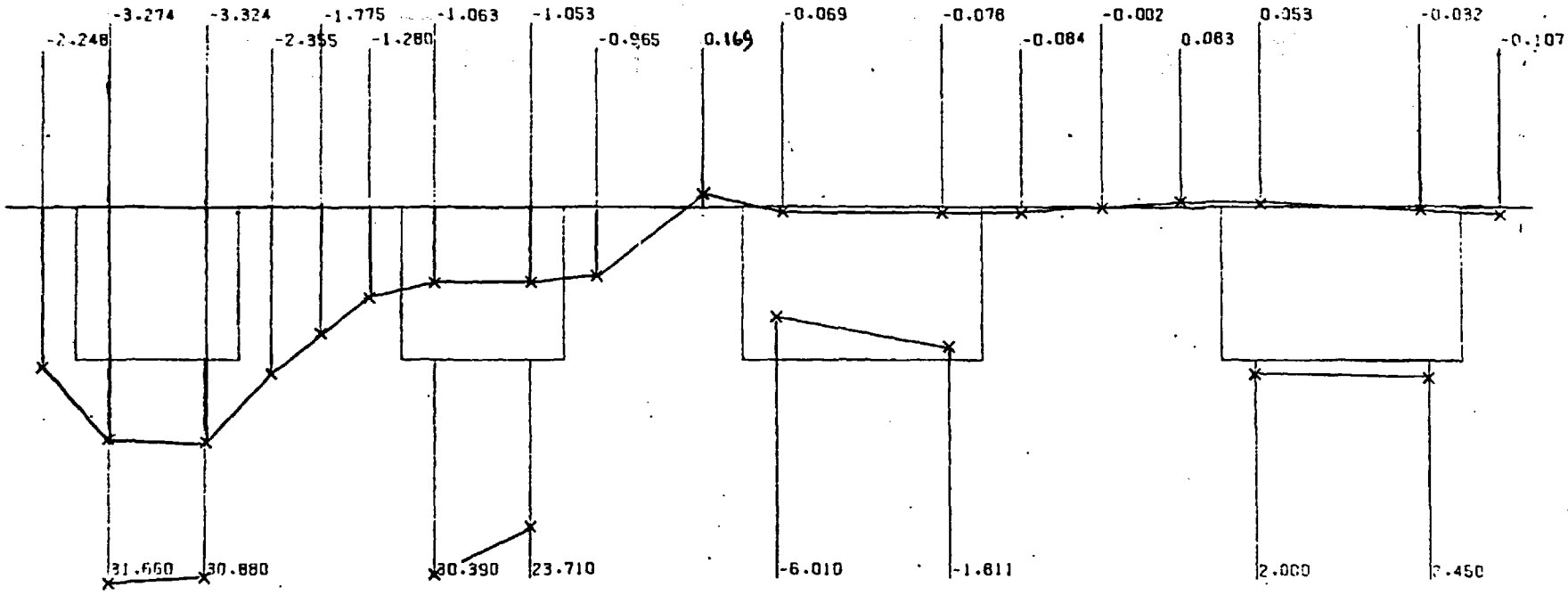


FIG247

LOAD CASE 77 SECTION 6-6 SECONDARY STRESS GAUGES
LONGITUDINAL STRESSES AT EXTREME FIBRES

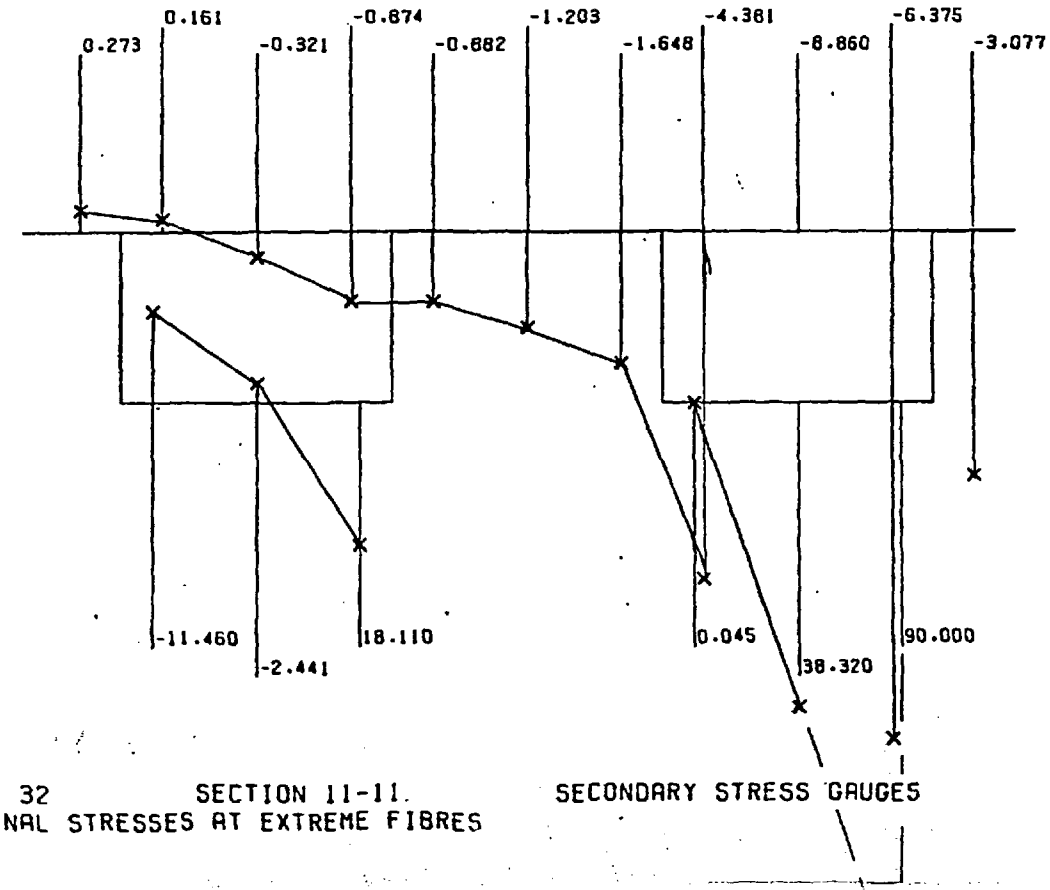


FIG248

LOAD CASE 32 SECTION 11-11. SECONDARY STRESS GAUGES
LONGITUDINAL STRESSES AT EXTREME FIBRES

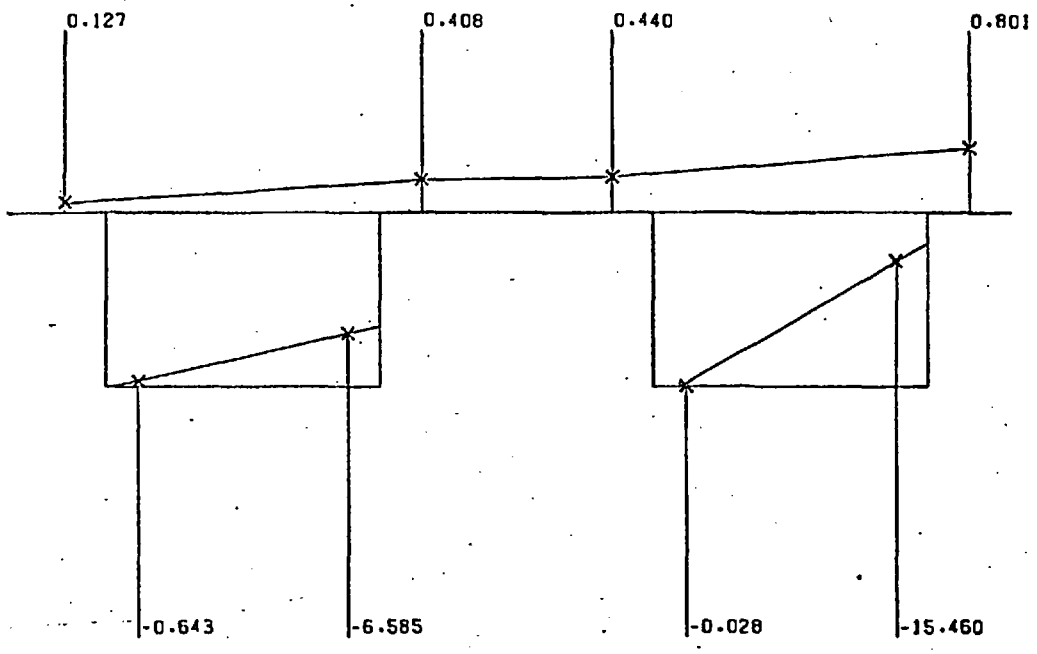


FIG249

LOAD CASE 73 SECTION 11-11 MAIN STRESS GAUGES
LONGITUDINAL STRESSES AT EXTREME FIBRES

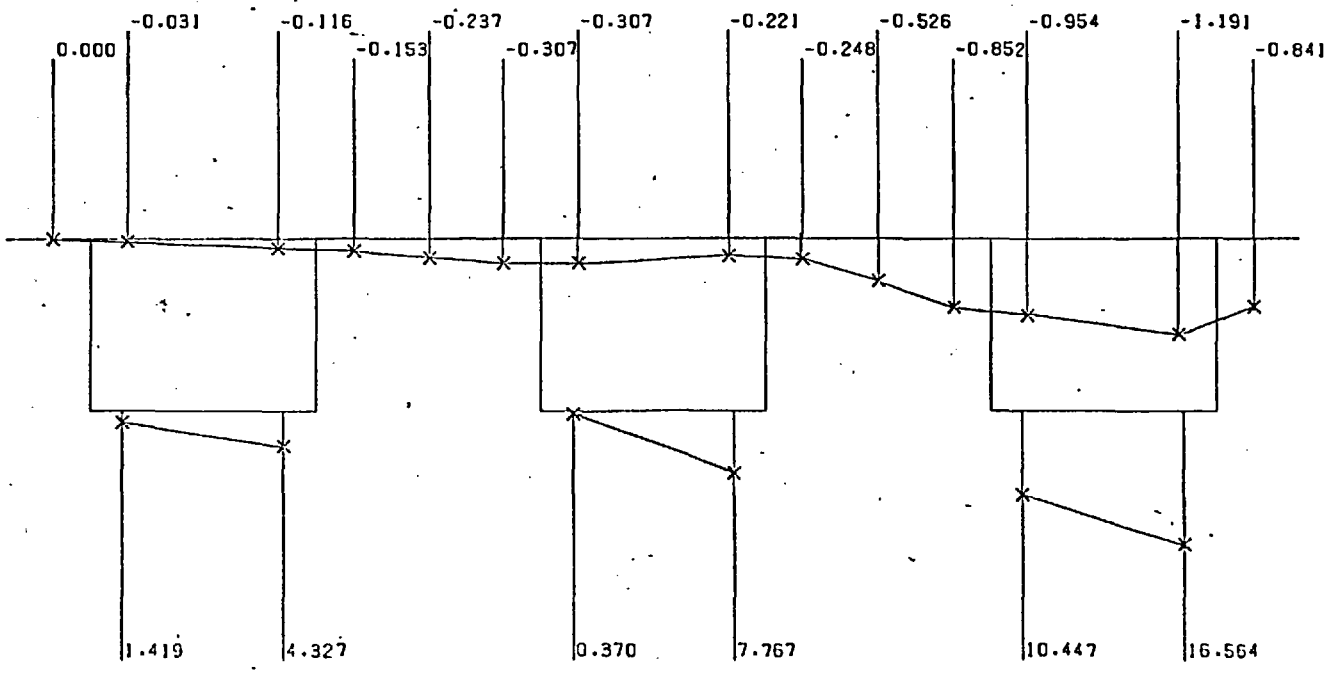


FIG250

LOAD CASE 1 SECTION 2-2 SECONDARY STRESS GAUGE:
LONGITUDINAL STRESSES AT EXTREME FIBRES

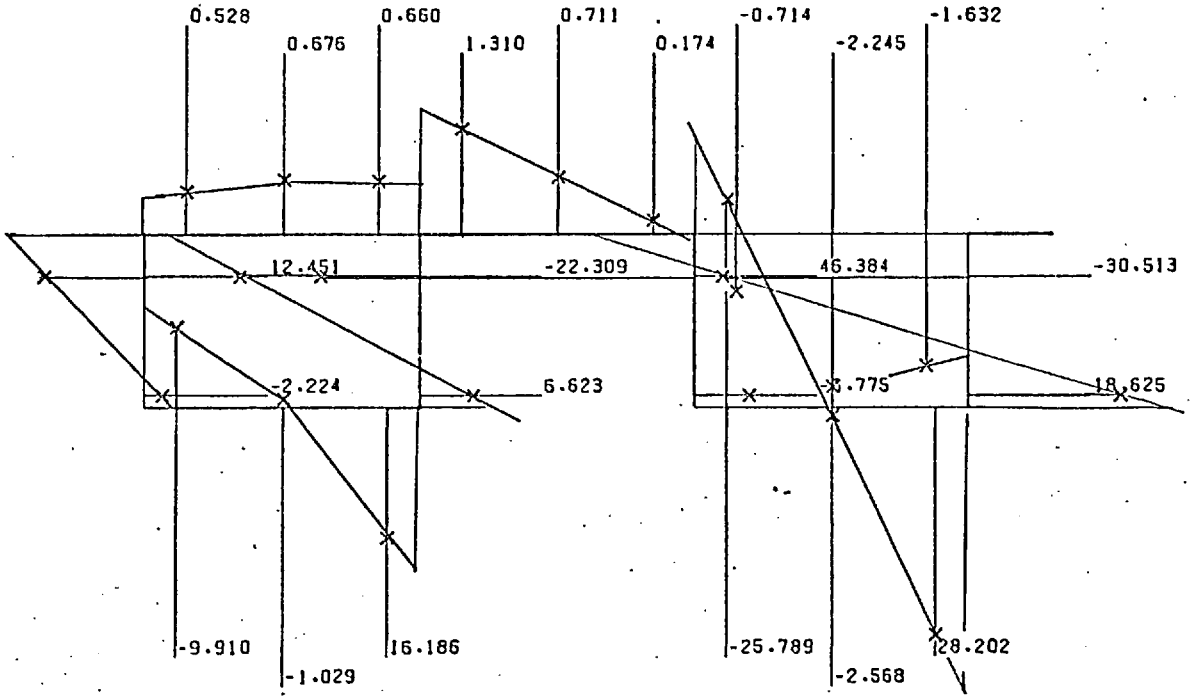


FIG251

LOAD CASE 10 SECTION 11-11 SECONDARY STRESS GAUGES
FLEXURAL COMPONENT OF TRANSVERSE STRESS

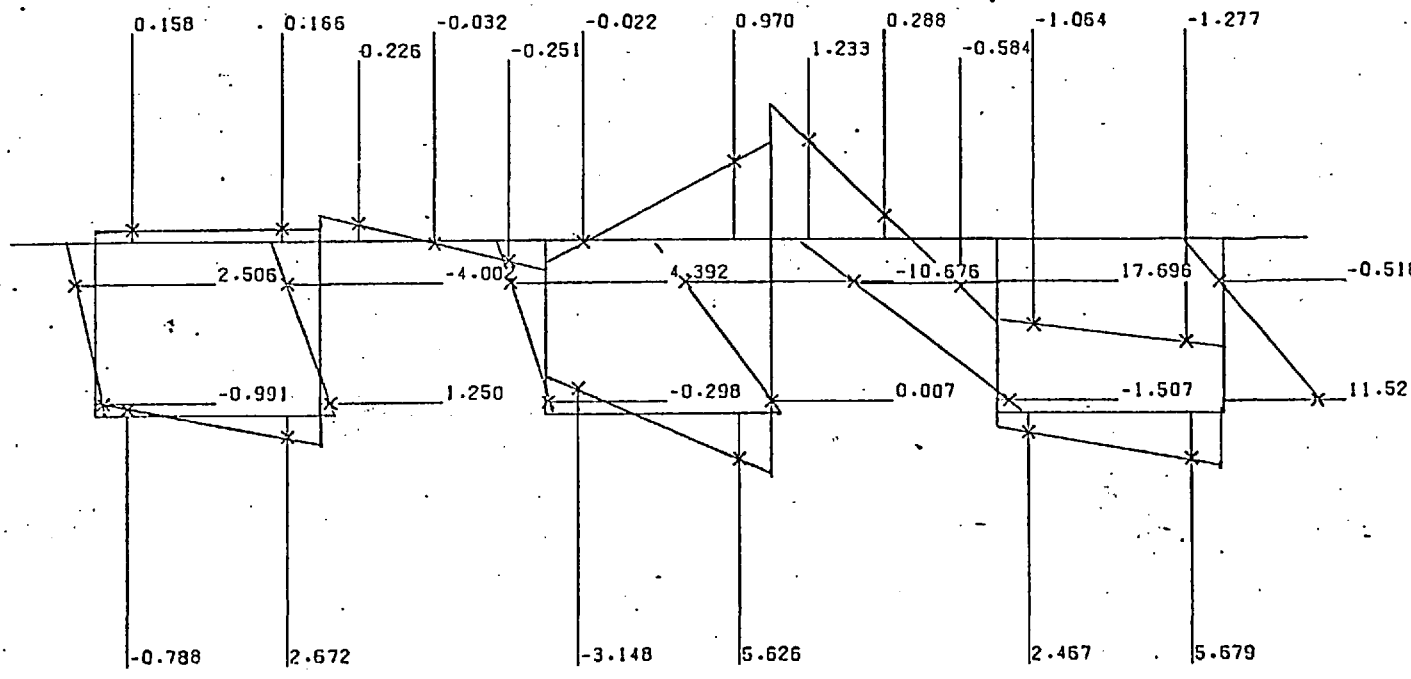


FIG252

LOAD CASE 1 SECTION 2-2 SECONDARY STRESS GAUGES
FLEXURAL COMPONENT OF TRANSVERSE STRESS

499

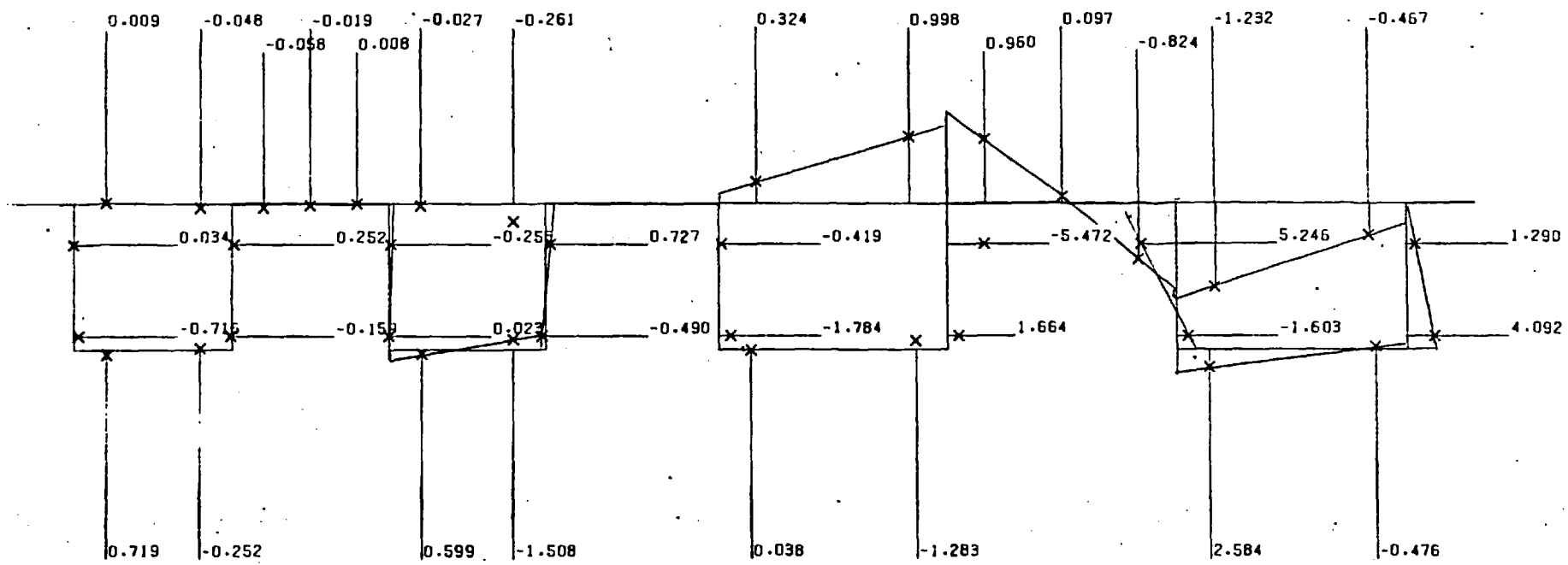


FIG253

LOAD CASE 5 SECTION 6-6 SECONDARY STRESS GAUGES
FLEXURAL COMPONENT OF TRANSVERSE STRESS

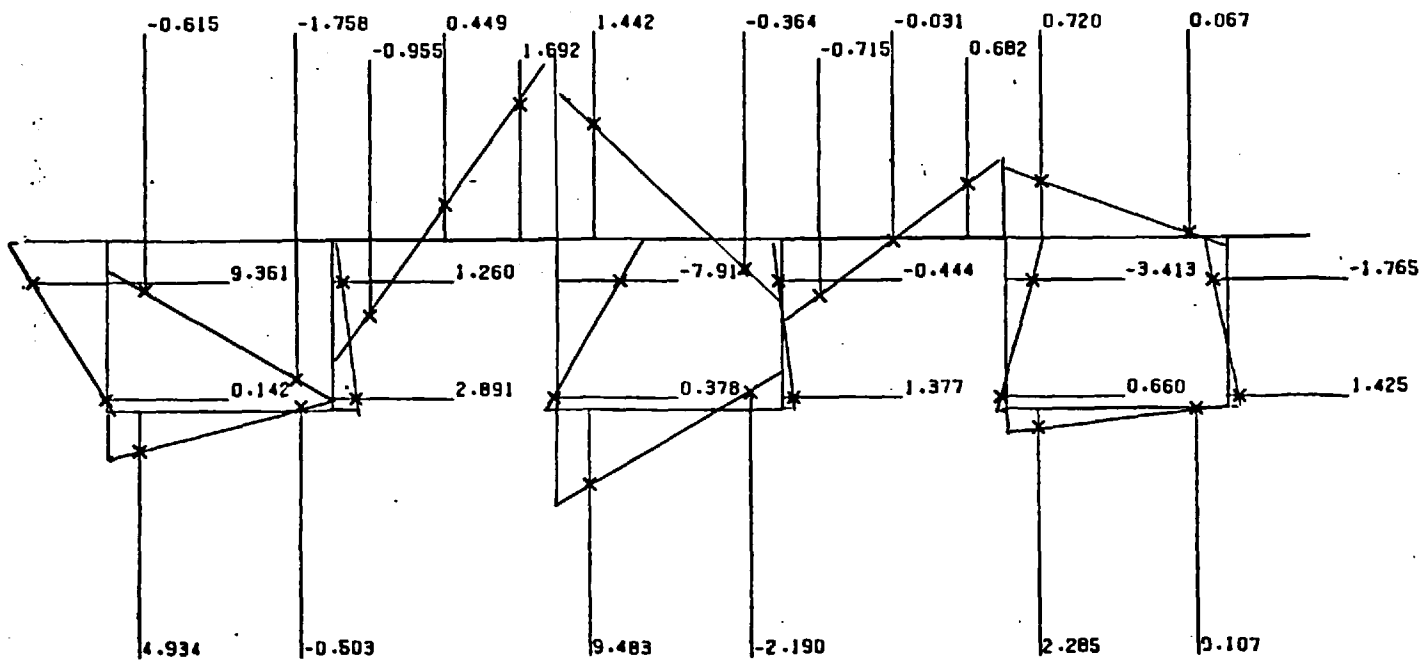


FIG254

LOAD CASE 4 SECTION 2-2 SECONDARY STRESS GAUGES
FLEXURAL COMPONENT OF TRANSVERSE STRESS

500

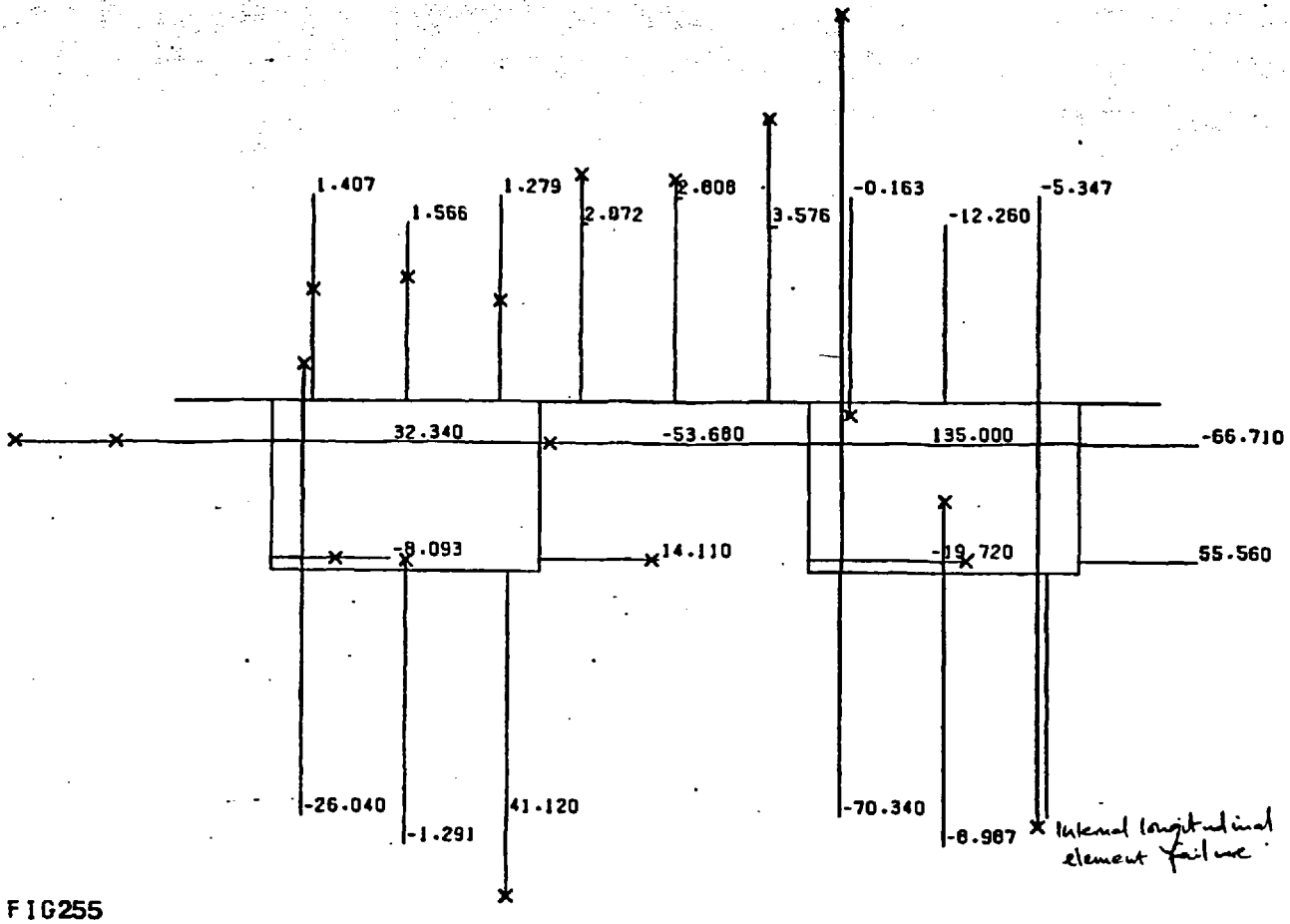


FIG255

LOAD CASE 32 SECTION 11-11 SECONDARY STRESS GAUGES
FLEXURAL COMPONENT OF TRANSVERSE STRESS

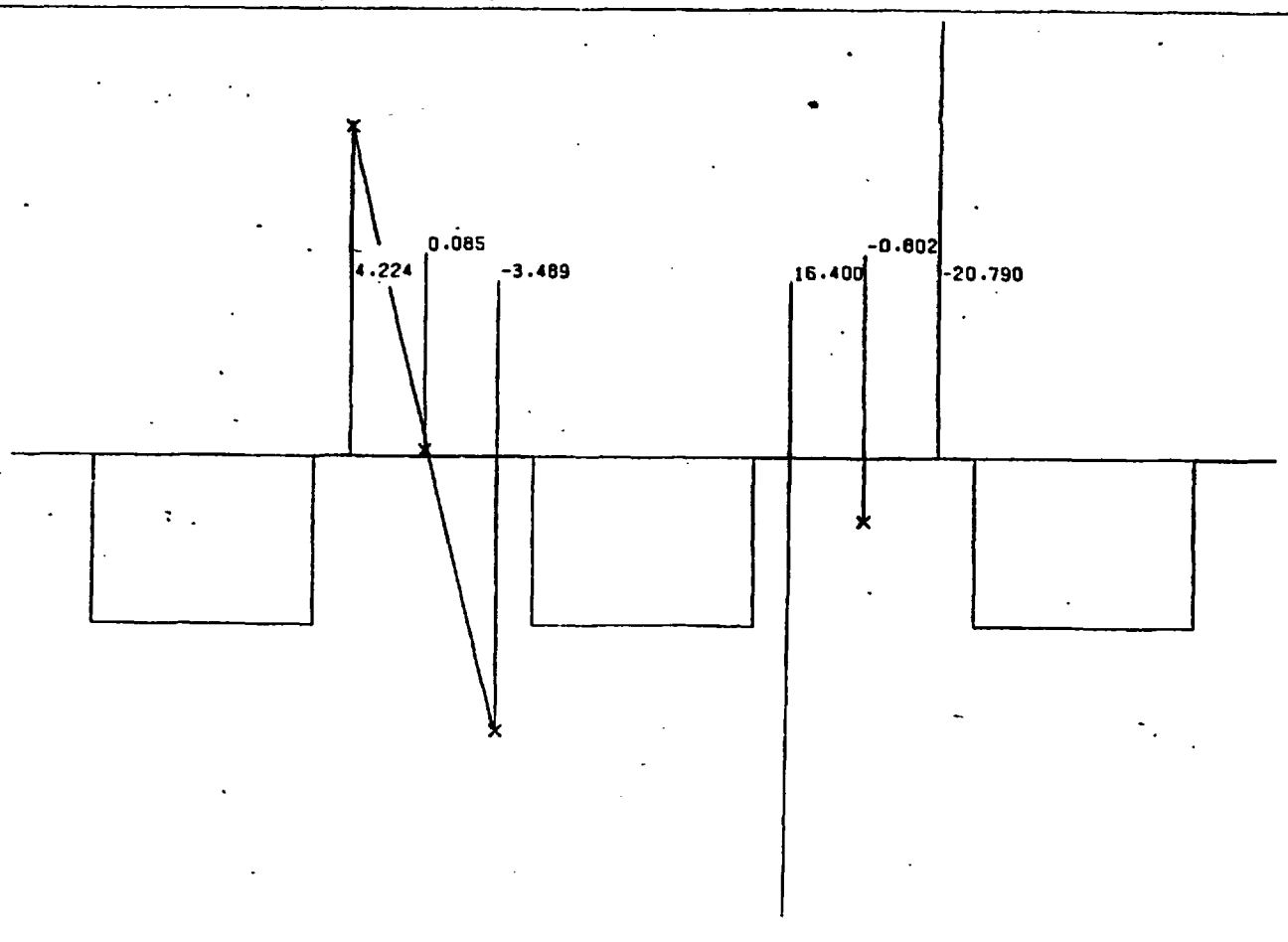


FIG256

LOAD CASE 16 SECTION 3-3 SECONDARY STRESS GAUGES
FLEXURAL COMPONENT OF TRANSVERSE STRESS

501

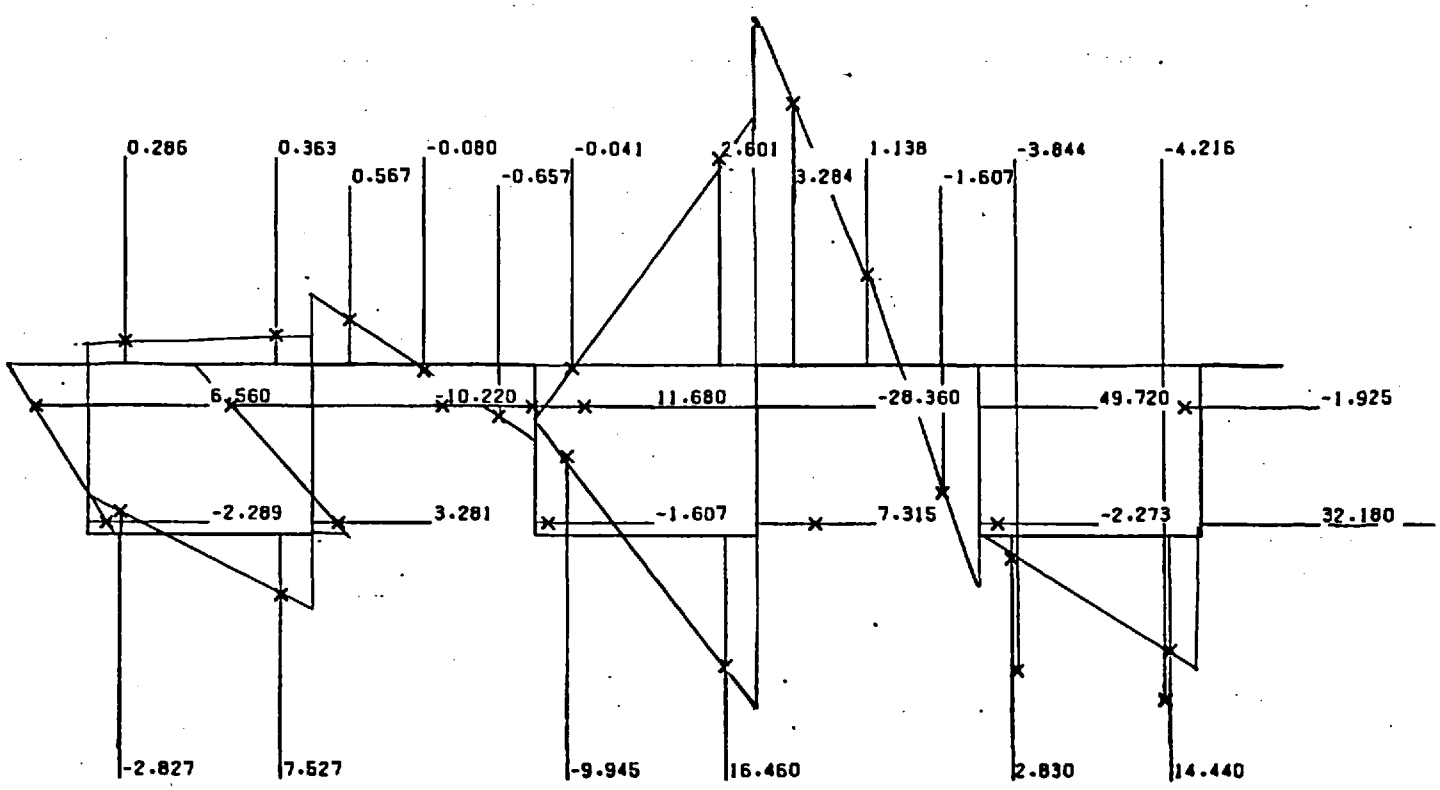


FIG257

LOAD CASE 16 SECTION 2-2 SECONDARY STRESS GAUGES
FLEXURAL COMPONENT OF TRANSVERSE STRESS

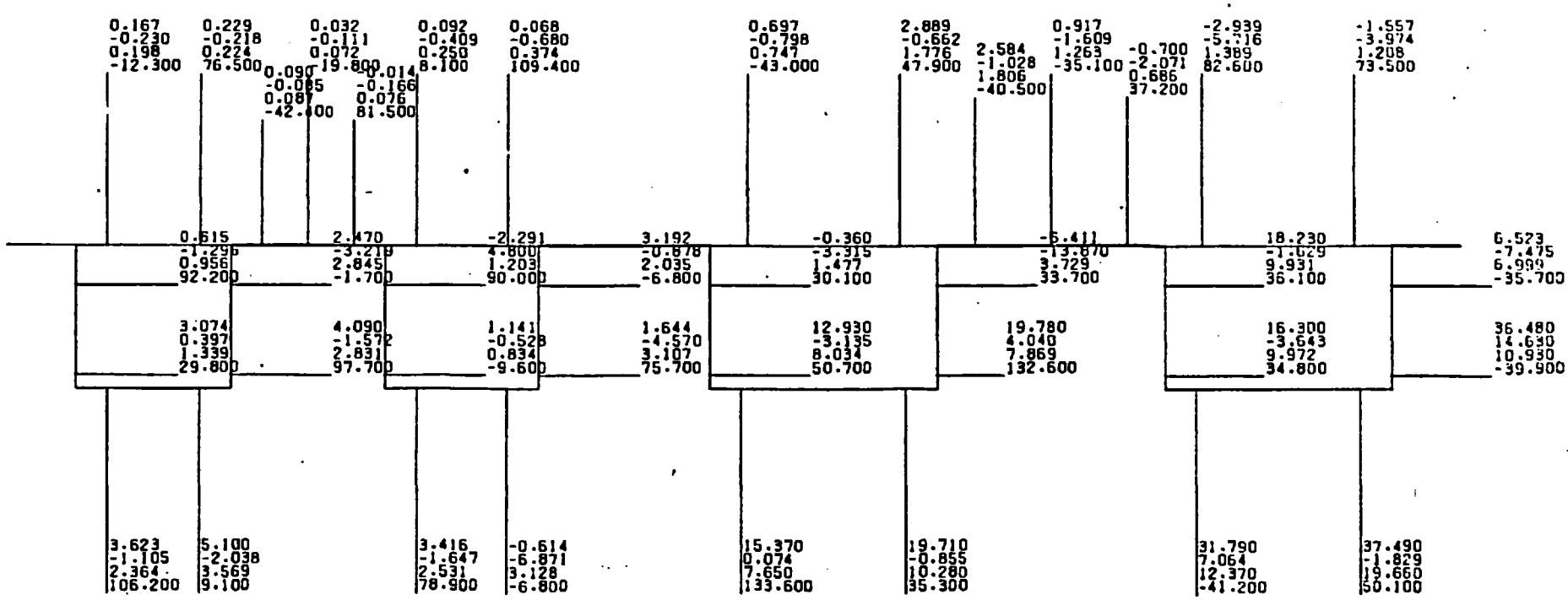


FIG258

LOAD CASE 73 SECTION 6-6 SECONDARY STRESS GAUGES
PRINCIPAL STRESSES.MAX. SHEAR.DIRECTION

502

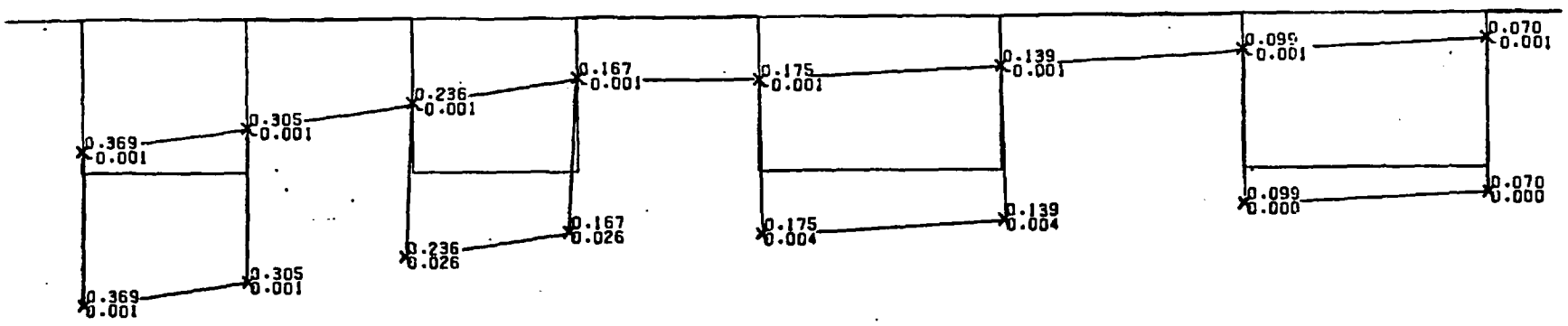


FIG259

LOAD CASE 9 SECTION 6-6
DEFLECTIONS

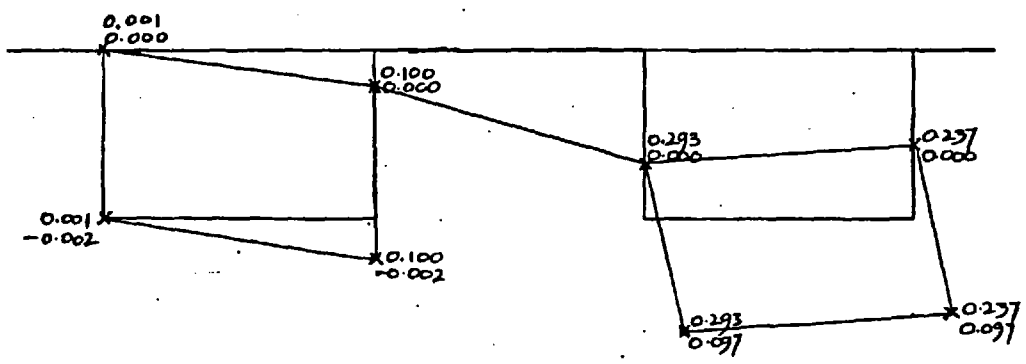


FIG260

LOAD CASE 10 SECTION 11-11
DEFLECTIONS

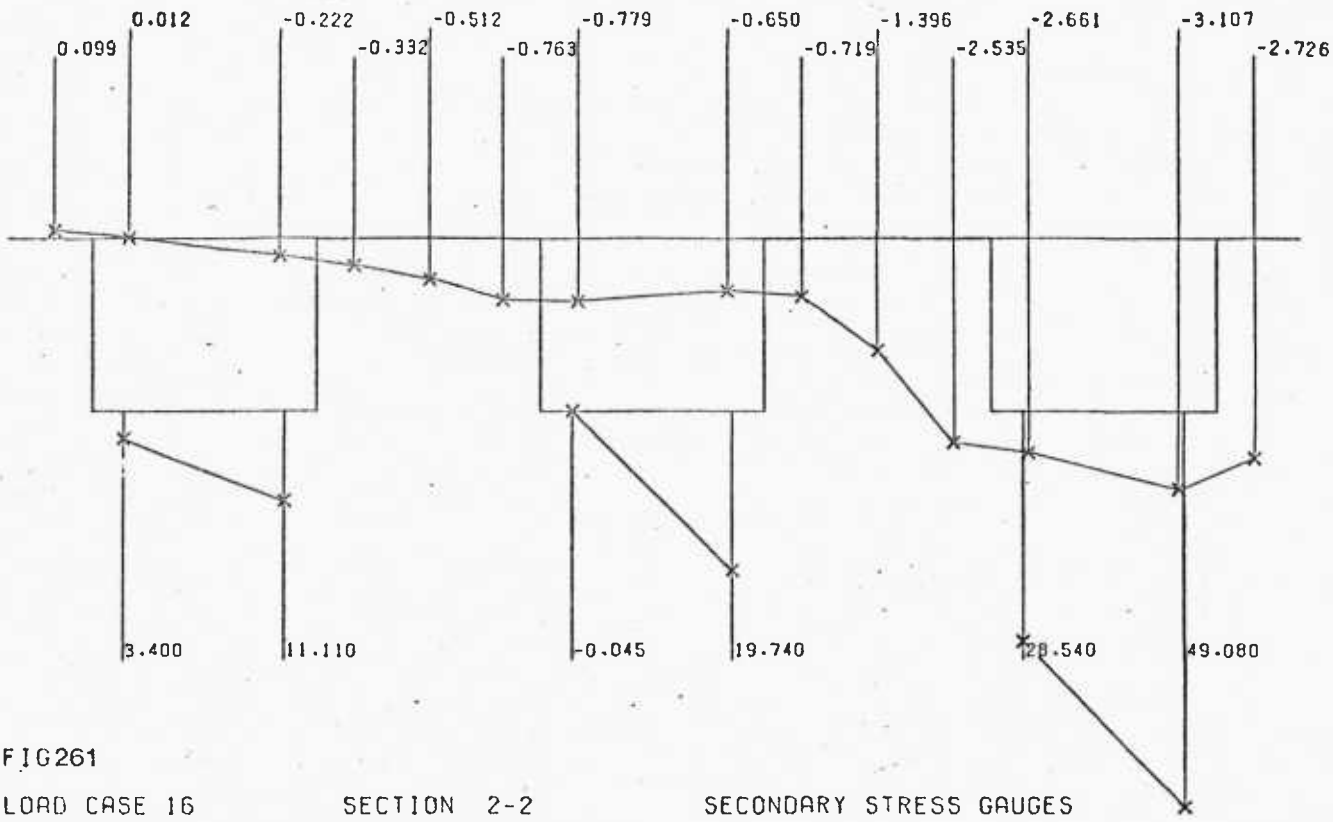


FIG261

LOAD CASE 16 SECTION 2-2 SECONDARY STRESS GAUGES
LONGITUDINAL STRESSES AT EXTREME FIBRES

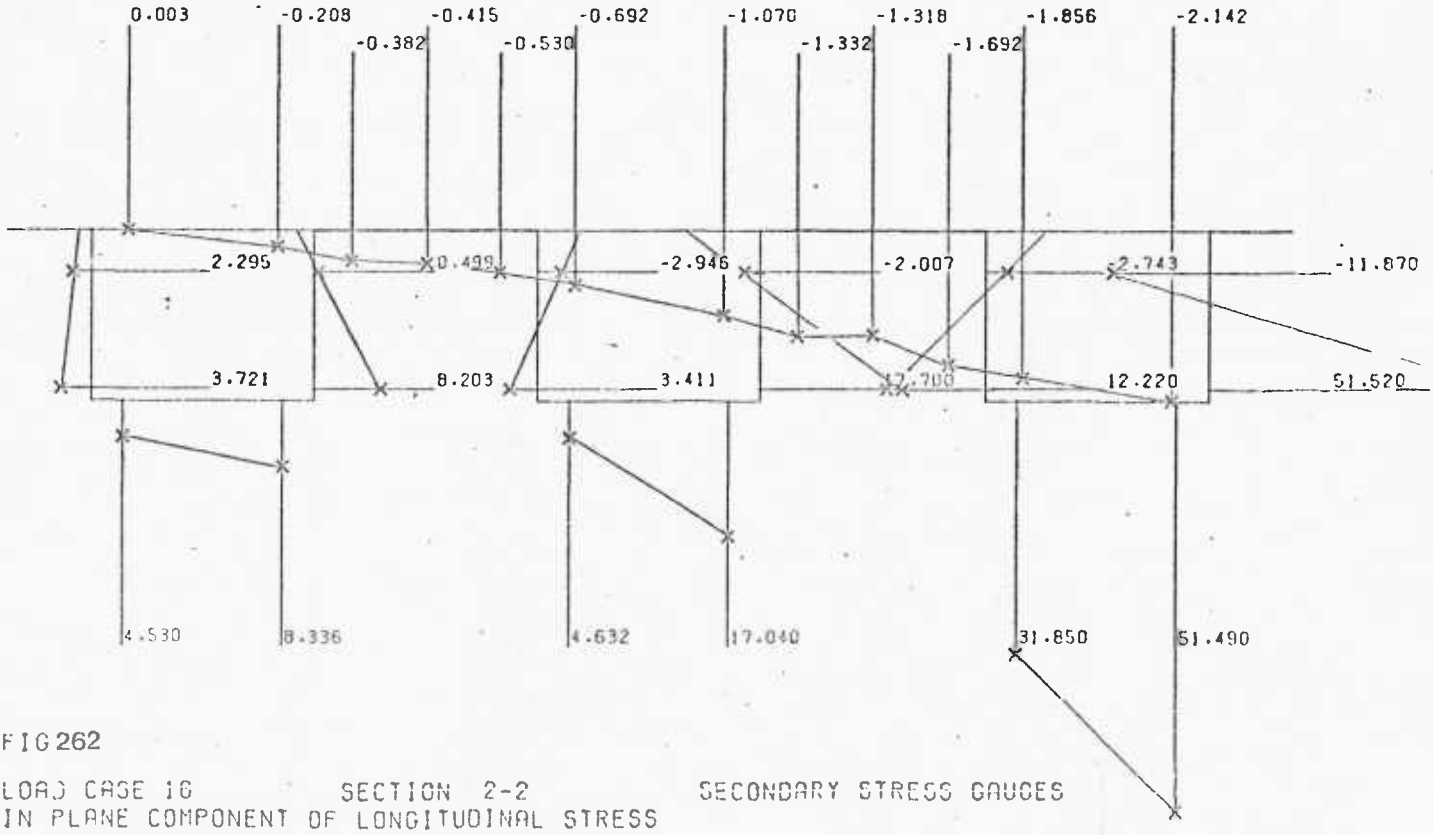


FIG262

LOAD CASE 16 SECTION 2-2 SECONDARY STRESS GAUGES
IN PLANE COMPONENT OF LONGITUDINAL STRESS

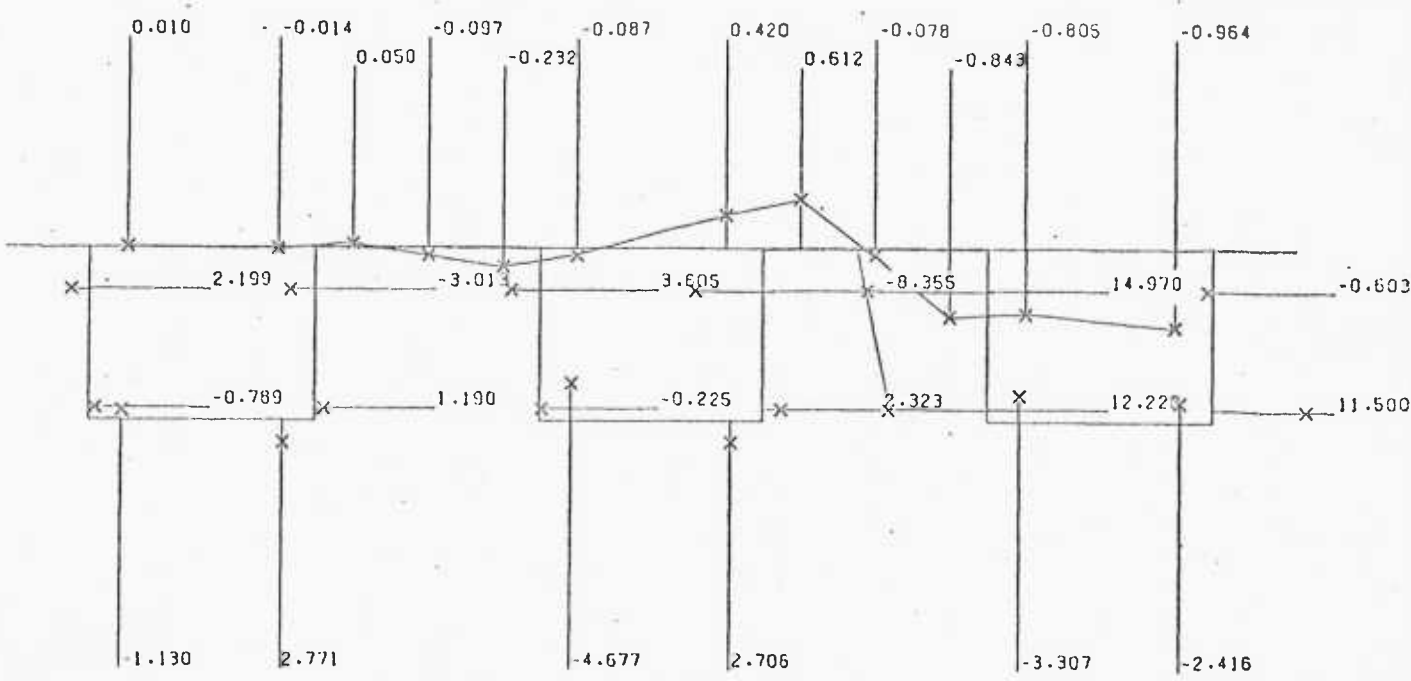


FIG 263 .

LOAD CASE 16 SECTION 2-2 SECONDARY STRESS GAUGES
FLEXURAL COMPONENT OF LONGITUDINAL STRESS

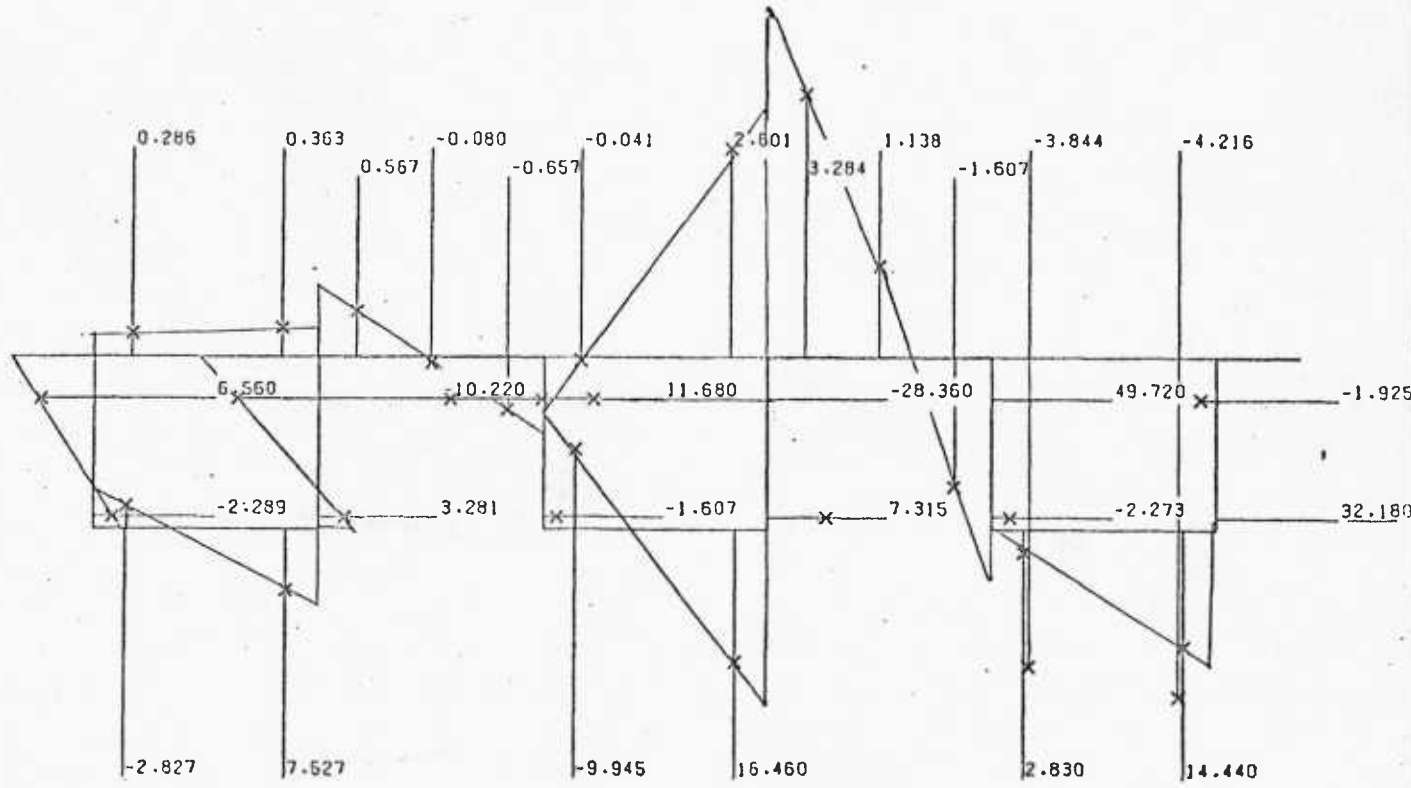


FIG 264

LOAD CASE 16 SECTION 2-2 SECONDARY STRESS GAUGES
FLEXURAL COMPONENT OF TRANSVERSE STRESS

505

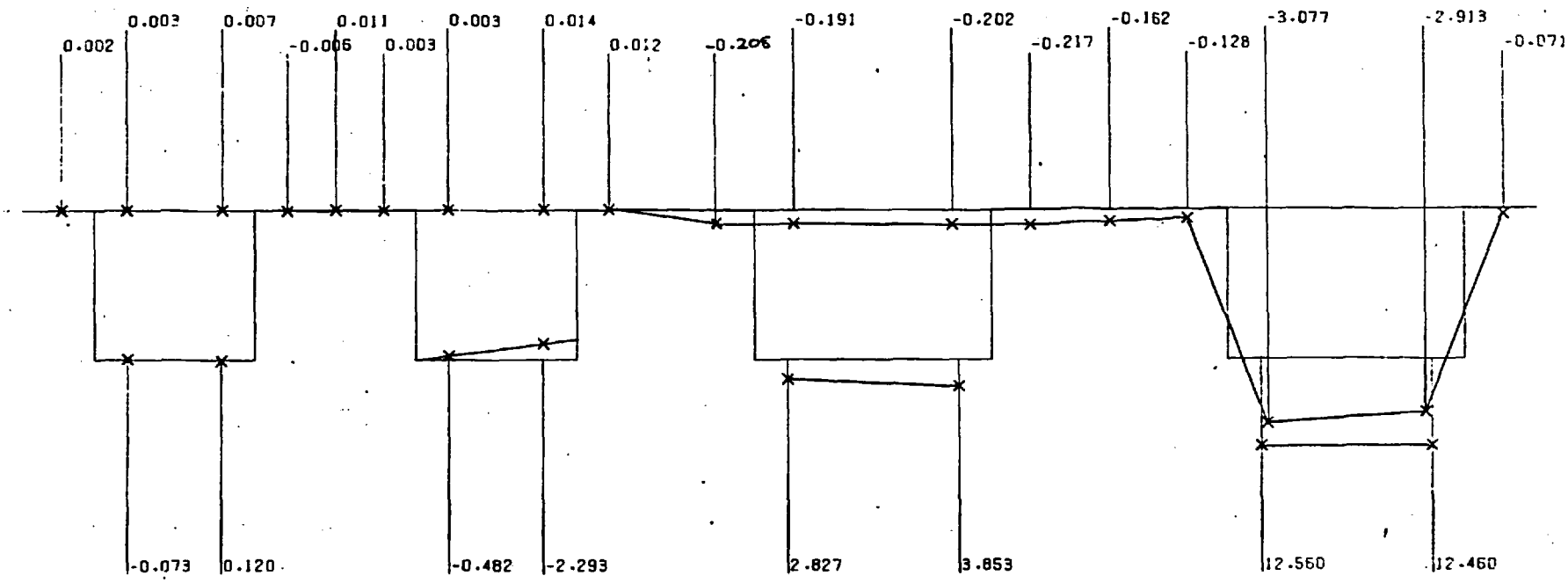


FIG265

LOAD CASE 82 SECTION 6-6 SECONDARY STRESS GAUGES
LONGITUDINAL STRESSES AT EXTREME FIBRES

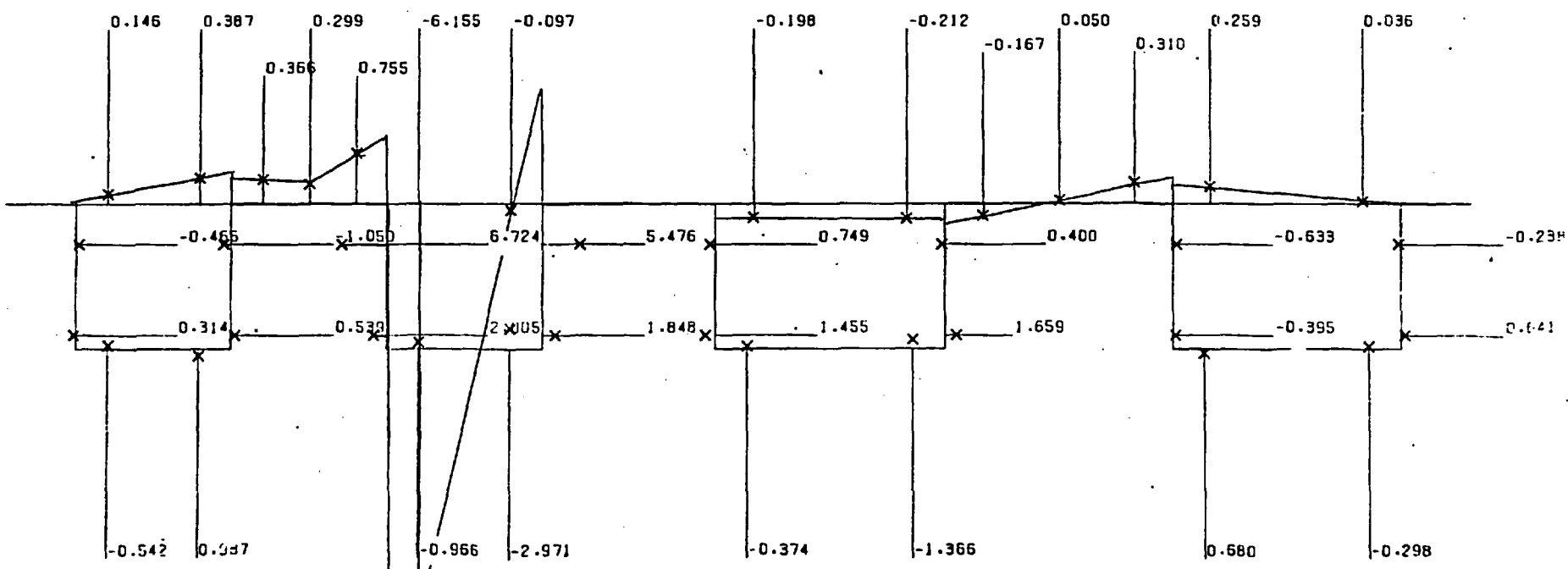


FIG266

LOAD CASE 84 SECTION 6-6 SECONDARY STRESS GAUGES
FLEXURAL COMPONENT OF TRANSVERSE STRES

506

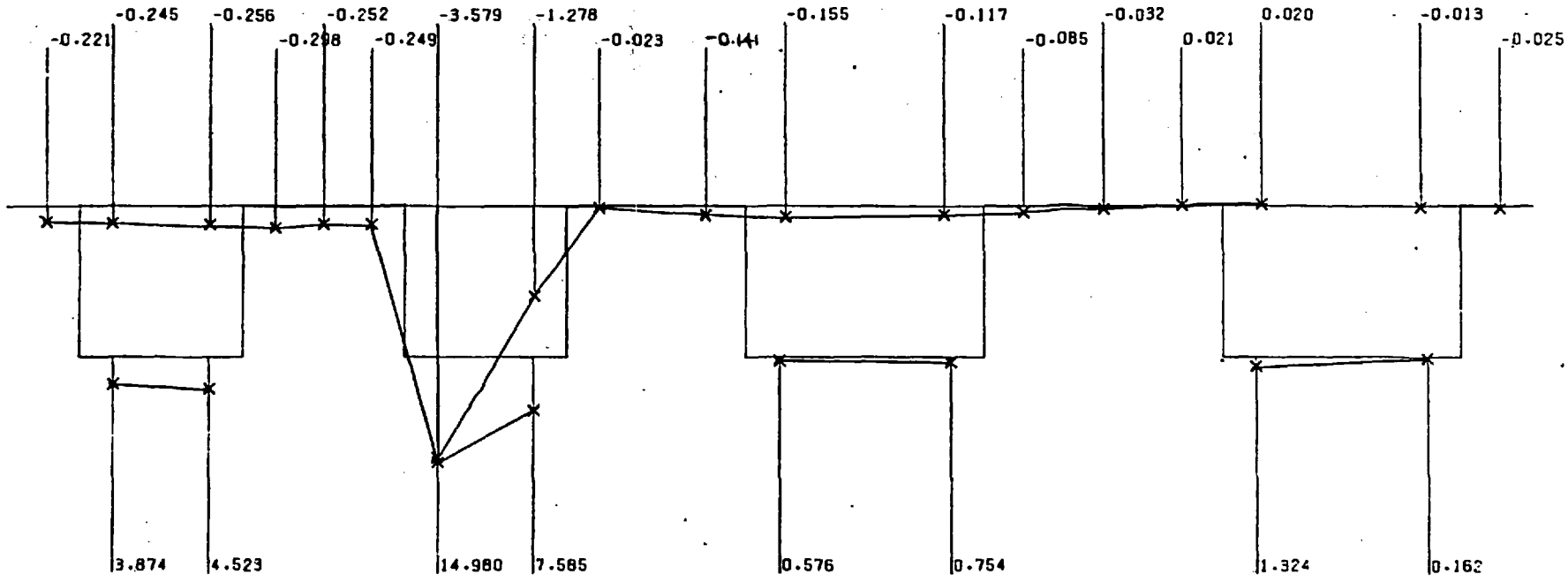


FIG267

LOAD CASE 84 SECTION 6-6 SECONDARY STRESS GAUGES
LONGITUDINAL STRESSES AT EXTREME FIBRES

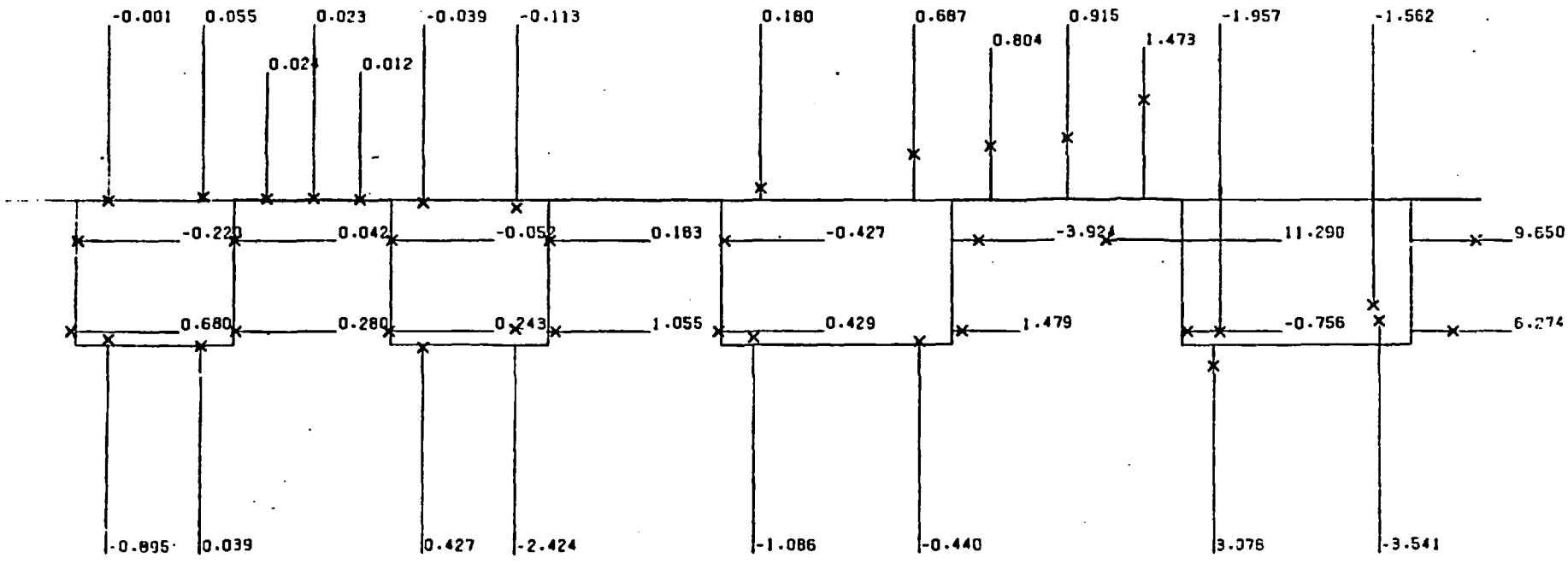


FIG268

LOAD CASE 82 SECTION 6-6 SECONDARY STRESS GAUGES
FLEXURAL COMPONENT OF TRANSVERSE STRESS

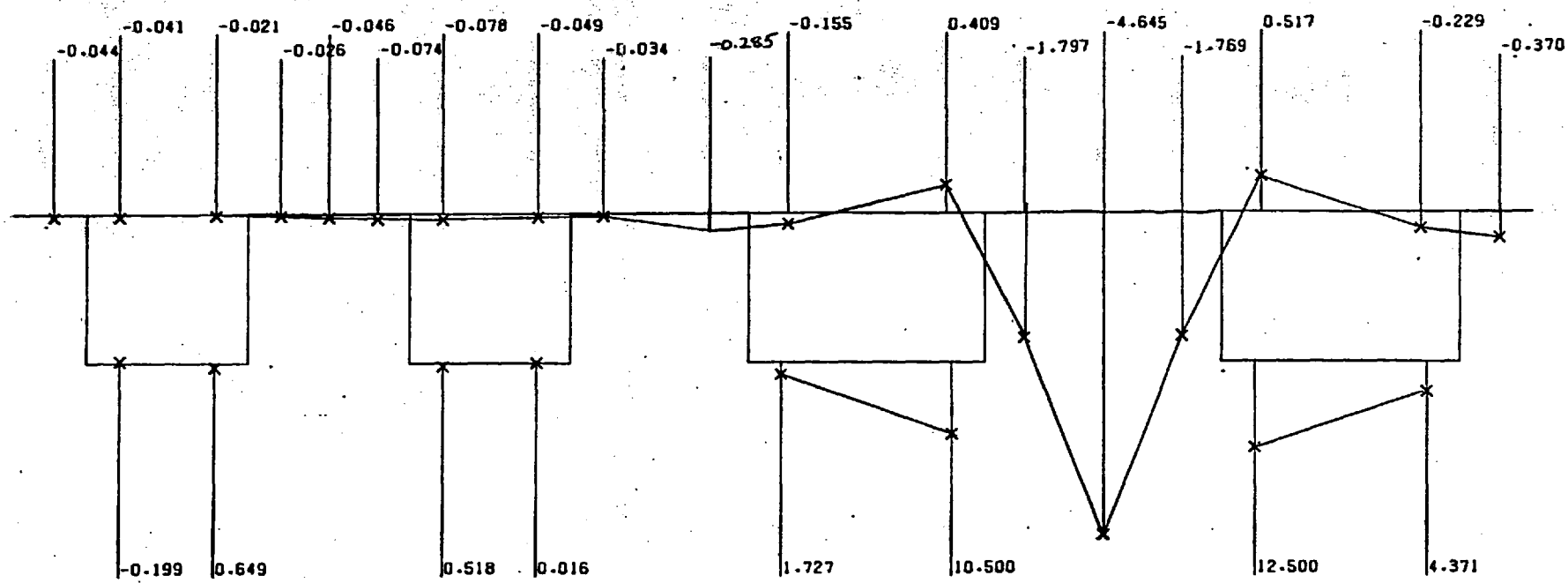


FIG269

LOAD CASE 69 SECTION 6-6 SECONDARY STRESS GAUGES
LONGITUDINAL STRESSES AT EXTREME FIBRES

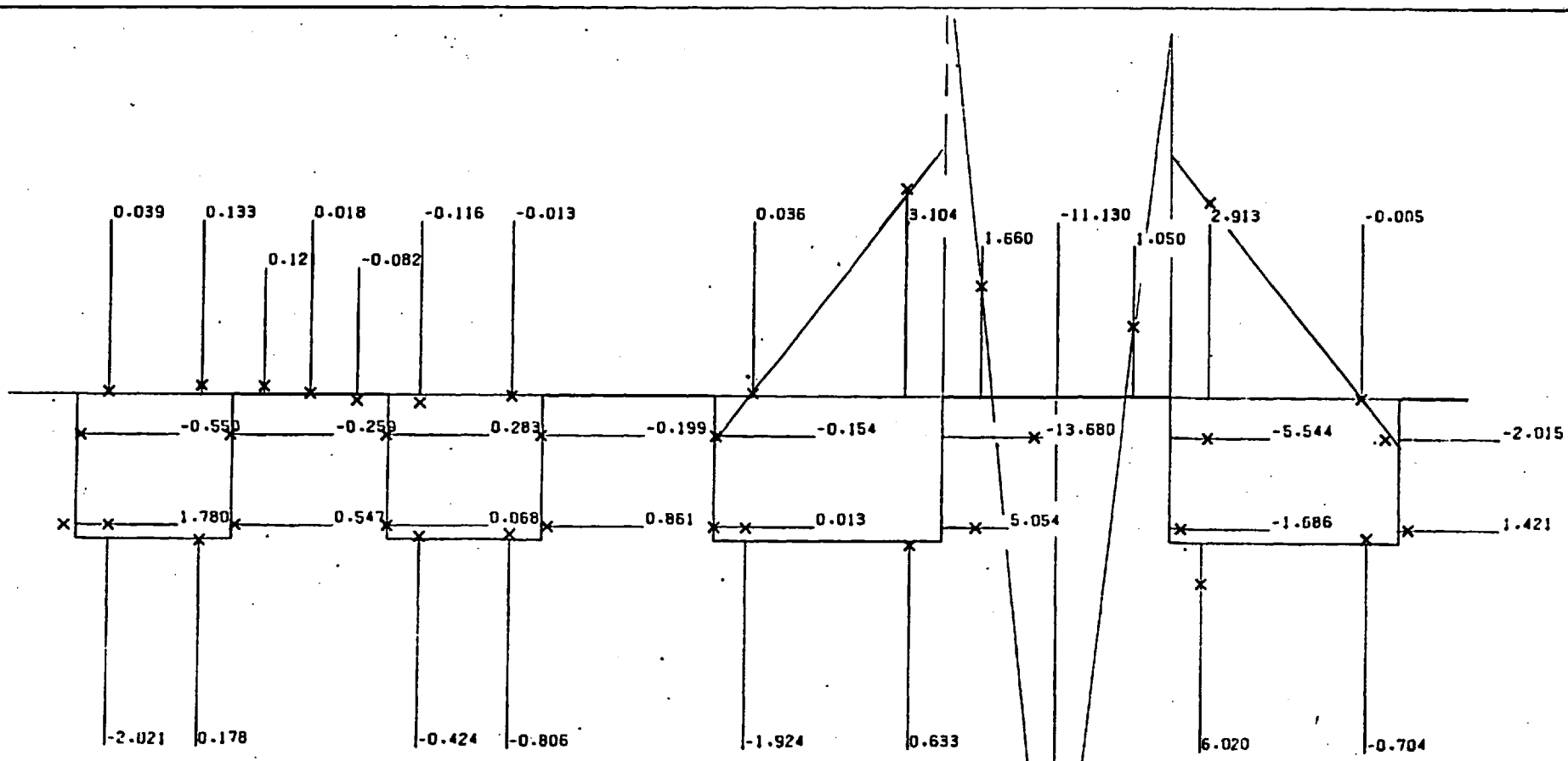


FIG270

LOAD CASE 69 SECTION 6-6 SECONDARY STRESS GAUGES
FLEXURAL COMPONENT OF TRANSVERSE STRESS

508

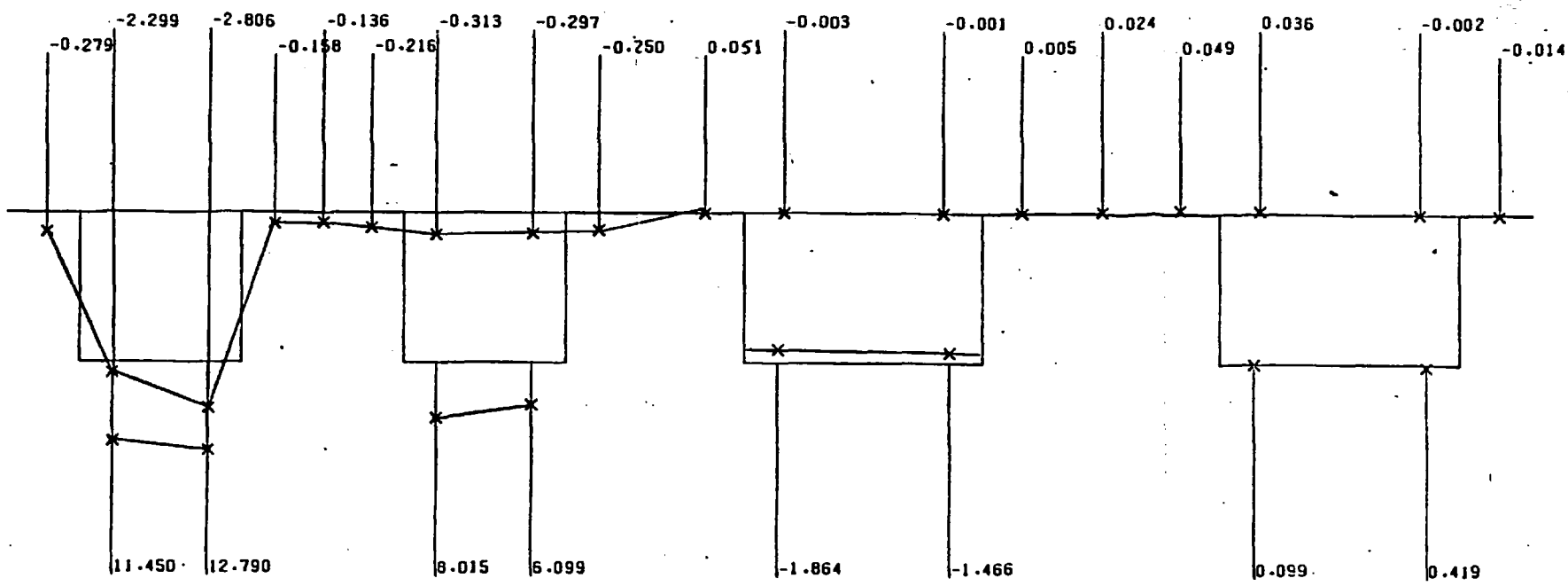


FIG271

LOAD CASE 71 SECTION 6-6 SECONDARY STRESS GAUGES
LONGITUDINAL STRESSES AT EXTREME FIBRES

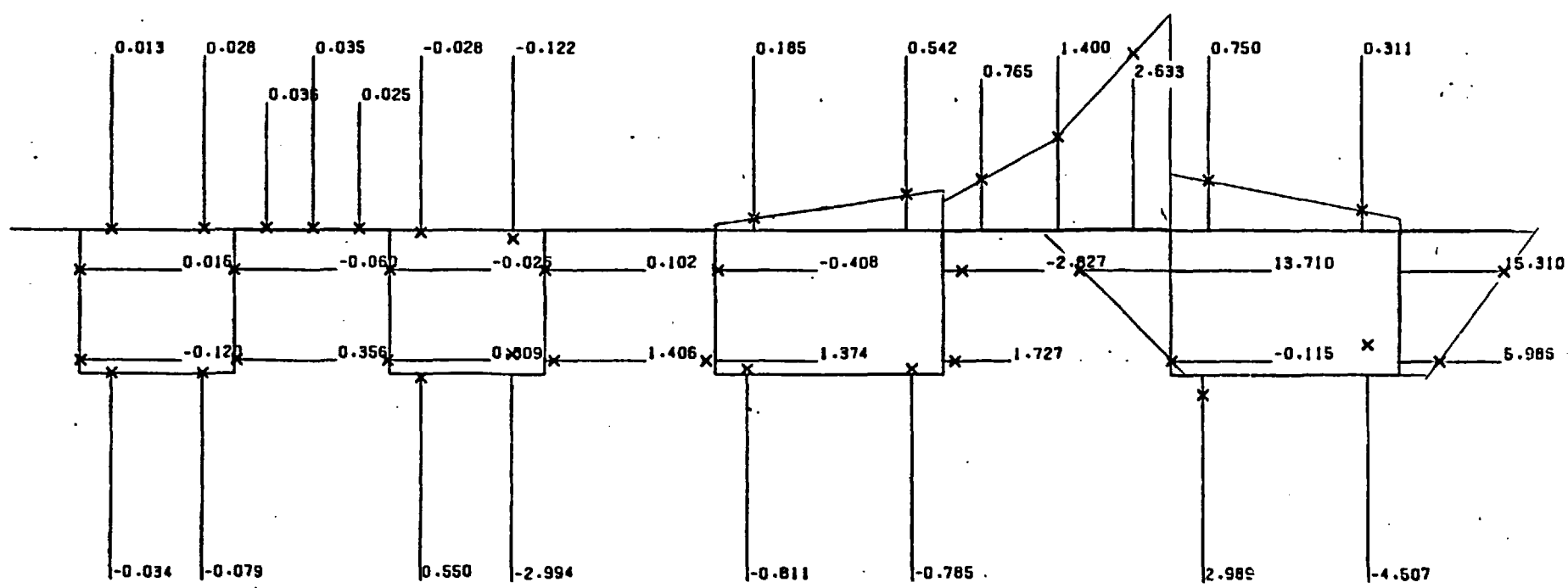


FIG272

LOAD CASE 68 SECTION 6-6 SECONDARY STRESS GAUGES
FLEXURAL COMPONENT OF TRANSVERSE STRESS

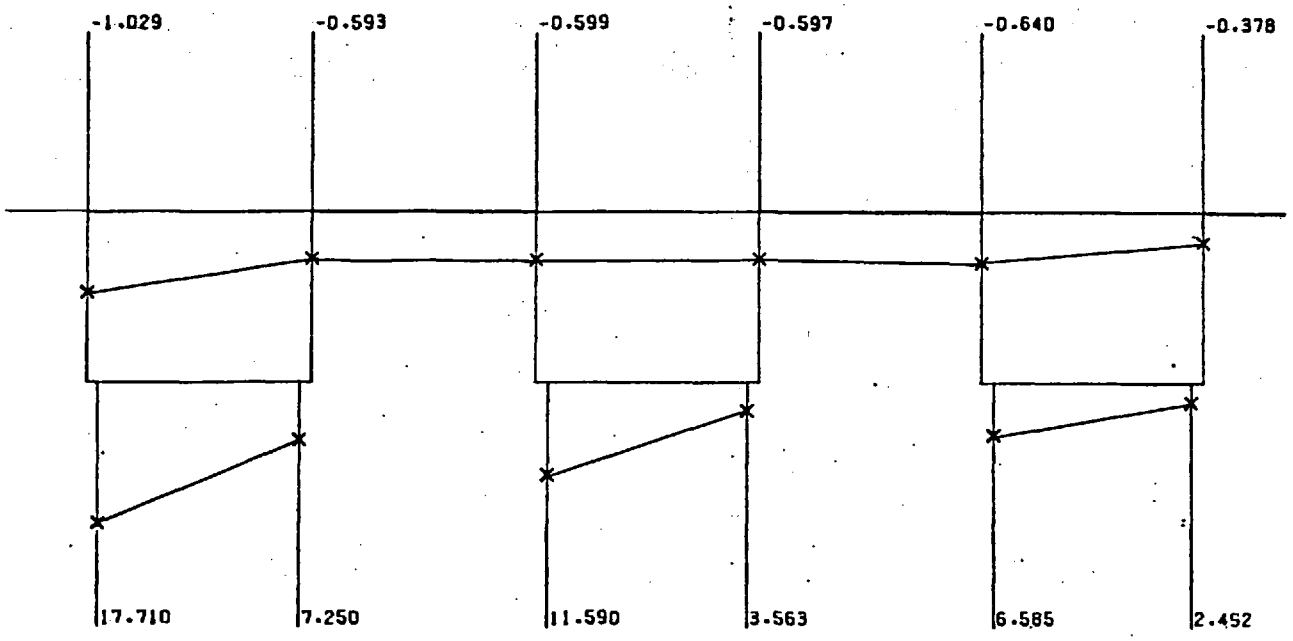


FIG273

LOAD CASE 88 SECTION 4-4 MAIN STRESS GAUGES
LONGITUDINAL STRESSES AT EXTREME FIBRES

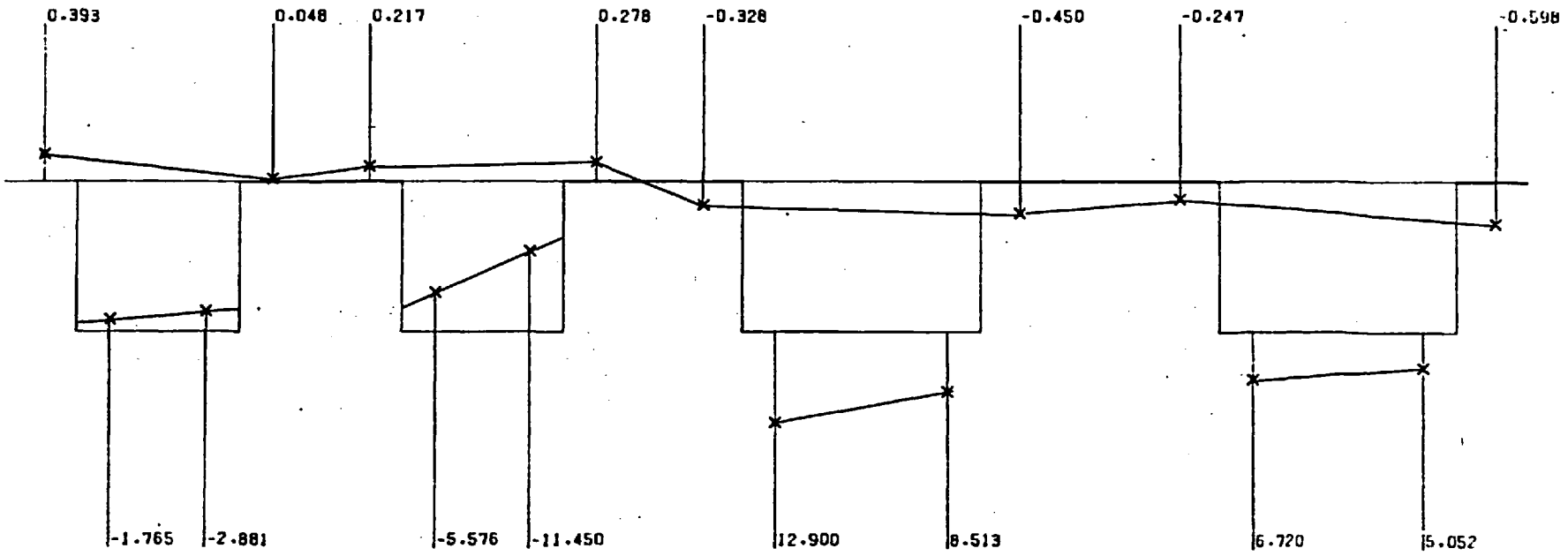


FIG274

LOAD CASE 88 SECTION 6-6 MAIN STRESS GAUGES
LONGITUDINAL STRESSES AT EXTREME FIBRES

510

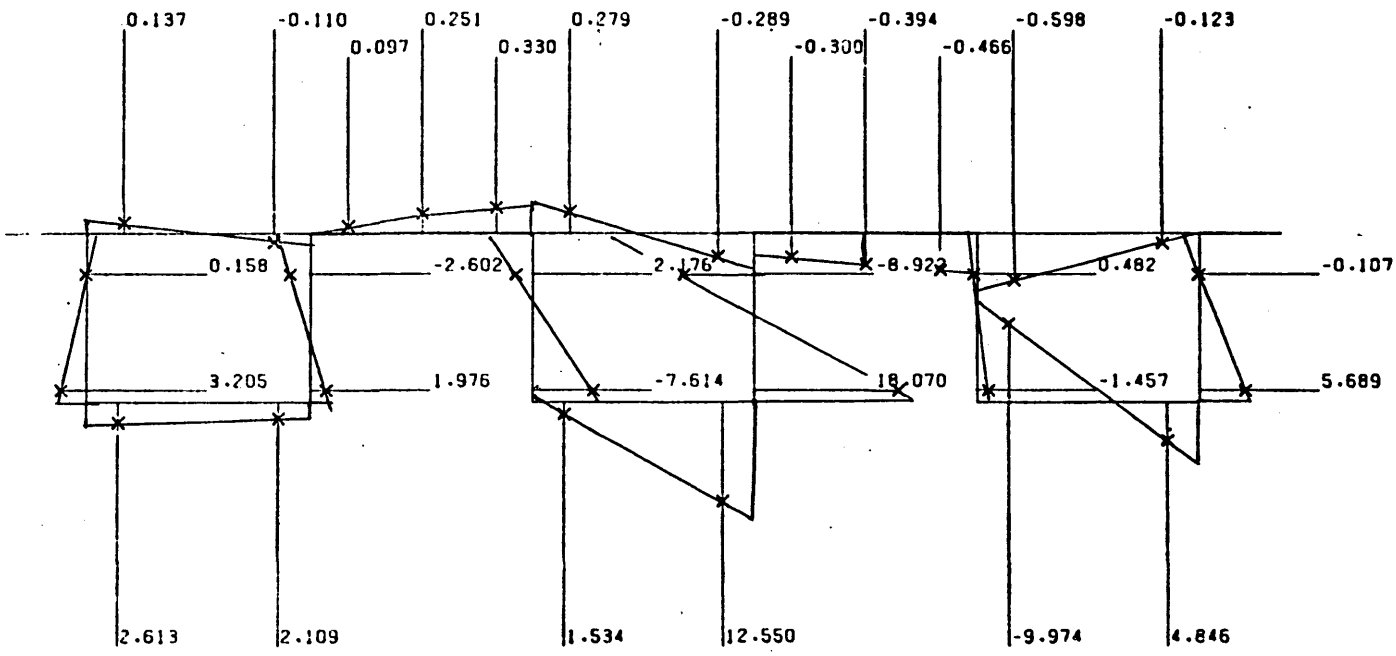


FIG**275**

LOAD CASE 88 SECTION 2-2 SECONDARY STRESS GAUGES
FLEXURAL COMPONENT OF TRANSVERSE STRESS

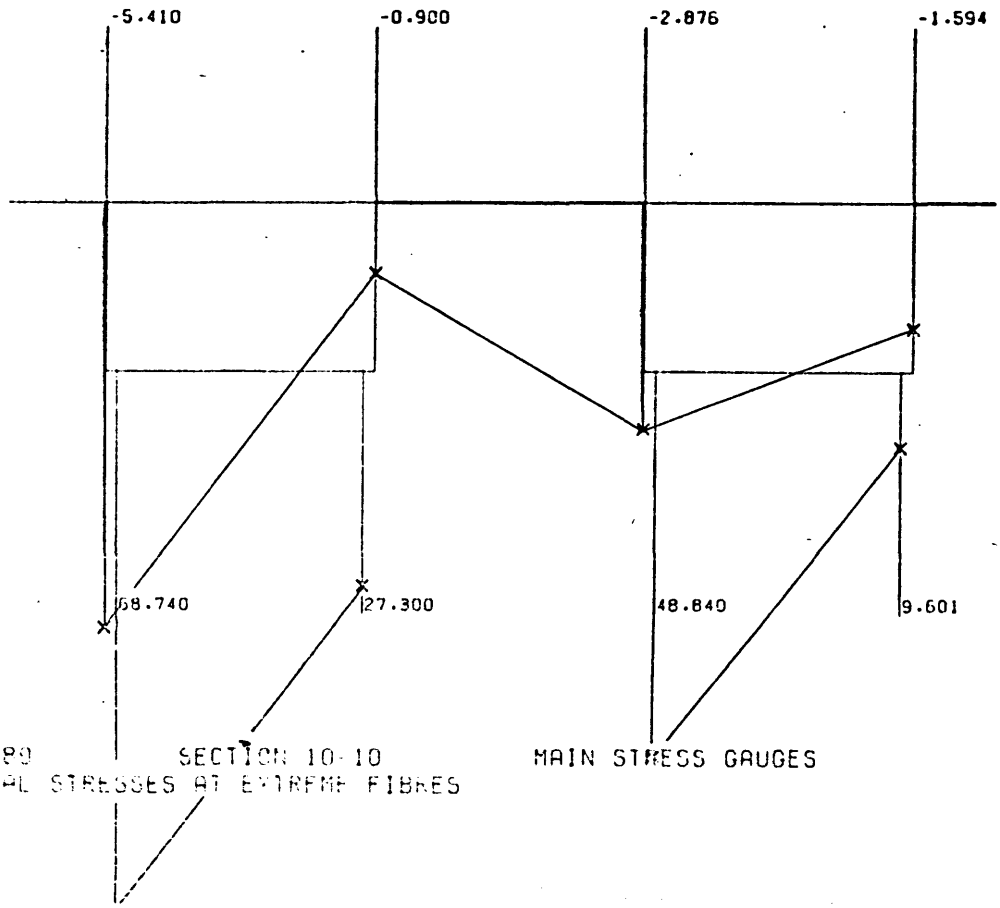


FIG**276**

LOAD CASE 89 SECTION 10-10 MAIN STRESS GAUGES
LONGITUDINAL STRESSES AT EXTREME FIBRES

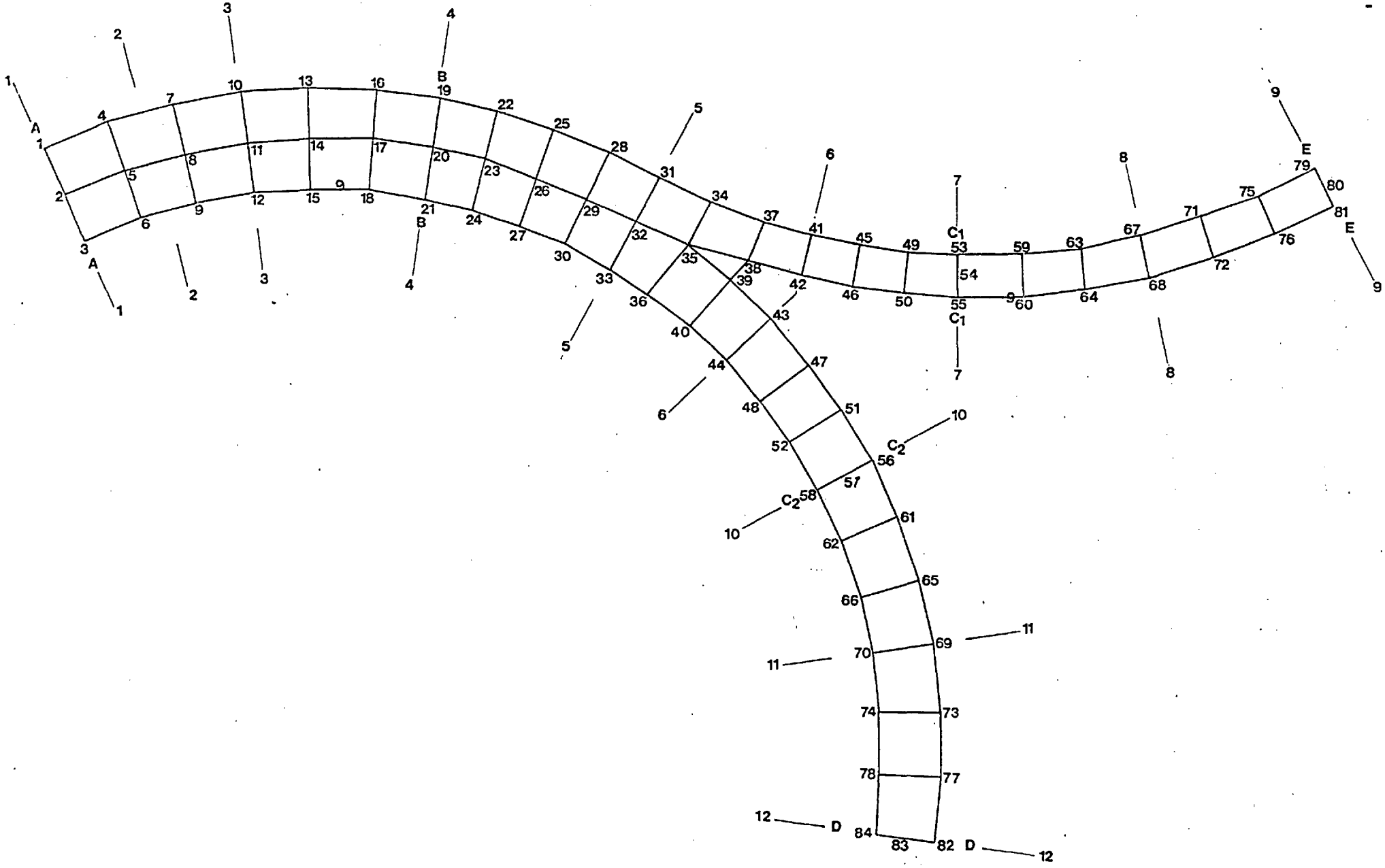


Fig.277 Model 4 Grid

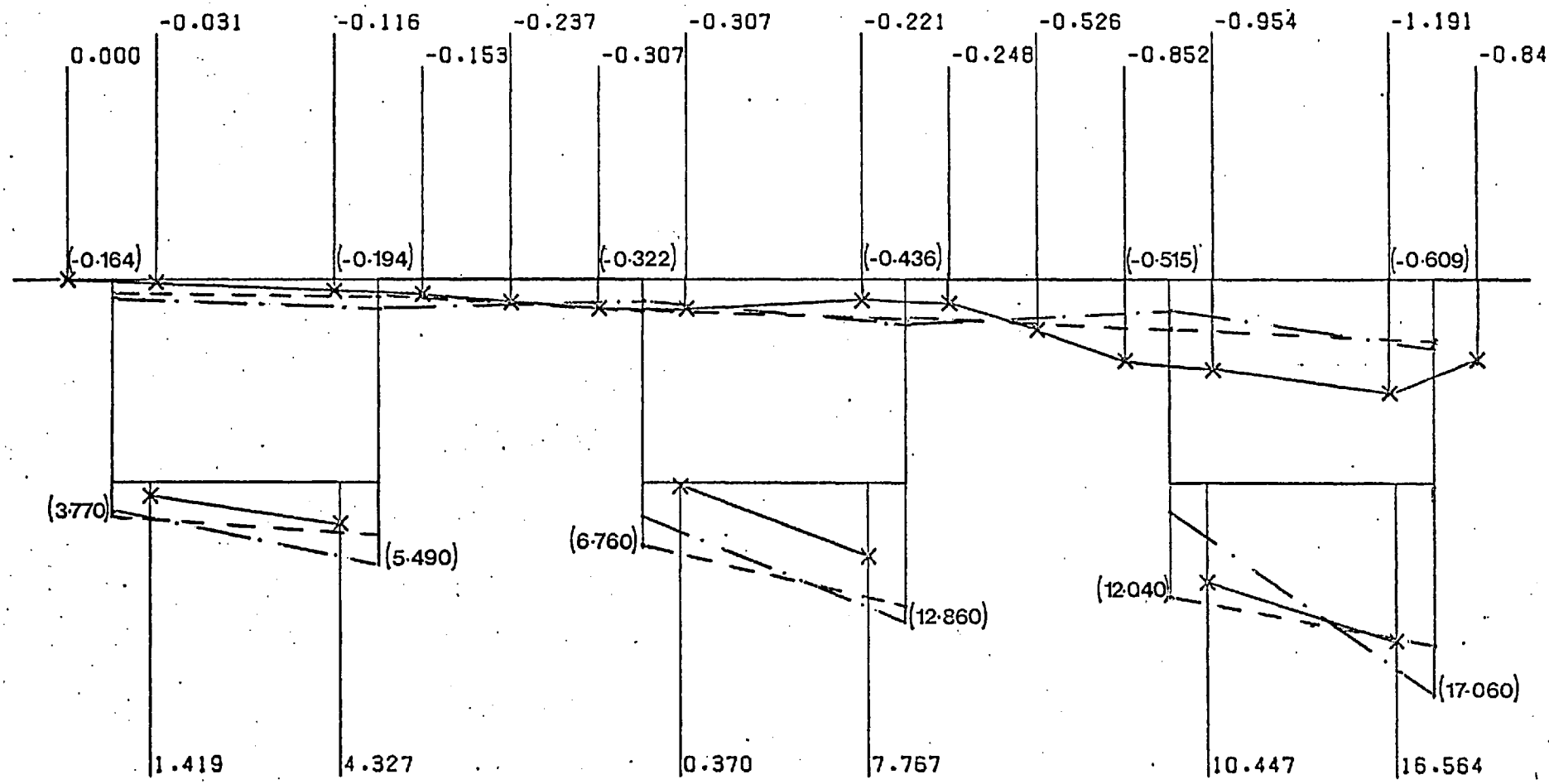


FIG 278

LOAD CASE 1 SECTION 2-2 SECONDARY STRESS GAUGES
LONGITUDINAL STRESSES AT EXTREME FIBRES

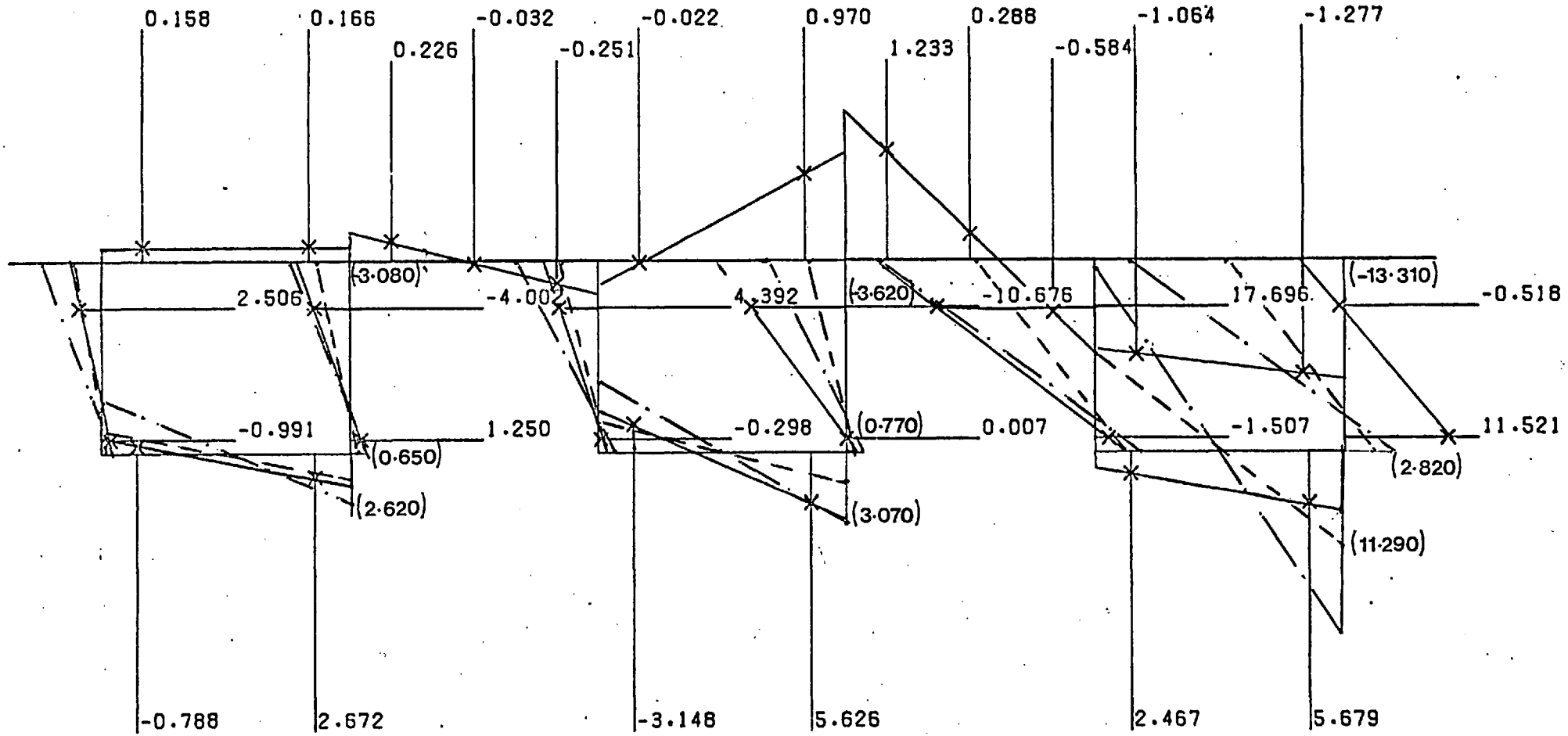


FIG 279

LOAD CASE 1 SECTION 2-2 SECONDARY STRESS GAUGES
FLEXURAL COMPONENT OF TRANSVERSE STRESS

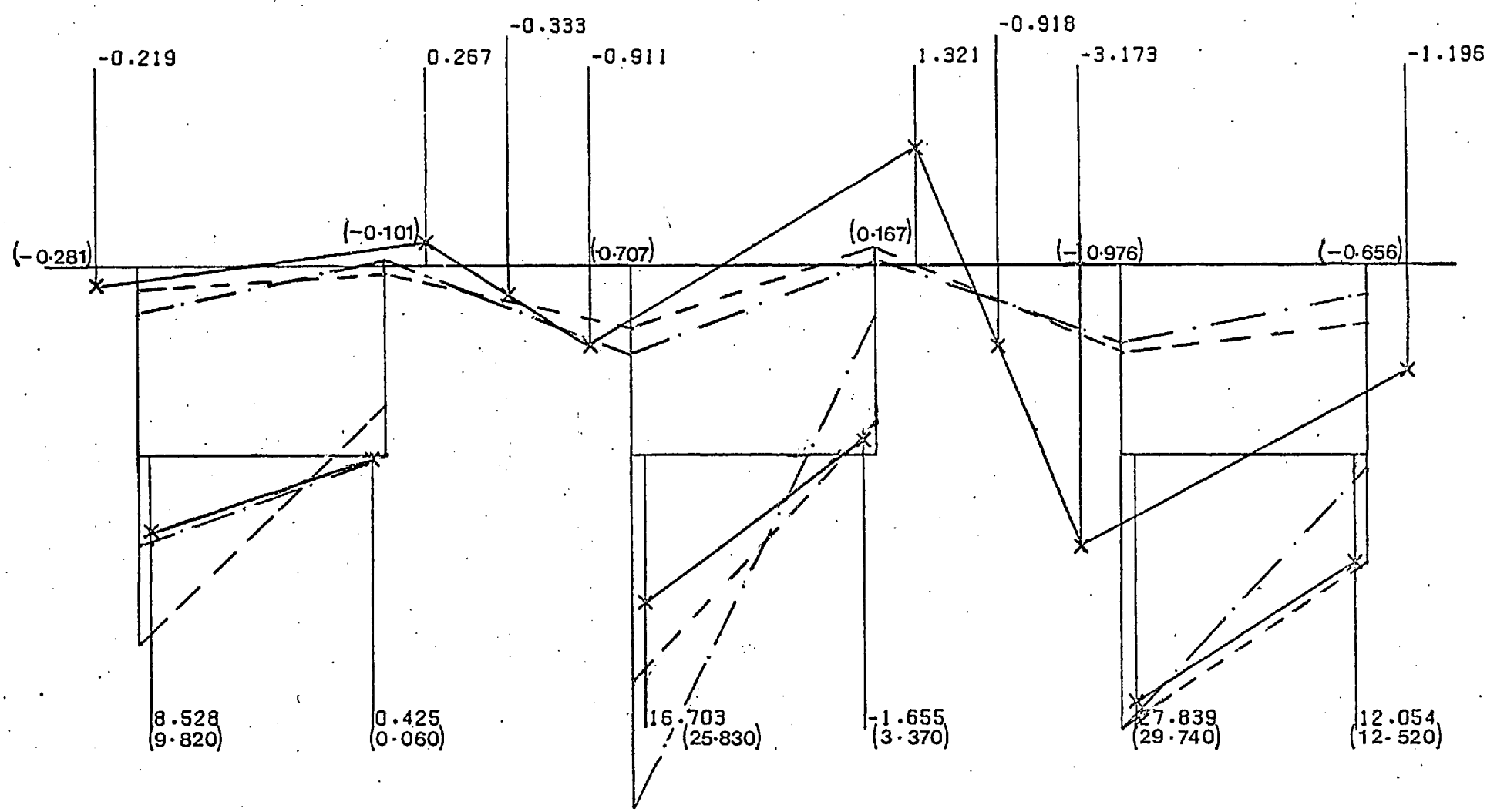


FIG 280

LOAD CASE 1 SECTION 3-3 SECONDARY STRESS GAUGES
LONGITUDINAL STRESSES AT EXTREME FIBRES

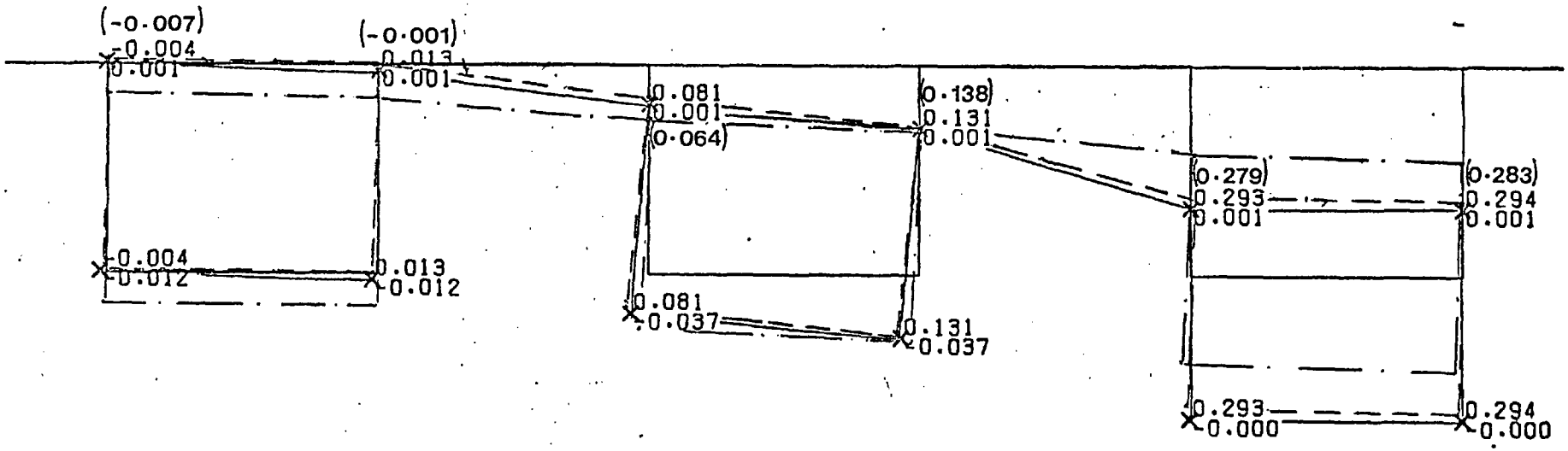


FIG.281

LOAD CASE 1
DEFLECTIONS

SECTION 3-3

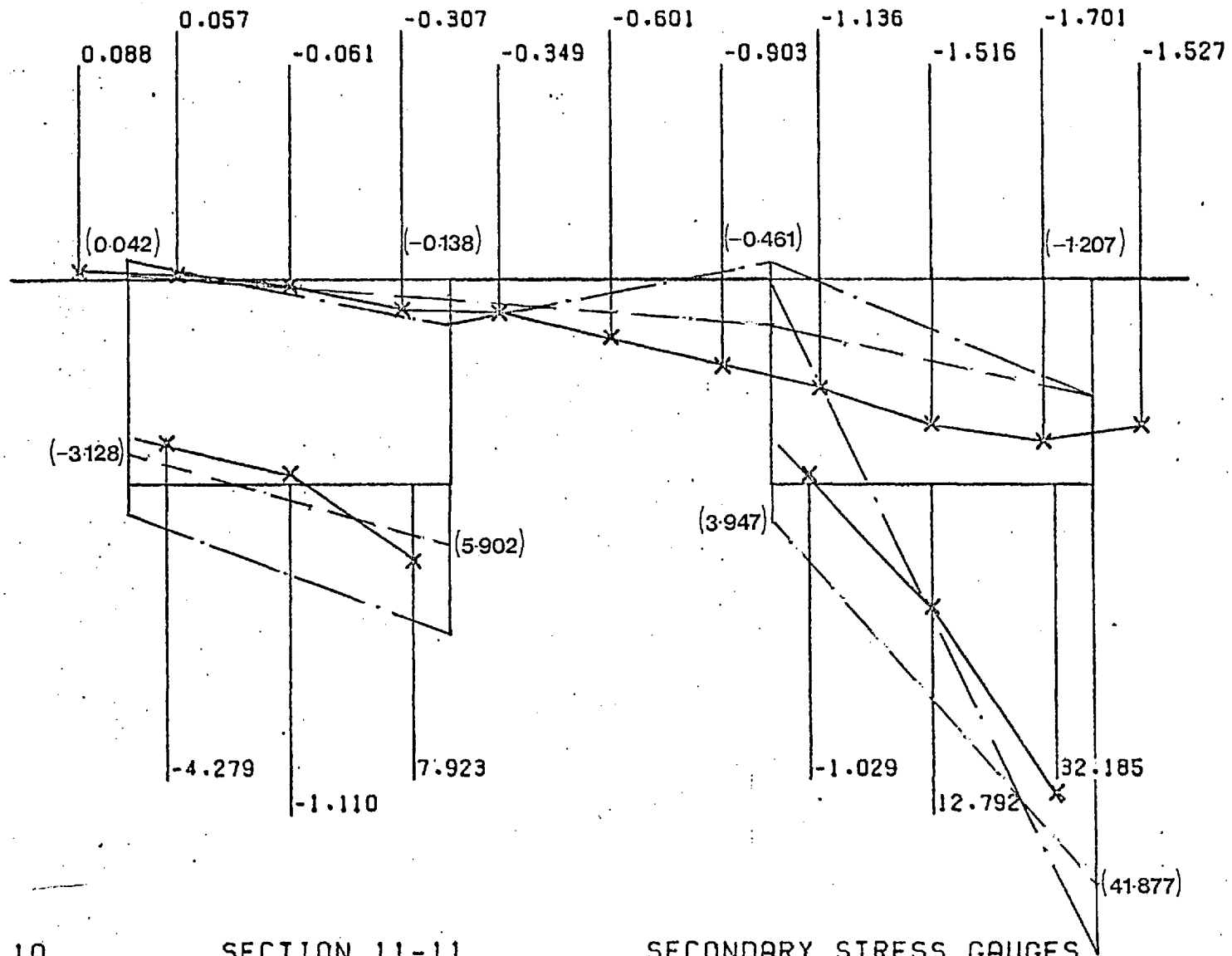


FIG 282

LOAD CASE 10 SECTION 11-11 SECONDARY STRESS GAUGES
LONGITUDINAL STRESSES AT EXTREME FIBRES

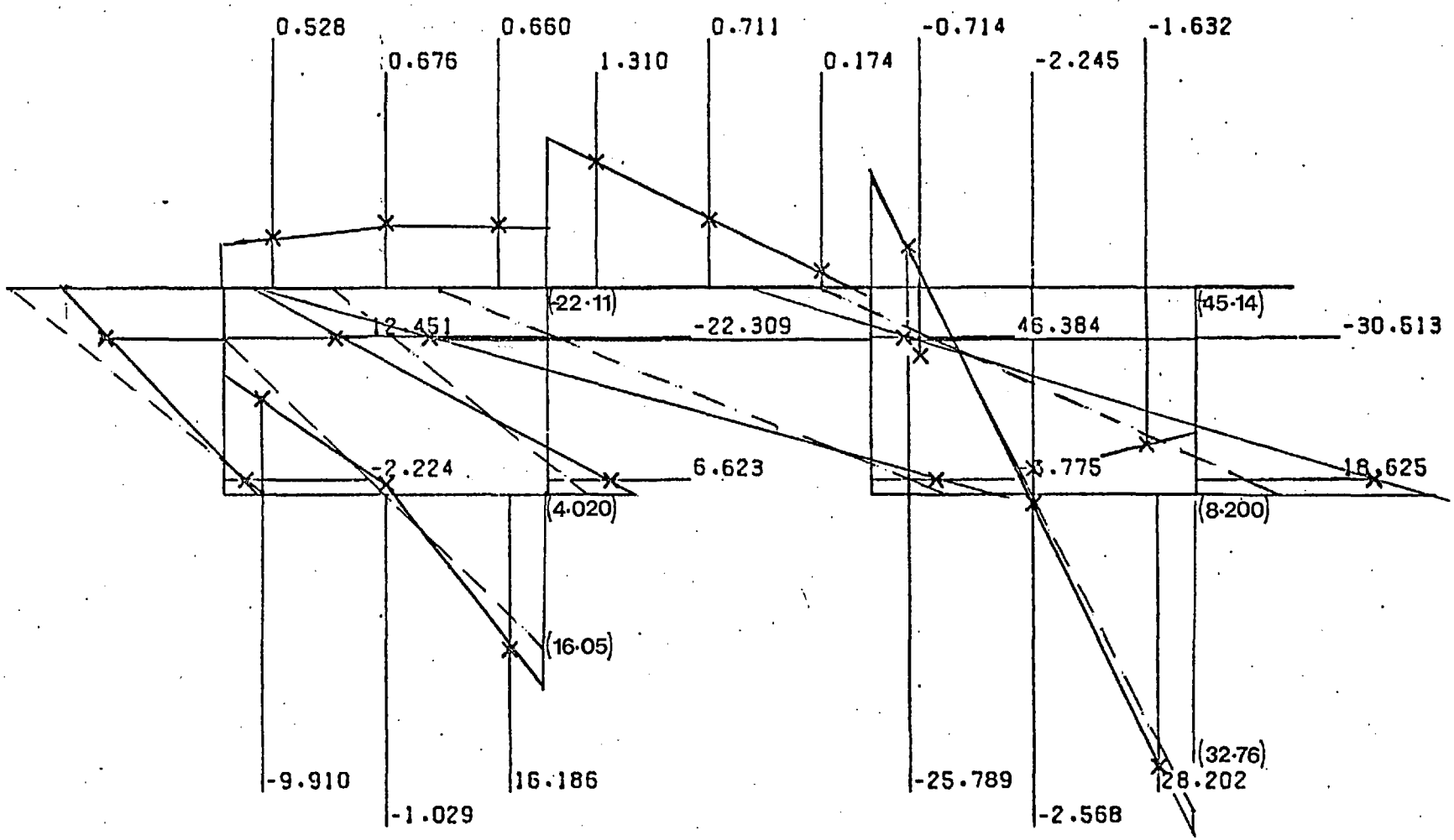


FIG 283

LOAD CASE 10 SECTION 11-11 SECONDARY STRESS GAUGES
FLEXURAL COMPONENT OF TRANSVERSE STRESS

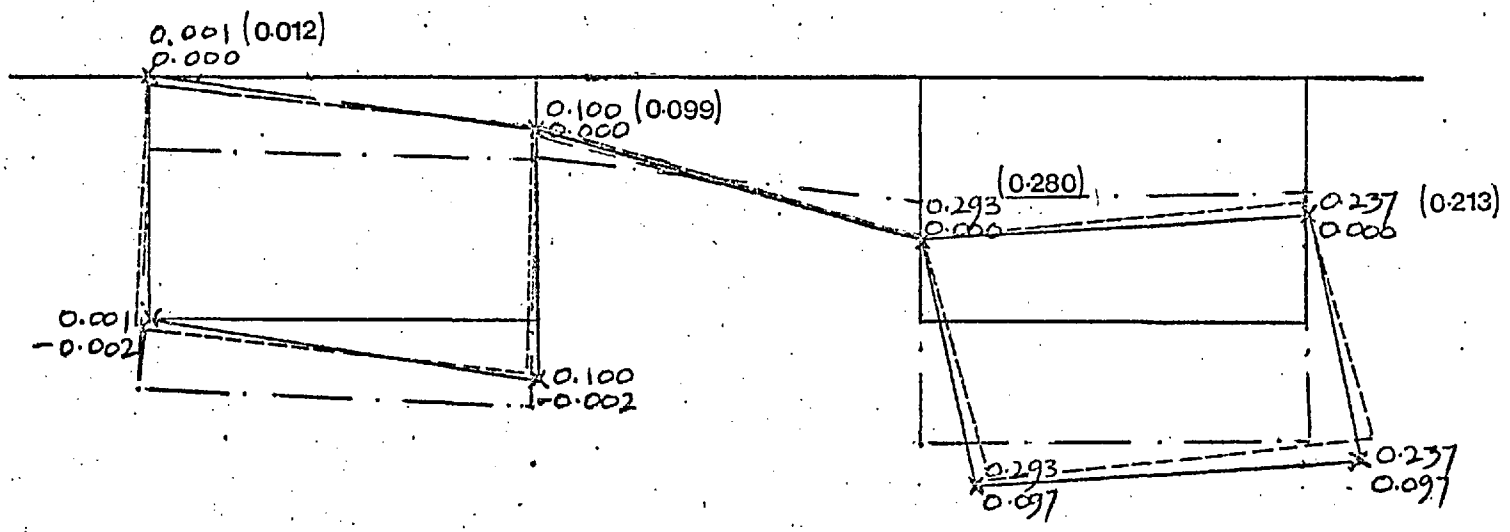


FIG 284

LOAD CASE 10
DEFLECTIONS

SECTION 11-11

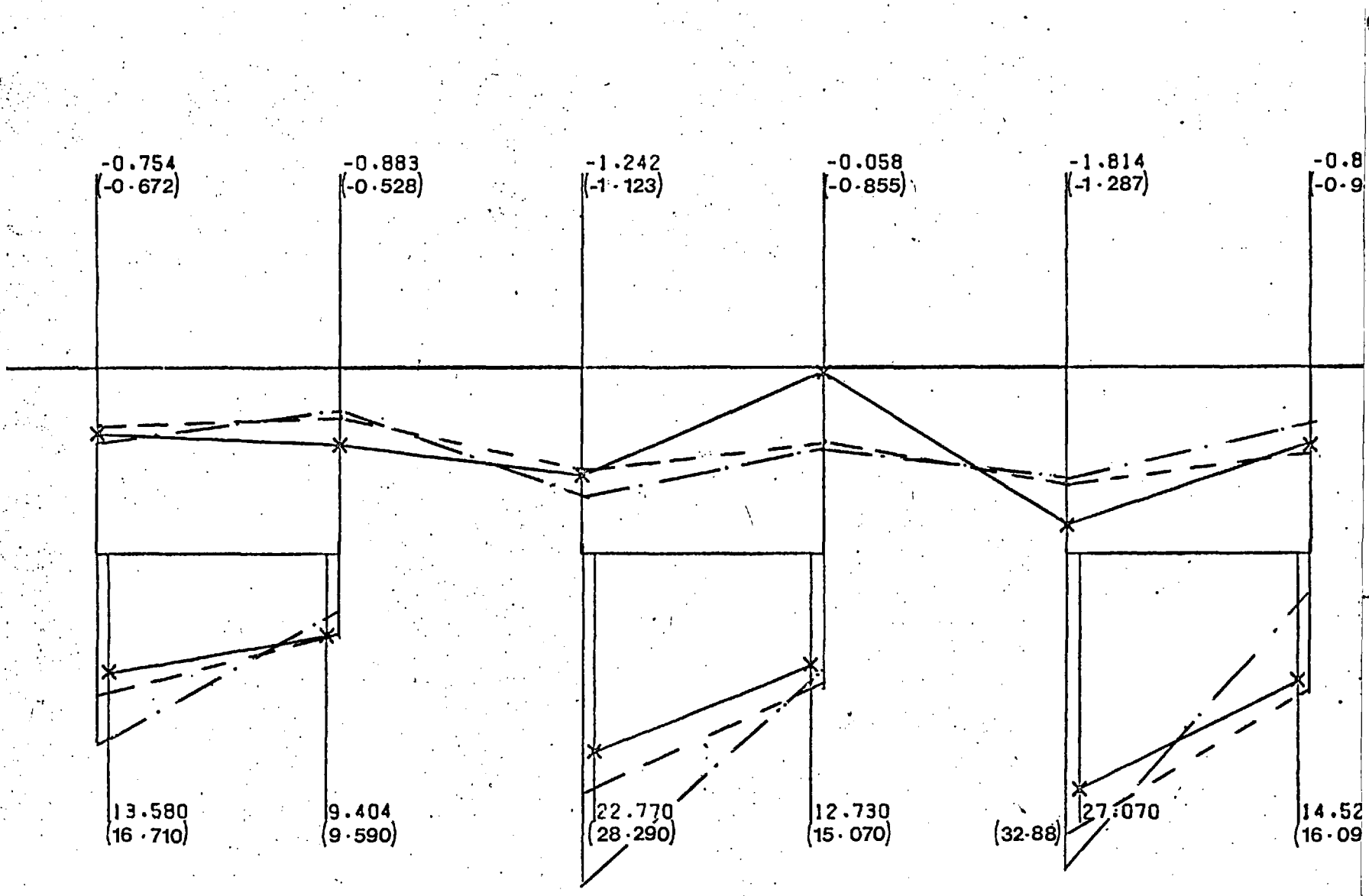


FIG 285

LOAD CASE 73 SECTION 5-5 MAIN STRESS GAUGES
LONGITUDINAL STRESSES AT EXTREME FIBRES

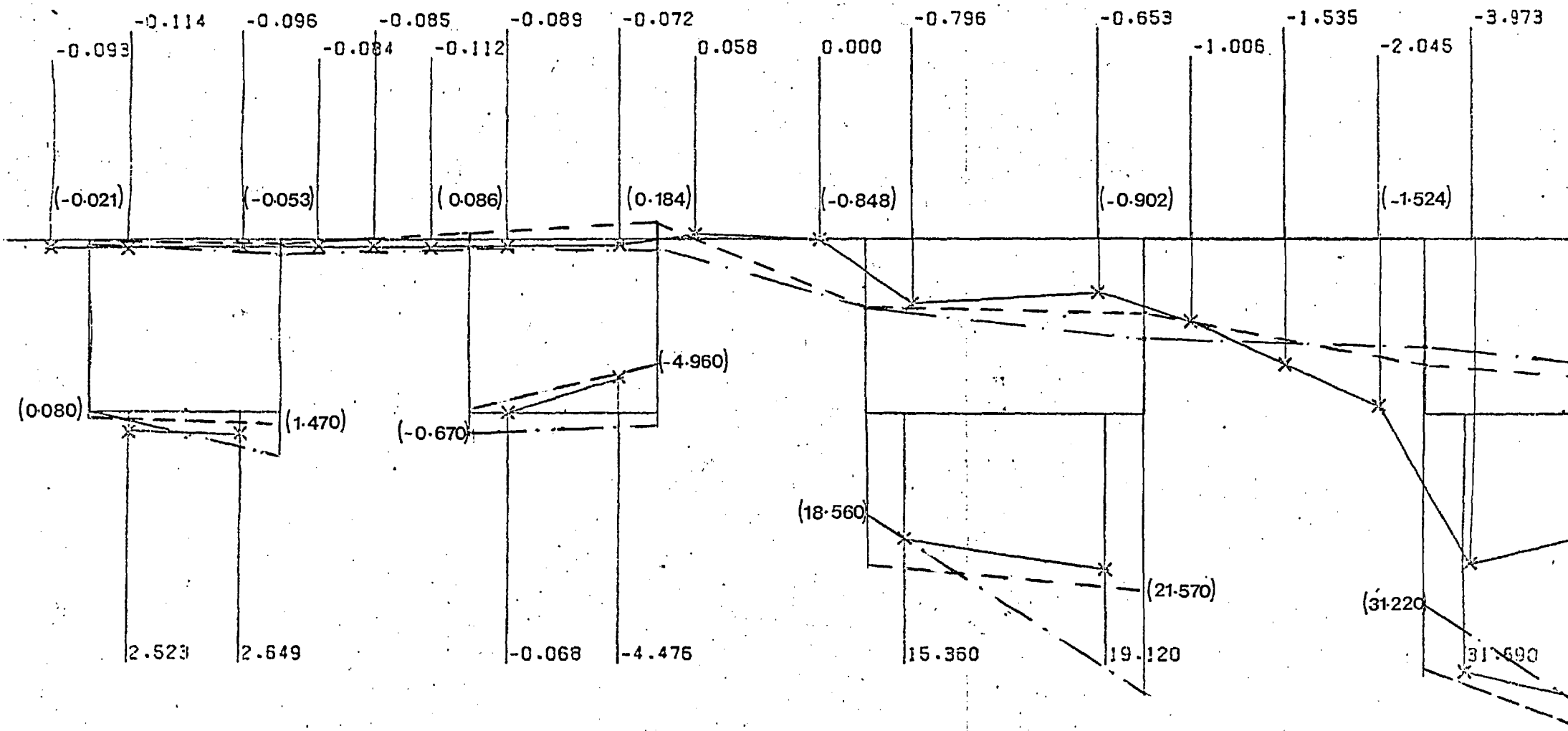


FIG 286

LOAD CASE 73 SECTION 6-6 SECONDARY STRESS GAUGES
LONGITUDINAL STRESSES AT EXTREME FIBRES

Deflection. coefficients

Model	0·408	0·516	0·726	0·984	1·584	1·782
GJ red	0·276	0·522	0·822	1·080	1·506	1·794
Full GJ	0·510	0·660	0·870	1·056	1·356	1·548

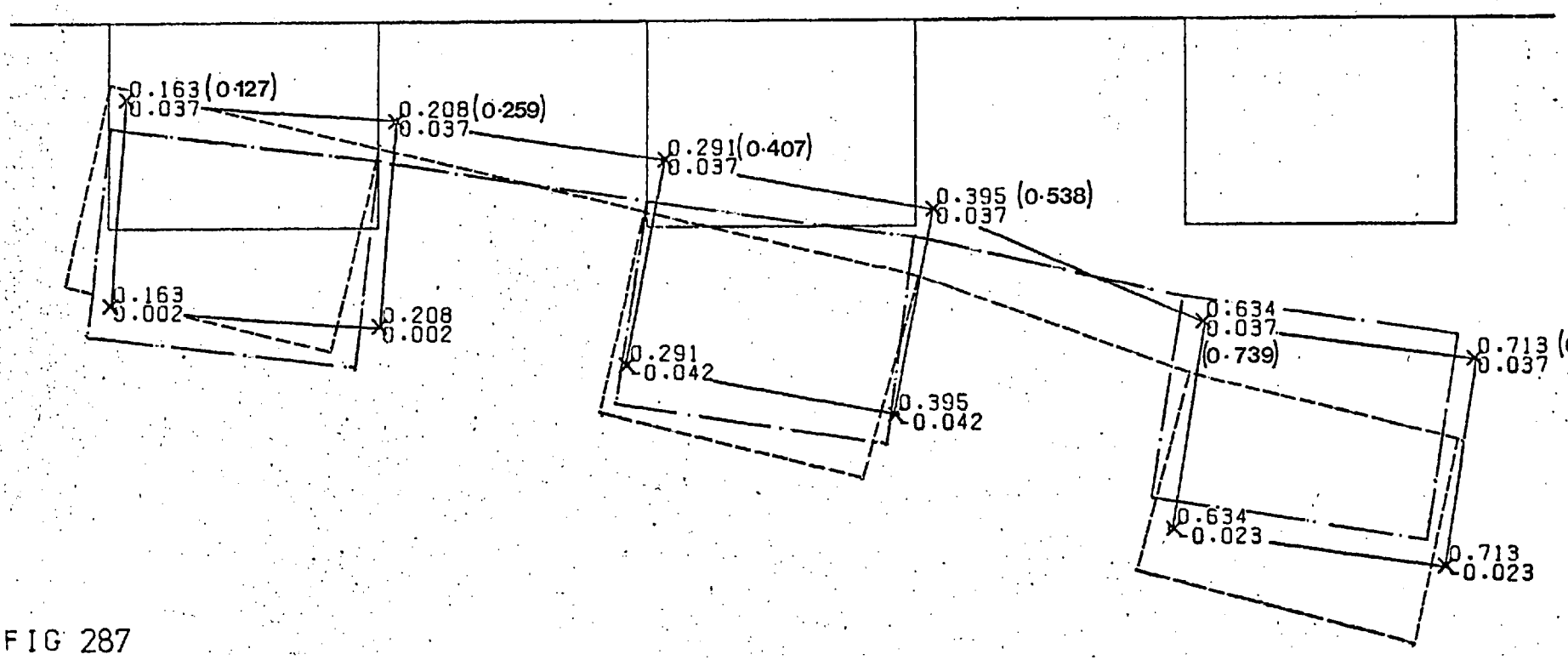


FIG 287

LOAD CASE 73 SECTION 5-5
DEFLECTIONS

	Deflection coefficients					
Model	0·352	0·445	0·560	0·568	0·788	1·040	2·001
GJ red	0·324	0·478	0·615	0·760	0·824	1·063	1·837
Full GJ	0·453	0·592	0·680	0·827	0·919	1·033	1·694

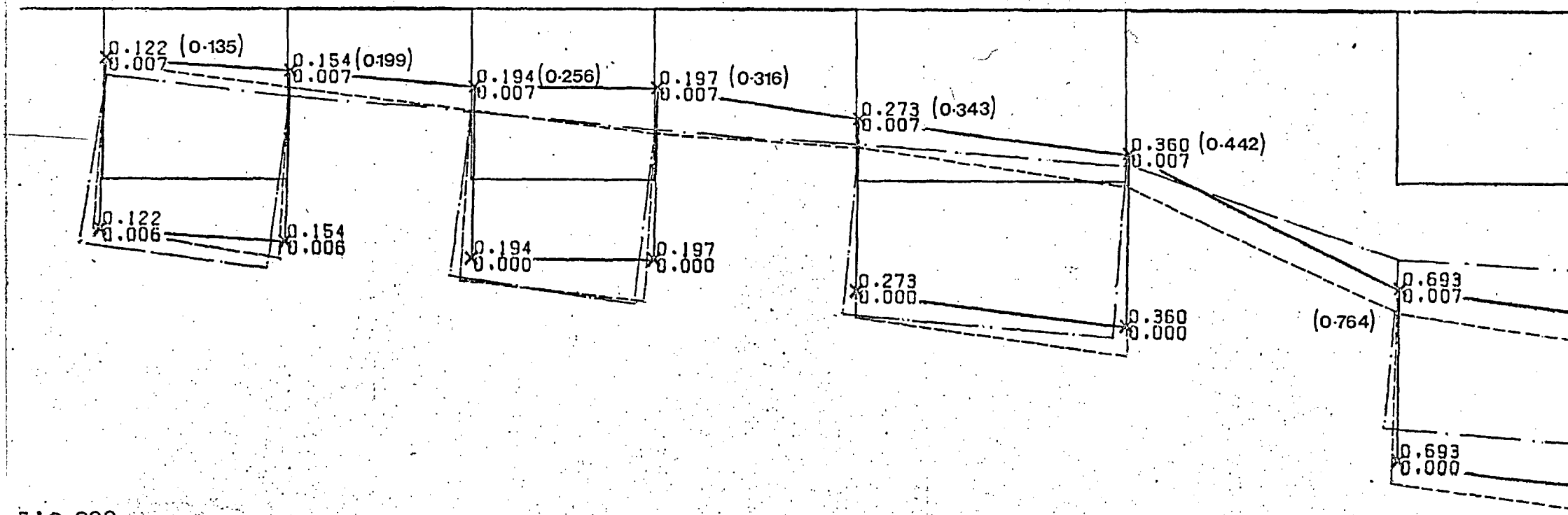


FIG 288

LOAD CASE 73
DEFLECTIONS

SECTION 6-6

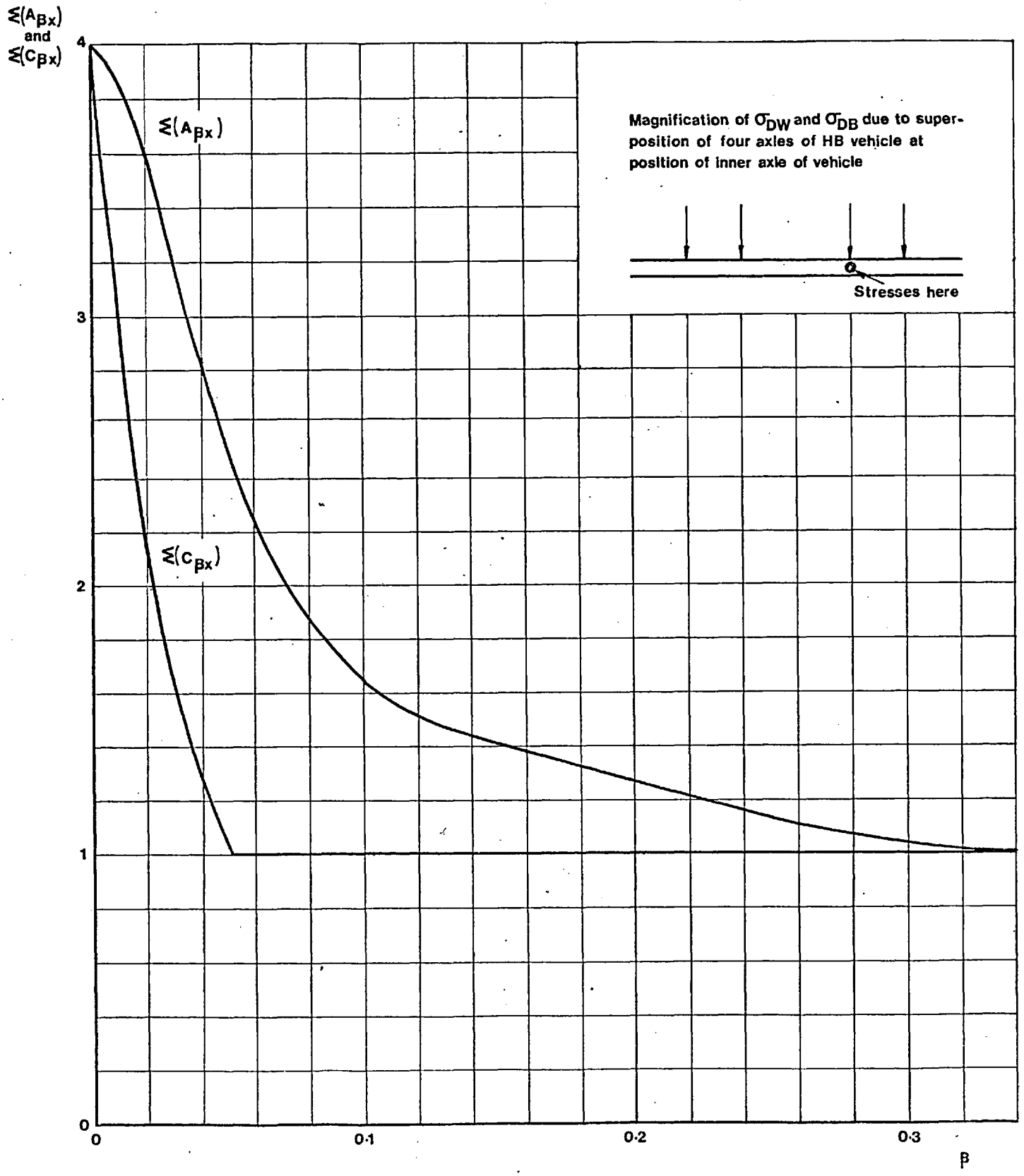

Σ(Aβx) and Σ(Cβx)
4
3
2
1
0
Σ(Aβx)
Σ(Cβx)
Magnification of σDW and σDB due to superposition of four axles of HB vehicle at position of inner axle of vehicle
Stresses here
0
0·1
0·2
0·3
β

Fig.289

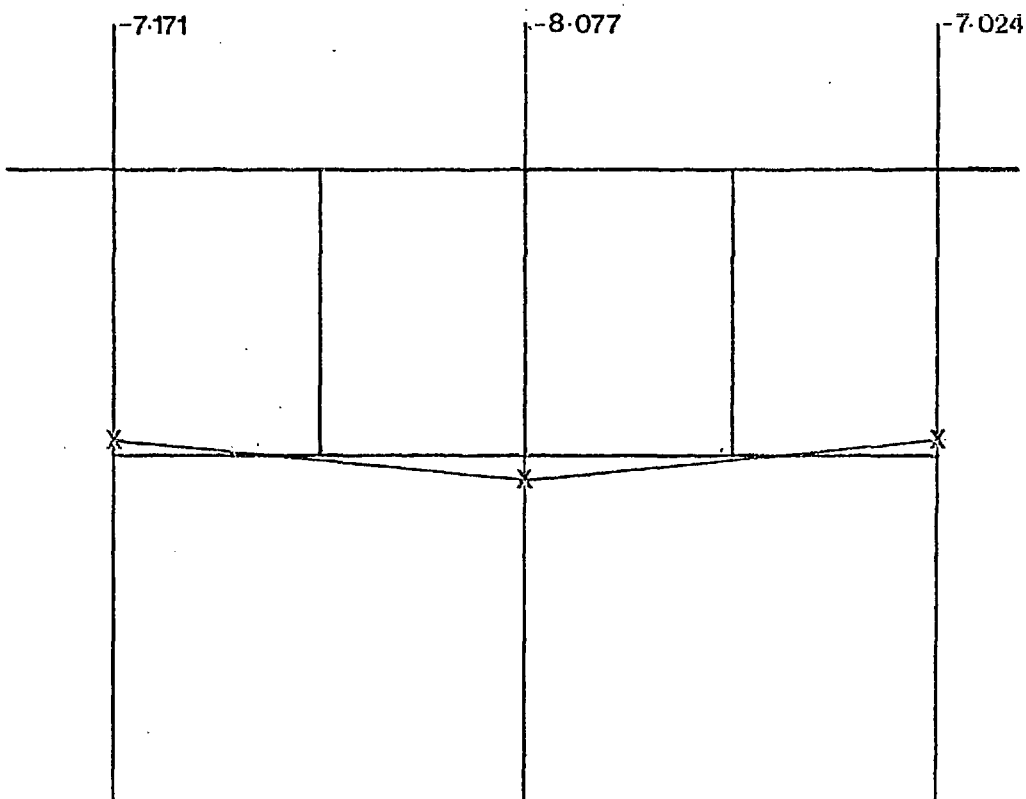


Fig.290 Bifurcated Elevated Highways Model 2 - Total longitudinal stresses at Midspan C,E given by main stress gauges

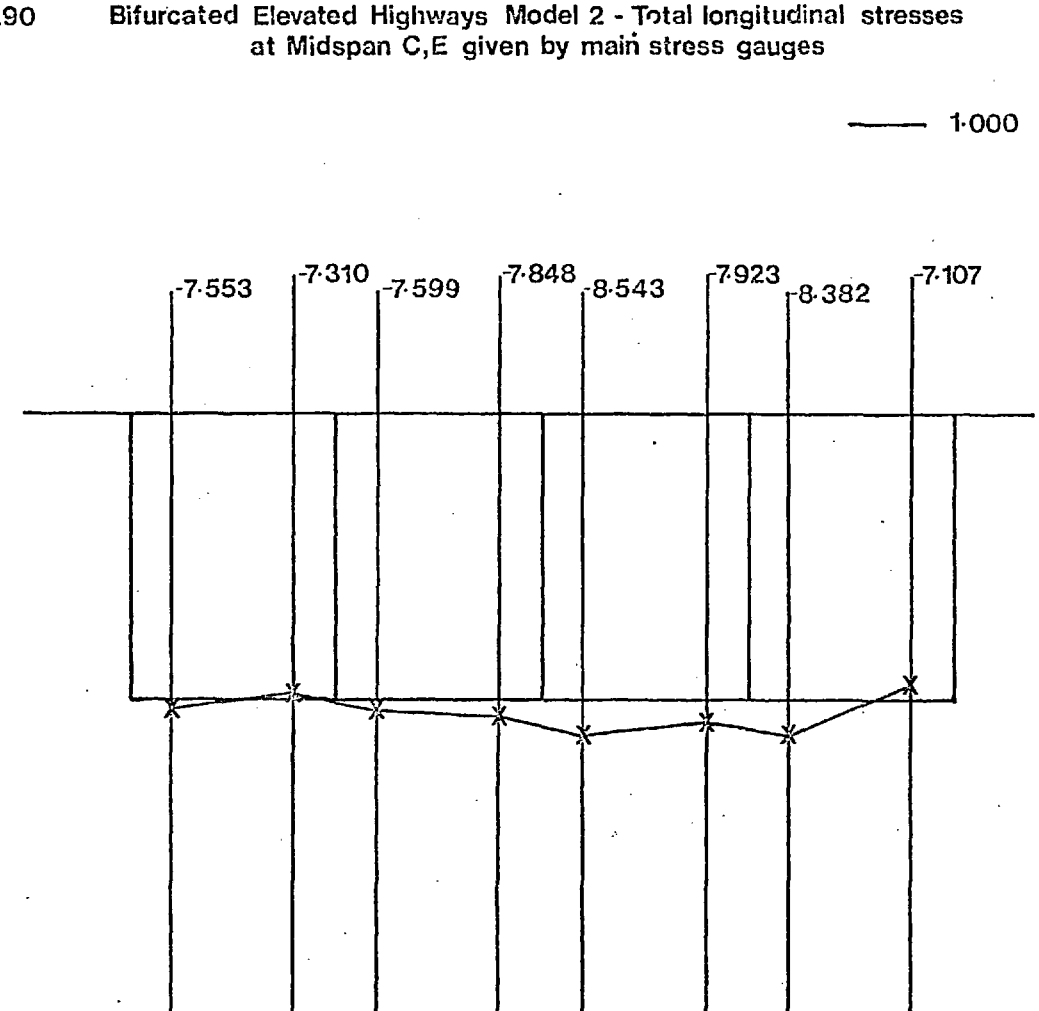


Fig.291 Total longitudinal stresses at Midspan C,E given by secondary stress gauges

NOTATION

A	enclosed area of box cross section
A_b	cross sectional area of bracing member
A_p	mid surface area of plate diaphragm
$A_{\beta x}$	coefficient from Equation D2
a	span of plate in transverse direction
b	spacing of transverse stiffeners
b_B	width of bottom flange between web centre lines
b_p	width of flange projection beyond web centre line
b_T	width of top flange between web centre lines
C_d	cross sectional warping property
C_1	coefficient from Equation 3.18
C_2	coefficient from Equation 3.18
$C_{\beta x}$	coefficient from Equation D2
c	slant height of box web between flange centre lines
D_B	transverse flexural rigidity of bottom flange
D_C	transverse flexural rigidity of web
D_T	transverse flexural rigidity of top flange
D_{YB}	as D_B
D_{YC}	as D_C
D_{YT}	as D_T
d_o	effective width of plate acting with transverse stiffener
E	Young's Modulus

E_b Young's Modulus of bracing members

F_B force in bracing member

F_D see Equation 2.3

G shear modulus

G_p plate diaphragm shear modulus

h depth of box

I_b second moment of area of beam on elastic foundations

I_c second moment of area of box cell

I_w warping second moment of area

I_x second moment of area about x axix

I_y second moment of area about y axis

I_1 second moment of area of top flange per unit length for transverse bending

I_2 second moment of area of bottom flange per unit length for transverse bending

I_3 second moment of area of web per unit length for transverse bending

J Bredt torsional constant

K distortional stiffness of box cell per unit length

K_{HB} HB summation coefficient from Figure 289

k foundation modulus of BEF

L box girder span

L_b length of bracing member

L_D diaphragm spacing

M bending moment in BEF

M_T torsional moment

M_x bending moment about x axis

m_D distortional bending moment per unit length

P antisymmetrical component of vertical loading

P_{HB} antisymmetrical component due to one axle of HB vehicle

P_{KE} antisymmetrical component due to knife edge load

P_{UDL} antisymmetrical component per unit length due to u.d.l.

P_1 antisymmetrical component of horizontal loading

P_{1B} contribution to P_1 of bottom flange radial force

P_{1T} contribution to P_1 of top flange radial force

P_{1W} contribution to P_1 of web radial forces

p applied distributed distortional load

Q diaphragm stiffness

Q_{BEF} shear force in BEF

Q_W distortional shear force

q dimensionless diaphragm stiffness

q_{BB} see Appendix B.3

q_{BC} " " "

q_{BT} " " "

q_{WB} " " "

q_{WC} " " "

q_{WT} " " "

q_W^* increase in Q_W per unit length

R BEF support reaction

R torsional stiffness reduction factor

R factor for simplification of β calculation from Figures B17-B20

R_B desired reduction factor for σ_{DW}

R_D torsional stiffness reduction factor when internal diaphragms present

R_W desired reduction factor for σ_{DW}

r radius of curvature

r_s error in σ_{DW} resulting from use of Equation 2.15

r_w ratio of warping stress at intersection of top flange and web to warping stress at intersection of bottom flange and web

r error in β resulting from use of approximate warping property $I_x/4$

S factor for simplification of β calculation

S section modulus of transverse stiffener and associated effective width of plate

S_B total radial force in bottom flange per unit length of span

S_T total radial force in top flange per unit length of span

t_B thickness of bottom flange

t_p thickness of plate diaphragm

t_T thickness of top flange

t_W thickness of web plate

U_D distortional strain energy

U_{DB} distortional bending strain energy

U_{DW} distortional warping strain energy

U_T torsional strain energy

U_1 contribution to U_D from top flange

U_2 contribution to U_D from bottom flange

U_3 contribution to U_D from web

u warping displacement

V redundant shear force at centre of bottom flange

V_D as V

v displacement along tangent to the section

W distortional deflection

x distance in spanwise direction

y perpendicular distance from neutral axis

y_s perpendicular distance from shear centre to centroid of top flange

$\bar{y}$ perpendicular distance from neutral axis to centroid of top flange

$\bar{y}_B$ perpendicular distance from neutral axis to centroid of bottom flange

$\bar{y}_T$ as $\bar{y}$

α ratio D_{YB}/D_{YT}

α_1 warping parameter

α_2 warping parameter

α_3 warping parameter

β distortional parameter (see Equation 2.14)

γ ratio b_B/b_T

δ_B change in length of diagonal for unit antisymmetrical loading

δ_D vertical distortional deflection at top of web

δ_G vertical rotational deflection from grillage analysis

δ_{HB} horizontal deflection at bottom of web

δ_T vertical torsional deflection at top of web

δ_{VB} vertical deflection at bottom of web

δ_b as δ_B

δ_1 vertical distortional deflection at top of web for unit antisymmetrical loading

ε strain

ε_x strain in x direction

ε_y strain in y direction

θ inclination of box web to vertical

θ_D equivalent distortional rotation

θ_G grillage rotation

θ_T torsional rotation

θ_1 angle between diagonal strain gauge element and direction of σ_1

λ ratio c/b_T

μ 10^{-6}

ν Poisson's ratio

ν ratio D_{YC}/D_{YT}

σ direct stress

σ_B longitudinal bending stress

σ_{DB} transverse distortional bending stress

σ_{DW} distortional warping stress

σ_L total longitudinal stress

σ_R radial component of longitudinal bending stress

σ_{RWB} radial stress at bottom of web

σ_{RWT} radial stress at top of web

σ_{TW} torsional warping stress

σ_W total warping stress

σ_x direct stress in x direction

σ_y direct stress in y direction

σ_1 maximum principal stress

σ_2 minimum principal stress

τ shear stress

τ_D shear stress in diaphragm

τ_{12} maximum shear stress

ψ_B displacement coefficient for bottom flange

ψ_C displacement coefficient for web

ψ_T displacement coefficient for top flange

ψ_b as ψ_B

Ω_d warping parameter